**Characterization and Mitigation of Crud at Pressurized Water Reactor Conditions**

by

Ittinop Dumnernchanvanit

B.S., Nuclear Science and Engineering
University of Illinois, Urbana Champaign, 2005

Submitted to the Department of Nuclear Science and Engineering
in partial fulfillment of the requirements for the degree of

Doctor of Philosophy in Nuclear Science and Engineering

at the

Massachusetts Institute of Technology

June 2017



Author .....
Department of Nuclear Science and Engineering
May 25, 2017

Certified by .....
Michael P. Short
Assistant Professor, Nuclear Science and Engineering
Thesis Supervisor

Certified by .....
Lin-wen Hu
Principal Research Scientist, Nuclear Reactor Laboratory
Thesis Reader

Accepted by .....
Ju Li
Batelle Energy Alliance Professor of Nuclear Science and Engineering
Professor of Materials Science and Engineering
Chair, Department Committee on Graduate Students

# Characterization and Mitigation of Crud at Pressurized Water Reactor Conditions

by

Ittinop Dumnernchanvanit

Submitted to the Department of Nuclear Science and Engineering
on May 25, 2017, in partial fulfillment of the
requirements for the degree of
Doctor of Philosophy in Nuclear Science and Engineering

## Abstract

The nuclear industry is no exception when it comes to those affected by fouling deposit problems. Fouling deposits on fuel rods in nuclear reactors, known as crud, can cause a variety of undesirable effects including axial power shifts, accelerated corrosion, increased primary circuit radiation dose, and possible fuel failure. This study revisits the crud problem once again using a newly constructed Internally Heated Testloop For PWRs (IHTFP) and new analytical techniques, and attempt to find a way to prevent or mitigate crud, or at least better understand it. This is the first time that fuel-rod coatings are examined as a way of countering crud growth. These coatings are chosen based on their surface chemical properties and robustness at PWR conditions. For the goal of gaining a better understanding of crud, this study is the first to apply fractal analysis to characterize crud. To achieve both of these goals, the IHTFP was built to obtain crud grown under the PWR thermal-hydraulic and chemical conditions. The crud-resistant coatings experiments show significantly reduced crud surface coverage, indicating reduced crud adhesion, for TiC and ZrN coatings. The results roughly agree with London-van der Waals theoretical force predictions, suggesting that London-VDW forces are responsible for the adhesion of crud to fuel cladding. This knowledge can be useful in designing better crud-resistant materials. The fractal analysis can provide a simple, effective way to characterize the macro-scale behavior of crud with its micro-scale properties. The fractal analysis experimental study found R2 values to be very close to one when applying the box-counting method to crud, which is one piece of evidence to support the usage of fractal analysis on crud. Moreover, a strong logarithmic relationship trend between fractal dimension and porosity was found. This relationship applies to both the IHTFP's and Westinghouse loop's crud, even though the two experimental setups used different crud precursors and heat flux. This could indicate that crud's fractal dimension is dependent only on porosity. This relationship could simplify crud modeling and lead to better predictions of crud's behaviors. Better predictions can lower margins, leading to more efficient reactors.

Thesis Supervisor: Michael P. Short
Title: Assistant Professor, Nuclear Science and Engineering

Thesis Reader: Lin-wen Hu
Title: Principal Research Scientist, Nuclear Reactor Laboratory

## Acknowledgments

I would like to extend my sincere gratitude to Professor Michael Short for his continuous support and guidance of this Ph.D project. With his patience, motivation and tremendous knowledge, we were able to undertake such ambitious project and complete it despite various technical hurdles. I was extremely lucky to be able to work, with someone as brilliant as Professor Michael Short. My admiration for him is not only confined to science but extend to the way he leads our research group, kept everyone motivated, and beyond.

Also, I am very grateful for having late Professor Mujid Kazimi as my former thesis reader, who gave a lot of great insights in all the committee meetings that we have had. It was my great honor to be able to receive comments and feedbacks from someone who is at the zenith of his field like Professor Mujid Kazimi.

I am also very lucky to have Dr. Hu as my thesis committee. She shared many important advice for both my thesis and experiment.

Professor Baglietto for reviewing and advising me on the thesis writing.

I am also incredibly fortunate to have Peter Stahle helping with the construction of the loop. Without his help and kindness, all the technical hurdles would have taken far longer and the crud loop would take far longer to complete.

Prof. Ron Ballinger for a donation of many of the components for the auxiliary loop, and letting us take many pieces of equipment from his lab.

I would also like to acknowledge Dr. Thomas Mckrell for his various helping advices during the IHTFP design and construction.

During the assembly of the crud loop, it would have been taken a lot longer if it was not for the skills and expertise of Naiqi Zhang.

Alexander Delmore, Gilberto Mota, and Sean Robertson for their help with building and running the IHTFP.

Special Thanks to Dr. Koroush Shirvan for his great help with his great help using Star-CCM+ program.

Dr. Moodera, Renan for his advice regarding sputtering coating of samples

Dr. Kurt Broderick for his many advice with the biphilic coatings.

Dr. Shiahn Chen for teaching me how to use scanning electron microscopes.

Vikash Kumar for his SEM expertise.

Miaomiao for her help with MAMBA-BDM

Lastly, I would like to thank my family and friends for their support through my many years at the institute as PhD student.

# Contents

# Chapter 1

# INTRODUCTION

## 1.1 Fouling in Energy Systems

Fouling is defined as an accumulation of unwanted substances on fluid-facing surfaces. The materials which constitute fouling deposit come in various forms, including materials such as corrosion products, organic materials, and living substances. It is usually detrimental to the system in which it occurs. Fouling deposits are a ubiquitous problem affecting a wide range of industries, such as coal power plants, petroleum refineries, nuclear reactors, shipping, and many other processes utilizing heat exchanger systems.

The accumulation of fouling deposits in any system can lead to various problems. In general, fouling deposits usually cause issues with decreasing heat transfer efficiency, increasing fluid friction, and increasing corrosion under the deposit [1]. For example, in a coal-fired power plant, fouling of heat transfer surfaces by the fly ash produced during coal combustion affects its main boiler. Ashes that accumulate on a boiler's heat transfer surface lead to decreased heat transfer, and have an adverse effect on the boiler's safety and cost [2, 3]. In petroleum refining and production, fouling can increase the resistance to heat transfer and fluid flow. This results in significant energy losses and safety concerns for petroleum refineries and pipelines [4].

To compensate for the effects that accumulating fouling deposits have on any particular process, system operators need to incur extra costs for maintenance, cleaning, and mitigation of the fouling deposits. In one study, the total fouling related costs for major industrialized nations were estimated at around US$4.4 billion annually [5]. In a less conservative estimate that includes the loss of production from fouling, the total effect of fouling on the economy could be as high as 0.25% of the GDP in industrialized nations [6]. The nuclear industry is no exception when it comes to those affected by fouling deposits. This thesis will focus specifically on fouling deposits that grow in nuclear reactor cores.

Inside nuclear reactors, zirconium alloy fuel claddings within the reactor vessel house nuclear fuel, normally based on uranium, used to create the nuclear reaction. Fouling on the surface of these fuel claddings still remains one of the main challenges in achieving higher burnup and power uprates for nuclear power plants [7, 8]. In the nuclear industry, this type of fouling deposit is known as Chalk River Unidentified Deposit (crud), named after the location (The Chalk River Laboratory in Canada) where it was first recorded. If the crud problem is ignored or left untreated, it can jeopardize the integrity of nuclear fuel rods [7]. A more detailed look at what fouling deposits in general and crud in particular are, and their effects on the systems on which they accumulate will be presented below.

### 1.1.1 What are Fouling Deposits?

Fouling is the accumulation of undesirable substances on top of fluid-facing surfaces. Examples of fouling include deposits in heat exchanger tubing, lime scale buildup inside pipes, or even layers of mussels growing on pipes near the sea. In most cases, these deposits are detrimental to the function of the system on which they accumulate. For instance, fouling deposits on a heat exchanger will decrease heat transfer and make that heat exchanger less effective. Fouling in filters can clog the filter, rendering it unusable [9]. In addition, fouling deposits on fuel rods of a nuclear reactor are detrimental to cladding surface heat transfer, and in the case of pressurized water reactor (PWRs) they accumulate boron used to control the nuclear reaction, causing axial power shifts and accelerated corrosion. Although the term "fouling deposit" is often used to describe situations where unwanted substances accumulate, the actual underlying process that causes fouling in different systems varies considerably from system to system. The section below introduces more details on various forms of fouling.

#### 1.1.1.1 Definition and Formation Mechanisms of Fouling Deposits

"Fouling" is a word used to describe the general phenomenon of the adhesion of unwanted substances or organisms to material surfaces. Within the umbrella of fouling, there are multiple mechanisms that are very different from each other in their nature. Fouling mechanisms can be categorized into six categories: particulate fouling, corrosion fouling, crystallization fouling, reaction fouling, biological fouling, and solidification fouling. This section will briefly explain each of these mechanisms with a few illustrative, real-world fouling deposit examples. For further details on each type of fouling, please refer to the background section 2.1.

**Particulate fouling.** The most important fouling mechanism upon which this thesis is focused is particulate fouling. This is the driving mechanism behind crud formation on the fuel rods within PWRs. It occurs in any system with fluids containing colloidal particulates. In particulate fouling,

particles are transported to heat transfer surfaces by a working fluid, where they can attach themselves by mechanisms such as adsorption [10] or adhesion [11]. One example of particulate fouling is the ash fouling in coal power plants, where ashes deposit in the convection area of the boiler. This happens because the inorganic elements that are vaporized during coal combustion may recondense upon contact with lower temperature surfaces, to form a type of glue between the ash particles and heating surfaces [12, 13]. Figure 1-1 shows fouling on the superheater tubes in a coal-fired power plant. The fouling can be seen as fluffy layers on the lower part of the superheater tubes.

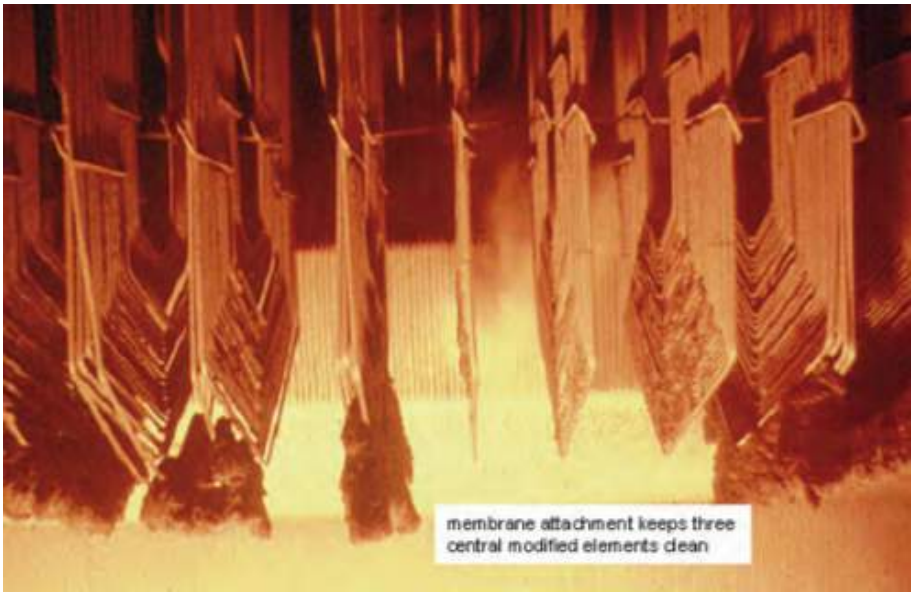


Figure 1-1: Ash fouling on superheater tubes in a coal-fired power station [14]. The fouling deposits are the fluffy layers on the bottom of the superheater tubes.

**Reaction Fouling.** Reaction fouling is caused by a chemical reaction inside the fluid stream within the system. Reactions between soluble precursors in the stream can turn into insoluble foulants, which sometimes deposit on surfaces. Metallic heat transfer surfaces can also act as catalysts for these chemical reactions [15]. Reaction fouling commonly occurs in the oil industry, where heat exchangers used in crude oil distillation plants can be fouled with asphaltenes. Food industries such as the milk processing industry may also experience chemical reaction fouling , by either protein or calcium ion adsorption [15]. Figure 1-2 shows the asphaltenes chemical reaction fouling on the heat transfer surface of a heat exchanger in a crude oil refinery.

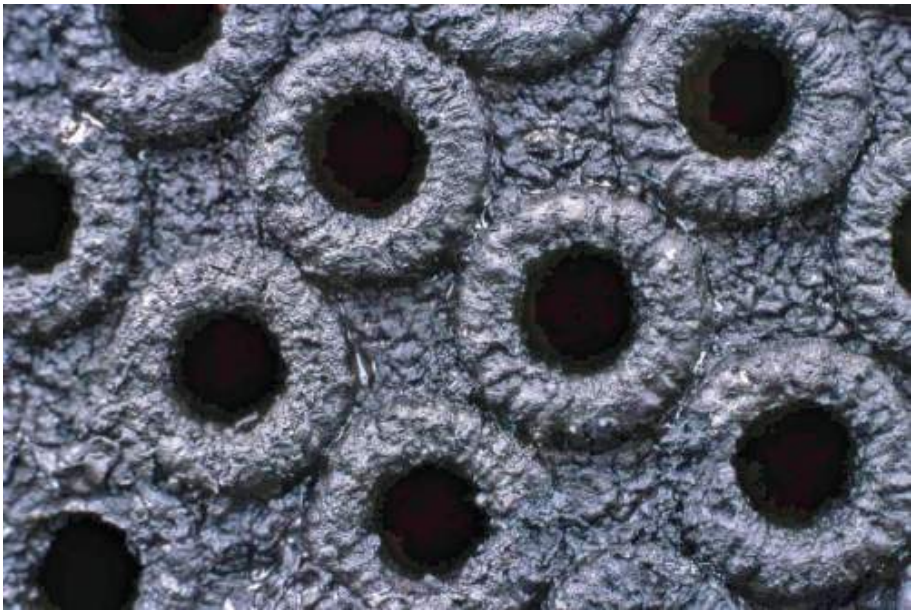

Figure 1-2: This image shows the asphaltenes fouling on the heat transfer surface of a heat exchanger in a crude oil refinery. This is a common type of chemical fouling [16].

**Corrosion Fouling** Corrosion fouling is similar to reaction fouling in that it involves chemical reactions. For reaction fouling, the reactions that produce fouling deposit precursors occur between constituents of the process fluid. On the other hand, for corrosion fouling, the reactions that produce fouling precursors occur between the process fluid and heat transfer surface [17]. When corrosion occurs on the heat transfer surface and the corrosion product is not soluble, it will accumulate on the originating heat transfer surface. One example of corrosion fouling is the reddish orange rust on carbon or low alloy steel. When steel corrodes, the iron oxide corrosion product does not form a protective layer, nor does it dissolve. Instead, the iron oxide accumulates as porous reddish corrosion fouling commonly referred to as rust [18]. Figure 1-3 shows an example of this type of corrosion fouling.

Figure 1-3: This image shows an example of corrosion fouling, in the form of red rust produced by the corrosion of low-alloy steel with surrounding water. The fouling material results from the reaction between the process fluid and heat transfer surface [16].

**Precipitation Fouling (Crystallization Fouling/Scaling)** Precipitation fouling, also known as crystallization fouling, happens when salts, oxides, or hydroxides from solution crystallize on the surfaces of fluid-facing materials. It occurs when the concentration of solutes exceeds the saturation concentration in the solvent. When this happens, solutes will start to crystallize, leading to the precipitation of solids on the fluid system surface. The reason that the concentration of solutes can exceed the saturation concentration could be driven by changes in temperature, or solvent evaporation. Particulate fouling typically occurs in liquid, soluble salt, or aqueous solutions. It could occur with both soluble salts with normal or inverse solubility [17].

Precipitation fouling is especially common in salts with inverse solubility. For salts with normal solubility, the solubility will increase with increasing temperature. On the other hand, the opposite will happen to salts with inverse solubility. In this case, the solubility of salt will decrease as the temperature rises. If a solution with inverse solubility is heated, crystalline precipitates will form and deposit on heat transfer surfaces [17]. If fouling happens from inorganic salts in water, it is called scaling. In the case that the precipitate settles because of gravity, the fouling layer is called sedimentation fouling. The most common example of precipitation fouling is the limescale deposit as shown in figure 1-4, commonly found throughout the world in residental and industrial water pipes. If a heat exchanger uses hard water, or water with a high mineral content, limescale may form as the water is heated causing the solutes with inverse solubility to precipitate. This phenomenon is shown in figure 1-4 [19, 20].

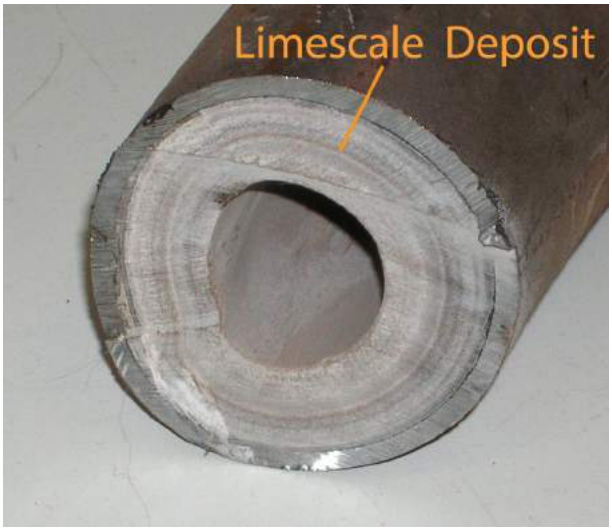


Figure 1-4: This figure shows a limescale layer in a heat exchanger pipe. Its thickness reduces the area through which the fluid can flow, and deteriorates the heat exchanging capacity of the pipe [21].

**Solidification Fouling (Freezing Fouling)** Solidification fouling or freezing fouling occurs when a component of the fluid freezes on a heat transfer surface, hence the name [9]. This solidification of fluid could lead, for example, to the separation of wax when a hydrocarbon-based process fluid comes into contact with a colder surface, fouling deposition in phenol coolers, and formation of ice layers in chilled water production. The parameters that may affect solidification fouling include temperature, mass flow rate, surface conditions, and the chemistry of the process fluid [17]. This type of fouling is very important to oil refineries and pipelines. The paraffin in crude oil can precipitate and accumulate into a fouling deposit under appropriate environmental conditions as shown in figure 1-5. These fouling buildups in oil pipelines and oil refineries can effectively choke the flow of hydrocarbon [9].

**Biofouling** When a fouling deposit is caused by biological organisms such as bacteria, algae, or barnacles and other sea creatures, it is called biofouling. Biofouling is generally controlled by the use of chemical agents such as chlorine [22, 23]. It can be separated into two types, microbial fouling, and macrobial fouling. Microbial fouling involves microorganisms such as algae, fungi, yeast, and bacteria. Macrobial fouling involves larger organisms such as barnacles, mussels, and sea vegetation [17]. Figure 1-6 shows a layer of barnacles macrobial fouling on a ship's hull. For nuclear power plants, this type of fouling often occurs in the systems that use sea water, such as the condenser in the secondary loop of boiling water reactors (BWRs) or the tertiary loop of PWRs [23].

**Composite Fouling** Lastly, in many cases, a fouling phenomenon can have multiple causes. Two or more fouling mechanisms mentioned above could be present in the same system. When this

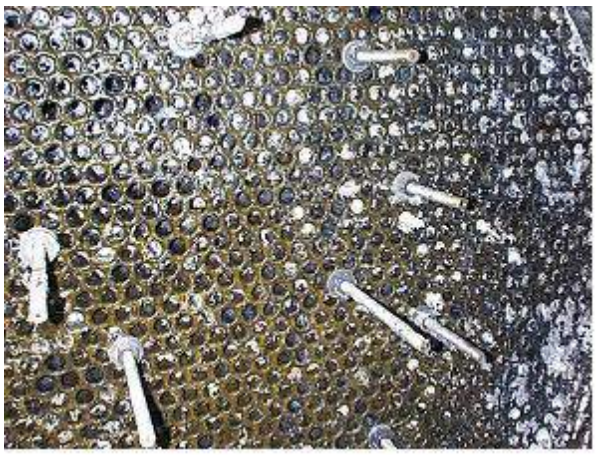

Figure 1-5: Solidification fouling in a petroleum refinery where paraffin solidified from a cooled petroleum product [16]. The dark layer covering the heat exchanger is the paraffin solidification fouling.

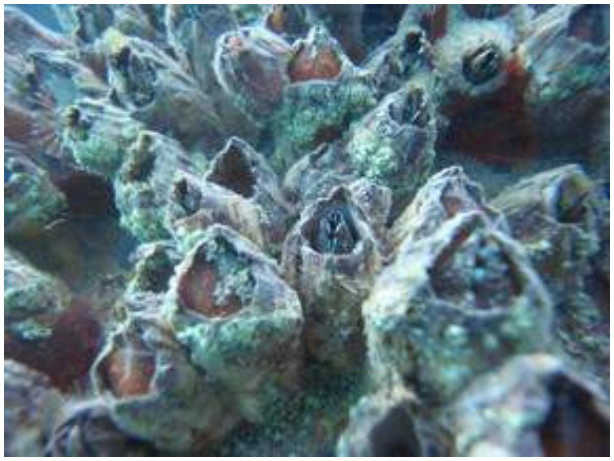

Figure 1-6: This is a zoomed-in image of biofouling caused by barnacles [24].

occurs, it is called composite fouling. One example of composite fouling is the fouling of condensers in power plants. In some cases, such as the one shown in figure 1-7, fouling could be a result of both scaling deposits as well as corrosion fouling [25, 26]. Another example of composite fouling is the fouling in oil pipelines and refineries. Both asphaltene or wax in crude oil can form a fouling layer in oil pipelines and refineries [9]. When composite fouling is present, the fouling problem becomes very complex [17].

Figure 1-7: Fouling deposits in the condenser of a power plant, composed of both precipitate fouling and corrosion fouling. The dirty yellow-green layers are caused by the scaling of calcium, while the reddish layers are iron oxide corrosion products [27].

#### 1.1.1.2 The Undesirable Effects of Fouling

Fouling is a ubiquitous problem affecting many industries. As mentioned earlier, the estimate of the cost due to fouling is a significant part of the GDP of industrialized nations [5, 6]. The effects of fouling vary among different systems in which it grows. The following subsections explain a few of the most notable detrimental effects of fouling.

**Undesirable Effects on Coal-fired Power Plants** In a coal-fired power plant, ash fouling of heat transfer surface is one of the main concerns for operation. The likelihood of ash fouling happening in a coal-fired power plant depends on its ash content and how the ash interacts in specific boiler conditions such as its temperature and oxidation condition [28]. The complexity of these interactions makes it very difficult to predict ash fouling. Ash deposits on a coal-fired boiler's heat transfer surfaces can reduce the power plant efficiency, or in extreme cases, lead to boiler shutdown [14]. A survey by the Electric Power Research Institute (EPRI) in the US showed that 7% of coal-fired power plant units suffer from frequent fouling, while another 40% experience occasional

problems with fouling [2].

**Undesirable Effects on the Petroleum Industry** Fouling deposits in the oil industry are formed from wax, asphaltenes, inorganic compounds, or all three. When waxes are present, they can increase fluid viscosity and form a layer on refinery or process tubing walls. These layers can constrict the flow through the filters, valves, or in some cases, pipelines. This leads to increased pumping energy and cost, or reduced crude oil production. When asphaltenes are present, they also form a fouling layer which leads to flow restriction, and forces the furnace to fire harder to compensate for the decreased outlet temperature [9, 29]. Overall, when fouling deposits occur in petroleum refineries, they can cause the loss of heat transfer, the blocking of process pipes, under-deposit corrosion, and localized hot spots. The increase in the heat transfer resistance and the blocked fluid flow can cause significant energy loss and safety concerns. These physical effects lead to production losses and heightened maintenance cost [9, 30]. Fouling therefore contributes directly to the emission of a significant amount of carbon dioxide in petroleum refining [4].

**Undesirable Effects on Ships** Biofouling deposits on ships result in a reduction of speed, an increase in the fuel and maintenance costs, and potentially accelerated corrosion. The reduction in speed is caused by an increase in frictional resistance of the hull when passing through the water. When fouling deposits are present on a ship's hull, the speed reduction of the ship may be on the order of several knots. Figure 1.1 shows the effect of fouling on different classes of military ships after six months out at sea. The figure clearly shows the significant fuel consumption effect that fouling deposits have on ships. Even in temperate water, the loss of speed could range from 1-2 knots, and the percentage increase in the fuel consumption to maintain certain speeds could be as high as 35%-50%. Note that in the table, the frictional resistance is assumed to increase by 1/4 percent per day. This is the British Admiralty's frictional resistance value for temperate water, based on its experience. In tropical water, British Admiralty suggested a frictional resistance of 1/2 percent per day, which will lead to even more speed reduction and fuel consumption [23, 31].

| Type of Ship | Standard Displacement (Tons) | Loss of Maximum Speed (Knots) | Percentage Increase in Fuel Consumption to Maintain a Speed of | |
|---|---|---|---|---|
| | | | 10 Knots | 20 Knots |
| Battleship | 35,000 | 1.5 | 45 % | 40 % |
| Aircraft Carrier | 23,000 | 1.25 | 45 % | 40 % |
| Cruiser | 10,000 | 1.25 | 50 % | 45 % |
| Destroyer | 1,850 | 2 | 50 % | 35 % |

Table 1.1: The effect of fouling on military ship speed and fuel consumption, after six months out of dock in temperate water. Frictional resistance is assumed to increase by 0.25% per day. The loss of speed can be significant as shown. The fuel consumption rate percentage increase after six months out of the dock in temperate water could be as high as 50% [31].

### 1.1.2 Crud: Fouling in Light Water-Cooled Nuclear Reactors

Crud is the term for fouling deposits that grow on fuel cladding inside light water reactor (LWR) cores. This thesis will focus on PWRs, as the effects of even a small amount of crud can be more severe. Note that the term "crud" had been with nuclear industry since 1959, when a research reactor in Canada, located at Chalk River, was testing corrosion of fuel element and found unidentified deposits covering the fuel elements [32]. It is known, that the term "crud" is a bacronym, coined after the discovery of the deposits. Therefore, this thesis will not capitalize the term as "crud."

To understand how crud deposits occur, one must understand the anatomy of a PWR. A PWR contains two coolant loops – the primary loop, and the secondary loop. Both use water as the coolant. The primary loop flows coolant through the reactor vessel where nuclear reactions take place. The coolant carries heat away from the reactor vessel to the steam generator, a large two-phase heat exchanger. The secondary loop then receives the heat from the primary loop through the steam generator. In the primary loop, coolant water is not supposed to boil, hence the high level of pressurization. To maintain the very high temperature of over 300 $^{o}$C, the coolant water inside the primary loop is pressurized to 15.5 MPa [33]. Figure 1-8 is a diagram of a typical PWR primary loop, showing the major components involved in the formation, transport, and deposition of crud. Figure 1-9 and 1-10 exhibit examples of crud deposit layers on BWR and PWR fuel rods, respectively. The following paragraphs will explain how crud forms in the reactor vessel part of the primary loop [34].

Usually, the primary loop's coolant contains dissolved species and suspended particulates. Some of these chemical species are intentionally added, while some are unavoidably present no matter what. For example, boric acid is intentionally added to control the nuclear reaction, by preferential neutron absorption. Others, such as nickel ferrites, are the result of corrosion of the alloys that made up the primary circuit, such as 300-series stainless steels and 600-series nickel-based alloys [33, 35]. Some of these dissolved species and suspended particulates can accumulate to form crud on the surface of the fuel rods' claddings, especially on the sections where sub-cooled boiling occurs [33, 36, 37, 38, 39].

Nickel ferrites, nickel oxides, and iron oxides constitute the majority of the particles that eventually deposit as crud [35]. The PWR water treatment system does not filter these particles well, because they are both too large to be filtered out by mixed-bed ion exchangers and too small for removal by typical particulate filters [40]. Therefore, only a small fraction of these crud-forming particles are properly filtered from the system. Most of these particles remain suspended inside the reactor primary coolant system, and eventually deposit on various surfaces inside the system [36, 41]. The number of suspended particles that form deposits depends on both their concentration within the coolant and the surface area of alloys in contact with the primary coolant. In a typical four-loop PWR, the total primary coolant surface area is approximately 25,000 $m^2$ [33]. The steam genera-

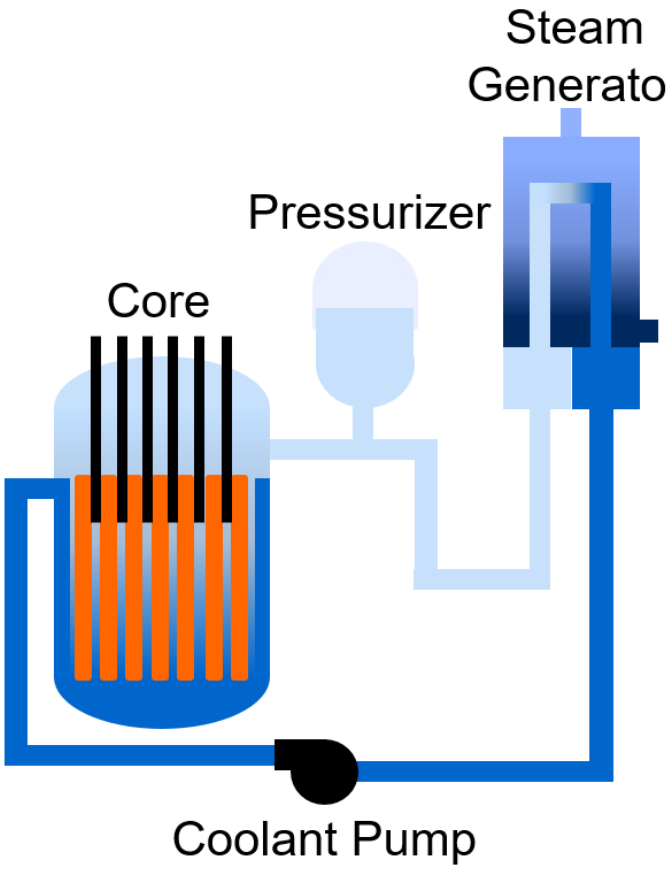


Figure 1-8: This figure shows the diagram of a typical PWR primary loop. The reactor vessel is where fuel rods are situated and where crud grows. The steam generator is where majority of crud particles originate.

tor has the greatest fraction, accounting for approximately 60% of the total primary loop's coolant surface area as an enormous bundle of bent tubes. The steam generator is typically made of nickel alloys, either alloy 600 or alloy 690, which explains the large nickel content commonly found in crud. Zirconium-alloy fuel cladding, where crud deposits, makes up 25% of the primary coolant contact surface area. The rest of the surface area is from the reactor vessel, pipes, and other components. Most of these components are made of stainless steel alloys, such as 304 or 316, while high pressure valves are often made of cobalt-bearing Stellite [33]. This primary coolant contact surface anatomy can partially explain the composition of crud, which is typically nickel ferrites, nickel oxides, iron oxides, and some zirconium oxides [35]. Finally, while the fuel rods do not form a majority of the reactor internal surface area, there is an expression in the nuclear industry: "There's no better filter than the fuel." This refers to the very high ability of fuel rods, especially those undergoing sub-cooled boiling, to trap particulates in the coolant as crud.

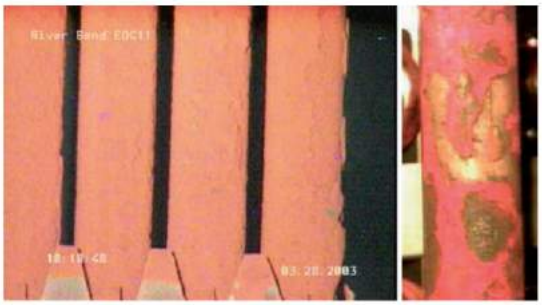

Figure 1-9: These two images show examples of heavy crud growth in a BWR at River Bend. Crud is the dirty-looking orange layer covering the fuel rods. The orange crud would suggest the presence of iron oxide, suggesting that there was high oxygen in that plant. It was observed that the thickest crud was very location specific in the River Bend core. [42]

### 1.1.3 Why Is Studying Crud Important?

Understanding crud is important because it places limits on reactor design and operation, which continue to be the main limiting factors for PWR operation even today. If left unchecked, crud can cause a variety of undesirable effects on the performance of the plant. Specifically, crud can worsen heat transfer, increase pressure drops, elevate primary coolant and surface radiation dose rates, cause crud-induced power shift (CIPS), and lead to crud-induced localized corrosion (CILC). The reduction in heat transfer, the pressure drop increase, and the CIPS still result in expensive actions, such as deoptimized fuel loading patterns or mandatory power level reductions, to offset their effects. CILC can lead to sudden fuel failure, and is much harder to predict [7, 33]. Finally, the activation of crud on fuel rods and its subsequent release into the primary coolant greatly elevates

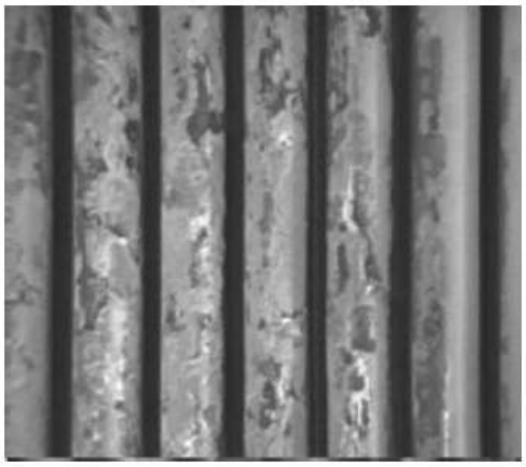

Figure 1-10: Crud deposit on PWR fuel rods in Three Mile Island Unit 1.

radiation dose levels throughout the primary system, creating safety issues for maintenance workers. The following subsections will explain the different types of undesirable effects that crud has on PWRs.

#### 1.1.3.1 Crud as a Bottleneck in Power Uprates

Crud represents one of the main challenges in achieving higher burnup and power uprates in PWRs [7]. Crud prevents the push for power uprates because if the power is increased in the reactor, it will be more likely for sub-cooled boiling events to occur on the surfaces of fuel rods. Sub-cooled boiling events aid the formation of crud. Therefore, unless the operators want to face serious negative effects that come with crud, they have no choice but to lower the power rating to mitigate crud formation.

Crud prevents the achievement of higher burnup by limiting the amount of boron that can be added to PWRs. According to the EPRI PWR Primary Water Chemistry Guidelines Volume-1 1999, having a pH below 6.9 when operating a PWR is not recommended [43]. The reason for this suggestion is that a lower pH leads to huge amount of crud by inducing faster corrosion rates on primary coolant-facing surfaces. Pushing for higher burn-up also means that more boron will have to be added to moderate the neutron flux at the beginning of nuclear fuel cycle. Adding more boron or boric acid will push the pH lower, unless extra lithium hydroxide (LiOH) or potassium hydroxide (KOH) is added to maintain the pH. Elevated levels of LiOH have been strongly implicated in accelerated corrosion in PWRs, making this course of action not preferred. If crud's limitation is removed, reactors can operate at a higher level of boron, lower pH, and higher burnup [43]. Therefore, solving crud problems will remove the design and operation limitations, leading to a more efficient reactor.

#### 1.1.3.2 Degradation of Heat Transfer

In the case that there is no crud, heat normally flows directly from cladding to coolant. On the other hand, having any layer including crud in the way, constitutes an extra thermal resistance. Even though fluid flows through crud, boron precipitation in the crud pores can lead to further heat transfer reduction. Jin/Short (2016) [44] demonstrated through modeling that crud can have a vapor dryout layer, accelerating film boiling. It is generally accepted that fouling deposits worsen heat transfer of the surface on which they grow. However, for crud, the issue is still left open for further research verification. Some studies suggest that crud may actually improve heat transfer, under certain conditions. This improved heat-transfer is the result of mechanism called "wick boiling" [36, 45]. More information on wick boiling can be found in this thesis' background chapter on crud's effects. Nevertheless, the uncertainties that go into heat transfer across crud would still be worrying to anyone operating or designing the PWR.

#### 1.1.3.3 Increased Pressure Drop

Similar to other types of fouling deposits, crud growth can also lead to a pressure drop within the system on which they grow. When crud grows, the roughness of the surface bordering flowing fluid may increase, since crud deposits are rougher than metal surfaces. crud's typical roughness is between 0.5 to 3.0 $\mu m$ [45], while typical metal roughnesses are below 0.15 $\mu m$ [46]. The resulting changes in surface roughness will lead to an increase in frictional pressure drop.

In nuclear reactors, this crud pressure drop effect may lead to various side effects depending on where the crud deposits grow. For example, if crud grows or accumulates on a venturi meter used to measure flow rate, the obstruction of the flow instrument can indicate a higher flow rate than reality. If crud grows in the nuclear reactor vessel's diffuser region, the increased pressure drop can lead to an earlier flow separation, which increases drag and prevents pressure recovery on the diffuser region [47].

#### 1.1.3.4 Crud-Induced Power Shift (CIPS)

During PWR operation, crud can worsen heat transfer from the fuel and accumulate boron. The accumulated boron in crud can cause a power distribution shift. Since boron absorbs neutrons, the places where crud grows and boron accumulates will absorb more neutrons, leading to localized suppression of the neutron flux. This leads to an undesired power distribution shift that can be called either axial offset anomaly (AOA) or crud-induced power shift (CIPS) [48, 49].

One example of such CIPS occurred at the Union Electric Company (UE) Callaway Plant, which was built by Westinghouse. The Callaway Plant is a PWR with a power rating of 3565 MWt. Beginning in cycle 4, the plant operator observed an unexpected power distribution shift towards the bottom of the core. Westinghouse and Union Electric Company concluded that the power

distribution shift was likely caused by the formation of crud [50]. In addition, more aggressive fuel loading patterns may be used if CIPS ceases to be an issue, or fuel fresh feed assemblies may be used in a loading pattern designed for the same burnup. Both of these strategies result in significant cost savings, reaching a few hundred thousand dollars per fuel cycle.

#### 1.1.3.5 Crud-Induced Localized Corrosion (CILC)

As mentioned earlier, crud can accumulate boron inside its layer. Other than that, crud can also induce a temperature rise, either by boiling point elevation due to concentrated soluble species or by inducing vapor dryout, and concentrate many chemical species. The slow fluid flow within crud slows or stops the flushing away of radiolysis products, resulting in a more chemically aggressive environment within any liquid trapped in the pores of crud. All these effects can contribute to heightened corrosion within the crud layer. This heightened corrosion is called crud-induced localized corrosion (CILC) [7]. It was reported by a few US PWR power plants between 1995 to 2000 that crud deposits worsened fuel corrosion. In particular, the TMI-1 experienced as many as nine failed fuel rods that were believed to arise from the heavy buildup of crud deposits at the upper spans on the outer surface of peripheral fuel rods [42]. Figure 1-11 shows an example of a fuel failure caused by the accumulation of a crud deposit. The hole on the middle fuel rod in the figure is a breach in fuel cladding.


Figure 1-11: Example of fuel rod failure caused by crud-induced localized corrosion (CILC) in the River Bend BWR [42]. At the end of cycle 11 at River Bend, six failed fuel assemblies were identified. The hole in the middle fuel rod in the image is one of the fuel failures. The orange coverings around the fuel rods are crud.

### 1.1.4 Obstacles to Eliminating Crud

Crud has been a problem in nuclear reactors for more than half a century, but still remains unsolved. One probable reason is the difficulty in studying and preventing it. Crud is extremely hard to obtain and work with because of its radioactivity. Recreating crud in a lab is also difficult because of the extreme PWR conditions, and the difficulties associated with precisely replicating the often unspecified or unknown conditions within a PWR. These following subsections will go into more detail on why it is difficult to study crud as well as the ways people had previously explored crud mitigation and prevention.

Real reactor crud samples are very difficult to obtain and are only available to few organizations, specifically those with the capability and hot cells to handle highly radioactive materials. Real reactor crud samples are also radioactive, leading to various problems with handling it for experiments. This is why it is rather rare to find literature that actually analyzes a reactor's crud. A more popular approach to studying crud is through growing it in ex-core experiments. However, the experimental approach to obtaining crud also has many disadvantages. First, growing crud similar to that in PWRs is hard because it is very difficult to recreate the reactor conditions. This is why there are only a few experimental loops worldwide capable of achieving this. Second, it takes a very long time to grow crud. In real reactors, crud grows in an environment where each fuel cycle lasts over a year and a half. That kind of experimental time span is impractical; therefore, in experimental loops, many parameters are tweaked to aid crud growth. Even so, it still takes at least two weeks to grow thick crud similar to that found in a reactor [8]. Many crud experiments will adjust various parameters to simplify the experiment. The obvious downside is that crud samples grown in those experiments may be different from those obtained from nuclear reactors.

The problem of crud has persisted for a very long time and there have been many attempts to prevent or mitigate it in the past. Many techniques for stopping crud had been experimented with and patented, but none have yielded effective results interesting enough to be applied to actual commercial reactors. These techniques include approaches such as electro-polishing of fuel rod surfaces, adding zinc, magnetic filtering, increasing coolant pH, and ultrasonic cleaning [51]. More detailed information for each of these techniques mentioned can be found in the background section. This thesis will address the crud challenge by using fuel cladding surface coating.

## 1.2 Objectives of the thesis

As shown in the previous section, the fouling deposits on fuel rods, or crud, still remains a significant problem for PWRs. The goal of this thesis is to revisit the crud problem once again, using a newly constructed PWR loop and new analysis techniques, and attempt to find a way to prevent or mitigate crud, or at least better understand it. For the goal of preventing or mitigating crud, our group is

the first to experiment with using fuel-rod coatings as a way of countering its growth. For the goal of gaining a better understanding of crud, our group is also be the first to apply fractal analysis to characterize crud. The following subsections will explain in more detail our actual goals for crud mitigation/prevention, crud analysis, and the way that we achieved them.

### 1.2.1 Our approach to obtaining Crud samples

As explained above, analyzing real crud isn't very practical in our case. The real reactor crud sample is very hard to obtain and has critical radioactive hazards. Our best options are to either use computer models to analyze crud or design an experiment that can simulate the conditions as close to that of the the real PWR as possible. Computer modeling of crud will be tackled by another part of our group. Therefore, this thesis will focus on an experimental approach to understanding and mitigating crud.

To be able to experiment with new techniques for preventing crud, as well as gain crud samples to analyze, we chose to build a facility, called the Internally Heated Testloop For PWRs (IHTFP) that can simulate conditions at the PWR fuel cladding surface. crud will be grown on this simulated PWR fuel cladding surface. The IHTFP has the ability to match the temperature and pressure in actual PWRs, as well as non-radioactive chemical conditions. The simulated fuel rod situated inside the IHTFP's autoclave is the place on which crud will grow. Crud from this facility is what we will use for analysis in the rest of the thesis. In the scope of this thesis, coatings will be applied to the simulated fuel rod surface. The detailed description of how the IHTFP facility was built and is operated can be found in Chapter 3, Design and Construction of the IHTFP.

### 1.2.2 Our approach to mitigating or preventing Crud

Our approach to mitigating or preventing crud will be to experiment with crud-resistant coatings that prevent the adsorption of crud particles onto fuel cladding surfaces. Various chemical surface-modification coatings will be tested to determine if any of them will prevent or mitigate the adsorption of corrosion-product particles. Preliminary results of the crud-resistant coating experiments done on a smaller scale in our group, shown in figure 1-12, motivated this approach due to their initial, qualitative success. Therefore, we are taking this experiment to the next step with an experiment using potentially crud-resistant materials in conditions very close to those found in reactors using the IHTFP.

### 1.2.3 Our approach to analyzing Crud

Another approach to the crud problem is to gain a better understanding of its surface coverage in order to adjust reactor parameters for better optimizations. Since industrially relevant parameters,

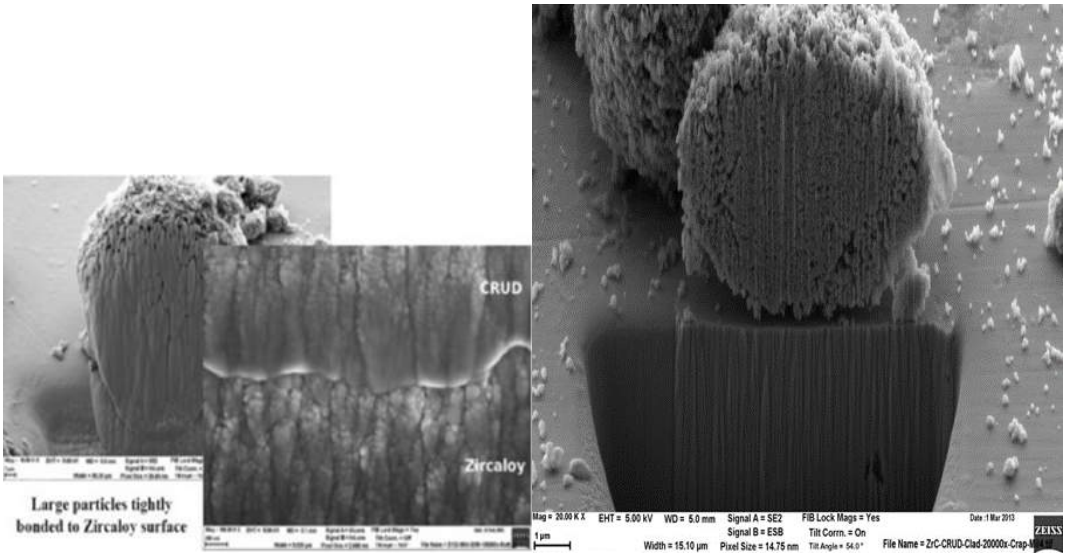


Figure 1-12: The two left pictures show how crud particles bonds to Zircaloy-4, while the right picture shows how crud particles do not bond to zirconium carbide. The figures show that crud bonds very well to the zircaloy surface while a clear separation can be seen in the right picture between the crud particle and the zirconium carbide surface [52].

such as the heat-transfer across crud, have been examined many times, especially by the industry themselves, we take a different approach and look deeper into the inner workings of crud. With the rise of more complex computer simulations aided by recent advances in modeling and simulation, we can now properly include many parameters, previously ignored for simplification, in our modeling of crud. The MAMBA-BDM model developed by our group treats crud as a chemical deposition in an environment that varies in concentration of soluble species and heating. The model is based on a complex fractal-based flow geometry, and uses fractal parameters to determine many crucial crud parameters, such as permeability and thermal conductivity. For example, the permeability is calculated by taking into account the porosity, tortuosity, and two fractal dimensions [7]. Despite the fractal parameter's usefulness in modeling crud structure, the fractal parameters of crud have never been measured. This thesis will bridge this gap by using experimental data to verify the assumptions made, and improve upon the MAMBA-BDM model. Specifically, we will examine both the porosity and the two fractal dimensions of crud. The detailed explanation of the parameter descriptions and the methods of acquiring those parameters are presented in the background section.

Other than analyzing crud from the fractal perspective, we also measure surface coverages of crud to quantify the crud resistance of a number of potentially crud-resistant coatings. The surface coverage analysis is done by applying image processing algorithms to separate the crud from the underlying surface. The surface fraction covered by crud can be used as a quantitative measurement of how effective each material is in mitigating crud. Even if an effective industry-ready crud-resistant material is not found by this thesis, these quantitative studies can lead to better understanding of

how crud and fouling deposits form in general.

## 1.3 Key Scientific & Engineering Contributions

This section lists the major contributions of this study. The first sub-section lists the engineering contributions regarding the designing, construction, and testing of the IHTFP. It provides an overview of how the IHTFP is unique when compared to other similar experimental loops around the world. The second sub-section lists the new scientific findings that were made in this thesis using the IHTFP. The section gives an overview of notable scientific results in this thesis, as well as how our scientific findings are unique.

### 1.3.1 Engineering Contributions

The main engineering contribution is the design and construction of the loop used to carry out the crud growth experiments. Our experimental loop setup has to simulate the extreme thermal-hydraulic and chemical conditions in a PWR. The whole section on design and construction of IHTFP has been allocated to explain how this engineering feat was carried out. The sections below will list the accomplishments from building this crud loop, as well as emphasize several aspects of the loop that make it stand out from other, similar loops.

**Simulating PWR Conditions** As mentioned earlier, the IHTFP has the capability to closely simulate PWR conditions. This is currently one of only a few known in the world outside of industry capable of simulating PWR conditions. The IHTFP grows crud on a simulated fuel rod, with geometry similar to that of real PWRs. The IHTFP can operate at a pressure of 155 bars and a temperature of 325 $^{o}$C, similar to the temperature and pressure conditions within a PWR. Other than this, the loop also has the capability to make the water mass flux within the test section match the actual PWR mass flux. The IHTFP can also be adjusted so that the Reynold's number within the test section is within the same order of magnitude as that found in a PWR. Moreover, the chemical conditions within the reactor are also simulated in the IHTFP by adding boric acid and lithium hydroxide in similar amounts to those of PWRs. crud precursor particles, in the form of nickel oxide ($NiO$), are added in large amounts to increase the crud growth rate. in addition, the IHTFP loop is made of 316 Stainless steel and therefore contributes to iron oxide ($Fe_3O_4$) source term natrually. This only leaves out radiation which is unlikely to affect crud growth. The summary of the IHTFP's conditions compared to the PWR's conditions is provided in table 1.2.

Finding a loop that can simulate PWR condition in a university setting is very rare. The only other similar setup that was built in a university setting, that we are aware of, is the loop built by Professor Ji Hyun Kim at Seoul National University. The loop at Seoul National University is used

| Condition | PWR | IHTFP |
|---|---|---|
| Pressure | 15.5 MPa | 15.5 MPa |
| Liquid Temperature | 287-324°C | 320°C |
| Reynolds Number | $5 \cdot 10^5$ | $1.62 \cdot 10^5$ |
| Mass Flux | $3500 kg/m^2 s$ | $1920 kg/m^2 s$ |
| $Fe_3O_4$, $NiO$ | 13-116 ppb | 20,000 ppb |
| Boron | 1400 ppm | $<$ 2000 ppm |
| Lithium Hydroxide | 3 ppm | ~2.2 ppm |
| pH | 6.9 | 6.9 - 7.4 |
| Dissolved Oxygen | $>$ 5 ppb | $>$1 ppb |
| Water Electrical Conductivity | ~11-23 $\mu S/cm$ | ~10-15 $\mu S/cm$ |

Table 1.2: This table compares conditions between that of the IHTFP and a typical PWR. Note that the IHTFP only contains nickel oxide (NiO) particles. The large amount of NiO was added to speed up crud growth. The lower-end value of pH was also chosen for the purpose of speeding up crud growth in the IHTFP [43, 53, 54].

for in-situ Raman and crack growth testing. Other loops that we are aware of are mostly operated by industry, such as Westinghouse's WALT loop and CRIEPI's crud loop in Japan. When compared to those loops, the IHTFP is still unique in its features that will allow unique experiments to be conducted. The explanations of some interesting unique features are listed below.

**Usage of large sapphire windows in the experimental autoclave with PWR thermal-hydraulic condition** Our crud loop is the first-of-its-kind to have sapphire windows as large as 2 cm. With the large sapphire windows, many possibilities open up. For example, the autoclave windows can be used for laser triangulation-based crud thickness measurement, Raman spectroscopy, and observation of sub-cooled boiling with a microscopic camera. The fact that the IHTFP contains three windows also makes it possible to take in-situ photographs and conduct high-pressure contact angle experiments.

**Internal rod heating instead of ohmic heating for fuel rod (Second-of-its-kind)** Normally, other experimental loops that simulate PWR conditions ohmically heat their test section, changing the electrochemical conditions on the rod surface. The IHTFP's heating rod is structured so that an electrically-isolated heating element is inserted inside a cladding, just like real PWRs. Internal rod heating with cladding is better than normal ohmic heating, because by using normal ohmic heating throughout the rod, the electricity flowing on the surface of the heating rod might interfere with the surface chemistry. This would have made it difficult to correctly gauge the crud resistance of candidate coatings.

### 1.3.2 Scientific Contributions

After the IHTFP was built, it was used to make three main scientific contributions. Most of our data from our crud loop were extracted from crud samples using scanning electron microscope (SEM) images. By applying image-processing techniques in many different ways, we were able to discover many interesting findings, briefly explained in the following list. More detailed information is provided in the discussion chapter of this thesis.

**First nanoscale cross-section characterization of PWR-representative crud morphology & composition.** In this study, the cross-section of crud is cut with a focused-ion beam (FIB) and analyzed at the nanoscale using a scanning electron microscope (SEM). With the high precision of the FIB and the SEM, we were able to observe and analyze the cross-section of crud at the nanoscale level. Although many SEM images of crud had been taken before, and cross-sectional images of crud already exist, this was the first time that crud's cross-section was observed at the nanoscale level. Using these cross-sectional images, we discovered that crud exhibits fractalline properties, and found a strikingly strong correlation between the fractal dimension and porosity. This correlation holds true across both the crud obtained from our facility and the crud provided to us by Westinghouse from their WALT loop facility.

**Crud fractal measurements.** As far as we are aware, this is the first time that fractal analysis tools have been applied to crud. Fractal analysis tools are still relatively new to the world of science and have recently gained popularity in their use for material analysis, especially for soil. Crud's composition, which is made up of particles, bears great resemblance to the composition of soil. Therefore, crud is a great candidate to apply fractal analysis tools. We chose the box-counting algorithm as a way of obtaining fractal dimensions from crud. The box-counting algorithm is one of the most commonly used fractal analysis tools with widespread usage in soil studies.

The fractalline properties of crud were examined. We found that fractal analysis via the box-counting method yields very low errors in the box-counting plots, supporting the theory that crud is fractalline. Although the low R-squared in the box-counting plot does not necessarily imply that the object of examination is a true fractal, the R-squared value as high as 0.9989 (figure 2-81) is very good evidence to support the theory that crud exhibits fractalline properties. In addition, fractal dimension vs porosity of crud was found to show a strong correlation. crud samples from our experiment, as well as crud samples received from Westinghouse's experimental loop, were both analyzed. We found that crud from both sources follows the same trend as shown in figure 2-81. Furthermore, fractal dimension and porosity's relationship to height position within crud layer was examined. The data was obtained by using computer code to repeatedly find fractal dimensions from cropped images of crud at different heights. From our experimental results, the crud's porosity

and fractal dimension decreases as the height position in crud layer increases.

**Testing of PWR-condition Crud-resistant materials** In this thesis, the crud-resistant coating approach to preventing crud was explored. Our results show an interesting relationship between the Hamaker constant (stickiness) of crud-resistant coating and the deposition of crud particles. Now that we know there is a relationship between the Hamaker constant and crud-resistant coating, the next step is to conduct experiments which will test crud-resistant coatings with Hamaker constants close to that of water.

## 1.4 Description of chapters

The thesis is organized so that, after the introduction, the background section will provide detailed explanations for all the science that is related to understanding this work. Next, details of the IHTFP will be covered in Chapter 3, along with its design and construction. Chapter 4 will then lay out the experimental plans, the test matrix, and analysis methodologies. After that, the experimental data will be presented, discussed and summarized. The description of each chapter is listed below:

**Chapter 2** Chapter 2 contains the scientific background that is needed to understand all the concepts related to the experiments. The first part of this chapter guides readers through what fouling deposits are in general, how they are formed, what their characteristics are, and their effects on the respective systems in which they are found. The second part narrows down the topic to just fouling inside nuclear reactors, or crud. This part expands on the previous section to dig deeper into crud's specific origins, characteristics, and effects on nuclear reactors. In this part, previous literature and previous attempts at experiments and modeling related to crud are examined. The third part ties together what is shown in the background section and digests the information to answer the question of what all this background implies about the experiments.

**Chapter 3** Crud grows in PWR conditions which are not easy to simulate experimentally. Therefore, lots of effort was put into building an experimental setup that can carry out the experiments we planned at PWR conditions. The detailed information of how the loop was built, as well as how to operate the loop, is presented in this chapter. This chapter is meant both as a complete guide to the operation of the IHTFP for future users, as well as to aid other researchers in constructing and running their own similar facilities.

**Chapter 4** Chapter 4 describes the experimental text matrix. It describes the kind of data we want to obtain, as well as the plan we went through to obtain it. The chapter provides descriptions

of the data processing and analysis methods that were chosen, as well as how they were done, and why they were done.

**Chapter 5** This chapter presents the resulting data and observations for both the fractal analysis and the crud-resistant coating experiment. The first part of this chapter deals with the image processing and analysis of crud samples obtained. The second part shows the results of the crud-resistant surface modification coating experiments. The third part ties the coating experiments' result to the Hamaker Constant. The last part of this chapter shows the new crud modeling results using the existing MAMBA-BDM code with our new experimental data as input parameters, to give a more realistic picture of the effects of crud on PWR operation.

**Chapter 6** From the results and analysis presented in chapter 5, this chapter processes the data a step further to yield meaningful scientific findings, and discusses the implications of these results. Both the results related to fractal analysis and results related to the crud resistant coatings will be reviewed in this chapter. Finally, for those conducting future experiments, the direction for this research's continuation and sources of error will be discussed in this chapter as well.

**Chapter 7** This chapter is the conclusion chapter that briefly summarizes the resulting scientific findings and their implications.

# Chapter 2

# BACKGROUND

## 2.1 Fouling and Adhesion in Energy Systems

Fouling of an energy system is the accumulation of an undesirable deposit on top of the fluid-facing surface. An example of fouling deposits include deposits in heat exchanger tubings, limescale buildups inside pipes, or even mussel layers growing on pipes near the sea. In some cases, these deposits are detrimental to the function of the system it grows on. For instance, fouling deposits on heat exchanger will decrease the heat transfer and make the affected heat exchanger less efficient. Fouling deposits in filters can clog the filters, rendering them unusable. Fouling deposits on fuel rods of nuclear reactors, called crud, are also detrimental to cladding surface heat transfer. In addition, crud deposits also accumulate boron which can cause power shift and accelerated corrosion.

### 2.1.1 Definition and Formation Mechanism of Fouling Deposits

Fouling deposits are accumulations of unwanted material on solid surfaces. Most types of fouling deposits are similar in that they lead to undesirable effects such as decreased heat transfer, increased pressure drop and under-deposit corrosion. The mechanisms which lead to the formation of these fouling deposits, however, can vary widely. Within this "fouling" umbrella, multiple mechanisms cause different types of fouling, which are very distinct from each other in their nature. Fouling mechanisms can be categorized into six categories: particulate fouling, corrosion fouling, crystallization fouling, reaction fouling, biological fouling and solidification fouling. This section explains each of these mechanisms, and shows their real-world fouling deposit examples. The most important fouling mechanism that will be focused on in this thesis is particulate fouling, which is the driving mechanism behind fouling deposits on the fuel rod within the pressurized-water nuclear reactor core.

**Particulate fouling** Particulate fouling is defined as the accumulation of suspended particles from the bulk fluid onto surfaces [10, 55]. One example of this type of fouling is ash fouling in coal-fired power plants. Ash-fouling causes problems for the boilers themselves [13], or the heat exchangers in the boilers' exhaust-heat recovery system [12]. Figure 2-2 shows an example of heavy ash fouling on superheater tubes in a coal-fired power plant. Ash fouling layers in coal-fired power plants can significantly deteriorate heat-transfer effectiveness and increase the pressure drop across the systems in which they accumulate. Another example of particulate fouling is the fouling of the Exhaust Gas Recirculation (EGR) cooler in diesel engines. Figure 2-1 shows EGR fouling in a diesel engine. EGR systems are used in modern diesel engines to reduce nitrogen oxide pollution. Particulate matters, consisting of soluble organic fractions (SOF), sulfates, and other solids, can accumulate on the walls of EGR coolers causing fouling problems. Similar to ash fouling deposits in a coal-fired power plant, EGR cooler's particulate fouling deposits lead to worsened heat transfer and increased pressured drop [56]. These, in turn, reduce the ability of the EGR to decrease nitrogen emissions.

Particulate fouling is the driving mechanism behind the formation of fouling deposits in nuclear reactors that will be the focus of this thesis. Suspended corrosion product particles are formed from the corrosion of surfaces in contact with primary loop water within the pressurized water reactor. The particles mostly come from the corrosion of the heat exchanger in the PWR's primary loop, called a steam generator. This is because the amount of surface area that can be corroded within the steam generator is significantly larger than the surface area of other loop components. These fouling particles eventually come into contact with nuclear fuel rods within the reactor vessels where they could get adsorbed to form fouling deposits on the nuclear fuel rods. The details of this process are explained in section 2.2 where the mechanisms of crud formation are described in detail.

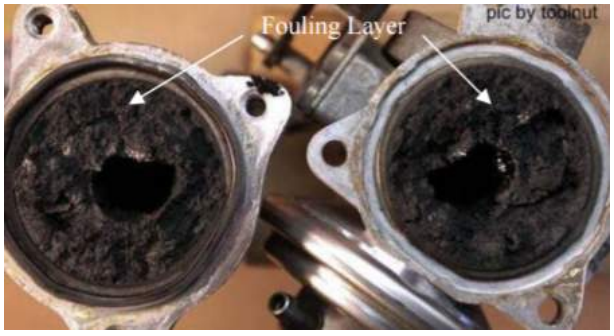


Figure 2-1: This image shows particulate fouling in the Exhaust Gas Recirculation (EGR) cooler in a diesel engine. [57].

**Reaction Fouling (Chemical-reaction fouling)** Reaction fouling is caused by chemical reactions inside the fluid stream, before they come into contact with system surfaces. Reactions between

Figure 2-2: This image shows ash fouling deposits on superheater tubes in a coal-fired power station [14].

soluble precursors in the stream could turn them into an insoluble foulant, which can deposit on the system internal surfaces. Chemical-reaction fouling is usually formed from organic chemical constituents. One of the important characteristics of reaction fouling is that the heat-transfer surface material is not one of the reactants in the chemical reaction that yields fouling material. However, even if the heat-transfer surfaces are not the reactant themselves, certain types of metallic heat-transfer surfaces could act as catalysts for these chemical reactions [58]. The chemical reactions which produce fouling constituents are usually complex. They can include mechanisms such as autoxidation, polymerization, cracking and coke formation [58].

Industries with processes that are susceptible to chemical reaction fouling include oil refining, petrochemical manufacturing, as well as food processing. Reaction fouling commonly occurs in the oil industry, where heat exchangers of the crude oil distillation plants can be fouled with asphaltenes [15, 58]. Before the primary distillation process of crude oil, the crude oil must be preheated to temperatures as high as 400 $^{o}$C. Under high temperature, the crude oil constituents may react to form solid materials that eventually deposit as reaction fouling deposits. In addition, chemical reaction foulings may also occur in the thermal cracking process, where heavy hydrocarbon fractions are transformed into lighter hydrocarbon fractions [58]. Food industries such as the milk-processing industry may also experience chemical reaction fouling [15, 59]. Fouling of plate heat exchangers in the dairy industry is caused by the accumulation of proteins that resulted from chemical reactions within the milk [59]. This form of fouling deposition leads to a progressive decline in efficiency and performance during operation [60]. The fouling of the heat exchangers in the diary industry is so significant that "cleaning in place" (CIP) must be employed every 4-8 hours under typical conditions [61, 62]. These adverse effects could result in production losses in the range of 15-20%, as well as various other problems such as increased water consumption, increased water treatment, and additional chemical usage [62]. The figure 2-3 shows the fouling deposit of a milk pipe in a milk-processing plant.

Figure 2-3: This image shows the reaction fouling of milk pipe in a milk-processing plant [62].

**Corrosion Fouling** Corrosion fouling is similar to reaction fouling in that it also involves chemical reactions. But instead of having a chemical reaction that occurs fully in the process fluid, corrosion fouling's reactions occur between the process fluid and heat transfer surfaces. When corrosion occurs on the heat transfer surfaces, and the corrosion products are not soluble, it will accumulate on the originating heat transfer surfaces [18]. When corrosion fouling occurs, it can potentially decrease heat transfer through the surface it grows on, as well as increase the fluid friction on the surface. One of the most common types of corrosion fouling is the iron oxide fouling on steel, especially carbon-steel layer. Iron oxide is formed from the bulk iron composition of steel and the oxygen in the environment or flowing fluid. Therefore, the reddish iron oxide rust layer is classified as corrosion fouling. Corrosion fouling is characterized by having two simultaneous electrochemical reactions [18]. The figure 2-4 summarizes the mechanisms behind these two simultaneous electrochemical reactions that create corrosion fouling. The metal material represented by the letter "M" is ejected from a metal anode to react with the water to form a metal hydroxide. The metal hydroxide can deposit on a nearby metal cathode and eventually lose its constituent water to become a metal oxide. Metal oxides and hydroxides are what comprise the corrosion fouling deposit in this case. On a metal surface that exhibits corrosion fouling, these anodes and cathodes are distributed throughout the metal surface in alternating areas of cathode and anode, with each anode and cathode pair taking up a tiny area of crystalline size. This is why corrosion fouling looks almost uniform when seen from the macro-scale point of view. Figure 2-5 shows a bad case of corrosion fouling within a heat exchanger pipe, where the pipe's inside surface has a thick layer of reddish-brown corrosion fouling. This corrosion fouling occurance in the Nuplas Industries polymer processing plant, shown in figure, forced them to go through regular cleaning of these pipes every 2-3 months [63]. The plant needs to shutdown during these cleanings, because it does not have a supply of cooling water, which leads to a loss of production.

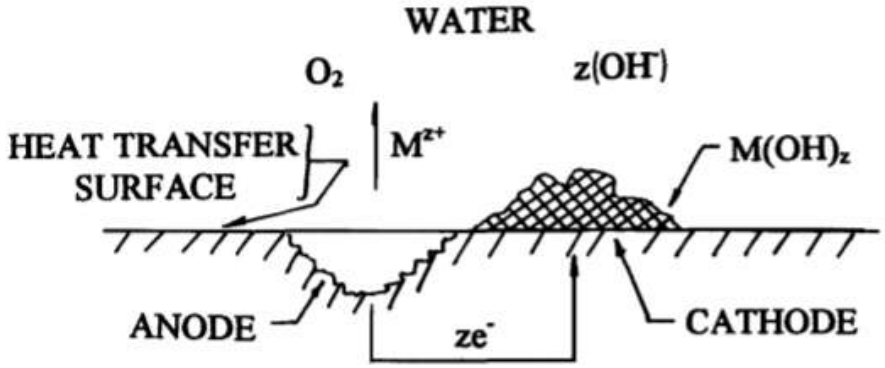


Figure 2-4: This figure shows the usual mechanism behind the corrosion fouling. The metal material represented by the letter "M" is ejected from a metal anode to react with water to form metal hydroxide, which can deposit on the nearby metal cathode. The metal hydroxide eventually loses its constituent water, and turns into a metal oxide. Metal oxides and hydroxides are what make up the corrosion fouling deposit [18].

Figure 2-5: This figure shows a corrosion fouling of steel within a cooling water pipe of an industrial heat exchanger of the Nuplas Industries plant [63].

The fact that crud is also caused by corrosion products can bring about confusion regarding whether crud is actually corrosion fouling rather than particulate fouling. Crud's corrosion product, however, does not originate at the heat transfer surface where it deposits. In PWRs, the relevant heat-transfer surfaces are those on fuel rods. The PWR fuel rod is usually made of zirconium alloy which will corrode into zirconium oxide. The fact that only a small amount of zirconium oxides is found when fouling deposits on PWR fuel rods are examined indicates that the corrosion of zirconium alloy from the heat-transfer surface isn't the cause of fouling on nuclear fuel rods (crud) [35]. As mentioned earlier, crud is made mostly of nickel ferrites, nickel oxides and iron oxides which are the corrosion products from other parts of the system, especially the heat exchanger. Therefore, in this case, corrosion product particles that form crud would count as suspended particles. This means that crud would be classified as particulate fouling.

**Precipitation Fouling (Crystallization Fouling/Scaling)** Precipitation fouling, also known as crystallization fouling, happens when salts, oxides or hydroxides from solutions gets crystallized on the surface. Precipitation fouling occurs when the concentration of solutes exceed the saturation concentration of the solvent. When this happens, solutes will start to crystallize, leading to precipitation of solids on the system internal surface. The reason that the concentration of solutes exceeds the saturation concentration could be driven by changes in temperature or solvent evaporation [19, 20].

Precipitation fouling is especially common in salts with inverse solubility. For salts with normal solubility, the solubility will increase with increasing temperature. For salts with inverse solubility, the opposite will happen and the solubility of salt will decrease as temperature rises. If a solution with inverse solubility is heated, crystalline precipitates will form and deposit on the nearby heat transfer surface. If fouling happens from inorganic salts in water, it will be called scaling. The most common example of this type of fouling is the limescale deposit. If a heat exchanger runs on hard water or water with high mineral content, limescale may form as the water is heated causing the solute with inverse solubility to precipitate [19, 20]. Figure 2-6 shows a thick limescale deposit in an effluent pipe of an oil refinery in Netherland. This particular deposit is made up of limescale as well as some trace of oil.

It can also be confusing whether crud can be identified as precipitation fouling as well. The bulk of crud made of crud particles is not classified as precipitation fouling because it is formed from suspended corrosion product particles, not from corrosion products in an aqueous form that crystallized into precipitates. In the case of crud, the corrosion product particles were formed from other parts of the loop and were floating in the coolant in solid form. On the other hand, for a fouling deposit to be classified as precipitation fouling, it should begin with having an aqueous form and then turn into solid form because of some changes to the fluid conditions. This process of precipitation also should happen near fouling deposition site for a particular deposit to be classified

Figure 2-6: This image shows a thick limescale layer in an oil refinery effluent pipe. The thick layer in the pipe is the limescale layer [64].

as precipitation fouling. In addition to crud particles, crud also accumulates other chemical species such as boron. These additional boron deposits could be classified as precipitation fouling.

**Solidification Fouling (Freezing Fouling)** Solidification fouling or freezing fouling occurs when a component of fluid freezes on heat transfer surface, hence the name. This type of fouling is very important to oil refining, as well as to chilled water production [9]. In oil refining, the solidification fouling process begins when paraffin waxes in crude oil solidify after coming into contact with a cooled surface. After that, these solid waxes get separated from the bulk crude oil to accumulate as solidification fouling deposits. Paraffin wax solidification is a good example of solidification fouling since the hydrocarbon constituent cools down at the condenser into solid form without any alteration of its chemical properties. The figure 2-7 shows condenser tubes in oil refinery covered in solidified hydrocarbon foulings. The hydrocarbon solidification foulings shown here would worsen heat transfer through the condenser, jeopardizing the condenser's efficiency. In chilled water production, the process of solidification fouling involves ice forming on the cooling surface. An ice layer covering cooling surface does not conduct heat very well, and prevents convective heat transfer. A worsened heat transfer between the cooled surface and the bulk chilled water leads to a worsened efficiency and a higher energy consumption within the chilled water system. Parameters such as temperature, mass flow rate, crystallization conditions, surface conditions and the chemistry of process fluid, can affect the formation of solidification foulings [17].

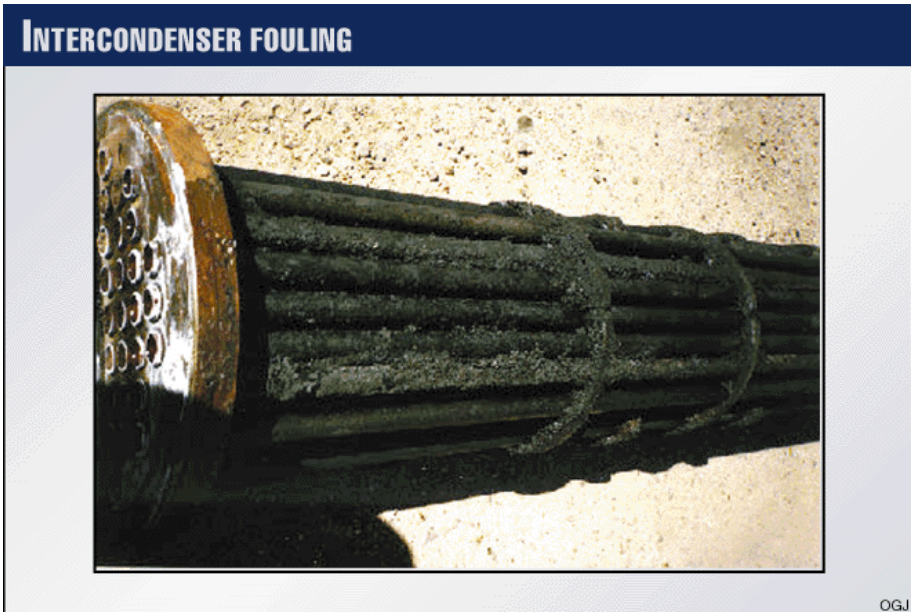


Figure 2-7: The condenser tubing shown in this image is covered in solidification foulings partially caused by solidified hydrocarbon [65].

**Biofouling** When biological organisms present in the liquid causes fouling, the fouling is called biofouling. Organisms such as algae, and barnacles can grow into an undesirable layer covering relevant surfaces. Biofouling can be caused by both microorganisms and macroorganisms. When microorganisms, such as algae, fungi, molds, yeasts and bacteria, cause biofoulings, the foulings are categorized as the microbial fouling subtype. When macroorganisms, such as barnacles, mussels, clams and weed, cause biofoulings, the foulings are categorized as the macrobial fouling subtype. Biofoulings usually form into uneven biofilms or slime layers. Many biofouling samples are also characterized as being deformable and filamentous [17]. Biofoulings cannot be prevented through strainers, and are generally controlled by the use of chemical agents such as chlorine. Biofoulings generally occur in systems that make use of cooling water in an open recirculation or once-through loop. In power plants, this type of fouling most commonly occurs in the systems that use sea water [22, 23], specifically in the seawater-cooled condensers of light water reactors and other power plants. The figure 2-8 shows the biofouling of a ship hull. The biofouling on the ship hull increases the fluid friction on the ship, slowing the ship down. This can translate into more fuel and maintenance costs for the ship. Other than increasing the fluid flow resistance, biofoulings may also promote corrosion fouling under the biofouling layers, especially in cases where iron oxidizing bacteria are present [17, 66].

**Composite Fouling** Lastly, in many cases, fouling phenomena can have multiple causes. Two or more fouling mechanisms mentioned above could be present in the same system. Fouling deposits caused by many different fouling mechanism is called composite fouling [25, 26]. In a system where

Figure 2-8: This image shows a ship hull covered with a biofouling layer [67].

there is composite fouling, the fouling problem becomes very complex with intertwined effects. These intertwined effects are not uncommon. For example, biofouling may cause under-deposit corrosion fouling [17]. These intertwined effects makes it very hard to properly characterize the fouling processes into a unified theory. The figure 2-9 shows an industrial heat exchanger with composite fouling layers grown on its surfaces. The composite fouling layers shown here are composed of both limescale precipitation foulings and algae biofoulings. The reddish brown rusty parts could also be corrosion foulings.

### 2.1.2 Important Parameters of Precipitation Fouling Deposits

With a clearer definition of what fouling deposits are, the next important information about fouling deposits is the parameters that characterize fouling deposits. Among these fouling deposit parameters, some will be chosen for use in our experiment and analysis. Although there are many types of fouling as shown in the previous section, there are several parameters describing fouling deposits that are useful in analyzing any types of fouling deposits. This section will define those parameters. The parameters will be separated into two main categories, the macroscopic parameters and the microscopic parameters.


Figure 2-9: This image shows foulings on an industrial heat exchanger. It is a combination of both limecale precipitation fouling as well as an algae biofouling [68].

#### 2.1.2.1 Macroscopic parameters

This section will explain the macroscopic parameters that are useful for characterizing the fouling deposit formations. Macroscopic parameters are very important to industries with fouling deposit problems, as they are directly related to how equipment performs. Each of the paragraphs below will explain what each macroscopic parameter is and how it relates to fouling deposits. The relevant macroscopic parameters include the fouling deposit's growth versus time, thermal resistance, and pressure drop change.

**Growth (Thickness) vs. time** Fouling deposit growth over time is the measurement of how quickly fouling deposits' thickness increase over time. Unfortunately, fouling deposits' growth is dependent on many conditions and is usually specific to systems. As explained previously, the fouling deposit term is very general, and is comprised of many distinct fouling mechanisms. Therefore, it is not surprising that, up to date, there is no united theory about how fouling deposits grow. This thesis will touch upon crud fouling deposit growth, where further details are shown in section 2.2.4.1.

**Thermal resistance** Fouling deposits can increase the thermal resistance on the heat transfer surface on which they grow. The convective heat transfer from the heat transfer surface to the bulk fluid is an efficient mode of heat transfer. With a fouling deposit layer on a heat transfer surface,

heat has to conduct through the fouling deposit layer before it can be carried away into the bulk fluid through the convective heat transfer. This can cause problems in systems, such as heat exchangers, where heat transfer is a crucial part of their operation. Worsened heat transfer leads to decreased efficiency of the system where fouling deposits accumulate.

**Pressure drop in system** The pressure drop is defined as the pressure difference between two points in a fluid flow system. The pressure drop between two flow areas across a uniform area flow channel is affected by the fluid flow friction, as well as gravity [54]. In the section of liquid flow area that has fouling deposits, the pressure drop can increase. This happens in various systems, such as heat exchangers or oil pipelines [9]. Further details on the pressure drop and its relation to crud can be found in the section 2.1.3.1.

#### 2.1.2.2 Microscopic parameters

The macroscopic parameters are definitely important, since they directly affect the growth of fouling deposits in the system. However, the microscopic parameters should not be overlooked, as they can provide useful insights into the science behind fouling deposits. Understanding the science behind fouling deposits can useful in predicting the macroscopic parameters. There are several microscopic parameters related to the characterization of fouling deposits, including porosity, permeability, fractal tortuosity dimensions, fractal area dimension, pore size distribution, thermal properties, and fouling deposit constituents.

**Porosity** Porosity is the fraction of empty spaces in a material compared to its total volume. The value varies from 0 to 1 with 0 meaning the material is solid. Porosity is important in the study of fouling deposits because it affects the flow of water within fouling deposits as well as the heat transfer through the fouling deposits layer. For our experiments, we will measure the porosity of fouling deposits from images of cross sections of crud.

There are many ways to measure porosity. The most basic method of measuring porosity is the water displacement method, where a porosity measurement is obtained from comparing the weight measurement of dry samples versus wet samples. Other than that, gas can also be used to displace pores instead of water. The equipment used to measure porosity using the gas expansion method is called Boyle's porosimeter. It consists of two chambers, the sample chamber containing the sample and the empty reference chamber, each with its own pressure gauge and a valve connecting them. In operation, the first reference chamber will be pressurized, and pressure will be measured. Then the valve between the two chambers will open letting the gas equilibrate between the two chambers, before taking a second measurement. Through equations relating volume and pressure, the volume of pores inside the sample can be derived. Both the governing equations and a diagram of Boyle's porosimeter described earlier are shown in figure 2-10. With Boyle's porosimetry technique, the data

obtained may be similar to figure 2-11. Typical volume used in Boyle's porosimetry is in the range of $10cm^3$ [69]. On the other hand, a thick crud sample of 50 microns thickness covering 10 $cm^2$ will have the volume of only 0.05 $cm^3$. Because crud has very small volume, Boyle's porosimetry method is not ideal for use on crud.

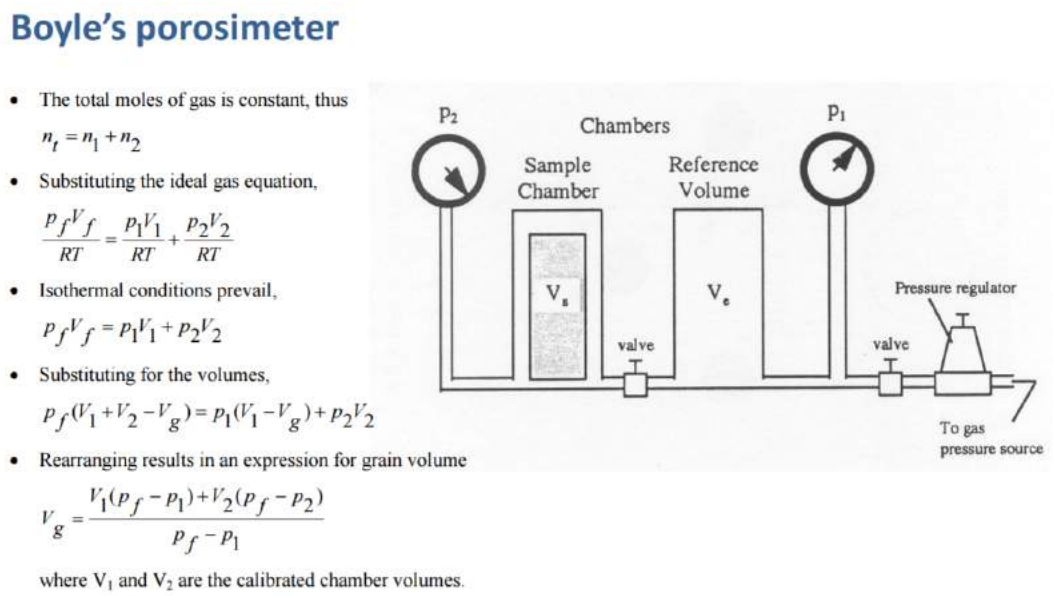


Figure 2-10: This figure shows the diagram of Boyle's porosimeter and the governing equation that can be used to calculate the volume of material without the pores $V_g$. [69]

Another method that can be used to measure porosity is mercury porosimetry. In this method, we infiltrate the deposit with liquid mercury and decrease the pressure to get both the porosity and the pore size distribution at once. An example setup used to for mercury porosimetry is shown in figure 2-12. Figure 2-13 shows a plot of typical data obtained from a mercury porosimetry experiment. From the graph, one can see that as the pressure increases, mercury does not infiltrate the sample at the same rate. The inflection point labeled A represents the break-through pressure that can be used to determine bulk or envelop volume. The difference between point A and B together can be used to determine the interparticle void volume. Lastly, point A and C can be used to determine the skeletal volume [71].

In this method, pore size ranging from 500 microns to 3.5 nm can be investigated [72]. The downside is that this method is destructive since the sample will be contaminated with mercury. Unfortunately, as stated earlier, crud is very thin and cannot be easily separated from its host surface. Therefore, we cannot practically apply mercury porosimetry since it requires a separated crud sample in a pressurized mercury chamber.

Another way to measure porosity is through converting a cross-section photo into a binary image, and then determining the amount of void in the binary image. This is usually more suitable for

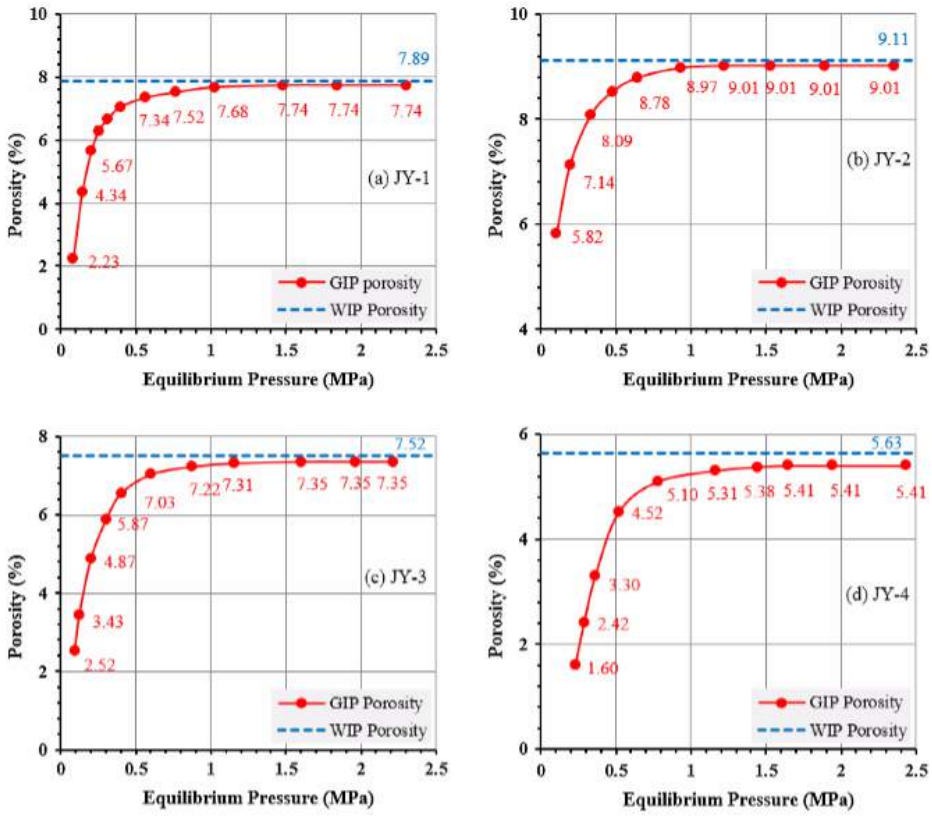


Figure 2-11: This figure illustrates resulting data from Boyle's porosimeter experiment [70]. The four graphs show the relationship between equilibrium pressure and measured porosity of gas shale plug samples measured at 25 ºC.

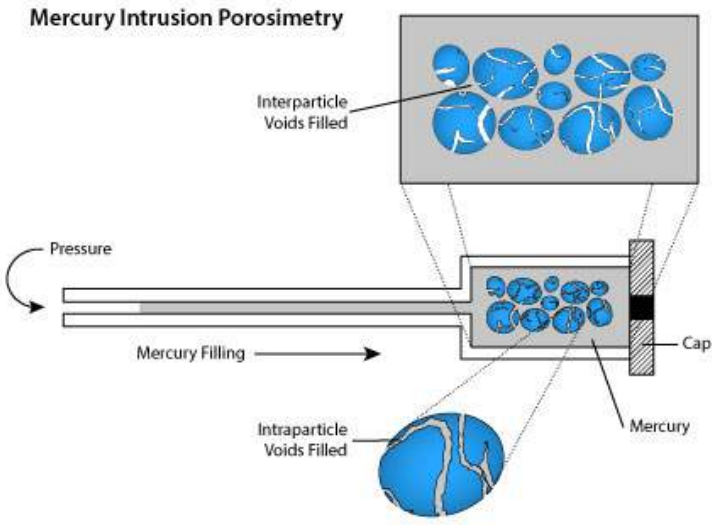


Figure 2-12: This figure shows the setup used to conduct mercury porosimetry experiments.

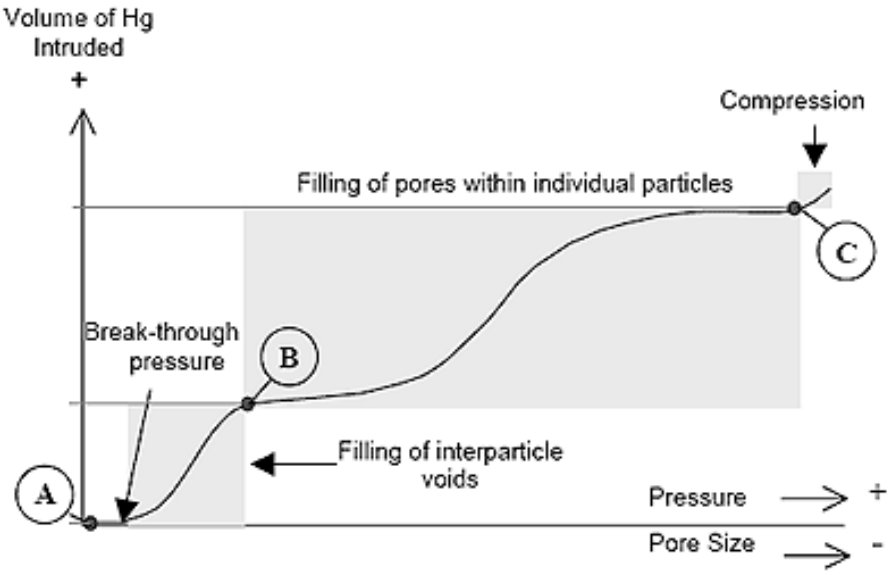


Figure 2-13: This graph shows typical data from a mercury porosimetry experiment [71]. As pressure increases, the increase in volume of mercury that infiltrates the sample will not be linear. The inflection points along the graph can be used to determine porosity and pore size distribution.

most cases of fouling deposit measurements because fouling deposit layers can be very thin, and it is therefore harder to separate them from the surfaces on which they grow. Using either the water displacement or gas expansion method without singling out the sample material is harder to carry out.

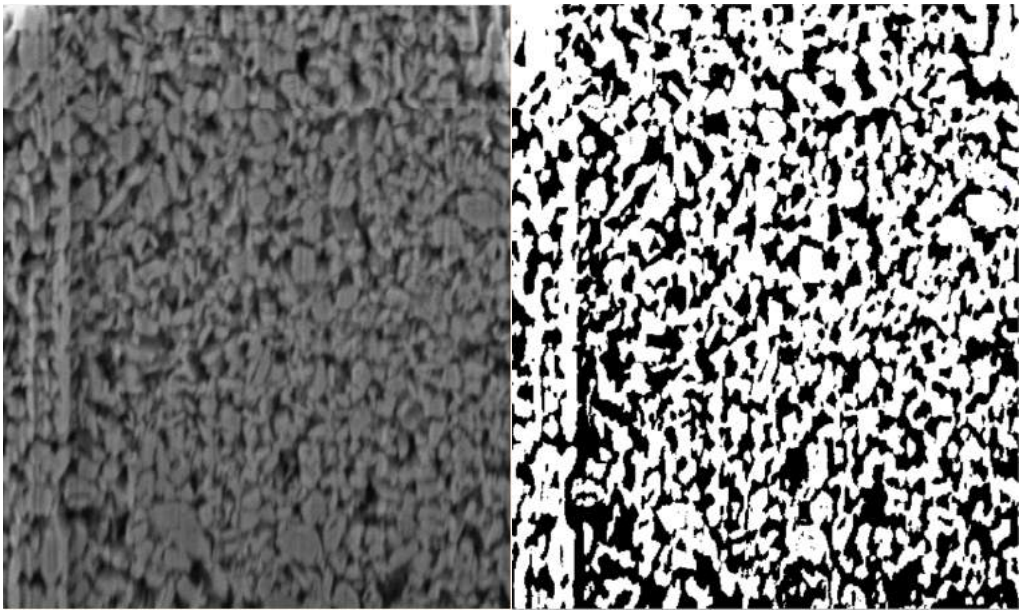

Figure 2-14: These two images show how an SEM image can be turned into a binary image where pores are represented by black pixel. The left image is the cross section SEM image of crud. The right image is the binary image of crud processed using an image processing algorithm. By counting the ratio of black pixel to all pixel, we can obtain the porosity of the material.

**Permeability** Porosity gives partial information about how fluid flows through a medium. The porosity parameter is blind to how the medium's structure is arranged. For example, a medium can have a large, straight tube-like structure in the direction of fluid flow that allows fluid to flow easily through it. Another medium can be composed of smaller tubes that coil around randomly leading to longer fluid paths. Both of these mediums described may have the same porosity if their volume composition ratio is the same, but obviously, fluid will not flow through them in the same way. The value that can better describe how fluid flows through a medium is its permeability. Figure 2-15 illustrates the above explanation. Both pictures have the same ratio of porous space to the whole volume, but water will will not flow very easily through the small channels of the right picture. Since permeability is the measure of how easily the fluid can flow or permeate through a material, the material on the right figure would have higher permeability than the left figure.

One way to calculate permeability is through the use of the fractal permeation model. The fractal dimensions can represent those missing pieces of information that porosity alone failed to describe. The fractal permeation model makes use of the fractal area dimension and the fractal tortuosity dimension to calculate the permeability. More details on the fractal permeation model are presented in section 2.3.5.

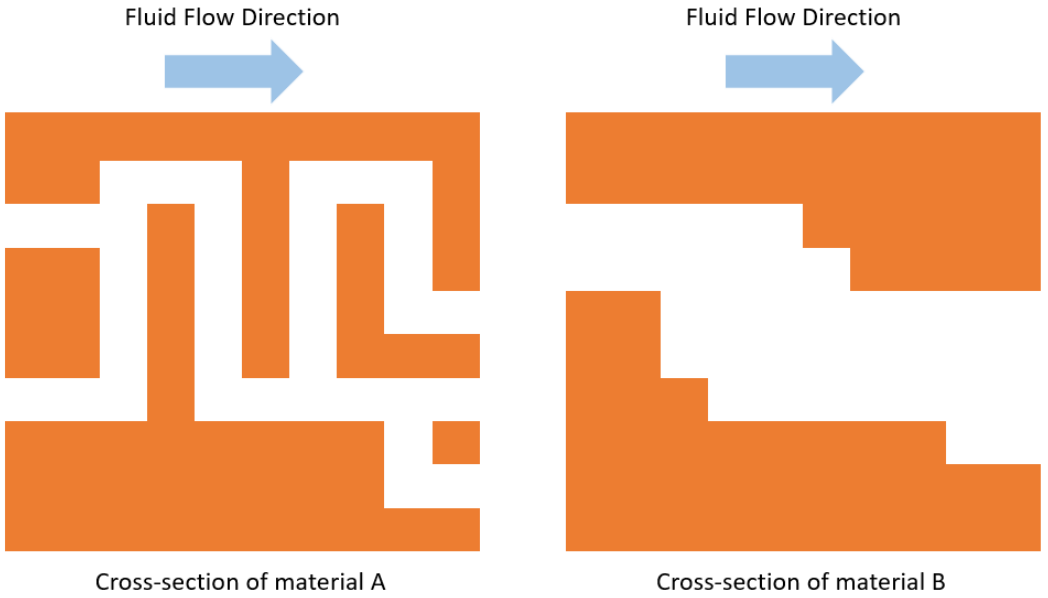


Figure 2-15: These schematics show cross sections of two materials with same porosity but different permeability. Smaller flow channels of the material A will generate more friction pressure drop. In addition, fluid has to flow through longer length in material A than in material B.

**Fractal tortuosity dimension** As explainted earlier, porosity alone isn't enough in characterizing the fluid flow. Tortuosity is the measure of how twisted the flow paths are within a porous material. The approach chosen to quantifying tortuosity in this thesis is through using fractal tortuosity di-

mensions. In our experiment, fractal tortuosity dimensions can be obtained through applying image processing techniques to scanning electron microscope (SEM) images. More detailed explanations of the fractal tortuosity dimension, and how they are obtained in our experiment, are offered in the section 2.3.6.

**Fractal area dimension** In addition to the fractal tortuosity dimension, the fractal area dimension is also needed for calculating permeability using the fractal permeability model. The fractal area dimension is the fractal dimension obtained from analyzing the cross-section image perpendicular to the flow. Other than using different images, the process of finding fractal area dimensions is the same as the process of finding the fractal tortuosity dimensions. Further details on the fractal area dimension can be found in the section 2.3.7.

**Pore size distribution** Some fouling deposit samples contain pores. These pores may come in different sizes depending on the type of fouling deposit and the environment in which fouling deposit grows. Pore size distribution is the plot with pore diameter on the x-axis plotted against the y-axis, which represents the number of pores that fall into the diameter or pore volume range. Pore size distribution can be useful in understanding the mechanism that governs the accumulation of the fouling deposits. Section 2.2.4.2 offers a more detailed explanation of pore size distribution specifically for crud.

**Thermal properties** Thermal resistance is very crucial parameter of fouling, especially for systems such as heat exchangers or nuclear reactors which requires low amounts of thermal resistance to work properly. However, in a more detailed study of fouling deposits, thermal resistance only may not be enough, and more thermal properties such as heat capacity, thermal expansion, and thermal stresses may be needed. Rigorous fouling deposit simulations such as MAMBA-BDM [7], are examples of usage that requires wider range of thermal properties than just thermal resistance.

**Fouling deposit composition** The composition of fouling deposits is very important in determining both the process at which fouling deposits grow and the effects that they might have on their host system. Fouling deposit composition varies widely depending on the type of fouling deposit and the system on which it grows. The composition could be living organisms such as barnacles and mussels, or non-living such as lime scale deposit. The composition can also be either organic compound, such as paraffin wax in the case of oil pipeline, or inorganic compound, such as nickel ferrite particles in the case of nuclear reactor. Section 2.2.4.2 offers a more detailed look at crud composition.

### 2.1.3 Effects of fouling deposits in heat transfer system

Fouling deposits usually cause adverse effects in the heat transfer system on which it accumulates. These adverse effects vary widely depending on the type of fouling deposits. Section 1.1.1.2 has already covered some examples of how fouling deposits affect chosen industries. Since most of those fouling, undesirable effects covered earlier are irrelevant to nuclear reactors, they will not be expanded upon this section. This section will focus, instead, on the effects of fouling deposits in heat transfer systems. Fouling deposits can degrade heat transfer and magnify the pressure drop across the heat transfer surface. The subsections that follows will go into details on how fouling deposits lead to the pressure drop and related heat transfer problems.

#### 2.1.3.1 Pressure drop

Pressure drop in fluid can be affected by a change in roughness or the reduction in flow area of the solid surface in contact with the fluid. Fouling deposits roughen the surface in contact with fluid flow, generating more pressure drop. Friction pressure drop in a cylindrical pipe system can be characterized by using the following Darcy-Weisbach equation [54]:

$$\Delta p = f_D \frac{L}{2} \frac{\rho V^2}{D} \tag{2.1}$$

where $\Delta p$, is the friction pressure drop across cylindrical pipe (Pa). $f_D$ is the friction factor. $L$ is the length of pipe (m). $\rho$ is the density of fluid ($kg/m^3$). D is the hydraulic diameter (m). Lastly, V is the velocity of fluid (m/s). The relationship between surface roughness and friction factor is shown in the following Nikuradze Diagram figure. The figure 2-16 shows that an increase in roughness will lead to an increase in the friction factor. Combined with the Darcy-Weisbach equation above, increasing the friction factor will directly increase the friction pressure drop. Therefore, the fouling deposit's rough surface will increase the friction pressure drop, which slows down fluid flow within the flow section. In addition, fouling deposits will take up flow space constricting the area which fluid can flow through. This constriction will have a direct effect on pressure drop as well.

Higher pressure drop is particularly a problem for these heat exchangers. For heat exchangers, pressure loss is actually considered to be a more severe problem than the loss of surface heat-transfer through fouling deposits. This is because pressure drop directly affects fluid velocity within the heat exchangers, and a change in fluid velocity has a large effect on the amount of heat removal. The pressure drop increase will also be more severe in smaller tubes of a heat exchanger. With smaller tubes, fouling deposit layers can take up a higher percentage of the flow areas, leading to a higher increase in pressure drop and a greater chance of clogging. Additional pumping or heating needed to counter this effect can be detrimental to the economics of the system [1].

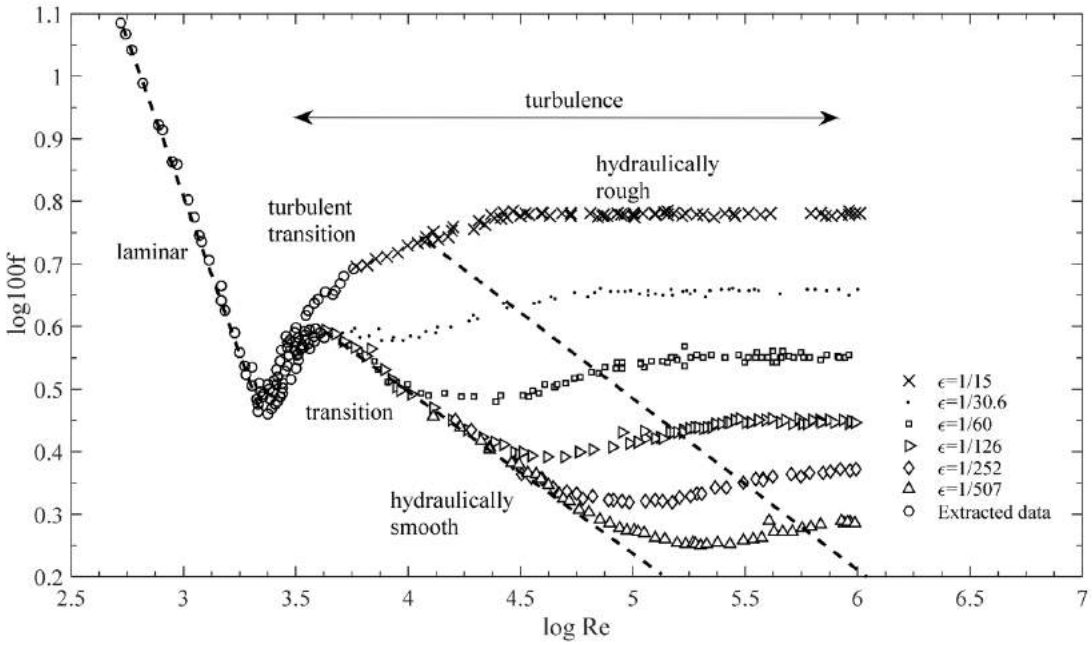


Figure 2-16: This Nikuradze Diagram shows the relationship between surface roughness and friction factor. The friction pressure drop is directly related to the friction factor. The diagram shows that as roughness increases, the friction factor also increases. This means that increasing the surface roughness will increase the friction pressure drop. Therefore, a fouling deposit's effect of roughening up the heat transfer surface can lead to higher friction pressure drop [73].

#### 2.1.3.2 Reduction in Heat Transfer Efficiency

Fouling deposits grow on the heat transfer surface that is in contact with the coolant water, which removes the heat from the heat transfer surface. Because the heat must now be conducted through fouling deposits before it can be removed with the coolant, the thermal resistance on the heat transfer surface will increase. Thermal conductivity of fouling deposit layers is also generally lower compare to the thermal conductivity of the heat transfer surface. Figure 2-17 shows that crud, especially a thicker layer, can lead to an increase in temperature [8]. The increases in temperature are most likely the result of decreased heat transfer in crud. This means that even though the fouling deposit layer is a lot thinner than the heat transfer surface layer, it can still cause significant thermal resistance. The worsened heat transfer could also lead to indirect negative effects. For example, in nuclear reactors, this worsened heat transfer causes heightened temperature on the fuel cladding which exacerbates problems such as corrosion and neutron flux imbalance. These issues will be explained in further details in the section 2.2.5 [1]. Other than this, higher temperature also means more boron compound precipitation due to inverse solubility.

In reality, crud's heat transfer behavior is not so simple as suggested by the Westinghouse's plot. If parameters, such as heat flux, were adjusted, the crud's heat transfer behavior shown in Westinghouse's plot might change completely. This complex coupling of variables is clearly demonstrated

in Jin/Short (2016) paper [44]. Further explanation of Jin/Short's findings are presented in section 2.2.6.1.

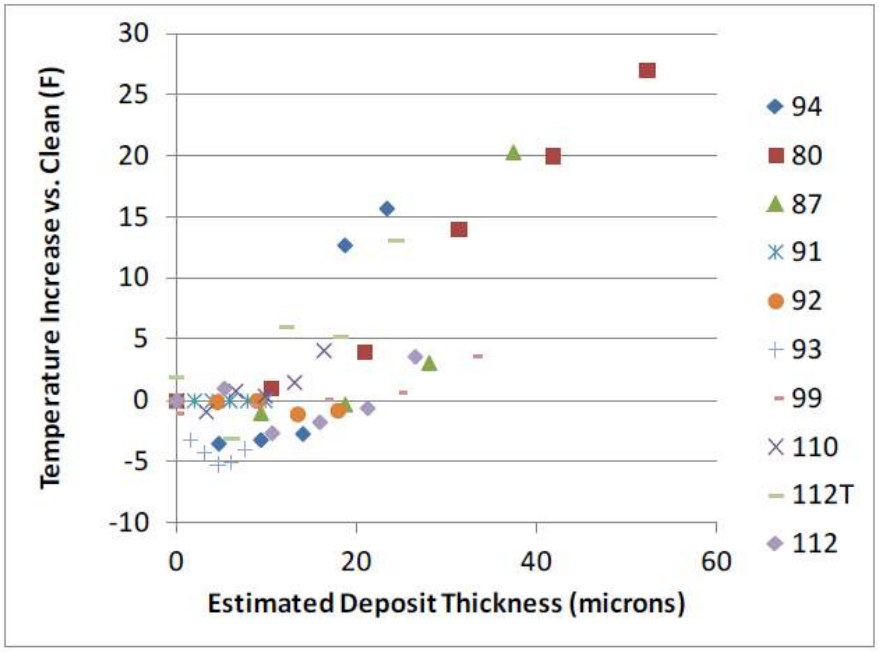


Figure 2-17: This figure summarizes the rod centerline temperature increase due to crud, in the Westinghouse's crud experiment. The difference in the rod centerline temperature between each crud-covered sample and a clean sample is plotted against estimated deposit thickness. The figure shows that crud, especially thicker ones, can lead to temperature increase by worsening heat transfer.

### 2.1.4 Fouling Deposit Mitigation Strategies in heat transfer system

Various methods have been developed to counter foulings in heat transfer systems. These methods can be classified into chemical methods and mechanical methods. Because the fouling deposit term covers a wide range of phenomenon as explained earlier, many of the fouling deposit mitigation methods are specific to only certain types of foulings. Nevertheless, they can serve as inspiration for how we may mitigate the type of fouling deposits relevant to us. The paragraphs below will give a quick overview of the fouling deposit mitigation methods that can be found in the literature.

**Chemical Methods** One way to achieve fouling mitigation is by adding special chemicals to a solution. Various ways that chemicals can be used to mitigate fouling include the use of sequestering agents, crystal modifiers and dispersants [74]:

- Sequestering agents can be used to dissolve away the fouling formations [74]. One example is the use of a hydrogen peroxide injection in PWR. Hydrogen peroxide is injected into the primary loop of PWR through CVCS, not long before an outage, to create an oxygen-rich

environment, thus allowing crud to detach and be removed through CVCS system [75]. Another example, also in the context of PWR, is the chemical cleaning process for a steam generator on the secondary loop [76]. The major ingredient that is used in the chemical cleaning process is hydrazine [76]. Hydrazine creates a reducing environment that dissolves away scale and sludge deposits. Although sequestering agent techniques are certainly useful as shown in these examples, they suffer from a limitation in that they usually modify the oxidation/reduction environment. Because of this, in PWR, they are either used before an outage or during outage cleaning.

- Crystal modifying agents, such as polycarboxylic acid, can be used to distort crystals. Distorted crystals have lower chance of settling on the heat transfer surface, and will therefore remain in the solution for longer [74]. Polycarboxylic acid is commonly used as industrial water scale inhibitor [77]. Its usage is widespread because it is efficient, easily prepared, and can be used in harsh environments. Crystal modifying agents are effective against calcium sulfate and calcium carbonate crystal [77]. However, their use in treating other types of crystals is still limited.

- Particulate fouling can be mitigated by chemical means using dispersant chemicals that reduce the surface tension of the deposits. Dispersant chemicals can help disintegrate colloidal particles into small fragments that do not settle easily on the heat transfer surfaces [74]. One example in the use of dispersant chemicals is for cleaning oil spills. Dispersants can be sprayed onto the surface of an oil slick to turn oil into small droplets that can mix with water. With regard to nuclear reactors, dispersants aren't widely used, most probably because of their organic nature. They will likely disintegrate in the harsh environment of nuclear reactors.

**Mechanical Methods** Mechanical methods of mitigating fouling deposits use physical means to break away fouling deposits. The list below presents some of the mechanical fouling mitigation methods found in the literatures:

- Mechanical or acoustic vibration on heat transfer surfaces can be used to break away fouling deposit layers. The advantage of this method of breaking away deposit is that it is less costly and does not require any significant upgrade to the reactor. The disadvantage, however, is that this method is more of a treatment than a cure or a prevention for crud problems, since it can only be done when the reactor is already shutdown. This means that a reactor operator will still have to deal with crud, but has a way of getting rid of it during a reactor shutdown, which happens about every one and a half years. Note that the acoustic vibration in the form of ultrasonic cleaning is already used in some PWR to clean up crud deposit, a form of particulate fouling [51].

- Another mechanical method of mitigating fouling deposits is the use of fluid shear stress at the heat transfer surfaces to break away the fouling deposits. For example, the fluid velocity can be increased to increase the shear stress, or the flow can be manipulated with a turbulence promoter so that the shear stress increases where deposits form [1]. The advantage of this method is that it can be done without any upgrade to the reactor. However, there are several disadvantages to this. First, increasing fluid flow will not always break away crud. Second, increasing the fluid velocity may exacerbate problems such as grid to rod fretting.

- In addition, temporary overheating can also be used to break up fouling deposits. In this method, heat transfer surfaces are heated to create enough thermal expansion on the heat transfer surface to break up the deposits [1]. The advantage of this method is that it does not require any upgrade. However, this is unlikely to be applicable to nuclear reactors, as heat flux cannot be easily controlled.

- Surface roughness also determines fouling deposit growth. Lowering the surface roughness decreases both the number of boiling nucleation sites and the adhesion of fouling deposit precursors to the surface. Theoretically, this method is interesting, but in application, crud grows more intensely anywhere there are defects [1]. Additionally, even if the initial fuel rod surfaces are polished, it is unlikely that they will stay smooth throughout operation with the harsh conditions inside nuclear reactors.

- Lastly, it is also possible to reduce the stickiness between the fouling deposit precursors and the heat transfer surface. This will prevent particles from sticking to the surface and forming into a fouling layer. This particular way of preventing the crud fouling deposit will be explored further in this thesis by experimenting with non-stick chemical surface modifications [78, 74, 1]. The disadvantage of this method is that the fuel rod coating will increase the fuel cost. The first advantage is that the coating can be deployed into the existing reactor fleet during routine fuel replacement without any upgrades to the existing reactors. The second advantage is that if this method works well, it will actually prevent the crud problem. This means that reactor operators will no longer have to worry about crud problems throughout reactor cycles.

## 2.2 Crud and Fouling in Nuclear Reactor Primary Circuits

Now that the background on general fouling deposits had been explained, this section will delve specifically into crud, which is one specific type of particulate fouling that grows on a nuclear reactor's fuel rods. The following subsections will explain what crud is, how crud grows, and how crud looks. Similar to the previous general fouling deposit section, more details about the parameters that are important in characterizing crud will be given. The effects of crud on nuclear systems will

also be discussed. Rather than repeat the topics that have been brought up in previously in our general fouling deposit section, the following subsections will attempt to narrow down topics that are specific to crud. Additionally, previous literature, on crud, as well as crud prevention strategies previously explored by others, will be discussed.

### 2.2.1 What is Crud?

Crud, or Chalk River unidentified deposits, is composed of layers of deposits from various chemical species present within the coolant of a light-water reactor (LWR). These chemical species are usually either corrosion products from various parts of the coolant circuit (especially the steam generator), or soluble boric acid added for controlling the reactivity in the reactor. These chemical species deposit at very low amount on parts of the fuel rods where boilings occur against the bulk coolant with a temperature lower than boiling point [79]. This boiling regime characterized by small bubbles and bulk coolant with a temperature lower than boiling point is called "sub-cooled boiling."

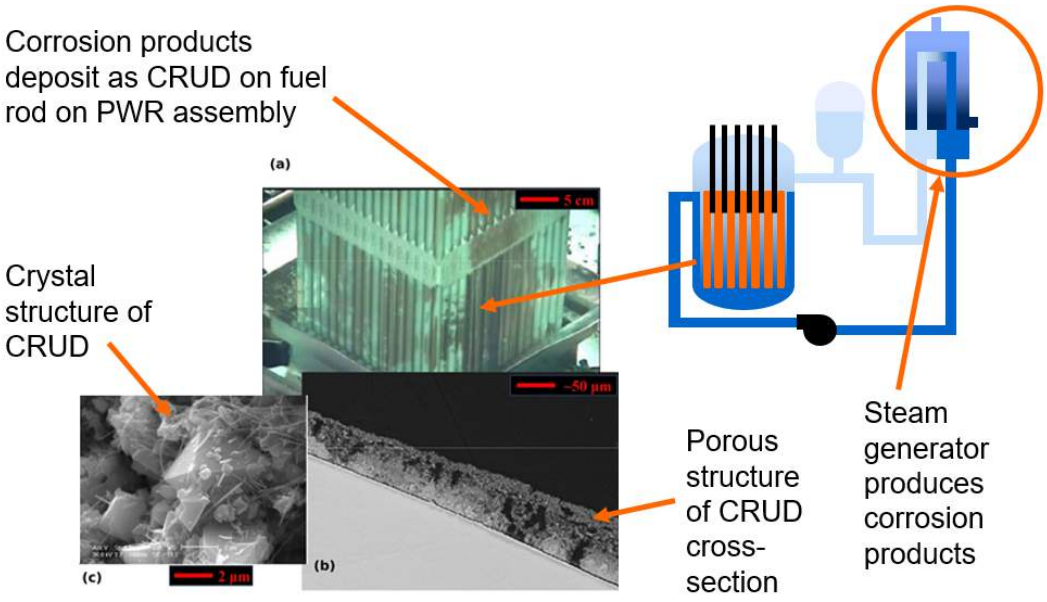


Figure 2-18: This figure shows images of crud at different magnifications. The right schematic is a diagram of the PWR's primary loop which includes the reactor. The arrow from the diagram going to the left shows that the fuel assembly image in (a) is taken from within the reactor vessel of the primary loop. The images marked by (a), (b), and (c) are the different stages of zoom for crud images. [7].

Awhile after a sub-cooled bubble is formed and grown at a nucleation site, the liquid layer separating the bubble and its substrate dries out. This causes corrosion particulates in the liquid layer to be deposited on the zirconium oxide substrate. Over time, these deposits grow into a crud layer. In PWRs, saturated nucleate boiling and film boiling on the fuel cladding surface are undesirable, and are suppressed through pressurizing the primary loop. The boron-10 isotope

in boric acid, intentionally added to PWR coolant, is used to control the reactor power level by absorbing neutrons. Subcooled boiling, which is allowed to occur on the hottest rods of the PWR core, can alter the localized concentration of the boron-10 isotope in the reactor through the process of selective distribution of the boric acid between the liquid and the gas phase [79]. As a result, subcooled boiling may cause a local change in the neutron flux and the power distribution with the high concentration of boron-10. Lithium hydroxide (LiOH) is another addition to the PWR coolant that counteracts the low pH induced by the addition of boric acid. Similar to boric acid, LiOH also concentrates on the boiling surface. LiOH is used to fix the pH within an optimal range (normally between 7.0-7.5) for minimizing the corrosion of pressure boundary materials [79]. Local changes in the LiOH concentration can therefore move the pH out of this range, and thereby accelerate corrosion.

### 2.2.2 Origins of Crud

This section will explain the origin of crud formations. It will cover the whole crud formation life cycle. The first subsection will cover the process whereby corrosion products from steam generator and reactor internals are released into the system as crud particles. The second subsection will explain how crud particles are transported to the reactor vessel, where they accumulate into a deposit, without getting filtered out. The last subsection will explain in detail how particles form into a crud layer on fuel cladding.

#### 2.2.2.1 Corrosion of reactor internals

The internal surfaces of a pressurized water reactor (PWR) are bound to corrode under the extreme conditions within the reactor. Of all the equipment in PWR, the steam generator is the origin of most crud particles or corrosion products. The steam generator has the most surface area in contact with reactor's coolant, as it consists of collections of coils of heat exchanger tubes, each with huge amount of surface area to volume ratio. More surface area leads to more places for corrosion, and therefore more crud particles. These crud particles or corrosion products get carried around the loop where some will deposit on reactor's fuel rods into crud layers. When steam generator replacement occurs, the corrosion product release is enhanced. This lead to more crud within the reactor core.

Several types alloys are used in the construction of PWR primary loop; some of these alloys can generate crud particles. PWR's primary loop is mostly composed of nickel-based alloys, stainless steel, and zirconium alloys. The following paragraphs describe alloy compositions, usage in PWR, and corrosion characteristics.

**Nickel-based Alloy** Nickel-based alloys, especially Alloy 600, are very commonly used in the construction of PWR primary loop. Table 2.1 shows the compositions of Alloy 600 and Alloy

690. Alloy 600 and 690 are nickel-chromium alloys with great corrosion resistance in a reducing environment. These alloys also maintains their properties up to temperatures in the range of 1000 $^{o}$C [80]. These properties make them ideal for their usage in heat exchangers. In PWR, Alloy 600 is most commonly used for steam generator tubings, general piping, pumps, and valves [81]. Because Alloy 600 is used in many components, especially steam generators, it is not surprising that a significant portion of crud precursor particles contain nickel. Table 2.2 shows that steam generator tubing, piping, pumps, and valves together already account for 73-90% of corroding surface. Because most of these equipment, especially the steam generator, is likely to be composed of alloy 600, the majority of crud-precursor corrosion products are likely to result from Alloy 600's corrosion. Alloy 690, on the other hand, can be used as a replacement of alloy 600 for reactor vessel head penetration nozzles [82]. This alloy exhibits better stress corrosion cracking properties than that of Alloy 600.

Several noteworthy studies has been done on nickel-based alloy's corrosion characteristics at PWR conditions. Carrette et al. [83] examined the corrosion scale mechanism for Alloy 690 with experimental oxide scale grown at PWR-condition for 2160 hours. They found that $NiFe_2O_4$ and $Cr_2O_3$ were the majority of oxides in the scale. Sennour (2008) [84] suggests that the oxide scale on Alloy 690 at PWR conditions may have a duplex structure as shown in figure 2-20. The right TEM image of figure 2-19 indicates that the top most part of oxide scale layer consists of separate particles. Although the internal oxide layer is not clearly shown in the TEM image, chemical analysis shown in the left graph of figure 2-19 clearly demonstrates this internal oxide layer. This chemical composition profile shows that at greater depth of around 140 to 200 nm, the composition matches that of Alloy 690 used for the test. As we get closer to the surface, we see the chromium-rich protective oxide layer (40 wt% Cr). This internal layer is shown in figure 2-19's TEM image to be compact and continuous. On the other hand, the external layer consists of scattered octahedral crystallites of a spinel oxide up to 100nm in size. Its composition is close to that of $NiFe_2O_4$. It is probably these particles that break lose from the surface to become crud particles in the coolant stream. The content and relative sizes of these particles certainly suggest so. Mossbauer spectroscopy examination of PWR crud samples, conducted by Sawicki (2010) [85], found that nickel ferrites ($NiFe_2O_4$) are predominant in crud.

| Alloys | Contents of different alloying elements/wt.% | | | | | | | | | | | |
|---|---|---|---|---|---|---|---|---|---|---|---|---|
| | Ni | Cr | Fe | C | Co | Mn | Al | Ti | Cu | Si | S | P |
| 600 | 72.80 | 15.80 | 9.60 | 0.06 | 0.01 | 0.82 | - | 0.20 | 0.01 | 0.31 | <0.001 | 0.008 |
| 690 | 59.31 | 29.20 | 9.94 | 0.018 | 0.014 | 0.31 | 0.13 | 0.27 | <0.002 | 0.27 | <0.0005 | 0.007 |
| Ni-30Cr | 69.15 | 30.35 | 0.25 | 0.002 | - | 0.02 | 0.06 | 0.04 | - | 0.1 | 0.0009 | - |

Table 2.1: Compositions by weight percent of typical Alloy 600 and Alloy 690 [86]. Ni-30Cr is an experimental alloy similar to Alloy 690 that was studied by Marchetti et. al.

| Component | Material | Fraction of Total Wetted Surface Area (%) | Fraction of Corroding Wetted Surface Area (%) |
|---|---|---|---|
| Piping, pumps, valves | Alloy 600 | 7-10 | 3-5 |
| Steam generator tubing | Alloy 600 | 50-65 | 70-85 |
| Steam generator Plenum | Carbon steel clad with Alloy 600 | 2-5 | 1-2 |
| Reactor fuel-rod | Zircaloy | 30-40 | N/A |
| Reactor vessel and internals | Alloy 600 or Carbon steel clad with Alloy 600 | 15-20 | 10-15 |

Table 2.2: This table, from Roy Castelli's book [81], demonstrates what materials are used at different parts of PWRs' primary loops. It is important to note that most reactor vessels are constructed using stainless steel, with rare cases of Alloy 600 [87]. The reason the Castelli chose Alloy 600 for this table is because it simplifies his later calculations.

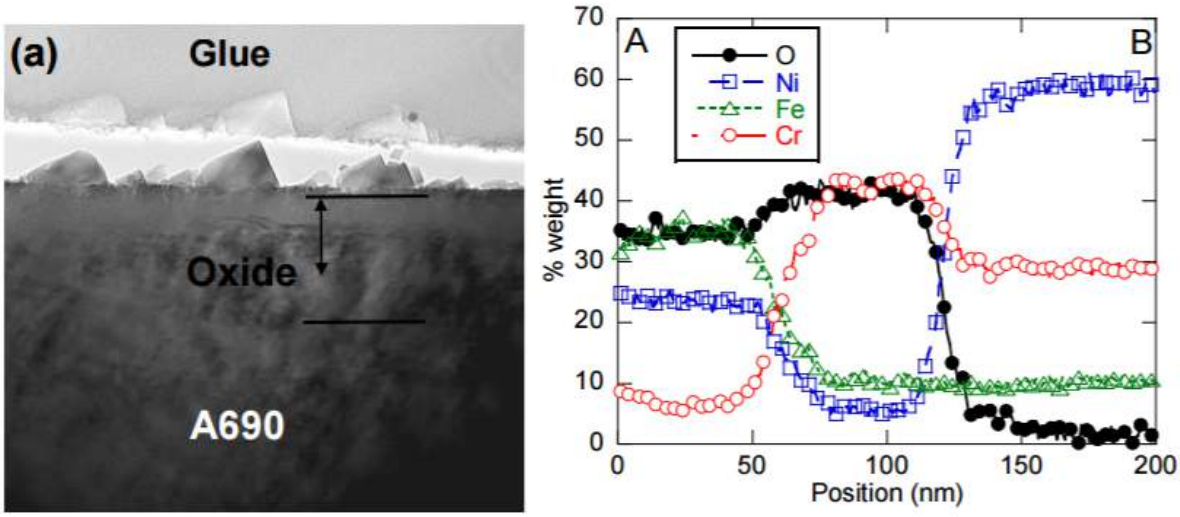


Figure 2-19: Sennour's examination of Alloy 690 [84] corroded for 858 hours at PWR conditions. The left image is the TEM cross-section analysis of the Alloy 690 sample and its oxide scale layer. The right graph gives the corresponding chemical analysis.

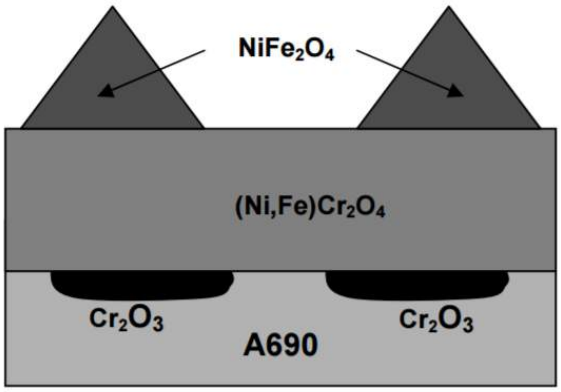


Figure 2-20: This schematics demonstrate the possible duplex structure of Alloy 600's oxide layer. [84].

**Stainless Steel Alloys** 304 and 316 stainless steel are most commonly used to construct the reactor-vessel internals [87]. Figure 2.3 shows the composition of 304 and 316 stainless steel. In general, 304 stainless steel are less expensive, but offers less corrosion resistance compare to its 316 counterpart. This is because 316 stainless steel contains 2 to 3 percent molybdenum as shown in figure 2.3. Molybdenum offers extra corrosion resistance especially against chloride.

Previous studies of stainless steel at PWR conditions such as that of Lister (1987) [88] and Terachi (2008) [89], suggest that stainless steel oxides also forms into two layers. The TEM cross-sectional image of 316 stainless steel oxide layer in figure 2-21 shows the compact, continuous inner oxide layer with high chromium content, and the outer layer composed of scattered iron oxide particles. Figure 2-22 shows the chemical composition of 316 stainless steel oxide film at different depths. The structure of a typical stainless steel oxide layer is summarized in figure 2-24's schematic. Similar to nickel alloy's case, the outer layer of magnetite ($Fe_3O_4$) and nickel ferrite ($NiFe_2O_4$) may detach from the surface to become crud precursor particles.

| Grade | | C | Mn | Si | P | S | Cr | Mo | Ni | N |
|---|---|---|---|---|---|---|---|---|---|---|
| 304 | Min. | - | - | - | - | - | 17.5 | - | 8.0 | - |
| | Max. | 0.07 | 2.0 | 0.75 | 0.045 | 0.03 | 19.5 | - | 10.5 | 0.10 |
| 304L | Min. | - | - | - | - | - | 17.5 | - | 8.0 | - |
| | Max. | 0.030 | 2.0 | 0.75 | 0.045 | 0.03 | 19.5 | - | 12.0 | 0.10 |

| Grade | | C | Mn | Si | P | S | Cr | Mo | Ni | N |
|---|---|---|---|---|---|---|---|---|---|---|
| 316 | Min. | - | - | - | - | - | 16.0 | 2.00 | 10.0 | - |
| | Max. | 0.08 | 2.0 | 0.75 | 0.045 | 0.030 | 18.0 | 3.00 | 14.0 | 0.10 |
| 316L | Min. | - | - | - | - | - | 16.0 | 2.00 | 10.0 | - |
| | Max. | 0.030 | 2.0 | 0.75 | 0.045 | 0.030 | 18.0 | 3.00 | 14.0 | 0.10 |

Table 2.3: This table shows the compositions of stainless steel 304 and 316 [90].

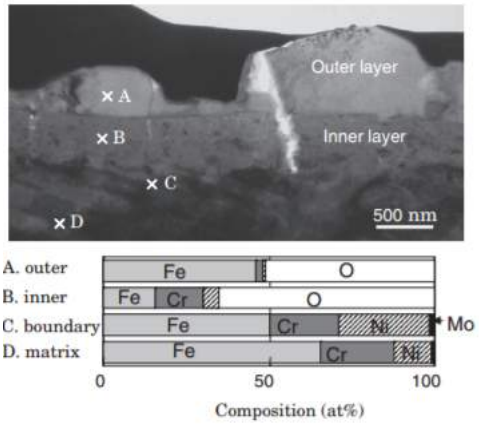


Figure 2-21: TEM image of the 316 stainless steel oxide layer and its composition at different depths. The compositions were obtained using TEM energy-dispersive X-ray spectroscopy (EDX). This oxide layer was grown at 320 ºC in water with 500 ppm boron, 2 ppm lithium, and 30 cc/kg-water of dissolved hydrogen [89].

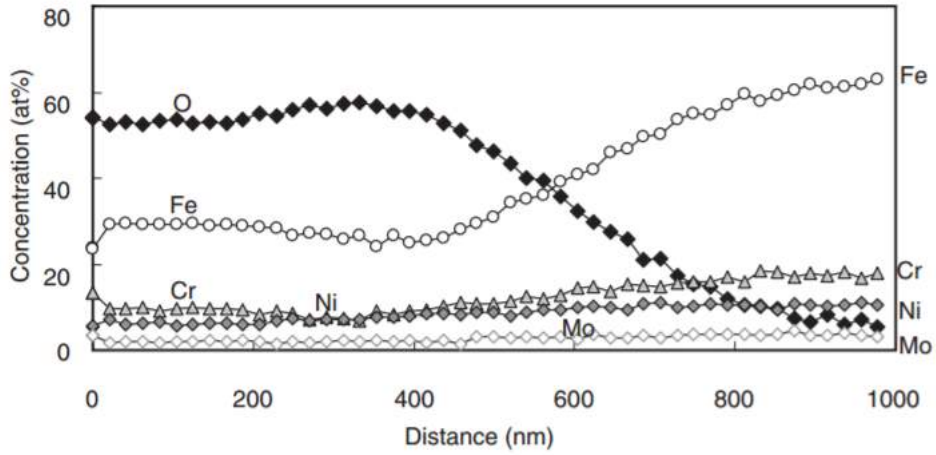


Figure 2-22: Composition depth profile of stainless steel 316 oxide films grown in experiments at 320 ºC for 380 hours. The measurement was done using Auger electron spectroscopy (AES) [89].

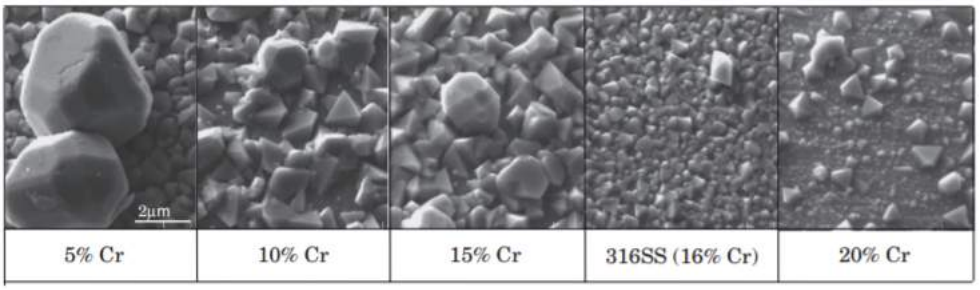


Figure 2-23: SEM images of oxide films, grown in experiments at 320 ºC for 380 hours. Each image shows a variation of 316 stainless steel with a different chromium composition [89].

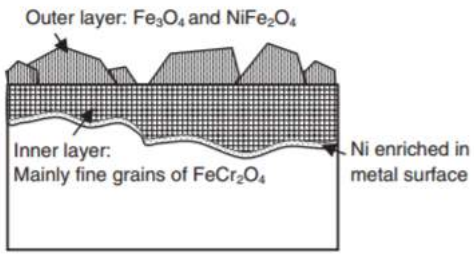


Figure 2-24: Schematic of stainless steel's oxide layer [89].

**Zirconium Alloys** Zirconium Alloys are used as fuel rod cladding in light water reactors (LWRs). Zirconium has a very low neutron capture cross section, making it ideal for cladding usages, as zirconium will not significantly suppress the neutron flux. Its surface also forms an oxide layer which protects it from further corrosion. Zirconium oxide do not play a significant role in crud growth as shown in the analysis of commercial PWR's crud by Sawicki (2010) [85] and Yeon (2010) [35].

#### 2.2.2.2 Mass transport in the primary circuit

The corrosion particles from the steam generator and pipes float around the PWR primary loop circuit, passing through the fuel assemblies in the reactor core. PWRs have the Chemical and Volume Control System (CVCS) that reduces corrosion particles to mitigate crud growth and reduces ions to mitigate corrosion processes. The dissolved ions are removed using mixed-bed ion exchangers. Larger particles are removed using filters. Unfortunately, most filters will only filter the corrosion particles down to 500nm in size [40], and ion exchangers will not remove things that are not dissolved. This leaves corrosion particles with sizes in between untouched by filters. Beyond this, O'Brien (2014), showed from the results of free energy calculations that nickel ferrites, the major corrosion particles, have a negative free energy for PWR conditions. This means that the corrosion particles are stable in the PWR condition and will not coagulate to form larger particles and be filtered out. O'Brien's calculations also show that the free energy of nickel ferrite is at minimum at around 50nm sized particle; then free energy increases as the particle size increase. This essentially means that we can expect lots of 50nm sized corrosion particle to be floating around. Floating corrosion particles move around the PWR primary loop until they eventually deposit on fuel rod surface as crud [40].

#### 2.2.2.3 Sub-cooled boiling and deposition

Although no one has actually observed crud growing in a PWR, to determine for certain how it is formed, the widely accepted theory is that it is formed by the dryout of liquid layer between the sub-cooled boiling bubbles and the boiling surface. As bubbles expand outward, the bulk of the bubbles expand faster than the base of the bubbles, leaving a liquid layer around the base of the

bubbles. The intense heat flux coming out of the PWR fuel rods quickly dries the layer of liquid out. This causes metal oxide particulates ($NiO$, $Fe_3O_4$, $NiFe_2O_4$) in the liquid layer to deposit on the zirconium cladding, via adsorption [91, 85].

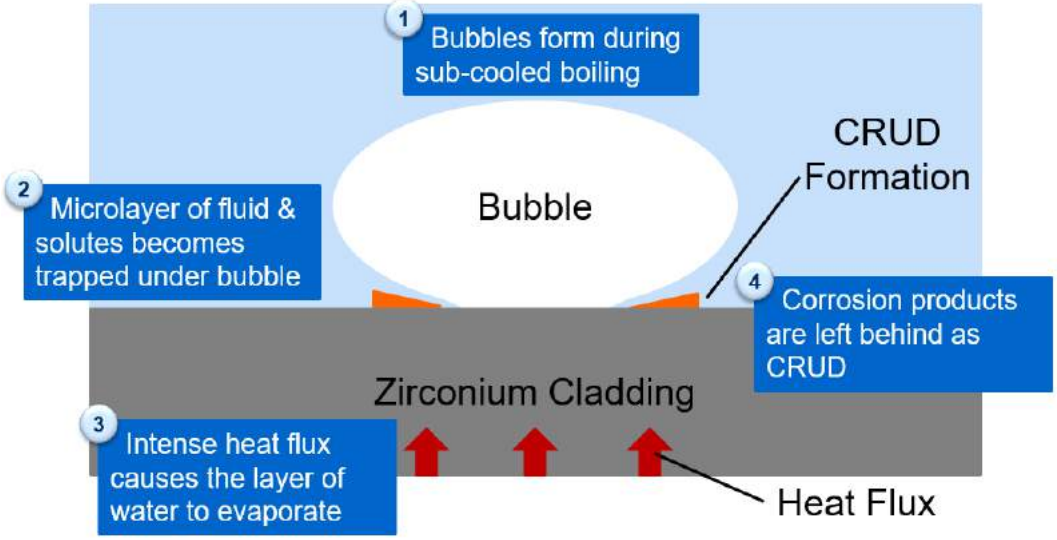


Figure 2-25: This figure shows the process of crud formation through sub-cooled boiling bubble as explained above.

There are many reasons to believe that crud deposition is likely caused by the sub-cooled boiling bubble's liquid layer dryout in PWR. One reason is that crud has ring-shaped deposition. Back before nuclear field was born, Partridge (1929), provided experimental evidence of ring-shaped boiling deposition which led to the theory of where there is a layer of water between the boiling surface and bubbles [92, 93]. Kobanov (1971) working in the nuclear field came up with similar theory about crud deposition through bubble formations [94, 93].

**Why allow boiling?**

There are many undesired consequences of boiling such as the formation of crud and the local concentration of chemical species such as boron-10 and LiOH. Nevertheless, most utilities still operate their PWRs with some sub-cooled boiling in the upper core region. In order to maximize the power output and reduce the fuel cost, the operators push the power profiles to their maximum limit, which is the point where there is limited sub-cooled boiling in the core. These issues become even more important with many utilities pushing the power of fuel assemblies beyond the original design levels for more efficient power generation [43].

The push for sub-cooled boiling is also driven by the increased heat transfer it offers. Figure 2-26, shows the plot of heat flux against temperature difference between the heated surface and water. From this graph and its label, we can see that boiling aids heat transfer until the point of

maximum heat flux. This is where film boiling occurs, where gas separates the heating surface from the water leading to immense lost of heat transfer. By pushing the reactor for sub-cooled boiling, reactor operators can exploit the enhanced heat transfer offered by the nucleate boiling regime.

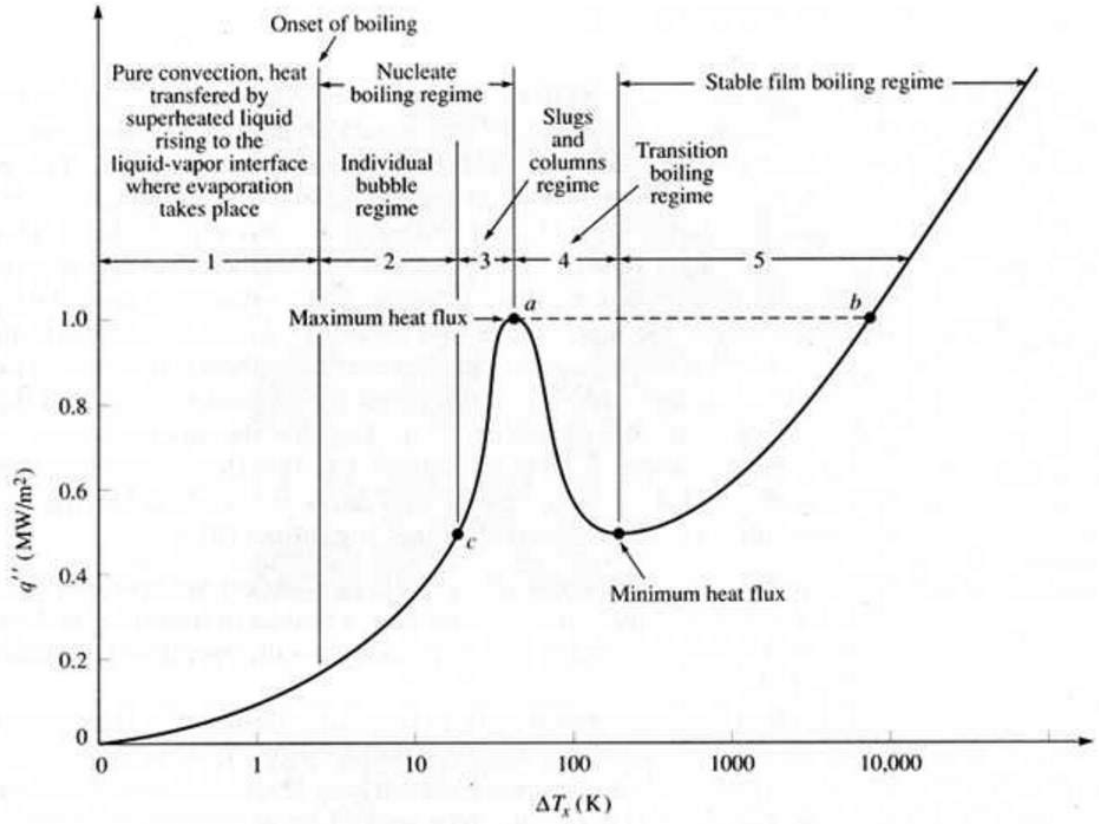


Figure 2-26: This is a plot of heat flux against temperature difference between the heated surface and water. The labels shows different boiling regimes. [95].

**What is sub-cooled boiling?**

The power in a PWR is maintained at levels that minimize sub-cooled boiling. Sub-cooled boiling can occur when the cladding temperature is slightly above the boiling point of water. At this point, the bulk coolant temperature will still remain below the boiling point [36]. In sub-cooled boiling, steam bubbles are formed on the surface of the cladding, but collapse as they travel into the the colder bulk coolant. Typically, the bubbles in PWRs are tiny in the range of micron because of the immense pressure in PWRs.

**Deposition of crud**

As mentioned above, once the boiling bubble's liquid layer dry out, crud particles deposit onto the surface. It should be noted as well that crud could form without boiling as well, although more

slowly [96]. The theoretical reason as to why the crud formation is faster with sub-cooled boiling may lie in the nature of surface energy. Surface energy grows very quickly as crud particles approach the surface. This means that the crud particles that are not close enough to the cladding surface will feel almost no surface force at all. Normal flow of liquid rarely gives particle a chance to get very close to the surface. However, with the presence of the boiling liquid layer, crud particles can get deposited close enough to the surface so that the surface force becomes significant enough to retain the crud particles at the surface. Other than this, the adhesion force in water is very low due to the Hamaker constant having a fluid (n=1.33) in between the crud particles and the cladding. However, when this microlayer of fluid dries out, that Hamaker constant should increase drastically due to fluid disappearing. A higher Hamaker constant will lead to a higher van der Waals force and stronger attraction of crud particles to the cladding surface. These reasonings are better explained in the section 2.4.2 about the Hamaker constant.

### 2.2.3 Characteristics of Crud

Now that we have explained what crud is and how it is formed, this section will delve into the unique characteristics of crud. It will provide illustrations as well as summaries of previous studies of commercial reactors' crud as well as crud grown in labs. The characteristics of crud, such as its porous structure and boiling chimneys, will be shown with actual images. Characteristics that will be reviewed include its look, its structure, and its composition.

#### 2.2.3.1 Examples of crud in PWR

In order to give a good picture of what commercial PWR's crud looks like, this section will present several figures of real crud samples examined in papers and reports. The left figure 2-27 shows crud deposits in macro scale. The row of cylinders in the picture represent fuel rods in the Three Mile Island One (TMI-1) nuclear reactor. The dirty patches are crud deposits grown on the fuel rods. The right figure 2-28 is a more zoomed-in image of how crud looks from a top-down angle. The pores are vapor chimneys, which can be found in many crud samples. The last figure 2-28 represents a very close zoom of crud's cross-section. Note its porous structure, as well as the long channels that represent boiling chimneys.

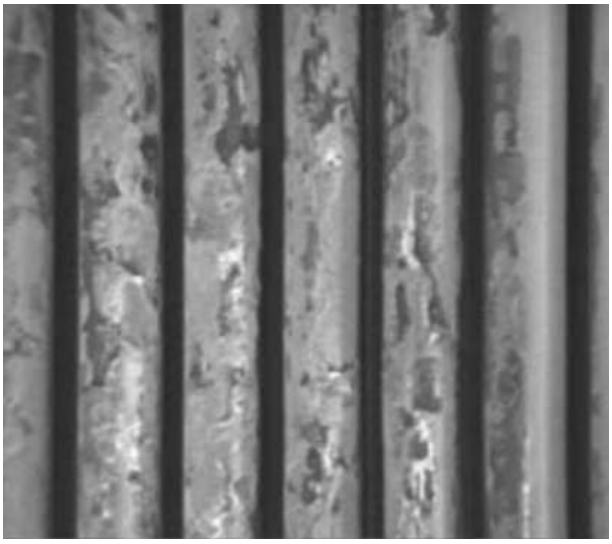

Figure 2-27: This picture shows the crud pattern in the TMI (Three Mile Island) fuel assumbly. The distinctive crud pattern of failed fuel rods at TMI-1 reactor was characterized by a mottled appearance with dark surfaces and a jagged patches of white [42].

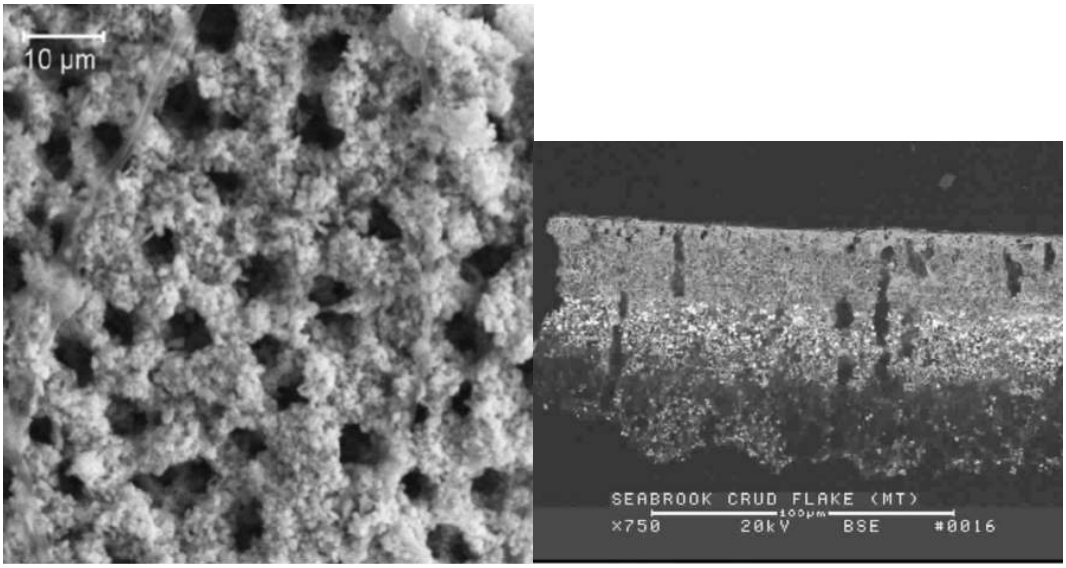


Figure 2-28: The left picture shows the top down view of a crud layer on the SEM (scanning electron microscope). The black spots are boiling chimneys where vapor bubbles exit crud layer [97]. The right picture shows the cross-section view of a crud sample from the Seabrook nuclear reactor. It can be seen here that crud is quite porous. The long channels going upward are most likely the boiling chimneys [97].

#### 2.2.3.2 Structure

Crud's structure is porous since it is composed of oxide particles sticking together with pores between them. In many cases, boiling chimneys distributed evenly all throughout crud can also be seen. They are composed of an agglomeration of crud particles sticking together into a layer. Yeon reported the porosity to be 60% for the crud from the Korean reactor that he studied. The boiling chimneys are believed to be the nucleation site where bubbles are ejected. Westinghouse's report shows crud's chimney diameter distribution, chimney density ($\#/m^2$), and chimney area (%), for each experimental trials. The crud chimney density range from $3.3 \times 10^8$to $7.8 \times 10^9$ $\#/m^2$. The chimney areas for different experimental trials range from 0.3% to 8.5% of the total surface area [8]. The following figure 2-29 is a graph of the median chimney diameter to crud thickness published by Westinghouse's WALT loop project [8]. Each data point represents a crud sample. The median chimney diameter ranges from being as low as only one micron to as high as ten microns. As the crud thickness increases, the median chimney diameter increases as well. These numbers and figure indicate that depending on the very exact condition at which crud is grown; its structure can vary quite a bit.

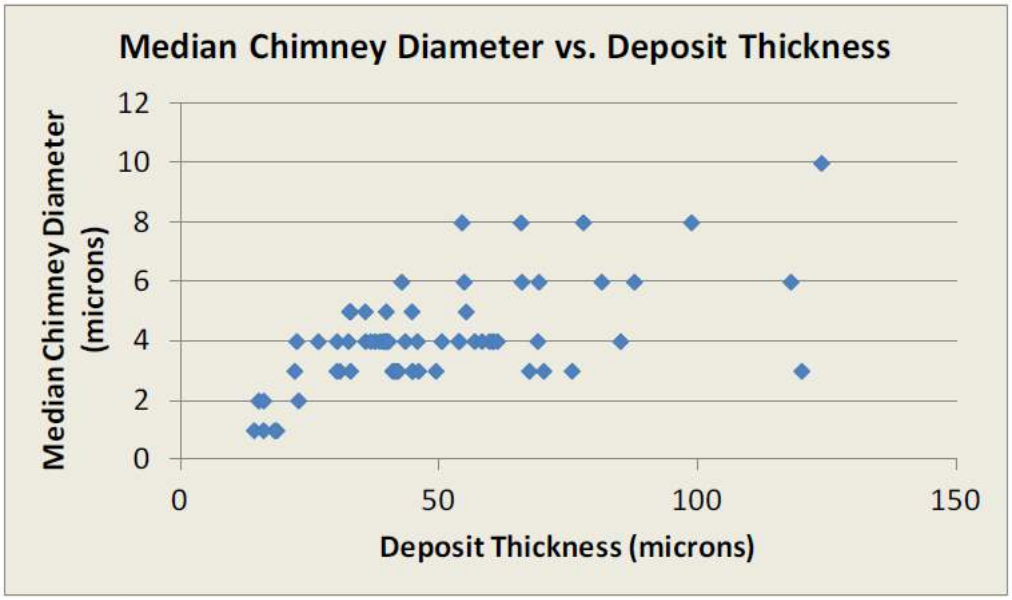


Figure 2-29: This figure shows the relationship between crud's median diameter and deposit thickness. This graph is derived from Westinghouse's data [8]. Each data point represents a crud sample.

The characteristics that are present in real reactors' crud and crud grown through experiments such as that of WALT (Westinghouse Advanced Loop Tester) loop, are shown to be quite similar. The following subsections showcase selected images from several studies that give interesting insights

into physical characteristics of crud.

**Jei-Won Yeon 2010** The 2010 study by Jei-Won Yeon, aimed to characterize the chemical composition of crud, also yielded useful SEM images that clearly show the general porous structure and boiling chimney in crud. In following figures 2-30, the zoomed in octaheral feature of crud on the top left figure shows that crud is composed of oxide particles sticking together. The "soft" crud picture on top right in following figure shows the darker area holes which are probably crud boiling chimneys [35]. Another important point to note, beyond crud's general structure, is that the "hard" crud shown in the bottom-left figure has no chimney. Since these images are taken from commercial reactor's crud, they provide a good evidence that not all crud will exhibit chimney structure.

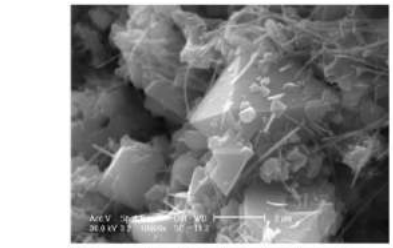

| Element | Cr | Mn | Fe | Ni | Zr | Total |
|---|---|---|---|---|---|---|
| At % | 0.72 | 1.95 | 46.07 | 25.91 | 25.35 | 100 |

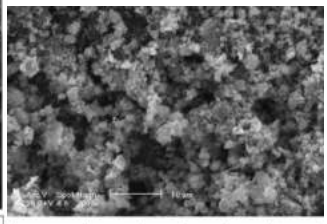

| Element | Fe | Ni | Cr | Zn | Total |
|---|---|---|---|---|---|
| Atomic % | 55.3 | 36.8 | 5.5 | 2.4 | 100 |

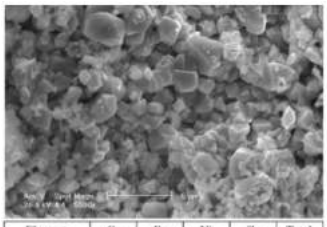

| Element | Cr | Fe | Ni | Zr | Total |
|---|---|---|---|---|---|
| Atomic % | 0.73 | 2.88 | 3.02 | 89.16 | 100 |

Table 2.
Elemental analysis data of the soft and hard cruds measured by ICP–AES. Unit is wt.%.

| Crud | Element | | | | | | | |
|---|---|---|---|---|---|---|---|---|
| | Co | Cr | Fe | Mn | Ni | Zn | Zr | Total |
| Soft | 0.0 | 8.3 | 29.1 | 0.0 | 60.6 | 0.6 | 1.4 | 100 |
| Hard 1 | 0.2 | 9.1 | 71.4 | 1.5 | 11.3 | 4.7 | 1.8 | 100 |
| Hard 2 | 0.1 | 9.3 | 61.7 | 0.5 | 5.5 | 22.3 | 0.6 | 100 |

Figure 2-30: This collection of figures exhibit the summary of Jei-Won Yeon's findings for structure and chemical composition of crud from PWR. The top-left picture shows the zoomed-in octahedral structure of crud crystals composed mostly of iron and nickel, surrounded by needle-like structures composed of nickel oxides. The top-right picture shows the SEM photo of soft crud and its elemental compositions. The bottom-left picture shows the SEM photo of hard crud and its elemental compositions. Lastly, the bottom figure shows table 2 from Yeon's paper summarizing his findings on the elemental composition of crud [35].

**Westinghouse's WALT loop 2008** The Westinghouse Advanced Loop Tester or WALT loop was used to simulate crud growth in the PWR conditions, and able to grow crud formation comparable to that of commercial PWRs. The report Westinghouse Advanced Loop Tester Update 2008, by G. Wang showcases both the picture of crud from PWRs and the picture of crud grown by WALT loop [8, 96]. These pictures are represented in the figure 2-32. Among the published results known to

us, WALT loop's crud growth test produced synthetic crud that has closest resemblance to reactor crud. In a later technical report published in 2011, Wang et. al. also shows some pictures such as figure 2-33 and figure 2-34. Those pictures in the 2011 technical report clearly show crud's porous and boiling chimney structures.

Another interesting finding is that the crud on a low heat flux, non-boiling surface is 14% lower than those on the boiling surfaces [8]. The crud in hot-spot boiling regions also exhitbits a more porous structure with channels that likely vent steam out of crud. On the other hand, the crud in the non-sub-cooled boiling portion of the rod does not have any visible channels within crud. Figure 2-31 shows this sub-cooled boiling vs non-sub-cooled boiling crud difference phenomenon.

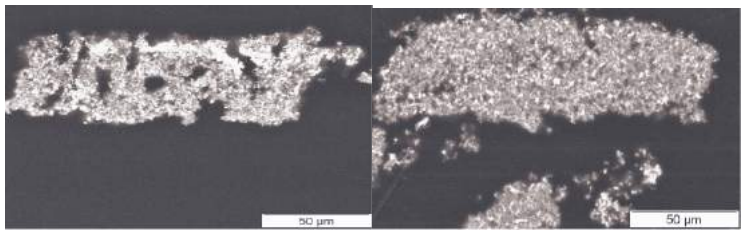


Figure 2-31: These two pictures shows cross section of crud obtained from the WALT loop. The left picture is from the crud sample taken from the hot spot on the heater rod with subcooled boiling. The right picture is taken from the crud sample in a non-boiling area. The left picture shows holes going through the crud that are boiling chimneys [8].

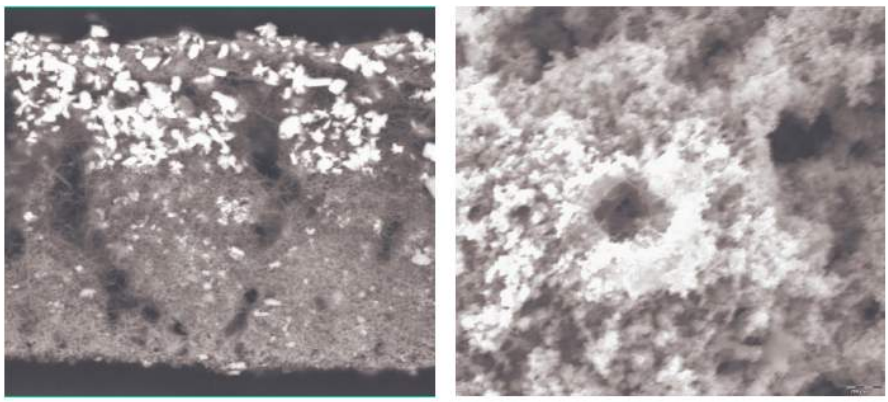

Figure 2-32: Westinghouse WALT loop 2008 report shows a comparison between actual reactor's crud and crud grown in WALT loop. The left picture shows the flaky structure of thick crud from the actual PWR that formed during AOA (axial offset anamoly). The right picture shows crud formation from the WALT loop. Both crud formations exhibit crud's porous characteristic [96].

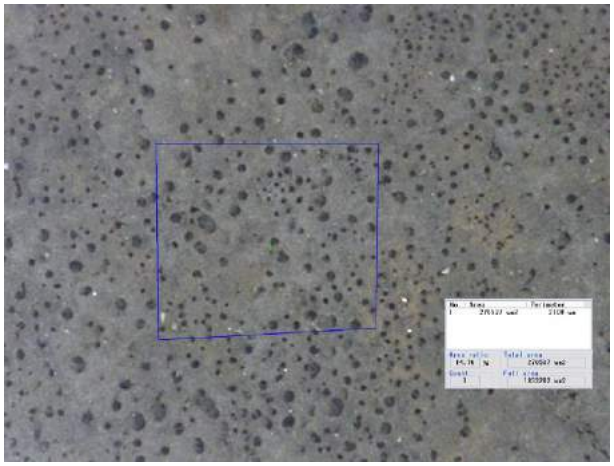

Figure 2-33: Top down view on crud formation grown in the WALT loop as shown in this figure shows its boiling chimney structure. This is obtained from technical report published by Wang on the WALT loop results in 2011 [8]. Scale bars not provided.

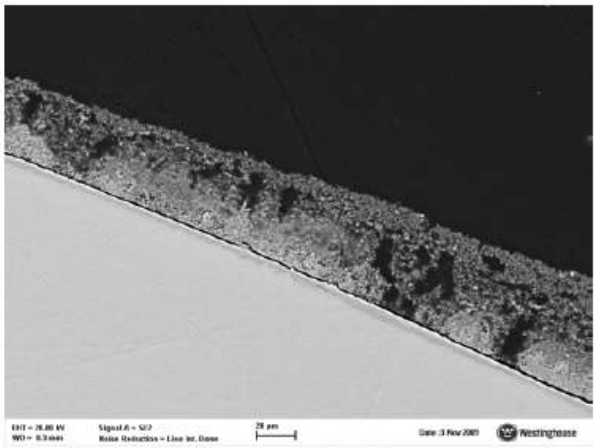

**TC2**

| Deposit (μm) | | ZrO2 | Porosity (%) | | Ni/Fe | |
|---|---|---|---|---|---|---|
| Total | Inner | (μm) | Total | Outer | Total | Outer |
| 54 | 27 | 4.4 | 60 | 76 | | |

Figure 2-34: Cross-section view on crud formation grown in the WALT loop as shown in this figure shows its porous structure. Similar to previous figure, this is obtained from the WALT loop report in 2011 [8].

#### 2.2.3.3 Composition

Although an actual crud deposit in the PWR is harder to obtain and analyze because of its radioactivity, there are still multiple analyses outlining the chemical composition of crud formation in the

PWR carried out in the past by various groups [35]. The general agreement is that crud is composed of iron or nickel combined in different forms [35, 91]. This section outlines some of the findings by different groups.

**Jei-Won Yeon 2010** The principle elements of crud layer were identified as nickel and iron by SEM (scanning electron microscope) and EPMA (electron probe micro-analysis) carried out by Jei-Won Yeon et. al. According to this analysis, crud composition will various depending on the different types of crud observed. For crud with octahedral crystal structure, the stoichiometric ratio of iron to nickel is approximately 2. The elemental analysis carried out can be used to deduce that the this type of crud is composed of NiO and $NiFe_2O_4$. Zirconium oxide crud fragments of 10-50 micrometers diameter were also observed in the crud samples [35]. These zirconium oxides fragments could originate from grid to rod fretting (GTRF). The previous figure 2-30 from Jei-Won Yeon summarizes his findings on the chemical composition of crud.

**J.A. Sawicki 2010** J.A. Sawicki carried out an analysis of crud deposits on PWR fuel rods that occurred from unexpected power shifts, using MossBauer spectroscopy. The analysis done on fuel crud scrapes found that the predominant species in crud is nickel-iron ferrite $Ni_xFe_{3-x}O_4$with a composition range $0.6 < x < 0.8$. Sawicki notes that this is markedly higher than the composition of $0.3 < x < 0.6$ found in PWR on low boiling duty [85].

### 2.2.4 Important Parameters of Crud Deposits

The previous section explains the characteristics of crud from commercial reactors or experiments that closely resembles the commercial reactors. This section will focus on the parameters that we might be able to obtain from this thesis' experiment. There are several parameters that are useful in analyzing crud. Many of them are inherited from general fouling deposit parameters. This section elaborates how the general fouling deposit parameters can be applied to crud, as well as expands the list of parameters with new crud-specific and experiment-specific parameters.

#### 2.2.4.1 Macroscopic Parameters

This section will explain the macroscopic parameters that are useful for characterizing crud formation, including the crud growth versus time, thermal resistance, and pressure drop change. Many of these parameters are general parameters that appears in other fouling deposits as well. For more general details of what these parameters represent, visit the previous section 2.1.2.1. The following paragraphs will dive deeper into how these macroscopic parameters might be measured in crud, as well as previous studies of crud that included these parameters.

**Growth (Thickness) vs. Time** Similar to other types of fouling deposits, crud growth vs time is also an important parameter. However unlike most fouling deposit, real reactor crud grows at extreme conditions and is therefore very hard to observe in-situ. The length of crud's growth time and the difficulty in observing crud in-situ makes it very hard to conduct crud growth vs. time experiment at close to PWR conditions. However, even crud experiments with conditions not close to that of commercial reactors can give insights into how commercial reactor crud might grow. In figure 2-35, the crud growth in terms of mass per area is plotted against time used to deposit. Notice that the time it takes form a deposit is in the range of hours; this is likely due to the use of metal ions to grow crud as opposed to suspended particles. Commercial nuclear reactor crud is composed mostly of suspended particles, since a significant amount of metal ions are removed using mixed-bed ion exchanger [40, 35].

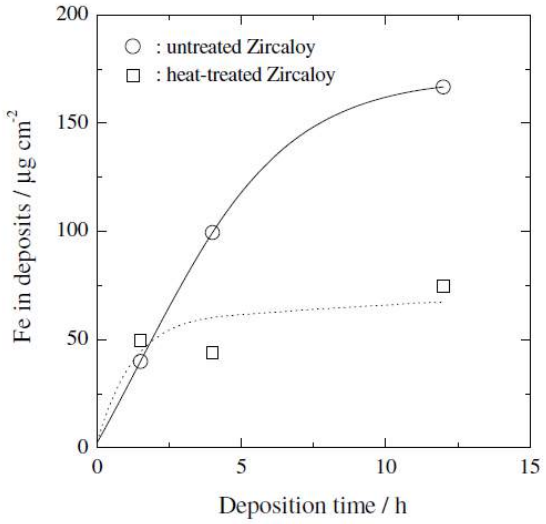


Figure 2-35: This graph from Jei-Won Yeon's paper shows crud deposition amounts in the unit of micro-gram per square centimeter plotted with the deposition time in hours. This graph was obtained from crud grown on an experimental loop that has the temperature of 215 Celsius, the pressure of 34 bars. Ion deposition is used instead of suspended particles deposition. Although the conditions do not match that of PWRs, it still give us an insight into what crud growth might look like [98]. Note that the graph also shows that heat-treated Zircaloy has an effect on crud growth; however, it has not yet been explained why that might be the case.

**Thermal resistance** Crud, just like any other fouling deposit, can increase the thermal resistance on the heat transfer surface on which it grows. The changes in the thermal resistance through the fuel rod cladding by crud is a huge concern for the nuclear industry. A lowered thermal resistance can lead to a higher temperature on the fuel rods as well as a less efficient heat transfer. Because

of this, the thermal resistance in crud was already widely studied by the nuclear industry, including the Westinghouse reports. Therefore, it will not be the main focus of the experiment. However, the determination of fractal properties of crud done in this thesis is particularly useful for determining heat transfer properties at micro level.

The MAMBA-BDM model paper [7] presents an approach to determining the thermal conductivity of crud that also utilizes fractal properties of crud. In this model, crud is separated into its solid and water parts. The solid part's overall thermal conductivity is defined as a volume-fraction average of individual components' thermal conductivities. Water's thermal conductivity is determined using the correlation:

$$k_f = 0.686 + 7.3 \times 10^{-10} P + 5.87 \times 10^{-6} (T - 415)^2 \tag{2.2}$$

where $k_f$ is the water's thermal conductivity; $P$ is the pressure in Pa; and $T$ is the temperature in degrees Kelvin. In crud or any multiple material medium, thermal conductivity will have contributions from both parallel and series conductance. A better way to understand parallel and series thermal conductance is to examine them in terms of parallel and series thermal resistance. In figure 2-36, the top diagram shows a system of two adjacent materials. When heat conducts from left edge at temperature $T_L$ to right edge at temperature $T_R$, it will have to go through material 1, then material 2, respectively. Therefore, heat flux going through both material 1 and 2 will face a total thermal resistance that is the sum of thermal resistance of both materials, similar to how electrical resistance work. In figure 2-36, the bottom diagram shows another system that illustrates the analogy between the parallel thermal resistance and the parallel electrical resistance. In crud, the interfaces between fluid and solid have very complex shapes. However, these complex interfaces, when zoomed in, are merely a combination of these simple parallel/series thermal resistance systems. Therefore, the overall thermal resistance can be modeled as a combination of series and parallel thermal resistance as follows [7]:

$$R_{CRUD} = \xi R_{series} + (1 - \xi) R_{parallel} \tag{2.3}$$

where $R_{CRUD}$ is the overall thermal resistance of crud; $R_{series}$ is the series thermal resistance; $R_{parallel}$ is the parallel thermal resistance; and $\xi$ is the parameter that defines how series/parallel character of crud combines. $\xi = 0$ refers to a system with all capillaries in the direction of flow, while $\xi = 1$ refers to a system with all capillaries in the direction perpendicular to flow. $R_{series}$ can be defined in the same way as its corresponding electrical resistance as follows [7]:

$$R_{series} = \varepsilon R_f + (1 - \varepsilon) R_s \tag{2.4}$$

where $R_f$ represents the fluid thermal resistance; $R_s$ represents the fluid thermal resistance; and $\varepsilon$

represents spatially dependence crud porosity. If we put the above equation in terms of conductivity instead, we get the following [7]:

$$k_{series} = \frac{1}{\frac{\varepsilon}{k_f} + \frac{1-\varepsilon}{k_s}} \tag{2.5}$$

where $k_{series}$ is the series thermal conductivity; $k_f$ represents the fluid thermal conductivity; and $k_s$ represents the fluid thermal resistance. Fractal properties can be used to help calculate the parallel thermal resistance/conductivity. In this case, the parallel thermal resistance/conductivity system is easier to characterize in terms of conductivity. The parallel thermal conductivity can be defined as follows, in the case that crud is assumed to have a spatially uniform microstructure [7]:

$$k_{parallel} = \frac{(2-D_f)\varepsilon\lambda_{max}^{D_T-1}[1-(\frac{\lambda_{min}}{\lambda_{max}})^{D_T-D_f+1}]}{t_{CRUD}^{D_T-1}(D_T-D_f+1)[1-(\frac{\lambda_{min}}{\lambda_{max}})^{2-D_f}]}k_f + (1-\varepsilon)k_s \tag{2.6}$$

where $k_{parallel}$ is the parallel thermal conductivity; $D_f$ is the area fractal dimension; $D_T$ is the tortuosity fractal dimension; $\lambda_{min}$ and $\lambda_{max}$ are the minimum and maximum crud pore size, respectively. In the end, the final value that we are trying to obtain is the overall crud thermal conductivity. The equation for overall crud thermal resistance, shown earlier, can be converted to its conductivity form as follows:

$$k_{CRUD} = \frac{1}{\frac{\xi}{k_{series}} + \frac{1-\xi}{k_{parallel}}} \tag{2.7}$$

where $k_{CRUD}$ is the overall thermal conductivity of crud. At this point we have a complete set of equations that can be used to calculate crud thermal conductivity with the help of fractal properties. This calculation of overall thermal conductivity, used in MAMBA-BDM, utilizes fractal dimensions $D_f$ and $D_T$. The assumptions were made for both values at the time when Short's (2013) paper was written. This thesis followed up to verify that those assumptions were valid.

Thermal resistance within crud has been studied extensively in the Westinghouse's WALT loop. One interesting WALT loop plot that gives insights into the behavior of crud's effective thermal conductivity is figure 2-37. This is a plot resulting from experiments on effective crud thermal conductivity versus heat flux. There is a weak relationship between effective thermal conductivity and heat flux. As heat flux increases, the effective thermal conductivity also increases slightly.There appears to be no real trend between the effective thermal conductivity and crud thickness. Figure 2-38 is a table showing the results for each of the test trials. Only the non-boiling cases were selected for this table. Although there are very few data points, we can still infer from those available that larger crud boiling chimney correlates with higher effective thermal conductivity. Crud density varies very little among non-boiling crud samples and does not seem to correlate in anyway with the effective thermal conductivity. Porosity, too, appears to have no effect on the effective crud thermal

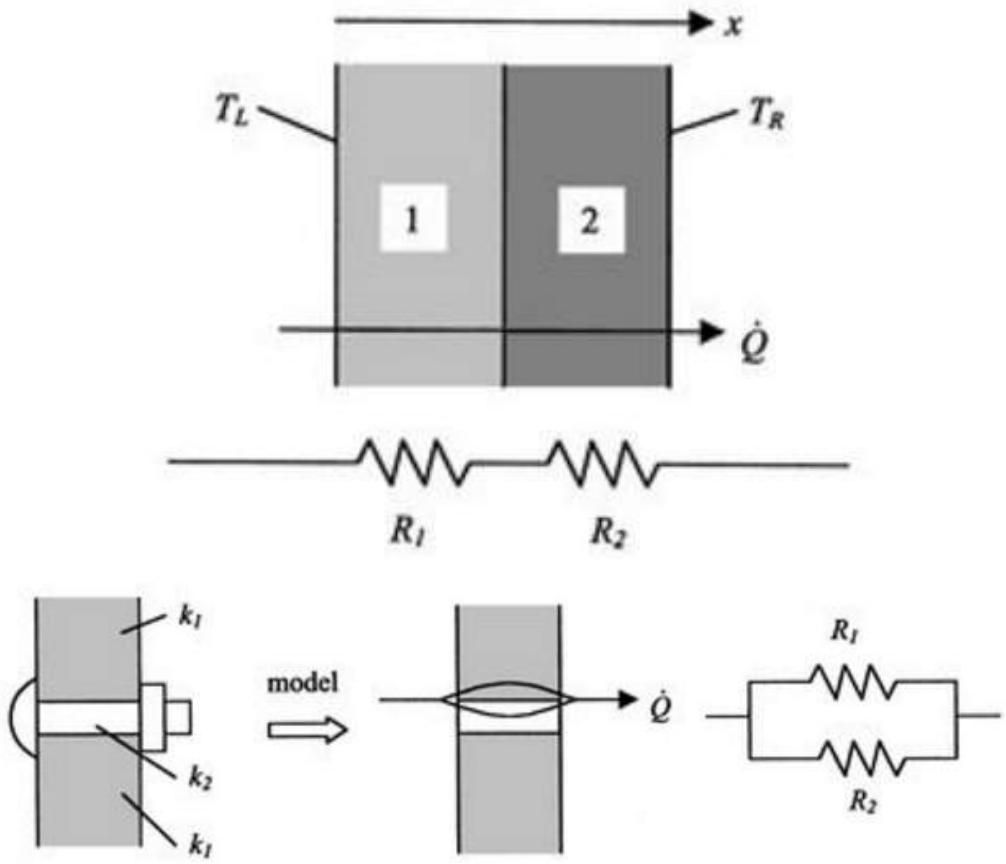


Figure 2-36: Top diagram illustrates the analogy where thermal resistance in series could be compared to electrical resistance in series. Bottom diagram illustrates a system where there is parallel thermal resistance, and how it can be compared to a parallel electrical resistance system [99].

conductivity. These inferences, however, could be misleading given that there are only a few data points. Also, experimental trials were not controlled in order to separately determine how single parameters affect crud. Further details of effective thermal conductivity in WALT loop can be found in section 2.2.6.2.

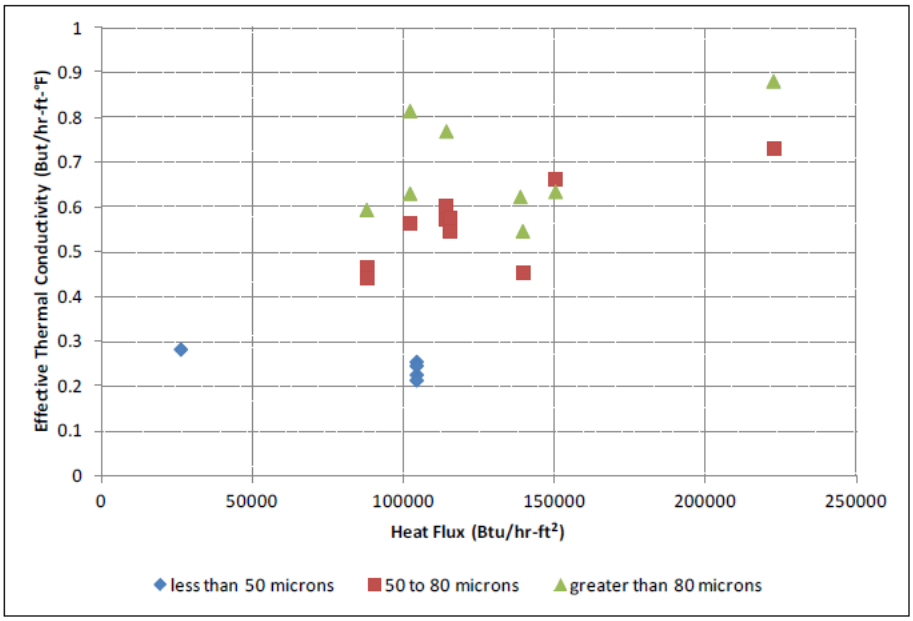


Figure 2-37: Plot of effective thermal conductivity versus heat flux [8].

**Pressure drop in system** As mentioned earlier in section 2.1.3.1, pressure drop can also increase in various systems such as heat exchangers or nuclear fuel rods, when there is fouling deposit formation. Doing experiments to measure pressure drop changes from crud formation will require a different type of setup that more closely simulates a reactor's fuel assembly. This is something that the IHTFP was not designed for. Since crud thickness is in a range of micron, it is also unlikely to obstruct the flow which makes pressure drop from crud less of a problem when compared to systems such as heat exchangers. The current IHTFP loop does not suffice for tackling this problem. An experiment conducted to gain data on crud's effect on pressure drop will benefit from having a test section and heating rod with shape more similar to that of the real reactor. One way that this experiment could be carried out is by measuring speed of water flow before and after crud had grown on the heater rod. Measuring the speed of water flow will require very sensitive flow meter. Because of its measurement difficulty and its relative unimportance to nuclear reactors, it will not be in the scope of this thesis.

| Rod | TC | Crud Thickness (microns) | Densified Crud Thickness (microns) | Microns Oxide | Porosity (%) | Crud Density (g/cc) | Chimney Density (#/m2) | Median Chimney Dia. (microns) | Ni/Fe | Effective Thermal Conductivity (Btu/hr-ft-°F) |
|---|---|---|---|---|---|---|---|---|---|---|
| 110 | 1 | 66 | 0 | 3.8 | 72 | 5.1 | 4.8E+08 | 6 | 0.32 | 0.4130 |
| 110 | X2 | 43 | 0 | 3.5 | 76 | 5.4 | 4.8E+08 | 6 | 0.34 | 0.4150 |
| 110 | X3 | 88 | 24 | 5.9 | 72 | 5.3 | 4.8E+08 | 6 | 0.41 | 0.5920 |
| 111 | 1 | 42 | 0 | 1.8 | 73 | 5.4 | 2.0E+09 | 3 | 0.44 | 0.3000 |
| 111 | 2 | 49 | 13 | 2.4 | 70 | 5.4 | 2.0E+09 | 3 | 0.55 | 0.3450 |
| 111 | 3 | 46 | 0 | 1.7 | 69 | 5.2 | 2.0E+09 | 3 | 0.44 | 0.3120 |
| 111 | 4 | 42 | 18 | 2.6 | 56 | 4.4 | 2.0E+09 | 3 | 0.55 | 0.3110 |
| 112 | 1 | 61 | 29 | 4.0 | 49 | 3.9 | 1.6E+09 | 4 | 0.70 | NA |
| 112 | 2 | 85 | 23 | 2.6 | 66 | 4.9 | 1.6E+09 | 4 | 0.49 | NA |
| 112 | 3 | 58 | 0 | 4.2 | 63 | 4.5 | 1.6E+09 | 4 | 0.36 | 0.3840 |
| 112 | 4 | 69 | 0 | 2.4 | 67 | 4.9 | 1.6E+09 | 4 | 0.41 | NA |
| 116 | 1 | 99 | 10 | 1.8 | 57 | 4.4 | 5.7E+08 | 8.0 | 1.43 | NA |
| 116 | 2 | 66 | 23 | 4.2 | 66 | 5.5 | 5.7E+08 | 8.0 | 3.17 | NA |
| 116 | 3 | 78 | 25 | 3.2 | 62 | 4.9 | 5.7E+08 | 8.0 | 1.05 | 0.8030 |
| 116 | 4 | 54 | 0 | 1.1 | 67 | 5.3 | 5.7E+08 | 8.0 | 0.94 | 0.5870 |
| 117 | 1 | 120 | 25 | 3.8 | 66 | 4.4 | 8.4E+08 | 3.0 | 1.98 | NA |
| 117 | 2 | 76 | 0 | 3.5 | 60 | 5.9 | 8.4E+08 | 3.0 | 3.13 | NA |
| 117 | 3 | 67 | 0 | 2.4 | 59 | 5.3 | 8.4E+08 | 3.0 | 1.97 | 0.4750 |
| 117 | 4 | 70 | 0 | 1.8 | 61 | 5.5 | 8.4E+08 | 3.0 | 2.49 | 0.4790 |

Figure 2-38: Summarizing table of measurements and calculations done using the WALT loop [8]. Only the data for non-boiling cases were selected in this case. TC 1-4 represent the locations that correspond to thermocouple 1-4, respectively.

#### 2.2.4.2 Microscopic Parameters

There are many microscopic parameters related to characterization of fouling deposits that we examine for our experiment including porosity, tortuosity, pore size/distribution, and composition. For more general details of what these parameters represent, visit the previous section 2.1.2.2.

**Porosity** For the experiments related to this thesis, crud's porosity will be obtained using SEM images, and image processing algorithms. First, grayscale SEM images will be processed into binary images using image processing algorithms, such as moment-preserving thresholding [100] or Otsu thresholding [101]. The black areas on binary images will represent the areas where water flows through, while the white areas represent crud particles. Porosity can then be obtained from binary images by counting the number of black pixels as pores, and taking the ratio of total number of black pixels over the total number of image's pixels. The equation below summarizes how porosity is obtained.

$$Porosity = (\#blackPixels)/(\#totalPixels) \tag{2.8}$$

**Fractal tortuosity and fractal area dimension** Similar to porosity's case, the image-processing algorithms can turn a grayscale SEM image to a binary image. The binary images can be used

obtain both the fractal tortuosity dimensions and the fractal area dimensions with the box-counting method. In crud's case, water flows in from the surface of the crud, and permeates through the crud until it eventually exits the chimney as bubbles. Therefore, the image that is perpendicular to flow is the top view of the crud. Since fractal area dimension is the fractal dimension obtained from plane perpendicular to flow, we use the top-down SEM image of crud for fractal area dimension analysis. On the other hand, the fractal tortuosity dimension requires an image that is parallel to flow. Therefore, a cross-section SEM image obtained from focused ion beam (FIB) cut is used to analyze fractal tortuosity dimension. According the MAMBA-BDM paper [7], the assumption that crud is a statistically self-similar porous solid across multiple length scales is based on the observations of SEM images of crud. The motivation in making this assumption is clear: numerous material properties can be obtained from using a few fractalline geometery parameters.

**Pore size distribution** One of the unique characteristics of crud is how it contains boiling chimneys distributed across its surface. Pore size distribution is one important parameter that can be used to characterize these boiling chimneys, if they are present. Pore size distribution is a distribution plot of chimney size in microns. X-axis on the plot will represent chimney size range, while the y-axis will represent the percentage of chimneys with a size that falls the the range. Pore size distribution can be found from analyzing the top-down image of crud in the SEM (scanning electron microscope). From an SEM image, pore size can be obtained from applying SEM software measurement tool.

**Composition** Composition of crud is a very important characteristic that can be used in calculating various values such as thermal conductivity. There are multiple ways of obtaining the composition of crud including the backscattering technique, SEM/EDX

The backscattering technique works by shining a beam, such as alpha beam or proton beam, into the material being tested. The beam that has been scattered back is then measured with the result in form of energy spectrum. The resulting energy spectrum will be different depending on what elements are involved. When beam is scattered against lighter element, it tends to lose more energy and therefore will create a peak at low part of spectrum. Real spectrum may be quite complicated and will involve many overlapping peaks that are hard to distinguish. Short simulation can be used to help determine the composition of any substrate. The simulation works by iterating the calculations until a convergence is reached. With a reasonable initial guess for the material composition, the convergence time can be shortened.

Another useful composition analysis technique is the transmission electron microscope (TEM). TEM is similar to SEM except that, instead of detecting the electrons that are scattered back from the sample, the technique detects the electrons that are transmitted through a very thin specimen. The different brightness/constrast can indicate different materials on the TEM images.

The advantage of TEM is that it can provide a highly detailed image with very high magnification, similar to SEM [102]. The general disadvantage of TEM is that sample preparation requires some work. In terms of usage for determining elemental composition, it suffers from the same problem as SEM; there is no spectra and therefore it is quite hard to figure what material is represented by different brightness and contrast. This lack of spectra can be solved by using add-ons such as energy-dispersive X-ray spectroscopy (EDX).

EDX is another useful analytical technique that can be used to analyze crud. EDX works by detecting X-rays that emerge from excitation of samples. EDX is great as an addon to either SEM or TEM, since SEM and TEM can provide an electron source for X-ray excitation. Figure 2-39 is an example of spectra that was obtained from a TEM with an EDX add-on. The spectra y-axis represents the detection count, while the x-axis represents the X-ray energy. Since X-ray excitation energies are unique to different types of elements, the X-rays detected will have peaks that represent different types of elements existing within the sample. These peaks are clearly shown in figure 2-39. EDX can be used in tandem with SEM/TEM images. Figure 2-40 shows a TEM image of a crud particle and its corresponding EDX spectra. EDX's advantages are that it can be used to analyze a very small area within a sample, that it is non-destructive, and it can be used together with SEM or TEM images. The limitation of using EDX is that it does not give any information on the type of chemical bonding the sample might have.

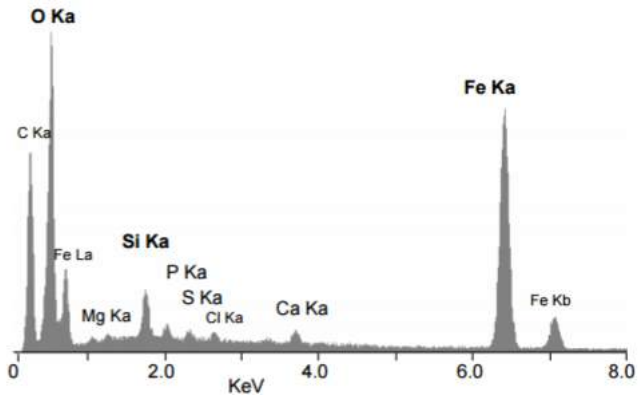


Figure 2-39: Example EDX spectra obtained from a TEM's EDX add-on. The spectra is from analyzing a sample of hydrothermal vent shrimp (Rimicaris exoculata ) [103].

Mössbauer spectroscopy is a spectroscopic technique that utilizes the Mössbauer effect [105]. The Mössbauer effect refers to the recoilless gamma ray emission and absorption, discovered by Rudolph Mössbauer. When gamma rays are emitted or absorbed into an atomic nucleus, conservation of momentum requires nucleus to recoil, although, Mössbauer found that nuclei in a solid crystal are not free to recoil. However, when the nucleus of a solid crystal emits or absorb gamma rays, some energy can still be lost to recoil. These recoil losses will always occur in discrete packets called phonons. These discrete energy losses can also be zero, in which case the event is known as being

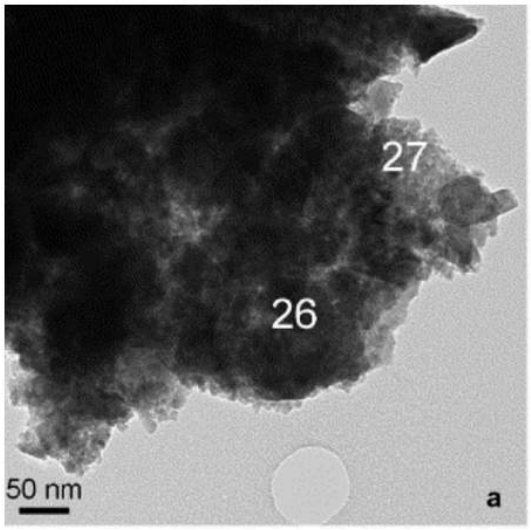


EDX data from fine-grained franklinite, sample A

| Element | Spectrum A-1 | | Spectrum A-26 | | Spectrum A-27 | |
|---|---|---|---|---|---|---|
| | wt% | at.% | wt% | at.% | wt% | at.% |
| Na | | | 3.8 | 8.9 | 5.1 | 11.5 |
| Al | 0.5 | 1.0 | 1.7 | 3.4 | 3.1 | 6.1 |
| Si | 0.3 | 0.6 | 0.9 | 1.7 | 1.2 | 2.2 |
| P | | | | | 1.9 | 3.2 |
| Cl | | | 1.5 | 2.3 | 0.9 | 1.3 |
| K | | | 0.5 | 0.7 | 0.6 | 0.8 |
| Ca | | | 0.7 | 0.9 | 1.1 | 1.4 |
| Cr | 16.0 | 17.7 | 1.5 | 1.6 | 0.4 | 0.4 |
| Mn | 2.2 | 2.3 | 3.9 | 3.8 | 5.1 | 4.9 |
| Fe | 47.9 | 49.4 | 51.8 | 50.1 | 46.6 | 43.7 |
| Ni | 4.6 | 4.5 | 2.5 | 2.3 | 1.3 | 1.2 |
| Cu | | | | | 0.6 | 0.5 |
| Zn | 26.0 | 22.9 | 27.8 | 23.0 | 25.6 | 20.5 |
| Sr | | | | | 0.2 | 0.1 |
| Zr | 2.6 | 1.6 | | | 6.4 | 2.5 |
| Ba | | | 3.3 | 1.3 | | |

Figure 2-40: The left image is a TEM image of crud $ZnFe_2O_4$ sample obtained from a commercial boiling-water reactor (BWR) [104]. The right table is the corresponding EDX spectra obtained from the same sample. Spectrum A-26 and A-27 corresponds to the location 26 and 27 on the TEM image, respectively.

"recoil free." Mössbauer spectroscopy is possible because having zero energy recoil loss means that gamma rays emitted by one nucleus can be resonantly absorbed by the same kind of isotope within another sample. This resonant absorption can be measured. Its resulting spectra can be used to obtain information about the chemical, structural, and magnetic properties of materials.

Mössbauer spectroscopy can give accurate data on the valence state of iron, as well as data on the various iron oxides in the sample [106]. In analyzing crystal structure, it can also be used to determine the coordinate number of iron atoms. The downside of Mössbauer spectroscopy specifically for usage in crud is that it requires crud to be removed from the cladding surface, so that its powder can be spread across the absorber for optimal experiment condition. Sawicki used Mössbauer spectra of iron-57 to determine the phase composition of iron-bearing compounds from crud samples scraped from Westinghouse's reactors. In the end, Sawicki found that crud samples used contained mostly nickel-iron ferrite $Ni_xFe_{3-x}O_4$in a composition range of $0.6 < x < 0.8$ [85].

X-ray photoelectron spectroscopy (XPS) is another technique that can be used to determine the composition of crud material. XPS is capable of measuring elemental composition at parts per million. In addition, empirical formula, chemical state, and the electronic state of elements can also be obtained. XPS's results provide a spectra of detection count value vs. the binding energy. Figure 2-42 is an example of XPS spectra. XPS works by irradiating the sample with an X-ray beam. The irradiation causes electrons to be ejected from the inner shells of the atoms. Detectors can then be used to obtain the kinetic energy spectra of electrons that escaped from the sample. Binding

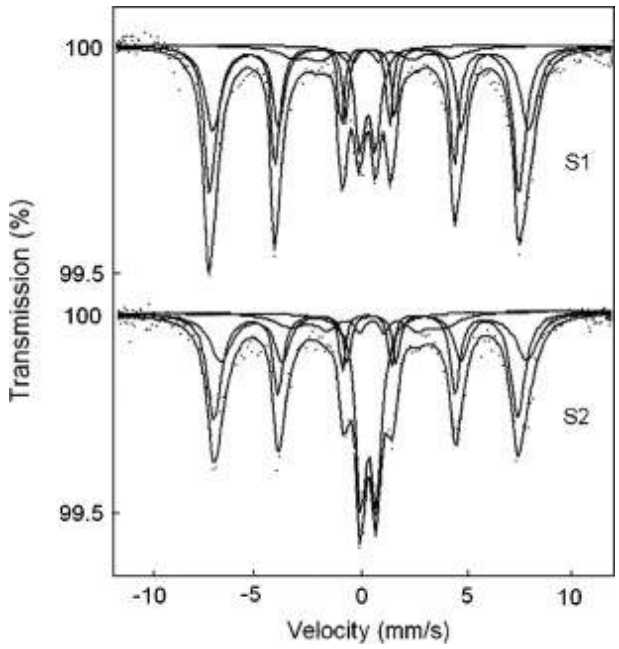


Figure 2-41: This is one of the Mossbauer results shown in Sawicki paper. It is a Mossbauer transmission spectra of iron-57. Sawicki fitted the spectra to reference patterns of $Ni_2FeBO_5$, $NiFe_2O_4$, $Ni_xFe_{3-x}O_4$ etc. [85].

energy can be inferred from the kinetic energy of escaped electrons. The main advantage of XPS is that it is able to distinguish chemical states of samples [107]. Despite its usefulness, XPS also has many limitations. It has a smallest measurement area limitation of around 10 m. It can only detect elements with an atomic number of 3 or greater. In addition, it also requires a high vacuum environment in which to work.

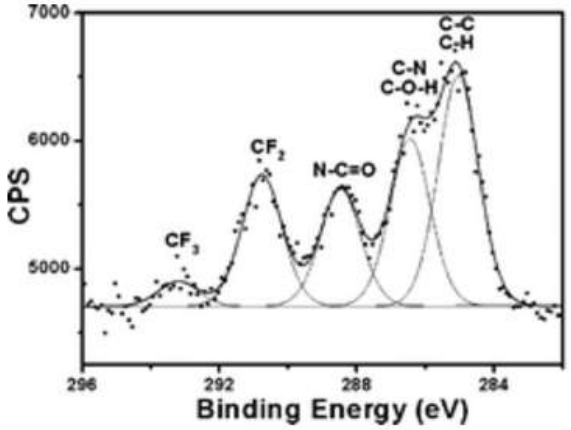


Figure 2-42: An example XPS spectra. [108]

### 2.2.5 Effects of Crud

Other than having the general adverse effects of fouling deposit explained in the section 2.1.3, crud also presents additional hassles to the reactor operation. This section will present these crud-specific adverse effects on the nuclear reactor. When crud is formed, the heat transfer mechanism changes from that of a normal convection with a limited sub-cooled nucleate boiling to another heat transfer mechanism called "wick boiling." Crud typically has porosity of roughly 60-80% depending on reactor conditions [37]. Crud is structured in a way that there are boiling chimneys penetrating the crud surface deep into the crud layer.

In wick boiling, liquid penetrates through the porous crud until it reaches the inner region where the temperature is above the saturation point and thus the water boils. The chimneys then serve as egress locations for the vapor produced [109]. Wick boiling can amplify the boron and the LiOH concentration as much as several tens of times beyond that of a normal clean surface during sub-cooled boiling [36]. As a result, crud can also cause an unwanted power distribution shift due to the elevated level of boron-10 absorbing neutrons. This power distribution shift in the core is generally termed an axial offset anomaly (AOA), or a crud-induced power shift (CIPS) [38]. Because of the increase in LiOH at the crud region, crud also causes crud induced localized corrosion (CILC) if the crud layer is thick enough. CILC can potentially lead to fuel failure. In addition, the clad temperature beneath the crud layer can be raised significantly because of wick boiling [36]. The sub-sections below will explain these effects in more detail.

#### 2.2.5.1 Crud-Induced Power Shift (CIPS)

CIPS is caused by boron that accumulates within the crud layer. In a PWR, reactivity control is done via control rods as well as via the addition of boric acid to absorb neutrons. Control rods are used for localized control of the reaction. At the same time, boric acid is used to control the average reactivity so it remains stable throughout the entire fuel cycle. During the cycle's beginning, the amount of fissionable fuel is at its highest and therefore reactivity will be high without any form of control. Boric acid is added to decreases the reactivity at this point in the beginning of a cycle. As time passes and fissionable fuel depletes, and boric acid quantity is reduced to increase the reactivity to the optimal point [7]. To illustrate why boron, especially boron-10, is the neutron absorber of choice, we can compare its cross section with other typical isotopes in the reactor. Figure 2-43, 2-44, 2-45, and 2-46 are the cross-sections of common isotopes in the nuclear reactor. Notice that boron-10 absorption cross section is far higher than any of its peers. As a result, boron, enriched to high amount of boron-10, is chosen as the ideal dissolved neutron absorber.

Boron atoms will accumulate in a crud layer, since the boiling process going on in crud will leave these strong neutron absorbers behind. Consequently, wherever there is crud, there will be more neutrons absorbed. This leads to lower neutron flux and therefore more power where crud

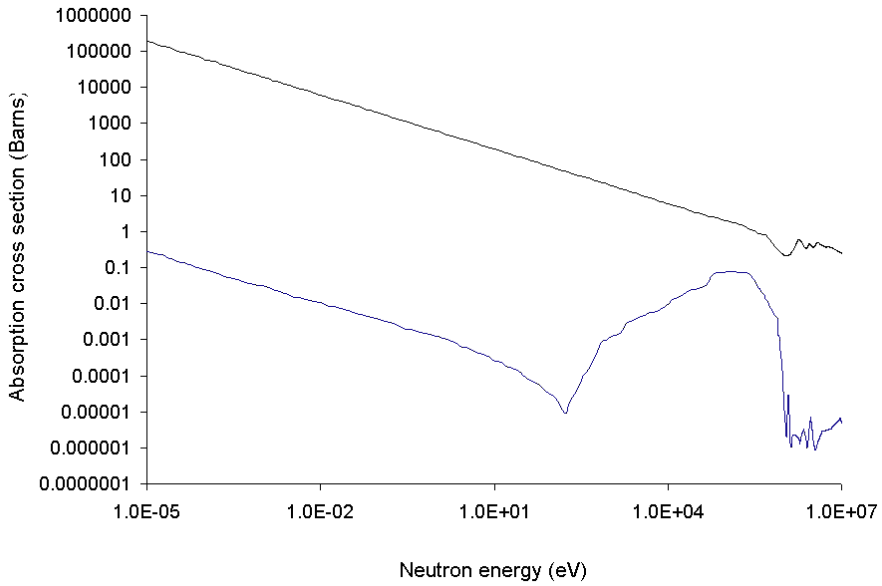


Figure 2-43: Capture cross sections vs energy of boron-10 vs boron-11 [110]. The top black line represents the neutron absorption cross section of boron-10 while the botton blue line represents the neutron absorption of boron-11. Notice that boron-10's absorption cross section is very high compare to to boron-11 and other isotopes shown in the next few figures

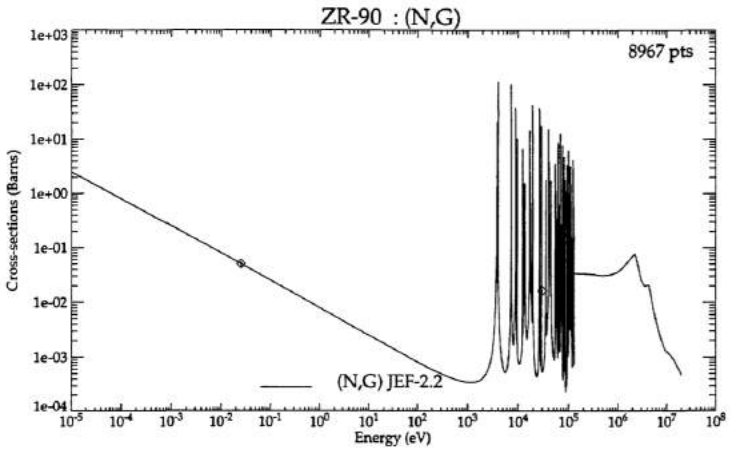


Figure 2-44: Capture cross sections vs energy of zirconium-90 [111]. Zirconium-90 is the most common isotope of zirconium.

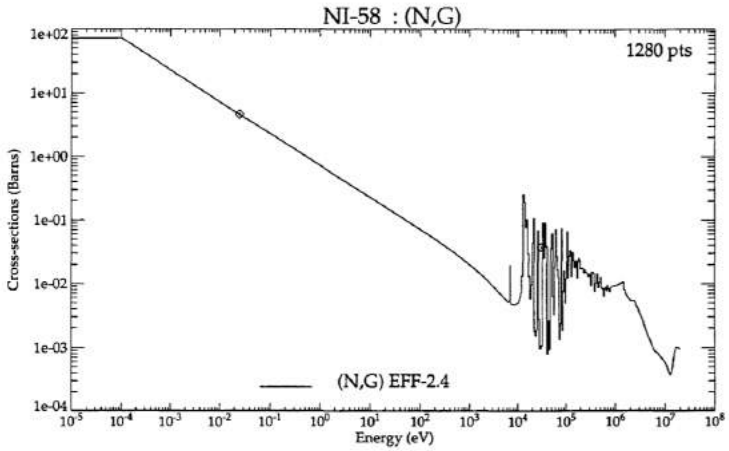


Figure 2-45: Capture cross sections vs energy of nickel-58 [111]. Nickel-58 is the most common isotope of nickel.

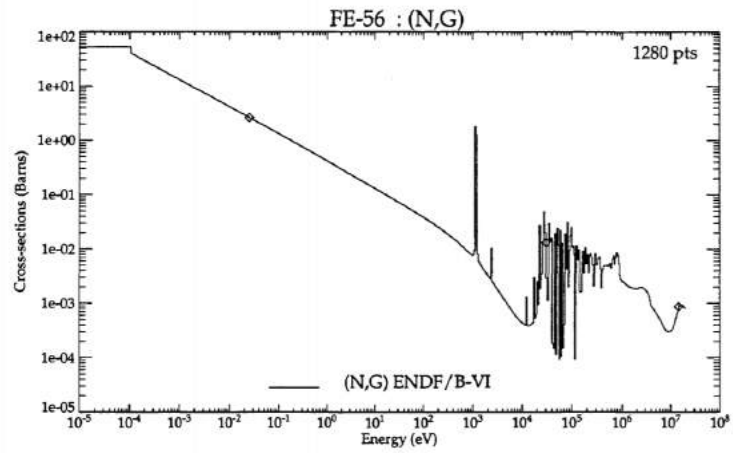


Figure 2-46: Capture cross sections vs energy of iron-56 [111]. Iron-56 is the most common isotope of iron.

forms. This power-shift is called crud Induced Power Shift (CIPS). In most cases, these power-shifts force reactor operators to operate at sub-optimal conditions. However, in extreme cases, it has been known to cause a reactor shutdown with the corresponding loss of approximately $1 million a day for the utility [7, 36].

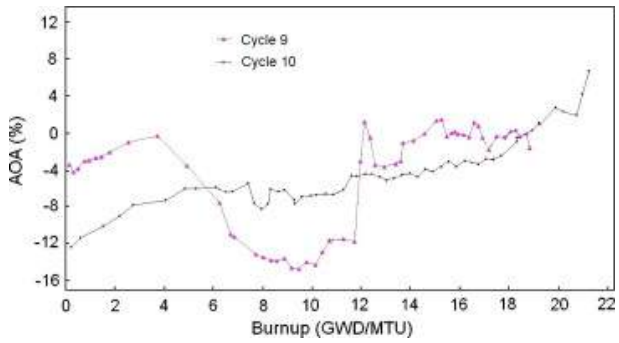


Figure 2-47: This is a plot of axial offset anomaly (AOA) or CIPS versus burnup during cycle 9 and 10 where crud was reported [85]. The name of reactor was probably proprietary and not mentioned in the Sawicki paper.

The decremental power-shift is not the less dangerous complication compared to the power-spike that reactors might experience when restarting the reactor with crud after a shutdown period. Some chemical species has increased solubility at lower temperature. This temperature dependence behavior of solubility is called retrograde or inverse solubility. Boric acid is one of the species which exhibits inverse solubility. This means that during shutdown, when the reactor will be at lower temperature, the boric acid is more likely to dissolve away from crud because of the increased solubility. If control rod is in the same position and reactor is turned on, reactor could experience dangerous power spike at crud location with now decreased boron. It is impossible to know how much boron is dissolved away from crud and therefore, control rod position must be adjusted to compensate for this effect. Note that CIPS used to be called axial offset anamoly (AOA), but the name has been changed to CIPS because we now expect it. Therefore it is not an anamoly.

#### 2.2.5.2 Crud-Induced Localized Corrosion (CILC)

Crud can cause accelerated corrosion where it is present. This happens due to both the thermal and the chemical exaggeration effects in the crud layer. The chemical effects are related to the boric acid accumulation. As water boils off in the crud layer, it leaves behind boron species. Boron is added to the PWR water to regulate neutron flux. Figure 2-48 shows that locations deep under the crud layer have a higher concentration of boron species. Figure 2-49 illustrate how pH changes with crud depth. From figure 2-49, the 35 m line shows that pH will continuously decrease as crud depth increases. The lower pH leads to increased corrosion. In the case of thicker 59 m crud, however, crud pH behavior is more complex, as shown in the same figure. Radiolysis of water inside reactors

also creates hydrogen which can become concentrated within crud [112]. Both of these phenomena contribute to enhanced corrosion within the crud layer

With respect to thermal effect, a crud layer has a higher temperature than a normal clean surface of a fuel rod. The heightened temperature is caused by a worsened heat transfer in crud. Figure 2-50 illustrates this heightened temperature effect [112]. Since higher temperature is directly related to higher corrosion rate, the surface under the crud layer experiences a higher corrosion rate as a result [7]. The profound effect that temperature has on corrosion can be shown using Arrhenius' equation. Arrhenius' equation describes the rate constant of a chemical reaction based on the absolute temperature and other constants. Arrhenius' equation is:

$$k = Ae^{-E_a/(RT)} \tag{2.9}$$

where $k$ is the rate constant; $T$ is the absolute temperature in K; $A$ is the pre-exponential factor which varies according to the type of chemical reaction involved; $E_a$ is the activation energy in $J/mol$ ; R is the universal gas constant in $J/K \cdot mol$. To show the effect of temperature on corrosion, we will calculate the temperature increase needed at typical PWR condition to double the corrosion within PWR. By taking $T_1$ as the initial temperature, and taking $T_2$ as the temperature needed to double the corrosion rate constant, we can obtain the following two equations:

$$k = Ae^{-E_a/(RT_1)} \tag{2.10}$$

$$2k = Ae^{-E_a/(RT_2)} \tag{2.11}$$

By solving these two equations for $T_2$ we get the resulting equation:

$$T_2 = \frac{E_a}{E_a - T_1 ln(2)} \tag{2.12}$$

This equation can be used to calculate the change in temperature that is needed to double the corrosion rate. For an example, we will calculate this change in temperature for iron oxide. According to Grosvnor (2005) [113], the activation energy of iron with oxygen as oxidant is roughly 32 kJ/mol. If we assume 573 K as the temperature which is typical of PWR, we get $T_2$ of 580.2 K. This means that only 7.2 K is needed to double the corrosion rate. This calculation emphasizes the profound effect that increasing temperature has on corrosion rate, and therefore, cladding integrity. As shown in figure 2-50, the temperature increase caused by thick 59 m crud could be as high as 55 K. This will lead to a quite severe CILC, and this is exactly what happened to several reactors. Several cases of CILC were reported between 1995-2000 [42]. Three Mile Island unit 1 (TMI 1) in particular had nine failed fuel rods that were caused by high amounts of crud at the upper span of

the fuel assemblies. The figure 2-51 shows photos of cross sections of failed fuel cladding.

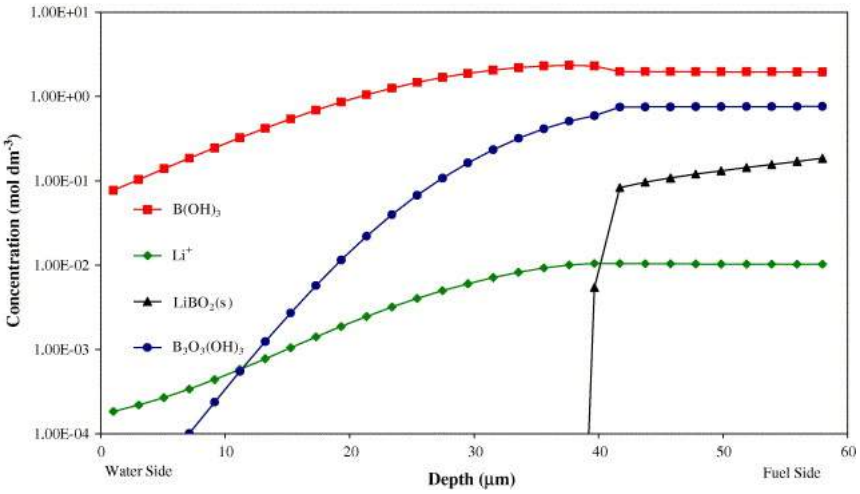


Figure 2-48: This graph, taken from Henshaw's (2006) paper, shows the relationship between boron concentration and depth. Generaly, we can see an increasing trend in the amount of boron as we go deeper into the crud [112].

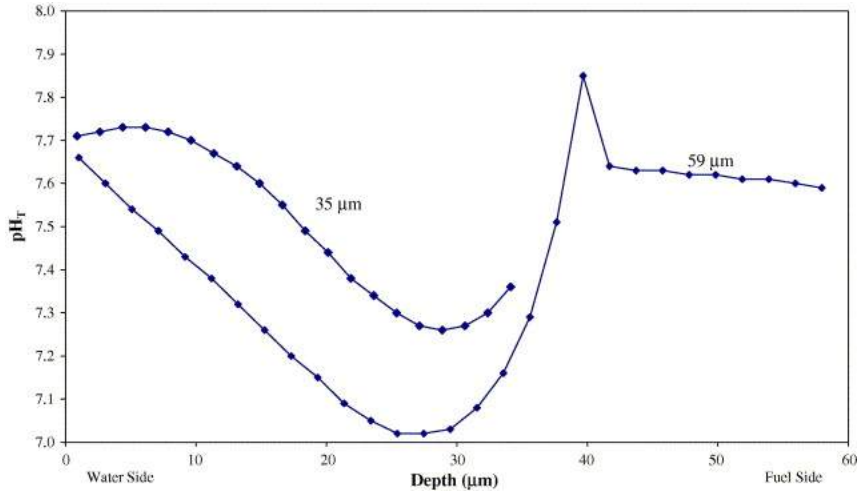


Figure 2-49: This graph, taken from Henshaw (2006) paper, shows the relationship between pH and crud depth [112]. The two lines represent the crud with thicknesses of 59 m and 35 m, respectively.

#### 2.2.5.3 Increased worker dose

Crud material can get activated by the radiation within the reactor. This combines with crud's ability to accumulate radioactive materials inside it, and therefore raises concerns about the extra radiation resulting from crud. The accumulation of activated materials in crud can lead to the increase in out-of-core radiation dose rate, since the radiation may penerate the reactor vessel as well as the containment structure in small amounts. In addition, activated materials in crud will also increase worker dose rate when fuel assemblies are moved around during refueling. Of all

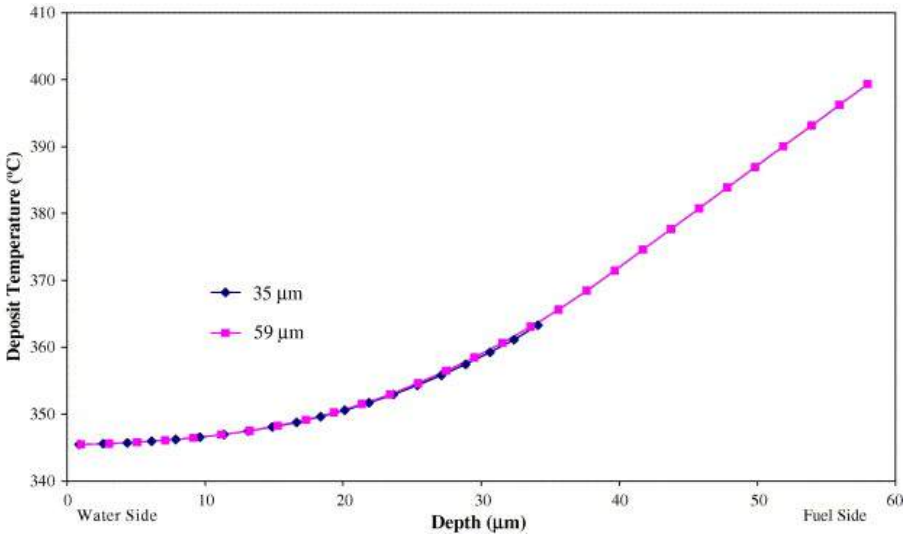


Figure 2-50: This figure shows the relationship between crud temperature and crud depth. The pink line represents the calculated numbers for crud with thickness of 59 m, while the blue line represents that of crud with thickness of 35 m [112]. It is clear from the graph that crud increases temperature on cladding surface. We can also see that thicker crud leads to more temperature increase.

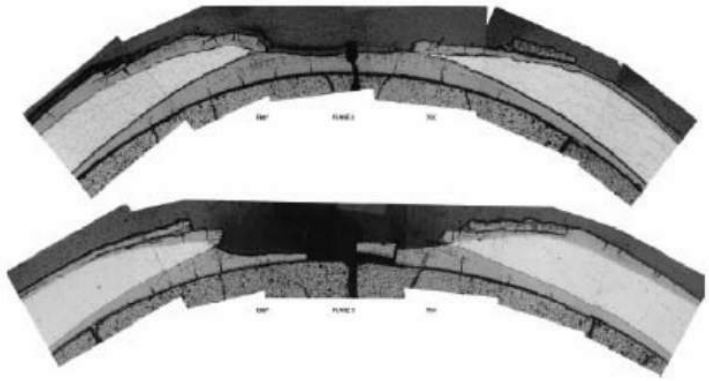

*FIG. 5.26. TMI 1, Cladding corrosion on a rod O11 at an elevation of 118.5 inches [5.46].*

Figure 2-51: This picture shows a cladding cross-section of damaged fuel from TMI 1. These fuel damages are caused by crud induced localized corrosion. These fuel failures happen at the elevation of 118.5 inches which are the upper most part of fuel assemblies. As mentioned earlier, the upper part of fuel assemblies are the parts that are likely to have sub-cooled boiling, and therefore crud buildup [42].

the radioactive isotopes, cobalt-60 is by far the most significant contributor to personnel radiation exposure, in the absence of any significant number of failed fuel rods [81]. Cobalt-60 decays with two very penetrating, energetic gamma rays with energy of 1.17 and 1.33 MeV. In addition, Cobalt-60 has a very long half-life of 5.271 years. Both its energetic gamma decay and its long half-life makes it especially dangerous to working personnels. Cobalt-60 is produced from elemental cobalt-59. This is why the ASTM specifications for both iron and nickel alloys used in nuclear reactors specify cobalt contents in tenths of weight percentages. Nevertheless, high cobalt content alloys are often used as bearings or wear pads in mechanical equipment such as pumps, valves, and control rod drive mechanisms. It is worth noting that there are other radionuclides that could effect personnels' radiation doses as well, but none is nearly as prominent as Cobalt-60 [81]. Crud is composed of corrosion particles from all around the reactor loop, including cobalt-59. When cobalt-59 particles deposit on crud layer, neutron flux could potentially turn it into the troublesome cobolt-60. This is why crud has such a profound effect on the radiation dose workers are exposed to. The ultrasonic cleaning technique has been implemented in several reactors to remove activated crud from the fuel claddings [51]. However, applying the ultrasonic cleaning technique on fuel rods also present workers with extra dose during the cleaning operation. Having the ability to mitigate crud will, in turn, mitigate this dose rate problem.

#### 2.2.5.4 Reactor Design and Operation Limitation

Other than affecting the how reactor operates directly, crud growth is also an important limiting parameter in reactor design and operation. According to EPRI PWR Primary Water Chemistry Guidelines Volume-1 1999 [43], having pH below 6.9 when operating the PWR is not recommended citing the reason that it leads to a huge amount of crud. The heightened amount of crud at low pH is likely due to the heightened corrosion of reactor internals driven by the low pH. This presents a balancing issue for reactor operators as lower pH also have benefits in terms decreasing the amount of corrosion. In modern-day PWRs where plant operators try to push for higher burnup, this becomes even more of a problem. Pushing for higher burnup means that more boron will have to be added to moderate the neutron flux at the beginning of the nuclear fuel cycle. Adding more boron or boric acid will push pH lower and as a result, many modern reactors will sustain a brief period of unfavorably low pH condition (less than 6.9) that could lead to crud buildups. Crud also limits the power output. If a reactor is adjusted for higher power, parts of the fuel assemblies, especially the upper parts could start to exhibit sub-cooled boiling. Since crud is directly ties to sub-cooled boiling this may lead to high amount of crud, which leads to many other problems [43].

#### 2.2.5.5 Conclusion on Effects of Crud

To summarize, crud issues contribute greatly to safety and economic concerns relating to the reactor. Therefore, mitigating or preventing crud is of a great interest to the nuclear industry. crud causes a reduced, unpredictable heat transfer, it induces a power distribution shift (CIPS), and it accelerates localized corrosion (CILC). For these reasons, crud creates operational difficulties because operators cannot properly determine the power safety margin. As a result, conservative assumptions must be assumed for the power safety margin. In some severe cases, as much as thirty percent reduction in power must be applied, causing a huge loss of revenue for the plant [36]. Even without crud growing in the reactor itself, just the knowledge that crud may grow presents engineering challenges when operating and designing nuclear reactors. Although crud causes relatively few direct problems today, potential crud problems deter PWR operators from power uprates because of the fear of crud problems reoccuring. Nuclear Energy Institute (NEI) made a prediction that nuclear power plants can theoretically add over 6,500-8,500 MWe from uprate alone [114]. This figure might not be far reaching since only 27 of 100 nuclear reactors in US had received extended power uprates [114].

### 2.2.6 Previous Studies on Crud

As explained earlier crud had always been a problem for commercial nuclear reactors. Therefore, it is not surprising that there had already been many studies on crud. These studies can be categorized into two approaches, the modeling approach and the experimental approach. The modeling approach uses computer models to simulate crud growth. The modeling crud growth subsection 2.2.6.1 below will show the evolution of crud computer models up to today. The experiments simulating crud in PWR conditions subsection 2.2.6.2 will showcase other crud loops similar to the IHTFP.

#### 2.2.6.1 Modeling Crud Growth

One way to gain a better understanding of crud growth and behavior is to model them. There have been many attempts to model crud's behavior. crud modeling is not new, and has been refined over time by different researchers across the world. Some of the earlier works are shown in the following paragraphs.

**Cohen (1974) Model** Cohen [37] developed a one-dimensional heat and mass transfer model which can estimate the temperature beneath the crud layer. This model assumes two mechanisms of heat dissipation; these are the axial conduction through the layer of crud in parallel direction to the boiling chimney, and the evaporation along the crud/Chimney boundary. While the model is successful in giving useful estimations of the axial temperature distribution through crud, it has drawbacks of not taking into account other variables such as chemical solutes and reactions. The distribution of heat transfer, fluid flow, and chemistry was also not fully coupled in the model.

In addition, it was later shown by Pan et. al, that the Cohen model appears to overestimate the concentration of boric acid [7].

**Pan (1985) Model** Pan [36, 115] developed a two-dimensional model and computed the temperature distribution as a function of depth and distance from chimney. As opposed to Cohen's earlier model, Pan's model loosely coupled heat transfer and fluid. In addition, transport of dissolved species in coolant were also included in the model. Pan's model performed parametric analyses of porosity, chimney population, system pressure, crud thickness, peak cladding temperature, and peak boron concentration. The disadvantages of Pan's model is that it ignores crucial phenomena, such as chemical precipitation, solubility limits for dissolved species, and boiling point elevation.

In Pan's model, the chemical concentration effects were simplified by treating the concentration of an "infinitely soluble" solute, $H_3BO_3(aq)$, as a result of wick boiling [7]. It accounts for changes in boiling surface and fluid transport due to porosity and tortuosity. Figure 2-52 summarizes one of Pan's result from his paper. It shows how the maximum concentration factor increases with crud thickness. Concentration factor is defined as the ratio of solute concentration in crud compared to bulk fluid. The maximum concentration factor was found to be in the region near the intersection of the heating surface and the chimney wall. Figure 2-52 clearly shows the significant effect crud has on solute concentration within crud. The assumption of infinite solubility, however, can potentially lead to an overestimate of boron concentration [7].

**Henshaw (2006) Model** Henshaw built upon Cohen's work [112, 36] by coupling thermal hydraulics and radiation water chemistry. Henshaw's work is focused modeling the coupled phenomena in the crud layer, such as conduction, porous medium flow, and dissolved species migration. Henshaw investigated, in particular, the complex chemical interactions associated with these coupled phenomena. The Henshaw model includes the concentration of multiple boron species coupled with a detailed chemistry model. Depletion of boron by neutron absorption, lithium monoborate precipitation, and wick boiling are all taken into account in the Henshaw model [7]. crud concentrations of soluble and gaseous species are allowed to vary along the axis of the boiling chimney. Henshaw's chemistry model, based on the work of Ellion et. al [116], is rigorous, with forty equations for radiolysis of water alone. Regarding crud's geometry, only single values of chimney spacing and size were used. Crud pore size and tortuosity were taken as constants [7]. Figure 2-53 shows one of Henshaw model's interesting result, crud temperature plotted against crud thickness. Each lines represents each amount of boron concentration. The graph indicates how boron can have an effect on deposit temperature. While this, by itself, is an interesting finding, it also shows how the coupling of physics complicates the modeling of crud. In addition to finding many relationships, such as the one shown in figure 2-53, this model is also capable of showing an elevated pH near the cladding wall that leads to zirconia instability.

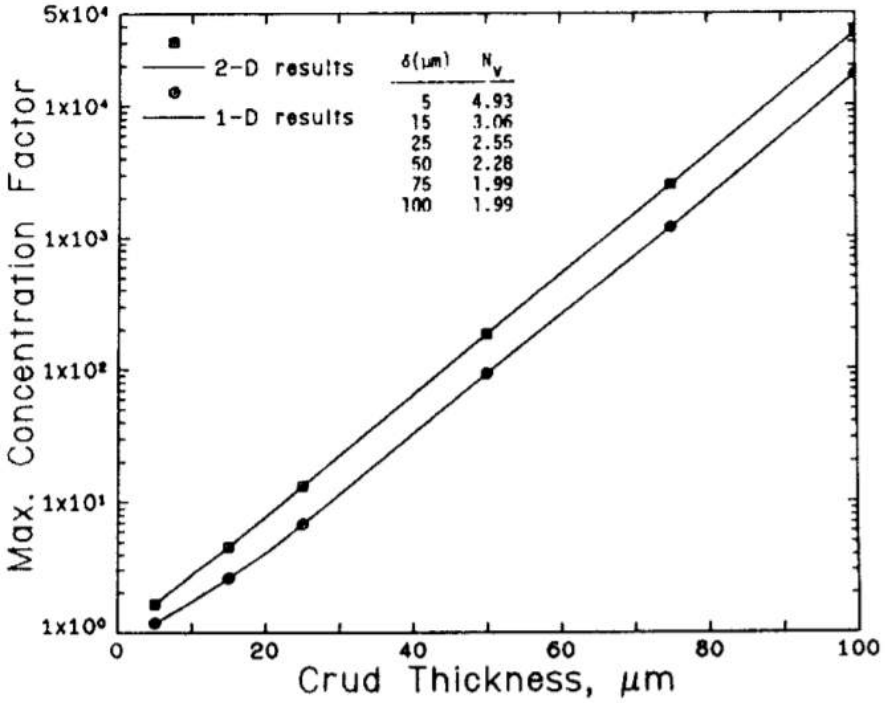


Figure 2-52: This figure shows the effect of crud thickness on the maximum concentration factor [115].

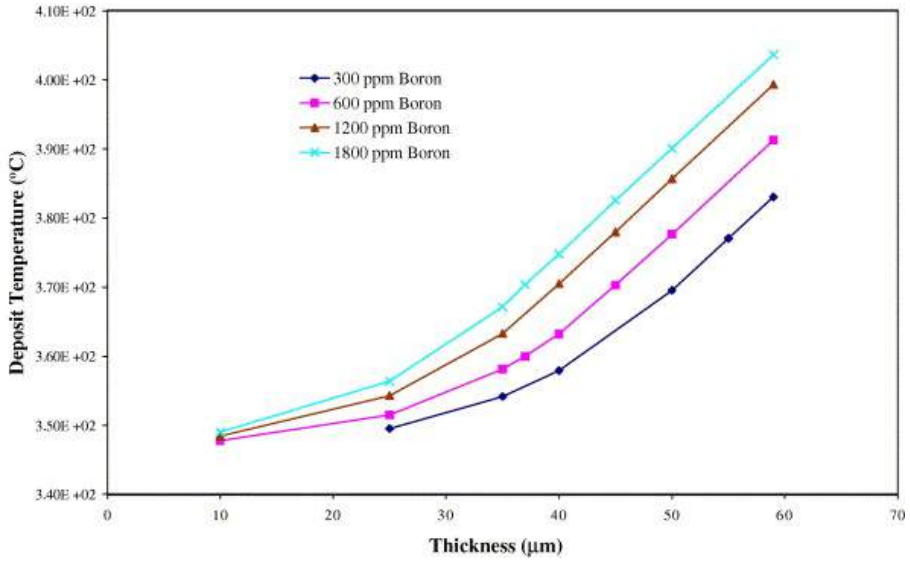


Figure 2-53: This graph shows the relationship between crud temperature, crud thickness, and boron concentration [112].

**Haq (2011) Model** Haq developed a two-dimensional model with more complicated assumptions and with the thermal hydraulics and the water chemistry coupled to each other [36]. His two-dimensional model simulates wick boiling phenomena in crud. Wick boiling is the term used to refer to the boiling through crud's chimneys. Similar to previous models, the boiling chimney's size and spacing were assumed to be constants. Although the Haq model is more rigorous in terms of coupling heat transfer, solute concentration, and coolant velocity, it lacks Henshaw's model meticulous chemistry details. The Haq model only addresses a single boron-bearing specie, $H_3BO_3$ [7].

One highlight of Haq's model is the ability to predict dependence of the thermal conductivity of crud on parameters such as chimney separation and crud thickness. This prediction is clearly shown in figure 2-54. Haq's model also illustrates the importance of coupling the physics. Haq's results examining the effects of coupling shows that values obtained from uncoupled models deviate from that of coupled models [7].

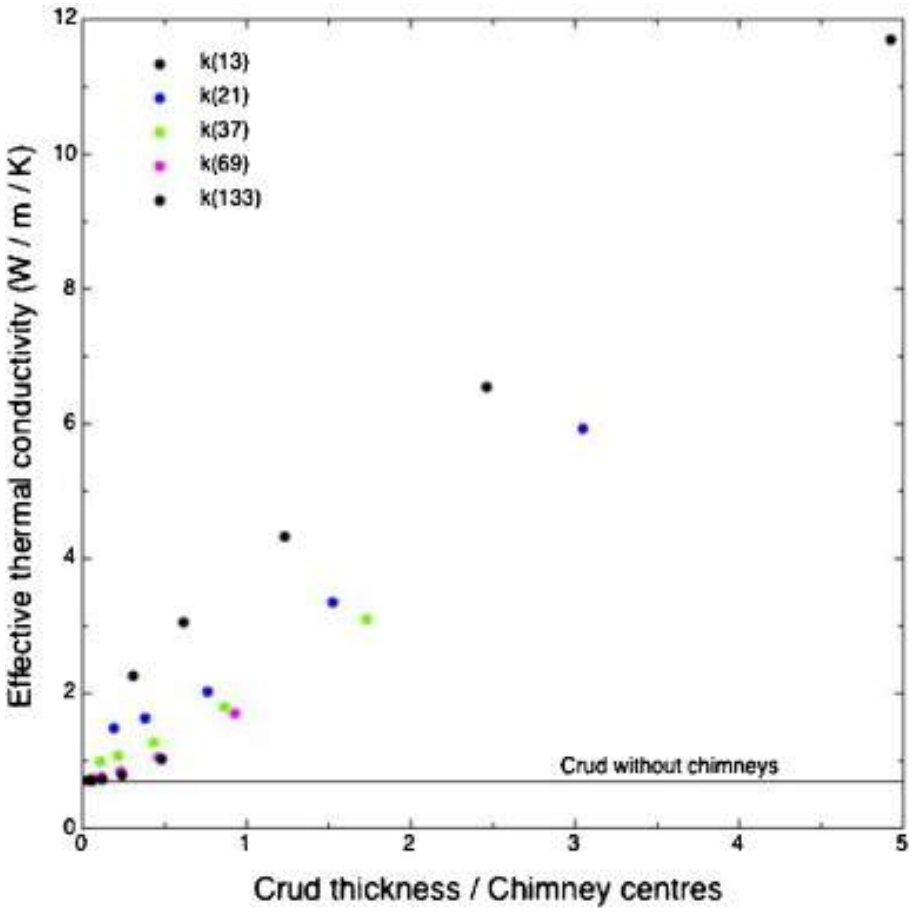


Figure 2-54: Haq model's result shows the dependence of effective thermal conductivity on the ratio crud thickness to chimney centers. "Chimney centers" is the term Haq used to describe the distance between chimney centers. The legend indicates that value of chimney centers [36].

**Short (2013) Model** Michael Short [7] developed a crud model that encompasses all coupled physical phemomena. The model is named MAMBA-BDM, and is based on MOOSE framework (Multiphysics Object Oriented Simulation Environment) [117]. MOOSE framework is geometrically agnostic and the crud model developed on it is scalable to the massively parallel, high performace computing that modern technology offers. In this model, most physical phenomena occuring in crud are simulated including the temperature, the fluid pressure, the fluid viscosity, the spatially-dependent material properties, the soluble boron concentration and the regions of boron oxide precipitation. The key assumption of this model is that crud is treated as statistically self-similar porous solid across multiple length scales. In other words, crud is assumed to exhibit fractal properties. With this assumption, the various material properties can be computed knowing fractal dimensions. Originally, assumptions were made regarding the fractal dimension values. Experiments performed as part of this thesis verified that the assumptions made are reasonable.

One of the most important highlights of Short model's finding is that superheating of liquid in crud cannot be ignored. All previous models assumed that there is no superheating in crud and that the transition to vapor happens at chimney boundary. This is because previous models impose boundary conditions on the crud chimney wall, where the chimney wall's temperature is assumed to be the saturation temperature. Figure 2-55 clearly shows that there should be liquid superheat in crud.

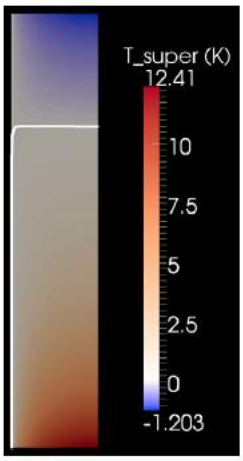


Figure 2-55: This figure shows temperature distribution within crud layer obtained from MAMBA-BDM [7]. The horizontal axis represents the distance from crud chimney's surface. In other words, the left boundary represents the crud chimney wall. The vertical axis represents the height within crud. This figure shows fluid super heating within crud.

**Jin/Short (2013) Model** The Jin and Short model accounts for two-phase fluid in the crud [44]. Short's (2013) paper emphasizes the importance of not assuming that temperature within crud will not exceed saturation temperature. This model follows up on Short's previous model to correct

for this fact by taking into account the two-phase fluid inside crud. Similar to the previous Short model, this model is implemented using MOOSE framework. The new Jin/Short MAMBA-2Phase model inherited most features from Short's previous work, MAMBA-BDM [7]. Separation of fluid phases was introduced that allows for the simulation of film boiling within crud.

Using their model, Jin/Short found that crud may have a double peak in effective thermal conductivity vs heat flux profile. Figure 2-56 clearly shows this double peak phenomenon in graph (d)-(f). One factor that determines whether crud exhibits a single or double peak effective thermal conductivity profile is its thickness. If crud is thin, the boiling situation within crud exhibits behavior similar to that of clean surface. At low heat flux, heat would conduct through a liquid-saturated crud layer. As heat flux increases and boiling occurs within crud, heat transfer will be enhanced. This is why we see the rapid rise in effective thermal conductivity. When heat flux increases enough that the boiling regime switches to film boiling, the effective thermal conductivity rapidly falls, since the gas film is not very good for heat transfer. On the other hand, if the crud is thick, there are more regime changes than just conduction, boiling within crud, and film boiling. Jin/Short expected nucleate boiling regime on top of a crud layer, in addition to the sub-cooled boiling regime within crud. Figure 2-57 demonstrates this idea.

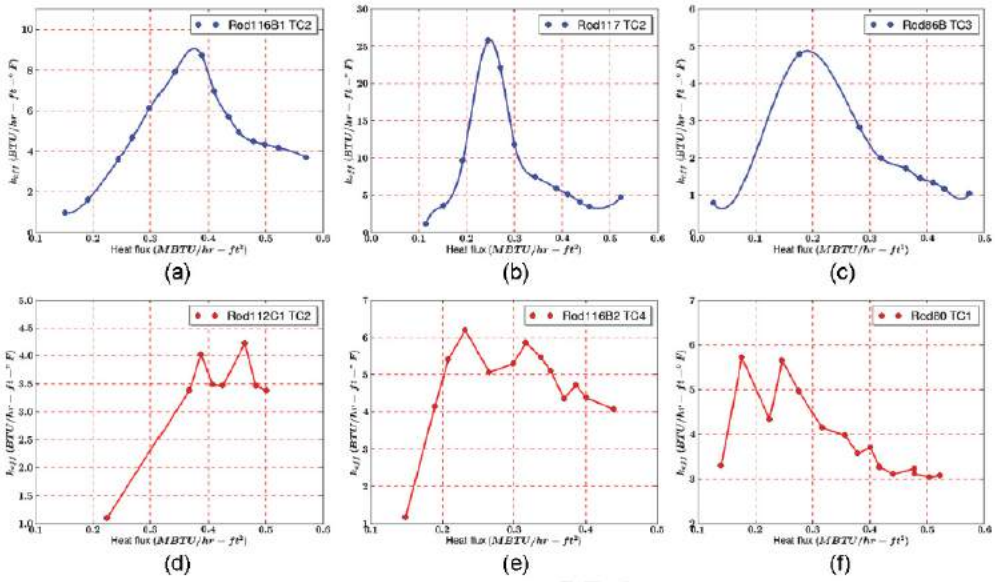


Figure 2-56: This figure shows the calculated effective crud thermal conductivity ($k_{eff}[BTU/hr - ft - {}^{o}F]$) vs heat flux ($k_{eff}[BTU/hr - ft - {}^{o}F]$) for various WALT loop rods [44]. Figure (a)-(c) only have a single peak, while figure (d)-(e) all have double peaks.

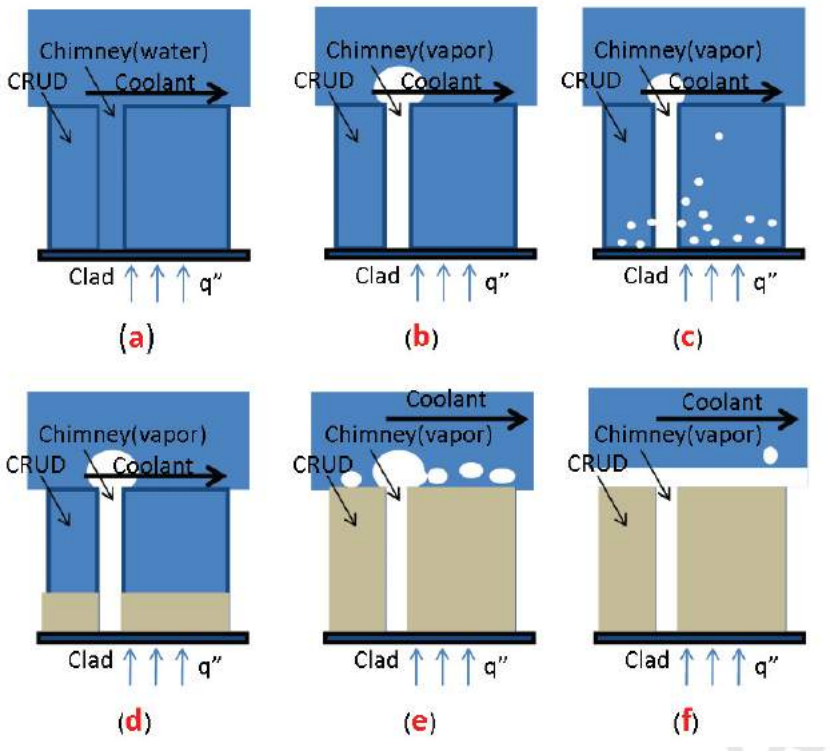


Figure 2-57: crud heat transfer regimes proposed by Jin/Short [44]. Regimes change as heat flux increases. The regimes are: (a) heat conduction by liquid and porous network; (b) wick boiling; (c) nucleate boiling adjacent to cladding surface; (d) film boiling within crud; (e) total crud dryout with sub-cooled boiling at the surface; and (f) film boiling at the crud surface.

#### 2.2.6.2 Experiments Simulating Crud in PWR Conditions

Actual experiments where crud is grown in PWR conditions are not common. There are only few attempts around the world to simulate crud growth at or close to PWR conditions. Most of the attempts are not university based, as PWR conditions are quite hard to achieve. We are aware of three other experiments done close to PWR conditions; they include the Westinghouse Advanced Loop Tester (WALT), the Japanese Central Research Institue of Electric Power Industry (CRIEPI) loop and the Korea Atomic Energy Research Institute (KAERI) loop.

**WALT (Westinghouse Advanced Loop Tester) Loop** The WALT loop is a large integrated crud loop built at the Westinghouse Science and Technology Department Laboratories in October, 2005. The WALT loop is heavily used to study heat transfer through crud, a topic critical to a reactor's operation. It was used to test for crud's thermal conductivity under a variety of conditions that PWR fuel rods can experience [96]. Being able to determine the thermal conductivity of crud means that the cladding surface temperature under the crud can also be obtained. A proper knowledge of the cladding surface temperature is needed to improve the ability to determine the margin to a potential cladding failure due to CILC [8]. Beyond this, the WALT loop is also used to assess zinc additions to PWR coolant, and to perform dryout and hot spot tests.

The thermal conductivity of crud has been examined using the WALT loop. The crud four-regime theory was developed using the experimental results [8]. As the amount of power and inlet temperature increases, the fluid conditions within crud changes. These changes in fluid conditions are categorized into four states, thus the name four-regime model. The first regime, the flooding model, is used to simulate the conditions of liquid flooding in crud chimneys and pores. This typically happens at low power and inlet temperature. The second regime, the mixture model, simulates conditions of vapor and liquid mixed in crud chimney or pores. Second regime usually occurs at medium to high power conditions in PWRs. The third regime is the dryout model. This model describes the dryout process that happens from the bottom to the top of crud layer. The fourth regime, the particle model, is for the condition where crud pores are filled or partially filled with some other solid particles. Another accomplishment of the WALT loop is the development of methodology for crud thermal conductivity measurement based on the crud four-regime theory [8]. According to this methodology, the effective thermal conductivity of crud can be found using the following equation:

$$k_{eff} = \frac{B_1}{\Delta t_1 - \Delta t_2} \tag{2.13}$$

where $k_{eff}$ is the effective thermal conductivity through crud; $\Delta t_1$ and $\Delta t_2$ are the temperature differences between the inner cladding surface measured using thermocouples embedded inside the

heater rod, and the water temperature; $\Delta t_1$ describes the temperature difference for a heater rod with crud, while $\Delta t_2$ describes the temperature difference for a clean heater rod. $B_1$ is the constant obtained using the following equation:

$$B_1 = \frac{q'''(r_2^2 - r_1^2)}{2} \times ln(\frac{r_3}{r_2}) \tag{2.14}$$

where $q'''$ is the volumetric heat flux; $r_1$ is the inner radius of the heater rod cladding ; $r_2$ is the outer radius of the heater rod cladding, which is also the crud layer inner surface radius; $r_3$ is the crud layer outer surface radius. This methodology of obtaining effective thermal conductivity of crud is certainly useful; however, there are still missing pieces that the crud four-regime model fails to pick up. Some of these missing regimes are found through simulation as descibed in Jin's paper (2016) [44]. Upon further examination with a more complex simulation, Jin found that there are also another two distinguishable scenarios for thin crud and thick crud, respectively.

The most important part of the WALT loop is the autoclave which houses the heater rod where crud grows. Water circulates around the rod in a loop to simulate fluid flow within the reactor. Flow is driven by the main pump attached to the inlet of the autoclave. The pressurizing pump is used to pressurize the system while the back-pressure regulator adjusts the amount of pressure. WALT loop's autoclave features a downcomer similar to those found in commercial reactor vessels. The temperature is maintained using the preheater wrapped around the autoclave, which heats the downcomer section. The heater rod itself is an electrical resistance heater rod with current applied throughout the rod. The benefit of using electrical resistance through the whole heater rod is that more heat flux can be obtained. However, this is also a disadvantage of the WALT loop as applying current through out the heater rod, including near heater rod surfaces, may interfere with the electrochemistry. Inaccuracy in electrochemistry may change the way crud grows, especially how crud particles adhere to the heater rod's surface. Figure 2-58 shows photos of the WALT loop.

The WALT loop's condition is very close to that of a typical PWR as shown in table 2.4. Its pressure, and heater rod diameter are the same as a regular PWR. Its heat flux is higher than an average PWR heat flux of 59.89 $watts/cm^2$ [53]. Its chimney inlet temperature is also higher than the PWR core inlet temperature of 292.7 C$^o$. These heighten temperature and heat flux values were chosen to promote faster crud growth. The WALT loop produces crud very similar to that of the reactor, as shown in the earlier figure 2-32. An example of typical data obtained from a WALT loop run is shown in figure 2-59.

**CRIEPI (Central Research Institue of Electric Power Industry) Loop** Similar to PWRs in other parts of the world, Japanese PWRs also have significant issues with crud deposition [118]. The Japanese CRIEPI loop is a large integrated crud loop, built to gain more understanding of these crud issues. Unlike the IHTFP that was built to explore the science governing crud deposition, CRIEPI

| Parameters | WALT Loop Values | PWR Values |
|---|---|---|
| System Pressure, MPa | 15.5 | 15.5 |
| Heat Flux, $watts/cm^2$ | 100.0 | 59.89 (average) |
| Inlet Temperature, C$^o$ | 332.0 | 292.7 |
| Heater Rod OD, mm | 9.5 | 9.5 |

Table 2.4: This figure shows WALT loop's operation condition. As explained earlier, its condition is very similar to that of PWR, with few tweaks to increase crud growth [53, 96].

Figure 2-58: The left photo shows the WALT loop's autoclave setup where the test section is located and the actual crud growth occurs. The right photo is the photo of the WALT loop's chemical control system [8].

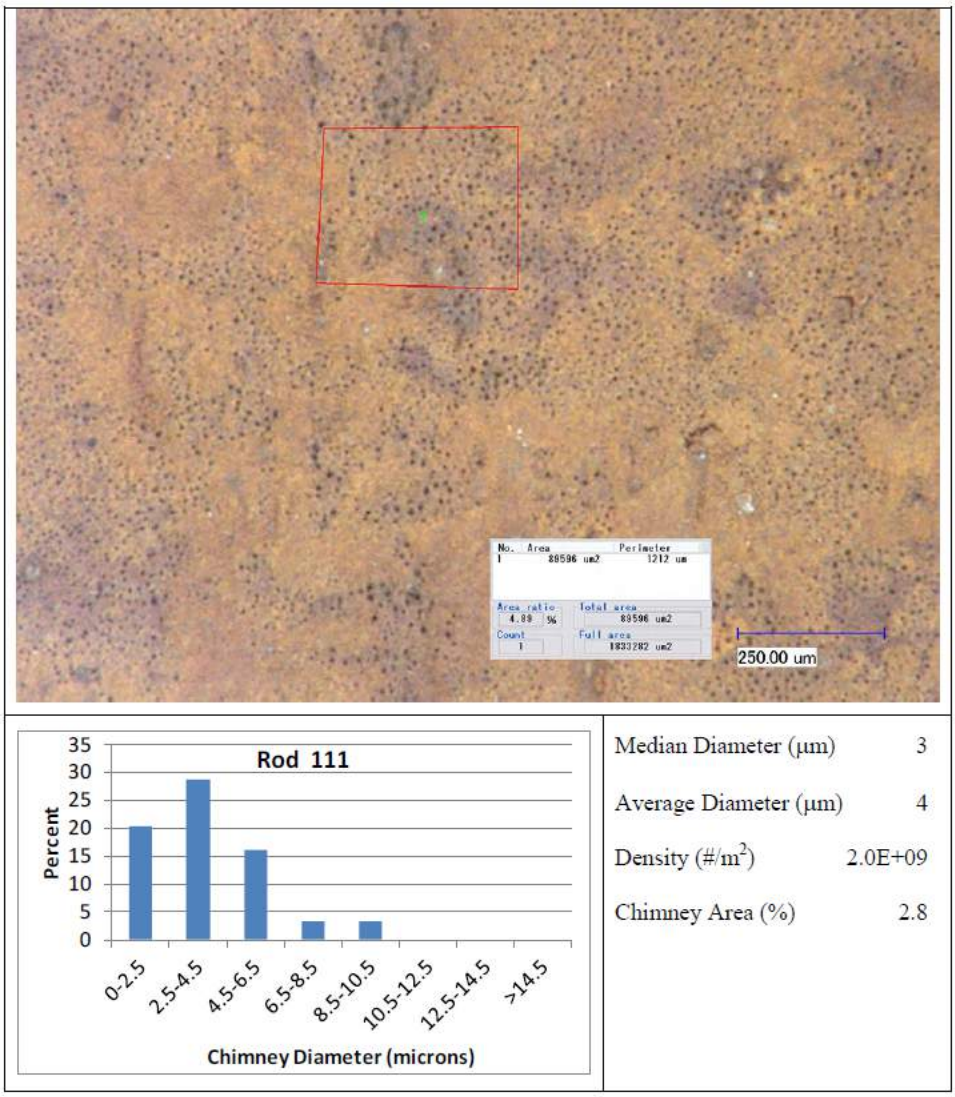


Figure 2-59: This figure shows data obtained from a typical WALT loop's run. The photo shows the top down image of crud in microscope. The crud boiling chimneys on this photo were counted, and their diameters recorded. The plot shows the distribution of chimney by its diameter. Bottom right of the figure shows that value for median and average diameter of chimneys, number density of chimneys, and the percentage of chimney area compared to the area of the whole image.

loop was built to clarify the contributing factors to crud deposition, the effects of crud on heat flux, and the effects of crud on water chemistry in PWRs. The water chemistry being examined includes boron, lithium, zinc, and dissolved hydrogen concentrations [118]. Because of its focus on clarifying parameters of real PWRs' crud, CRIEPI loop's design emphasis is on the accuracy of conditions at which the crud is grown. Size and cost wise, it is many times larger and more expensive than the IHTFP, but also simulates the PWR conditions better than the IHTFP. Each CRIEPI loop's test runs for around 1000-2000 hours [118], which is significantly longer than the IHTFP's runs that last for around 340 hours. It is the only other loop that we are aware of that features a sapphire window. In CRIEPI loop's case, the sapphire window is a lot smaller than that of the IHTFP and is used only for the in-situ Raman spectroscopy.

| | Test specimen | Japanese PWR cladding |
|---|---|---|
| Material | Zircaloy-4 | Zircaloy-4 |
| Outer diameter ($mm$) | 10.72 | 10.72 |
| Inner diameter ($mm$) | 9.48 | 9.48 |
| Heat flux ($W/cm^2$) | 0 - 80 | 60 - 144 |

Table 2.5: Comparison of tube design between the CRIEPI loop's test specimen and PWR cladding [118].

| Thermal hydraulic paramter | Test condition | Typical PWR condition |
|---|---|---|
| Bulk water temperature ($^oC$) | 325 | 325 |
| Pressure ($MPa$) | 12.5 | 15.5 |
| Fluid velocity ($m/s$) | 0 - 7.6 | 3 - 4 |
| Pitch length ($mm$) | - | 14.1 |
| Hydraulic diameter ($mm$) | 12.9 | 12.9 |
| Perimeter length ($mm$) | 33.7 | 33.7 |
| Cross-section of the flow path ($mm^2$) | 108.3 | 108.6 |
| Steaming rate ($kg/sec \cdot m^2$) | 0 - 12 | 0.3 - 0.6 |
| Heat flux ($W/cm^2$) | 0 - 80 | 60 - 144 |

Table 2.6: Comparison of thermal hydraulic parameters between the CRIEPI loop's test specimen and PWR cladding [118].

The CRIEPI loop's crud deposits have thicknesses of several to 10 microns and compositions that include iron-nickel oxide and zirconium oxide when there is no zinc injection [118]. In experiments with zinc injection, crud deposit to several microns thick with the main oxide being grains and needles of $NiFe_2O_4$. $NiO$, which easily formed under the low dissolved hydrogen condition, were detected as well [118]. $NiO$ needles, detected in the US and Korean PWR, were not detected in this study [35, 79].

One of the crucial accomplishments of CRIEPI loop's experiments is the modeling of crud density using water chemistry. The iron and nickel concentrations in the crud layer deposited on the zircaloy-4 surface can be calculated from the following equation [118]:

$$D_{p,a} = (\frac{C_{cb,a}UVtp_p}{vL} - C_{d,a}M_aV)/S \tag{2.15}$$

where $C_{cb,a}$ is the concentration of material $a$ in bulk water $(g/L)$; $U$ is the boiling rate constant (heat flux $(W/cm^2)$ divided by steaming rate $(kg/s \cdot m^2)$); $V$ is the mass of the test solution (L); $t$ is the test time (hour); $v$ is the fluid velocity (m/s); $L$ is the evaluation length (m); $C_{d,a}$ is the concentration of material $a$ at dissolution $(mol/L)$; $M_a$ is the molecular weight of material $a$; and $p_p$ is the crud particle precipitation parameter. $p_p$ can be further dissociated into the following equation [118]:

$$p_p = p_{p,DH} \times p_{p,Ni} \times p_{p,B} \times p_{p,T} \tag{2.16}$$

where $p_{p,DH}$, $p_{p,Ni}$, $p_{p,B}$,and $p_{p,T}$, represent the effects on precipitation parameter by dissolved hydrogen level, nickel concentration, boron concentration, and cladding temperature, respectively. Since parameters other than the precipitation parameter $p_p$ are usually known in experiments or PWRs, CRIEPI data was used to determine the precipitation parameter. The precipitation parameters found are summarized in the figure 2-60. Subsequent verification of the model using Japanese and US PWRs data shows that the model is decent at predicting crud density, as shown in figure 2-61. The only deviation in figure 2-61 is the data point for Japanese PWR-A (3 cycle fuel) which was caused by the effect of crud release from fuel cladding during the three start up and shut down processes [118].

| Test condition | | | Fe | Ni |
|---|---|---|---|---|
| $p_{p,DH}$ | DH < 10 $cm^3$·STP/kg | | $1\times10^{-5}$ | $1\times10^{-5}$ |
| | DH > 10 $cm^3$·STP/kg | | $1\times10^{-5}$ | $1\times10^{-5}$ |
| $p_{p,B}$ | High B | 1800 ppm | $1.0\times10^{-3}$ | $6.0\times10^{-4}$ |
| | Middle B | 1200 ppm | $8.0\times10^{-4}$ | $5.0\times10^{-4}$ |
| | Low B | 350 ppm | $3.5\times10^{-4}$ | $8.0\times10^{-6}$ |
| $p_{p,Ni}$ | High Ni | >33 ppb | $1.5\times10^{-2}$ | $1.5\times10^{-2}$ |
| | Middle Ni | 10 ppb to 30 ppb | $1.0\times10^{-2}$ | $1.0\times10^{-2}$ |
| | Low Ni | < 10 ppb | $6.0\times10^{-3}$ | $6.0\times10^{-3}$ |
| $p_{p,T}$ | Surface temperature of Zry-4 specimen = 325°C | | $1.0\times10^{-3}$ | $1.0\times10^{-3}$ |

Figure 2-60: Table showing the precipitation parameters obtained from the CRIEPI loop's experiments [118].

**KAERI (Korea Atomic Energy Research Institute) Loop** Another experimental setup worth noting is the setup used by the Nuclear Chemistry Research Division, KAERI, in cooperaion with Korea Advanced Institute of Science and Technology (KAIST). This setup is is shown

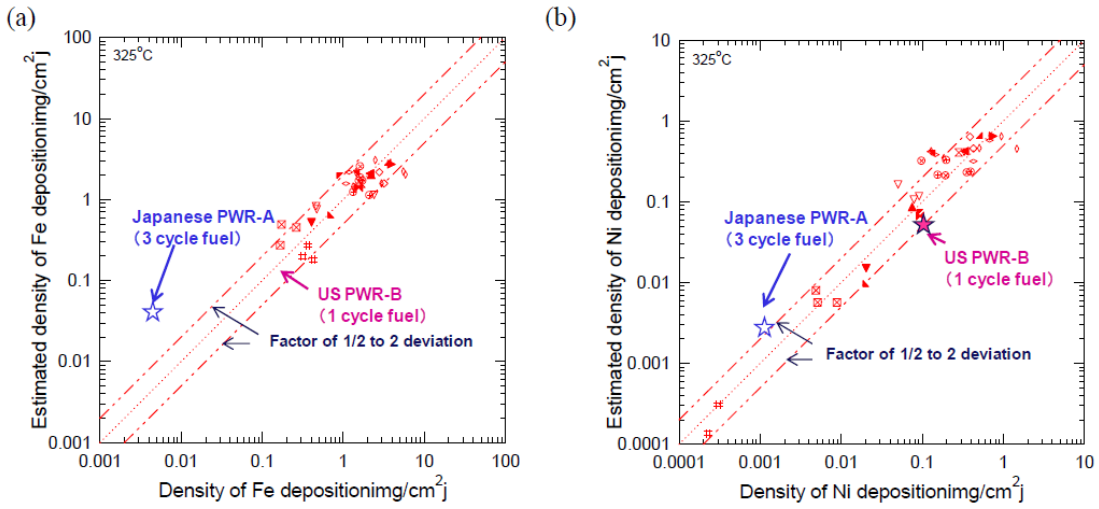


Figure 2-61: Relationship between CRIEPI's crud density model calculations (red lines), experimental data from CRIEPI's loop (red dots), and data from PWRs [118].

in a paper by Jei-Won Yeon published in 2006. It was used to examine the deposition behaviour of corrosion products on the Zircaloy heat transfer surface. It can reach PWR conditions with the maximum temperature of 300 C°, the maximum pressure of 160 bars, and the flow rate of 3mm/s. It is a great example of an experiment done in a university setting, as oppose to an industrial or government settings [98]. Figure 2-62 is the schematic diagram of KAERI's loop.

The KAERI's loop yielded many useful results. Table 2-63 is an example of data obtained by using the KAERI's loop. The table illustrates how iron ions can act as a glue that help crud particles stick to heated surface [98]. In addition to this finding, Yeon also found that dissolved hydrogen, similar to dissolved iron oxide, can promote crud growth, and that heat treated Zircaloy is effective in reducing iron oxide deposition.

## 2.2.7 Prevention or Mitigation of Crud

There are many ideas that have been put forth to reduce the crud growth rate, none of which have worked very effectively. The subsections below will give details about crud prevention and mitigation methods. These methods will be categorized into four main approaches: primary water chemistry modification, ultrasonic cleaning, fuel shuffling schemes, and surface modification.

### 2.2.7.1 Primary water chemistry modification

Modifying the primary loop's water in PWR can help with crud mitigation. As mentioned earlier, current PWR reactor operators achieve some degree of crud resistance by limiting their coolant pH greater 6.9. Other than this pH limitation, there are also the methods of filtering coolant and particulate scavenging, which will be explained in the following subsections.

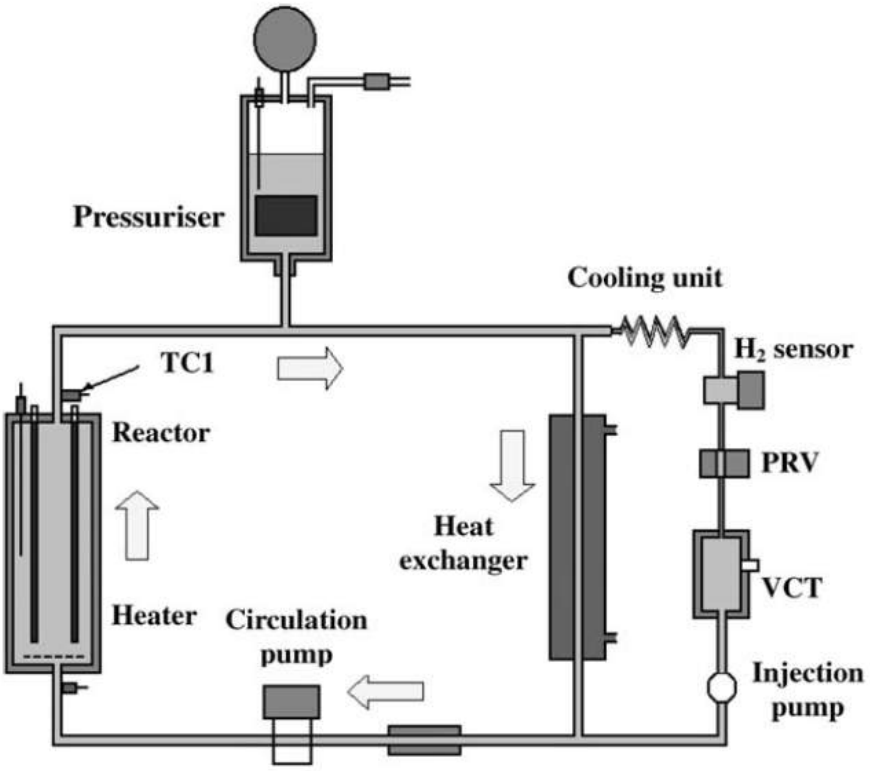


Figure 2-62: Schematic diagram of the KAERI loop [98].

Effects of $Fe^{2+}$ ions on the deposition of suspended hematite on the heat exchanging Zircaloy surface

| Deposition solution (μg/ml Fe) | Amount of deposits (μg Fe/$cm^2$) | Layer |
|---|---|---|
| Suspended hematite (30) | < 0.1 | – |
| Suspended hematite (30) + $Fe^{2+}$ ions (50) | 2.3 | Outer |
| | 10.5 | Inner |

Figure 2-63: Example of an interesting result from the KAERI loop [98]. This table shows two trials of crud growth experiment. The first trial contains only hematite particles as crud precursor. The second trial includes both hematite particles and the iron ions as crud precursor. The table shows that the amount of deposit is significantly higher for the trial with iron ion included. This led to the theory that iron ion may act as a glue to make hematite particles stick to the heated surface [98].

**Filtering coolant** The filtering of coolant in nuclear power plants to get rid of unwanted chemicals is a common practice. The Chemical and Volume Control System (CVCS) in a PWR can filter out most corrosion particles. The physical filters can filter out larger particles, while the mixed-bed demineralizers can remove ions from the coolant water. However, particles in the range of 50 nm are small enough to avoid capture by the CVCS, while large enough to make removal by mixed-bed demineralizer improbably. These corrosion particles are what constitute most crud seen in PWR reactors. O'Brien (2014), has also shown that the first principle calculation predicts stable 50 nm-sized nickel ferrite particles in PWR coolant. Therefore, this common method of filtering coolant will not be enough to prevent the crud formation [40].

**Particulate Scavenging and Filtration** Panson (1989), proposed a solution whereby zirconium oxide particles are injected into coolant. The zirconium oxide particles will attract corrosion products floating in the reactor coolant, and then accumulate into larger particles. These larger particles can be easily filtered out via Chemical & Volume Control System (CVCS) to reduce the amount of crud depositing on the fuel rods [119]. Panson mentioned that although the invention was described in terms of zirconium oxide particles, any other particles that may attract corrosion products may be use as well. Zirconium oxide was chosen because it was already known that zirconium oxide layers on cladding do attract crud. In addition, adding zirconium oxide particles to the reactor does not introduce any new chemical species to the reactor. Information about how zirconium oxide particles might interact chemically corrosion products was not included in the patent. The patent's expectation that these zirconium oxides can attract a significant amount of particles is based on providing a sufficiently large amount of particles, so that their cumulative surface area can compete with the surface area of fuel elements [119]. Panson suggested that a one pound batch of 10 m spherical particles would have a surface area of $1 \times 10^6\ ft^2$, whereas the typical core surface area in a conventional reactor is about $6 \times 10^4\ ft^2$.The lack of any further studies of this method suggests that it may not be feasible. One important question can be raised regarding the actual attractiveness of zirconium oxide particles to the corrosion products. crud in reactors forms on heated surfaces, especially those that exhibit sub-cooled boiling. It is unlikely that these zirconium oxide particles will be nearly as effective as heated fuel rods in attracting crud.

**Magnetic Filtering** Emory (1983) proposed magnetic filters for the PWR primary coolant. This method uses very strong magnet to separate corrosion particles from the PWR primary coolant. As mentioned earlier, the current CVCS systems are usually blind to particles small enough to slip through physical filters and large enough that they do not dissolve into ions. Using magnetic filters will remove any iron and nickel particles that would otherwise deposit as crud, regardless of their size [120]. Although no further information regarding Emory's experiment was published after the conference, there are others who revived the studies of magnetic filtering in more recent years. Song

et al. [121] published his magnetic filtering experimental results, suggesting that magnetic filters can be quite effective in removing magnetite. Figure 2-64 demonstrates the efficency of magnetic filters on magnetite. At lower flow rates, the magnetic filter can easily reach 90% efficiency.

The major disadvantage of this technique is that it is only effective against magnetite. The magnetic properties in other corrosion products including nickel ferrite is significantly weaker [121]. More recent examinations of the composition of commercial reactors' crud such as that of Sawicki (2010) [85] and Yeon (2010) [35], demonstrate that crud composition includes significant amounts of nickel-ferrite. This is probably one of the reasons that led to the loss of interest in the use of magnetic filtering in recent years.

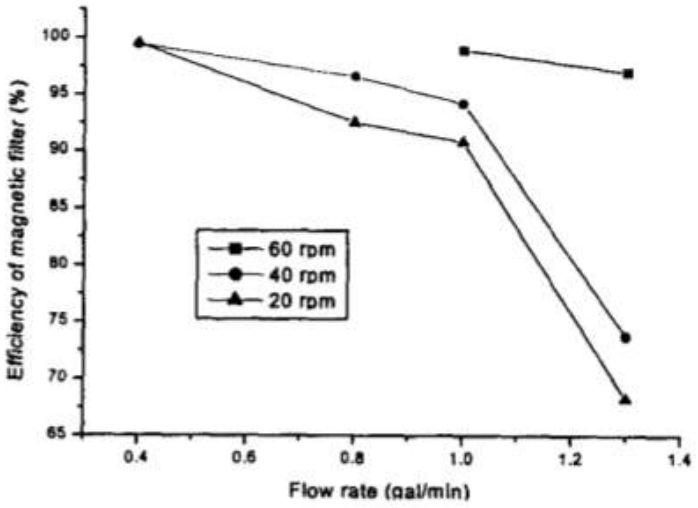


Figure 2-64: The efficiency of magnetic filter versus flow rate in the experiment conducted by Song et al [121]. Each line represents a rotation speed of the alternating magnetic filter used. Note, however, that magnetite was used for the experiment; nickel ferrite particles, which are found abundantly in crud, were not examined.

#### 2.2.7.2 Surface modifications

Other than modifying the water chemistry in PWRs to eliminate any crud particles inside the PWR water coolant that could accumulate as crud, the PWR cladding can also be modified so that even if there are crud particles in the PWR coolant, they will not be able to stick easily to the cladding to form crud. There are many ways that cladding surfaces can be modified to achieve crud mitigation. The paragraphs below will give details on some of the possible methods, including the electropolishing method, the polishing patterns method, and the coating method. Note that the coating method will be the focus of this thesis experiment.

**Electropolishing** Byers [79] mentioned that electropolishing can eliminate surface defects that can act as a bubble nucleation site. Since crud deposition is most likely caused by bubbles, elimi-

nating nucleation sites will mitigate crud growth. Without nucleation sites, there will not be any sub-cooled boiling and therefore crud will be mitigated, at least theoretically. However, actual experimentation reveals that in a rod with very low roughness, boiling will be concentrated at any little scratches on the rod surface. This leads to a very rapid crud growth at those scratches [79]. In addition, even if this method worked, having no nucleation sites and boiling means significantly less heat transfer. PWR specifically use sub-cooled boiling to maintain effective heat transfer; therefore, this may lead to significant efficiency loss.

**Polishing Patterns** Byers proposed another solution where the sub-cooled boiling regions of the cladding might receive extra polishing. This method is similar to the electropolishing method, but with only some areas being polished. In a 2004 , William A. Byers, filed a patent for "crud-resistant nuclear fuel cladding". crud-resistant fuel claddings in this patent are claddings with patterns of surface roughness designed to minimize the build-up of thick crud. Parts of a cladding that could experience more crud growth are polished very finely to eliminate any surface defect greater than 0.1 microns. With bubble nucleation sites eliminated, there will be fewer sub-cooled bubbles appearing. If bubbles do appear, they will appear randomly on the polished surface, not at specific nucleation spots causing crud buildup. With this, the tendency of crud to grow in big patches will be reduced [79]. In a place where there is less sub-cooled boiling, coarse finish is given to the cladding. This makes the coarse-finished area attract more crud particles that would otherwise build up on other areas. With the polishing patterns, thinner and more evenly distributed crud should be obtained, as opposed to a large, thick patch.

The advantage of this technique is that it is can be applied to fuel rods without any upgrade to the reactor. One major disadvantage, on the other hand, is that does not prevent crud, but is only a way to cope with a crud problem. Therefore, it may be not be worth the extra cost that will come with manufacturing polishing patterns. Another major disadvantage is that the polished surface may not stay polished very long inside the harsh conditions within the reactor.

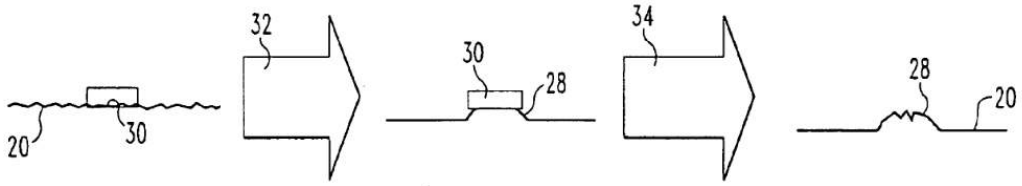


Figure 2-65: Diagram of how one might create an electropolishing pattern [79]. Number 20 represents the surface of cladding; number 30 represents the electropolishing mask that is immune to electropolishing; number 32 represents the electropolish step; number 28 is the cladding surface after electropolishing that had not been polished because of the presence of electropolishing mask; number 34 represents the last step where the electropolish mask is remove.

**Coatings** In this method of crud prevention or mitigation, the fuel rod claddings will be coated with materials that will lessen the adsorption of crud particles to the surface of fuel claddings. With less adsorption, even if there is subcooled boiling and the crud particles have the chance to touch the cladding surface, they will not stick to the surface. As a result, crud may not form. To our knowledge, we are the only group that is experimenting with using a coating method as a means to prevent or mitigate crud in PWR [7]. One reason that coating has not been well-explored by previous literature could be that it is more difficult from both a scientific perspective and from a manufacturing perspective. As to the scientific perspective, it is very hard to find something that can withstand the conditions within PWRs. The harsh condition rules out most of the organic materials that are usually useful when it comes to coating. From a manufacturing perspective, coatings will increase the cost of fuel, especially if the material used is rare or exotic. However, since we have seen from previous literature that other simpler approaches had been exhausted, the coating approach now returns as an attractive candidate for crud prevention. Crud prevention through cladding coating techniques will be a focus of this thesis.

#### 2.2.7.3 Ultrasonic cleaning

Acoustic vibration can be used to break up crud layers, making it easier to flake off from the surface. Ultrasonic cleaning utilizes acoustic vibration at a high frequency to clean out crud layer during refuel [51]. This method is already in use in some PWRs, but it is very limited in usefulness, since it can only be done during refueling. Ultrasonic cleaning had been shown to be effective for removing crud in PWR and mitigating the CIPS problem. In addition, it was shown that reducing crud also reduces the radiation dose to personnel during refueling [51]. This reduction in radiation exposure was clearly shown in the Callaway PWR's case, where around 50% reduction in radition dose rate was observed following the ultrasonic cleaning of crud. Modeling calculations of radiation dose rate by both Westinghouse and General Electric agreed with the magnitude of radiation reduction observed at the Callaway PWR [51]. This might not be surprising, given the fact that Cobalt-60 plays a huge role in worker dose rate, as mentioned earlier in section 2.2.5.3. Removing crud is essentially removing the largest source of Cobalt-60 [51]. This technique's major disadvantage is that it cannot be done while the reactor is online for obvious reasons. As a result, it becomes only a temporary treatment to the crud problem rather than a final solution.

#### 2.2.7.4 Fuel shuffling schemes

Fuel shuffling schemes to minimize subcooled boiling is another method used to mitigate crud formation. In nuclear reactors, different fuel assemblies have different amounts of burnup unless the assembly is new. Fuel with higher burnup will generate less neutron flux, while fuel with lower burnup will generate more neutron flux. If fuel assemblies are not shuffled, the cluster of fuel assemblies

with lower burnup may become a hot spot. Using this method, fuel assemblies are shuffled so that the local power peaks in the reactor will not be as high. With lower power peaks, the chance that subcooled boiling will occur will be lower. One of the most common nuclear fuel assembly loading patterns is called "Ring-Of-Fire." Figure 2-66 is a diagram of fuel assemblies with the Ring-Of-Fire pattern. Number 204 and 206 on the figure represent new and once-through fuel assemblies respectively. In this pattern, new fuel assemblies are placed in ring shapes as shown in the darker pattern shading in figure 2-66, and thus the name "Ring-Of-Fire." The rest of the new fuel assemblies are placed in checker pattern in the center part of the reactor core. The Ring-Of-Fire pattern is optimized for longer cycle length, higher average enrichments and higher fuel duty [122]. Higher fuel duty is due to the increase in sub-cooled boiling, enhancing the effectiveness of heat transfer [122]. Larger amounts of sub-cooled boiling, unfortunately, also cause more crud growth. Patents such as that of Lukic [122], suggest methods of arranging fuel assemblies so that they discourage crud growth problems. A Fuel-shuffling scheme as a method of crud reduction has the obvious disadvantage of decreasing the overall efficiency of the reactor, since a reactor with less sub-cooled boiling also has less heat transfer, and therefore, less power.

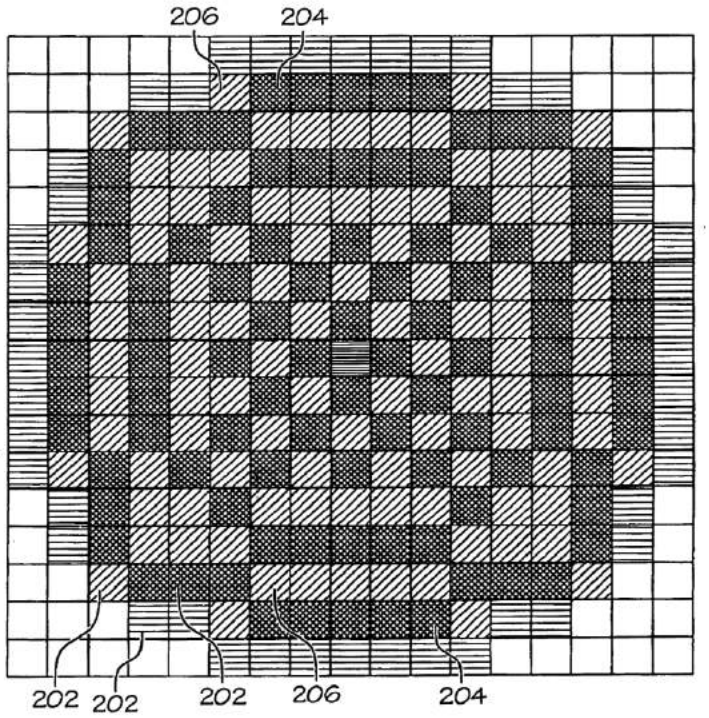


Figure 2-66: Diagram of conventional ring-of-fire fuel assemblies loading pattern. Each small shaded square tiles represents a top-down view of fuel assemblies in a nuclear reactor. Number 202 represents multiple types of fuel assemblies; number 206 represents a once-burned fuel assemblies; number 204 represents new fuel assemblies [122].

## 2.3 Fractal Analysis for Crud

Fractals are geometric shapes that can be split into parts, each of which is a smaller-sized copy of the whole [123]. Before Mandelbrot's breakthrough in the fractal world, Euclidian or standard geometry failed to properly describe the shape of many things occurring in nature which are extremely irregular and fragmented. For example, the shape of a cloud, a mountain, a coastline or a tree, cannot be easily described using a simple Euclidian geometry such as a sphere, a cone or a circle. Fractal geometry, the new geometry of nature, were developed by Mandelbrot. Fractal theory describes a family of shapes which Mandelbrot called fractals. According to Mandelbrot, the most useful fractals involve chances and both their regularities and their irregularities are statistical . The shapes described tend to exhibit "scaling," which means that their irregularities or fragmentations are identical at all scale.

The motivation for applying the fractal analysis to crud is to verify that crud actually exhibits fractalline properties. Such analysis also allows us to determine the actual properties of crud, such as its fractal dimensions. This is useful because we can use fractal dimensions to calculate the permeability of water flowing through crud as well as the thermal conductivity of crud. The MAMBA-BDM model, developed by Short [7, 44], simulates the conditions within PWR crud. One area that is still missing experimental data is the permeability of crud, which was previously estimated. The present thesis will attempt to fill in the missing permeability experimental data by applying the fractal analysis box-counting method on the scanning electron microscope images obtained from crud grown using the IHTFP.

This section will explore the use of the fractal theory in the characterization of crud formation. First, an introduction on how a fractal is related to crud will be given. Then the fractal dimension, one of the core of fractal theories, will be explained. After that, the specific topic of why the fractal dimension is used in this thesis, and how that relates to the fractal permeation model, will be explained. With the theories explained, the thesis will go on to elaborate the method used in this thesis to examine crud fractal properties.

### 2.3.1 Fractals in Nature

Fractals are quite common in nature. Natural occurances of fractal include objects such as ocean coastlines [124, 125], rivers [126, 127], mountains [128], vegetables/plants [129], snowflakes [130], ant nests [131], and termite mounds [132]. In fact, the motivation for making the fractal theory by Mandelbrot, was to characterize the complexity in nature that cannot be explained with the Euclidean geometry. The following figures 2-67, 2-69, and 2-70 shows some examples of fractal occurance in nature.

For any of these natural fractals, fractal dimensions can be obtained using different methods.

Fractal dimensions of broccoli were found by Kim to be around 2.7-2.8 [133] by using the original equation describing fractal dimension proposed by Mandelbrot 2.3.4 (uncertainties not provided). Another paper found the fractal dimension of pepper, eggplant, and tomato leaves to be 1.099, 1.1306, and 1.1518, respectively [134]. This second paper uses the box-counting method to find the fractal dimensions. The box-counting method will be described in detail in section 2.3.9.2. The box-counting graph is this second paper has the $R^2$ of 0.9962 for pepper leaf, 0.9913 for eggplant leaf, and 0.9972 for tomato leaf (section 2.3.10 explains $R^2$ in more detail).

Kolwankar (2014) [135] obtained a fractal dimension for the Varasgaon and Panchet reservoir shown in the right image of figure 2-68. The reservoirs' edge borders mountains so that the reservoirs' edge acts similar to lines that trace around the mountains at a constant height from sea level. This makes it a perfect candidate for the fractal analysis of mountains. The photo of the two reserviors were manually processed into a binary image as shown in the top right image of figure 2-68. After that, an edge detection algorithm was used to obtain the reservoir's edges as shown in the bottom right image of figure 2-68. By utilizing the box-counting method, Kolwankar found the fractal dimension of $1.32 \pm 0.02$ for the Varasgaon and Panchet reservoirs.

One simple way to obtain the fractal dimension of a snowflake similar to that shown in the top image of figure 2-71, is by treating the snowflake as the Koch snowflake. The Koch snowflake was first described by Helge von Koch in 1904 [130]. The bottom image of figure 2-71 demonstrates the progression of Koch snowflake pattern. The Koch snowflake has a fractal dimension of 1.26. Lightning such as that shown in figure 2-70, also clearly exhibits fractal patterns. Agoris (2002) [136] examined the fractal dimension of lightning with box-countin method, and found that fractal dimension of lightning varies from 1.10 to 1.32 (uncertainty not provided).

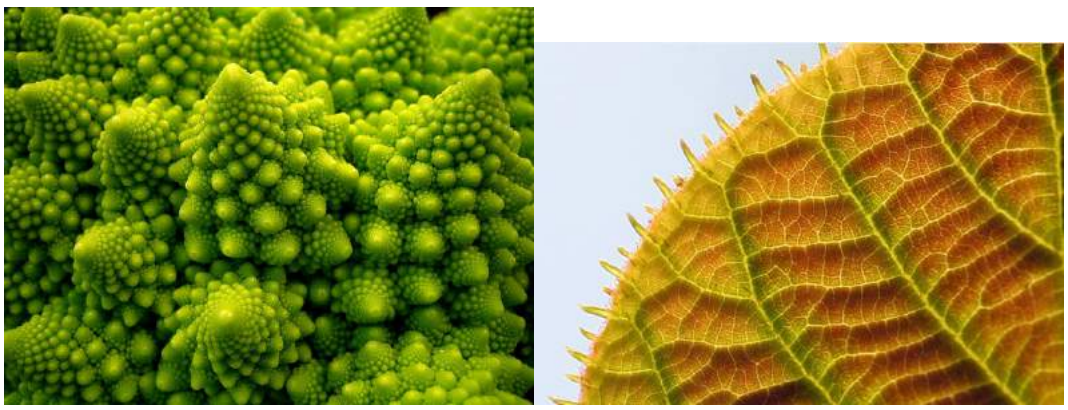

Figure 2-67: The left photo shows elaborate zoomed-in 3D fractal patterns in Romanesco Broccoli. The right photo shows fractal patterns that exist in a leaf [137].

The following table 2.7 exhibit fractal dimensions of various coastlines calculated using measuring rod method. These values were obtained by University of North Carolina. The Measurement rod is another method used for measuring coastline as first suggested by Mandelbrot himself. It is useful

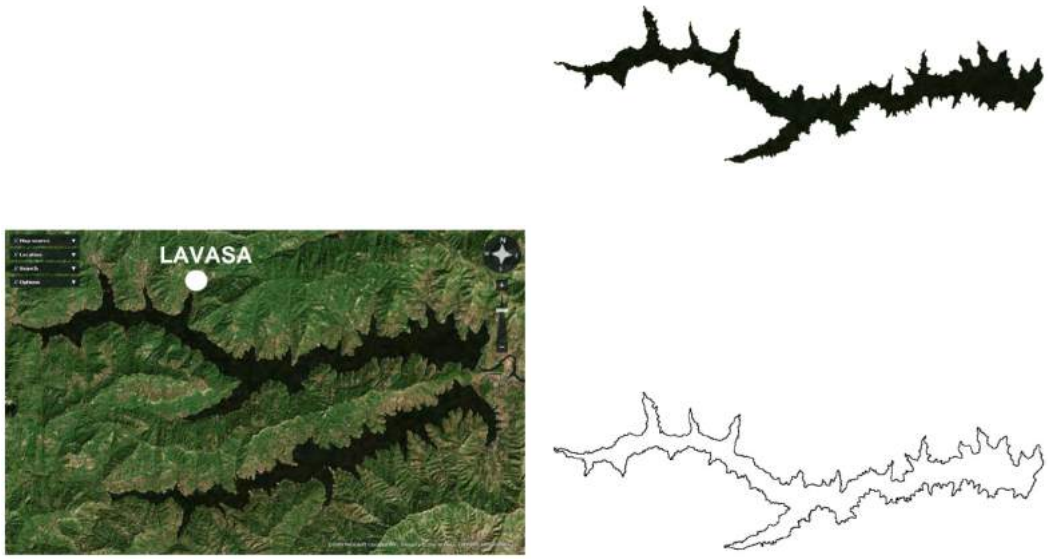


Figure 2-68: The left figure shows the original photo of the Varasgaon and Panchet reservoir . The top right figure shows the manually processed binary image of the lake. The bottom right image shows final image used for determining fractal dimension that was obtained by using an edge detection algorithm [135].

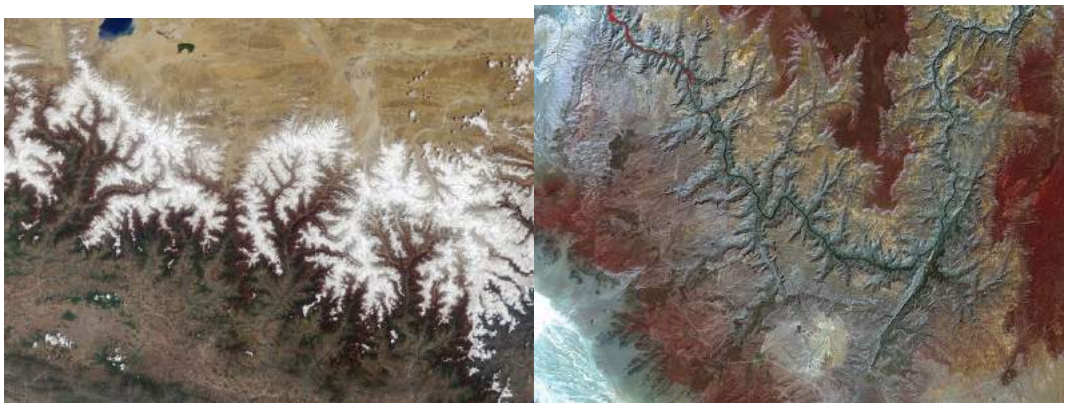

Figure 2-69: The left photo shows beautiful fractal patterns on the top view of a mountain range. The right photo shows fractal occurance in top-view of Canyon. Fractal arrangements play a huge role in shaping the geography [137].

Figure 2-70: This photo is a picture of fractal patterns in lightning [137].

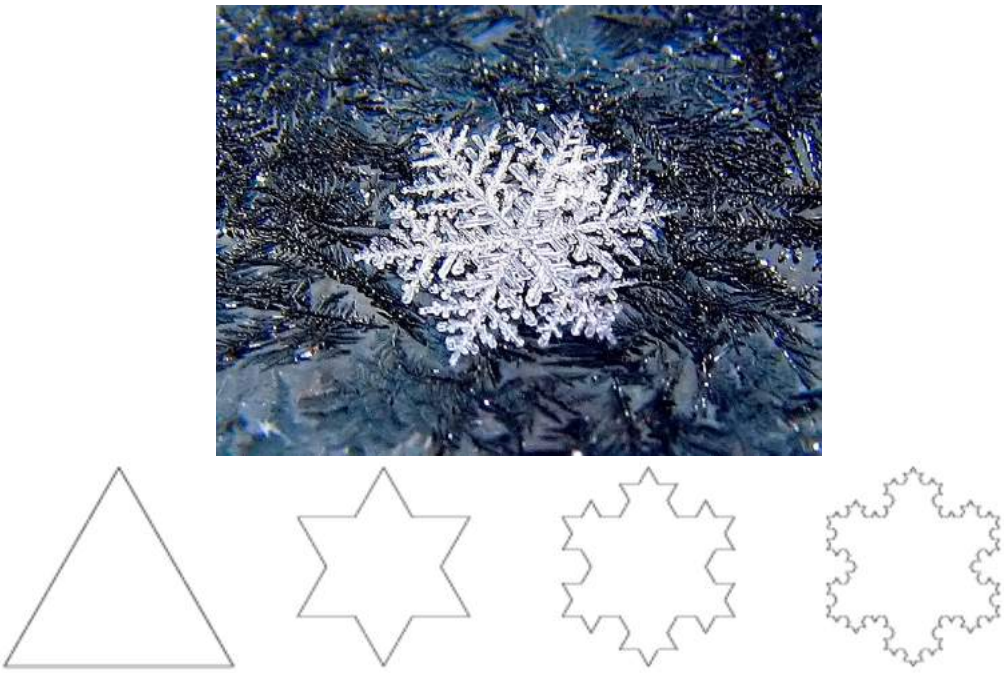

Figure 2-71: The top photo shows a zoomed-in snowflake with fractal patterns [137]. The bottom diagram shows the Koch snowflake which was inspired by a real snowflake [138]. The Koch snowflake starts with a simple equilateral triangle. Each step of Koch snowflake fractal pattern adds more equilateral triangles to each edge from the previous step.

for measuring fractal dimension of fractal lines.

| Country's coastlines | Fractal dimension |
|---|---|
| South Africa | 1.05 |
| Australia | 1.13 |
| Great Britain | 1.25 |
| Norway | 1.52 |

Table 2.7: This table shows the fractal dimension of coastline calculate by using the measurement rod method [139].

### 2.3.2 Crud Fractal Analysis Problem

Although the fractal analysis is becoming widely used in fields that try to characterize porous materials such as in soil science [140, 141, 142], it has never been used to analyze crud before. This study on the fractal properties of crud is the first of its kind. The MAMBA-BDM model, developed by our research group, uses estimated fractal properties as input parameters when calculating the permeability of crud. With real experimental data on these fractal properties, the MAMBA-BDM will be able to model crud even more accurately than before [7, 44], and this thesis will quantify changes in crud's predicted effects using these measured fractalline properties.

The MAMBA-BDM model itself is a significant leap in crud simulations when compared to its

predecessors. In older crud models, simplifications were made, such as infinitely soluble species, one-dimensional analysis, constant material properties, liquid saturation, and decoupled physical phenomena [7]. These assumptions were undesirable, but the older crud models required simplifications because of the limitations in the computing power. The MAMBA-BDM exploits the new advances in high-performance computations to enable crud to be simulated more accurately than ever before.

### 2.3.3 How is Fractal Related to Crud?

When talking about fractals, many people will relate fractals to perfect mathematical fractals that can be rendered into beautiful images. However, Mandelbrot's purpose for creating the fractal theory was actually very practical in its nature. The intention was not create aestheticallly pleasing fractals that show the beauty of mathematics, but rather to develop a new geometry of nature that can describe more complex shapes in the natural world that cannot be described with Euclidian or standard geometry [123]. Crud formation is just one of the countless products of nature that fractal theory was made to describe.

According to Mandelbrot's 1977 book Fractal Geometry of Nature, "Scientists will (I am sure) be surprised and delighted to find that not a few shapes they had to call grainy, hydralike, in between, pimply, pocky, ramified, seaweedy, strange, tangled, tortuous, wiggly, wispy, wrinkled and the like, can henceforth be approached in rigorous and vigorous quatitative fashion [123]." Certainly, crud is very complex and irregular that it cannot be quantify easily with Euclidian geometry. One approach, when examining systems that are too complex to be described easily in mathematical terms, is to use experiments to determine important data such as permeability that can be used for practical purposes. However, in the case of crud, its tiny size make it virtually impossible to conduct experiments to find microparameters such as the permeability. Section 2.1.2.2 previously described how crud samples are too small for porosity measurement using typical methods, such as Boyle's porosimeter and mercury porosimeter. This is why we turn to the fractal analysis for a more rigorous characterization of crud's properties.

### 2.3.4 Fractal Dimensions

The fractal parameter that we are measuring using experimental data is the fractal dimension. To understand the concept of fractal dimension, let's first review what a dimension means. A line has a dimension of one because the movement of a point on the line is restricted to one axis. Likewise, a plane has two dimensions because the movement of a point on the plane is restricted to two axes, and a cube has three dimensions because the movement of a point on the cube can be in the direction of its length, width, and height. One important aspect to notice is that lines, planes and cubes are all self-similar. This means that it can be separated into smaller pieces while maintaining the same

geometric shape. For instance, a line can be separated into three lines, with each of the three lines having similar shape to the whole and having magnification factor of three compare to the whole [143]. As stated by Mandelbrot, the fractal dimension is the ratio between the logarithm of the number of self-similar pieces to the logarithm of the magnification factor [123].

$$Dimension = \frac{log(numberOfSelfSimilarPieces)}{log(magnificationFactor)} \tag{2.17}$$

With this definition, the line which can be separated into three self-similar pieces with the magnification factor of three now has a fractal dimension of one corresponding to the actual Euclidean dimension. This procedure can be further generalized for cutting a line into N-pieces yielding the exact same dimension of one. Similarly, a plane can be cut into nine equal pieces of similar shape to its parent with a magnification factor of three. Generalizing this, a square plane can be cut into $N^2$ equal pieces with similar shapes to its parents with magnification factor of N. Using Mandelbrot's definition of the fractal dimension, we yield a fractal dimension of two for planes, corresponding to the planes' Euclidean dimension of two. Similarly, a cube will have three dimensions using this procedure [143].

Now that we have established a connection between the fractal dimension and the Euclidean dimension, we can use Mandelbrot's definition of the fractal dimension above to calculate the actual fractal dimension of certain true fractals, such as Sierpenski triangles. Sierpenski triangles can be broken down into three self-similar pieces with a magnification factor of two or nine pieces with a magnification factor of four, as shown in figure 2-72 [143]. Using Mandelbrot's fractal dimension formula in equation 2.3.4, the Sierpenski triangles yield a fractal dimension of:

ln(3)/ln(2) = 1.58

ln(9)/ln(4) = 1.58

Generalizing this to N we get:

$$\frac{ln(3^N)}{ln(2^N)} = \frac{N * ln(3)}{N * ln(2)} = 1.58 \tag{2.18}$$

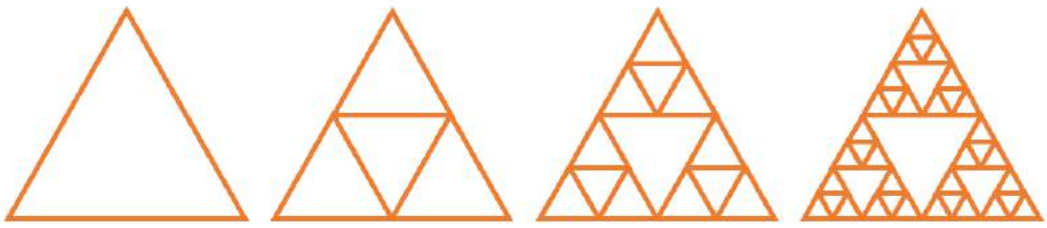

Figure 2-72: Sierpenski triangles. Notice that in each drawing, the triangles can be divided into three similar shapes that are half the size of originals. This means that the number of self similar pieces per division for the fractal dimension formula is three while the maginification is two.

Fractal dimension, in a sense, is a ratio that provides information on the complexity of a self-similar shape. Note that there cannot be true fractals in nature [144]. A true fractal, by mathematical definition, should scale to infinity; this can never happen in the real world. In real world applications, the data we obtain will always exhibit an imperfect self-similarity. For instance, the coastlines will exhibit a self-similarity in some range of scale only. Of course, the fractal nature of coastlines can only be seen when observing them from very far away, such as on satellite images or maps. When we are at the beach, the coastline's fractal nature is almost unnoticable. Romanesco broccoli also exhibits fractal structure, as shown in section 2.3.1. Again, the fractal nature of romanesco broccoli cannot extend infinitely; it is obvious when zoomed in enough that romanesco broccoli is composed of plant cells. Any fractal structure in nature cannot continue forever; it must end somewhere. It is obvious that zoomed in close enough, there will always be atomic structure where fractals in nature cannot continue its self-similarity property. In the case that fractal analysis is done using images, the resolution of images most likely will breakdown self-similarity long before it actually does so in nature. Nevertheless, characterizing the fractal dimension from images will give data that are useful for characterizing the samples.

There are two main reasons why we are interested in the fractal analysis of crud. First is that it can be used to predict the permeability via a fractal permeation model. By knowing the permeability from the fractal dimension, the thermal conductivity can be calculated with the heat transfer equation shown in next section 2.3.5. The second reason is that knowing the fractal dimensions might give us a better understanding of how crud forms, and possibly give an insight into how crud can be mitigated. For this purpose, the fractal dimensions of different areas and heights will be investigated to see if there is any inherent pattern that can be explained.

### 2.3.5 Fractal Permeation Model

As mentioned earlier, crud has a porous structure which allows the water to permeate through. It also contains boiling chimneys which act as nucleation sites for sub-cooled boiling bubbles. Water inside the crud turns to gas and combines into bubbles which exit out of crud chimneys. (It is unknown whether the water turns into gas while inside crud's porous structure or at the inside of the chimney.) This means that the rate at which bubbles exit chimneys will depend on how quickly water can permeate through crud. Porosity alone does not suffice in describing how fluid flow through crud, as explained earlier in section 2.1.2.2. Permeability, on the other hand, can be used to characterize fluid flow through crud. The permeability through porous medium such as crud can be described using Darcy's law equation shown below:

$$Q = -\frac{\kappa A(p_b - p_a)}{\mu L} \tag{2.19}$$

$Q$ is the total volumetric flow rate in $m^3/s$; $\kappa$ is the effective permeability in $m^2$; $A$ is the flow area cross-section in ; $p_b - p_a$ is the total pressure drop in Pa; $\mu$ is the fluid viscosity in Pa $\cdot$ s; L is the length over which the pressure drop is taking place in m. Darcy's law equation essentially describes diffusive fluid flow through medium. Darcy's law can be extended to take into account fractal geometry. The permeability is a function of the geometry which can be quantified by the fractal area dimension $d_N$ and the fractal tortuosity dimension $d_T$ as well as the volume fraction, $v_f$ [145]. Through using Darcy's law and the determination of the total volumetric flow rate $Q$ in $m^3/s$, the effective permeability $\kappa$ in $m^2$ can be obtained as follows:

$$\kappa = \frac{\mu L_0 Q}{\delta A_0} = g_q \lambda_{max}^2 \beta^{1+d_T} \frac{(1 + d_N(1 - \alpha^{D+d_T-d_N}))}{3 + d_T - d_N} \tag{2.20}$$

[145, 7]

Apart from those variables described above, $\delta A_0$ is the flow area cross-section in $m^2$; $\alpha$ is the minimum to maximum pore size ratio; $\beta$ is the maximum pore size in $m^2$; $g_q$ is $\pi/128$; D in the equation represents the dimensionality of the material, either 1D, 2D, or 3D. Lastly, figure 2-73 below further shows what $\lambda$, and $L_0$ in the equation above represent in a porous structure system.

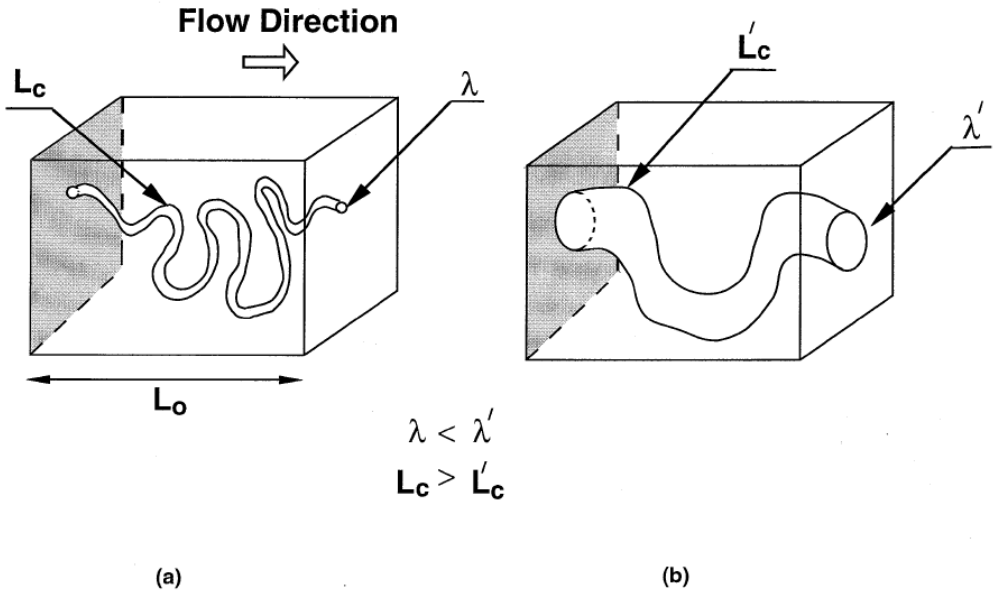


Figure 2-73: A simplified diagram of the capillaries inside a porous structure. $\lambda$ and $\lambda'$ are the pore sizes and $L_c$and $L_c'$ are the tortuous length of the capillary [145].

When analyzing a 3D porous system, fractal dimensions can be further separated into the fractal area dimensions and the fractal tortuosity dimensions [145]. The fractal area dimensions and tortuosity dimensions can be used to calculate the permeability as mentioned above. The following sections will go into detail about what the fractal tortuosity and the fractal area dimensions rep-

resent. By knowing the fractal permeability, it is possible to calculate the thermal conductivity of crud layer using the thermal conductivity equation. The governing equation for temperature field is as follows [44]:

$$-\nabla \cdot (k_{CRUD} \nabla T_l) + \rho c_p \tau (\frac{\kappa}{\mu \epsilon} \nabla P_l) \nabla T_l \tag{2.21}$$

Where $P_l$ is the pressure distribution in Pa, $T_l$ is the temperature distribution in K, $k_{CRUD}$is the solid/fluid averaged fractalline crud thermal conductivity in $W/m^2K$ , $\rho$ is the fluid density in $kg/m^3$, $c_p$ is the specific heat capacity of the fluid in $J/g$, $\tau$ is the tortuosity, $\mu$ is the fluid viscosity in Pa $\cdot$ s, $\epsilon$ is the porosity of the crud, and $\kappa$ is the crud permeability in $m^2$ found through fractal permeation model. This equation is used in the two-phase crud model also developed by our group [44] to predict the thermal conductivity of crud. If we can replace the estimated fractal dimension value with the experimental fractal dimension value, this model can be made even more accurate.

### 2.3.6 Fractal Tortuosity Dimension ($d_T$)

As mentioned in previous sections on microscopic parameters, tortuosity describes how twisted the flow pathways are. The fractal tortuosity dimension, $d_T$, represent the extent of convolutedness of capillaries pathways. In 2D, the fractal tortuosity dimension can range from 1 (straight path) to 2 (curve that filled the whole plane). Tortuosity literally represents how tortuous the flows in the capillaries are, therefore, the images to analyze in order to get the fractal tortuosity dimension would have to be parallel to flow path [145]. In crud, it is expected that the water flows down into a crud layer and exits again as steam from boiling chimneys. Therefore, images parallel to flow paths can be found using the cross-section images of crud layers. By applying the box-counting method 2.3.9.2 on the images, the fractal tortuosity dimensions can be obtained.

Fractal tortuosity dimension can be used for both calculating the fractal permeability, as well as the overall thermal conductivity through crud. By utilizing fractal dimensions, Short (2013) [7] was successful in incorporating microstructure properties into his MAMBA-BDM model which allows greater flexibility and accuracy in the modeling of crud layer. Section 2.3.5 presents rigorous details of how permeability can be calculated using fractal dimension. Section 2.2.4.1 delves deeper into the details of how overall crud thermal conductivity can be calculated by utilizing fractal dimension values.

### 2.3.7 Fractal Area Dimension ($d_N$)

The fractal area dimension can be used along with the fractal tortuosity dimension to calculate the permeability of a structure using the fractal permeability model. As opposed to the fractal tortuosity dimension, the fractal area dimension is obtained from analyzing the image perpendicular to the

flow. In a crud layer, the images perpendicular to the fluid flow should be the top-view of crud since water flows upward through boiling chimneys. Similar to the fractal tortuosity dimension, the fractal area dimension can be obtained by applying the box-counting method 2.3.9.2. Instead of applying the box-counting method to the image parallel to flow in order to obtain the fractal tortuosity dimension, we apply box-counting method to the image perpendicular to flow in order to obtain the fractal area dimension.

### 2.3.8 Methods for Obtaining Fractal Dimension

Now that the fractal dimensions have been explained, the next question is how are these fractal area dimensions and fractal tortuosity dimensions obtained. In their review, Lopes and Betrouni [140] summarized the useful methods for estimating fractal dimensions into three categories: the box-counting method, the fractional brownian motion (FBM) method, and the area measurement method.

**Fractional brownian motion (fBm) methods** Brownian motion exhibits two important properties: it has independent increments, and the probability distribution of a brownian motion point in the future would be a gaussian distribution with an expected value of 0. Fractional Brownian motion (fBm) is a generalization of brownian motion, where the increments of fBm can be dependent to the past increments. The fBm's probability distribution is also gaussian. One way to understand what fBm represents is to look at it in terms of a covariance. A covariance of two brownian motions is given by:

$$Cov(B_s, B_t) = E[B_s B_t] - E[B_s]E[B_t] \tag{2.22}$$

where $B_s$ and $B_t$ are two brownian motions at time $s$ and time $t$; $Cov(B_s, B_t)$ is the covariance of $B_s$ and $B_t$; $E[B_s B_t]$ is the expected value of $B_s$ multiplied by $B_t$; and $E[B_s]$ and $E[B_t]$ are the expected values of $B_s$ and $B_t$, respectively. Since we know that the expected value of brownian motion is zero, the equation can be simplified to:

$$Cov(B_s, B_t) = E[B_s B_t] \tag{2.23}$$

Solving for the expected value and assuming that t > s will yield [146]:

$$Cov(B_s, B_t) = E[B_s B_t] = s \tag{2.24}$$

The covariance of the two brownian motion simpifies to $s$. A fractal Brownian motion's expected value of the intensity difference between two points is zero, while the square of the difference is

proportional to the distance between the points at a power 2H [140]. This means that the covariance of fBm is given by [123]:

$$E[B_s^H B_t^H] = \frac{1}{2}(|t|^{2H} + |s|^{2H} - |t-s|^{2H}) \tag{2.25}$$

where $B_s^H$ and $B_t^H$ are two fBms; and $H$ is the Hurst index. If Hurst index is 1/2, then this equation simplifies to that of the Brownian motion resulting in $s$ as shown above. If Hurst index is more than 1/2, then the increments are positively correlated. On the other hand, if the Hurst index is less than 1/2, the increments are negatively correlated. The fractal dimension of an n-dimension fractal Brownian functions (fBfs) is given by:

$$D = n + 1 - H \tag{2.26}$$

Fractal brownian motion can be used to find the fractal dimensions of images by treating the images as 2D fBfs. The fBm method is particularly useful in estimating the fractal dimensions, because most fractals in the physical world are fBfs [147]. Two fBm algorithms are commonly used to estimate fractal dimensions of images: the variogram method, and the power spectrum method.

The variogram method makes use of the fact that it is possible to model a 2D fBf image given a fractal dimension [140]. This method basically obtain the fractal dimension by solving an inverse problem using a 2D fBf image as an input. An example of this method's usage is shown in figure 2-74. The variogram method provides robust estimations of fractal dimensions [140]. The advantage of this method is that it is applicable to irregularly distributed data. Its disadvantage is that is tends to be unstable for images with higher fractal dimensions [140].

The power spectrum method, on the other hand, is based on the use of fourier transform. For each image line height profile that together forms an image, a power spectrum is found by applying the fourier transform and taking the square of its amplitude. After that, these power spectra are averaged. The slope of the log-log plot of the averaged spectra can then be used to determine the fractal dimension. Figure 2-74 shows a resulting plot given by this method.

**Area measurement methods** Area measurement methods examine the structuring elements at various scales. The fractal dimension is obtained first, by finding the best-fit line of the log-log plot of scales and areas of signal intensity surface. To get an intuitive sense of what the area measurement method actually does, lets first take a step back, and look at the problem in terms of lines. Afterward, we can generalize the technique to areas. For example, lets look at a sample problem where we will try to determine the total length of the Britain coastline. One way to achieve this is by taking measuring sticks and placing them around the coastlines as shown in figure 2-75. Unfortunately, as shown in the figure, using measurement sticks of different lengths will actually

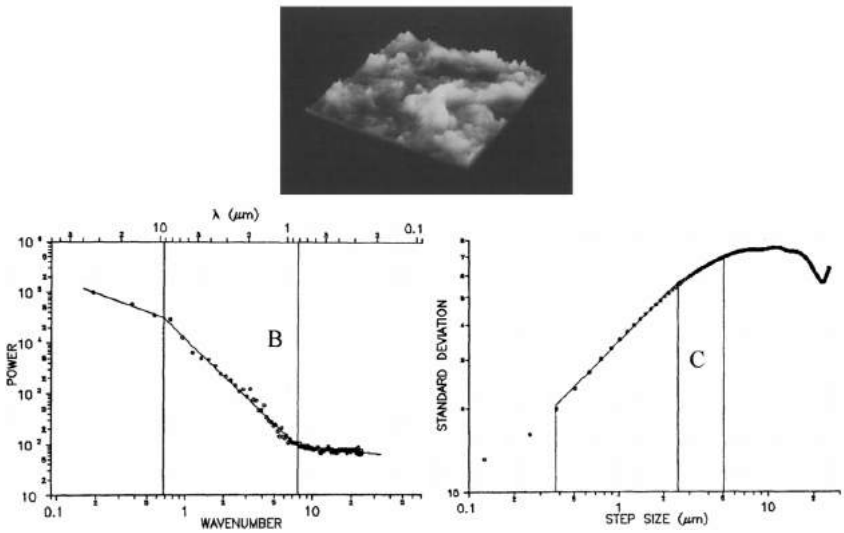


Figure 2-74: Figure demonstrating the usage of the power spectrum technique. The top image is an SEM image of a lithogenic quartz particle at 3000x magnification. The bottom left image is the plot obtained using the power spectrum method. The bottom right image is the plot obtained using the variogram method [148].

change the lengths measured. With a longer measurement stick and small magnification factor of $r = 1$, the perimeter $N$, was found to be 9. As the size of the measurement stick increases, we can see that the perimeter $N$ also increases. Recall earlier, that the one way fractal dimension can be calculated is by using the equation:

$$Dimension = \frac{log(numberOfSelfSimilarPieces)}{log(magnificationFactor)} \tag{2.27}$$

In the same way, a similar equation can be applied to coastline using equation [149]:

$$Dimension = \frac{log(N)}{log(r)} \tag{2.28}$$

If we graph the log-log plot of the above equation for multiple values shown in figure 2-75, we get the plot in figure 2-76. In this case the fractal dimension, which represents the slope of the graph, is found to be 1.21 [149]. This method of finding the fractal dimension is called the "measurement stick method." Now, if we extend this type of analysis to three dimensions using different types of structure element, we get the area measurement methods.

The most often-used, area measurement methods include the isarithm method, the blanket method, and the triangular prism method. The isarithm method uses the complexity of contour lines to approximate the complexity of a surface. This method is very similar to the measurement stick method, but instead of tracing a line around a 2D shape, isarithm method traces contour lines around a 3D surface. Each isarithm or contour line traces around a 3D surface at constant elevation. Note that in this context, the 3D surface is the 2D input image with its brightnesses as

elevations. The fractal dimension of the image can then be taken as the average of contour lines' fractal dimension, plus one. Example data obtained from this method is shown in figure 2-77. The blanket method [150] covers a 3D surface with a blanket of thickness 2. The blanket upper surface and lower surface are defined by dilatation and erosion of the image. Asvestas et al. (1998) found that this method is only efficient when theoretical value of fractal dimension is low.

The triangle prism method compares the total surface area of triangular prisms with a single tile-projection area in the log-log form [151]. To describe this method more intuitively, we should recall the measurement stick method mentioned earlier. Now, instead of using measuring sticks to cover a 2D perimeter, this method uses triangle tiles to cover a 3D surface area. Figure 2-78 illustrates how a surface area can be covered with triangles. Notice, from the figure, that the surface area is divided into tiles, each containing four triangles. These tiles would correspond to the measurement sticks of the measurement stick method. From the second diagram in figure 2-78, notice that these tiles can be projected on to the ground plane as squares. Similar to how the magnification factors in the measurement stick method dictates the measurement stick lengths, the magnification factor in the triangular prism method dictates the tile-projection area size. We can then plot the log of surface area versus the log of tile-projection area size, and apply a linear fit. The fractal dimension is calculated as $2 - s$, where $s$ is the slope of the linear fit. Figure 2-79 illustrate an example of the usage of the triangular prism method.

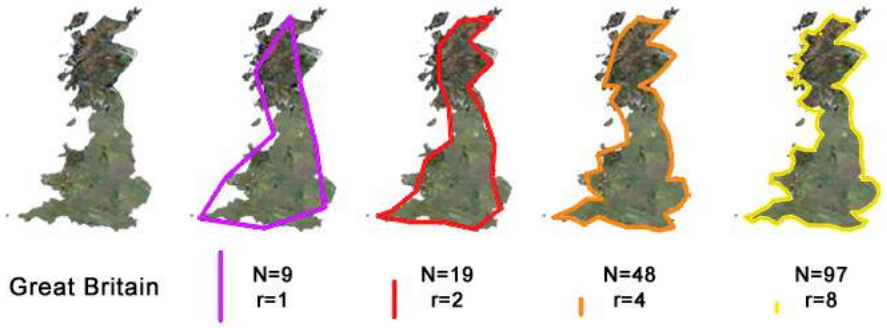


Figure 2-75: This figure shows how measurement sticks of different lengths can be applied to Britain's coastline. [149].

**Box-counting method** This is the method used to analyze crud in this thesis; Therefore, it will be explained more extensively in section 2.3.9.2.

### 2.3.9 Obtaining Fractal Dimensions via Box-Counting Method

For the scope of this experiment, the relevant method which is used to obtain fractal dimensions is the box-counting method; therefore, this subsection will focus on the box-counting method [140].

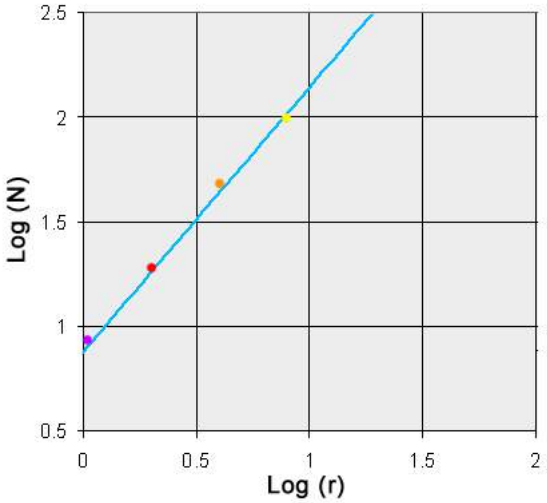


Figure 2-76: A plot of log of perimeter $N$ versus log of magnification factor $r$ [149]. The data points are obtained from figure 2-75 . The slope of this plot is the fractal dimension of Britain coastline.

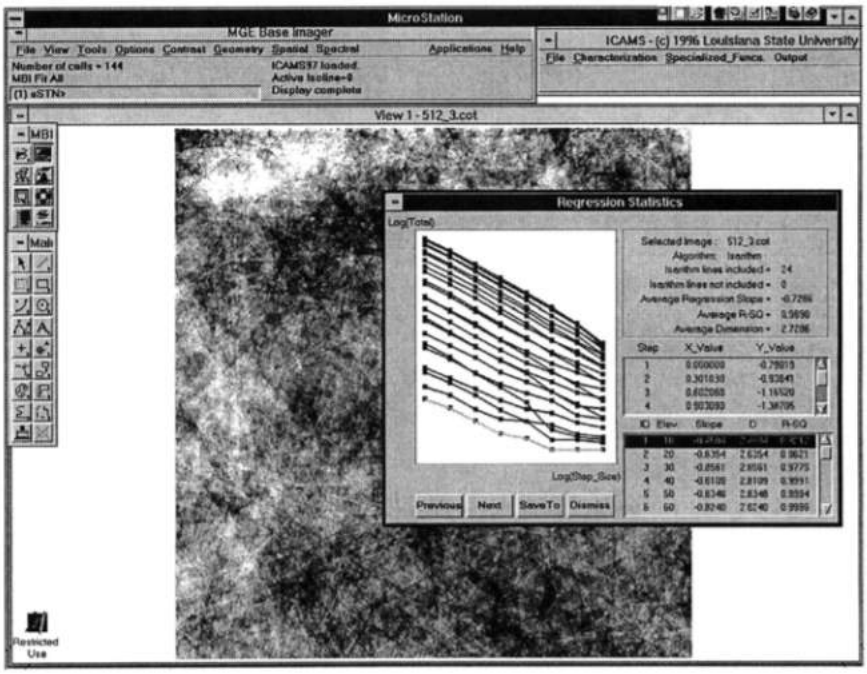


Figure 2-77: An output of the isarithm method using ICAM software. The input image in the background is a simulated surface with a fractal dimension of 2.7 [152].

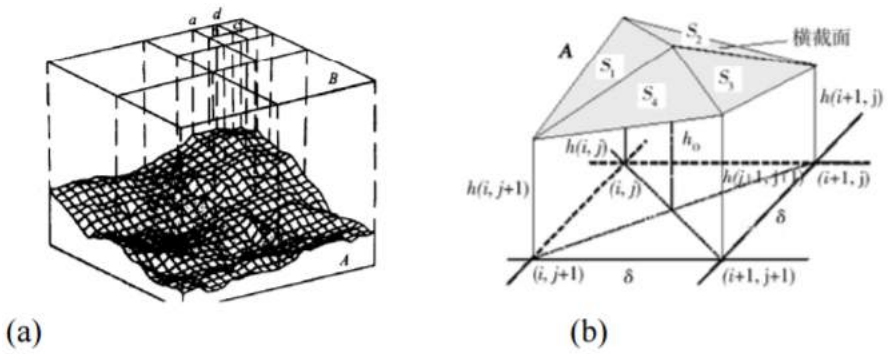


Figure 2-78: This figure illustrates how the triangle-prism surface area measurement method covers a surface area with triangles. (a) is the projection network covering a surface area. (b) is the projection grid, which represents each tile in the projection network [151].

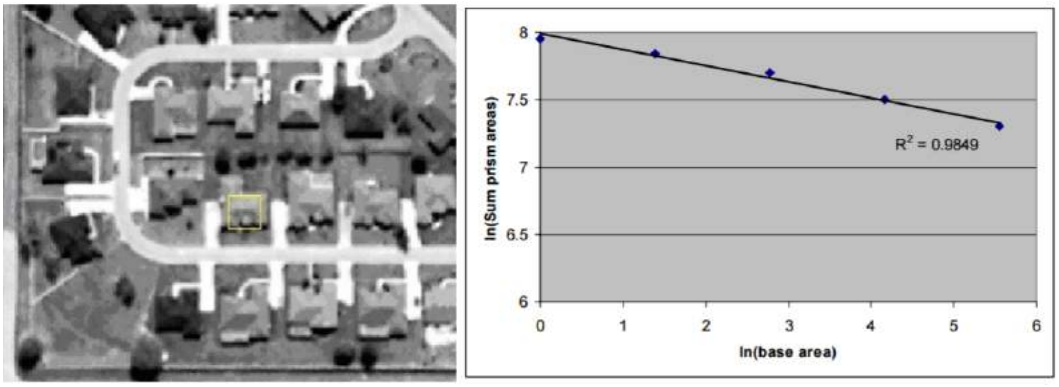


Figure 2-79: This figure illustrates the usage of triangular prism method. The left image is the input image. The right plot is the log-log plot obtained using the triangle prism method [153].

The following subsection will first discuss how the images can be preprocessed for use in box-counting analysis. After that, it will go into details regarding box-counting method and its variation.

#### 2.3.9.1 Preprocessing images for the box-counting method

The box-counting method requires a binary image as an input. Image processing algorithms can turn the grayscale images from SEM into binary images, where the black area represents water flow and the white area represents crud particles. These binary images can then be analyzed with the box-counting method to yield fractal tortuosity dimension. In crud's case, water flows in from the surface of the crud, and permeates through the crud, until it eventually exits the chimney as bubbles. Therefore, the images that should be perpendicular to flow are the top views of crud. These images are used to obtain fractal area dimensions. On the other hand, the images that should be parallel to flow are the cross-sectional view of crud. Similarly, those images can be used to obtain the fractal tortuosity dimension.

**Huang** Huang (1995) [154], introduced an image thresholding technique that tries to minimize the measurement of fuzziness of an input image. Huang's technique can use the Shannon's entropy function to estimate fuzziness of the image. Since Shannon entropy also appears in max entropy and Li thresholding technique, it will be expanded here.

To get an intuitive sense of what the Shannon entropy is, lets consider two systems that outputs some strings made up of letter A, B, C, and D. For example, the systems may output something similar to "ACDABBDA." First system will output all letters at 25% chance, while the second system will outputs 80% of letter A, 10% of letter B, and 5% of letter C and D. Now we might ask; what is the number of yes/no questions we would expect to ask to correctly predicts what letters appear from the systems. For example, we might first ask "Is it is either A or B?", then if the answer is correct, we can ask the question "Is it A?" to narrow down on either A or B. If the answer to the question "Is it is either A or B?" is a no, then we can deduce that the answer will be either C or D. We can then ask the question "Is it C?" to get the correct answer. Each of these questions would correspond to a "bit" of information, a term popularized by computer science. The information size would be the average number of bits (yes/no question) required to correctly identifies each element. In this case we have just examined, the information size would be 2, as we always require two yes/no questions to correctly predict the answers. The information size does not have to be an integer as we will see shortly.

In the first system with equal probability of all letters, asking the questions "Is it is either A or B?", "Is it A?", and "Is it C?." is the most efficient way to get a correct answer. That would correspond to using the following binary encoding: "00" for A, "01" for B, "10" for C, and "11" for D. Now if we look at the second system with 80% probability that it will output letter A, it would

be beneficial to instead ask the question "Is it A?" first. Then if it is actually A, which is very likely, we don't have to ask any further question. If it is not A, then we can ask "Is it B?" If it is not B then we can ask "Is it C?" to narrow down on the correct answer. This corresponds to binaries with: the letter A as "0," B as "10," C as "110," and D as "111." It is important to notice that on average, we do not have to ask as many questions as the previous first system case. The expected number of questions that have to be asked can be calculated as follow:

$$\#questions = p_A \times 1 + p_B \times 2 + p_C \times 3 + p_D \times 3 \tag{2.29}$$

where $p_A$, $p_B$, $p_C$, and $p_D$ are the probabilities of getting letter A, B, C, and D, respectively. The reason $p_A$ is multiplied by 1 is because getting a "yes" in the question "Is it A?," means that only one question is asked. Similar logics can be used for the rest of the equation. Plugging in the probabilities above for second system, we yield only 1.1 expected number of questions, and therefore, 1.1 information size. This is less than the 2 questions or bits required for the first system. This essentially means that the second system is producing less information because there is less uncertainty in its output. Shannon calls this measure of average uncertainty, "entropy", denoted by $H$. Generalizing the above equation that was used to determine the number of questions, we get:

$$H = \sum_{i=1}^{n} p_i \times (\#bits)_i \tag{2.30}$$

The number of bits can be simplified further, arriving at the Shannon's formula for entropy as follows:

$$H = \sum_{i=1}^{n} p_i \times log_2 p_i \tag{2.31}$$

This Shannon's entropy formula is what Huang, max entropy, and Li's thresholding techniques use in deriving their algorithm.

**Intermodes** The intermodes image thresholding technique [155] assumes that the histogram of image brightness has two peaks. The input brightness histogram is iteratively smoothed until there are only two local maxima left. The threshold is then obtained by averaging the brightnesses at the two local maxima. This method works best when there are two very clear peaks. Its advantage lies in the relatively simple math and algorithm implementation. In crud's case, the SEM photos of crud do not always exhibit two clear peaks; therefore, this algorithm is not applicable.

**IsoData** The isodata [156] is an iterative image thresholding technique. The algorithm starts by taking some initial threshold that divides the image into the object and the background. An iteration starts by computing the average brightnesses of the pixels from the object and the background. Then,

the average of those two values is computed, and compared to the threshold. This iterative process will repeat until the threshold is larger than the computed average of those two values.

**Li** Li (1993) [157] proposed a thresholding technique that finds threshold by minimizing the cross entropy between the input image and the image divided by some threshold. The cross-entropy measures the information theoretic distance between the two distributions. In Li's method, cross entropy is formulated in a pixel-to-pixel basis.

**Max Entropy** The max entropy thresholding algorithm [158], tries to maximize the sum of entropy of the two classes (background/object). The advantage of this algorithm lies in its general nature that stems from using a global objective property of the brightness histogram.

**Mean** The mean thresholding technique [159] is exactly as the name implies; threshold is computed from taking the mean average of the image brightness. It is usually inaccurate, but because of its simplicity and speed, it is usually used as an initial guess for image thresholding techniques that require an initial estimate for iteration.

**Minimum Error** The mininum error thresholding technique [160] assumes that there are two normally distributed peaks in an image representing the object and the background. There will be a part where these two peaks overlap, which in this case, is taken as the error. The mininum error thresholding technique finds a threshold that minimizes this error value.

**Minimum** The mininum thresholding technique [161] assumes that there are two peaks on the brightness histogram. The histogram is iteratively smoothed until there are only two local maxima. The threshold is taken as the minimum brightness value between these two local maxima. Minimum thresholding is simple to implement. However, it only works when the image's brightness histogram exhibits two peaks.

**Moments** The moment thresholding technique by Tsai (1985) [162] finds a threshold that preserves the first three moments of the original image. For an image with $N$ pixels, the image's $j$th moment $m_j$ is defined as the following [163]:

$$m_j = \frac{1}{N} \sum_i i^j h_i \tag{2.32}$$

where $i$ represents each brightness value on the image's brightness histogram; $h_i$ represents the total number of pixels with the brightness value of $i$. Now, we consider $p_i = h_i/N$. In the case of the resulting binary image, there would be only $i = 0, 1$. $p_0$ would then represents the overall probability of getting a black pixel in the thresholded image. The threshold $t$ for the image's

brightness histogram can be obtained by finding $t$ as $p_0$-tile, where $p_0$ is given by the following system of equations [163]:

$$p_0 = \frac{z - m_1}{(c_1^2 - 4c_0)^{1/2}} \tag{2.33}$$

$$c_0 = \frac{m_1 m_3 - m_2^2}{m_2 - m_1^2} \tag{2.34}$$

$$c_1 = \frac{m_1 m_2 - m_3}{m_2 - m_1^2} \tag{2.35}$$

$$z = \frac{1}{2}((c_1^2 - 4c_0)^{1/2} - c_1) \tag{2.36}$$

By computing, the $p_0$ from this system of equation we get the ratio of black pixels to total pixels. This value, along with the brightness histogram, can be used to determine the threshold. This technique along with Otsu technique, are the thresholding techniques chosen for analyzing crud.

**Otsu** Otsu thresholding algorithm [164] tries to minimize the intra-class variance. The classes are the object and background divided by threshold. The intra-class variance is defined as a weighted sum of variances of the two classes as follows:

$$\sigma_w^2(t) = \omega_0(t)\sigma_0^2(t) + \omega_1(t)\sigma_1^2(t) \tag{2.37}$$

where $\sigma_w^2(t)$ is the weighted sum variance; $\sigma_0^2(t)$ and $\sigma_1^2(t)$ are the variances of the two classes (black/white) separated by a threshold $t$; $\omega_0$ and $\omega_1$ are the probabilities of the two classes. The probability of each class is computed by summing the values within the class and divide it by the total value of the two classes combined. Otsu demonstrated that minimizing the intra-class variance is essentially the same as maximizing the inter-class variance. Inter-class variance can be formulated as follows:

$$\sigma_b^2(t) = \omega_0(t)\omega_1(t)[\mu_0(t) + \mu_1(t)]^2 \tag{2.38}$$

where $\sigma_b^2(t)$ is the inter-class variance; $\mu_0(t)$ and $\mu_1(t)$ are the class 0 and class 1 mean values, respectively. This equation forms the basis of the Otsu thresholding algorithm. The algorithm loops through all possible thresholds to determine the maximum value of $\sigma_b^2(t)$. Otsu threshold is another image thresholding algorithm chosen for crud analysis. It usually gives very similar result to the Moment thresholding algorithm.

**Percentile** The percentile method [165] simply assumes that the fraction of foreground pixels is 0.5. This method is very simple, but also often inaccurate. It cannot be used for crud analysis since it will always give a 50% black and 50% white image which is not very useful for determining the porosity.

**Renyi Entropy** This method [158] is similar to the max entropy method. The only difference is that this method uses Renyi's entropy instead. Renyi's entropy is a generized form of Shannon's entropy

**Shanbhag** Shanbhag (1994) [166] proposes an image thresholding algorithm based on utilizing the information measure. In this method, the original image is treated as two fuzzy sets. The "membership coefficient of the pixels" to a set is defined as the measurement of uncertainty in assigning them to the specific class (black/white) [166]. The membership of pixels ranges from 0 to 1. The zero value represents the minimum uncertainty in assigning the image to a specific class. This thresholding method involves the "defuzzification" process where a crisp set of pixels in the image is obtained as a result. "Information" is supplied in transforming the two fuzzy sets of the original image to the two crisp set.

**Triangle** In the triangle thresholding method [167], a line is drawn between the maximum and minimum value of the histogram as shown in figure 2-80. A second line, normal to the previous line, can be traced until it hits the histogram as shown in the figure. The second line is maximized by moving it along the first line, and the threshold is taken as where this maximized second line hit the histogram. Because triangle thresholding algorithm is a geometric method, it cannot perceive whether the data is one-sided. It merely assumes that the maximum peak is near one end of the brightness histogram.

**Yen** Yen (2002) [168] proposed a thresholding technique based on two factors: the discrepency between the thresholded and original images, and the number of bits required to represent thresholded image. A cost function that take these two factors into account will be determine. Yen's technique finds a threshold that minimizes this cost function.

**Choosing the image thresholding techniques** These 15 image thresholding algorithm are present in the ImageJ software, along with the ImageJ's default thresholding algorithm which is a variation of the isodata algorithm. ImageJ was used to test one or two different images from each sample that we have, to determines which image thresholding algorithm is versatile enough to be used across all of our data. Both moment and Otsu thresholding algorithms were shown to be the

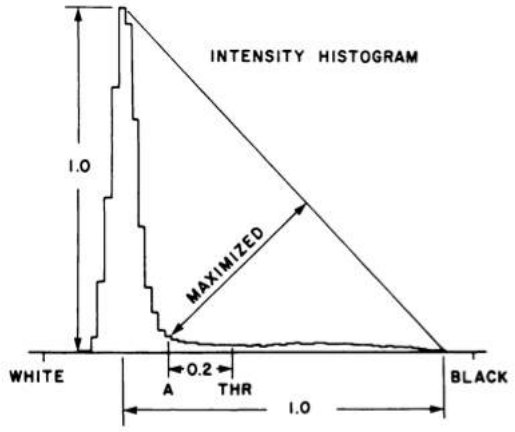


FIG. 2. Determination of the global search threshold for each picture. The threshold (THR) was selected by normalizing the height and dynamic range of the intensity histogram, locating point A as shown, and then adding a fixed offset.

Figure 2-80: This figure demonstrates how the triangle thresholding method works [167].

most versatile for its use in crud analysis. Therefore, both algorithms were rewritten in a python script used to automate the crud image analysis.

#### 2.3.9.2 Box-counting method

The box-counting method is the method utilized most often to estimate of fractal dimensions for real world application. It is frequently used in wide range of applications including soil science [140, 141, 142], material science [169, 170], and more. Its simplicity, robustness, and automatic computability are features that recommend it as the chosen method for many purposes [140]. The box-counting method is used for analyzing complex patterns by breaking data, typically images, down into smaller box-shaped pieces. The method is similar to zooming in and determining how the details changed with the scale. In this method, the image is covered with a grid of some box size, and each grid is analyzed for its features. For instance, the traditional fixed grid scan box-counting method will divide the 2D/3D image into a grid of some specified pixel sizes. The number of boxes or cubes with filled pixels can then be counted. To obtain the fractal dimension, the value of the logarithm of the box count, ln(N), and the value of the logarithm of the box size, ln(r), can be plotted. An example plot is shown in figure 2-81. The linear regression can be used to obtain the slope. The absolute value of slope represents the fractal dimension $D$.

How well each data point fits onto the linear regression line is one of many indications that the system being analyzed exhibit fractalline property [123]. There are three scanning strategies for the box-counting method, including the fixed grid scan, the sliding box scan, and the local dimension scan. The fixed grid scan can be used to analyze images for fractal dimensions. The sliding box

scan is more applicable for doing lacunarity analysis. Subsampling or the local dimension scan finds the fractal properties only locally, and therefore does not fit the scope of this thesis. The following subsections will explain each type of scans in more details.

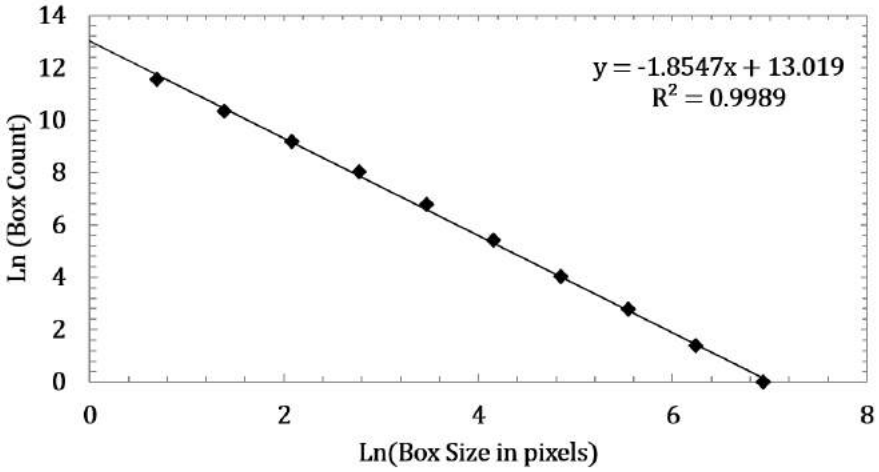


Figure 2-81: Plot of ln(box count) to ln(box size in pixels). The absolute value of the slope of its linear regression line is fractal dimension.

#### 2.3.9.3 Fixed Grid Scan

If box counting is applied on a completely filled area (which means all boxes will go toward box count), the fractal dimension (ln(Box Count)/ln(Box Size)) will be two. This is because, in this case, all the boxes will be counted. In any fixed grid scan, the number of total boxes used including the one that was not counted will be around the square of box size [123]. The figure 2-82 shows how the fixed grid scan works.

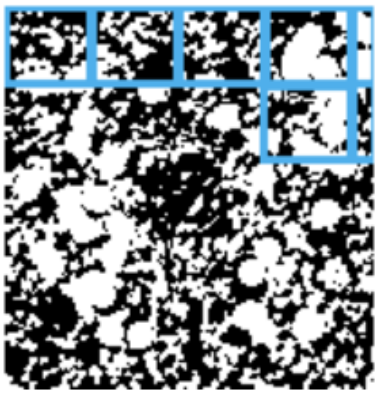

Figure 2-82: This figure shows the traditional fixed grid scan where boxes do not overlap [171].

#### 2.3.9.4 Sliding Box Scan

For sliding box scan, each box will slide along the image overlapping the previous placements. Figure 2-83 shows how the sliding box scan works. This type of analysis is often used for analyzing textures in lacunarity analysis. In fractal analysis, lacunarity represents the size distribution of gaps or holes in a fractal. It measures how patterns fill space. Patterns with larger gaps generally have higher lacunarity [172]. Lacunarity can also quantify other pattern features such as "rotational variance". If a pattern changes by a significant amount once rotated by 90°, that will have high lacunarity. Figure 2-84 illustrate the explanations of lacunarity provided above.

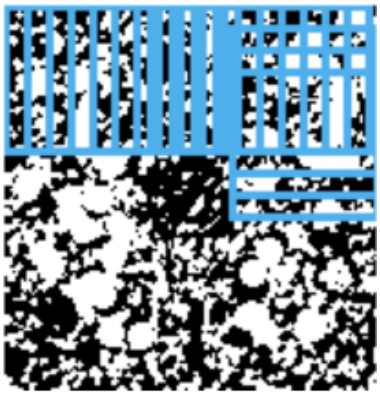

Figure 2-83: This figure shows the sliding box scan where boxes can overlap each other [171].

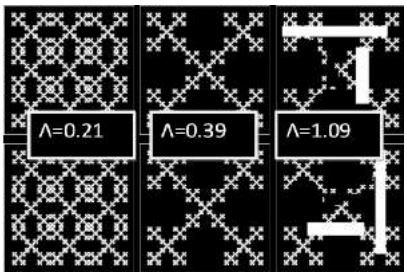


Figure 2-84: This figure illustrates what lacunarity represents. The label on each set of two images represents the lacunarity as calculated by the ImageJ software. Each set of images represents the same pattern with a 90° difference in rotation. The right most image has the highest lacunarity because, once rotated, the image is different than the original image. The left most image has lower lacunarity than the middle image because its pattern contains fewer or smaller gap [172].

#### 2.3.9.5 Subsampling and local dimension scan

This type of method is used to determine the local variation as opposed to the global measure that describes the entire image. Subsampling, as the name implies, will move the box according to some feature related to pixels of interest. For instance, the local connected dimension box-counting algorithm will count boxes concentrically focused on the pixel of interest. The figure 2-85 shows

how the subsampling scan works. This type of method is particularly useful in the case that fractal dimension is expected to change significantly with scale [171].

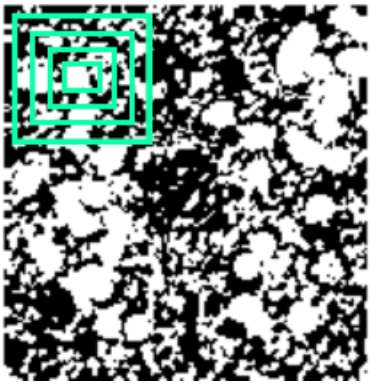

Figure 2-85: This figure shows how local connected dimension box-counting algorithm works. Local connected dimension box-counting algorithm is one example of subsampling and local dimension scan. The figure shows how boxes can be laid concentrically focused on each pisel of interest [171].

### 2.3.10 Uncertainty for Fractal Parameters

Many papers such as that of Pitchumani (1999), did not address the issue of uncertainty for fractal parameters [145]. In other papers, such as "The spatial distribution of soils across Europe: A fractal approach" by Ibanez (2009), the coefficient of determination $R^2$ of the regression and the standard error of the estimate of fractal dimension ($D$) were recorded [173]. In the papers that do address uncertainties, there are two important values that are used to estimate the uncertainty of the fractal dimensions derived from box-counting method. These two values are the standard deviation around the regression line (also called the standard error of the estimate) and the R-squared of regression line. Note that the largest and smallest length scales where the box-counting line fit works can also be useful, if a deviation from box-counting line fit can be seen. The standard deviation around the regression line is the usual method for estimating the error for fractal dimensions. This can be used to make error bars in a graph with fractal dimensions representing y-axis. The standard deviation around the regression line can be calculated as follows:

$$\sigma_{est} = \sqrt{\frac{\sum (Y - Y')^2}{N}} \tag{2.39}$$

where $\sigma_{est}$ is the standard error of the estimate or the standard deviation around the regression line; $Y$ is an actual value; $Y$ is a value predicted by the regression line; finally, $N$ is the number of values used to make the regression line.

Papers such as "Using fractal geometry to determine phytotoxicity of landfill leachate on willow" by Bailowiec (2010), uses the standard deviation of regression line and the standard error of mean [174]. Bailowiec's paper examined the effect that landfill leachate has on plants. The paper describes

the experiment where leachate solution was applied on willow shoots to see its effects on the plants. Fractal dimensions of leaves were one of the parameters used to determine the difference between plants that were affected by leachate solution and those that weren't [174]. The conclusion was that leaf length and fractal dimension are shown to be good indicators of plant response to toxicants in their environment . Another way to determine how close the data are to the regression line that was fitted, is by using the R-squared value. The R-squared (or the coefficient of determination) is the percentage of response variable variations that is explained by the fitted line. The R-squared values range from -100% to 100% where 0% R-squared means that none of the variability in data is explained by the fitted line, 100% R-squared means that the model explains all the variability in data, and -100% R-squared is a perfect anti-correlation. The R-squared is important to investigate when using the box-counting method to get fractal dimension, because it also tells us if it makes sense to apply the box-counting method in a particular case.

## 2.4 Adhesion Forces

crud is formed when the liquid layers between the bubbles and the cladding surfaces dry off and deposit crud particles on to the surfaces. When crud particles come into contact with cladding surfaces, they may stick to the surface to start a crud layer formation or they may not stick and get washed away later. How well crud particles stick to the cladding surfaces is related to the surface forces between the two bodies.

### 2.4.1 Types of Adhesion Forces

There are many types of surface adhesion forces including Coulombic forces, magnetic forces, chemical bonding, hydrogen bonding, and van der Waals forces. These forces are briefly described in the following subsections.

#### 2.4.1.1 Coulombic Force

Coulomb or electromagnetic force attracts or repulses particles or objects according to their electrical charge. When charges of two objects of interest are the same, they repel each other. When charges of two objects are different, they attract each other. In the crud particles to cladding surface system, the Coulombic force is unlikely to play any role. This is because it is likely that neither crud particles nor cladding surfaces are charged.

#### 2.4.1.2 Magnetic Force

The magnetic force results from the electromagnetic force. It occurs whenever there is a moving charge. When two objects contain charges that move in the same direction, magnetic force will

generate an attraction between them. Likewise, when two objects contain charges that move in the opposite direction, repulsive magnetic force will be created. The movement of charges within objects may be inherent to the material, in which case these objects are natural magnets. On the other hand, the movement of charges within objects may also happen because electric current is flowing through the objects. In this case, the object would be an electromagnet. Neither crud nor fuel rod cladding surfaces are a natural magnet. They also should not act as electromagnet as there should be no current flowing through both crud and fuel rod during reactor operation. Therefore, magnetic force will not be considered as an adhesion force affecting crud particles.

#### 2.4.1.3 Chemical Bonding

Chemical bonding is the attraction between atoms caused by either the electrostatic force between atoms of opposite charges (ionic bond) or the sharing of electron between atoms (covalent bond). In the case of crud particles to cladding surfaces system, there is no trace of any chemical reaction that should result in the case that chemical bonding does play a role in crud growth. Therefore, it will be neglected in this study.

#### 2.4.1.4 Hydrogen Bonding

When a hydrogen atom and an atom with high electronegativity (tendency to attract electron) is attached together with covalent bond, the shared electrons will spend more time at the highly electronegative atom. This creates an imbalance of charge between the hydrogen atom and the atom it attaches to. This charge imbalance may cause one side of the molecule to electrostatically attract another molecules that also have a charge imbalance. This electrostatic interaction is called "hydrogen bonding". Since neither crud particles, nor cladding surfaces contain hydrogen, this type of force can be neglected.

#### 2.4.1.5 Van der Waals Force

Van der Waals forces' is the interaction between molecules with induced dipoles [175]. It is usually relatively weak, but in case of crud particles, it is still very relevant due to the lack of any other forces, as explained earlier. More details on this particular force will be explained in detail in the next section.

### 2.4.2 Van der Waals forces and Hamaker constant

There are many interactions between two bodies that contribute to surface forces, for example, structural, hydration etc., depending on the nature of the system. One very important interaction that is always present is the van der Waals interaction. Van der Waals forces is a term used to

define physical attractive/repulsive forces driven by dipolar interactions created by the materials' geometry and fluctuation of its electron cloud [176].

Although the van der Waals force is always present in any system, its importance varies depending on its relative strength and the existence of other forces. In the crud particle to cladding surface system, van der Waals force can be the major contributing force since there are no other known interaction forces we are aware of. The van der Waals force can be separated into three types:

- The Keesom force characterizes the interaction between two permanent dipoles.
- The Debye force characterizes the interaction between one permanent dipole and one induce dipole.
- The London or dispersion force characterizes the interaction between the two induced dipoles.

Between two molecules, each of these types of van der Waals force has an interaction free energy which varies with the inverse sixth power of the distance. Its effect is non-negligible from a separation distance of around 1 Angstrom to several nanometers [177].

One way to determine how van der Waals forces affect the bulk properties for materials is by using the model developed by Lifshitz [176]. Lifshitz's model of van der Waals forces is based on quantum electrodynamics. Instead of looking at individual atoms, Lifshitz's model treat material properties as a continuum. In Lifshitz's theory's treatment of materials, there are time variances of electron clouds and fields between materials, which lead to exchanges in virtual photons at complex frequency [176]. These exchanges create the van der Waals forces we observed. These exchanges are also directly related to the dielectrical properties of the material which can be measured by using VEELS or ellipsometry explained in detail in section 2.4.2.8. The Lifshitz theory can be expressed in terms of the Hamaker constant. The Hamaker constant can be used to assess the magnitude of van der Waals interaction on a macro-scale.

Hamaker uses pair-wise summation of all atoms in the macroscopic bodies to calculate the distance dependence of free energy [175]. Ultimately, we are interested in calculating the stickiness of crud resistance coating by examining van der Waals forces at a macro-scale. We suspect that the Hamaker constant might be useful in predicting how well crud particles can be adsorbed to the cladding surfaces.

Between semi-infinite parallel plates with a separation distance L, a van der Waals free energy $V_{vdW}$, per unit area, can be expressed as [175]:

$$V_{vdW} = -\frac{A_{Ham}}{12\pi L^2} \tag{2.40}$$

A is the Hamaker constant. The van der Waals interaction free energy is directly proportional to the Hamaker constant. The van der Waals forces are effective only up to an order of hundreds

of angstroms. When molecules are too far apart, van der Waals' forces decay very quickly. This outer regime with diminished van der Waals forces is called the retarded regime. In our usage of the Hamaker constant, we focus on the non-retarded regime when the interacting bodies are close together, all Hamaker constants we calculated will be non-retarded Hamaker constants. The Hamaker constant depends on the properties of the two materials and the media in between. The $L^{-2}$ term is the distance dependence of van der Waals interaction. This distance dependence will vary with the type of geometry of the system from $L^{-2}$ for parallel plate shown to $L^{-1}$ for two spherical particles. A system of a crud particle near a cladding surface can be represented by a system of a spherical particle near a flat surface. Therefore, the van der Waals interaction energy (J) calculation for the system of a crud particle and a cladding surface is the calculation for a spherical particle near flat surface. This is given by the equation [175]:

$$E_{vdW} = -\frac{A_{Ham}}{12}(\frac{1}{x} + \frac{1}{1+x} + 2ln(\frac{x}{1+x})) \tag{2.41}$$

where $E_{vdW}$ is the van der Waals interaction energy; $x$ is defined as $d/z$ where $d$ is the diameter of particle and $z$ is the distance from sphere surface. From this equation, we can see that the as the spherical particle gets very close to the surface ($z$ close to 0), the equation will turn into:

$$E_{vdW} = -\frac{A_{Ham}d}{12z} \tag{2.42}$$

This equation shows that as $z$ becomes very close to 0, the van der Waals interaction force will grow very quickly. For crud, this probably explains the reason why crud formation is usually observed more in a system with some occurance of boiling bubbles. In a normal fluid flow environment inside a reactor, it will be rare for crud particles to be able to get very close to the surface for these van der Waals forces to become relevant. However, when there is boiling present, there will be a liquid layer drying off because of intense heat flux, as explained earlier. The dry-off event gives crud particles chances to get very close to the cladding surface so that the van der Waals forces will strengthen enough to make crud particles stick to the surface.

In our experiment, the factor that we are trying to manipulate in this system is the cladding surface material. Other factors that will contribute to particle size and particle-surface separation distance are controlled through adding similar-sized particles in all trials, as well as controlling the fluid flow and the heat flux through cladding. Therefore, the only relevant variable in the van der Waals interaction equation is the Hamaker constant $A_{Ham}$. This is why we will be exploring the Hamaker constant of each surface-modification coating material. In this thesis' result section, the relationship between the Hamaker constant and the crud growth will be analyzed [175].

The Hamaker constants of two different materials can be estimated using the Hamaker constant of each material. The estimation formula is as follows:

$$A_{12} = \sqrt{A_{11}A_{22}} \tag{2.43}$$

Where $A_{11}$ is the Hamaker constant between homogenous material type I, $A_{22}$ is the Hamaker constant between homogenous material type II, and $A_{12}$ is the Hamaker constant between material type I and type II. If there is third media, the estimation formula is as follows [11]:

$$A_{132} = (\sqrt{A_{11}} - \sqrt{A_{33}})(\sqrt{A_{22}} - \sqrt{A_{33}}) \tag{2.44}$$

Where $A_{132}$ is the Hamaker constant between material type I and II with material type III as medium. In the system of crud particles and cladding surface, type I and type II materials represent the crud particle material and the cladding surface material. Type III material is the water coolant fluid in this system. Experiment data on Hamaker constant is hard to obtain from literature. For the Hamaker constant on two types of materials with a medium, Lifshitz's "macroscopic theory" can be used to obtain Hamaker constant from dielectric constants that are more widely available in the literature. Lifshiftz relates Hamaker constant to dielectric constant as follows [11]:

$$A_{132} = \frac{3}{4}kT(\frac{\epsilon_1 - \epsilon_3}{\epsilon_1 + \epsilon_3})(\frac{\epsilon_2 - \epsilon_3}{\epsilon_2 + \epsilon_3}) + \frac{3h}{4\pi}\int_{v_1}^{\infty}(\frac{\epsilon_1(iv) - \epsilon_3(iv)}{\epsilon_1(iv) + \epsilon_3(iv)})(\frac{\epsilon_2(iv) - \epsilon_3(iv)}{\epsilon_2(iv) + \epsilon_3(iv)})dv \tag{2.45}$$

Where $\epsilon_1$, $\epsilon_2$ and $\epsilon_3$ are the static dielectric constants of the three media, $\epsilon(iv)$ are the values of $\epsilon$ at imaginary frequencies. The first term in the equation represents the static (Coulombic), or zero energy, attractive term. The second term represents the dynamic term due to virtual photons, which itself is due to differing oscillations in frequency/magnitude between the electron clouds of the three materials. This equation is only an approximation that includes the first few terms of an infinite series. The approximation is valid because the first few terms account for most of the contribution to value [11].

Using rigorous Lifshitz theory has many important disadvantages. First, the dielectric constant must be known for all frequencies, which means it is not very useful given the difficulty even in obtaining even a single dielectric constant value. The equation is also lengthy and the analytical solution involves very difficult calculations. In the case of crud particles to cladding coating materials, we can make some approximation because of our cladding coating material properties. Because materials chosen for cladding coatings are non-conductive materials with relatively low indices of refraction, higher-energy terms contribute far less than the lower-energy term [178]. The following subsections explain different forms of approximation commonly used to estimate the Hamaker constant.

#### 2.4.2.1 Approximating the Hamaker constant

In this thesis, the Hamaker constants will be calculated for the homogenous material with vacuum medium (vacuum Hamaker constant). Then the relation $A_{132} = (\sqrt{A_{11}} - \sqrt{A_{33}})(\sqrt{A_{22}} - \sqrt{A_{33}})$ can be used to calculate the Hamaker constant for the heterogenous materials and a water medium. The Hamaker constant for the heterogenous materials with a water medium will be obtained for both the room temperature conditions (more accurately) as well as the PWR temperature conditions (less accurately).

There are many approaches that can be used to obtain the vacuum Hamaker constant. They include the Tabor Winterton approximation [11], the single oscillator model approximation [11]„ the surface energy approach [11], the simple spectral method [179], and the full spectral method [179]. Relevant to the scope of this thesis are the Tabor Winterton approximation, the surface energy approach, and the single oscillator model approximation. The simple spectral method and full spectral method require knowledge of the full spectrum of the index of refraction of the specific material. This is not easily obtainable in literature at the time of writing, as most of materials used in this thesis are uncommon. The following subsections will explain the Tabor Winterton approximation, the surface energy approach and the single oscillator approach model approximation, all relevant to this thesis [11].

#### 2.4.2.2 Tabor-Winterton Approach:

By assuming that absorptions occur within a single frequency, the Lifshitz equation can be simplified down to the Tabor-Winterton approximation given by the following equation [11]:

$$A_{132} \approx \frac{3}{4}kT(\frac{\epsilon_1 - \epsilon_3}{\epsilon_1 + \epsilon_3})(\frac{\epsilon_2 - \epsilon_3}{\epsilon_2 + \epsilon_3}) + \frac{3h\nu_e}{8\sqrt{2}} \frac{(n_1^2 - n_3^2)(n_2^2 - n_3^2)}{(n_1^2 + n_3^2)^{1/2}(n_2^2 + n_3^2)^{1/2}\{(n_1^2 + n_3^2)^{1/2} + (n_2^2 + n_3^2)^{1/2}\}} \tag{2.46}$$

Where $A_{121}$ is the Hamaker constant unit in zJ. $n_1$, $n_2$ is the index of refraction of visible light between the vacuum and the material, for the material one and the material two. $\epsilon_1$, $\epsilon_2$ are the dielectric constant for the material one and the material two. $h$ is the Planck's constant or $1.055 \times 10^{-34}\ J \cdot s$ and $\nu_e$ is the plasma frequency.

Plasma frequency is used to describe the rapid oscillations of the electron density in a media [180]. The oscillation of electron density occurs because of coulombic force constantly pushing and pulling the electrons. For example, consider a system with electrically neutral plasma. This system starts off stable with no movement. If electrons in this stable system are perturbed, Coulomb force will pull the electron back to the same spot [180]. However, because an electron may still retain its energy, the motion will overshoot to the point where Coulomb force will try to push the electron back to the same spot. This cycle repeats at some frequency called plasma frequency. With thermal

motion of electrons ignored, the charge density oscillates at the plasma frequency given by:

$$\omega_{pe} = \sqrt{\frac{n_e e^2}{m_e \varepsilon_0}} \tag{2.47}$$

where $\omega_{pe}$ represents the plasma frequency (rad/s); $n_e$ represents the number density of electrons; $e$ is the electron charge; $m_e$ is the effective mass of electrons; and $\varepsilon_0$ is the vacuum permittivity constant ($8.854 \times 10^{-12} F \cdot m^{-1}$).

This full Tabor-Winterton equation is useful, given that we have the complete data for dielectric constant or index of refraction at high temperature. However, such data is very difficult to obtain. Alternatively, the Hamaker constant can be obtained by using the following expression:

$$A_{132} = (\sqrt{A_{11}} - \sqrt{A_{33}})(\sqrt{A_{22}} - \sqrt{A_{33}}) \tag{2.48}$$

where $A_{22}$ and $A_{11}$ are vacuum Hamaker constants of material 2 and material 1 respectively; $A_{33}$ is the vacuum Hamaker constant of water. Vacuum Hamaker constants of materials are slightly easier to obtain in the literature. One limitation is that Hamaker constants data is limited to only certain temperatures. However, the data from Lefevre's paper indicates that for a solid homogenous material system with a vacuum medium, the increase in temperature from 25 C$^{o}$ to 350 C$^{o}$ has little influence on the Hamaker constant [181]. Therefore, we can assume that solid's vacuum Hamaker constant ($A_{22}, A_{11}$) do not change with temperature. Further details regarding the temperature's effect on the Hamaker constant can be found in section 2.4.2.6. Water's Hamaker constant, on the other hand, is affected by the temperature. Water's Hamaker constant changes in accordance to its change in the dielectric constant and the index of refraction. Both the dielectric constant and the index of refraction of water do change with temperature. To get the vacuum Hamaker constant for any of the three materials ($A_{11}, A_{22}, A_{33}$), the Tabor Winterton approach can be used assuming a vacuum medium and a homogenous material. If the material is assumed to be homogenous, the equation can be further simplified down to [11]:

$$A_{131}^{TWA} = \frac{3}{4} kT(\frac{\epsilon_1 - \epsilon_3}{\epsilon_1 + \epsilon_3})^2 + \frac{3\pi\hbar\nu_e}{8\sqrt{2}} \frac{(n_1^2 - n_3^2)^2}{(n_1^2 + n_3^2)^{3/2}} \tag{2.49}$$

Where $\hbar$ is the Planck's constant or $1.055 \times 10^{-34}\ J \cdot s$ and $\nu_e$ is the plasma frequency which is approximately $3 \times 10^{15}$ Hz. $n_1$ and $n_3$ is the index of refraction of the visible light for the material I and vacuum. $\frac{3\pi\hbar\nu_e}{8\sqrt{2}}$ is approximately $2.635 \times 10^{-19}$ J $\cdot$ rad.

As shown in the following table 2-86 of vacuum Hamaker constants, Hamaker constants produced by the Tabor Winterton approximation for high index of refraction materials such as titanium dioxide and silicon nitride does not match well with the actual force measurement. As stated in the Ackler 1996's paper, the Tabor Winterton approximation can produce values comparable to other techniques

when refractive indices are below 1.8 separated by vacuum. In the table, note that for $TiO_2$ and $Si_3N_4$, the Tabor Winterton approximation did not give a very good value. Both $TiO_2$ and $Si_3N_4$ has a high index of refraction of 2.71 and 2.03, at 500 nm wavelength [179, 182, 183].

**TABLE 2**
**Vacuum Hamaker Constants for Ceramics—$A_{1v1}$ (Vacuum) (zJ)**

| Method | Force measurement | | Physical property measurement | | | |
|---|---|---|---|---|---|---|
| Tech.: Material | Surface force apparatus | Atomic force microscope | Tabor winterton approx. | Single oscillator approx. | Simple spectral method | Full spectral method |
| Mica | 135 (36)<br>100 (33) | — | 100 (1)<br>84.8 | 84 (48) | 100 (10) | 69.6 |
| $Al_2O_3$ | — | — | 140 (1)<br>137 (9) | 113 (48) | 150 (49) | 145.1 (9) |
| $SiO_2$ | 50–60<br>(55) | — | 63 (1)<br>56 (9) | 64 (48) | 65 (10)<br>65 (49) | 66 (9) |
| $Si_3N_4$ | — | — | 218 | 147 (48) | 180 (49) | 174 |
| $TiO_2$<br>Rutile | — | — | 430 (1)<br>401 (9) | 199 (48) | — | 173.1 (9) |

Figure 2-86: This table shows the value of the Hamaker constant calculated using different approaches. The Taber-Winterton approach that we planned on using is not very accurate for materials with high index of refraction [179].

#### 2.4.2.3 Single Oscillator Model Approach:

The single oscillator model is similar to the Tabor Winterton approximation. It is derived similarly to the Tabor Winterton approximation, but with the electronic structure of material modeled as a single oscillator. The Tabor Winterton approximation's major weakness is that the oscillator frequency was assumed to be constant for all materials. This leads to erroneously large Hamaker constants when index of refraction is large. The single oscillator model, on the other hand, is derived with the oscillator frequencies that vary with bandgaps. The following equation gives the Hamaker constant derived from the single oscillator model [179]:

$$A_{131} = \frac{312(n_1^2 - n_3^2)^2}{[(n_1^2 - 1)^{1/2} + (n_3^2 - n_1^2)^{1/2}](n_1^2 + n_3^2)^{3/2}} \tag{2.50}$$

Where $A_{131}$ is the Hamaker constant in zJ. $n_1$, $n_3$ is the index of refraction of visible light for the material one and vacuum. The single oscillator model can be used to get a decent approximation of the Hamaker constant for a material with high index of refraction where the Tabor Winterton approximation does not work as well [179].

#### 2.4.2.4 Surface Energy Relation to Hamaker:

The surface free energy results from the van der Waals' forces, in the material with non-hydrogen bonding liquid and solids. For those types of materials, the surface energy can be obtained from a

Hamaker constant with the following expression [184]:

$$\gamma_n = \frac{A_n}{24\pi D_0^2} \tag{2.51}$$

Where $\gamma_n$ is the surface free energy of the material $n$ and vacuum, $A_n$ is the the Hamaker constant of the material $n$ in vacuum, and $D_0$ is the intermolecular 'cut-off' distance. In other words, $D_0$ is the cut-off distance between molecules where forces between surfaces is assumed to be negligible. Israelachvili notes a surprisingly good agreement between theory and experiment is achieved when the $D_0$ value of 0.165 nm is used for small molecules [11].

For the scope of this thesis, most surface-modification materials tested have no hydrogen bonding. Therefore, the assumption that the surface free energy results from the van der Waals's force as described by the Hamaker constant will hold. As a result, this expression relating the surface free energy to the Hamaker constant can be used to calculate the Hamaker constant given the surface free energy of a material. Similar to the Tabor-Winterton approximation, the expression $A_{132} = (\sqrt{A_{11}} - \sqrt{A_{33}})(\sqrt{A_{22}} - \sqrt{A_{33}})$ can be used to obtain the Hamaker constant for crud particles to material surface with water as a medium [11].

#### 2.4.2.5 Additional knowledge useful for calculating Hamaker constant

Properly calculating the Hamaker constant from the information available in current literatures sometimes requires additional, non-obvious knowledge. This following sub-sections explain how the dielectric constant can be used to obtain the index of refraction, as well as how the critical surface free energy of liquid on a solid can be used to obtain the surface free energy of a solid.

#### 2.4.2.6 Effect of temperature on Hamaker constant

As mentioned earlier, temperature has little influence on a solid's Hamaker constant. For example, in a system with a homogenous alumina material and a vacuum medium, the Hamaker constant calculated by Parsegian (2006) [185], went from 14.5 J at 300 K to 15.2 J at 800 K. This confirms the weak effect of temperature on the van der Waals forces of a solid material. On the other hand, temperature has a more profound influence on the water's Hamaker constant. At room temperature, the dielectric constant of water is 80 and refractive index of water is 1.333. Using the Tabor Winterton approximation equation for the vacuum Hamaker constant, $3.7 \times 10^{-20}$J can be obtained which matches with value published by Israelachvili in 1992 [11]. Increasing the temprature to 350 celsius will make water's dielectric constant decrease to 13.05, while the refractive index will decrease to 1.187. Using the Tabor Winterton approximation on these two values will yield $1.65 \times 10^{-20}$J. This is the water vacuum Hamaker constant value that will be used for the rest of the thesis.

Therefore, in the final calculation for the system with a crud particle, the surface-modification

material, and a water medium, using the expression $A_{132} = (\sqrt{A_{11}} - \sqrt{A_{33}})(\sqrt{A_{22}} - \sqrt{A_{33}})$, the assumption that the solid Hamaker constant $A_{11}$ and $A_{22}$ does not change with temperature will be made. On the other hand, the water's Hamaker constant, $A_{33}$ will be calculated using Tabor Winterton approximation with high temperature data.

#### 2.4.2.7 Index of refraction and dielectric constant relationship

Where the index of refraction's data is not available directly, the index of refraction data can be obtained from the dielectric constant data for a non-magnetic material. This sub-section explains the derivations to obtain the index of refraction from the dielectric constant. The index of refraction can be defined by:

$$n = \frac{c}{c_m} \tag{2.52}$$

Where n is the refractive index, $c_m$ is the speed of light through a medium in m/s, and $c$ is the speed of light through a vacuum in m/s. But the speed of light can also be defined in terms of the electrical permittivity $\epsilon$ in F/m and the magnetic permeability $\mu$ of the material in F/m. Replacing the speed of light with the electrical permittivity and the magnetic permeability, we get:

$$n = \frac{c}{c_m} = \sqrt{\frac{\mu\epsilon}{\mu_0\epsilon_0}} \tag{2.53}$$

For a non-magnetic material, the magnetic permeability $\mu$ is equal to $\mu_0$ which is the magnetic permeability for vacuum. Therefore the equation can be simplified to:

$$n = \frac{c}{c_m} = \sqrt{\frac{\epsilon}{\epsilon_0}} \tag{2.54}$$

The dielectric constant is the ratio of the electrical permittivity between a material versus vacuum:

$$\kappa = \frac{\epsilon}{\epsilon_0} \tag{2.55}$$

Therefore, the relationship between the index of refraction and the dielectric constant for a non-magnetic material becomes the following [186]:

$$n = \sqrt{\kappa} \tag{2.56}$$

#### 2.4.2.8 Critical surface tension of solid and, the surface free energy of solid relationship:

Fox and Zisman et al. [187], found in 1950, that the plot of cosine of the wetting angle versus the surface tension of wetting liquid, gave a straight line. Extrapolating this line to the zero wetting angle allows Zisman's critical surface tension to be obtained. This is shown in the following figure 2-87. The liquid with a surface tension below the critical surface tension of surface will wet the surface [188, 187]. Gardon (1965) expanded on on Zisman's work to include the relationship between the critical surface tension of a solid and the surface free energy of a solid. Gardon suggested the following relationship [189]:

$$\gamma_s = \gamma_c/\phi^2 \tag{2.57}$$

Where $\gamma_s$ is the solid surface free energy and $\gamma_c$ is the critical surface tension for the solid. $\phi$ can be further decomposed into the following expression:

$$\phi = \phi_I \phi_V \tag{2.58}$$

Where $\phi_V$ is one, if molar volume of the two components are the same. If the ratio of the molar volume is as large as 5 or as small as 0.2, $\phi_V$ may be as low as 0.93 [189]. $\phi_I$ characterizes the nature of the interaction forces in two phases. If the two phases only depend on dispersion forces, the value will be almost one. This relationship is useful in the case of $TiB_2$ where data is very limited. However, $TiB_2$ has been actively studied for its relationship to liquid alumnium, which makes the critical surface tension data available. Using this relationship developed by Gardon, the critical surface tension can be used to determine the surface free energy, which can then be used for obtaining the Hamaker constant.

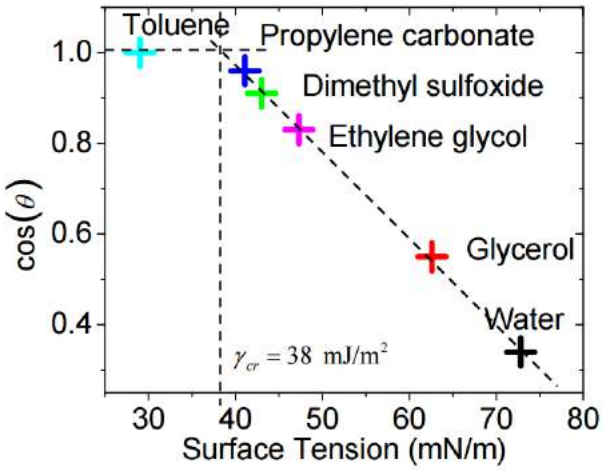


Zisman plot for PMMA using various testing liquids

Figure 2-87: This Zisman plot shows the linear relationship between the surface tension of wetting fluid and the contact angle on solid [190].

**Measuring the dielectric/refractive properties** There are several ways that dielectric/refractive properties can be measured for materials, including the valence electron energy loss spectroscopy (VEELS) and the ellipsometry technique.

Ellipsometry technique can be used to investigate dielectric properties of thin films. Ellipsometry works by measuring the change of light polarization when it reflects off or transmits across sample materials [191]. A light source used by an ellipsometer emits incident light with known polarization. This incident light interacts with the sample material upon hitting, through reflection, absorption, scattering, and/or transmission. The interactions will emit light back to the detector with a different amplitude and phase shift. This process is shown in figure 2-88, which demonstrates how an ellipsometer works. Ellipsometers do not directly give optical constant values. The data of amplitude ratio upon reflection and phase shift must be analyzed with models such as Forouhi Bloomer model [191].

Another useful technique for measuring dielectric/refractive properties of material is the VEELS. The VEELS technique is a subset of electron energy loss spectroscopy (EELS). EELS equipment itself usually comes as an add-on to TEM which can provide EELS with the electron source. EELS works by bombarding the sample of interest with a beam of electrons that have a narrow range of kinetic energies. When passing through the material, electrons may undergo inelastic scattering causing it to lose some energy. A spectrum of energy loss can then be obtained similar to that shown in left graph of figure 2-90. From the spectrum of energy loss, optical properties can be calculated with results similar to that shown in the right graph of figure 2-90.

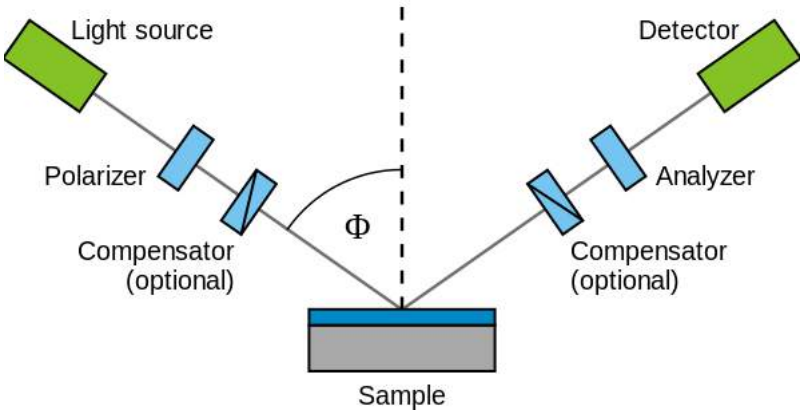


Figure 2-88: Diagram demonstrating how the ellipsometry technique works [192].

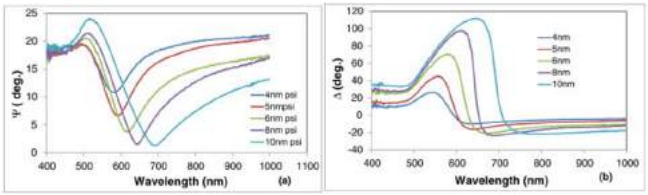


Figure 2-89: Example data obtained by applying the ellipsometry technique on gold [193]. In the left graph, the ratios of reflected to incident light amplitude are plotted against the wavelengths. In the right graph, the phase shifts are plotted against the wavelengths.

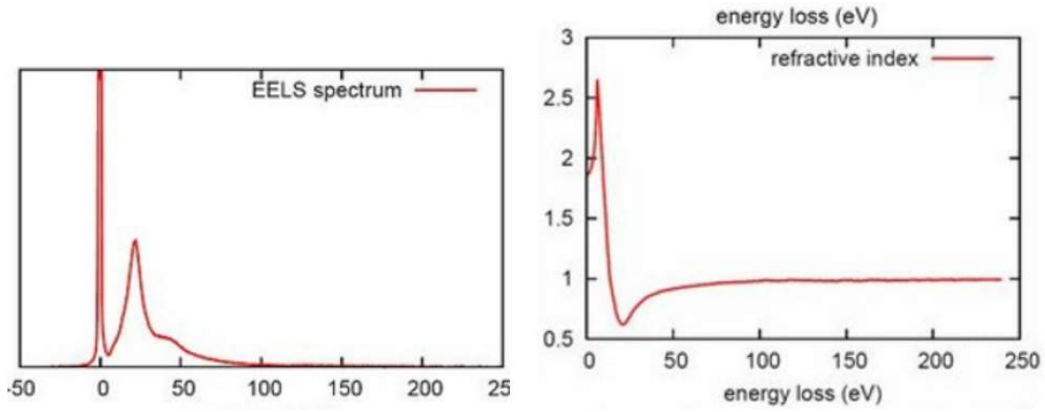


Figure 2-90: An example VEELS spectrum and its corresponding refractive indexes obtained from the VEELS spectrum [194]. The material used was SiN.

#### 2.4.2.9 Implication of Van der Waals Force Background

The equation 2.49 suggests that if the dielectric constant $\epsilon_1$ and the refractive index $n_1$ are low, the Hamaker constant will also be very low. If the materials used for crud-resistant coating is non-magnetic, the equation 2.56 demonstrates that lowering $n_1$ value will also lower the $\epsilon_1$. This means that low index of refraction should correspond to the low London-dispersion Hamaker constant.

## 2.5 Implications of Background to Controlling Crud

The previous background sections should provide enough details to understand the theories behind crud, from its origins, to its effects, to the mechanisms of its formation, to ways of preventing it completely. This last section will be dedicated to explaining what this valuable background knowledge implies about how crud growth can be controlled, as well as the benefits of controlling crud. The first subsection will breakdown the approaches to preventing and mitigating crud, and touch upon how we are dealing with each approach. The second subsection will briefly summarize the benefits of crud prevention and mitigation.

### 2.5.1 The approaches to preventing and mitigating crud

To summarize what was covered earlier in the background, crud is formed through the deposition of suspended particles. The dryout of the liquid layer between sub-cooled bubbles and the heat transfer surface aids the deposition of suspended particles. In each of these summarized processes, if even one part of the process can be prevented, it might be possible to prevent the formation of crud altogether. This implies that to prevent crud from growing, there are three main approaches that can be taken:

- The first approach is to get rid of particles that cause crud formation in the first place. This might involve some sort of filtering technique. The problem with trying to get rid of crud particles is that the particles are very hard to filter out. As mentioned previously, nuclear reactors do have their own filtration systems that includes both physical filters designed to capture larger particles, and ion exchanger filters designed to capture ions and very small particles. However, there are specific particle sizes around 50 nm that are capable of evading both types of filtration system. Nevertheless, using this approach, a patent suggesting magnetic filtration systems [120] as well as a patent suggesting the use of floating zirconium oxide particles to capture crud particles have been filed [119]. Since this approach to crud prevention has already been examined many times, we will take a different approach to crud prevention.

- The second approach in dealing with crud is to prevent crud particles from sticking to the heat transfer surfaces. This is the approach that is explored in this thesis. Our idea is to coat

nuclear fuel rods with substances that will prevent adsorption of crud particles to the heat transfer surfaces. The atomic-force microscopy (AFM) technique and material properties, such as Hamaker constant, were used to identify multiple material candidates that crud particles might not be attracted to. These materials were tested in IHTFP to determine if any of them will be successful in preventing or mitigating crud formation.

- The third approach that can be used to deal with crud is to manipulate boiling. crud is formed from the dryout of liquid layer under the boiling bubble. If the bubble is mitigated or manipulated, this dryout of liquid layer may be mitigated or prevented. Without the dryout layer, crud might not grow. This approach to crud prevention will be explored after the completion of this thesis. More in-depth details on the manipulation of boiling approach will be presented in the discussion section.

### 2.5.2 Benefits of crud prevention and mitigation

PWR's design and operation contain many limitations due to the presence and effect of crud. If crud is prevented or mitigated, these limitations will be removed, allowing for more efficient reactors to be designed and built. Because crud-resistant fuel rod cladding coatings are applied on fuel assembly, their deployment to the existing fleet of reactors should be simple. There is no need for any expensive upgrades or changes of equipment for the reactor itself. The fuel assembly with crud-resistant coating upgrade can be deployed the next time fuel is depleted. Since fuel rods are replaced about every one and a half years, the existing fleet of reactors can easily yield the benefits of crud prevention coating. Removing operation limitations related to crud should allow the existing reactors to run more efficiently. Specifically, the fear of crud and its effects forces operators to put caps on reactor's operating parameters, such as the choice of pH and the choice of power rating. Without fear of crud, reactor operators can comfortably push for a lower pH and a higher power rating. With crud-resistant coatings, it will also be possible to push for a higher fuel burnup and power uprates, as more boric acid can be added at the beginning of nuclear fuel cycle without the concern about the pH dropping below 6.9.

The power uprate is especially important in the current environment where not many new nuclear reactors are being built, while the list of reactors being shutdown is ever-growing. Wisconsin Kewaunee, Southern California Edison, Florida Crystal River, Nebraska Fort Calhoun and New York FitzPatrick, are some of the plants that have been or is set for shutdown in recent years [195]. With these reactors shutting down without new reactors being built, power uprates will be the only way to maintain the amount of nuclear power generation. The section 2.2.5.5 clearly shows that there are still huge gaps for improvement through power uprates, that have yet to actualize. This huge improvement gap is not surprising, as power uprates may jeopardize the reactor with problems

such as crud. With crud problem gone, however, there will be one less deterrent to nuclear reactor power uprates. The power uprates may become attractive again and significant amounts of power generation can be obtained without building a single new reactor.

# Chapter 3

# DESIGN AND CONSTRUCTION OF THE IHTFP TEST FACILITY

## 3.1 Experimental Overview

The most accurate way to obtain data regarding the growth of crud would be to acquire actual crud samples from a reactor. Obtaining the samples directly from a reactor, however, is impractical for many reasons. crud from a reactor is extremely hard to extract given its hazardous environment. In addition, it will also be very hard to handle samples as crud accumulates a dangerous amount of radioactive materials. For our experimental objectives, which involve cladding coating tests, obtaining reactor samples is even more impractical, since a reactor remains in operation for around 18 months. This means it will take 18 months to obtain a sample set. Testing cladding coatings without proper experimental evaluation of what they will do in the reactor also raises concerns regarding safety. Other than that, crud growth in a reactor is unpredictable, making it even more impractical to attempt crud experiments with a reactor.

It is unlikely that radioactivity has significant effects on crud growth and characteristics. Therefore, if an experimental loop can be built to simulate most of the conditions within the reactor except for radiation, it should still be able to produce crud formations with similar characteristics to those found in the reactor. Omitting the radiation conditions allows us to operate the loop more easily. The IHTFP will allow crud growth experiments to be carried out at experimental thermal hydraulic and chemical conditions similar to those found in a pressurized water reactor (PWR). Samples obtained will be easy to handle and should imitate reactor crud quite well.

Additionally, the construction of the IHTFP will create many new experimental capabilities/possibilities, since it will be the first loop outside of the Nuclear Reactor Laboratory (NRL), or even at MIT that is built to simulate PWR conditions. For example, the Buongiorno group has planned an

experiment that will study the contact angle of surfaces at high-pressure and high-temperature conditions, something that has never been done before, since the hurdle of recreating PWR conditions is quite high.

## 3.2 Introduction

The IHTFP is built to simulate the conditions inside a PWR including temperature, pressure, flow, and coolant chemistry. It works by driving flow through the autoclave, where PWR conditions that induce crud formation are simulated. The autoclave contains a heating rod which contains an electric isolated resistance heater, to simulate an actual PWR fuel rod. This introduction to the design and construction of the IHTFP will give the reader a good idea of how the system works, without delving into exhaustive technical details or the actual steps needed to operate the loop.

### 3.2.1 Overview of the crud loop

The IHTFP is made up of two main systems, the main loop and the auxiliary loop, as shown in Figure 3-1. The main loop is the part that is pressurized and heated to PWR conditions. Water also circulates within the loop to imitate the thermal-hydraulic condition of PWRs in the autoclave. The auxiliary loop is where the water storage tank is situated. It is used mainly for chemistry control. The auxiliary loop is where the main loop obtains its water and retrieves its water input supply. This auxiliary loop is maintained at room temperature, slightly pressurized with argon to avoid oxygenating the test water. The control program, shown in figure 3-2, is used for data acquisition and control of the loop. Its bottom diagram lays out the main loop (bottom left) and the auxiliary loop (bottom right). Measurement associated with each piece of equipment in the loop is displayed side by side. In the case where a piece of equipment can be turned on/off via the control program, an on/off button is also provided.

### 3.2.2 Main Loop

The main loop's function is to simulate the thermal hydraulic condition of the PWR. To simulate thermal hydraulic conditions, pressure, temperature, and flow will be carefully controlled. By regulating these three factors, PWR conditions within the autoclave flow channel can be achieved, and crud can be grown on the heating rod in the autoclave. The high-pressure condition in the main loop is maintained using a pressurizing pump. A high temperature is maintained using the autoclave heating rod as well as the heating tapes around the loop. Flow is maintained with the circulation pump.

The water in the main loop will be kept at a high temperature at all times. Heat loss occurs through insulation and the pressurizing pump cold water input. Having water circulate without

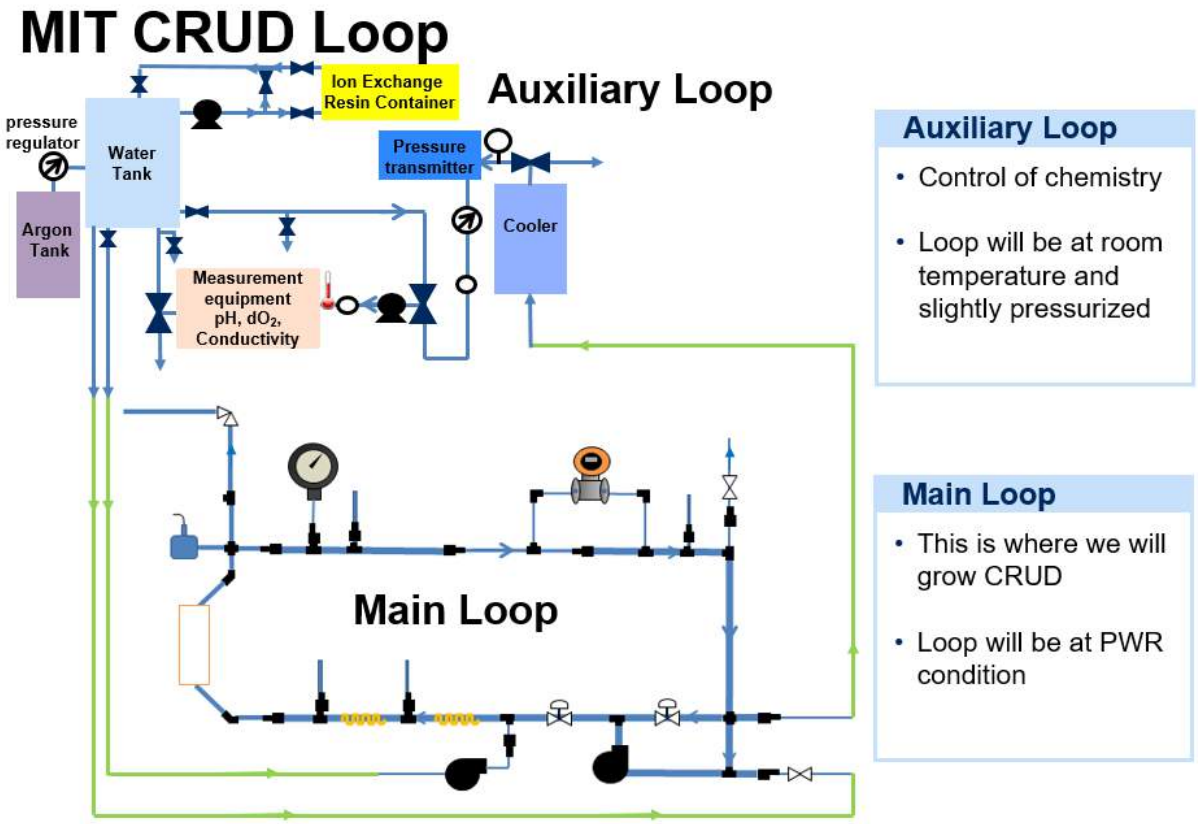


Figure 3-1: Diagram demonstrating the two most important parts of IHTFP, the auxiliary loop and the main loop. The diagram shows how both loops are connected. The auxiliary loop provides water to the main loop at the input of the pressurizing pump. The main loop outputs the water to be cooled down at the sample cooler. After that point, the pressure is regulated at the back-pressure regulator in the auxiliary loop. In addition, the water chemistry monitoring tools and cleanup systems are in the auxiliary loop.

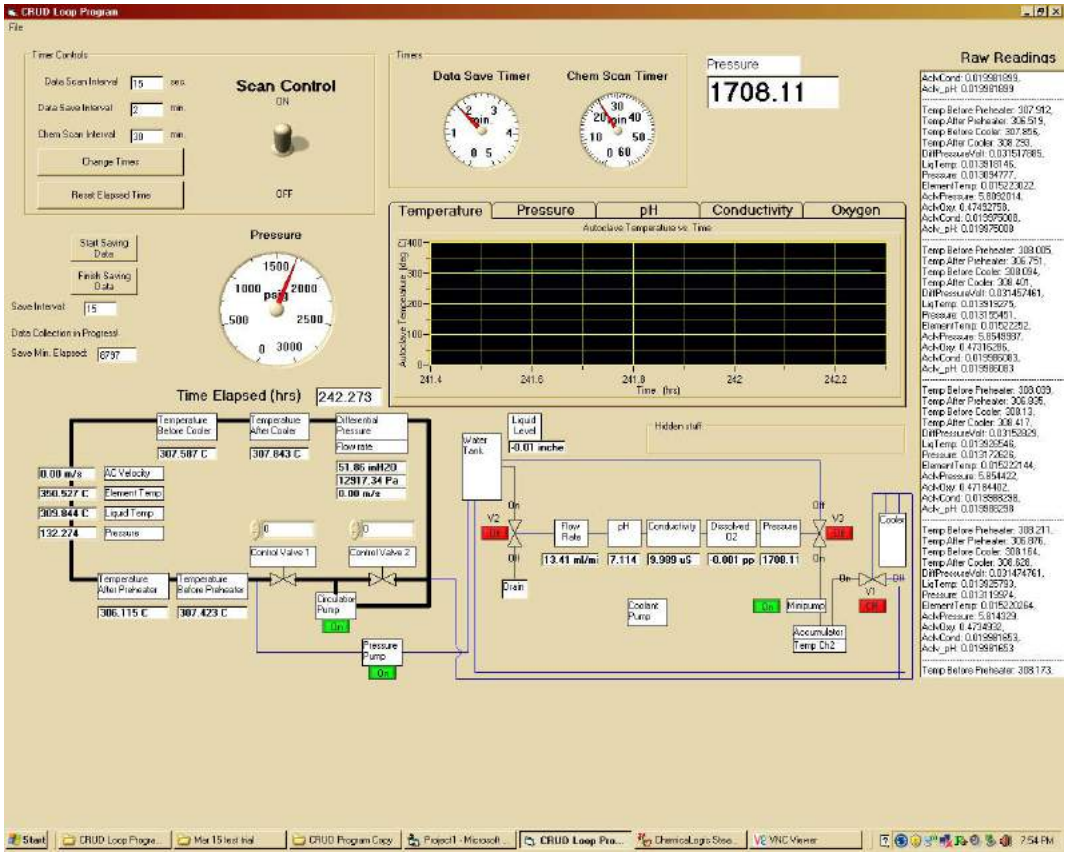


Figure 3-2: This is the illustration of how the crud loop control program looks. It is laid out in a simplified diagram of the loop, where data readings will be shown at the related equipment locations. This control program can be used to control valves and pumps as seen by their on/off function buttons.

lowering the water flow temperature provides the advantage of having less heat loss. The power usage to get the temperature to 320 °C is quite high, making it one of our limiting factors in building the loop. The downside of this design is that the corrosion products coming from the loop's tubing will not get removed easily, and can, therefore, affect the experimental results. However, since our goals, including the testing of coatings and the fractal analysis of crud using scanning electron microscope images, do not require very precise chemistry, it remains an attractive design choice. In addition, this internal corrosion of the main loop is an added benefit, as it provides a more natural source term from 316 stainless steel corrosion to better simulate conditions inside a real PWR. The decision to go with this design made it possible to build the crud loop within our budget constraints. The following subsections explain how pressure, temperature, and flow control are accomplished in the IHTFP.

#### 3.2.2.1 Pressure Control

Pressure control is accomplished by the pressurizing pump and the back pressure regulator, as shown in figure 3-4. The pressurizing pump is a positive-displacement pump that will keep pumping in water at a defined flow rate of up to 67 mL/min. The pressure is kept under control by the back-pressure regulator. The back-pressure regulator will release the pressure pumped up by the pressurizing pump just enough to maintain the pressure. Pressure is monitored by the pressure transmitter connected to the autoclave, and additionally by the pressure gauge in the main loop and the pressure gauge on the auxiliary loop. The pressure switch helps shut down the electrical system in the case of an emergency pressure spike. The pressure relief valves will release the pressure, pushing the steam to the top of the building when there is an emergency pressure increase. Additionally, the pressurizing pump also has its own safety relief valve for handling a pressure emergency in case all other prevention mechanisms fail. More information on how this system works is provided in section 3.6.1.3.

#### 3.2.2.2 Temperature Control

For the temperature control, as shown in figure 3-4, two separate systems are used to maintain the autoclave temperature. First, the autoclave heating system is the system attached to the autoclave itself. Second, the loop heating system operates the heaters that are placed throughout the loop. The autoclave heating system includes the heating rod and its internal thermocouples and the controller box. Figure 3-3 is a photo of the autoclave controller box. The heating rod is used to heat up water flowing in the main loop system, as well as provide heat flux for sub-cooled boiling. The element temperature or the centerline temperature of the heating rod is measured by the thermocouple embedded within the heating rod. The element temperature is the temperature that is used to regulate heat supplied to the heating rod. As the heat density coming from the autoclave

heating rod is a lot higher than that of a typical heating rod, it may take few seconds before the heating rod becomes too hot and gets destroyed. Therefore, trying to achieve control using the liquid temperature will give temperature feedback that is too slow to react to rapid temperature changes. Because temperature control in the heating rod is very delicate, an "on-off" control of the heater will not work, as 100% "on" power, in many cases, can quickly burn out the heater. The control box help achieves this fine temperature control using a transformer to control the input voltage. The control box's element temperature panel (left-most panel) can be utilized to adjust the temperature setup. The proportional-integral-derivative (PID) setup allows the control box to stabilize the temperature at any given point. A PID controller controls a feedback mechanism, whereby it continuously calculates the difference between a specified setpoint and a measured process variable, and then applies corrections based on proportional, integral, and derivative terms. In the autoclave heating system, the liquid temperature is measured with the thermocouple situated on the top of the autoclave, right where liquid leaves the autoclave. The liquid temperature is displayed on the middle panel of the autoclave's control box. This liquid temperature panel is used for monitoring only and does not have anything to do with the control of temperature. The last panel of the autoclave control box is used to monitor the pressure within the autoclave, in units of bars. Again, this panel does not directly control pressure within the system.


Figure 3-3: Photo of the autoclave control box.

Because the autoclave heater cannot provide enough power to heat the whole loop beyond approximately 230 °C, additional heating is needed. This extra power is provided by heating tapes. The loop heating system controls the heating tape throughout the loop's tubing. Figure 3-4 below shows the pre-heaters or the heating tapes at only a few spots; in the real loop, the heating tape was installed at almost every possible spot to maximize the heat input. As the heating tapes have low energy density, they will not fail even if driven at full power without a heat sink. Therefore,

temperature control of these heating tapes does not have to be as delicate. As a result, the liquid temperature is chosen to control these heating tapes instead of individual heating tape's temperature. Additionally, the liquid temperature is ultimately the temperature that we want to control in the loop system. Unlike the autoclave, where the heating rod also plays a major role in defining heat flux and sub-cooled boiling, the temperatures of heating tapes are not essential for the experiment. Controlling the heaters with the liquid temperature also allows us to control all the loop heaters through just one point without installing thermocouples on every heater in the loop. This simplification adds huge benefits regarding debugging the loop. Although there are four thermocouples throughout the loop used to monitor temperature, only the exterior thermocouple situated at the autoclave output is relevant to loop heater control. The autoclave output exterior thermocouple is a dual junction thermocouple, which means that it can output temperature to two thermocouple lines. The first thermocouple wire goes to the computer for display on the computer screen, shown in figure 3-2. The second thermocouple wire goes to the heating tape proportional-integral-derivative (PID) controller. This single controller regulates the heating tape throughout the loop. Unlike the autoclave heating rod, which has the luxury of a large transformer to control power input, this single controller only turns heating tape power on/off. When this controller clicks on, all of the loop's heating tapes will heat up. This control method is very crude but works well, and has huge benefits when it comes to simplifying the loop. PID control allows this controller to stabilize the temperature in an acceptable way even with no variable heating. The autoclave heating system and the loop heating system combine to make the crud loop capable of heating itself to 320 Celsius or more and providing enough heat flux (up to 206 $kW/m^2$) for growing crud on the testing samples on the heating rod in the autoclave. More information on how this system works is provided in section 3.6.1.2.

#### 3.2.2.3 Flow control

Flow control is achieved by using a combination of the circulation pump, the differential pressure transmitter, and the control valves, as shown in figure 3-4. The circulation pump is a centrifugal pump that drives flow through the loop. Since the circulation pump with a variable speed function add-on is very expensive, we use the control valves to regulate the flow instead. Control valves regulate the flow by constricting the flow path. There are two control valves to prevent damage to the circulation pump in the case of a control valve failure, or an accidental control valve shutoff. Both of these control valves are shown in figure 3-4. The main control valve in series with the circulation pump is the one regulating the flow. The control valve parallel to the circulation pump is left slightly open to let the water through in case the main control valve fails, and to help quench pump-induced flow vibrations. The differential pressure transmitter is the chosen method for measuring the flow through the loop. At this temperature, pressure and flow rate, there is no flow meter on the market

except those that are custom made. Those custom made flow meters are extremely expensive and do not make much sense for this project. Therefore, a differential pressure transmitter is used as a way to circumvent this problem. By knowing the difference in pressure between the flow area of different sizes, Bernoulli's equation can be applied to calculate the flow rate from a given differential pressure. More information on how this system works is provided in section 3.5.3.

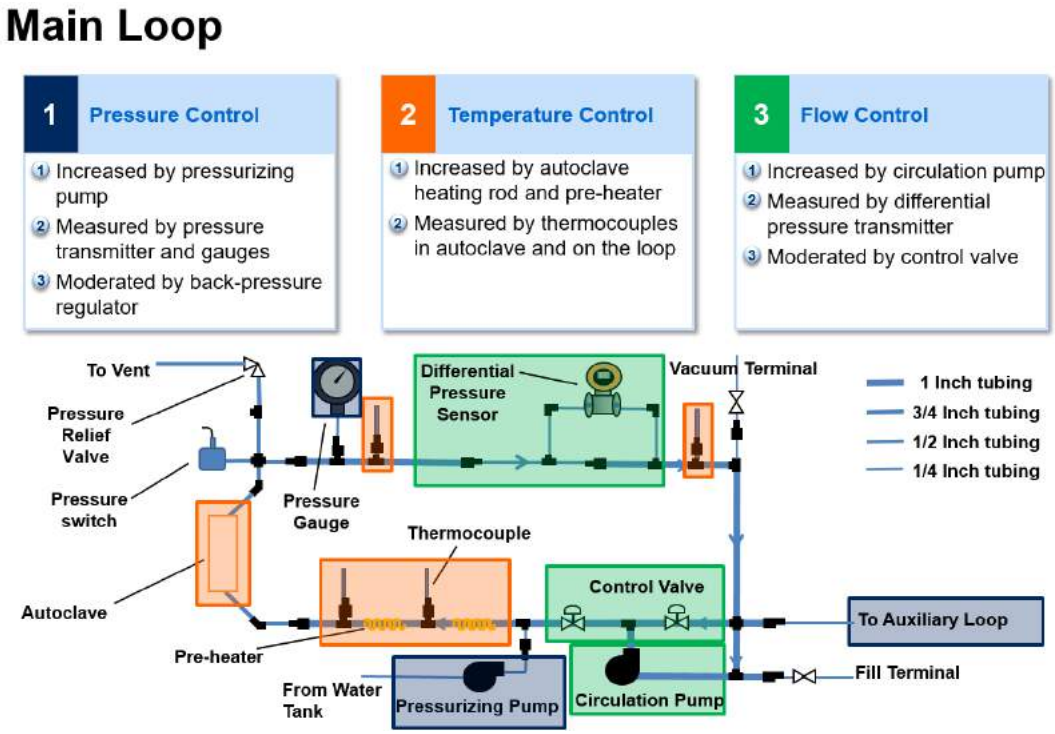


Figure 3-4: This diagram shows different parts of the main loop and their functions.

### 3.2.3 Auxiliary loop

The main loop needs the auxiliary loop to store its input/output water and control the loop chemistry. Figure 3-5 is a diagram of the auxiliary loop. The water tank in the auxiliary loop is where water that will be injected into the main loop is stored. On startup, the water tank is used to mix the boric acid, the lithium hydroxide, and the nickel oxide crud particles together. The process starts by first cleaning up the water to make sure that the chemicals added are the only chemicals existing in the water. Cleaning up the water first also prevents non-crud fouling of the crud loop. The most important part of cleaning is the ion exchange resin. During cleaning, input tap water is circulated using a small pump, through the ion-exchange resin container, to exchange out any ions that exist within the water. As ions in water get filtered out, the water's conductivity as measured by the conductivity sensor goes down. During the cleaning run, valves can be configured so that water is drawn from the tank through measurement equipment to monitor the conductivity and

dissolved oxygen in the water. This ion cleaning process is slow and can take as long as two days to complete depending on the content of tap water and how new the ion-exchange column is.

After the water in the tank has been rinsed of ions (approximately 0.09 $\mu S/cm$ conductivity), the next process is to get rid of the dissolved oxygen in the water. This process is done by bubbling argon through the water. The bubbling continues until the dissolved oxygen is below 5 ppb. After both dissolved oxygen and conductivity are low enough, the chemicals can be added to the water tank via the airless injection port on the top of the water tank. After the chemicals are added, the valves can switch flow to bypass the ion-exchange resin container, turning the auxiliary loop into a mixing loop. The mixing occurs by taking water from the bottom of the tank and releasing it at the top, while maintaining an inert argon cover gas.

When the chemicals have been well-mixed as determined by the stabilization of conductivity and pH, the water tank will be ready for input into the loop. The main loop is filled through its fill port, which connects to the water tank. Pressurizing the loop will take a lot longer if there are gas pockets in the loop, since they would compress and store energy. Two loop-filling methods can eliminate these gas pockets — the vacuum method and the argon gas method. The vacuum method uses a vacuum pump to eliminate any gas in the loop. Once the loop is under vacuum, it can be filled through its fill port. The argon gas method, on the other hand, pressurizes the water in the water tank with argon gas. When we open the fill port, pressurized water will rush into fill the loop. Gas pockets can be cleared from the loop by releasing the tube-connection nuts where there are gas pockets. More information on these two methods can be found in section 3.9.4.

When the loop is filled, and the fill port is closed, the pressurization process can begin. The part that drives this process is the pressurizing pump which is the only water input during operation. It draws water directly from the water tank to pressurize the loop. The output for the main loop is connected to the auxiliary loop via a sample cooler which cools down the water to near room temperature. Cooled down water passes through the pressure gauge and pressure transmitter to measure its pressure. The back-pressure regulator acts as a pressure boundary between the high-pressure system and the low-pressure system of the crud loop (more detail in section 3.6.2.5). It releases flow just enough to maintain the setpoint pressure. The water then gets directed through measurement equipment to ensure it has the desired chemical properties. After that, the water is released into the water tank, completing the water cycle during operation.

## 3.3 Crud Loop Preliminary Design

### 3.3.1 Design Considerations

The design of the IHTFP involves finding a balancing point among many trade-offs. Many design considerations go into designing the extreme temperature, pressure, and flow loop with limited

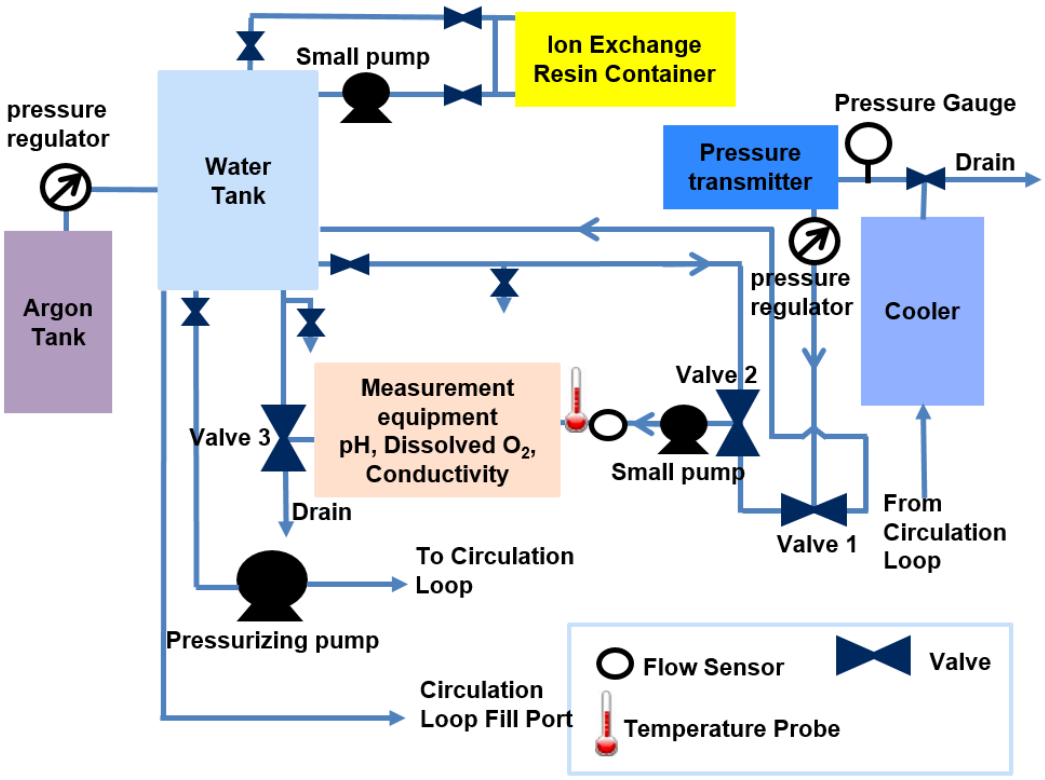


Figure 3-5: This diagram shows different parts of the auxiliary loop and their functions.

resources. These design considerations play major roles in choosing IHTFP design parameters and deciding what equipment to purchase for the loop. Considerations that play a major role in our design and purchase decision includes the following:

**Data Accuracy:** Data accuracy is the most important aspect of the IHTFP's design considerations. Ideally, the loop should be able to produce good quality, useful data in a reasonable amount of time. One good way to get the crud data representative of PWR crud is to imitate conditions within the PWR in the experimental setup. The IHTFP is designed in such way that makes it capable of imitating the PWR thermal hydraulic and chemical conditions as closely as possible. The heating rod within the autoclave where samples are placed imitates the fuel rod of the reactor. The autoclave test section is designed so that the Reynold's number and the mass flux imitate the conditions within a PWR. All the supporting mechanisms in both the main loop and the auxiliary loop work together to help crud grown in the loop exhibit characteristics that are as close to crud grown in an actual PWR as possible.

One might ask if PWR conditions are truly necessary, since simulating PWR conditions is extremely hard to achieve compared to the normal atmospheric pressure pool-boiling facility, and accurate imitation of PWR conditions might not be worth the trouble. However, both the low-

pressure aspect and the no flow aspect of the simpler facility have downsides when it comes to growing crud. A pool-boiling facility has several critical disadvantages. Firstly, PWR crud formation is a balance between the crud layer forming and eroding at the same time. With a pool-boiling facility, a crud formation experiment lacks this flow. This will lead to more crud growth. In our experiment specifically, the materials that would otherwise be crud resistant might not look that way in a pool boiling experiment. Things are worse if the pool boiling facility has its heating plate on the bottom of the autoclave. In that case, crud particles may settle just like any other sediment system without any flow.

Having less pressure and temperature leads to results that will likely not represent the real reactor. Inaccurate pressure changes properties, such as the contact angle shown later in chapter 4. Changes in contact angles can change how bubbles form, and thus may affect how crud grows. Most of the relevant properties that could affect the crud growth change with temperature, including properties such as the boiling bubble sizes, the surface tension of water, and the water viscosity. Having both the high pressure and high temperature together is difficult to achieve. However, for the crud growth experiment, increasing one cannot be done without increasing another. The crud growth experiments need sub-cooled boiling to work. When the temperature is high, the pressure must also increase to prevent liquid from turning into vapor. When the pressure is high, the temperature will also need to increase, or there will be no boiling and no crud.

**Cost:** High temperature and pressure equipment are extremely expensive. To be able to build the whole loop with limited funding, equipment must be recycled from other experiments when possible. Also, some consideration is given to expense when functionally equivalent equipment with lower cost can be substituted. For example, a flow meter that can properly measure flow rate at this extreme condition is only available as custom made equipment, and is extremely expensive. Therefore, it is replaced with a differential pressure transmitter and an orifice, which can also be used to obtain flow rate with some additional calculations using Bernoulli's equation. This saves cost by a factor of more than ten times compared to a custom piece. Another example of a cost-saving initiative is the use of control valves instead of a circulation pump's variable speed add-ons. A circulation pump with variable speed setup is extremely expensive, double the cost of a normal circulation pump. Since control valves cost a lot less than a circulation pump, using control valves in this case saved an enormous dollar amount of costs. Reusing equipment such as the dissolved oxygen sensor, the conductivity sensor, the pH sensor, the sample cooler, relays, and the temperature controller, etc., makes the cost of acquiring that equipment virtually free, while promoting recycling in the community.

**Safety:** The IHTFP will be running at PWR conditions, which are very dangerous. Therefore, safety is of the utmost importance. Figure 3-6 summarizes the safety systems used in the IHTFP.

Multiple redundant safety features are present throughout the loop. For pressure safety, there are three pressure relief valves — one attached to tubings in the main loop, and other two attached to the autoclave itself and the pressurizing pump, respectively. Having three redundant pressure relief valves is one way to make sure that even if one of the relief valves fails to open, there are others to compensate. Other than this, the pressure pump will shut off on its own without human intervention once the pressure becomes too high. The pressure switch also shuts down the whole electrical system in the case of a pressure emergency.

Polycarbonate sheets are used to protect people within the crud loop room in case high system pressure ejects a piece of the loop. Polycarbonate is the same material that is used for making bulletproof equipment in the security industry, so the person behind the glass can feel assured nothing will easily penetrate the polycarbonate sheet. Nevertheless, even with many redundant safety systems, it is still a dangerous experimental setup, and extreme caution must be taken when operating it.

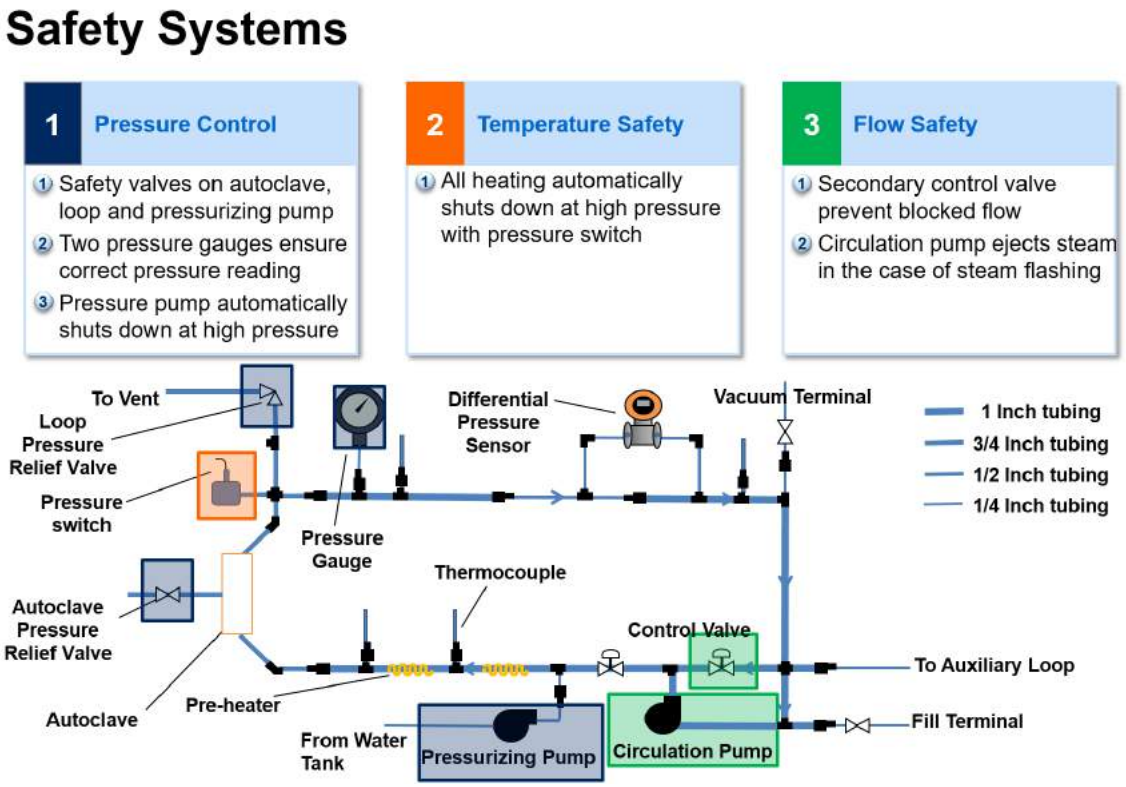


Figure 3-6: This is the diagram of the safety system elements within the loop.

**Space & Mobility:** The whole loop, including the control computer desk, must fit in its designated room which has usable space of only around 17 feet by 12 feet. The loop must also be able to fit through a normal door which is around 6.5 feet by 3 feet. This is necessary to make the loop portable as a unit. Disassembling the whole loop for moving is impractical since it entails a high

risk of damaging equipment during disassembling and reassembling of the equipment, which can also take many man-hours. The heated part of the loop usually becomes so sealed by heat that it becomes extremely hard to disassemble. In our experience, parts were thrown away because the tubing was bent from too much force in disassembling.

During its life-time, the loop has already been moved two times. During the initial construction phase of the loop, the room that the loop was supposed to be placed in was not ready yet. To avoid reassembling the crud loop many times, it had to be built with mobility in mind. For this purpose, the loop can be separated into three major parts that can be moved separately. All three major parts are designed to fit through a common door size of 6.5 feet by 3 feet. Two parts that make up the main loop are designed so that they can be easily lifted with a pallet jack. Practical mobility is another reason why the main loop was designed to have a three-dimensional structure. With its three-dimensional structure, a pallet jack can easily lift the loop with good balance.

**Simplicity:** The first few iterations of the IHTFP in its construction phase had too much emphasis on cost and too little emphasis on simplicity, which led to a higher probability of failure and a more arduous task debugging the loop. One example of this mistake is the usage of the accumulator in an attempt to match the flow rate of pH, dissolved oxygen, and conductivity measurement equipment. The original pressurizing pump had a flow rate that was too low, so the loop output flow rate was too low for equipment to measure properly. The previous solution to this was to use an accumulator that accumulates output water. From time to time, the computer would let some water from the accumulator through the measuring equipment to take the measurement. Although this system can save some cost of buying a new pressurizing pump, it presented a myriad of problems that delayed experiments. In the end, the old pressurizing pump was replaced with a new one featuring a higher flow rate, which functions very well, making the experiment a lot smoother. Learning from mistakes such as this, the design add-ons included subsequently were required to be as simple as possible.

In the same way, simplicity influenced our decision to use only one liquid temperature for central control of all heaters in the loop. Before the decision, the initial plan was to have a separate temperature controller for each heating element. Each temperature controller would take input from the thermocouple embedded between the heating tape and the stainless steel tubing. The motivation back then was to make sure that the heater did not burn out. Fortunately, it was later found that because heating tapes have very low heat density, there is no need to worry about heater burn-out, even if it was put to 100% power for a long time. Therefore, the loop was simplified to having just one controller that takes the liquid temperature at the autoclave output as an input. This was a great time-saving decision, as lots of man hours would have been spent maintaining the complex electrical system for loop heating. If there were one controller for each heater in the loop, the maintenance work for the loop heating system would have taken at least quadruple the time.

Moreover, the loop's electrical circuit will become an even more complex and less comprehensible to outsiders.

**Maintenance:** Easy maintenance and ability to debug the loop is another vital design consideration. A significant amount of time was spent doing maintenance and figuring out problems with the loop. Therefore, designs must also make the loop maintenance easy. There are two main categories of ways that make the loop easy to maintain. First, the loop should be designed so that it is easy to access its equipment for maintenance. Accessibility is one of the reasons why the loop structure is built as a sturdy three-dimensional rigid structure as opposed to a two-dimensional structure to hold up the tubings. The three-dimensional structure allows operators to climb up the loop to get at necessary parts without using a ladder, which is more dangerous as it can slip. No maintenance procedure for crud loop requires a ladder except refilling the loop which is done approximately once every two months. Second, the loop should be very simple as mentioned previously.

### 3.3.2 Crud Loop Design Parameters

The IHTFP design parameters were chosen to best match those found in a reactor as possible. The table 3.1 summarizes the conditions in the IHTFP compared to those in a PWR.

| Condition | PWR | IHTFP |
|---|---|---|
| Pressure | 15.5 MPa | 15.5 MPa |
| Liquid Temperature | 287-324°C | 320°C |
| Reynolds Number | $5 \cdot 10^5$ | $1.62 \cdot 10^5$ |
| Mass Flux | $3500 kg/m^2 s$ | $1920 kg/m^2 s$ |
| $Fe_3O_4$, $NiO$ | 13-116 ppb | 20,000 ppb |
| Boron | 1400 ppm | $<$ 2000 ppm |
| Lithium Hydroxide | 3 ppm | ~2.2 ppm |
| pH | 6.9 - 7.4 | 6.9 - 7.4 |
| Dissolved Oxygen | $>$ 5 ppb | $>$1 ppb |
| Water Electrical Conductivity | ~11-23 $\mu S/cm$ | ~10-15 $\mu S/cm$ |

Table 3.1: This table compares conditions between that of the IHTFP and a typical PWR. Note that the IHTFP only contains nickel oxide ($NiO$) particles, because the 316 stainless steel tubing of the IHTFP provides a natural $Fe_3O_4$ source term. The large amount of NiO was added to speed up crud growth. The lower-end value of pH was also chosen for the purpose of speeding up crud growth in the IHTFP [43, 53, 54].

As seen in the table above, the IHTFP can easily reach and operate at the PWR pressure. The pressure has profound effects on boiling and how bubbles form. Therefore, the loop was designed to get to 15.5 MPa, matching the PWR conditions. For temperature, the IHTFP can run at a temperature higher than the hot section of PWR. The high temperature was chosen to speed up crud growth. Since crud is formed from boiling, higher temperature and more boiling are expected to produce more crud growth. It generally takes over a year and a half for crud to grow in a

PWR. However, we do not have the time luxury to grow crud for a year. This significant time limitation drove the crud loop design parameters to support a higher crud growth rate. Reaching these high temperatures was extremely difficult and introduced many unexpected problems, but was nevertheless necessary to achieve the higher growth rate.

Reynold's number and mass flux are intertwined with each other. The experimental loop's liquid is fixed as water at PWR conditions. The only two parts left to adjust that will affect Reynold's number and mass flux, are the flow velocity, as well as the flow area size and shape. The flow area shape and size is limited severely by equipment prices. A larger flow area requires a larger, thicker and more expensive autoclave.

### 3.3.3 Pressure Drop Calculations

The pressure drop calculations were done on an Excel spreadsheet using the Darcy-Weisbach frictional pressure drop equations. In case of straight tubings, the equation for frictional pressure drop is shown below [54]:

$$\Delta p = f_D \frac{L}{2} \frac{\rho V^2}{D} \tag{3.1}$$

where $\Delta p$, is the friction pressure drop across cylindrical pipe (Pa). $f_D$ is the friction factor. $L$ is the length of pipe (m). $\rho$ is the density of fluid ($kg/m^3$). $D$ is the hydraulic diameter (m). Lastly, $V$ is the velocity of fluid (m/s). In the case of straight tubings, the friction factor can be calculated with the following equation [54]:

$$f_D = 0.184 Re^{-0.2} \tag{3.2}$$

This equation does not consider how the friction factor varies with roughness, probably since roughness' effect is not pronounced in the turbulent regime that both PWRs and the IHTFP operate in. In case of tube constrictions, expansions, and elbows, the following pressure drop equation can be used:

$$\Delta p = K \frac{\rho V^2}{2} \tag{3.3}$$

where $K$ is the loss coefficient and $V$ is the average velocity of fluid (m/s). A 90-degree elbow is assumed to have $K$ coefficient of 0.5, while 45-degree elbow is assumed to have $K$ coefficient of 0.3 [196]. In case of tube constrictions, the loss coefficient $K$ can be calculated as follows [54]:

$$K = \frac{(1 - \frac{A_2}{A_1})}{2} \tag{3.4}$$

where $A_1$ and $A_2$ are the inlet and outlet area size ($m^2$) respectively. In case of tubing expansions, the loss coefficient $K$ can be calculated as follows [54]:

$$K = (1 - \frac{A_1}{A_2})^2 \tag{3.5}$$

In the Excel calculations, the flow rate is assumed to be 11 liters/minute, which would correspond to a flow speed of 3.07 m/s in the test section. The following Table 3.2 summarizes the results obtained from the Excel pressure drop calculation. The pressure drop of the loop as a whole is still lower than the pump specification with a significant margin. The remaining pressure drop will be incurred across the control valves used to control the flow rate. This margin will allow for future upgrades without worrying about the pressure drop constraint.

| Loop Section | Additional Assumptions | Pressure Drop (Pa) |
|---|---|---|
| Autoclave Test Section | ID = 0.0175 m, OD = 0.02 m | 5239 |
| Autoclave Inlet Constriction | Assume flow area goes from 3/4-inch tube to test-section | 282 |
| Autoclave Outlet Expansion | Assume flow area goes from test-section to 3/4-inch tube | 371 |
| Straight Tube (1/2-inch OD) | Length = 10 inches, Thickness = 0.035 inch | 30 |
| Straight Tube (3/4-inch OD) | Length = 47 inches, Thickness = 0.049 inch | 284 |
| Straight Tube (1-inch OD) | Length = 249 inches, Thickness = 0.065 inch | 377 |
| Tube Elbows (3/4-inch, 45-degree) | K = 0.3, No. of elbows = 2 | 134 |
| Tube Elbows (3/4-inch, 90-degree) | K = 0.5, No. of elbows = 2 | 223 |
| Tube Elbows (1-inch, 90-degree) | K = 0.5, No. of elbows = 6 | 211 |
| 1-inch to 1/2-inch Tubing constriction | - | 172 |
| 1-inch to 3/4-inch Tubing constriction | - | 30 |
| 1/2-inch to 1-inch Tubing expansion | - | 260 |
| 3/4-inch to 1-inch Tubing expansion | - | 26 |
| Pressure Drop without Pump and Valve | - | 8055 |
| Pump | Flow of 11 liters/minute has ~12m head (figure 3-52) | 72398 |
| Control Valve | Adjust to match target liters/minute | 64343 |

Table 3.2: This table shows the pressure drop across each section of the IHTFP.

### 3.3.4 Heater Calculations

#### 3.3.4.1 Heat transfer calculation

In the crud loop, it is very hard to measure the temperature exactly at the surface of the cladding. Having a thermocouple on the surface of the cladding can obstruct the flow leading to changes in the result. Therefore, it is best to obtain the temperature of the surface of the cladding through

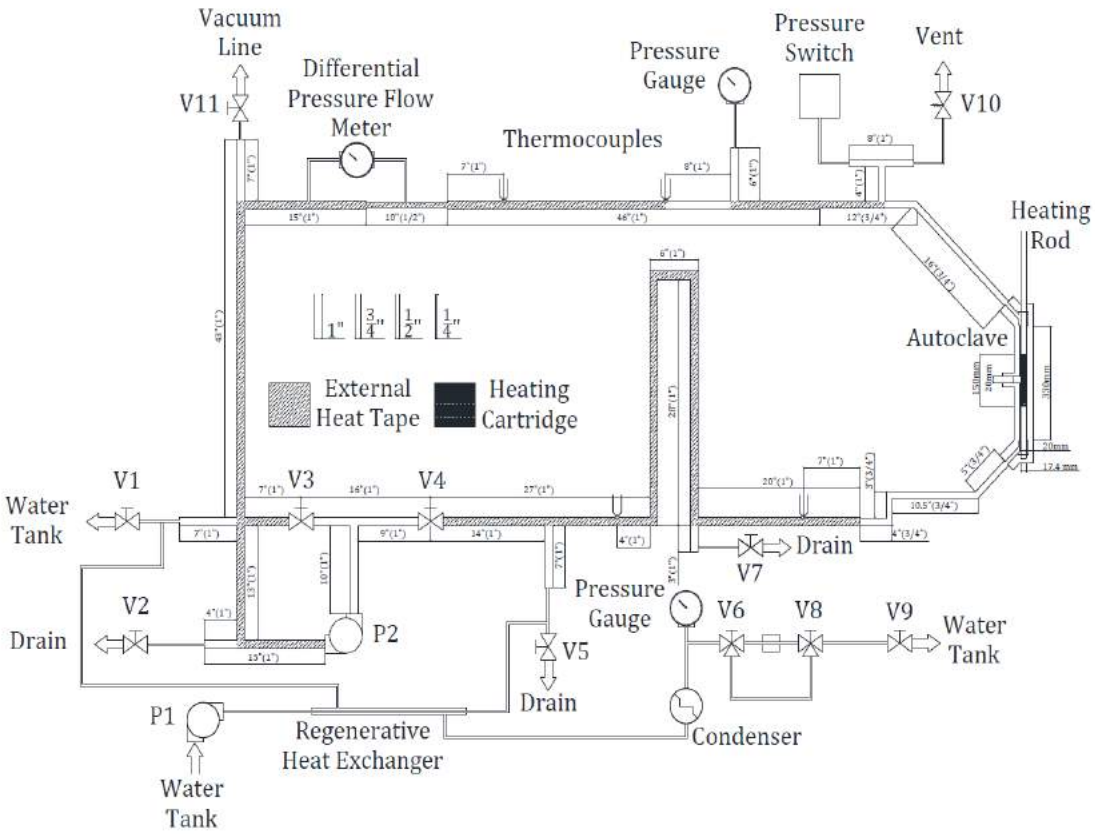


Figure 3-7: Diagram of the main loop with tube lengths labeled, by Sean Robertson.

calculations, given that we know the heating rod centerline temperature and the liquid temperature. When building the crud loop, rough heat transfer calculations [54] are used to determine the difference between the temperature at the heating rod centerline ($T_{max}$) and the temperature of the outer surface of the heating rod cladding ($T_{co}$). To accomplish this, we start with the heat conduction equation in a cylindrical geometry.

$$\frac{1}{r}\frac{d}{dr}(kr\frac{dT}{dr}) + q''' = 0 \tag{3.6}$$

Integrating this equation then dividing it by $r$, we obtain:

$$k\frac{dT}{dr} + q'''\frac{r}{2} + \frac{C_1}{r} = 0 \tag{3.7}$$

By taking this equation, moving all terms with r in it to the other side, then integrating both sides, we get:

$$-\int_{T_{max}}^{T} k\,dT = \frac{q'''}{4}(r^2 - R_v^2) + C_1 ln(\frac{r}{R_v}) \tag{3.8}$$

This equation can then be used to derive the temperature difference between the heating rod centerline ($T_{max}$) and the inner surface of the cladding ($T_{ci}$), as well as the temperature difference through the cladding ($T_{ci} - T_{co}$). When combined, we can get the temperature difference between the heating rod centerline temperature and the temperature at the outer surface of the cladding.

$$T_{max} - T_{co} = (T_{max} - T_{ci}) + (T_{ci} - T_{co}) \tag{3.9}$$

To obtain the temperature difference from $T_{max}$ to $T_{ci}$, we assume that the heat flux at the center of the heating rod is zero. This assumption can be converted to the following boundary condition:

$$q''|_{r=0} = -k\frac{dT}{dr}|_{r=0} = 0 \tag{3.10}$$

Applying this boundary condition to the heat conduction equation with $r = 0$, we get the following:

$$C_1 = 0 \tag{3.11}$$

Now plugging $C_1 = 0$ and $R_v = 0$ back into the equation 3.8 we get:

$$-\int_{T_{max}}^{T} k\,dT = \frac{q'''}{4}r^2 \tag{3.12}$$

At the inner surface of cladding, $r = R_{ci}$, the temperature is represented by the value $T_{ci}$. Plugging these values into the equation 3.12, the following equation is obtained:

$$-\int_{T_{max}}^{T_{ci}} k\,dT = \frac{q'''}{4}R_{ci}^2 \tag{3.13}$$

Converting this equation to linear heat rate using energy balance $q' = \pi R_{ci}^2 q'''$, we obtain:

$$-\int_{T_{max}}^{T_{ci}} k\,dT = \frac{q'}{4\pi} \tag{3.14}$$

With the assumption that k is constant at $k_{heater}$ , we can derive the following equation:

$$T_{max} - T_{ci} = \frac{q'}{4\pi k_f} \tag{3.15}$$

In the similar way we can derive $(T_{ci} - T_{co})$. Starting with knowing that volumetric heat generation $q'''$ should be 0, we simplify the equation 3.8 to the following:

$$-\int_{T_{max}}^{T} k\,dT = C_1 ln(\frac{r}{R_v}) \tag{3.16}$$

We also know that the following the heat flux equation must apply:

$$q''|_{r=R_{ci}} = -k\frac{dT}{dr}|_{r=R_{ci}} \tag{3.17}$$

And that the heat flux $q''$ is equal to $q'' = \frac{q'}{2\pi R_{ci}}$ in the heated section of the rod. By plugging this information into the equation 3.7, we yield:

$$-\frac{q'}{2\pi R_{ci}} + \frac{C_1}{R_{ci}} = 0 \tag{3.18}$$

$$C_1 = -\frac{q'}{2\pi} \tag{3.19}$$

With the assumption that k is a constant at $k_{heater}$, we can derive the following equation:

$$T_{ci} - T_{co} = \frac{q'}{2\pi k_c} ln(\frac{R_{co}}{R_{ci}}) \tag{3.20}$$

Combining these derivations using equation 3.9 we get the following equation :

$$T_{max} - T_{co} = \frac{q'}{2\pi}(\frac{1}{2k_{heater}} + \frac{1}{k_c} ln(\frac{R_{co}}{R_{ci}})) \tag{3.21}$$

We can use this equation to calculate the temperature of the cladding's outer surface knowing

the heating rod centerline temperature (element temperature). The input values to the equation are shown in the table 3.3. From using these values and the equation 3.9, we find $T_{max} - T_{co}$ to be 95.1 ºC. Since the element temperature measurement which measures the centerline temperature outputs around 420 ºC depending on the heater rod used, the outer cladding temperature where crud grows should be around 325 ºC. Note that these calculations are not entirely accurate since they do not include the full effect of fluid flow. Rigorous fluid dynamic calculations would require computer simulation. However, these rough calculations are suffice for this thesis since the results do not depend on the heat flux or fluid flow.

In actual experiments, liquid temperature was maintained around 310 ºC in most experiments. If we take the Febrary 12, 2016 experimental trial for an example, we would have an average pressure of 120 bars. The saturation temperature at 120 bar is 324.7 ºC according to ChemicaLogic SteamTab software [197]. This translate to $T_{wall} - T_{sat}$ value that is smaller than 1 ºC. A typical boiling regime graph shown in figure 3-8 shows that 5 ºC to 10 ºC would be the regime for subcooled boiling. However, it is important to note that 420 ºC may not be the exact rod centerline temperature due to inexact placement of thermocouple in the heating cartridge, and that the actual rod centerline temperature may be higher. Some heater rods showed the element temperature to be as high as 470 ºC. We had issues with multiple heater rods burning out as a result of lowering the pressure and pushing the temperature. Therefore, we refrain from pushing the calculated wall temperature beyond the saturation temperature. Again, note that the usage of figure 3-8 is only an estimate since this figure is used in pool boiling cases. The real temperature difference required for flow boiling would be slightly higher.

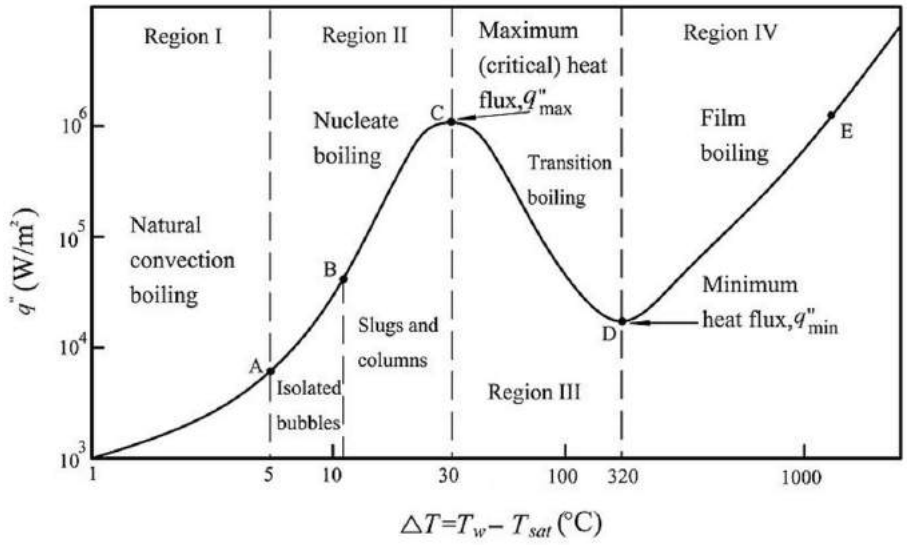


Figure 3-8: Plot of the boiling regime, heat flux versus the difference between wall and saturation temperature [198].

| Parameter | Value |
|---|---|
| $k_{heater}$ | 15 W/m · K |
| $k_{cladding300C}$ | 18.8 W/m · K |
| $q'$ | 1700 W |
| $R_{ci}$ | 12.5 mm |
| $R_{co}$ | 18.0 mm |
| $T_{max} - T_{co}$ | 95.1 °C |

Table 3.3: This table summarizes different parameters that are used to calculate the temperature difference between the centerline temperature and the cladding outter temperature $T_{max} - T_{co}$. The $k_{heater}$ is the thermal conductivity of the nichrome heater. The $k_{cladding300C}$ is the thermal conductivity of stainless steel cladding and ring at 300 °C. The q' is the linear heat rate of the autoclave heater rod. The $R_{ci}$ and $R_{co}$ are the cladding inner diameter and the cladding outer diameter that includes the sample ring. From this information, we found a $T_{max} - T_{co}$ value of 95.1 °C.

### 3.3.5 Autoclave Geometry Considerations

The design of the autoclave must allow experiments carried out in its test section to imitate the conditions in a PWR as closely as possible. In addition, we also want to include the autoclave windows which can be used for laser-triangulation-based crud thickness measurement, observation of subcooled boiling, Raman spectroscopy, and contact angle measurement. At the same time, the autoclave must be within a reasonable cost range. Figure 3-9 shows the final autoclave design as rendered by the autoclave manufacturer. Water flows in from the bottom slanted autoclave inlet through the center test section, and out through the top inlet. The middle section contains the autoclave windows. The following section explains the considerations that went into designing different parts of the autoclave.

**Autoclave Windows** One of the aspects that make this crud loop the first of its kind is that its autoclave has three two-centimeter-diameter-sized windows that can be used to observe crud growth in situ. These windows will open up a wide range of possibilities for using this autoclave, including using laser triangulation to observe crud thickness in situ, using Raman spectroscopy in situ to observe crud formation, and using laser techniques for high-pressure contact angle experiments.

**Autoclave Inner Shape** The autoclave inner shape is designed to be as thin as possible while maintaining a reasonable mass flux and Reynold's number. The heating rod in the middle of the annulus has 17.5 mm diameter while the real reactor's fuel rods have only 9.5 mm diameter. The reason that IHTFP's heating rods must be thicker is that the electric resistant heating it uses

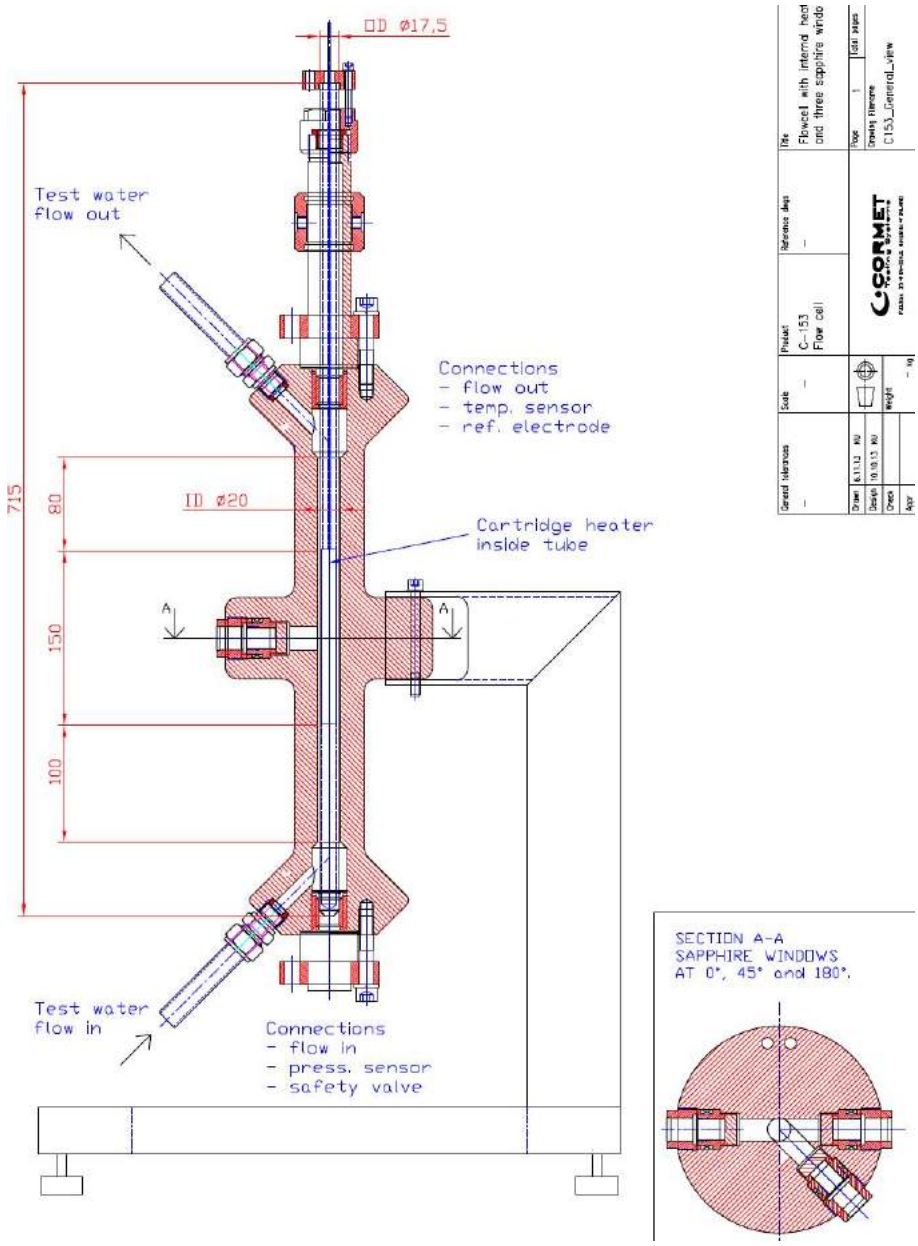


Figure 3-9: Final autoclave design as rendered by the autoclave manufacturer Cormet Oy.

has lower heat density than the uranium pellet inside commercial reactors. Therefore, to obtain a reasonable heat flux for crud generation, we need to use a heater rod with larger volume and diameter. Nevertheless, the mass flux and the Reynold's number is comparable to that of the real PWR as shown in the section 3.3.2.

The inner test section is designed to be very small because it saves the amount of metal that must be used to contain the pressure. The finite element stress analyses determined that stress concentrations are very high at the window holes. This issue is made worse by having a larger autoclave. Therefore, the autoclave inner shape is designed to be just large enough for proper flow conditions while small enough to require only minimal reinforcement to combat the stress concentrations. Section 3.3.7 gives more detail on the finite element stress analyses. The computational fluid dynamics (CFD) models showed that the inner section of 20 mm is optimal for this case before the addition of sample rings. Therefore, this size was chosen as the autoclave inner diameter (test section outer diameter). More detail on CFD models can be found in section 3.3.6.

The slanted inlet and outlet allow the flow to stabilize quicker in the autoclave, as they eliminate any sharp, perpendicular turn in and out of the autoclave. Having the slanted inlet and outlet also leads to less flow friction. The slanted inlet and outlet also avoid the equipment and flanges on the top and bottom of the autoclave, making the autoclave easier to manufacture and maintain.

**Autoclave Outer Shape** The autoclave outer shape design was a direct result of stress analysis. The autoclave manufacturer decided on the final autoclave's outer shape, as shown in the figure 3-9, with the result of its final stress analysis investigations. The design has its window holes on a large cylindrical section because that is where the stress is most concentrated. This design also allows for easier manufacturing.

**Adding Rings** crud could be grown directly on the heater rod. However, this means that the costly heater rod cannot be reused. In addition, the heater rod's size is quite long, which makes it less versatile when it comes to applying crud-resistant material coatings, and when it comes to post-experiment analysis. A better way to do the experiments is to cover the heater rod with sample rings, and grow crud on these rings instead. Figure 3-10 demonstrates how sample rings cover the heater rod. There are two main reasons we want to add a ring structure on to the fuel rod. The first reason that is because of the limitation in the size of the e-beam or the sputtering chamber. To coat the crud-resistant materials on the whole heating rod would require an enormous sputtering chamber which is not readily available to us. Second, the ring structure allows us to replace only the ring part for each trial of the experiment. Replacing only a small sample ring as opposed to the full heating rod will also save significant consumable costs. The only downside to using the ring is that it might disturb the flow profile within in the autoclave. The CFD models were used to verify that this flow disturbance effect is acceptable for crud growth experiments. After that, observations from

the real test shown that the window section's crud samples do not show any significant deviation from other crud samples.

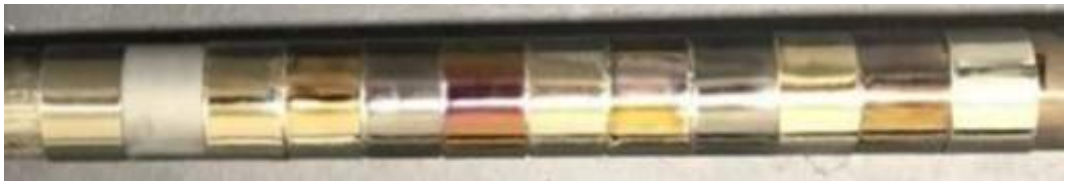

Figure 3-10: Sample rings covering the heater rod. Sample rings are where we grow crud. Different ring colors are due to different types of coatings applied. From right to left, the samples are coated with 316 stainless steel, $ZrC$, $ZrN$, $TiC$, $TiN$, $Al_2O_3$, $TiO_2$, $TiB_2$, $ZrO_2$, $MgO$, $Ti_2AlC$, and zircaloy, respectively.

### 3.3.6 Computational Fluid Dynamics (CFD) Model

Computational fluid dynamics (CFD) analysis was performed for the autoclave, specifically on the region with the sapphire viewing windows. The CFD was done to ensure that the flow conditions in the autoclave will represent the flow conditions in real reactors, and to ensure that the windows will not disturb the flow patterns. The CFD of the system without the sample ring shows little disturbance of flow on the surface of the heating rod by the window section, as shown in figure 3-11 and 3-12.

When the decision was made to use sample rings, tests needed to be conducted to determine their effect on crud growth. In the system with sample rings, the CFD results showed that the flow stabilizes very quickly after initial disturbance at the beginning section of the sample ring, as shown in figure 3-12. The windowed flow section of the autoclave was shown to slightly alter the flow profiles in the system with sample rings, as shown in figure 3-13. This flow profile disturbance led to the decisions to place four dispensible stainless steel rings without a surface modification coating where the window section is. Fortunately, experiments showed that there was no significant difference between crud grown near the window and those far away from the window. This fact confirms that window section is not an issue that will affect data accuracy.

### 3.3.7 Finite Element Stress Analysis

The goal of using an in-house finite-element stress analysis is not to build an exact autoclave design, but instead to gain more understanding of the type of equipment that is needed to carry out the task. Before working with a manufacturer, we must ensure that the kind of autoclave contemplated, which includes sapphire windows, at PWR pressures and temperatures, is a feasible design goal. The finite element stress analysis verified that the autoclave with the parameters we are looking for could be built within our lab constraints. It also narrows down the optimal design that fits the need

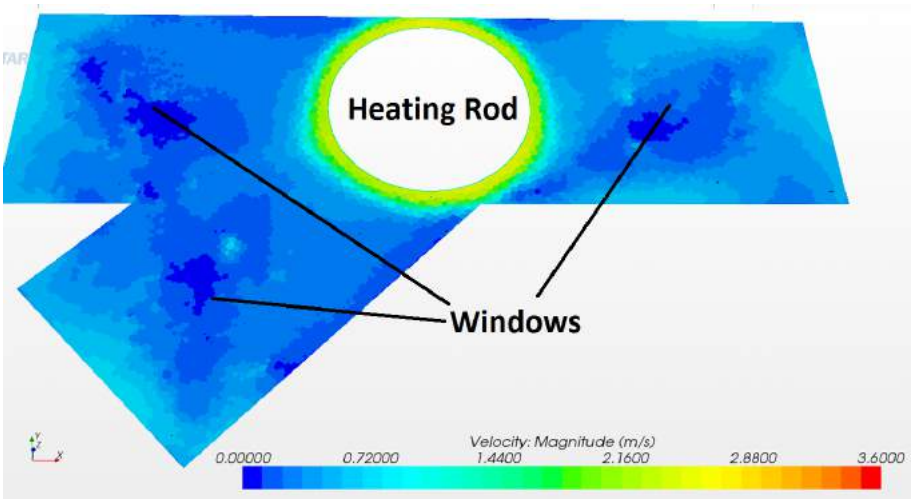


Figure 3-11: CFD horizontal cross-sectional plot of flow velocity for normal cladding case. The cross section is taken at the windows' center.

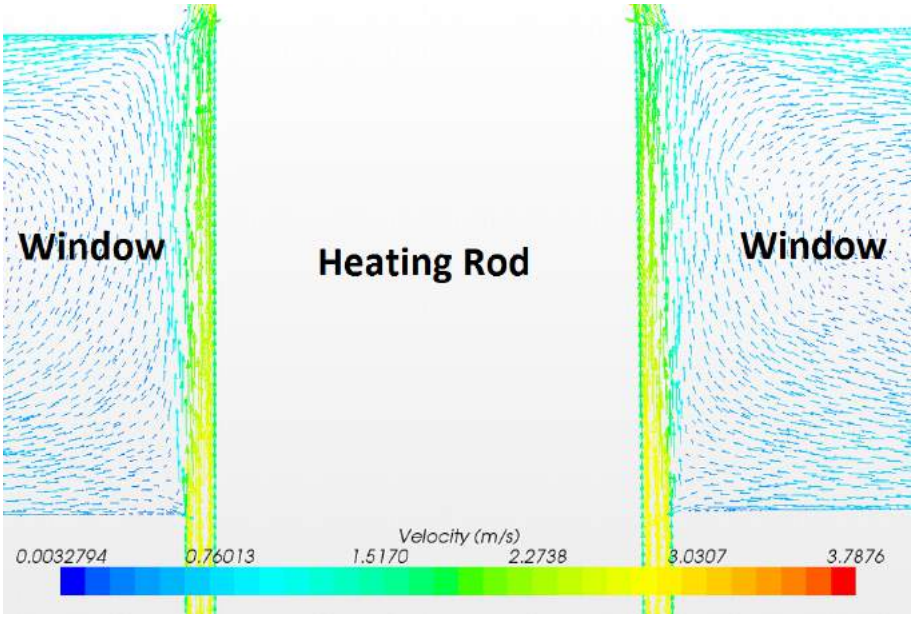


Figure 3-12: CFD vertical cross-sectional plot of flow velocity for normal cladding case. The cross section is taken at the windows' center. Arrows represents the direction of flow velocity at each point.

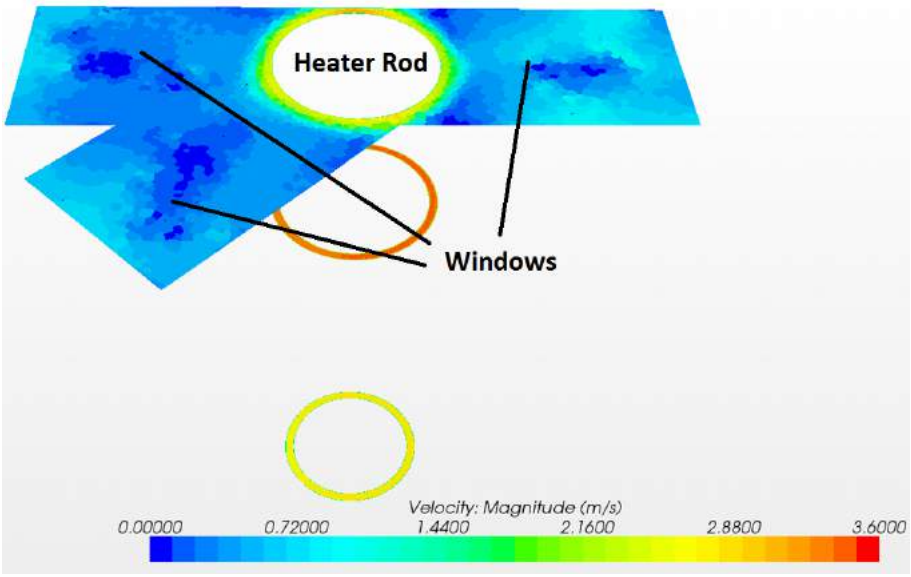


Figure 3-13: CFD horizontal cross-sectional plot of flow velocity for the case with a sample ring covering the cladding. The cross section is taken at the windows' center.

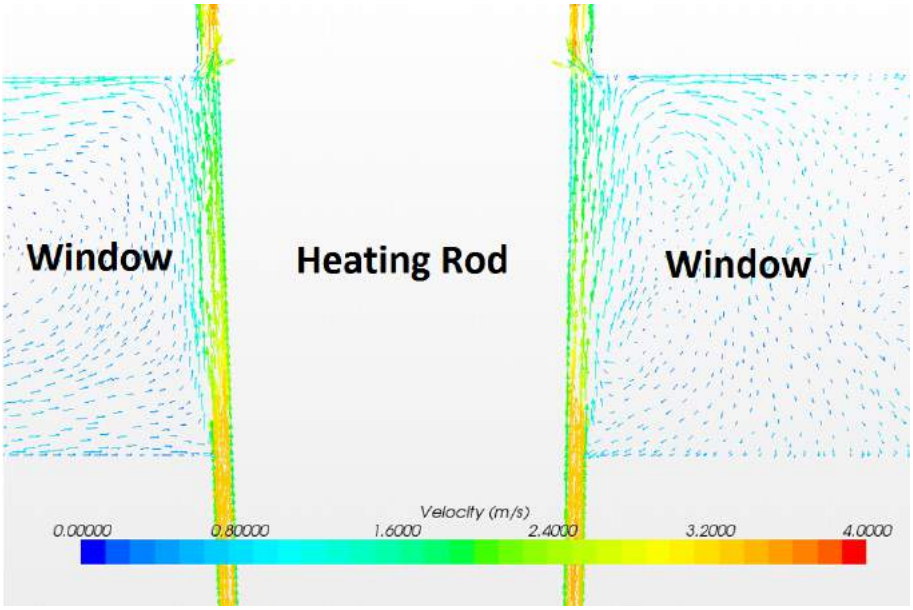


Figure 3-14: CFD vertical cross-sectional plot of flow velocity for the case with a sample ring covering the cladding. The cross section is taken at the windows' center. Arrows represents the direction of flow velocity at each point.

of the study, before the detailed manufacturing tasks are relegated to Cormet Oy, the company that manufactured the crud loop's autoclave. The final calculation and testing of stress for licensing was left to the autoclave manufacturer.

Specifically, the finite-element stress analysis makes sure that the stress concentration caused by drilling the autoclave for windows is not too high. Other than this, the diamond-sapphire window was examined with a view toward how well it holds against the high PWR pressure. One important piece of information obtained from finite-element stress analysis was that stress concentration is very significant at the location of the window holes. A larger diameter autoclave previously designed with a window would require an autoclave that is extremely thick. Figured 3-15 demonstrates how the maximum von Mises stress concentration decreases with thickness, in a system with an autoclave under 2250 psi pressure. The autoclave has 8 cm inner diameter and 2 cm windows. The graph demonstrates that even if we almost double the autoclave thickness, the von Mises stress concentration only decreases from around 19 to 14 ksi. The 316 stainless steel at 315 $^{o}$C has the yield strength of 32 ksi [199]. In the autoclave's high-pressure and high-temperature conditions, a safety factor of at least 3 times would be preferred. Instead, the preliminary simulation shows that the stress concentration is reduced significantly when the size of the autoclave is reduced instead. Because of this, we arrived at a much thinner autoclave design with a flow section of only 2 cm in diameter. It is important to note that the autoclave flow-section size reduction is limited by the size of its heater rod. The heater rod size is limited by the heat flux constraint. A smaller heater rod provides less heat flux, and therefore, less crud growth. In addition to examining the autoclave, stress analysis was also used to examine the effect of thickness of sapphire window on the stress concentration. Figure 3-16 demonstrates thickness affects von Mises stress concentration. Figure 3-17 shows an example of the typical result of stress analysis.

## 3.4 Crud Loop Parameter Controls

Section 3.2.2 gives general information on the control of IHTFP's pressure, temperature, and flow. This section delves into specific details on the equipment used to control the IHTFP.

### 3.4.1 Pressure Control

As mentioned earlier, the pressure control of the system is done using two main pieces of equipment — the pressurizing pump, and the back-pressure regulator. The pressurizing pump supplies the system with a small flow rate, but with very high force. The back-pressure regulator will let the water out of the system just enough to maintain a steady pressure in the system. In case the back-pressure regulator fails to release the pressure, multiple safety systems are put in place to avoid any danger. These safety systems include the main loop safety valve, the autoclave safety valve, the

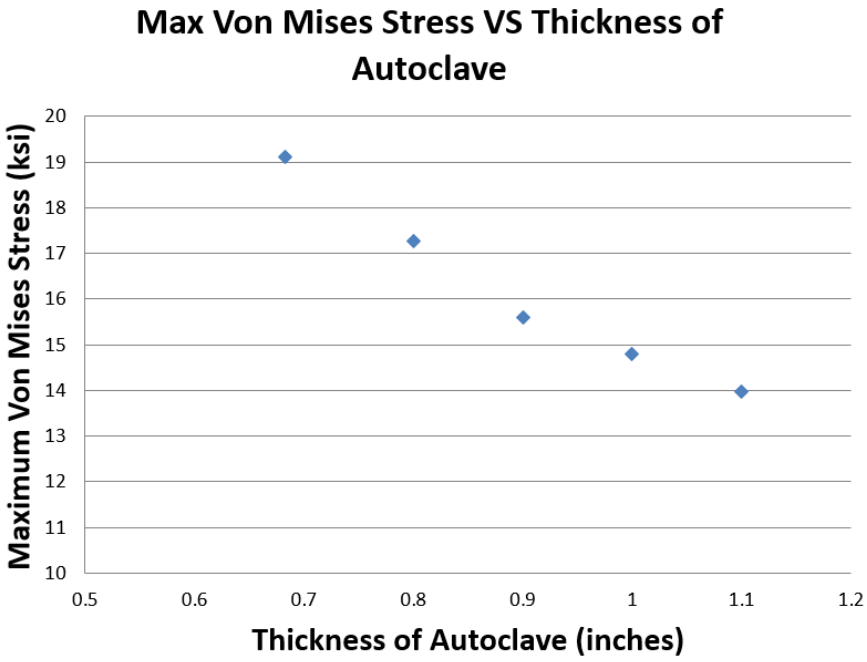


Figure 3-15: This is a plot of maximum von Mises stress (ksi) vs thickness of the autoclave (inches). This analysis is done for an autoclave with 8 cm inner diameter with windows that are 2 cm in diameter, under 2250 psi pressure condition.

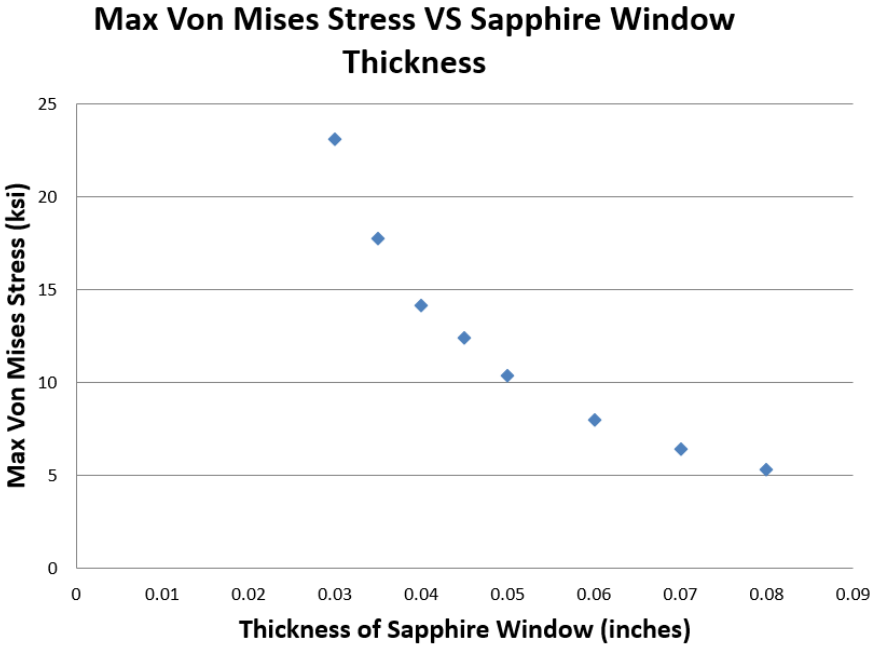


Figure 3-16: This is a plot of maximum von Mises stress (ksi) vs thickness of the sapphire window (inches). This analysis is done on a sapphire window with 2 cm diameter attached to an autoclave with 8 cm inner diameter, under 2250 psi pressure condition.

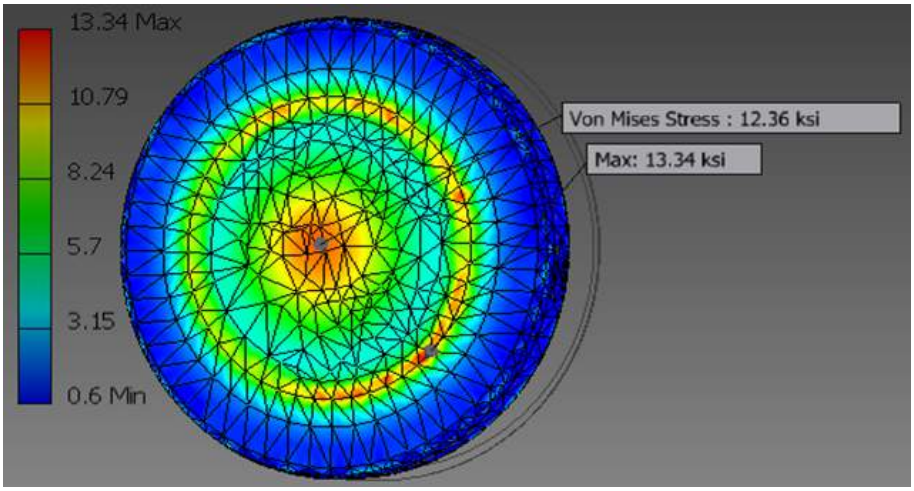


Figure 3-17: Example finite element stress analysis applied on a sapphire window. Red parts are where most stress concentrates.

pressure switch, and the pressurizing pump's safety system.

The pressurizing pump can be turned on and off via the computer which controls the relay in the crud loop relay box (see Section 3.7.2 for electrical diagrams). The back-pressure regulator can be adjusted manually. Caution must be taken when adjusting the back-pressure regulator. Proper protective equipment is required if the adjustment is made during high pressure. The pressurizing pump can be adjusted for a different flow rate. Increasing the pressurizing pump flow rate can help the loop pressurize quicker and get the necessary flow rate for purposes of measurement. Adjustment can be made by turning the stroke adjustment knob on the pressurizing pump that will increase or decrease the stroke length. Increasing the stroke length will increase the flow rate as the stroke rate will remain steady. Note that during the heating of the loop, it is advisable to decrease the flow rate as much as possible (without falling below the instrumentation required flow rate) to lessen the heat loss.

### 3.4.2 Temperature Control

As mentioned in the introduction, the crud loop uses two heating systems to control its temperature — the loop heating system and the autoclave heating system. Both systems are completely separate with their own heaters and control boxes. The autoclave heating system provides the necessary heat flux to carry out the experiments while at the same time providing the loop with a significant heat source. The loop heaters' sole purpose is to heat up the coolant water enough to get to the PWR temperature conditions. These sections below will describe the specifics of each heating system.

**Loop Heating System** The loop heating system is the heating system that spans over the whole loop. This heating system consists of many heating tapes placed all around the loop. The main

controller for this system is the Omega CN9000 temperature controller, which essentially controls all of these heating tapes. The Omega CN9000 temperature controller takes only one input from the dual junction thermocouple situated on the top of the loop near the autoclave, likely to be the highest temperature section of the loop. This dual junction thermocouple measures the liquid temperature. The slower temperature feedback caused by using liquid temperature is acceptable for two reasons. First, even if the loop heaters remain fully on without any water flow, the heaters will still not burn out. Second, the temperature changes when the loop is set at high temperature are very slow, and therefore a slow temperature feedback will suffice. See section 3.9.7 for more information on how to operate the autoclave temperature controller.

**Autoclave Heating System** The autoclave heating system is the heating rod inside the autoclave where we grow crud. The autoclave's heating rod is controlled using a West 6100 temperature controller on the autoclave controller box provided by Cormet Oy, the manufacturer. The temperature control uses the heating element temperature as feedback, as opposed to the liquid temperature. See section 3.9.7 for more information on how to operate the autoclave temperature controller.

### 3.4.3 Flow Control

In a crud loop, liquid flow through the main loop is driven by a centrifugal pump. The centrifugal pump can be turned on/off using the control program on the computer. The flow rate can be adjusted to a desired point by using the control valves, shown in figure 3-18. Control valves' stems can be adjusted using the CM10 control panels, shown in figure 3-19. The red values on CM10 control panels are process variables or PV. The green values are setpoints or SP. Process variables and setpoints are used by PID controllers to adjust valve openings. Since the flow driven by the centrifugal pump is usually very steady in normal experimental conditions, adjusting the control valves' opening manually will suffice. Therefore, process variables and setpoints can be ignored. The yellow values on CM10 control panels are the valve opening in percent with high percent meaning the valve is almost close. These values can be adjusted via the up/down button in manual mode.

## 3.5 Crud Loop Measurement and Instrumentation

### 3.5.1 Pressure Measurement

The pressure measurement can be obtained from multiple types of equipment at multiple points on the experimental setup. Having multiple places to get pressure readings is beneficial because we will be able to determine the pressure even if some of the pressure reading equipment breaks down. Beyond this, in case there is some malfunction or clog in some part of the loop, the problem can be recognized earlier because we know the pressure readings everywhere in the loop.


Figure 3-18: Photo of IHTFP's control valve 2.


Figure 3-19: Photo of CM10 control panels used to manipulate control valves in the IHTFP.

There are two pressure transmitters in the loop. One is on the autoclave. It reads the pressure inside the autoclave and displays the number on the West 6100 panel on the autoclave controller. Another pressure transmitter is connected before the back-pressure regulator. This one will read to the computer. Aside from the pressure transmitters, there are also three pressure gauges at the pressurizing pump, at the top of the main loop and above the sample cooler. These pressure gauges should be more reliable than the other forms of measurement with electronics, since the latter can give an inaccurate reading caused by data transfer inaccuracy or digital error in the electronics.

### 3.5.2 Temperature Measurement

Temperature measurement in the loop is done at six points, two in the autoclave and four on the tubings of the loop. Two temperatures are measured in the autoclave, the liquid temperature and the element temperature. Both readings are shown and labeled on the autoclave controller box. The liquid temperature is taken at the top section of the autoclave. The element temperature is the temperature measured at the inside of the autoclave heater rod. The element temperature thermocouple is embedded inside the heating element, press-fitted into the heating rod. The temperatures are measured outside the autoclave in four spots. All of these spots measure liquid temperature within the crud loop's tubing. This is clearly shown in the diagram 3-4.

### 3.5.3 Flow Measurement

The flow must be maintained so that the mass flux and the Reynolds number imitate the PWR as closely as is reasonable. The velocity of 3 m/s was chosen for most of our experiments because that will bring the Reynolds number and the mass flux condition close to that of the PWR's, while not being so fast that it presents a significant vibration that can make crud loop deteriorate quickly.
[1]

In the IHTFP, the flow measurement is done using the differential pressure transmitters. The reason for using these transmitters is that at PWR temperature and pressure conditions, other types of flow meters will not be able to withstand the harsh pressure temperature and flow rate. In this flow measurement system, which is basically a venturi flow meter, the water flows through a small section made of ½-inch tubing as opposed to the surrounding 1-inch tubing. Each end of the differential pressure transmitter is connected to the ½-inch tubing and the 1-inch tubing. When the fluid flows through tubings with different flow areas, it will have different pressures according to the Bernoulli's equation (see Equation 3.23). The differential pressure measured from the transmitter can be used to calculate the actual fluid velocity using the Bernoulli's equation. These ideas are better demonstrated in figure 3-20, which is a schematic of a venturi flow meter.

[1] We tested flow velocities much higher than 3 m/s, and they caused significant loop vibrations. This shows that we did all our pressure/flow calculations correctly, but other considerations keep us from raising the flow rate.

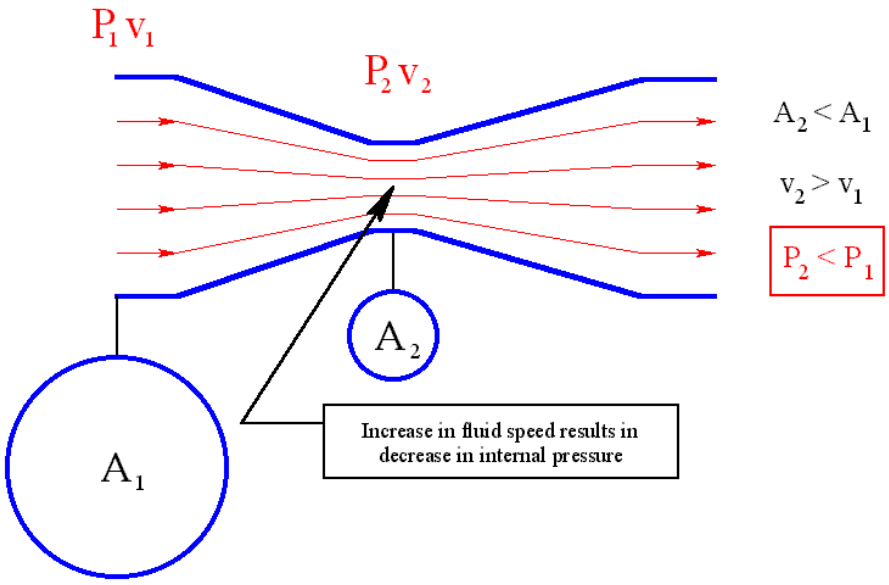


Figure 3-20: Schematic of how a venturi flow meter works.

**Calculation for Differential Pressure Drop:** The differential pressure drop in unit $inch-H_2O$ $\Delta P_{inch-H_20}$ displays on the meter. This can be converted to the Pascal unit using the following conversion equation:

$$\Delta P_{Pa} = 249.09 * \Delta P_{inch-H_20} \tag{3.22}$$

To convert the differential pressure drop to the fluid velocity, we start from Bernoulli's equation:

$$\frac{p_1}{\rho} + V_1^2 + gz_1 = \frac{p_2}{\rho} + V_2^2 + gz_2 \tag{3.23}$$

Since the two tee fittings where the differential pressure transmitter's nodes are connected at the same height level, the gravity term can be ignored, leaving the following equation:

$$\frac{p_1}{\rho} + V_1^2 = \frac{p_2}{\rho} + V_2^2 \tag{3.24}$$

By rearranging the equation above, the following equation can be obtained:

$$\frac{2(p_1 - p_2)}{\rho} = V_2^2 - V_1^2 \tag{3.25}$$

Since the pressure at two locations is measured in the same tube, the mass flow rate at both locations must be the same, leading to the following relationship:

$$\dot{m}_1 = \dot{m}_2 \tag{3.26}$$

$$\rho_1 A_1 V_1 = \rho_2 A_2 V_2 \tag{3.27}$$

$$A_1 V_1 = A_2 V_2 \tag{3.28}$$

$$V_2 = \frac{A_1}{A_2} V_1 \tag{3.29}$$

Plugging this equation back into the rearranged Bernoulli's equation, the following equation is obtained:

$$\frac{2(p_1 - p_2)}{\rho} = (\frac{A_1}{A_2})^2 V_1^2 - V_1^2 \tag{3.30}$$

Velocity $V_1$ can then be obtained from the above equation:

$$V_1 = \sqrt{\frac{\frac{2(p_1 - p_2)}{\rho}}{((\frac{A_1}{A_2})^2 - 1)}} \tag{3.31}$$

This equation is used to obtain the flow velocity in the autoclave from the differential pressure value measured.

| Parameter | Value |
|---|---|
| Differential Pressure ($inches - H_2O$) | 6.0 |
| Water Density ($\frac{kg}{m^3}$) | 667.4 |
| 1-inch Tubing Inner diameter (inches) | 0.834 |
| 1/2-inch Tubing Inner diameter (inches) | 0.402 |
| Autoclave Inner Diameter (mm) | 18.0 |
| Autoclave Outer Diameter (mm) | 20.0 |

Table 3.4: This table summarizes different parameters affecting mass flow rate. The values shown are values that are usually present in the loop.

### 3.5.4 pH Measurement

According to the EPRI PWR Primary Water Chemistry Guidelines [43], the pH should be between 6.9 to 7.4. A pH lower than 6.9 is expected to generate heavier core crud deposits, by inducing more rapid corrosion. In the IHTFP's case, the goal is the grow crud regardless, so there is no need to follow the 6.9 pH guideline directly. Lithium hydroxide is used to control the amount of pH in the reactor, partially to offset the boric acid used to control neutron reactivity. EPRI's guidelines allow boron to be added as the situation requires, to optimize the reactor. Lithium hydroxide is then added, just enough to maintain the pH of above 6.9.

In the IHTFP's case, the interest lies in simulating the PWR conditions as closely as possible.

Therefore, the typical boron concentration of 1400ppm and lithium hydroxide of 3ppm is used. The lithium hydroxide amount is taken from the graph 3-21 by EPRI. If 1400 ppm of boron is traced up to 3 ppm of lithium, we can see that the point lies within the band for pH of 6.9-7.0.

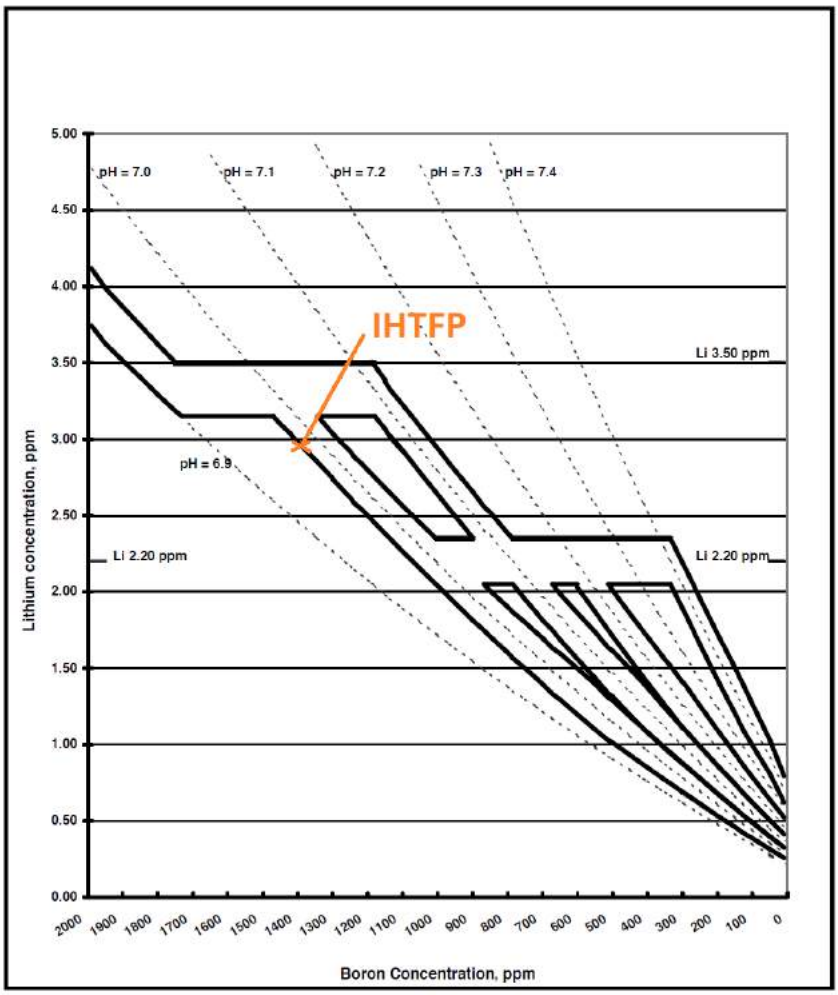


**Figure 3-2d**
**Coordinated Chemistry at Elevated pH$_T$ (>6.9)**
**Example Li/B Programs (plotted at T$_{rc}$=300°C)**

Figure 3-21: Figure from the EPRI PWR Primary Water Chemistry Guidelines [43], showing how the boron concentration relates to the lithium concentration at 300 °C. This table was used to make the decision regarding the lithium concentration for the crud loop.

### 3.5.5 Dissolved Oxygen Measurement

The dissolved oxygen level is an important measurement to keep track of because it can increase or decrease both the general corrosion and the possibility of stress corrosion cracking. In the real reactor, dissolved oxygen concentrations can be controlled with plant heat-up by venting and vacuum filling, followed by the used of hydrazine or hydrogen for residual oxygen scavenging [43]. In the

IHTFP's case, an easier method is employed where dissolved oxygen is bubbled out with argon from an argon tank.

As seen in the figure below, the EPRI Primary Water Chemistry Guidelines suggests that the oxygen concentration for the PWRs should be measured every three weeks and should be less than 5 ppb, or else action level one is required. "Action level one" means that action should be taken to bring the dissolved oxygen level down. If that does not happen within a week, a shutdown is recommended. In the case that the measured dissolved oxygen is between 5 ppb and 100 ppb, the reactor can continue to operate but needs further investigation into the cause of the higher dissolved oxygen. At 100 ppb of measured dissolved oxygen, the EPRI suggestion is to shut down the plant. Therefore, our aim for the loop is to get 5 ppb or less during an experimental run to imitate normal PWR conditions, and to keep the loop from corroding.

| Control Parameter | Sample Frequency | Action Level | | |
|---|---|---|---|---|
| | | 1 | 2 | 3 |
| Chloride, ppb | 3/week | - | >150 | >1500 |
| Fluoride, ppb | 3/week | - | >150 | >1500 |
| Sulfate, ppb | 1/week | - | >150 | >1500 |
| Lithium, ppm | 3/week | - | - | - |
| Hydrogen, $cc(STP)/kg - H_2O$ | 3/week | <25,>50 | <15 | <5 |
| Dissolved Oxygen, ppb | 3/week | >5 | - | >100 |

Table 3.5: This is a table of recommended water chemistry parameters and action levels from EPRI PWR Primary Water Chemistry Guidelines [43]. The important point from this table is the recommended dissolved oxygen level in ppb. If the dissolved oxygen level is beyond 5 ppb, it is recommended by action level one that the level should come down within a week or else shutdown is recommended. If dissolved oxygen is beyond 100 ppb, it is recommended by action level three to shut down the reactor right away.

### 3.5.6 Conductivity Measurement

In the EPRI PWR Primary Water Chemistry Guidelines, the conductivity of water should be in accordance with the chemical additions. Therefore, there is no direct commandment on what the conductivity should be. There are, however, EPRI guidelines on the relationship between conductivity values and the concentration of boric acid and lithium hydroxide, as shown in figure 3-22. In the case of the IHTFP, the conductivity measurements are very useful for monitoring what is going on in the loop during the ion-exchanger cleaning.

For the crud Loop, the initial conductivity before adding any substance can be cleaned with the ion-exchanger down to around 0.09 $\mu S/m$. The conductivity should be a good representation of the amount of ions floating in the system. If there are too many unexpected ions inside the water prior to any addition of our chemicals, these ions might cause an unexpected build-up of harmful deposits. For example, calcium deposits can build up and ruin the tubing system. In addition, without the proper cleaning of ions, these ions may interact with other things in the loop and affect

the results of the crud buildup experiment. Once the conductivity has reached that 0.09 $\mu S/cm$ point or lower, chemical additions including the boric acid, the lithium hydroxide, and the nickel oxide crud particles can be added.

| | Lithium (ppm Li) | | | | | | | | | | | | | | | |
|---|---|---|---|---|---|---|---|---|---|---|---|---|---|---|---|---|
| **B (ppm)** | **0.00** | **0.25** | **0.50** | **0.75** | **1.00** | **1.25** | **1.50** | **1.75** | **2.00** | **2.25** | **2.50** | **2.75** | **3.00** | **3.25** | **3.50** | **3.75** | **4.00** |
| **0** | 0.1 | 8.5 | 16.9 | 25.4 | 33.8 | 42.3 | 50.7 | 59.1 | 67.6 | 76.0 | 84.4 | 92.8 | >100 | >100 | >100 | >100 | >100 |
| **50** | 0.6 | 2.9 | 5.7 | 8.5 | 11.3 | 14.2 | 17.0 | 19.8 | 22.6 | 25.5 | 28.3 | 31.1 | 34.0 | 36.8 | 39.6 | 42.5 | 45.3 |
| **100** | 0.9 | 2.9 | 5.7 | 8.5 | 11.3 | 14.1 | 16.9 | 19.7 | 22.5 | 25.3 | 28.1 | 31.0 | 33.8 | 36.6 | 39.4 | 42.2 | 45.0 |
| **150** | 1.1 | 2.9 | 5.7 | 8.4 | 11.2 | 14.0 | 16.8 | 19.6 | 22.4 | 25.2 | 28.0 | 30.8 | 33.6 | 36.5 | 39.3 | 42.1 | 44.9 |
| **200** | 1.3 | 2.9 | 5.6 | 8.4 | 11.2 | 14.0 | 16.8 | 19.6 | 22.4 | 25.1 | 27.9 | 30.7 | 33.5 | 36.3 | 39.1 | 41.9 | 44.7 |
| **250** | 1.5 | 2.9 | 5.6 | 8.4 | 11.2 | 13.9 | 16.7 | 19.5 | 22.3 | 25.0 | 27.8 | 30.6 | 33.4 | 36.2 | 38.9 | 41.7 | 44.5 |
| **300** | 1.6 | 3.0 | 5.6 | 8.4 | 11.1 | 13.9 | 16.6 | 19.4 | 22.2 | 24.9 | 27.7 | 30.5 | 33.2 | 36.0 | 38.8 | 41.5 | 44.3 |
| **400** | 2.0 | 3.0 | 5.6 | 8.3 | 11.0 | 13.8 | 16.5 | 19.2 | 22.0 | 24.7 | 27.4 | 30.2 | 32.9 | 35.6 | 38.4 | 41.1 | 43.9 |
| **500** | 2.3 | 3.1 | 5.6 | 8.3 | 10.9 | 13.6 | 16.3 | 19.0 | 21.7 | 24.4 | 27.1 | 29.8 | 32.6 | 35.3 | 38.0 | 40.7 | 43.4 |
| **600** | 2.6 | 3.2 | 5.6 | 8.2 | 10.8 | 13.5 | 16.2 | 18.8 | 21.5 | 24.2 | 26.8 | 29.5 | 32.2 | 34.9 | 37.6 | 40.2 | 42.9 |
| **700** | 2.9 | 3.2 | 5.6 | 8.2 | 10.8 | 13.4 | 16.0 | 18.6 | 21.3 | 23.9 | 26.6 | 29.2 | 31.9 | 34.5 | 37.2 | 39.8 | 42.5 |
| **800** | 3.3 | 3.4 | 5.6 | 8.1 | 10.7 | 13.3 | 15.9 | 18.5 | 21.1 | 23.7 | 26.3 | 28.9 | 31.5 | 34.2 | 36.8 | 39.4 | 42.0 |
| **900** | 3.6 | 3.5 | 5.7 | 8.1 | 10.6 | 13.2 | 15.7 | 18.3 | 20.9 | 23.5 | 26.1 | 28.7 | 31.2 | 33.8 | 36.4 | 39.0 | 41.6 |
| **1000** | 4.0 | 3.7 | 5.7 | 8.1 | 10.6 | 13.1 | 15.6 | 18.2 | 20.7 | 23.3 | 25.8 | 28.4 | 31.0 | 33.5 | 36.1 | 38.7 | 41.3 |
| **1100** | 4.4 | 3.9 | 5.8 | 8.1 | 10.6 | 13.0 | 15.5 | 18.1 | 20.6 | 23.1 | 25.7 | 28.2 | 30.7 | 33.3 | 35.8 | 38.4 | 40.9 |
| **1200** | 4.9 | 4.1 | 5.9 | 8.2 | 10.6 | 13.0 | 15.5 | 18.0 | 20.5 | 23.0 | 25.5 | 28.0 | 30.5 | 33.1 | 35.6 | 38.1 | 40.6 |
| **1300** | 5.3 | 4.3 | 6.0 | 8.2 | 10.6 | 13.0 | 15.4 | 17.9 | 20.4 | 22.9 | 25.4 | 27.9 | 30.4 | 32.9 | 35.4 | 37.9 | 40.4 |
| **1400** | 5.8 | 4.6 | 6.2 | 8.3 | 10.6 | 13.0 | 15.4 | 17.8 | 20.3 | 22.8 | 25.2 | 27.7 | 30.2 | 32.7 | 35.2 | 37.7 | 40.2 |
| **1500** | 6.2 | 4.9 | 6.3 | 8.4 | 10.7 | 13.0 | 15.4 | 17.8 | 20.3 | 22.7 | 25.2 | 27.6 | 30.1 | 32.6 | 35.0 | 37.5 | 40.0 |
| **1600** | 6.7 | 5.3 | 6.5 | 8.5 | 10.7 | 13.0 | 15.4 | 17.8 | 20.2 | 22.6 | 25.1 | 27.5 | 30.0 | 32.4 | 34.9 | 37.3 | 39.8 |
| **1700** | 7.2 | 5.6 | 6.7 | 8.7 | 10.8 | 13.1 | 15.4 | 17.8 | 20.2 | 22.6 | 25.0 | 27.5 | 29.9 | 32.3 | 34.8 | 37.2 | 39.7 |
| **1800** | 7.8 | 6.0 | 7.0 | 8.8 | 10.9 | 13.2 | 15.5 | 17.8 | 20.2 | 22.6 | 25.0 | 27.4 | 29.8 | 32.3 | 34.7 | 37.1 | 39.6 |
| **1900** | 8.3 | 6.4 | 7.3 | 9.0 | 11.0 | 13.2 | 15.5 | 17.9 | 20.2 | 22.6 | 25.0 | 27.4 | 29.8 | 32.2 | 34.6 | 37.0 | 39.5 |
| **2000** | 8.9 | 6.8 | 7.5 | 9.2 | 11.2 | 13.3 | 15.6 | 17.9 | 20.2 | 22.6 | 25.0 | 27.4 | 29.7 | 32.2 | 34.6 | 37.0 | 39.4 |

Figure 3-22: Conductivity of a solution with boric acid and lithium hydroxide at 25 ºC [43]. If both lithium hydroxide and boron added to the IHTFP dissolved completely and mixed very evenly, we should obtained the maximum of 30.2 $\mu S/cm$ conductivity since we added 1400 ppm boron and 3 ppm lithium hydroxide. However, in reality, that does not always happen , and lower conductivity can be expected.

## 3.6 Crud Loop Components (and Equipment Selections)

The first and primary component is the main loop, where the experiment will take place. It is where the water is heated to 320°$C$ and pressurized to 155 bars to simulate the condition of a PWR. The figure 3-23 below, revisited from the introduction, shows how the two loops are connected. The main loop's input is connected to the output of the auxiliary loop. The main loop also dumps the output water into the auxiliary loop.

### 3.6.1 Main Loop

The main loop, as shown in figure 3-4, is where the crud growth experiment will take place. The most important part of this loop is the autoclave. Within the autoclave is a test section with a heating rod in the center and the water flowing in an annulus around the heating rod. This test section is where we make the conditions match that of the PWR to simulate the crud growth at PWR condition. The sample rings are placed on the heating rod inside the test section. The rest of the loop exists to get conditions within the test section to match PWR conditions. This loop's

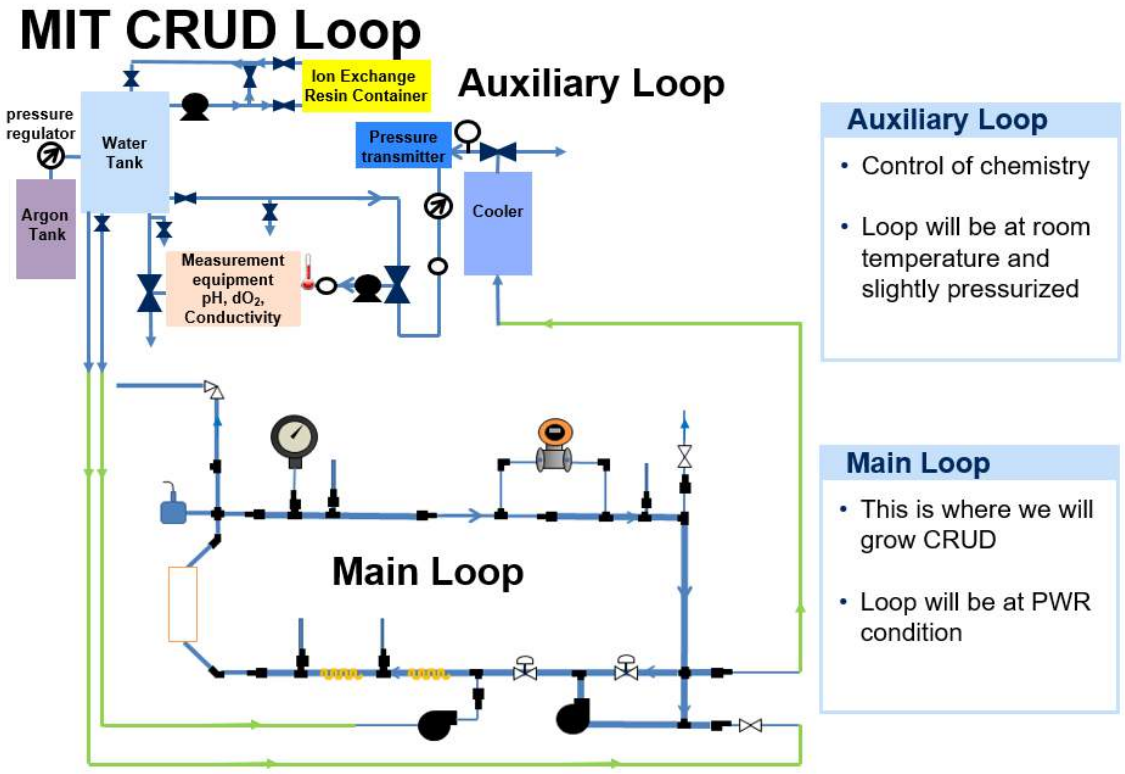


Figure 3-23: This is a diagram demonstrating the two most important parts of crud loop, the auxiliary loop, and the main loop. The diagram shows how both loops are connected. The auxiliary loop provides water to the main loop at the input of the pressurizing pump. The main loop outputs the water to be cooled down at the sample cooler. The pressure boundary is located at the back-pressure regulator in the auxiliary loop.

water is heated to 320 $^{o}$C, pressurized to 155 bars, and given flow rate of roughly 2.5-3 m/s in the autoclave, to simulate conditions within the PWR. Figure 3-25 shows different pieces of equipment within the main loop.

**Design Considerations** Many design considerations go into building the main loop the way it is currently. First off, the loop supporting structure is constructed in the rectangular box shape because this structure is very sturdy. It can withstand heavy weight of equipment such as the autoclave and the control valves without any problem. Other than that, the sturdy structure allows easier maintenance, since the structure can be climbed to reach any point in the loop without the inconvenience of using a ladder. The loop can also be moved relatively easily. The middle section can be detached separating the main loop into two large sections. Each of these can then be transported as a whole with the use of a forklift or a palette jack. Unistrut beams were chosen as the structural building blocks because they are modular, allowing easier loop modification. Stainless steel was chosen as the structural material because of its strength and low price.

Figure 3-24: This figure shows the photos of the main loop from different angles. Notice the autoclave on the left of both pictures wrapped in the heat insulators. This autoclave is where the experiment is carried out.

#### 3.6.1.1 Autoclave Components

The autoclave is the main part of the loop. It is the place where the crud growth will take place. The rest of the system is built to help this part simulate the condition within the PWR reactor vessel. The autoclave is shown in the figure 3-24 on the left of both photos wrapped in the beige heat insulation blankets. The autoclave has many components attached to it to control and regulate the conditions inside the autoclave vessel which will be explained below.

**Autoclave Vessel** The autoclave vessel, shown in figure 3-26, is the actual vessel where simulated the PWR fuel rod will be placed. Water will flow in from the bottom of the vessel at 45-degree

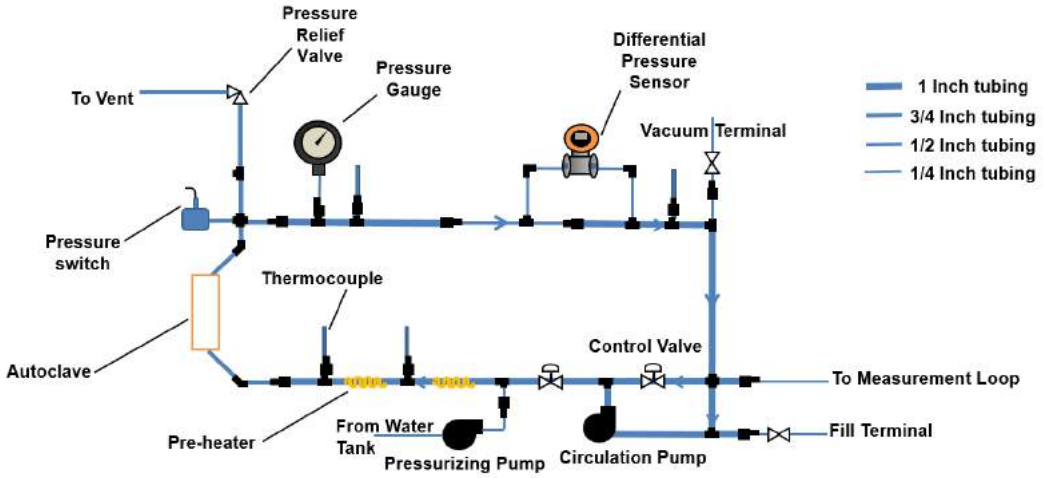


Figure 3-25: Diagram of the main loop with equipment labels.

angle, then travel up the annular flow section with the electric resistant heater inside the simulated fuel rod, which simulates a PWR fuel rod. The autoclave test section diameter is 20 mm. This autoclave is also special because it has three sapphire windows attached which open up a wide range of opportunities, including the use of laser triangulation to measure the crud thickness in situ, the use of Raman spectroscopy to measure the crud composition in situ, and the measure of the contact angle with a laser.

Figure 3-9 is a diagram of autoclave's final design. The autoclave vessel has two flanges on the top and bottom. The bottom flange will remain sealed most of the time. The top flange can be taken off along with the sample fuel rod. The top flange contains a graphite gasket at its larger opening to seal the autoclave. On the top section of the top flange, a rubber o-ring acts as a seal. The top most part of the autoclave top flange is a polyacetal plastic cap that pushes down on the fuel rod to prevent it from getting pushed up by the pressure inside the autoclave. The reason that this part is made of polyacetal and not metal is to keep the heating rod from being grounded. Grounding the heating rod could affect electrochemistry on the surface of the heating rod which is not desirable in the crud growth experiments. In addition, direct measurement of the electrochemical potential (ECP) inside the autoclave are only possible if the rod itself is ungrounded. Since this rubber o-ring, as well as the polyacetal cap, cannot withstand high temperatures, the top part must be actively cooled with the cooling system from the auxiliary loop. This autoclave has been custom manufactured by Cormet Oy, a company from Finland.

**Autoclave Heater** The autoclave heater lies within the test section of the autoclave vessel. It is composed of the internal cartridge heater, press-fitted into the heating rod cladding. The internal cartridge heater is 150 mm long and has a diameter of 12.5 mm. The heating rod cladding also has an inner diameter of 12.5mm and an outer diameter of 17.5mm. The heating rod cladding is 715 mm


Figure 3-26: Photos of the autoclave vessel.

in length. The maximum power of the heater is 1750 Watts. Figure 3-27 is a photo of an example autoclave heater rod with a heating cartridge press-fitted inside. Figure 3-28 is a photo of a heating cartridge before being press-fitted inside the heating rod cladding. Figure 3-29 is a diagram of an autoclave heater.

The heating rod is designed so that electricity runs through only the middle heating cartridge part, as opposed to the whole rod. This design preserves the electrochemistry of the heating rod surface, so it is not interfered with by electricity flow. This preservation of the electrochemistry is important to the crud-resistant coating experiments because changing the electrochemistry at the surface can potentially change the adsorption of crud particles at the sample surface, and therefore give inaccurate data. Other similar facilities, such as the WALT loop, do pass current directly through the tube, since they are not as concerned with surface electrochemical potentials.

Figure 3-27: Photo of an autoclave heater rod with heating cartridge press-fitted inside.

**Autoclave Control Box** The autoclave itself features a control system that can be used to monitor the pressure as well as the temperature of the heating element and the liquid inside the

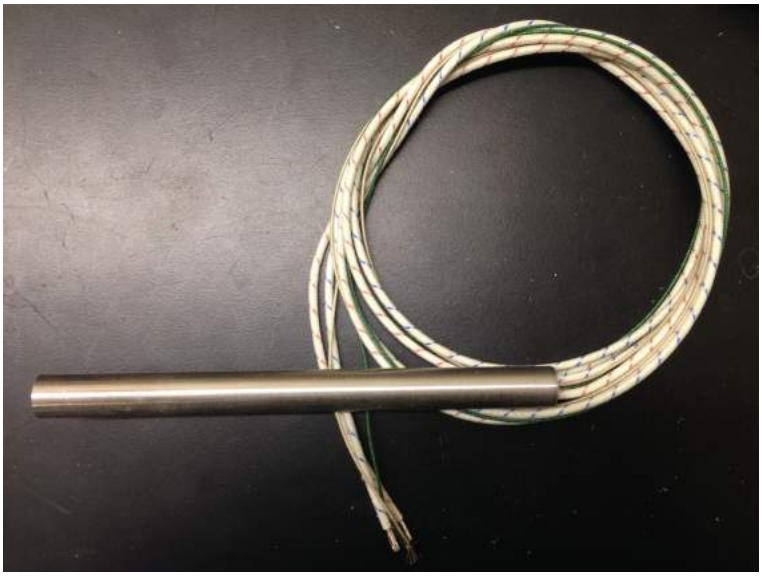

Figure 3-28: Photo of heating cartridge before being press-fitted inside an autoclave heater rod.

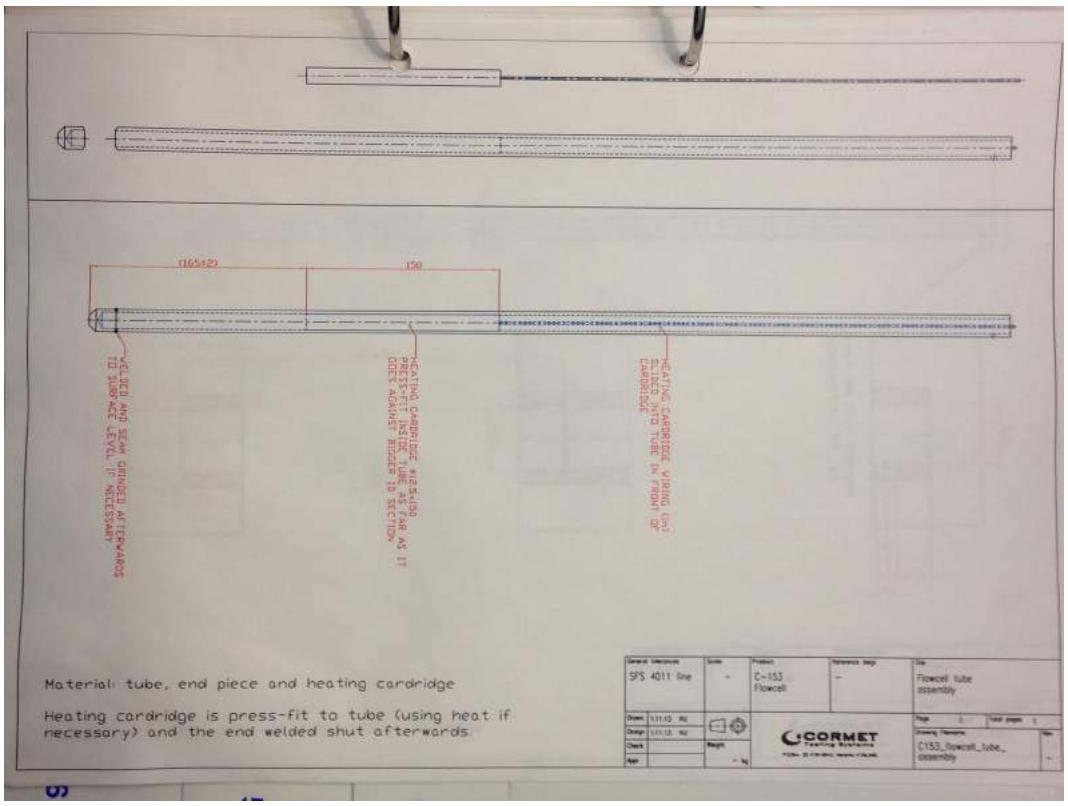


Figure 3-29: Diagram of an autoclave heating rod. Top part shows the heating cartridge and its tube shell separately. Bottom part shows a labeled diagram when both of them are combined.

autoclave vessel. This information is also passed on to the computer so it can be displayed on the autoclave control program and recorded in data files. The heater element temperature controller can be used to ramp up the heater element temperature in a controlled fashion. This variable control of temperature is made possible by a large transformer inside the heater box that can be used to adjust the voltage and the power supplied to the heater. The autoclave control system also has a breaker and two fuses as protection against a sudden power surge. The whole autoclave control system is packed nicely into a box, as shown in figure 3-3. Figures 3-91 and 3-92 are diagrams of equipment inside the autoclave control box.

**Autoclave Flow Meter** The flow meter attached to the autoclave stand, as shown in figure 3-30 and 3-31, is used to monitor the flow rate of the cooling water. This flow meter's reading indicates the flow output throughout the cooling water system. The cooling water flow rate can be adjusted by turning the yellow valve at the sample cooler's cooling line outlet. Adjusting the yellow valve at the sample cooler's cooling line will redirect water to either the autoclave cap or the circulation pump. The yellow valve is in the left photo of figure 3-30. The model number is Kytola EH-4AA-H.

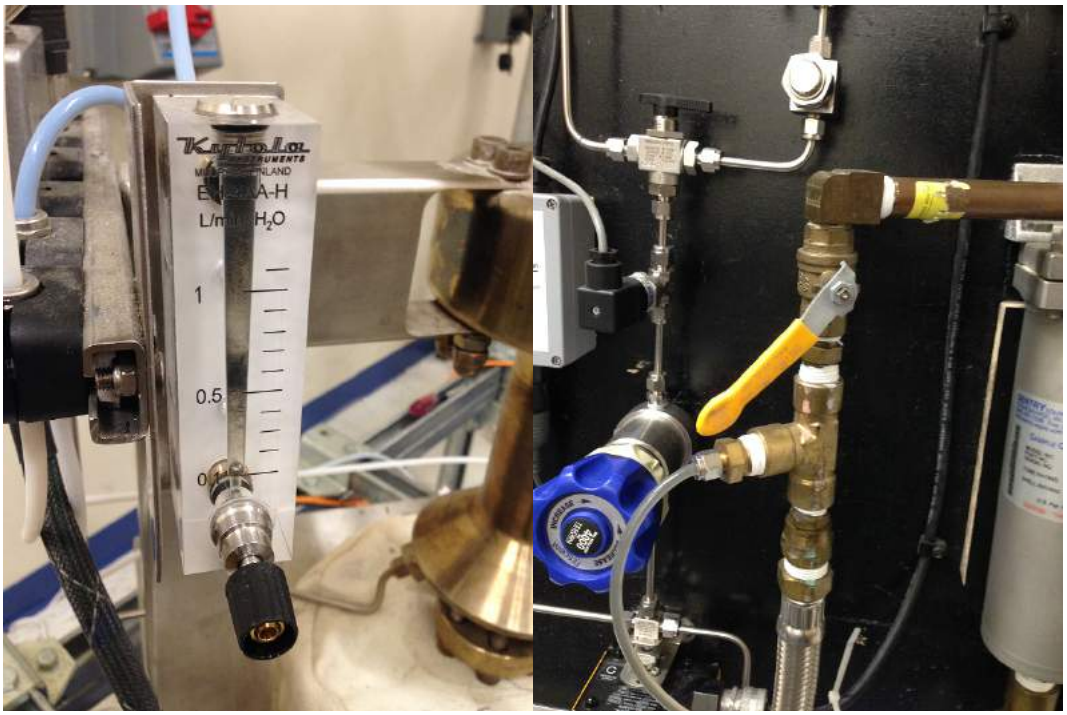


Figure 3-30: Kytola EH-4AA-H flow meter attached to the autoclave assembly. It measures flow of the autoclave cooling water system.

**Autoclave Pressure Transmitter** This pressure transmitter, as shown in figure 3-32, is used to measure the pressure within the autoclave, and is attached to the tubing that connects directly to the autoclave. It transmits data to the autoclave control box to display on the control box panel.

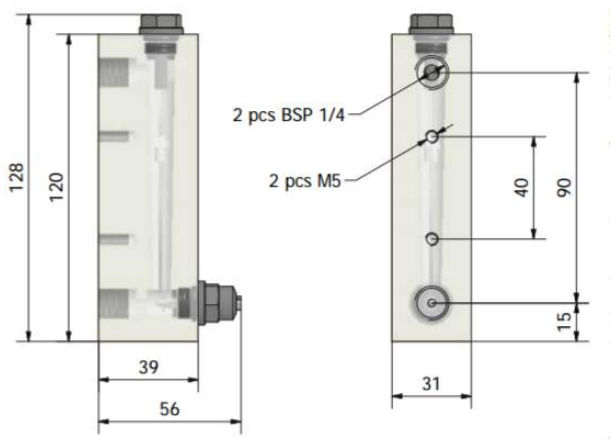


Figure 3-31: Autoclave flow meter diagrams [200].

Additionally, the signal is also relayed from the autoclave controller to the computer for display purposes. The autoclave pressure transmitter is manufactured by Keller with model number P-25Y. This pressure transmitter is essentially the same as the pressure transmitter in the auxiliary loop as shown in section 3.6.2.4.

Figure 3-32: Photo of autoclave pressure transmitter.

**Autoclave Safety Valve** The autoclave safety valve, as shown in figure 3-33, is a redundant safety valve which will release steam into the room once the pressure goes to around 3500 psi. It is the last resort protection in the case no other systems are operational including the main loop safety valve, the pressure switch, etc. The release pressure can be set to anywhere between 3000-4000 psi

by turning the knob on top of the valve with a wrench. The autoclave safety valve is manufactured by Swagelok with model number R3A-F.

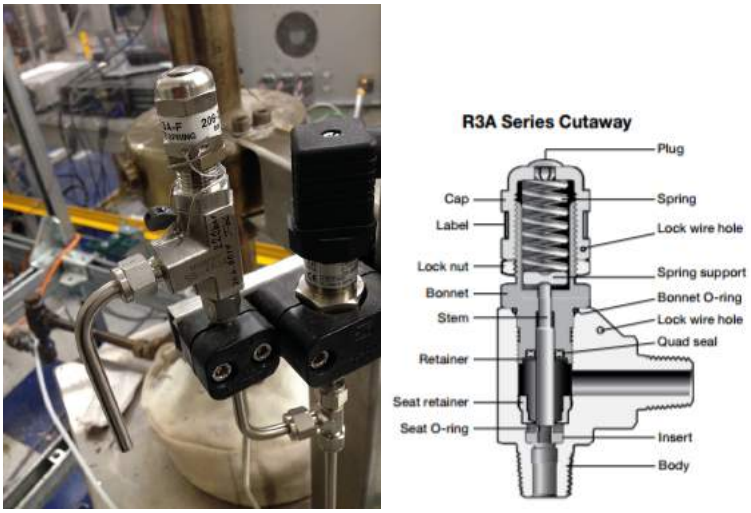


Figure 3-33: Photo (left) and diagram (right) of the autoclave safety valve [201].

#### 3.6.1.2 Heating Tape Control Components

As mentioned earlier, there are two heating systems in the main loop. One is in the autoclave heating rod which is situated inside the autoclave vessel. Another is the heating tape system. This heating tape system is comprised of all the heating tape installed on tubings in the loop. The following section explains what each component in this heating tape system is and its importance in the heating tape control system.

**Main Loop Temperature Probes** The main loop temperature probes, shown in figures 3-34 and 3-35, are the temperature probes outside the autoclave. They are used to monitor temperature at different spots throughout the loop. There are four main loop temperature probes. Three of them are normal single-junction thermocouples that output only to the CN9000 temperature controller. The thermocouple near the autoclave outlet is a dual-junction thermocouple that outputs to both the temperature controller and the computer. They are each inserted into their thermowell, which can withstand the loop's high pressure. The tip of the thermowell is submerged into the area with flowing water along the tubing system. Figure 3-35 demonstrates how thermowells work. Thermowells attach to the loop through 3/4-inch pipe connections. These pipe connections, as well as other pipe connections in the loop's hot area, use Xpando for sealing purposes. More information on the Xpando seal can be found in section 3.6.1.6. The temperature probes are manufactured by Omega with model numbers of M12KSS-U-0250-SL for a single-junction type and M12KSS-U-0250-DUAL for the dual-junction type. Thermowells are also manufactured by Omega with a model

number of 3/4-260A-U15/8-304SS-F.

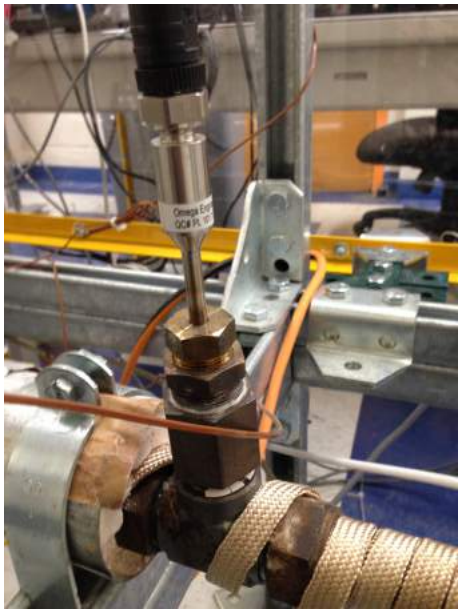

Figure 3-34: Photo of a temperature probe fitted inside a thermowell attached to loop tubings. Heating tape can be seen wrapped around loop piping, along with insulation on the lower left of the figure.

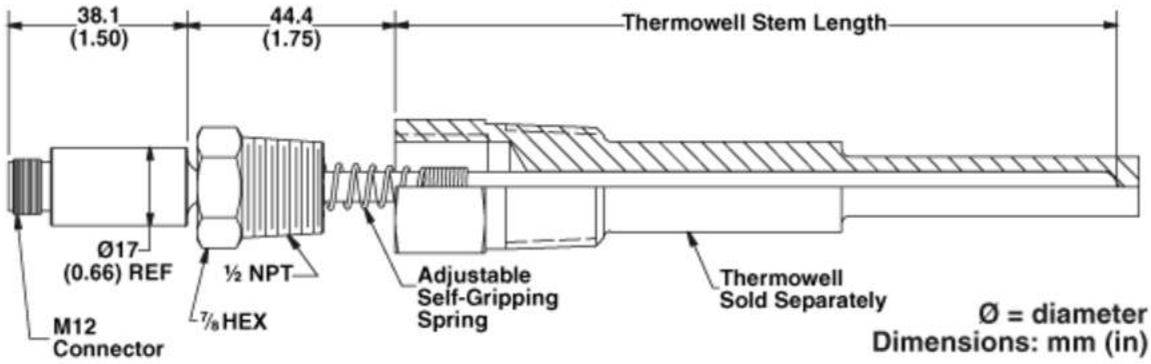


Figure 3-35: A diagram demonstrating how thermowells work [202].

**Main Loop Heating Tape** Heating tapes, as shown in figure 3-36, are wrapped around most of the main loop tubings. They work to give more heat to the system so that a resulting temperature close to that of the PWR can be achieved. The heating tapes used are an extreme temperature heating tape wrapped in fiberglass which can withstand temperatures up to 760 $^{o}$C. This allows them to be driven at full power without too much care for heat sinking, adding features without sacrificing simplicity.

There are two main types of heaters we used, both of which have the length of 8 feet and the

power of 624 Watts. The 120V type heater has a higher current of 5.2A, while the 240V type has the current of 2.6A. The reason that the heating tape is separated into two types is that the 240V plugs which are meant for heaters do not give enough Amps to be able to get the loop to the PWR temperature on its own. Therefore, a 120V plug must also be used to draw more current to heat up the water.

When running the loop near PWR temperature, the heating tape will be heated to a very high temperature. As a result, it may become white and brittle, as shown in figure 3-37. It is recommended not to move the tapes in any way, because the outer fiberglass will flake off, rendering the heating tape unusable. Since the flow rate used in the loop to match the PWR condition is quite high, the vibration is quite significant. This vibration can, over time, cut the fiberglass insulation out of the heating tape wire if they are not kept clear of the aluminum insulation cover.

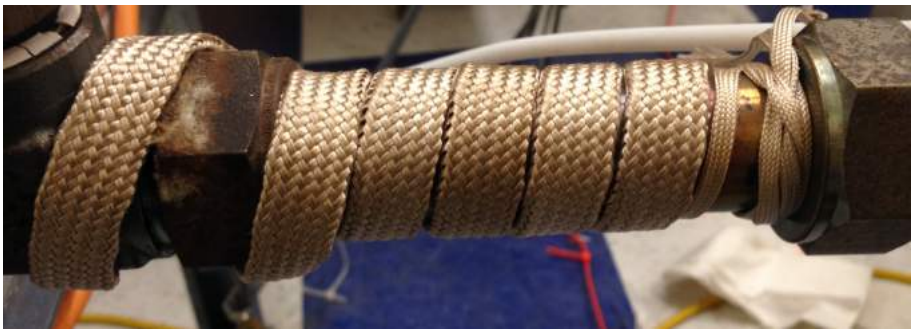

Figure 3-36: Photo of a new heating tape wrapped around main loop tubings.

Figure 3-37: This heating tape becomes white and brittle after several experimental runs.

**Latching Relay System** The latching relay system is used to make sure that once there is an emergency shutdown for some reason, the heating system will stay off. For instance, if there was an overpressure and the pressure switch turned the heating system off, we do not want the heating system to be on again as soon as the pressure is lowered. If there is something wrong with the loop that causes it to shutdown, we need to inspect it before continuing the run to make sure that the loop will be safe. Section 3.7.2.4 delves into greater detail of the latching relay system that is used to control the heating tapes. Figure 3-89 is a diagram of the latching relay system system.

**Temperature Controller** The temperature controller, as shown in figure 3-38, is of type CN9000A by Omega Engineering. Only one temperature controller is used to control all heating tapes wrapped around the main loop tubings. This temperature controller takes the input as the liquid temperature from the top-left dual junction thermocouple near the outlet of the autoclave. It is a proportional-integral-derivative controller, which means it has better ability to stabilize temperature than the normal on/off controller.

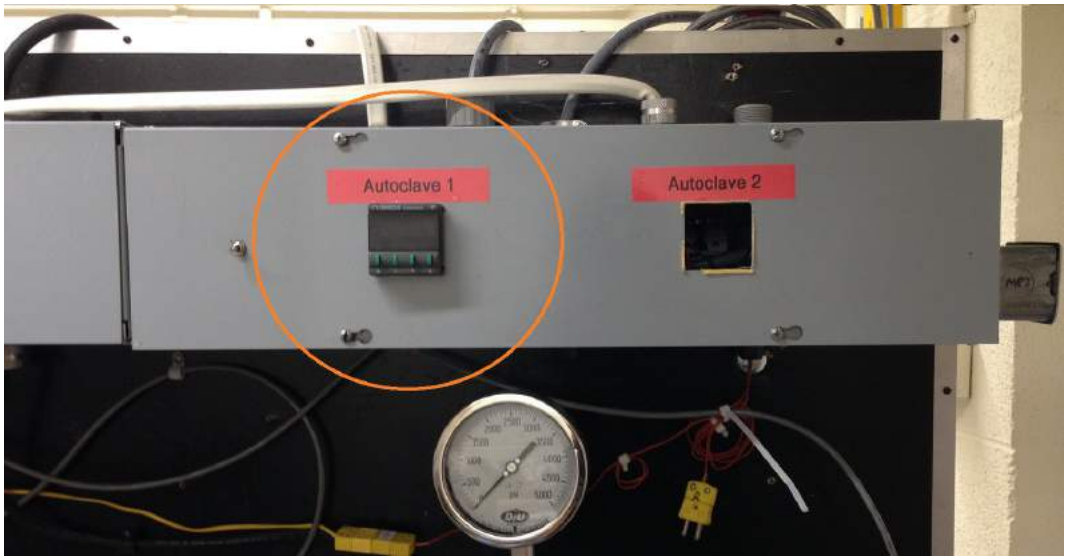


Figure 3-38: Photo of heating tapes temperature controller.

**Solid State Relays** Since the voltage and current we are controlling are very high, we cannot run the current through the temperature controller without having it burn out. Therefore, intermediate relays are needed to connect the heaters with the rest of the temperature control system. The intermediate relays in the crud loop heating system are the solid state relays in the temperature controller box. Two solid state relays, shown in figure 3-39, are used in the system, one for the 240V heaters and another for the 120V heaters.

**Heater Duplex Receptacles** These duplex receptacles act as an intermediate connection between individual heaters and the heating control system. They are included to facilitate the task of connecting and disconnecting individual heaters, making it a matter of simply unplugging and plugging in the individual heater plug. There are two duplex receptacles for 240V heaters which are connected to the thick white power line. Another duplex receptacle is for the 120V heaters which are connected to the gray power line. Figure 3-40 is a photo of one of the duplex receptacles. These heater duplex receptacles are sold by McMaster-Carr with model numner 1826T4.

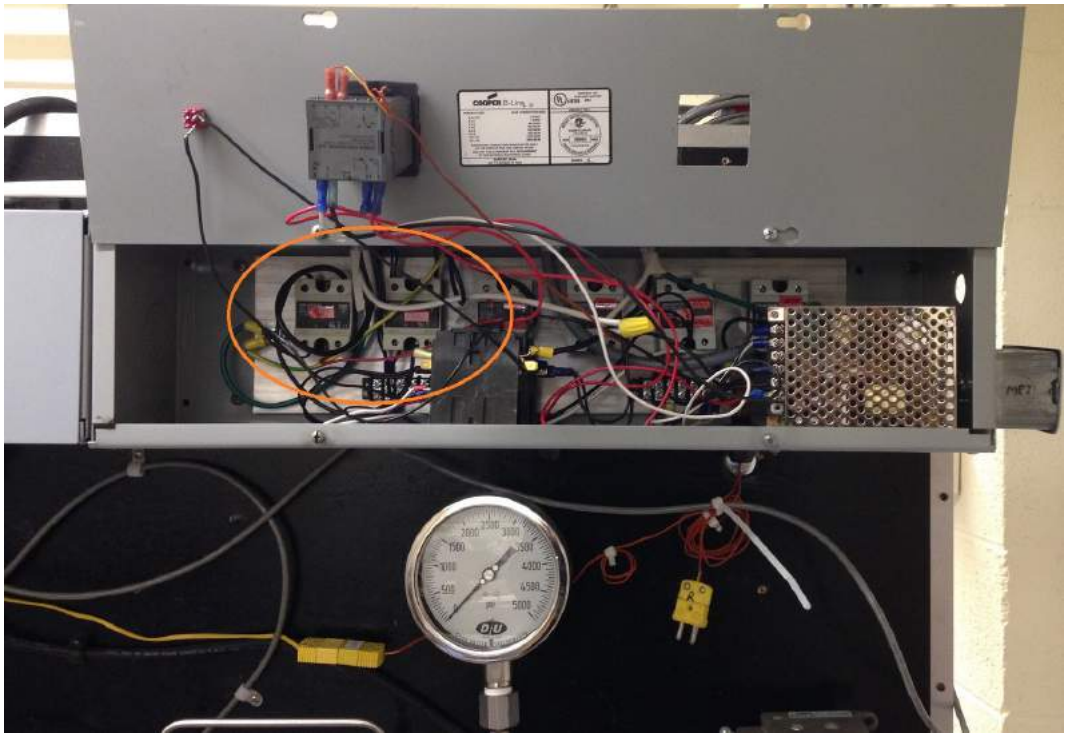

Figure 3-39: Photo of solid state relays.

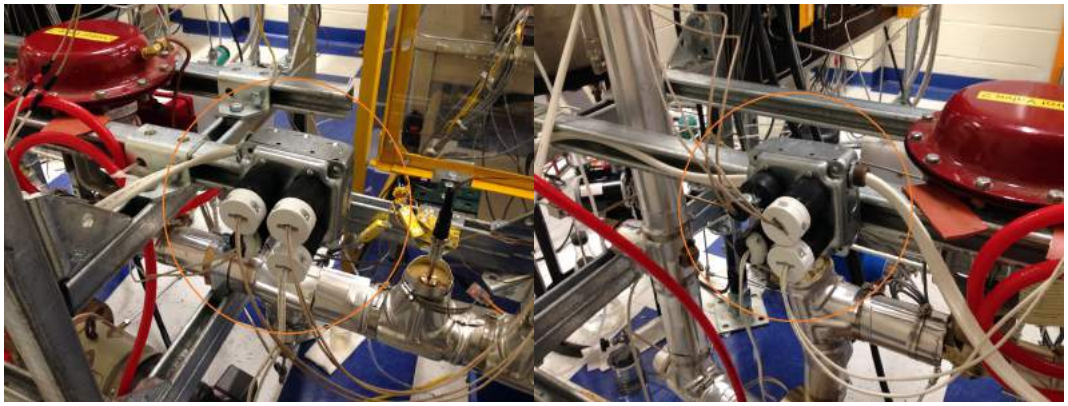

Figure 3-40: Photo of the two heater duplex receptacles. Each duplex receptacle distributes power to four heating tapes.

**Heater Emergency Switch** The emergency switch, as shown in figure 3-41, is the smaller red manual switch which is not attached to the wall. It is used to shut down only the heaters in the system. To shut down the whole system (not recommended), the emergency power-off switch attached to the wall both inside and outside the crud loop room can be used. The reason that this system is not connected to the pressure or flow control system is that we still want the water to be pressurized and running for a while after shutting down the heaters. If the pressurizing pump is shut down during an emergency, the quick decrease in pressure will cause the water inside the loop to flash to steam, and this could damage the system. Leaving the circulation pump on will help with cooling the whole loop evenly. This emergency switch was sold by McMaster-Carr with model number 7480T11.

Figure 3-41: Photo of emergency switch for the heating tapes.

#### 3.6.1.3 Pressure Control Components

**Pressurizing Pump** The pressurizing pump is used to pressurize the system to 15.5 MPa. It is a positive-displacement pump (diaphragm pump) which works by using a piston. A diagram of pressurizing pump is shown in the following figure 3-43. When piston gets pulled back, the diaphragm also gets pulled back. As a result, the water is drawn in to fill the chamber. The discharge ball of this pump chamber is pushed on its seat while the suction ball is opening the suction side. As a result, water will not be drawn from the outlet, because the discharge ball, on its seat, will block the flow. Water comes in through the inlet passing through the suction ball, filling up the chamber. When the piston gets pushed forward, the reverse happens. Water is pushed away from the pump chamber out through the discharge balls, while the inlet is blocked with suction balls on its seat. This stroking action repeats to pump the water slowly through the diaphragm pump.

The current pressurizing pump is the Ecoflow model LDB1V-M910 manufactured by LEWA. The pump can achieve a maximum flow rate of 82 ml/minute (1.3 gallons/hour). Unlike a circulation pump where flow rate varies with the pressure drop, the pressurizing pump always maintains the flow rate specified by stroke length regardless of pressure drop. The pump's driving motor is a


Figure 3-42: Photo of emergency switches inside the room (left) and outside the room (right). These switches will close down all power including that of pressurizing pump. They should only be used as last resorts.

1730 rpm AC motor. The pressurizing pump's stroking speed is 138 strokes/minute. The internal pressure relief valve of the pressurizing pump is set to 170 bars. The maximum allowable working pressure for the pressurizing pump is 391 bars.

When using the pressure pump, the valve leading up to the pressure pump inlet must be checked so that it will not obstruct flow. Failure to do this may result in diaphragm damage to the pressurizing pump. If the diaphragm of the pump is damaged, pump oil will mix with water making it difficult and potentially very costly to clean. When repairing the pressure pump or emptying the loop, this same valve must be closed. The pump flow rate can be adjusted via the adjusting knob on its side. The flow rate can be adjusted from 82 - 8.2 ml/minute, all the while maintaining a stroke rate at 138 strokes/minute.

**Pressure Gauge** Extra pressure gauge on the main loop, as shown in figure 3-45, serve two purposes. First, they are used to supplement the electronic measurement and to make sure that the electronic system is not malfunctioning. Second, pressure gauges also give a measurement of local pressure. They can be used to determine if there is any extreme pressure difference in the loop caused by some problem such as clogging of tubes. This pressure gauge is manufactured by Helicoid with model number 2314.

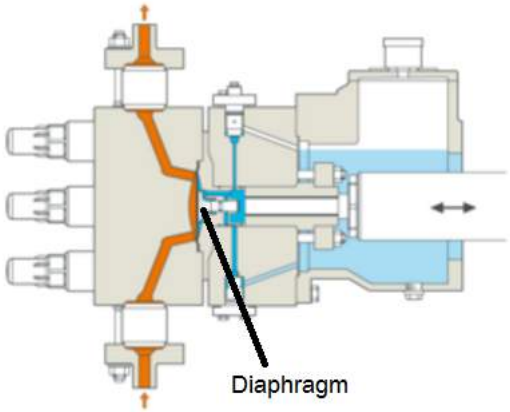


Figure 3-43: This figure shows the cross-section diagram of a generic LEWA diaphragm pump [203]. The orange shaded parts are the water. The white parts at the inlet suction and outlet discharge holds the suction balls and the discharge balls.

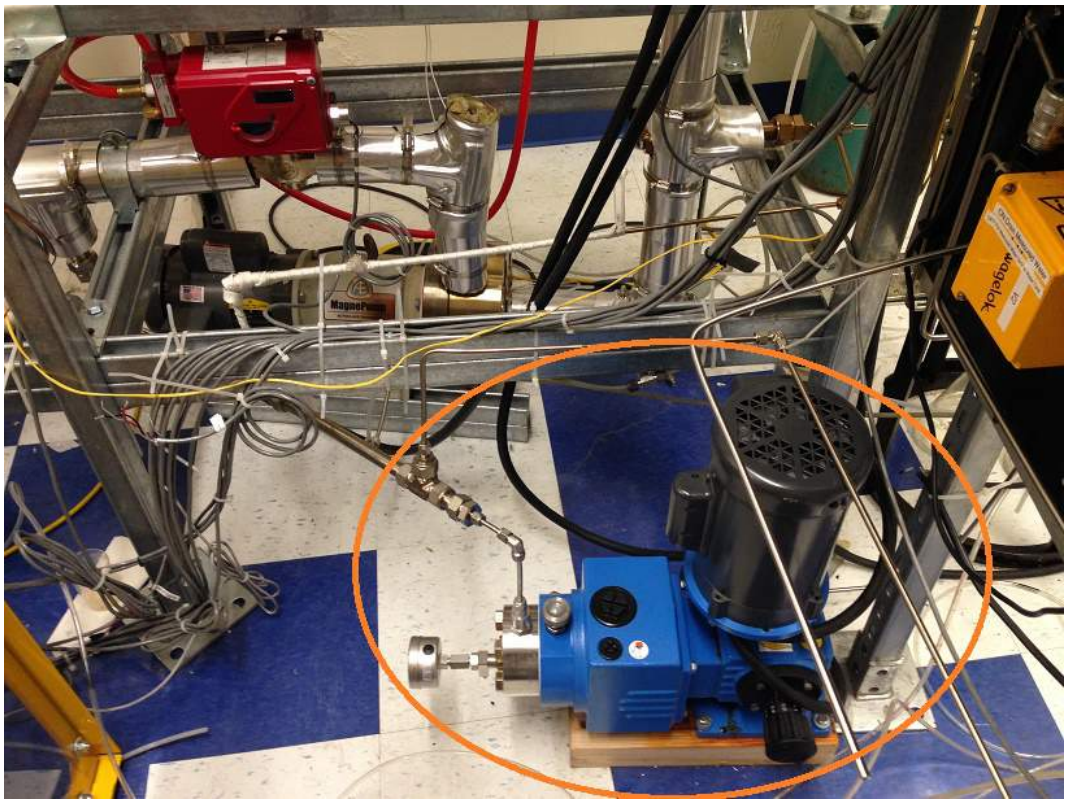

Figure 3-44: This photo shows the pressurizing pump installed on crud loop.

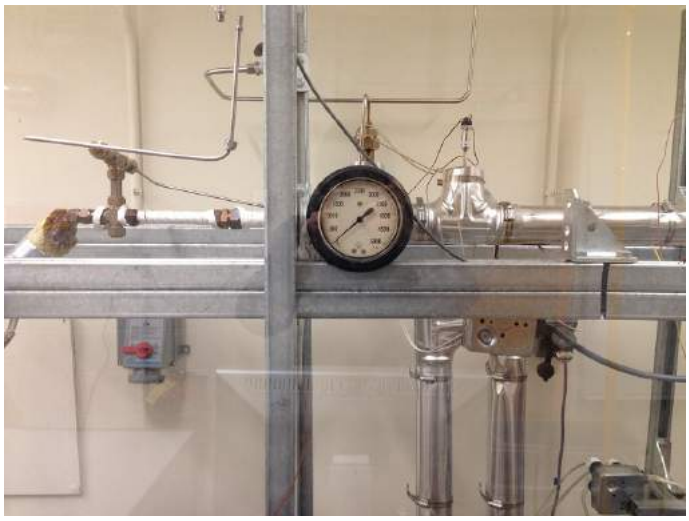

Figure 3-45: Photo of a physical pressure gauge attached to the loop.

#### 3.6.1.4 Flow Control Components

**Differential Pressure Transmitter** A differential pressure transmitter can be used to obtain the difference in pressure at two points. Together with the orifice and some additional Bernoulli equation's calculations, the loop flow speed can be obtained. More detail on these calculations can be found in section 3.5.3. In the IHTFP, the differential pressure transmitter, as shown in figure 3-46 and 3-47, is used to determine flow speed. This differential pressure transmitter can measure a pressure difference from 0 to 37.3 kPa (150 $inch - H_2O$). This differential pressure transmitter is manufactured by Kobold with model number PAD-HEE3S2NS00.

**Control Valves** The control valves are used to control the flow speed of the water around the loop. The control valve in series with the circulation pump is the main control valve that will be used to adjust the speed of the flow. This control valve is connected to the PID controller that will adjust the valve's opening depending on the input received from the computer which represents the velocity of the system. However, in reality, since the flow rate driven by the circulation pump is very steady, a manual adjustment of the control valves to constant opening amount will suffice for the flow control without any PID functions.

When using the control valves, caution must be taken to make sure that valve is not pushed too far. Pushing the valve too far will cause damage in the packing and therefore a leak during pressurization. The reason for using any control valve, when variable speed pumps are available, is that the variable speed pumps cost significantly more than a pump with a control valve. Figures 3-18 and 3-48 show photos of a control valve on the IHTFP and a diagram of the control valve, respectively. These control valves are manufactured by Badger Meter with model number RCV 1711.

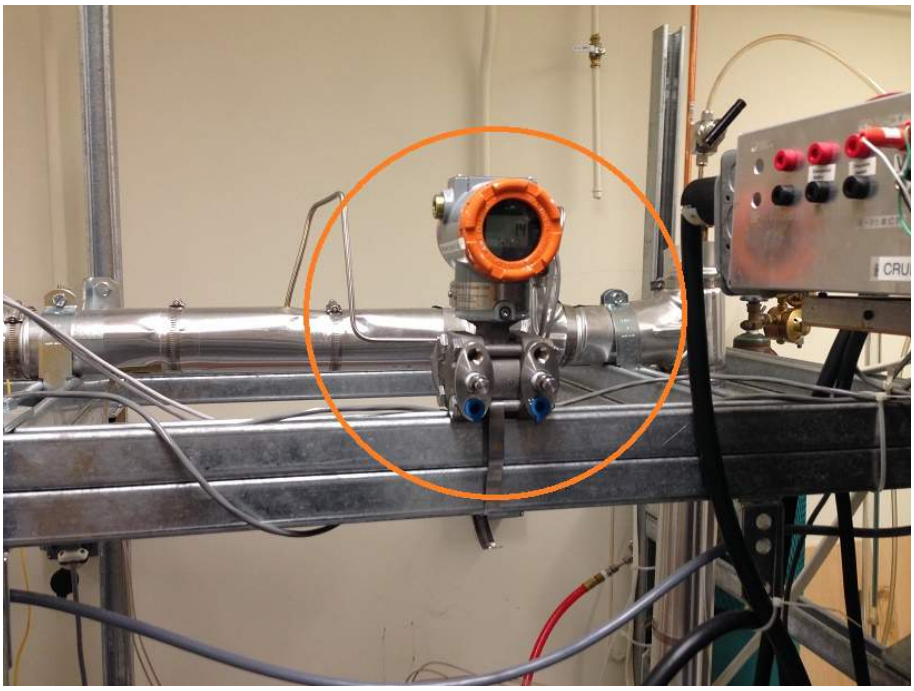

Figure 3-46: Photo of Kobold differential pressure transmitter.

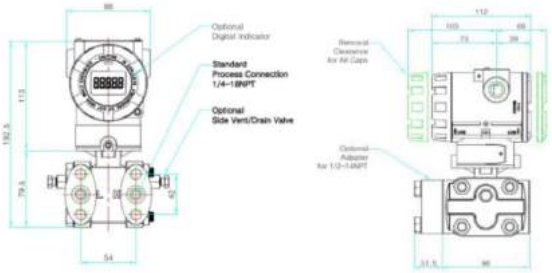


Figure 3-47: Kobold differential pressure transmitter diagram [204].

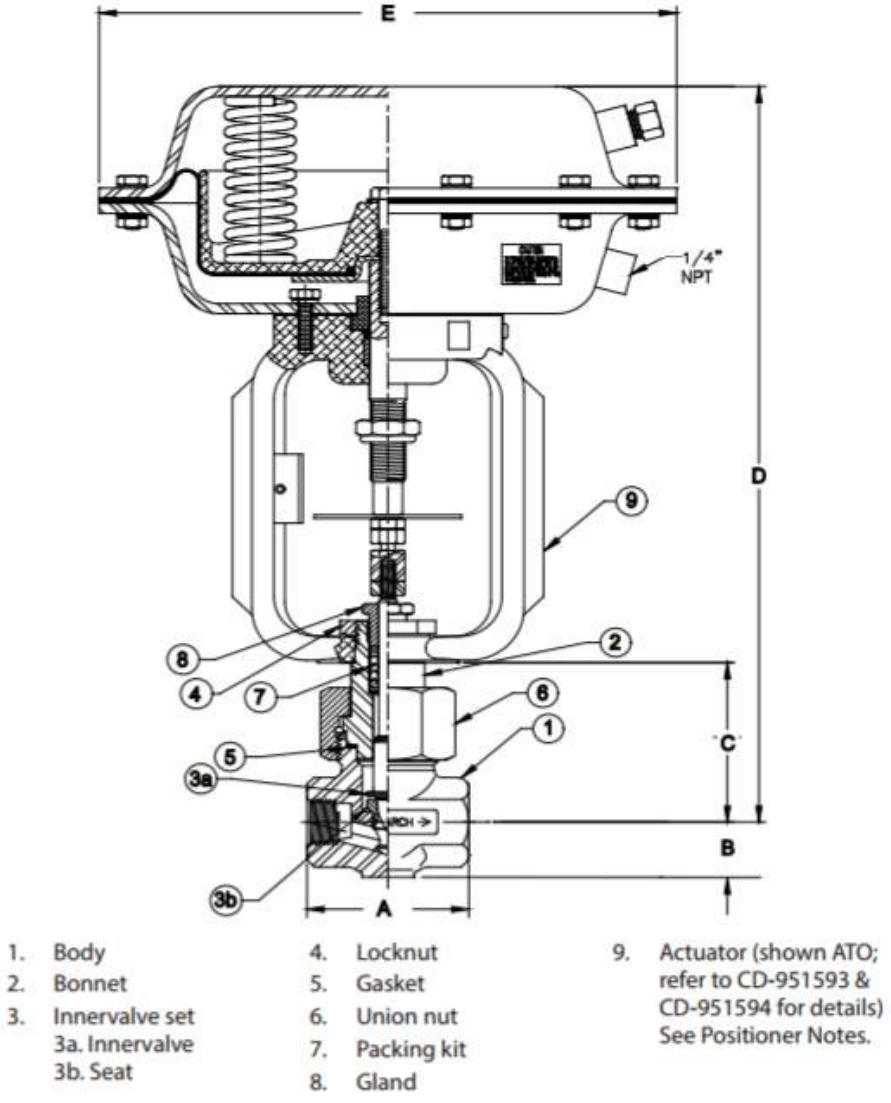


1. Body
2. Bonnet
3. Innervalve set
   3a. Innervalve
   3b. Seat
4. Locknut
5. Gasket
6. Union nut
7. Packing kit
8. Gland
9. Actuator (shown ATO; refer to CD-951593 & CD-951594 for details) See Positioner Notes.

Figure 3-48: Schematic of a control valve [205].

**Compressed Air Pump** The compressed air pump, as shown in figure 3-49, is used to supply compressed air to the control valves. The control valves need a pressure of at least 30 psi to operate. They use the gas pressure to close and open the valve. We did not use a gas tank for supplying the pressure to the control valves because the gas tank would exhaust very quickly given the gas leakage from the control valves. The compressed air pump is situated in a storage room near the crud loop room to save room space. The compressed air runs from its room through copper piping into the crud loop's room where it is attached to the control valves. The compressed air pump will be triggered, each time its pressure falls below a set pressure. This pump is manufactured by Speedaire with model number 5Z645C.

Figure 3-49: Photo of compressed air pump.

**Circulation Pump** The circulation pump, as shown in figures 3-50 and 3-51, is a centrifugal pump that is used to drive the flow around the loop. The pump is a magnet drive pump, which means it uses a magnet to couple the pump turbine with its motor. Using magnetic coupling as opposed to physical coupling is done to prevent any leaking. A small leak at a pump's direct coupling could lead to water exiting the loop, and other undesirable things such as oxygen going in. If the pump's turbine is directly coupled to the pump motor, there must be a connecting hole in the pressurized part of the pump to make this direct coupling happen. A leak in that connection, even if it is tiny, will have an effect on the water chemistry of the loop over time. For our purposes, we cannot tolerate much chemistry change, since the system will be at high pressure and temperature where corrosion is a huge issue. The loop will run for week-long experiments, which provides plenty of time to degrade the system's water chemistry. The pump's ability was chosen using the flow rate versus the pressure head graph as shown in the figure 3-52, with the criteria of getting enough flow rate,

while having redundant power. As seen on the flow rate versus pressure head graph, the flow rate can be adjusted by adjusting the pressure head. In the IHTFP, the pressure head can be adjusted via the control valve. The circulation pump is manufactured by Autoclave Engineers with model name 3/4 HP Magnepump.

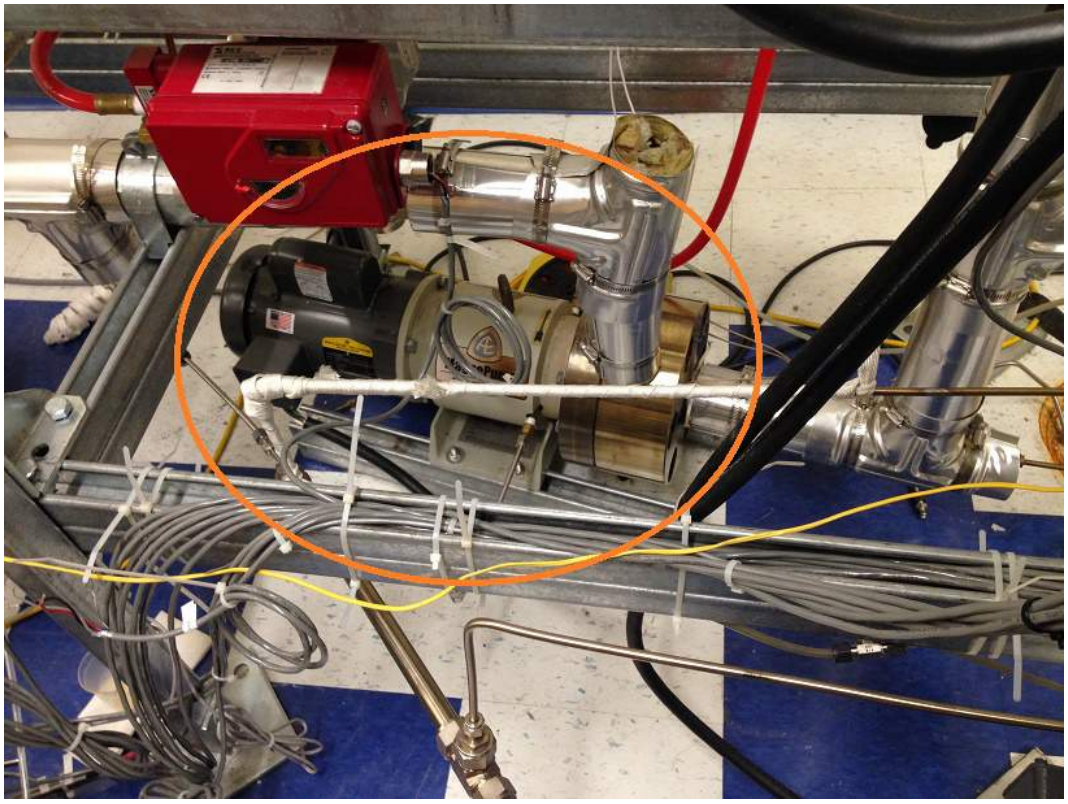

Figure 3-50: Photo of circulation pump that drives the main loop flow.

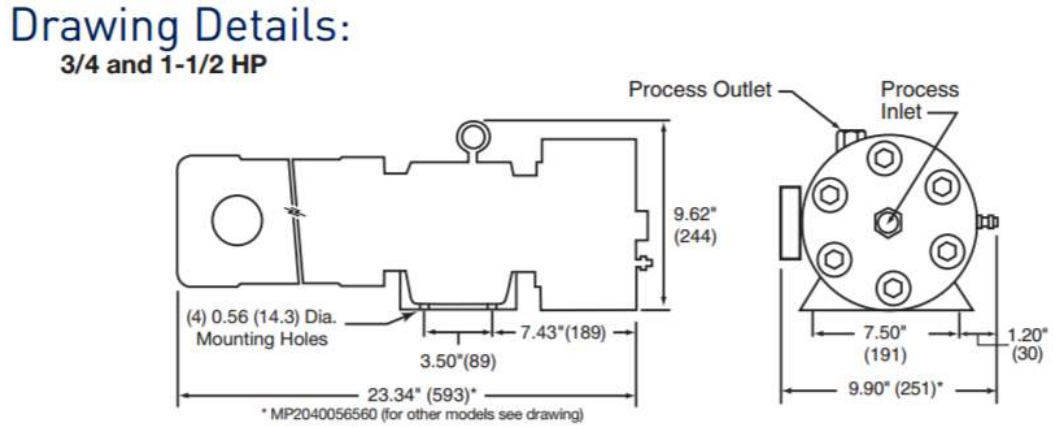


Figure 3-51: Drawing of the circulation pump [206].

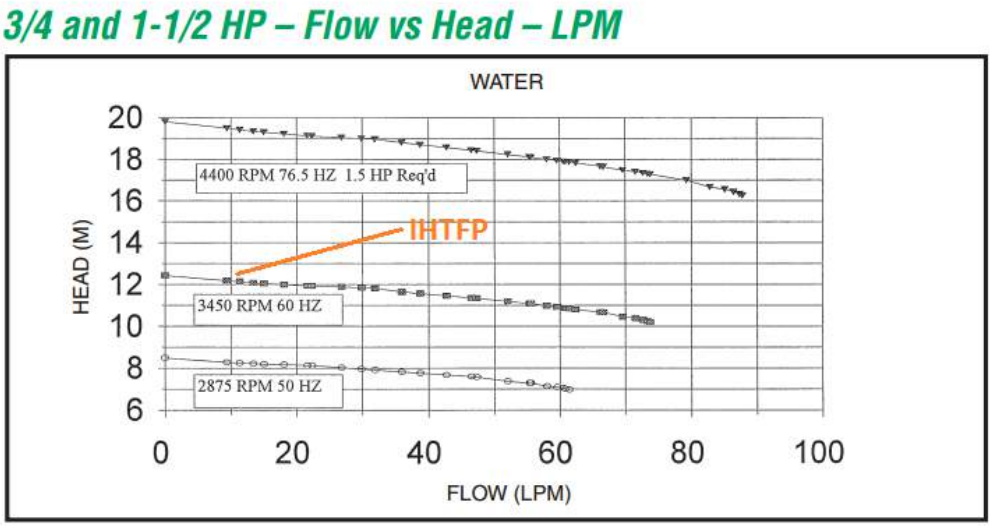


Figure 3-52: This graph shows the magnet pump's flow vs. head graph as seen in its documentation. The pump used for the IHTFP is represented by the middle line [206].

#### 3.6.1.5 Safety Components

**Main Loop Pressure Relief Valve** The pressure relief valve, as shown in figure 3-54 and 3-53, will release steam into the tube directed to the ceiling vent when the pressure in the loop is higher than 3000 psi. The ceiling vent tube is connected all the way up to the roof of the building where the steam will be released from a chimney. This pressure relief valve is used as a last resort to prevent the loop pressure from rising to a dangerously high level. This main loop pressure relief valve is manufactured by Autoclave Engineers, and is part of their RVP series, with part number 5RVP9072.

**Pressure Switch** The pressure switch is one of the many safety features on the crud loop. It is a switch that will shut down the system once the pressure becomes too high. This pressure switch is connected to the heating system and will trip the heating system if the pressure goes above approximately 2500 psi. The latching relay is used along with this switch to make sure that the heating system will stay off until someone comes in to check up on the crud loop and make sure that there is nothing seriously wrong with its operation. The reason that the pressure switch is only connected to the heating system is that the system should still be pressurized and the water in the system should still flow while the loop cools itself down. If the pressurizing pump and the circulation pump is tripped as well, the decrease in pressure and flow rate while the temperature remains high will cause the water inside the system to flash. This is very undesirable because of the decreased heat removal and the increased corrosion. After the heating system has been shut down for a while, the computer will automatically shut down the pressurizing pump and the circulation pump.

It is crucial to note the importance of the pressure switch's role in closing down the heating

Figure 3-53: Photo of main loop RVP pressure relief valve.

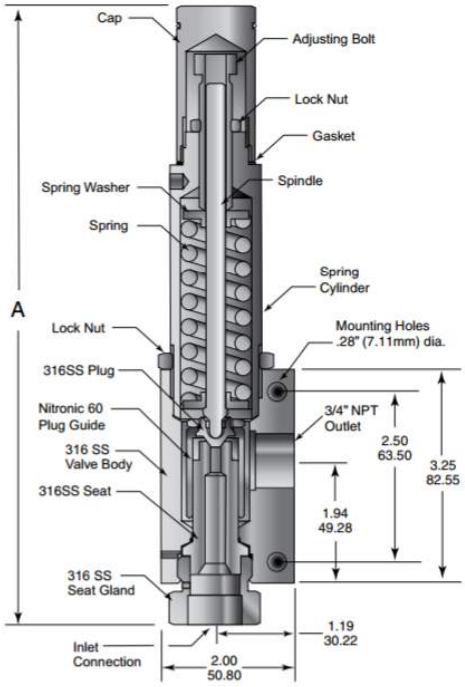


Figure 3-54: Diagram of main loop RVP pressure relief valve [207].

system. In case the water is heated, and pressure is high, any leak or detached part will be very dangerous as the steam quickly expands. The system will take a while to return to normal pressure as water flashes to steam. In the case where water is not heated, water will only expand by a tiny amount and the system will come down to normal pressure very quickly, and therefore is not as dangerous. The pressure switch makes sure that the heating system will turn off and stay off any time there is a significant overpressure. Figure 3-56 shows the inside of a pressure switch. The gold color hex in the center can be used to adjust the trigger pressure. The IHTFP's pressure switch current setup triggers at approximately 2500 psi. This pressure switch is manufactured by Omega with model number of PSW-133.

#### 3.6.1.6 Other Components

**Piping & tubing** All tubings in the loop are made of 316 stainless steel and manufactured by Swagelok. They have working pressure ratings of at least 2800 psi and over 10,000 psi burst pressure. It is highly advised that the tube should not be used above 2800 psi for an extended period, but if pressure runaway ever happens, the tube will be able to withstand the pressure as high as 10,000 psi for a short time. The tubing sizes used are 1/8, 1/4, 1/2, 3/4, and 1 inch.

In high-temperature and high-pressure conditions, corrosion poses a huge problem to the integrity of the loop. Therefore, the 316 stainless steel is chosen instead of the more widespread 304 stainless steel because of the superior corrosion resistance imparted by having 2-3 percent molybdenum [90].

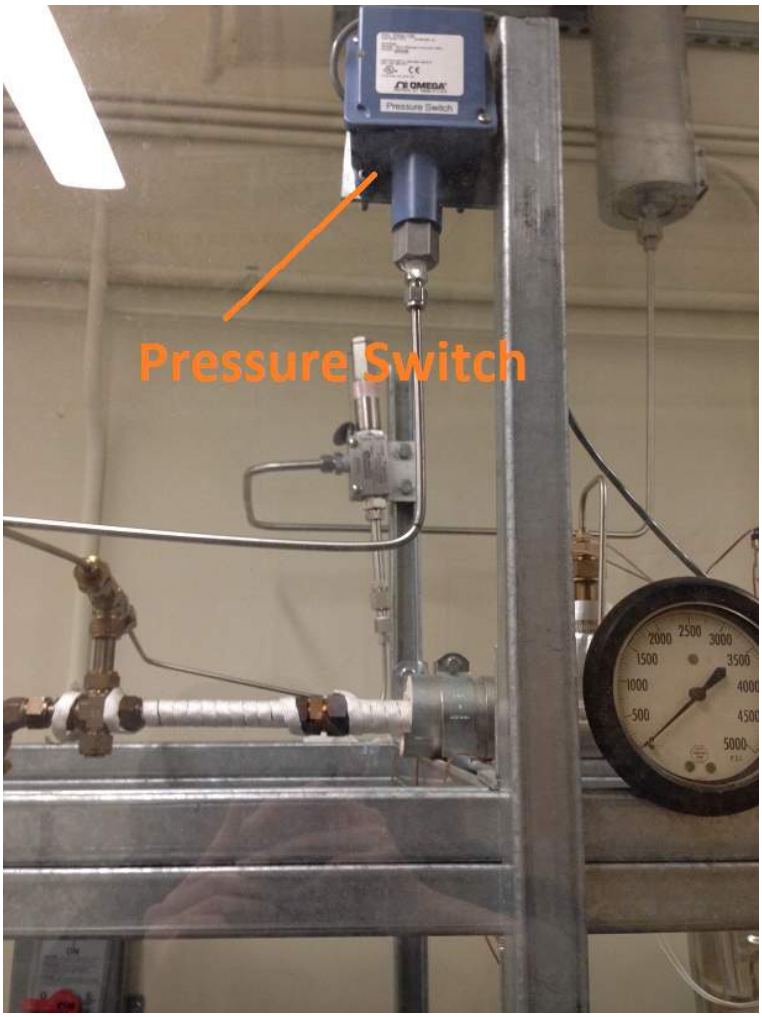


Figure 3-55: Photo of the pressure switch attached to the IHTFP.

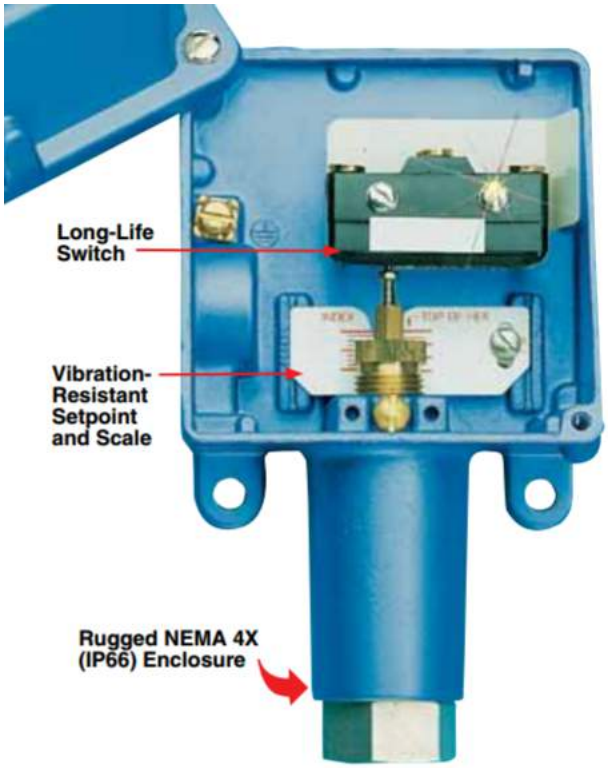


Figure 3-56: An inside of an Omega PSW pressure switch [208].

Beyond that, it is also easier to clean and fabricate. Tubings in the cold parts of the crud loop are also 316 stainless steel. Malleable nylon and vinyl tubing have been tried in the cold regions of the system, but resulted in an oxygen leak into the system. Therefore, they were replaced with steel. Most tubings on the main loop are larger than the rest of the loop at one inch in diameter because the pressure drop must be maintained at a low level to get the high-speed flow of the PWR condition. The larger the diameter of the tubings, the less pressure drop they create.

**Xpando Seal** In normal circumstances, pipe connections are sealed with the help of teflon tape. However teflon tape has a 327 $^{o}$C melting point. Since the IHTFP has the capability to rise above that temperature, teflon tape would not be ideal for the IHTFP. The solution to this problem is to use the Xpando seal. Xpando seal is capable of withstanding high pressure up to 5000 psig and high temperatures up to 537 $^{o}$C. These properties easily satisfy the pressure and temperature requirements of the IHTFP. The only downside of using Xpando is that its application isn't as simple as teflon tape.

To apply Xpando seal, mix Xpando powder with some water until the mixture has the thickness of a thin paste. Then a spatula can be used to apply the Xpando mixture on to the male pipe thread. After that, the pipe threads can be joined together. A 24-hour wait is required for the Xpando to dry, and be ready to withstand the IHTFP conditions. In the IHTFP, the connections that require

Xpando seal are the control valve connections and the thermowell connections, as shown in figure 3-57. Figure 3-58 is a photo of an Xpando powder can.

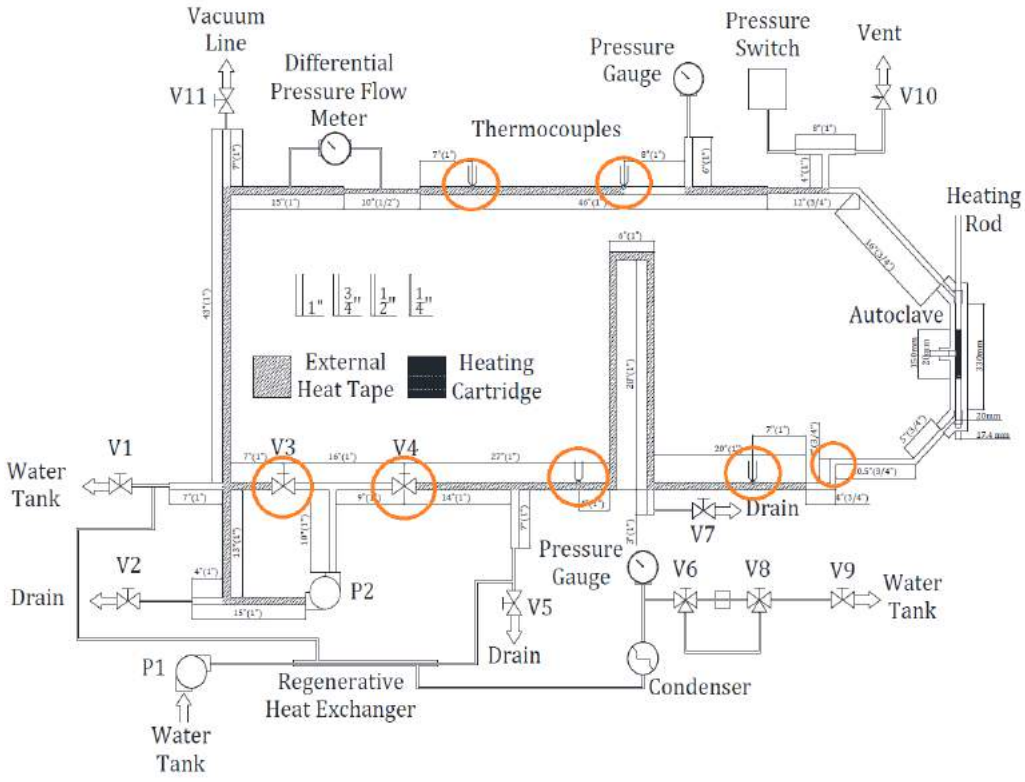


Figure 3-57: Main loop diagram with parts that need Xpando circled in orange.

**Main Loop Tubing Insulation** The ceramic wool insulation wrapped with aluminum sheet jacket, as shown in figure 3-59, is used to insulate most sections of pipe. The ceramic wool is chosen as the insulator for its ability to withstand the very high temperatures we operate at, as well as for its ability to insulate heat very well. The aluminum jacket is used to contain the ceramic wool around the tubings. Since inhalation of the ceramic wool or any other long biopersistent dust particles over an extended period of time has the potential to cause tumors, it is strongly advised to put on masks covering one's nose when removing or assembling ceramic wool insulations. The ceramic wool insulations are manufactured by Industrial Insulation Inc.

### 3.6.2 Auxiliary Loop

As first stated in the introduction, the auxiliary loop's main function is to control the chemistry, store the water, and act as input/output for the main loop. The auxiliary loop consists of three major loop systems. First, the main part of the auxiliary loop is the sub-loop that helps control the chemical parameters and provides the water input into the main loop. This sub-loop will be at


Figure 3-58: An Xpando powder can.

Figure 3-59: Ceramic wool heat insulator. Yellow ceramic wool is covered by its aluminum sheet jacket.

room temperature and almost at atmospheric pressure. The second sub-loop is the cooling water loop that helps cool the water coming out of the main loop into the auxiliary loop, as well as other equipment, including the autoclave and the circulation pump. The third sub-loop is the deionization system which is used to clean (deionize) and mix the water in the water tank. For simplicity, we have grouped the three sub-loops together in the auxiliary loop system as they all operate at room temperature and close to atmospheric pressure. This section will delve deeper into details of what each piece of equipment on the auxiliary loop does, and how to use them. The figure 3-60 shows what make up the auxiliary loop.

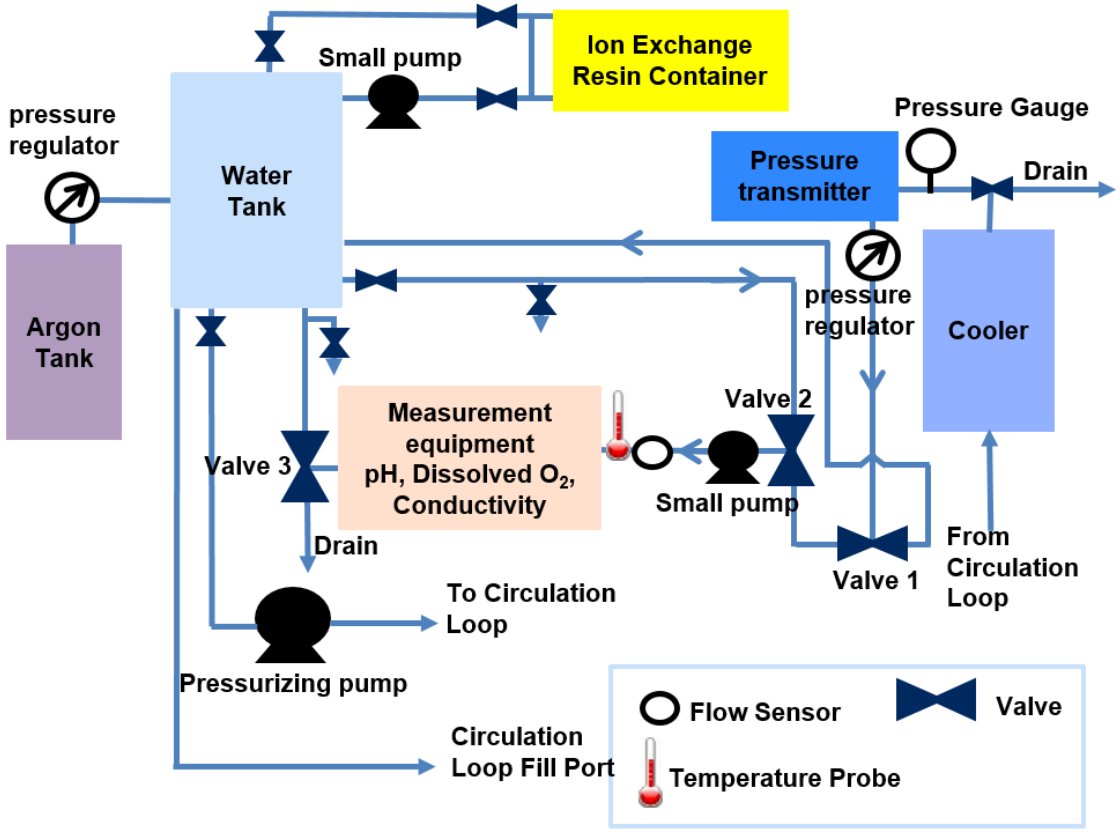


Figure 3-60: This diagram shows different parts of the auxiliary loop and their functions. It should give a better overall picture of what is going on in the loop before delving deeper into what each instrument does.

#### 3.6.2.1 Water Chemistry Measurement Equipment

The chemistry measurement equipment on the crud loop comes in a set manufactured by Mettler Toledo. This set can be used to measure the oxygen, the conductivity, and the pH of water. The measurement of water chemistry is important because an uncontrolled loop chemistry may affect the data, as well as damage the loop. For example, a high amount of oxygen can quickly corrode the loop, while a high amount dissolved calcium can lead to the scaling and clogging of the loop.

Figure 3-61: This is the photo of the auxiliary loop. The auxiliary loop is used to measure and regulate the loop chemistry.

The whole chemistry measurement equipment assembly is manufactured by Mettler Toledo.

**Transmitter Monitor** This blue transmitter with a green screen, as shown in figure 3-62, is used to read the data signals from the dissolved oxygen, the pH, and the conductivity sensors. Through its connections on the back side of the board, this transmitter can also relay the data analog signal to the computer's Agilent control unit to be displayed on the computer. Data output from the transmitter monitor is in the form of current measured in ampere units. Therefore, the data line must be connected to the analog reader with ampere input. It is also possible to connect the data line to the reader with voltage inputs and use resistor to convert the ampere to the voltage. The transmitter monitor can also be used to set the settings of each of these three pieces of equipment. This transmitter monitor is manufactured by Mettler Toledo with the model name of Thornton 770 Max. Figure 3-63 is a photo of this transmitter monitor's backside. Its outputs to computer are labeled. The channel 1, 2, and 3 cable connect to the conductivity sensor, dissolved oxygen sensor, and pH sensor, respectively.


Figure 3-62: Photo of Mettler Toledo Thornton 770MAX display screen.

**Dissolved Oxygen Sensor** The oxygen sensor, as shown in figure 3-64, is used to measure dissolved oxygen within the water in units of ppm. The settings for this unit can be controlled through the Mettler Toledo transmitter monitor. It is recommended that the dissolved oxygen level

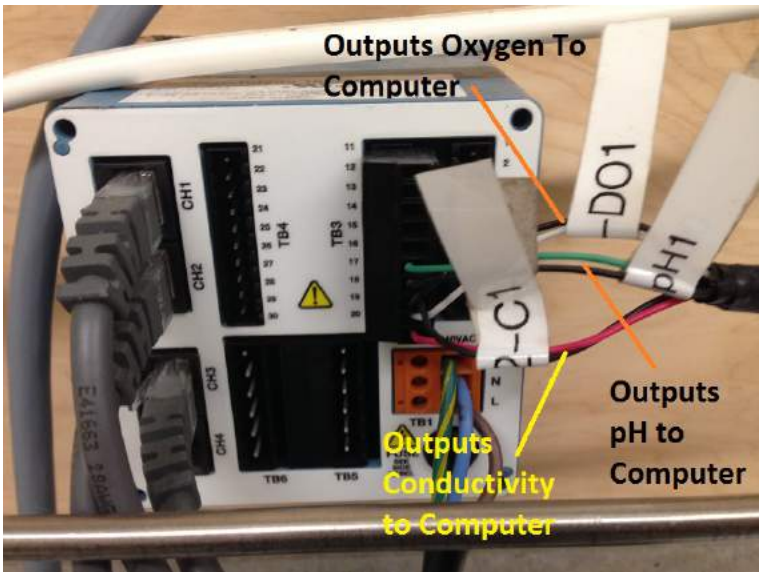


Figure 3-63: Photo of Mettler Toledo Thornton 770MAX transmitter's back side.

should be below 5 ppb during experimental runs to prevent corrosion. The oxygen can be lowered by bubbling argon through the water tank for several hours to a day depending on the oxygen level. A high oxygen level may also be indicative of a leak in the system. This dissolved oxygen sensor comes with the Mettler Toledo Thornton 770MAX assembly.

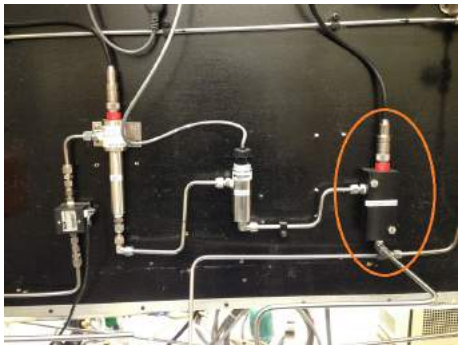

Figure 3-64: Photo of dissolved oxygen sensor.

**Conductivity Sensor** The conductivity sensor, as shown in figure 3-66, can determine the amount of ions in the loop. The conductivity measurement can be used to make sure that the water is completely cleaned of ions before we add in any other chemicals. Before adding any chemicals to the loop, it is recommended that the loop be deionized down to around 0.09 $\mu S/cm$ as recommended by the autoclave manufacturer. This conductivity sensor has a range of 0.05 $\mu S/cm$ to 10,000 $\mu S/cm$ and will output a 4-20 mA signal. The conductivity sensor's model name is Thornton 1000-30.

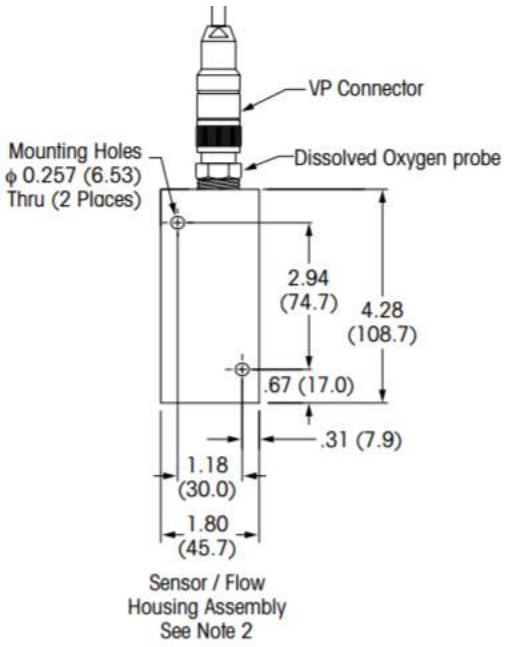


Figure 3-65: Dissolved oxygen sensor diagram [209].

**pH Sensor** The pH sensor, as shown in figure 3-67, is used to monitor pH to make sure that it is similar to that of the reactor, approximately 6.9-7.4 [43]. Note that this sensor needs a minimum of 50 ml/minute flow rate to give proper readings. The EPRI's lower limit pH recommendation [43] is there to prevent crud buildup. Therefore, it is recommended that this loop should operate at EPRI's lower limit since our goal is to grow crud. Lower pH helps corrode the inside of the main loop, naturally simulating the corrosion of primary loops in PWRs. This corrosion is good for us, since it adds more realism to the experiment. The sensor assembly's model is 770MAX pHure Sensor. Figure 3-68 is a diagram of a pHure sensor assembly.

#### 3.6.2.2 Flow Sensor

The flow sensor, as shown in figure 3-69, measures flow output in ml/minute and outputs the readings in analog form to the computer. The flow sensor attached in series with the measurement equipment is useful in determining if the measurement equipment has enough flow rate to work properly. Having a flow rate through the measurement equipment of 50 ml/minute or more is recommended for accurate measurement readings. The flow sensor's input and output lines are only 1/8-inch in diameter. Because of its tiny size, it is this equipment that is most likely to clog in the measurement system. This flow sensor is manufactured by Omega with model number FLR1000 ST. Figure 3-70 is a dimensional diagram of a FLR1000 ST flow sensor.

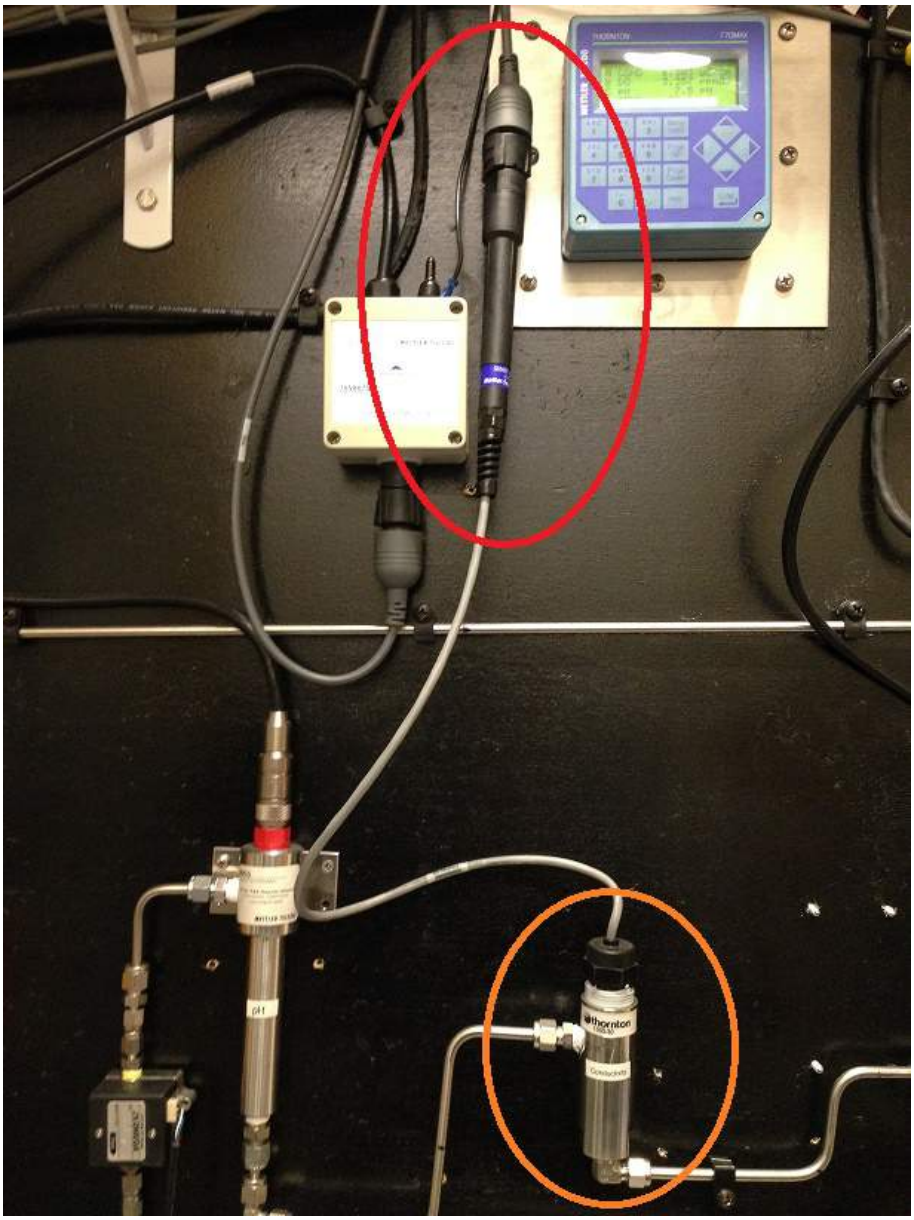


Figure 3-66: Photo of conductivity sensor (circled in orange) and its accompanying smart signal adapter (circled in red).

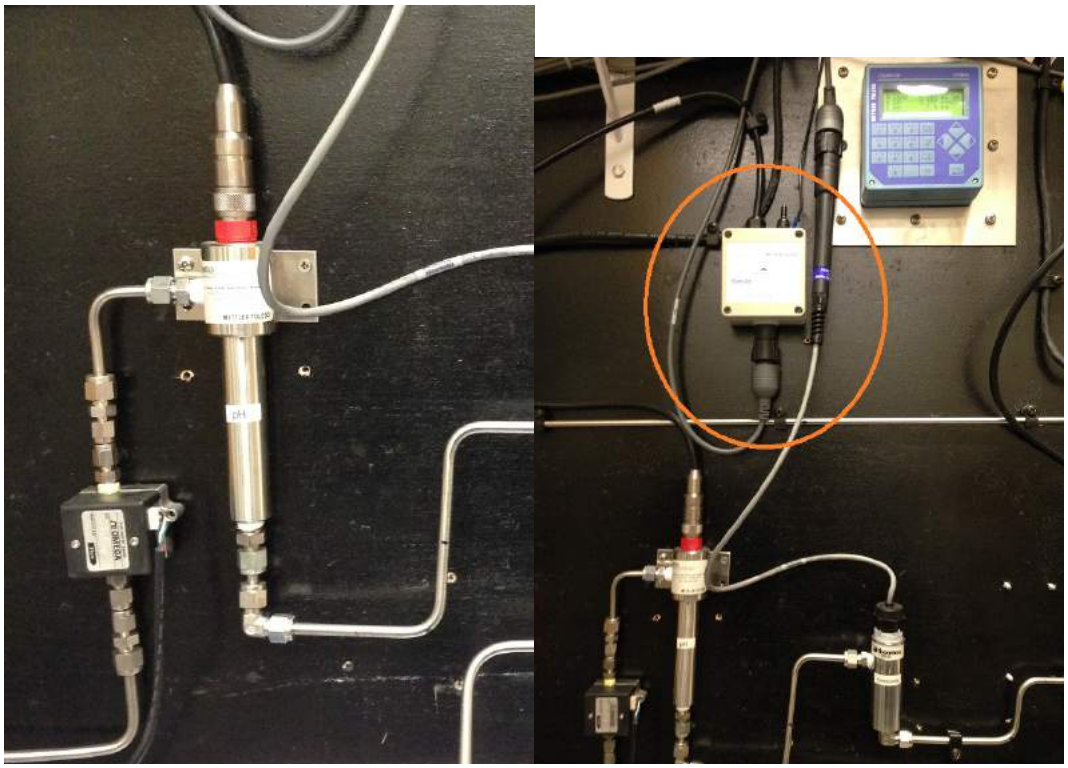

Figure 3-67: Photo of the pH sensor (left) and its amplifier (right).

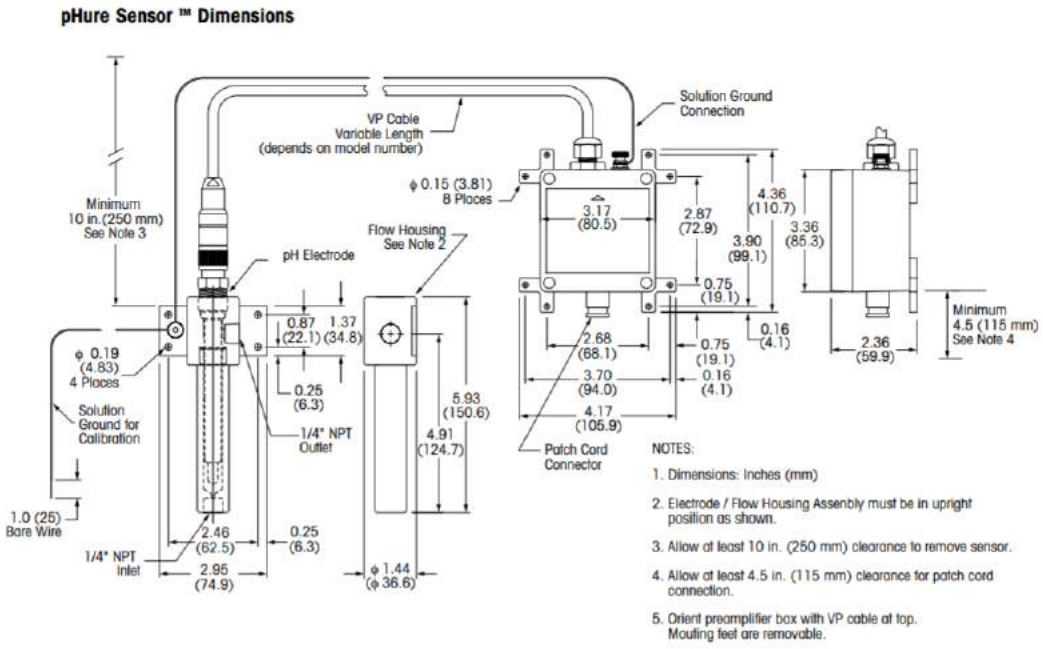


Figure 3-68: Diagram of pH sensor assembly [209].

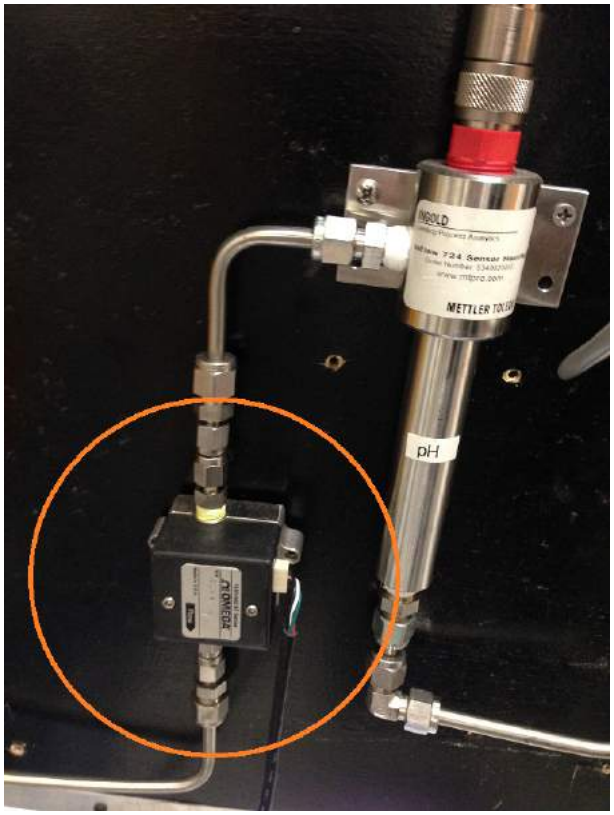


Figure 3-69: Photo of auxiliary loop flow sensor.

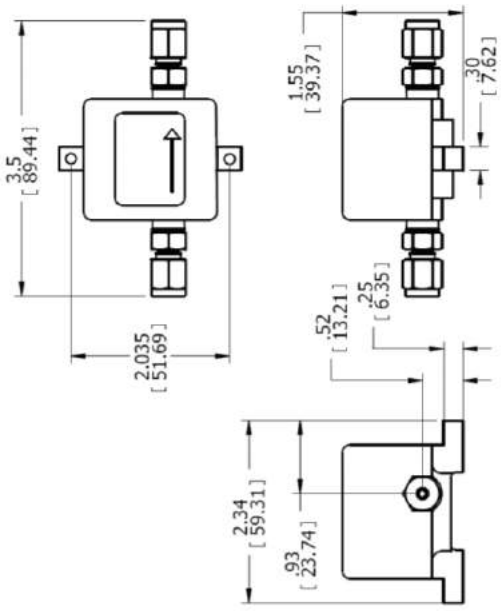


Figure 3-70: Dimensional diagram of flow sensor [210].

#### 3.6.2.3 Valves and Actuators

The valves and actuators in the auxiliary loop are used to control the direction of flow within the loop. Figure 3-71 is a photo of the valve and actuator. The three electric valves attached to the actuators are all three-way valves. These three-way valves can let water flow from the center inlet to either the right or the left end outlets. The arrows marked on the valve shows which end outlet is open for flow. The reason an electric actuator is needed is that the manipulation of valves is required when taking measurements of the loop's chemistry. While the loop is running no one should be near it, and therefore, there will be no one to adjust these valves for taking needed measurements. The valve system, therefore, must be controllable from the computer. This remote control of the valves is where the electric actuator comes in. This valve and actuator assembly is manufactured by Swagelok with model number MS-141ACX. Figure 3-72 is a dimensional diagram of the valve actuator.

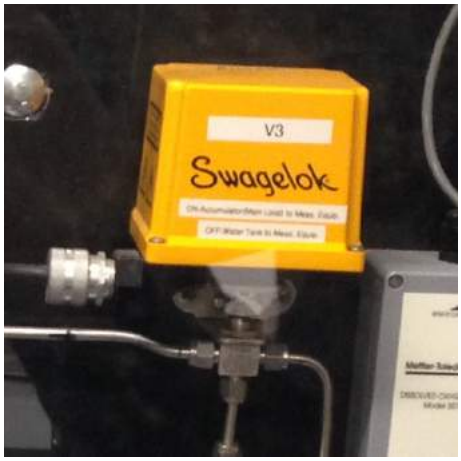


Figure 3-71: Photo of valve and its actuator. The valve is the part attached to tubings while the actuator is the yellow box.

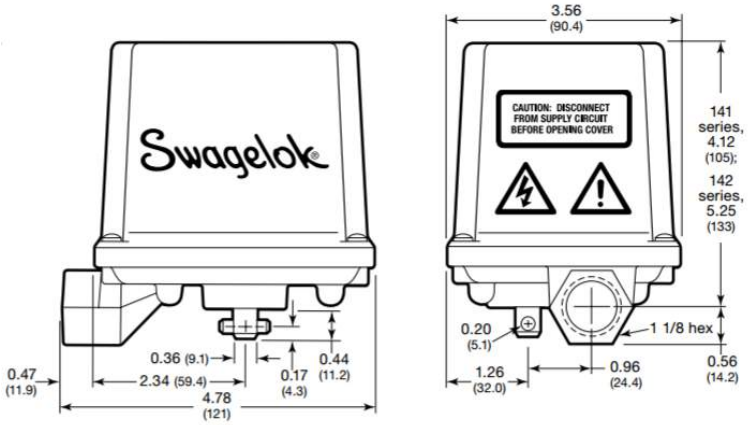


Figure 3-72: Dimensional diagram of valve and a Swagelok valve actuator [211].

#### 3.6.2.4 Pressure Transmitter

Another pressure transmitter, as shown in figure 3-73, is attached to the loop just before the back pressure regulator. It verifies the pressure measurement made by the autoclave pressure transmitter. Its functionality is the same as the autoclave pressure transmitter. This pressure transmitter is manufactured by Wika with model number A-10.

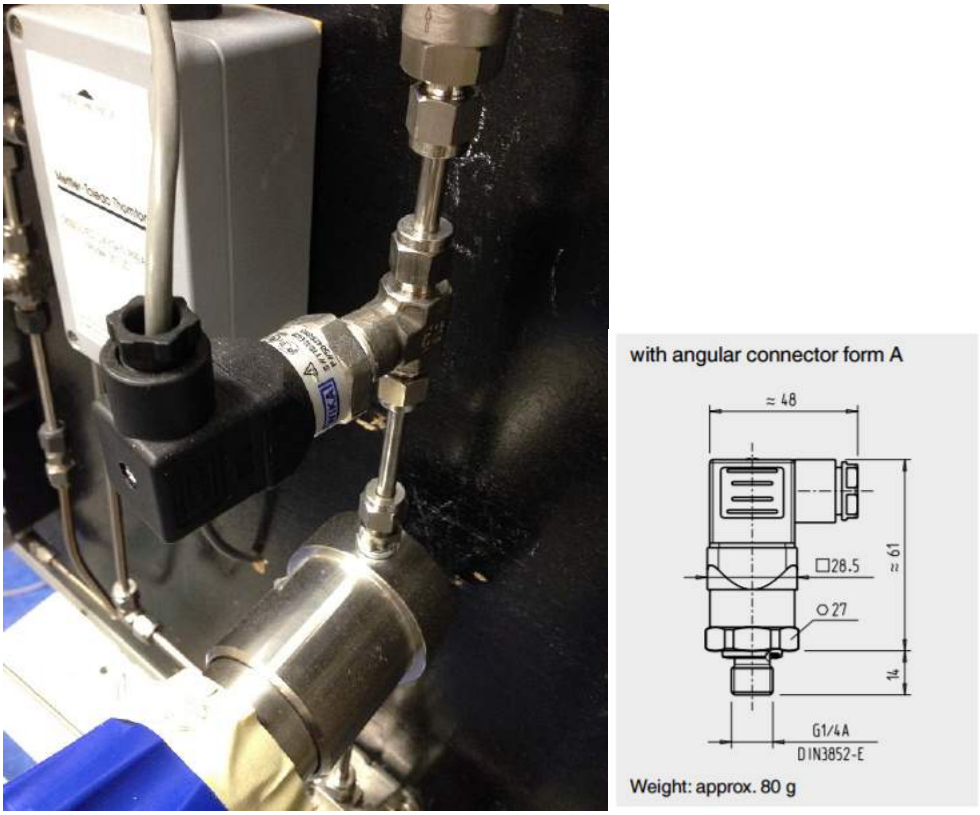


Figure 3-73: Photo (left) and diagram (right) of WIKA pressure transmitter [212].

#### 3.6.2.5 Back Pressure Regulator

The back pressure regulator, as shown in figure 3-74, can be used to set the pressure in the loop. As shown in the figure 3-75, the inlet of the back pressure regulator has high pressure, while the outlet will have almost atmospheric pressure. When the pressure is not as high as the adjusted pressure, no water will leave the regulator. When the pressure on the inlet side increases to become high enough to push the diaphragm, some water is let through the regulator until the pressure drops down again. When the adjusting knob is turned, the spring becomes tightened, pushing down the diaphragm with greater force. As a result, more pressure is needed from the inlet side to push up the diaphragm and let water flow out of the outlet. The back pressure regulator is placed after the sample cooler, as it cannot tolerate a high-temperature environment. This back-pressure regulator

is manufactured by Tescom with model number 26-1763-24-114.


Figure 3-74: Photo of back pressure regulator.

#### 3.6.2.6 Sample Cooler

The sample cooler, as shown in figure 3-76, is used to cool the water as it flows into the auxiliary loop. By cooling the water down, we make sure that the equipment in the auxiliary loop will not be damaged from the extreme temperature. Equipment such as the back-pressure regulator, the pressure transmitter, and the measurement equipment cannot withstand the extreme temperatures found within the main loop. The sample cooler is a heat exchanger that dumps heat from the high-

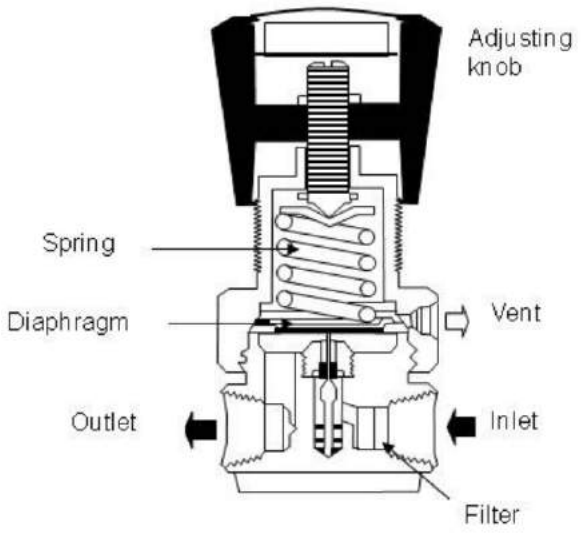


Figure 3-75: A labeled diagram depicting an overview of back pressure regulator [213].

temperature line from the main loop onto the cooling loop. Figure 3-77 is the performance curve of this sample cooler. Note that the flow rate we use this sample cooler for is 80 mL/min or 0.02 GPM. In this case, the approach temperature is virtually zero (the process fluid outlet temperature very close to inlet cooling fluid temperature), and the sample cooler's performance is far more than what we actually need. This sample cooler is manufactured by Sentry Equipment with model number TLF-4225.

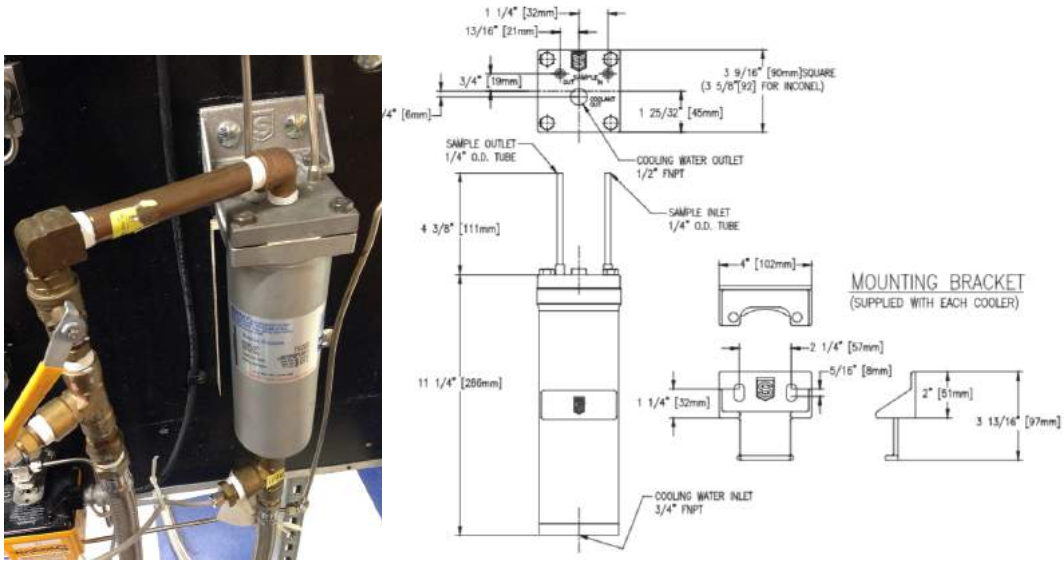


Figure 3-76: Photo of sample cooler (left) and dimensional diagram of sample cooler (right) [214].

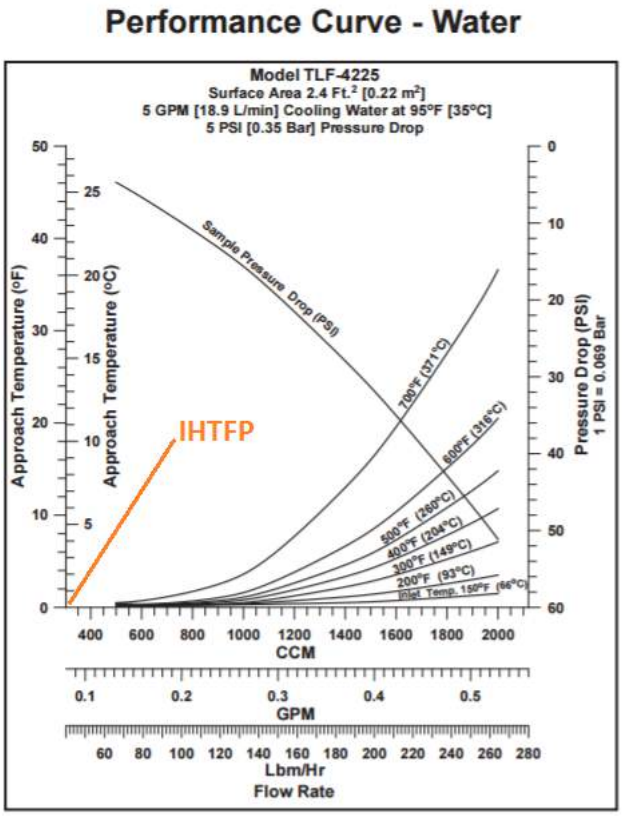


Figure 3-77: Performance curve of sample cooler [214].

#### 3.6.2.7 Water Tank

The water tank in the auxiliary loop is used to store water that will be used to circulate in the main loop. It is where water is added to the loop. The top lid can be unscrewed open to pour in tap water. The raw tap water can be deionized by the deionization system attached to the water tank. The mixture of chemicals such as boric acid and lithium hydroxide can be added from the top of the lid after the water is cleaned through an injection port. The water tank can hold approximately 120 liters of liquid when full to the top. Its height is approximately 90 cm, and its diameter is approximately 41 cm. The glass column on the side of the tank is used to see the water level in the tank. Figure 3-78 shows photos of the water tank. Figure 3-79 is a schematic of the water tank. Note that the deionization loop is used for both cleaning and mixing the water (more information on this in section 3.9.2.4).

Figure 3-78: The water tank photo (left), the water tank lid photo with the chemical injection port circled (top right), and the zoomed in chemical injection port.

#### 3.6.2.8 Argon Tank

The argon tank is used for bubbling argon into the water tank to remove oxygen. When argon is bubbled inside the tank, the argon bubbles remove dissolved oxygen from water releasing it on top of the water tank where the bubbles pop. The gas exhaust then removes that additional argon along

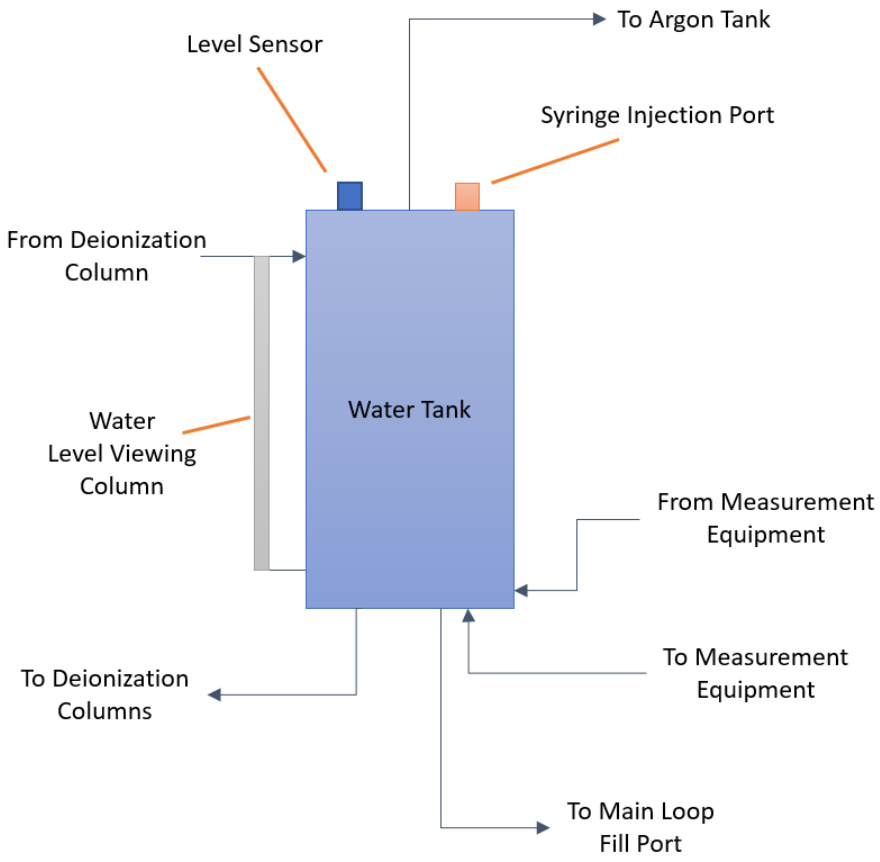


Figure 3-79: Schematic of the water tank.

with oxygen from the top of the tank. Argon is used instead of nitrogen because it was found that bubbling nitrogen causes pH to rise slightly, as nitrogen creates trace amounts of nitric acid when dissolved in water..

#### 3.6.2.9 Deionization System

The deionization system, as shown in figure 3-80, is used to lower the ion concentration of water in the water tank to an acceptable amount for the experiment, which is around 0.1 $\mu S/cm$. Additionally, the valves can also be set up to bypass ion-exchanger columns. In that case, the deionization system will act as a water tank mixer instead. This functionality is useful when mixing the chemicals to make sure they are distributed evenly throughout the water tank. The deionization system consists of the two mixed-bed ion exchanger columns and a pump. The model number for the ion exchanger is US Water Systems Dual 4.5" x 20" DI Filters 1.5 GPM.

The mixed-bed ion exchanger columns are cylindrical containers of ion-exchange resin beads. When water flows through the beads, ions in the water will be absorbed by the beads. Ion-exchange resin beads work by trapping unwanted ions and releasing the ions that combine with water. Ion-exchange resin beads are fabricated from organic polymer substrate and are usually porous, providing a large surface area to trap and release ions. The small pump in the deionization system is used to draw the water from the bottom of the water tank into the deionization columns. The output water from the deionization columns is ejected into the top of the water tank. The small pump in the deionization system is used to draw the water from the bottom of the water tank, push the water through the deionization columns, and out into the top of the water tank.

Figure 3-80: This is a photo of the two ion-exchanger columns connected to the deionization system. The lower left green pump is the small pump used to drive the deionization system.

#### 3.6.2.10 Gas Exhaust Flasks

When bubbling argon through the loop, there must be an exhaust where the argon gas can leave the tank. A bare exhaust that just lets argon gas out of a port will interfere with the dissolved oxygen level. The interference happens because the exhaust will also let the oxygen from the air into the tank. Although it may seem counter-intuitive that the oxygen from the air can seep in while the argon gas is rushing out, it is an observable effect. Without the gas exhaust flasks, we were not able to get the dissolved oxygen level below 200 ppb. After the gas exhaust flasks were installed, the oxygen could go down to almost zero ppb. To prevent the outside oxygen from seeping in through the exhaust, we use a system where the exhaust gas bubbles through two flasks of water. The exhaust gas can leave the system in the form of bubbles, but the air outside cannot go back through the exhaust because it cannot penetrate the water to get to the bubbling tube. Both flasks, as shown in figure 3-81, function in the same way to make sure that no oxygen will get into the loop through the exhaust.


Figure 3-81: Gas Exhaust Flasks.

#### 3.6.2.11 Neslab Cooling Water Heat Exchanger System

This heat exchanger system, as shown in figure 3-82, cools down and drives the cooling water around the loop to cool the sample cooler, the circulation pump, and the autoclave. Water in this system is at atmospheric pressure. This cooling water heat exchanger inputs and outputs water from the building's cooling water. The water from the building is used to cool down, by heat exchange, the cooling water that goes through the whole crud loop. Note that the building water and the crud

loop's cooling water run in a separate loops and do not mix. The crud loop's cooling water can be added in from the hole on top of heat exchanger system designated for monitoring and adding its cooling water. Maintaining the flow rate reading of 0.5 liters/minute on the Kytola flow meter in the autoclave assembly is ideal. This Neslab heat exchanger is manufactured by Thermo Scientific with the model name Neslab System II. The temperature of Neslab heat exchanger system can be adjusted via the the screw shown in figure 3-82. The control valve located in the cooling water inlet line will regulate flow rate based on the heat load and the temperature adjustment. The current set point maintains the outlet temperature at approximately 35 ºC.

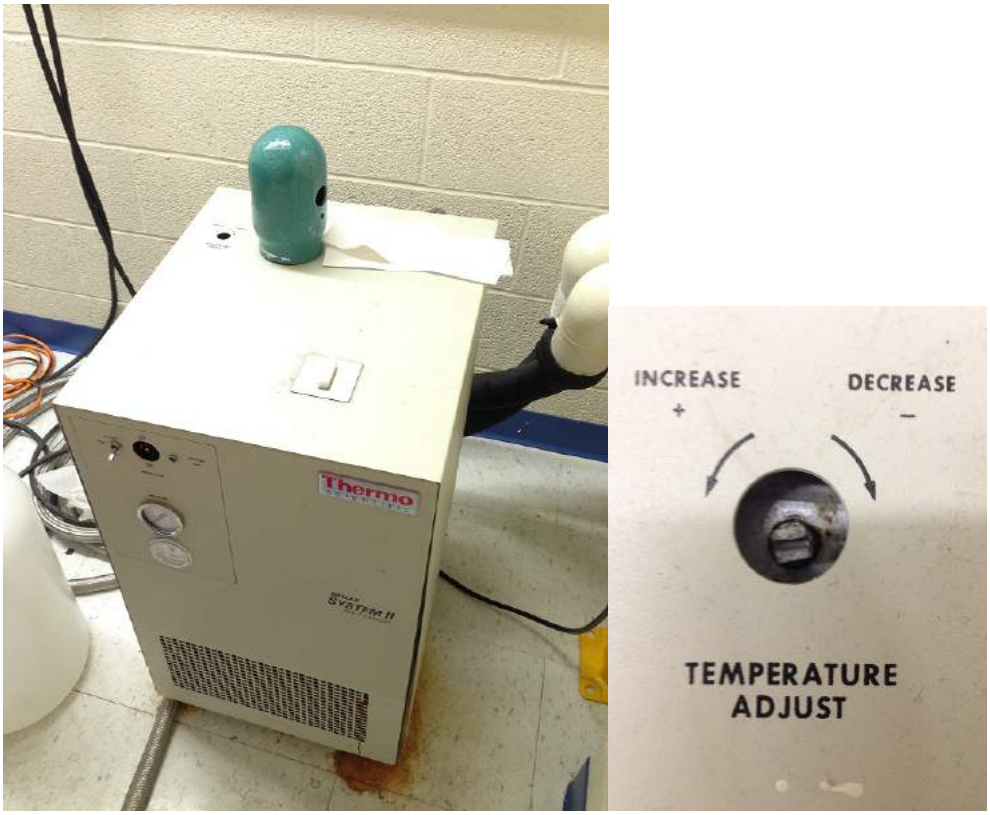


Figure 3-82: The left photo shows the Neslab cooling water heat exchanger system. The lid near the front of the system can be used for filling water. The right photo shows the Neslab cooling water heat exchanger temperature adjustment screw.

## 3.7 Data Acquisition and Control System

### 3.7.1 Control Program

The control program, written in Visual Basic, is used to monitor parameters and control equipment in the crud loop from the computer. The control program usage includes:

- Turning on/off valves 1, 2, 3 in the auxiliary loop

- Turning on/off mini-pump for the auxiliary and deionization loop
- Turning on/off circulation pump for the main loop
- Reading data from the four loop thermocouples
- Reading heating rod centerline and liquid temperature from autoclave control box
- Reading pressure from autoclave control box and auxiliary loop pressure transmitter
- Reading dissolved oxygen, pH, and conductivity data from the Thornton 770MAX measurement equipment assembly
- Saving the data

All these data reading and on/off commands sending actions are done through the Agilent control unit attached to the computer. More information on the agilent control unit can be found in section 3.7.2.1.

Once the control program starts, the scan control is switched on to initialize its operation. The program then starts reading from the circuit board, and clicking sounds are heard. After a set scan interval, this scanning as indicated by repeated clicking. The control program panel 3-2 shows a simplified layout of the crud loop with important equipment in the white boxes. Beside the boxes are the data readings associated with each equipment along with its unit. Additionally, for equipment that can be controlled through the program, the on/off button is provided to turn that equipment on and off. V1, V2 and V3 are valves with electric actuators that can be turned on/off via the green/red buttons. To save the data, the save intervals can be specified in minutes, by clicking on the "start saving data" button. After this is done, the save minutes elapsed will start counting the minutes since the save start. Once the experiment is done, we can click "finish saving data" to stop the count and save data. Data are saved in form of multiple text files to the path specified in the Visual Basic code. The default path is "C:\crud_DATA." Note that the control program is not used for safety at all since the computer can be unreliable.

### 3.7.2 Electronics

Other than the controller box provided by Cormet Oy for the autoclave, the two primary electrical systems in this loop consist of the system controlled by the crud loop relay box, and the system controlled by the heating tape controller box. The crud loop relay box controls most functions in the loop except the heating tapes. The heating tape controller box has the single job of controlling all the heating tapes on the loop. Figure 3-83 is an overview diagram of the IHTFP electronics system. The arrows represent the direction of data transfer. As shown in the diagram, the computer uses Agilent data acquisition and control unit to interface with the loop. The Agilent unit accepts

data from the autoclave control box, loop thermocouples, and the Mettler Toledo sensors. These data are displayed on the computer. The computer control program controls the circulation pump, the pressurizing pump, the mini pump, and the valve actuators, through the Agilent unit and the crud loop relay box. The heating tape controller system controls the heating tapes using data from a dual junction loop thermocouple. The autoclave control box controls the autoclave heater with autoclave element temperature data. In addition, the autoclave control box also reads the autoclave liquid temperature and the autoclave pressure.

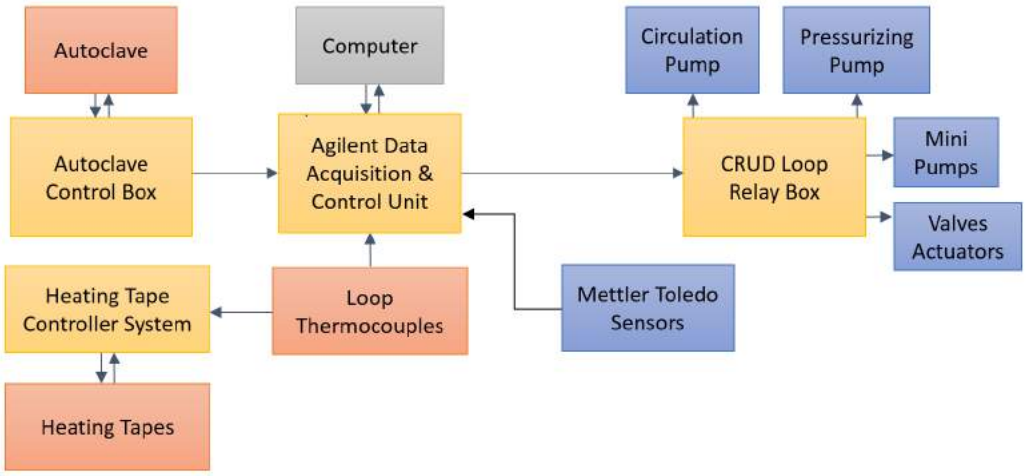


Figure 3-83: Overview electronics diagram of the IHTFP. The arrows represent the direction of data transfer.

#### 3.7.2.1 Agilent Data Acquisition and Control Unit

The Agilent data acquisition and control unit, as shown in figure 3-84, is an interface between the computer and the rest of the loop. As mentioned earlier, the computer's crud loop program can read data from and send on/off commands to the Agilent unit attached to the computer. Specifically, the Agilent unit can use the thermocouple board to read input analog voltages and translate them into digital signals for the computer. Its relay board translates digital on/off command signals from the computer to relay signals that can be used to control loop equipment. All the data inputs used in this loop are analog inputs. All the outputs are on/off command signals. This data acquisition and control unit is manufactured by Agilent with model number 34970A. The multiplexer board used to read data has model number of 34902A. The relay board has model number of 34903A. Its Figure 3-86 demonstrates how the Agilent unit connects to other electronics in the IHTFP. For data reading purposes, data input lines from the equipment are connected directly to the reader board on the Agilent control unit. For sending on/off commands, the Agilent control unit connects to crud loop relay box or valves relay casing which acts as intermediaries.


Figure 3-84: Photo of Agilent data acquisition and control unit's frontside (left) and backside (right).

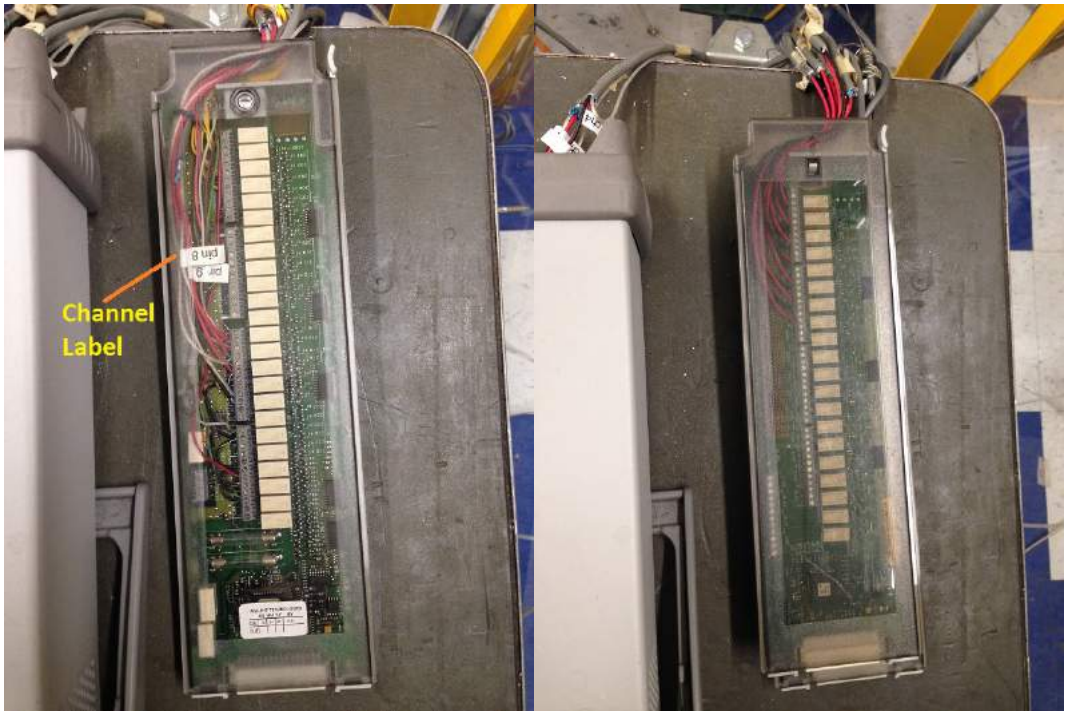


Figure 3-85: Photo of Agilent data acquisition board (left) and relay board (right). Each wire is labeled with the channel it connects to. More information on wiring can be found in subsection 3.7.2.5.

### 3.7.2.2 Crud Loop Relay Box

The crud Loop relay box, as shown in figure 3-87, acts as an intermediary between the crud loop control program and all pumps in IHTFP. The main reason to have the crud loop relay box is that there will be a voltage overload if high voltage equipment wires are wired directly to the relay box. Therefore, intermediate relays are needed to lower the voltage first. The crud loop relay box is a collection of relays used to control the equipment in the loop other than the heating tapes and the valve actuators. It also provides duplex boxes, so it is easy to plug pieces of equipment into the system. The pressure switch is also wired through here to shut down everything in the case of an overpressure emergency. Figure 3-86 demonstrates how the crud Loop relay box connects to other electronics in the IHTFP. In addition, valve actuators relay wires are also wired through the crud loop relay box, which does nothing to it. The reason for putting those connections through the crud loop relay box is to make it easier to disconnect and organize wires when moving the loop to other rooms. Lastly, the crud loop relay box also houses a power supply which powers all relays in the crud loop relay box and the valves relay casing.

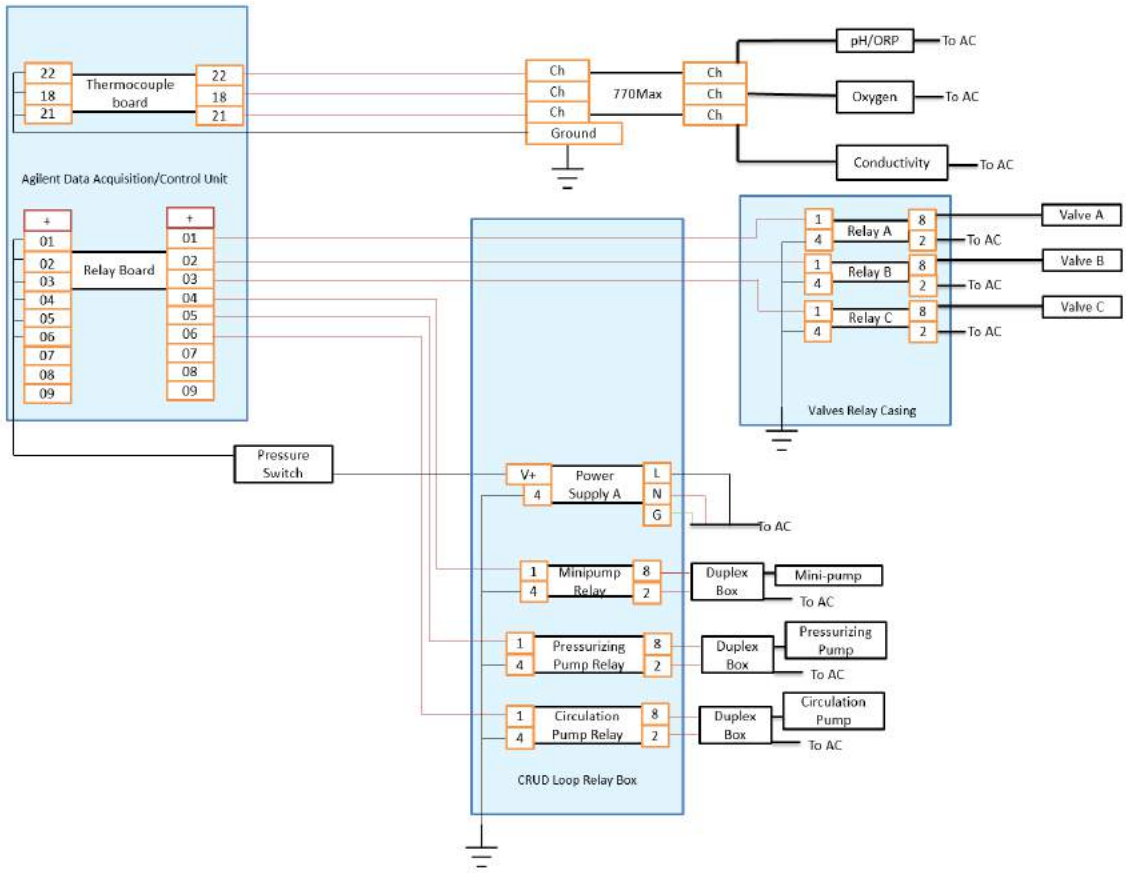


Figure 3-86: This diagram illustrates the simplified electric wiring diagram of crud loop relay box system, valve relay casing, and Agilent data acquisition/control unit.

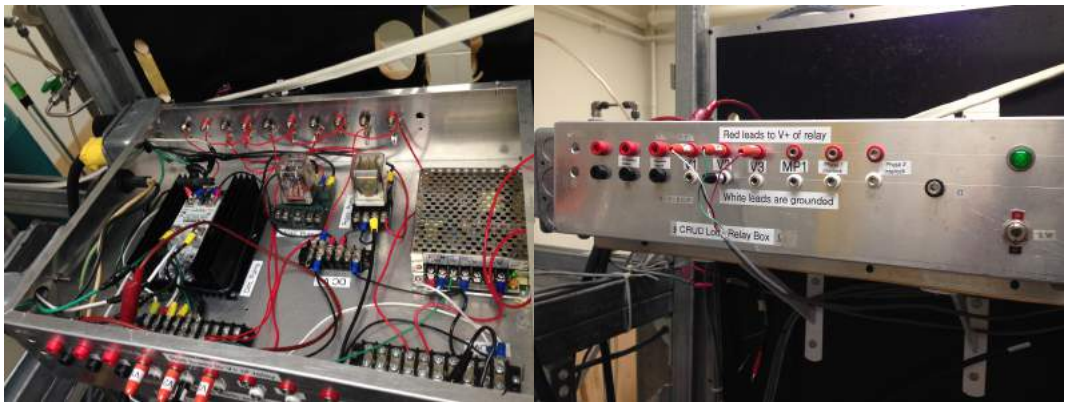


Figure 3-87: Photo of crud loop Relay Box.

#### 3.7.2.3 Valves Relay Casing

Similar to the crud loop relay box, the valves relay casing acts as an intermediary between the low voltage Agilent unit and the high voltage valve actuators. The valves' on/off signals are relayed from the Agilent unit through the crud loop relay box and gets relayed to a higher voltage at the valves relay casing. All of these connections are shown in figure 3-86. Figure 3-88 is a photo of valve relay casing. The three valve relays can be seen on the right-hand side.

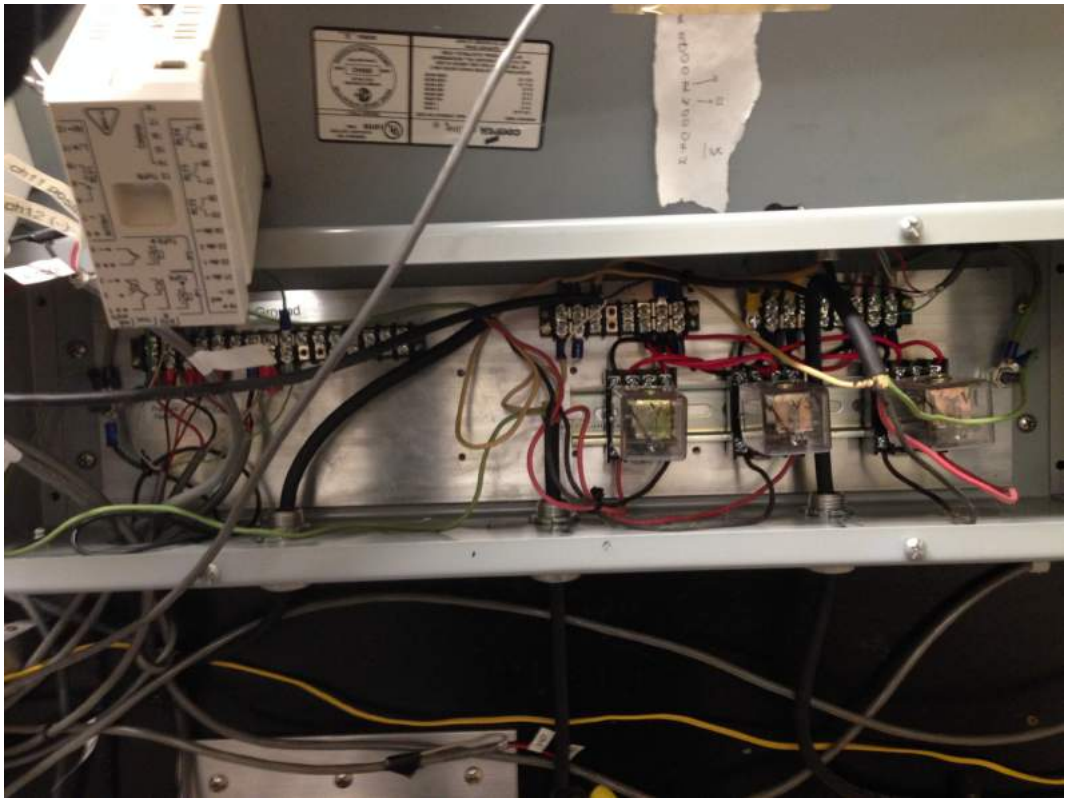

Figure 3-88: Photo of valves relay casing.

### 3.7.2.4 Heating Tape Controller System Wiring Diagram

The heating tape system wiring is set up to control the heating tapes outside the autoclave, as well as to shut down the system in case the emergency or pressure switch activated. The following figure represents the wiring within the control box. The gray box represents the wire coming in from different places. The power is drawn from the 120V AC and the 240V AC lines. The solid state relays (SSR) are intermediate relays that allow the high voltage and current to go through it to the heaters. Without the intermediate relays, the wires in the normal relays will burn out from the high current. Each solid state relay operates with either the 120V AC line or the 240V AC line. The DC power supply provides the power to turn the solid state relays on and off. The PID controller gives on/off signal to the solid state relays by cutting or bridging the DC power supply to the solid state relays. The rest of the system are parts of the latching relay circuit, which is also connected to the emergency button and the pressure switch, as seen in figure 3-89. Figure 3-90 is a photo of the heating tape controller system's casing, with each piece of equipment labeled.

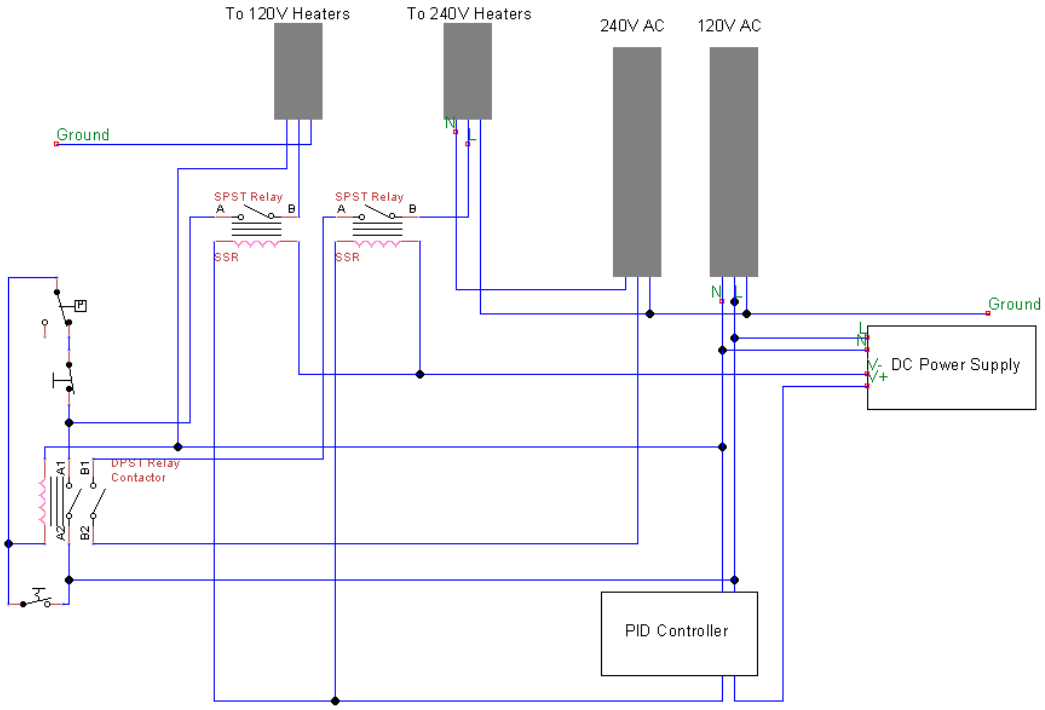


Figure 3-89: This figure illustrates the electric wiring diagram of heating tape controller system box.

### 3.7.2.5 Connecting Plugs

The IHTFP electronics can easily be separated from the Agilent control unit. All connecting plugs on the crud loop are labeled with the socket that it connects to. In the case that the labels are damaged

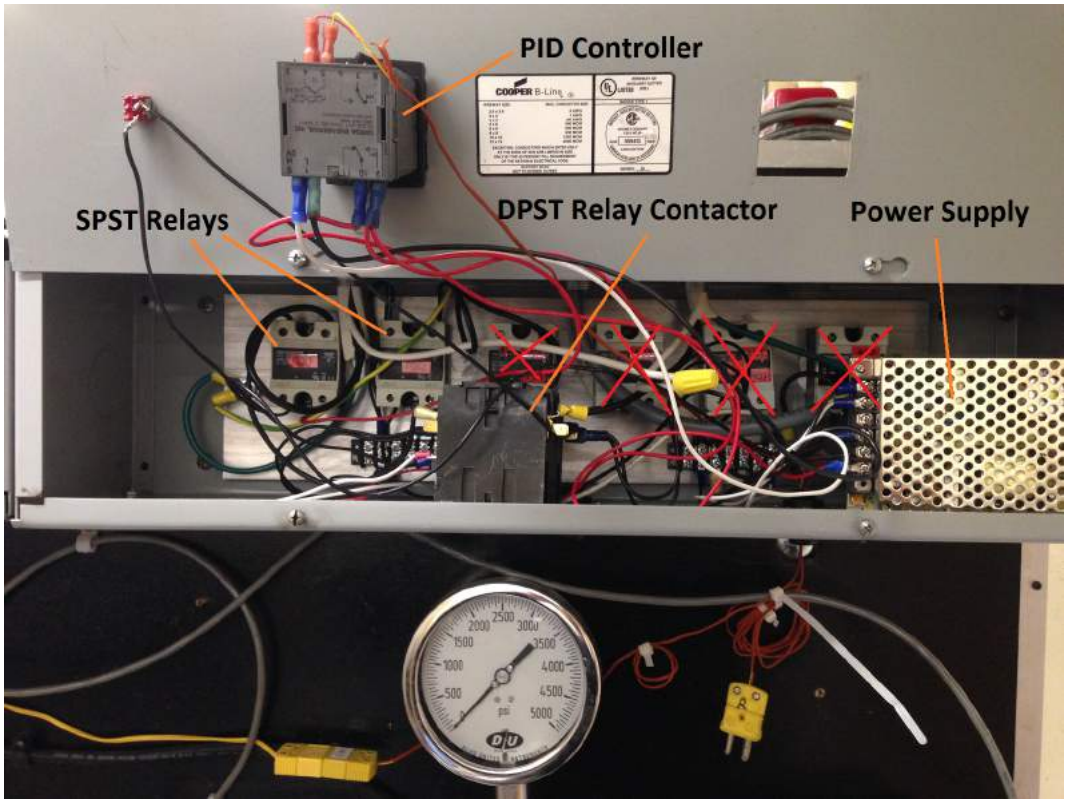


Figure 3-90: The heating tape controller casing with each components labeled. Note that the relays crossed in red are those that are not used.

or lost, the following list gives guidance as to where to connect different equipment. Alternatively, this list can be obtained by looking into the Visual Basic code that makes up the program. The crud-loop relay box part shows the connections that go directly to the crud loop relay box. The crud-loop computer inputs list shows the connections that go onto the reader channels on the board attached to the Agilent control unit.

**Crud Loop Relay Box**

1. Valve 1: Ch 1
2. Valve 2: Ch 2
3. Valve 3: Ch 3
4. Minipump: Ch 4
5. Pressurizing pump: Ch 5
6. Coolant pump: Ch 10

**IHTFP Computer Reader**

1. Temperature before heater: Ch 1, Thermocouple reader
2. Temperature after heater: Ch 2, Thermocouple reader
3. Temperature before cooler: Ch 3, Thermocouple reader
4. Temperature after cooler:Ch 4, Thermocouple reader
5. Differential Pressure: Ch 9, Voltage reader
6. Liquid Temperature: Ch 12, Voltage reader
7. Pressure: Ch 13, Voltage reader
8. Element Temperature: Ch 14, Voltage reader
9. Autoclave Pressure: Ch 15, Voltage reader
10. Auxiliary Loop Flow: Ch 16, Voltage reader
11. Liquid Level: Ch 17, Voltage reader
12. Oxygen: Ch 18, Voltage reader
13. Conductivity: Ch 21, DC current reader
14. pH: Ch 22, DC current reader

#### 3.7.2.6 Heating Tape Controller System Wiring Diagram

The autoclave control box controls the heat output of the autoclave heating rod. Figure 3-29 is a diagram of the autoclave heating rod control system. This system uses element temperature to calculate the power output of the autoclave heating rod. Unlike the loop heating tape which can only turn on/off, the autoclave heating rod's power output can vary from 0 to 100%. This is made possible with the transformer circled in orange on figure 3-29. The power output of the autoclave heater rod can be adjusted by adjusting the voltage output of the transformer. Another important part to note in the autoclave heating rod control system diagram is the two fuses. These two fuses will blow in the case that too much power is drawn, in order to save the system. Power overload usually happens when the heating rod failed from short circuiting. Figure 3-92 is a diagram of the rest of autoclave controller box, which reads liquid temperature and pressure, display them on controller's screens, and output those signal to the computer.

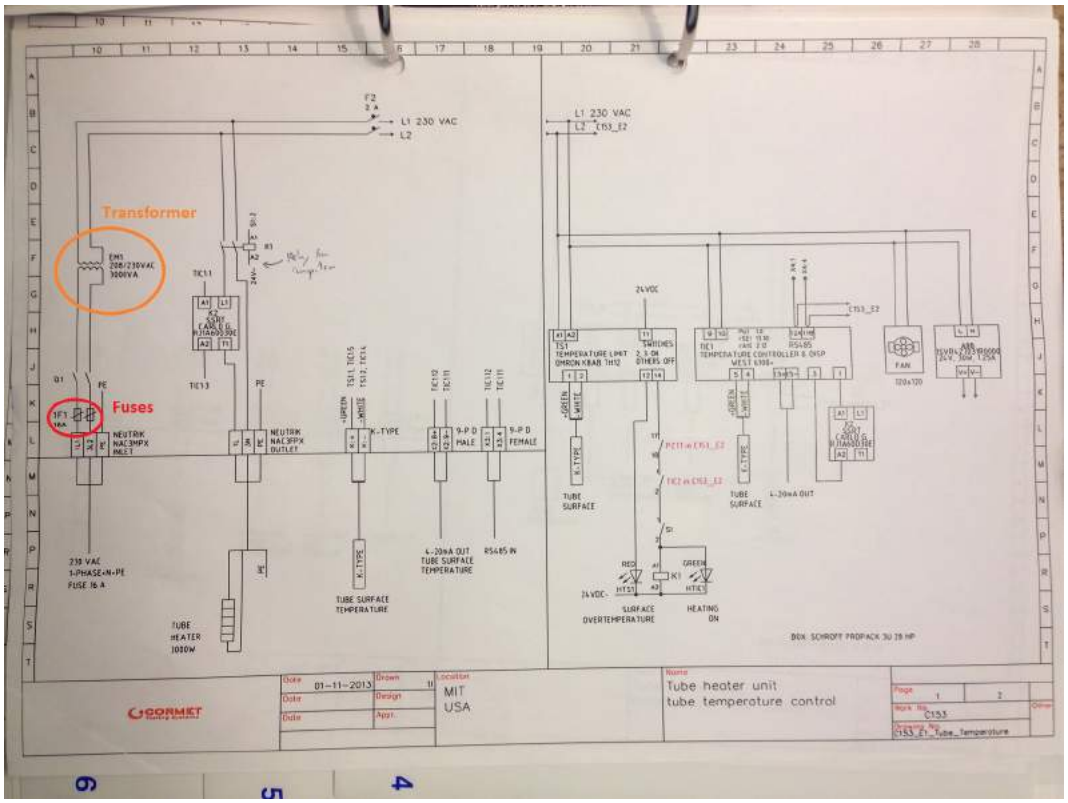


Figure 3-91: Diagram of the autoclave control box temperature control system. Transformer, circled in orange, enables the variable adjustment of autoclave heating rod's power. Fuses, circled in red, will blow to save the system if too much power is drawn.

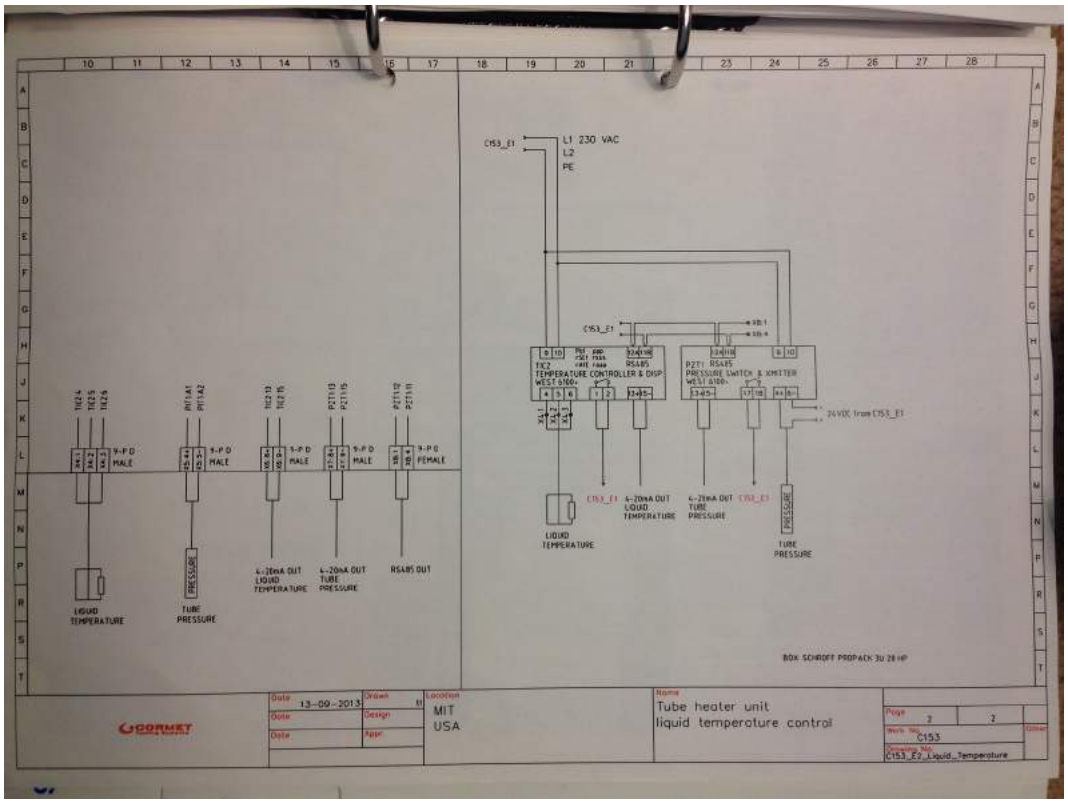


Figure 3-92: Diagram of the autoclave control box temperature control system.

## 3.8 Safety Systems

Running any system at conditions similar to that of PWR is dangerous. In the crud loop, multiple redundant safety systems exist, with their primary task to ensure that no one operating the system will be injured. Additionally, some safety systems are there to ensure that there is no equipment damage in unexpected circumstances. The figure 3-6 shows the diagram of the safety systems within the crud loop. The subsections below will delve into the details of the safety systems in the crud loop.

### 3.8.1 Safety Relief Valves

There are multiple redundant safety valves within the system so that at least one should be functional in case other valves fail. There are three safety valves. The first one is attached directly to the autoclave. The second one is attached to the top part of the loop. The third valve is internal to the pressurizing pump. The safety relief valve on the loop will be release once pressure reaches 3,000 psi. The pressure relief valve attached to the autoclave will also release at 3,000 psi. The internal pressure relief valve in the pressurizing pump will release at 170 bar. Section 3.6.1.1 gives more detail of the R3A-F safety valve attached to the autoclave. Figure 3-93 shows the safety valve

attached to the pressurizing pump. Lastly, section 3.6.1.5 provides further detail on the 5RVP9072 safety valve attached to the main loop.

Figure 3-93: Safety valve attached to the pressurizing pump is circled in orange.

### 3.8.2 Pressure Switch

The pressure switch will shut down the electrical system once its set point is reached. The pressure switch's set point can be adjusted by opening up its covering and adjusting the bolt within. The last adjustment of pressure switch will cause it to trigger at approximately 2,500 psi. At that point, it will cut the power to the pressurizing pump, and the pressure should not increase further to trigger the safety valves. Figure 3-55 shows a photo of the pressure switch. Figure 3-56 illustrates how the pressure switch works. Section 3.6.1.5 delves into deeper detail about our pressure switch.

### 3.8.3 Closed Room

The system is placed in its own specialized room to prevent any danger it might pose to other lab members. The room is equipped with specialized tubing connected to a safety valve that will shoot steam straight to a vent on the building's ceiling in the case emergency safety valves open. Figure 3-94 shows this specialized vent system. When the loop is running, this room will be locked with a "danger" sign posted on the door.

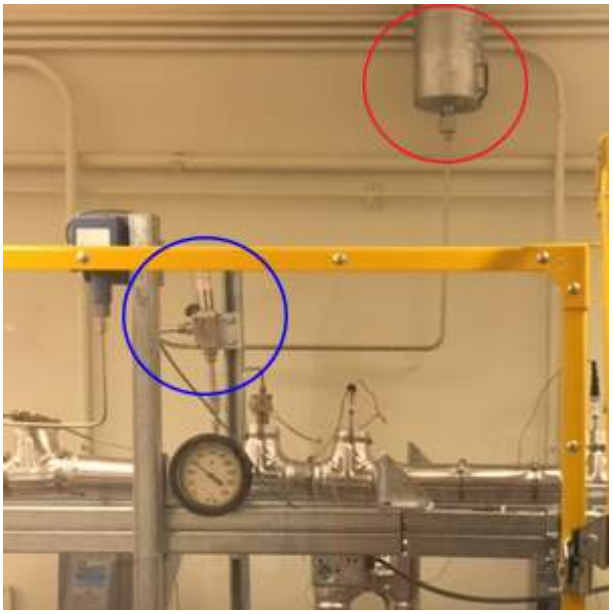

Figure 3-94: Specialized steam vent system. The main loop's safety valve, circled in blue, is connected to the steam vent, circled in red.

### 3.8.4 Polycarbonate Shield

The loop also has a polycarbonate shield placed around the control computer to prevent any danger from the loop in case of a steam leak or if a flying object is ejected by a pressure release. Polycarbonate is the same material that is used in the security industry for bulletproof purposes, so it is highly unlikely that any flying object will penetrate it. Even with the polycarbonate shields around the workstation, it is not recommended to stay in the room while the loop is running. Figure 3-95 is a photo of a polycarbonate shield.

### 3.8.5 Electrical System

All the electrical plugs in the room are connected to the breaker. Therefore, in the event of a short circuit, the breaker will automatically shut down the whole system, preventing damage to the circuit or a nearby human. The autoclave control box also comes with its own internal breaker and two fuses for this purpose. Nevertheless, the loop operator must be sure to unplug all equipment when working with any of the control boxes' internals.

## 3.9 Operation of the IHTFP

Now that we have presented most information regarding how the loop works, and what each piece of equipment does exactly, this section will pull everything together and set out a procedure on how to operate the loop. Through our experiences operating the loop, we have found many nuances that

Figure 3-95: Polycarbonate shield panel.

contribute to a smooth system operation; most of these are present in the following sections. Figure 3-96 summarizes the operating procedure of the IHTFP.

### 3.9.1 Precautions before operating the loop

At the outset, to manipulate anything in the loop, always check that all the heating systems and the pressure systems are properly closed. This includes not only checking the computer screen, but also physical gauges, as the computer may exhibit error. All unused electric plugs should be unplugged. In addition, also be sure to wear proper protection when working with chemicals related to the loop. Nickel oxide particles used as the crud precursor are carcinogens and exposure to them should be very limited. The ceramic wool insulation dust can cause lung complications.

### 3.9.2 Preparing the Water

To imitate the water chemistry within nuclear reactors, there are several steps that have to be taken in preparing the water. They start with filling up the water tank and deionizing it, then removing its dissolved oxygen. This is done because, before adding any chemical into the system, we need to have very pure water that must be properly deionized with dissolved oxygen removed. After the water has been cleaned, boric acid, lithium hydroxide and nickel oxide crud particles can be added.

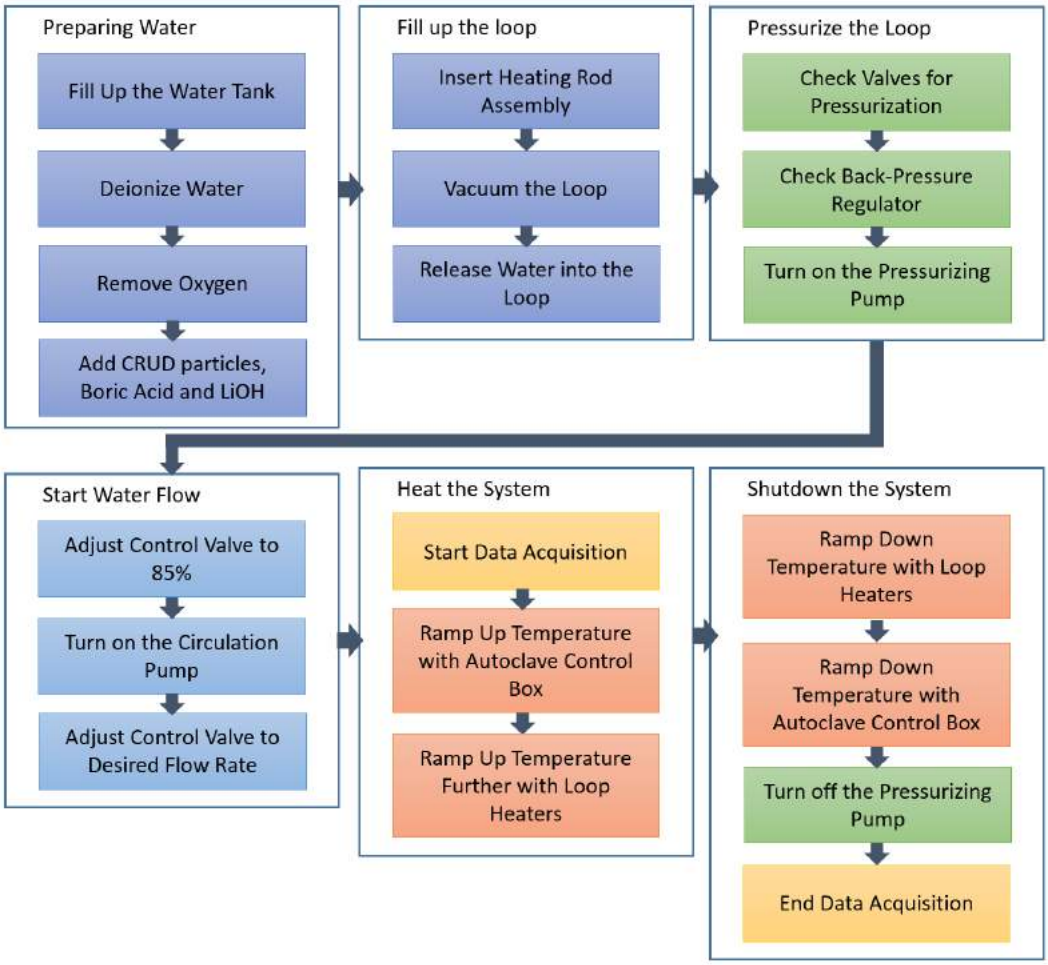


Figure 3-96: Diagram summarizing the operating procedure of the IHTFP.

#### 3.9.2.1 Filling Up the Water Tank

Before filling up the water tank, make sure that all the leftover water is drained. The tap water can be used to fill the tank since we have the mixed-bed ion exchanger attached to the water tank. To fill the tank, first, remove the lid of the water tank, then fill the water tank using any type of water container available. The usual way the loop is filled is by using a plastic tank to transfer water from the main lab.

#### 3.9.2.2 Deionizing the Water

The deionizing loop in the back of the auxiliary loop board is used to deionize the water in the loop and bring the conductivity down before any additive chemical is added. To deionize the water, turn the valves on the deionization loop so that water is redirected into the deionization columns. Then turn on the mini pumps on the control program. The deionization loop pump will drive the water through the deionization column where the ion-exchange beads will remove ions from the water. The ideal amount for conductivity before adding other chemicals should be around 0.09 $\mu S/cm$. This may take up to two days to complete depending on the conditions of the ion-exchanger columns.

#### 3.9.2.3 Removing Oxygen

In the crud loop, the target dissolved oxygen is less than 5 ppb similar to the reactor. The oxygen can be removed by bubbling argon into the tank. We usually use 99.998% high purity argon for this purpose. The connections on top of water tank provide a way to connect to argon tank for this purpose. To bubble argon, simply connect the tube fitting from the argon tank into the middle connection on top of the water tank. Make sure that another valve on top of the water tank is open to allow for a gas outlet.

To remove the dissolved oxygen, first make sure that the argon tank is hooked up to the water tank's bubbler-port which is at the center of the water tank lid. Then check if the exhaust gas port, which is the port on the side of the water tank lid with valve attached, is properly connected to the gas exhaust system. To let gas bubbles into the water tank, slowly turn on the gas valve, first by turning the knob on the gas regulator, so the knob moves outward. When the knob moved out to the point where it almost gets detached, we can start to open the gas tank knob very slowly. After the pressure on the high-pressure reader jumped up, stop turning the gas tank knob, and start to turn the gas regulator knob slowly, so it moves inward toward the gas regulator body. At some point, the gas exhaust flasks will start bubbling. Usually, there is a delay between when the knob is turned and when the flask bubbles so turn a little at a time and wait for 30 seconds or so each turn. When the flask bubbles very slowly, turn the knob back out a bit. The best point the regulator knob should be at to save the most gas is where gas bubbles once in a long time, and even without the bubbles, the dissolved oxygen level does come down. One trick to adjust the flow rate of the argon

gas is by using the valve at the water tank lid's center. This valve will give a much better precision than using the gas regulator valve. The markings on the valve can also be used as guidance to get the right flow amount.

Next, we want to redirect the water from the water tank into measurement system so we can get the dissolved oxygen measurement and see it decrease to the point we want. Make sure all the manual valves that allow the water from water tank through the measurement equipment are open. Then redirect the valve just before the measurement equipment to let the water flow from the water tank to the measurement equipment. When done, open the measurement pump from the computer user interface to pump the water from the water tank. Now the measurement of water properties in the water tank can be read from the computer user interface. Wait as the dissolved oxygen concentration lowers to the proper amount. When the dissolved oxygen is the proper amount, the gas tank valve and the gas tank regulator valve should be closed. Then disconnect the tube fittings from the top of the water tank and reconnect the fitting to the connection it was at before it was used for oxygen removal.

#### 3.9.2.4 Adding Crud Particles, Boric Acid and Lithium Hydroxide

Once the oxygen and ions in the water have been removed, the crud particles, the boric acid, and the lithium hydroxide can be added. Usually, 20 $\mu g/ml$ crud particles are added. The calculation of how many grams of crud particles that should be added, is done by using basic unit conversions combined with the fact that the water at the full tank is around 120 liters. Note that the calculation should also be adjusted for the density of water which will decrease a good amount going from 25 ºC to 310-320 ºC. With completely full tank of 120 liters, and operating temperature of 310 ºC, the amount of chemicals to add are the followings: 3.53 g of nickel oxide (20 $\mu g/ml$), 170.7 g of boric acid (1400 ppm), and 0.3657 g of lithium hydroxide (3 ppm).

The boric acid is added to the system to simulate the reactor condition. In the commercial PWR, boron is added to control the number of neutrons. For our experiments we use 1400 ppm of boron for the reasons explained in "pH Measurement" section 3.5.4. The lithium hydroxide is added to partially neutralize the boric acid both in the reactor and in the crud loop. For the crud loop, 3 ppm of lithium hydroxide is usually added. The chemical injection port on the top is the port sealed with rubber, as shown in figure 3-97. Injecting the solutions through the rubber with a syringe is the easiest way to add the chemicals without introducing oxygen into the system. Another alternative approach is to remove the small rubber seal as well, for an easier injection. A slower alternative approach is to remove the top of the tank and pour in the solution of nickel oxides crud particles, boric acid, and lithium hydroxide.

In all experiments conducted for this thesis, nickel oxide particles used are nickel(II) oxide nanopowder with particle sizes less than 50 nm and purity of 99.8%. Boric acid used has the

following impurities: <0.0001% of Arsenic, 0.0005% of Calcium, 0.0002% of Chloride, <0.0005% of heavy metals (such as lead), and 0.0005% of other impurities that are insoluble in methanol. Lithium hydroxide used has 99.995% purity.

Figure 3-97: Top lid of the water tank. The chemical injection port is circled in orange.

### 3.9.3 Top Flange and Heating Rod Assembly Insertion

To insert the top flange and the heating rod assembly, slowly lowers the heating rod down the autoclave test section without letting the heating rod touch the autoclave or at least touch as little as possible. Then, place the cylinder that is covering the heating rod into its hole, holding the heating rod in place. Adjust the graphite gasket on to its spot, then lower the whole top flange assembly down to make it sits on the graphite gasket. After that make sure all of the following procedures are carried out to make the autoclave ready for operation:

- Put together the top flange assembly as shown in figure 3-98.
- Insert the whole assembly onto the autoclave opening shown in figure 3-99.
- All six large bolts, shown in figure 3-98, must be tightened. When tightening the large bolts, tighten them a bit a time and go around in a circle. If one bolt is tightened very far in while other bolts are still quite loose, there will be an imbalance in load on the soft graphite gasket which can damage the gasket. The autoclave manufacturer does not specify the exact torque to use for this purpose. In our experience, we tighten the bolts as hard as we can using just an Allen wrench.
- The top plastic cap's bolts, shown in figure 3-98, must be tightened.
- The top cap holding the heating rod in should be screwed into place and tightened.
- The cooling line to the top flange, shown in figure 3-98, must be connected.

- Make sure that the thermocouple line and the heating rod power line are plugged to the sockets shown in figure 3-100.


Figure 3-98: Photo of top flange heating rod assembly. Each component mentioned in the insertion instruction is labeled.

Figure 3-99: Photo of the autoclave's top opening where the top flange can be inserted.

### 3.9.4 Filling Up the Loop

It is crucial that after the loop is filled, there should be little to no air inside the loop. Having even a little amount of air inside the loop cause the loop to pressurize very slowly. Two ways that were used to achieve this includes using the vacuum pump to get rid of the air and using the gas to push the water from the tank out through the loop to replace air in the loop with water. The vacuum pump method is preferred over the gas method since it requires less work and is usually better at making sure that there is no air pocket in the loop.

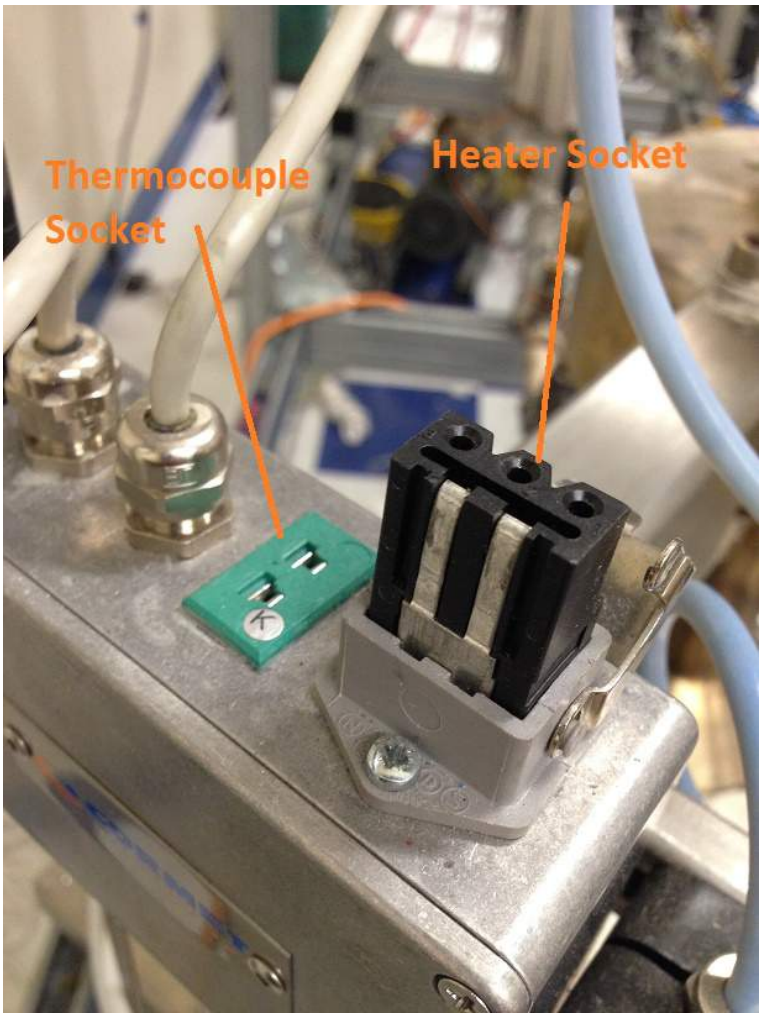


Figure 3-100: Photos of sockets where the heating rod's wiring should be plugged to.

**Filling the loop with the vacuum pump method** For the vacuum pump method, start with making sure that there is no water left in the loop that will damage the vacuum pump. Then, close all the loop drain valves as well as the valve connecting the loop to the water tank. After that, connect the tubings from the vacuum pump to the valve on top of the loop near the water tank. Open that valve, and vacuum the loop for at least 20 minutes to clear any air inside. After that close the valve to the vacuum pump and open the valve leading to the water tank to let the water fill the loop for around 5 minutes. If there is no leak, the loop should be filled with water without any air gap. The valve connecting the water tank directly to the loop can then be closed.

When first starting up the vacuum pump by plugging it into the wall, it is recommended to stand back in the case that pump has accidently been filled with some water. In that case, the pump may splash out a huge amount of oil. If the pump does not turn on when plugged into the wall, try resetting it with the red button on the back of the pump. One trick that works quite well with when using the vacuum pump method is to turn the black valve near the sample cooler, so the flow toward the back-pressure regulator is blocked. Doing this will prevent the water from rushing in through the back-pressure regulator when doing the vacuuming. If this black valve leading to sample cooler was closed for vacuuming, make sure that it becomes open when pressurization starts, or it will cause a pressure overrun.

**Filling the loop with the argon gas method** For the gas method, starts by connecting the tube from argon tank to the inlet near the side of the water tank. Then on the crud loop, open the top valve near to the water tank as well as the valve connecting to the water tank to let the water fill up the loop. Adjust the gas tank valve to pressurize the water tank, so the water is pushed out to replace air and fill the whole loop. When the loop is filled, and water came out of the top valve, close the top valve. Then go through each connection to the equipment that may have an air gap in them and release its nut to let water pushes all the air out.

### 3.9.5 Pressurizing

#### 3.9.5.1 Conditions required

Before pressurizing, make sure that all connections are tight and all the equipment are operational. Other than that, check to make sure that all the valve positions lie in the proper spots. The following figure 3-101 show which valves should be checked before commencing pressurization procedures. Other than the valves from the figure 3-101, if the black three-way valve 3-102 between the sample cooler and back-pressure regulator was closed for vacuuming, make sure that it is open. Otherwise, there will be a pressure overrun.

Next, make sure all the pressure readings are working correctly. There are four places on the crud loop where the pressure can be monitored, which includes the two pressure gauges and the

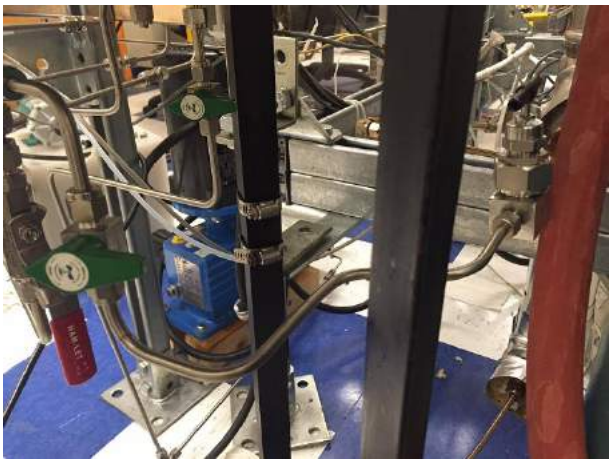

Figure 3-101: This photo shows the two green valves and the fill valve that should be checked before pressurizing. The nearer green valve on the left and the black needle valve on the right should be properly closed when pressurizing. Moreover, the farther green valve in the middle going to the pressurizing pump must be open for flow. Otherwise, the pressurizing pump may be starved of input water leading to damage.

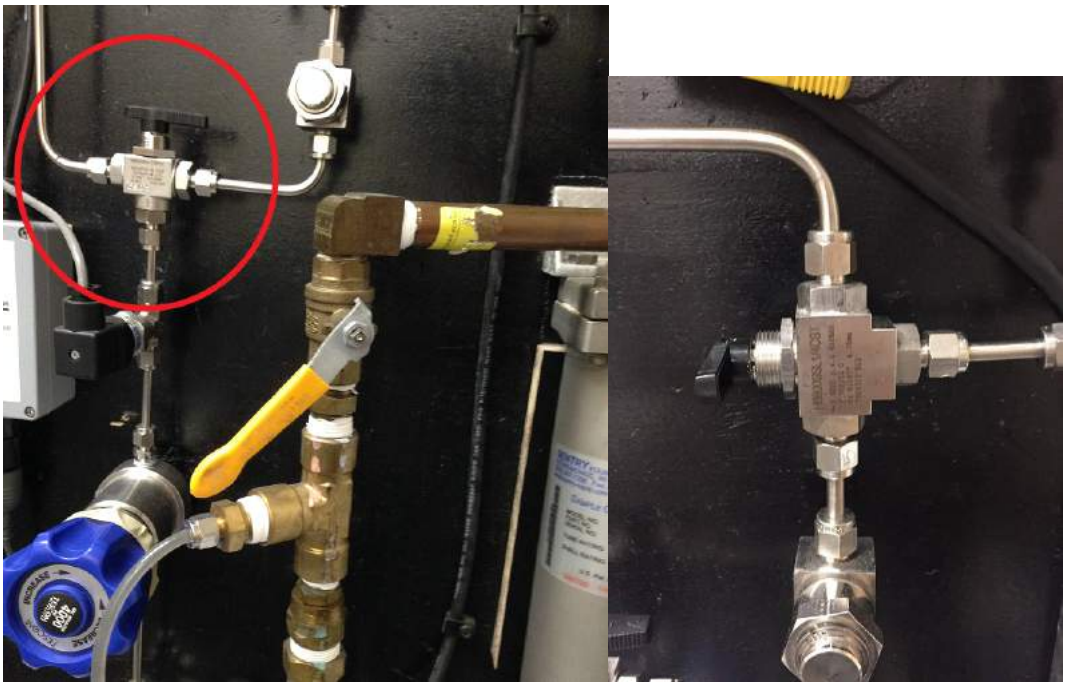

Figure 3-102: The left photo shows the black valve, circled in red, that connects to the sample cooler and the back pressure regulator. The valve can be closed in the position shown in the right photo.

two pressure transmitters. The two pressure gauges include one on the top mid section of the main loop and another on the auxiliary loop. The pressure transmitter data can be read from both the autoclave controller for the autoclave pressure transmitter or the computer. The redundant measurements are done to make sure that the whole loop is getting pressurized, as well as for the pressure reading comparison.

#### 3.9.5.2 Back-pressure regulator valve position

In the case that the back-pressure regulator's position is unknown, turn the back-pressure regulator out all the way down to a low pressure for safety. In the case that the back-pressure regulator valve remains unchanged from the last experiment and the current experiment requires the same condition, there is no need to adjust the back-pressure regulator during start-up.

#### 3.9.5.3 How to begin pressurizing

After all of the necessary conditions are met, the pressurization can commence. Simply go to the control program and click the pressure pump button to turn it on. If everything goes well, the pressure displayed on the autoclave heater controller box, the computer screen, and the gauge will begin rising. It is recommended to look at the autoclave's heater controller box's panel as that usually gives the quickest and the most accurate reading of pressure.

If the back-pressure regulator was set to the lowest pressure, slowly turn up the pressure, then wait for the actual pressure to catch up. Repeat this process until the pressure reached the desired point. Otherwise, if the back-pressure regulator was left at the position from the last experiment, watch closely as the pressure rises with the mouse on the pressure pump button on the control program ready to turn the pump off if there is pressure overrun.

#### 3.9.5.4 Start data acquisition

Data acquisition can commence once the loop has been pressurized. To start data acquisition, put in 15 minutes or any other save interval preferred in save interval box, then press the "Start Saving Data" button. At the end of the experimental run, click on "Finish Saving Data" to stop the data reading interval and record the data to the file. After that, check if the data were properly saved by going to the save path specified in the Visual Basic code. The default path is "C:\crud_DATA."

### 3.9.6 Flow Control

After the loop is pressurized, the flow should be turned on before the loop heating starts. Turning on the flow will distribute the heat more evenly across the loop. To start the flow, adjust the control valve 2 to around 85% closed and turn on the circulation pump. Adjust the control valve opening

until the differential pressure regulator reads the desired value. The control valves' openings can be adjusted via its PID controllers on the auxiliary loop. In a manual control mode, the higher percent on the control screen corresponds to a smaller control valve opening.

### 3.9.7 Heating the System

Once the water inside crud loop has been pressurized to the required point, and the flow in the loop is stable, the loop will be ready for heating. Heating the loop to PWR conditions requires both heating from the autoclave and heating from the heater tapes. This section will give guidance on how to heat up the system. It will provide information on how to operate both the autoclave heater rod controller, as well as the heater tape controller.

#### 3.9.7.1 How to Operate Autoclave Heating Controller

The autoclave heating system that is used to control the autoclave has three mounted controllers, one for the heating element temperature, one for the liquid temperature and one for the pressure. The heating element temperature is the value that will be used as the main control parameter. The others can only be used to set a limit to the pressure and the temperature. The following paragraphs describe the basic functions needed to control the West 6100+. It provides just enough information to get started on using the West 6100+ control unit. For detailed information, the West 6100+ documentation, available online, has an extensive list of what could be done with it.

There are four buttons from the left to the right of the controller panels including the auto/manual, the down, the up and the return button. These buttons can be used in a combination to achieve more functionalities. The default screen, as shown in figure 3-103, will display the current temperature (ºC) on top and the set point temperature (ºC) below. This default screen is known as the operation mode. The first button auto/manual allows the user to switch between the manual and the automatic control. In the manual control mode, the power is set to an exact percentage. In the automatic control mode, the controller will automatically adjust the power output percentage so that the temperature will reach the set point established by the human operator. In the IHTFP's case, automatic control is always used. Always be very cautious about switching to manual control. When switching to manual mode, the controller will maintain its power output. Therefore, when the power is 100% during the automatic mode, the 100% power trend will continue, which could quickly lead to film boiling and heater burn out in a low-pressure setting. The up and down buttons are for the adjustment of the current adjustable number displayed on the screen.

In any mode, pushing the return button will allow the user to navigate the functionalities within the particular mode. In the operation mode, the return button will allow the user to investigate and set the target temperature set point (SP), the current temperature set point (SPrP), and the temperature ramp point (rP). A human operator can adjust these set points. In automatic mode,

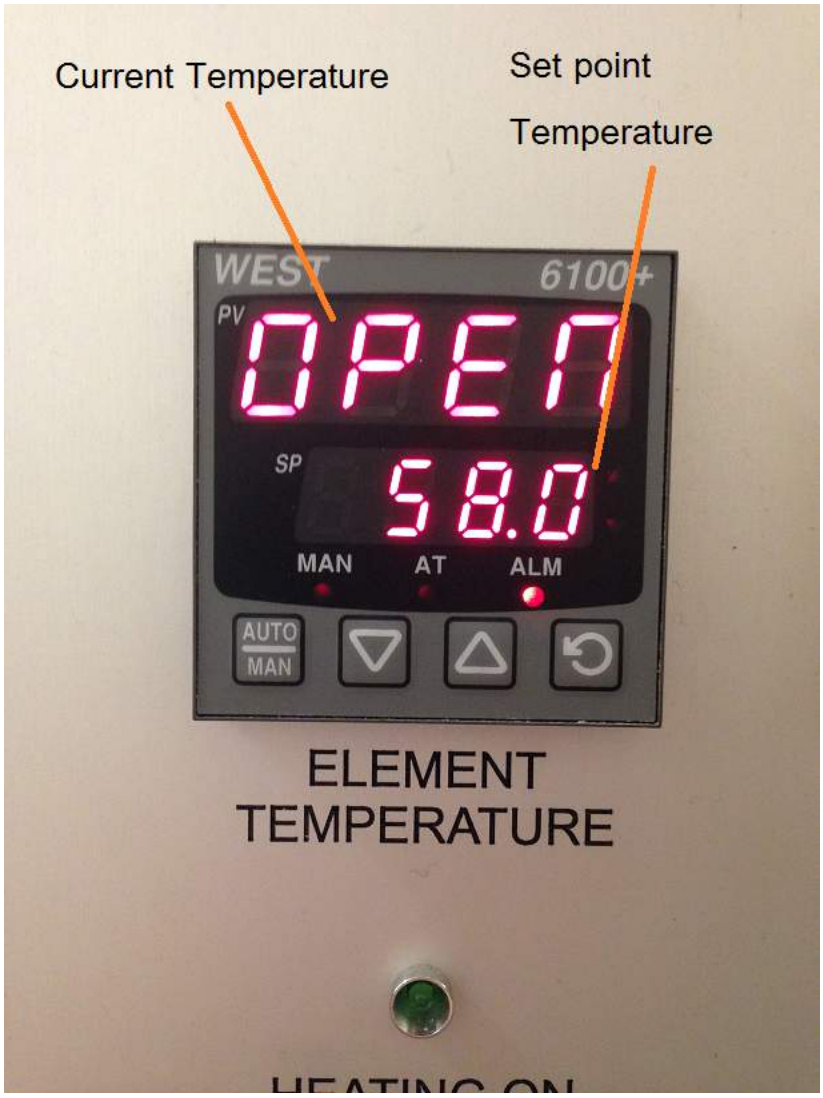


Figure 3-103: West 6100+ default control screen that displays the current and set point temperature. Note that the current temperature displays "OPEN" because the loop was shut down with heating rod thermocouple detached.

the controller will adjust the power so that the temperature will reach the set point. Once the target set point is changed, the current set point that the controller is trying to match will not become the new target set point right away. It will slowly ramp up to target set point according to the speed set by the ramp point (rP). The speed set by ramp point is in the unit of degree Celsius per hour.

The mode menu can be accessed by pushing the up button and the return button at the same time, then using the up/down buttons to navigate the menu to see other modes. Pushing the return button on any mode will swap the controller into that mode. Moreover, from within any mode, pushing the up button and the return button at the same time will take the operator to the mode menu. The menu will start with OPtr which means operation mode, the home mode of the controller. Other modes include the setup mode (SEtP), the configuration mode (ConF), the information mode (inFo) and the auto-tune mode (Atun). For most usages, the operation mode and the setup mode are the most useful. The operation mode is the default display mode, while the setup mode can be used to adjust the PID parameters. To find out more about adjusting the PID controller for proper parameters in the case of manual adjustment, consult the documentation of West6100+ control unit.

#### 3.9.7.2 How to Operate Heating Tapes

The Omega CN9000 temperature controller controls all of the heating tapes. Since the temperature difference across the loop is not very high, and we are operating the heaters at far below their maximum temperature, we use only one temperature controller to control all the heaters in the loop for simplicity. The first heating system is connected to a latching relay. Connecting the system to the latching relay means that if the system was previously shut off, the latching relay button, on the same control box as the Omega CN9000 temperature controller, must be manually switched on by a human operator for the heating system to work again. Before trying to turn on the latching relay, also make sure that the red emergency button is not in off mode. If the latching relay system successfully turned on, a clicking sound will be heard once when the latching relay button is pressed down. If there were two clicking sounds when the latching relay button was pressed, and when the latching relay button was released, it is likely that the emergency button is still in an off mode or the circuit has been damaged. Once the latching relay is properly turned on, the Omega CN9000 temperature controller can be used to control the output of all the heating tapes on the loop.

The controller is also attached to the dual junction thermocouple on top of the crud loop near the autoclave. Knowing the temperature of only one part of the loop is enough for temperature control in this case because the temperature difference across the whole crud loop with water flowing in normal circumstances does not exceed 2-3 $^{o}$C. The Omega CN9000 temperature controller does not do variable control heating. It will only turn the heater on/off according to the PID functions programmed into it. As a result, the heating tape temperature will fluctuate significantly. The temperature of the loop heating tapes can be adjusted manually on the CN9000 temperature controller.

By pressing the star key on the Omega CN9000, the current temperature set point will show up. By pressing both the star key and up/down key on the Omega CN9000, the temperature set point can be adjusted.

#### 3.9.7.3 Heating up the System

When heating up the system, always make sure that the temperature does not rise too fast. When the temperature rises too quickly, the thermal expansion of connections anywhere in the loop, especially in the autoclave, could expand at a different rate causing a leakage. To achieve the slow temperature rise, the operator can use the autoclave heating rod with a variable heat adjustment to heat up the system in the beginning until the temperature starts to plateau. When that happens, turn on the heating tapes, and set a new target temperature for the autoclave heating rod. Let the system continues heating until the required point. From our experience, ramping the temperature faster than 100 ºC per hour could lead to leakage that can be seen in form of steam rising from the loop, especially from the autoclave. Figure 3-104 is a flow diagram showing how to heat up the IHTFP.

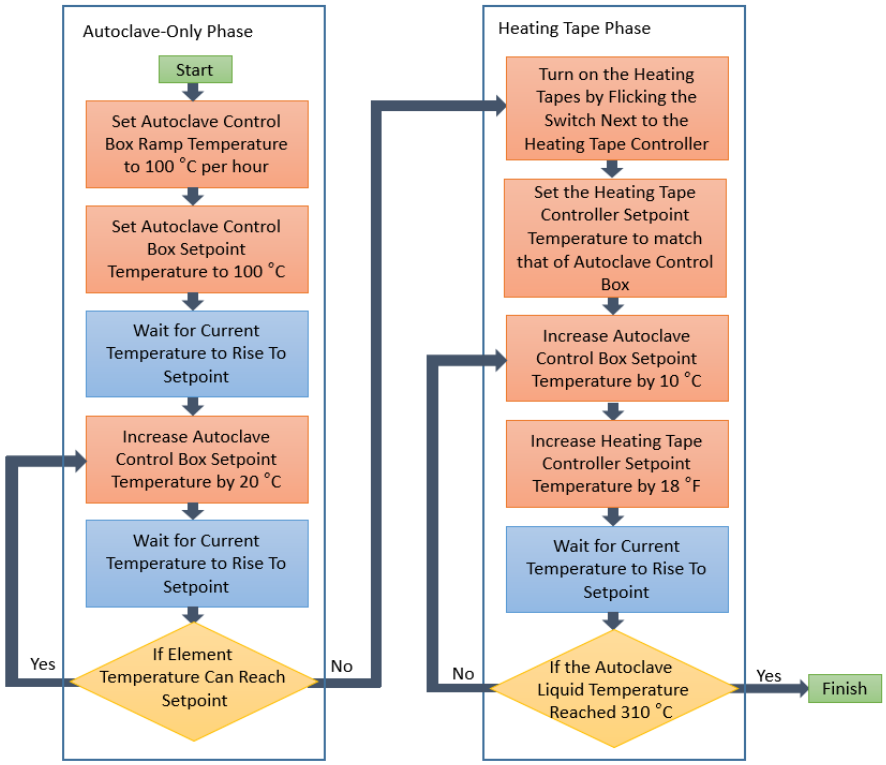


Figure 3-104: Diagram summarizing how to heat up the IHTFP.

### 3.9.8 Cooling the System

When cooling down the system, make sure that system is not cooled down too quickly. Powering down the temperature ramp is limited by the possibility of the water liquid flashing and leaking from an unequal thermal contraction in the equipment. When the water is cooled down too rapidly, and the pressurizing pump cannot keep up, the water in the system can flash to steam which can potentially damage to the circulation pump. The circulation pump has its steam vent to protect itself. This steam vent will shoot out steam in the case of flashing. Cooling down too rapidly will also cause some equipment to contract faster than others. This different amount of contraction can lead to a leak, or even worse, a broken Xpando seal which is tough to fix. To cool the system down slowly, start with decreasing the temperature on the Autoclave control box since the autoclave has a variable heat resistor. The usual speed the loop is powered down is at 200 $^{o}$C per hour.

### 3.9.9 Depressurizing the System

Once the system has been cooled below 100 $^{o}$C, it can be depressurized. Depressurizing the system involves just shutting down the pressurizing pump from the control program screen and waiting for the pressure to come down. Even without adjusting the back-pressure regulator, the pressure will usually come down on its own. After the loop has been depressurized, do not drain the loop until the water hits around 40 $^{o}$C to avoid any hot water splash burn.

### 3.9.10 Draining the Loop

The loop contains two valves on the bottom of the loop for draining water, as well as a Swagelok cap that can be taken off to let the water out. These two drain valves and the cap are shown in the figure 3-105 below.

When draining the loop, be sure to close all the valves leading to the loop to prevent the water from rushing in from the water tank. These valves to the water tank are the valve leading to pressurizing pump, the valve between the sample cooler, and the valve at the back-pressure regulator's input. Figures 3-101 and 3-102 show the valves that should be closed during the draining to avoid water rushing in from the water tank. Figure 3-101 shows the three valves which should be closed. The closer green valve and the black needle valve are on the fill line and lead directly to the water tank. Therefore they should be closed. The farther green valve connects the water tank to the pressurizing pump. This valve should be closed as well since the water can seep through the pressurizing pump into the loop. The valve in figure 3-102 should be closed because water may actually seep backward through the back-pressure regulator as well.

After all the valves are in the right position, some parts of the loop must also be disconnected to let the air inside the loop. The input air will replace water allowing more water to be drained.

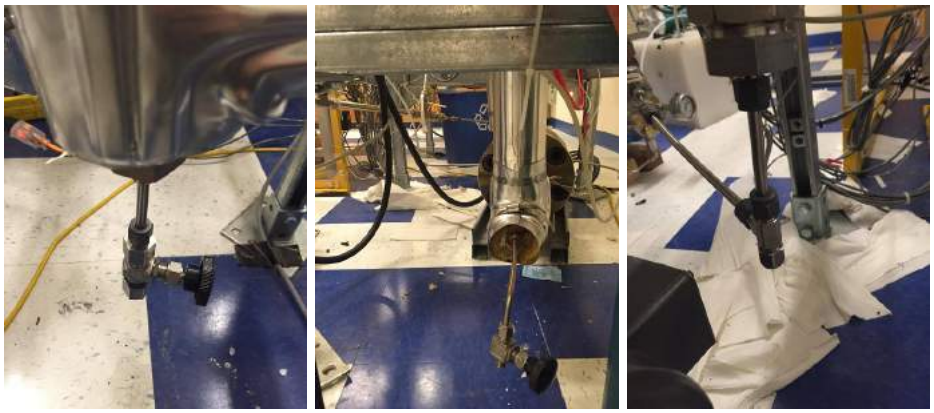

Figure 3-105: These three photos show the ports that must be opened for all the water in the loop to be drained. The first valve is the valve on the bottom of the loop near the autoclave which should drain the water from the autoclave and the tubings near it. The second valve is used to drain the circulation pump and the tubings near it. The cap is used to drain the water near the pressurizing pump.

This way the more water will easily drain out. The parts to disconnect to let air into the system includes the quarter-inch tubing line connecting to the pressure switch, the loop safety relief valve, and the differential pressure transmitter.

### 3.9.11 Top Flange and Heating Rod Assembly Removal

Before pulling off and separating the top flange assembly from the rest of the autoclave, make sure to do the following:

- All of the six large bolts on the autoclave must be loosened. When loosening the large bolts, loosen them a bit a time and go around in a circle. If one bolt is loosened too far out while other bolts are still quite loose, there will be an imbalance in load on the soft graphite gasket which can damage it.
- The cooling line to the top flange must be disconnected.
- The thermocouple line and the heating rod power line should be disconnected.

After these steps are done, top flange assembly will be ready to be separated. To separate the top flange assembly, slowly pull it vertically without having the heating rod touching the autoclave wall. Do this as slowly and carefully as possible to prevent damage to samples.

### 3.9.12 Safety Precautions During Loop Operation

Always stay behind the polycarbonate shield when operating to loop to avoid any danger in the case of any accident. Always keep the emergency stop button on the table near you in the case the loop

needs to be stopped right away. Avoid being in the crud loop room during loop operation. Always monitor the coolant flow rate using the flow meter attached to the autoclave. Shut down the loop if there is not enough coolant flow.

## 3.10 Maintenance of the Loop

There is equipment in the loop that will need maintenance replacement from time to time. For most equipment, a maintenance procedure is well written within its documentation. However, there are a few maintenance procedures that are not in the documentation. The following section explains those maintenance procedures for the loop.

### 3.10.1 Replacing Autoclave Windows

The sapphire windows may corrode after multiple experimental runs, as shown in figure 3-106. Window replacement can be done by first removing the outer window casing. Then, using the puller tool provided to screw into the window assembly. Once the puller is in place, apply just enough force to pull out the inner window casing. To reinsert the window casing simply push the window assembly into its spot. After that, the outer casing can be tightened into place. When tightening the window casing, first do it by hand. This is to prevent cross threading. Then tighten properly by applying the torque of 100 Nm with a torque wrench.

Note that great care must be taken when removing and inserting the outer casing of the window. Always check to make sure the thread is in the right spot before starting to apply the torque on the wrench. If the torque is applied inappropriately and the cross threading happens, it will take a lot of work to fix, especially if the damaged thread is on the autoclave itself. The recommended way of fixing cross threading is by grinding the crossed part down so the thread can slide in again. The sapphire window assembly may break during removal so the windows should be removed only when necessary.

### 3.10.2 Replacing the Argon Tank

When argon tank runs out, it can be detached by removing the gas regulator and its holder. After removing the connections, roll the gas tank out towards a gas cart. Used argon tanks must be transferred to the building NW13's docking area for disposal. To replace argon tank, simple latch the holder on it and thread in the gas regulator.

Figure 3-106: A new autoclave window (left) versus a used, corroded autoclave window (right).

### 3.10.3 Replacing Vacuum Pump Oil

The vacuum pump oil can be replaced, simply by draining the oil from the bottom of the pump into a disposal container. Then pour the new oil in from the top input opening. Fill the oil to the marking on the side of the vacuum pump.

### 3.10.4 Replacing the Ion-Exchange Column

After a while of use, usually after cleaning two full tanks of tap water, the ion-exchange column will start to become less effective in filtering ions from water. The symptom of this happening is that it may take as long as two days to clean up ions within the water. To replace the ion-exchange column, first, close down the two valves leading to the ion-exchange columns. Doing so prevents the water from gushing out during replacement. Then, use the white plastic ring given with the ion-exchange column to screw out the ion-exchange column holder. Then replace the ion-exchange resin column inside with a new column. After that, proceed to put the whole ion exchange column and its holder back in the same place with the help of white plastic ring.

## 3.11 Troubleshooting

There are many cases where there will be issues that prevent the operation of the loop. This section here present common problems, how to check for them and suggest how to fix them. Consult documentations for the specific piece of equipment if the common fixes do not work.

### 3.11.1 Troubleshooting in the Case Pressurization is Not Achieved

There are many cases where there will be issues that prevent the operation of the loop. Most of the time, similar problems occur. This section presents these common problems, how to check for them

and suggest ways of fixing them. Consult the documentations for a specific piece of equipment if these common fixes do not work.

**Wrong Valve Position** In the case that some of the valves are not properly turned, the loop will not pressurize. The valves to check includes the valve letting the water from the water tank into the pressurizing pump, and the needle valves on the fill line.

**Needle Valve Leakage** The needle valve leakage is another common problem. The sign of this is water seeping out of the needle valve stem. In this case, the problem usually goes away after the valve stem is tightened. If the problem persists, new valve replacement is typically the best choice as they are not too expensive compared to manhour of fixing the valve.

**Control Valve Stem Leakage** Control valve stem leakage could also happen. The sign of this is the water seeping out of the control valve stem. Usually, this problem can be addressed by tightening the valve stem. In a rare case, tightening the valve stem may not work. In that case, the packing or the O-ring may be damaged. There are two options to solve the packing or the O-ring problems. One of the ways is to take apart the control valve according to the manual to check for damage in the packing or the o-ring. If either the packing or the O-ring is broken, replace the broken packing or O-ring with a new spare part. The second way is to ship it to the manufacturer to have it fixed.

**Tube or Pipe Connection Leakage** There could be a leak in some tube or pipe connections. Running the pressurizing pump at a high flow rate for a while might reveal where the leak is occurring.

- If the leak comes from the tube connections, this issue can usually be fixed by tightening the nuts. Make sure that the nuts are not overtightened, or there is a risk of damaging the tubing seal which leads to a leak as well. In the case that a tubing connection is damaged, the tube section including nuts, and ferrules must be replaced.

- For a pipe connection, replacing the seal is the usual way to approach the problem. There are two types of seals that are applied on the pipes, the Teflon tape seal for low-temperature connections, and the Xpando seals for high-temperature connections. For the Teflon tape seal, the pipe connection can be undone and the Teflon tape will usually easily unwound. Replace the Teflon tape and put the pipe connection back again and the connection should work. For the Xpando seals, releasing the pipe connection must be done very carefully to avoid having broken Xpando debris fall into the tube. The connections can then be cleaned of the Xpando material using any available equipment that can scrape off the debris. In the case the Xpando debris falls into the tube, it can be removed either by vacuuming, removing with Kimwipe, or

removing the whole three-way section to take the debris out. Once the connections are clean, mix the Xpando with water to get a thickness of a thin paste and apply them to the pipe male connection. After putting the pipe connection back together, Xpando will need 24 hours to dry before it can be used without leaking.

**Autoclave Window Leakage** A leak could also occur at the autoclave windows. One possible test for this is first to close down the system and drain the whole loop. Then vacuum out the loop. If there is a leak at the window, you will be able to hear the wheezing sound from the window. Otherwise, if no sound is heard, it is also useful to plug the window with your palm to see if there is a leak which will provide suction. If another person is present, you can also have another person look at the autoclave controller for you to see if the pressure changes when you plug the window with your palm. Usually, a leak in the autoclave window means that either a part of the window glass corroded away, or that the window is not properly tightened. In the case that tightening the window does not work, see the section "Replacing autoclave window" 3.10.1, for how to change the autoclave window.

**Pressurizing Pump Problem** The pressurizing pump could be a problem as well. One possible test for this issue is to replace the tubing going to the pressurizing pump with a short tubing leading to a pressure gauge and to a pressure relief valve. Once the replacement is done, try pressurizing a little to see if the pressure will go up with that small system. Be ready to click the off button for the pressurizing pump all the time. An extreme caution must be used when doing this test, since a small system will pressurize very quickly, so it will be easy to get a pressure overrun without great care. If the pressurizing pump does not pressurize, it is recommended to send it manufacturer, unless the pump is already old at the time of reading.

### 3.11.2 The Autoclave Controller Box Remains Shutdown

If the heater is not turned on at all, first check if the heater is properly supplied with power by examining different wires with a voltmeter. If the heater is properly supplied with power, the next most common cause is that there was previously a power surge. The following fixes work most of the time to combat this issue. If none of the following fixes work, it is likely that the heater burned out and must be replaced.

**Turn On the Internal Breaker** The autoclave controller comes with an internal breaker built-in that will turn off in the case of power surge. To activate the internal breaker again, first, check to make sure that power is not supplied to the autoclave heater controller. Then open the top cover by loosening the screws on the back of the heater controller. Once the heater controller's top is opened, the internal breaker switch is located near the heater controller front panel towards the right-hand

side, when looking in from the front panel. Flick the switch and close the heater controller box properly before testing if the fix worked.

**Replace the Fuse** If turning on the breaker switch does not work, another issue could be that the fuse was blown. On the back of the autoclave heater controller towards the right-hand side, there are two black rubber circles with a slotted screw head. Those parts can be unscrewed out to reach the fuses. Once the fuse is found, test its integrity by using a voltmeter to check the resistance across the fuse. If one fuse was found to be blown with infinite resistance, the operator should replace that fuse with a new one. The fuse should be the 500 Voltage and 16 Amps type. After the fuse is replaced, close up the heater controller box. Then, test if the fix worked.

### 3.11.3 Neslab Heat Exchanger Stopped Working

The two most common problems which made the Neslab heat exchanger stop working are either the temperature of the coolant became too high or that its coolant level is too low.

**Coolant Water Level Too Low** To determine if the water level is the issue, simply check the water level by opening to the top hatch leading to the water. If it is low, fill it up to almost full. Usually, if the water level became low not too long after the last change, it indicates that the loop might have a leak. In that case, it is recommended to go through all the connections to test for a leak as well.

**Temperature Level Is Too High** The temperature of the coolant can be checked from the front of the Neslab heat exchanger. The most common reason for the rise in coolant line temperature is that the building's cooling line was shut down, and therefore there isn't a place to dump heat. To determine if the building's cooling line is the problem, check the incoming cooling line to see if it is cold. If the building's cooling line is hot, then you will have to wait for building's cooling line to be fixed.

### 3.11.4 Failure to Get to the Desired Temperature

If the temperature does not increase to the desired PWR temperature, even when all the heaters are running at full power, several issues might be the cause. The following three issues are the most common ones.

**Leak in the System** A leak in the loop will drain away its energy as heated water exits the loop. A symptom for a leak is that it is harder than usual to pressurize the system. Moreover, when the pressurizing pump is closed, the pressure falls quicker than usual. In the case that there

is an unknown leak, you may have to go through all the connections in the loop to see which one is causing the problem. One way to find out where a leak that cannot be detected at low pressure is to pump the loop with very high flow rate from pressurizing pump. After a while, close the pressurizing pump and inspect the loop for any dripping.

**Heating Tape Failure** It could also be that some of the heating tapes failed. To check this, test the resistance of all heaters using their plugs after the loop had been shut down. If there is indeed a failed heating tape, replace it accordingly. When replacing a heating tape, wear a gas mask when removing the insulation covers. The ceramic wool heat insulator's dust can be damaging to the lungs.

**Too Much Pressurizing Pump Flow Rate** If the pressurizing pump's stroke length is too high, the pressurizing pump may dump too much cold water into the loop. This influx of cold water will cool down the loop making it harder to increase the temperature. The easy fix for this is to turn down the pressurizing pump's stroke length. An ideal pressurizing pump stroke length is where the measurement loop measures around 60 ml/minute.

## 3.12 Example Raw Data Outputs from the Loop

If the data file is saved for the experiment run, there should be several text files that contain the data for the loop. Each of them is a dataset for a specific type of loop data output. The following figure 3-107 is the excel file made from compiling the several text files together in different columns. Figure 3-108 shows the graph of temperature vs time for an experiment conducted on February 12, 2016. "Autoclave liquid temperature" measures the water temperature at the top part of the autoclave. "Autoclave Element Temperature" measures the temperature within the heating rod. Figure 3-109 shows the four spots in which the loop temperatures are measured, corresponding to figure 3-108's labels. Note that the temperature differences in water across the loop are minimal, due to the fact that the distance that water travels in IHTFP is very short compared to the distance water travels through in PWRs. Figures 3-110, 3-112, 3-113, 3-114, and 3-115, are the graphs of oxygen concentration, conductivity, pH, differential pressure and pressure versus time, respectively, for the February 12, 2016 experiment. Since there was a dissolved oxygen anomaly in the February 12, 2016 experiment, figure 3-111 was selected to show a typical dissolved oxygen graph without any anomaly.

The following list gives a brief explanation of what each of these output columns represent:

- Pressure: This value represents the pressure of the whole system. It reads from the pressure transmitter near the back-pressure regulator.

| Pressure | Liquid Temperature | Element Temperature | Differential Pressure | Dissolved O2 | pH | Conductivity | Temperature before cooler | Temperature after cooler | Temperature before preheater | Temperature after preheater |
|---|---|---|---|---|---|---|---|---|---|---|
| 154.535 | 33.604 | 33.757 | 12.6 | 0.007 | 6.859 | 8.724 | 34.163 | 34.471 | 33.857 | 34.133 |
| 155.185 | 34.27 | 33.863 | 12.58 | 0.006 | 6.859 | 8.722 | 34.16 | 34.443 | 33.836 | 34.121 |
| 154.002 | 69.469 | 69.606 | 16.35 | 0.006 | 6.898 | 8.619 | 67.865 | 69.082 | 67.988 | 69.011 |
| 155.221 | 92.786 | 92.963 | 16.39 | 0.007 | 6.898 | 8.293 | 91.894 | 92.827 | 91.575 | 92.627 |
| 152.59 | 122.779 | 183.191 | 16.42 | 0.005 | 6.895 | 8.019 | 121.423 | 122.282 | 120.273 | 121.373 |
| 155.513 | 156.356 | 246.529 | 16.19 | 0.006 | 6.883 | 8.255 | 155.273 | 155.952 | 153.611 | 154.629 |
| 155.413 | 180.825 | 280.228 | 15.87 | 0.005 | 6.885 | 8.235 | 179.564 | 180.039 | 177.469 | 178.386 |
| 153.196 | 192.871 | 250.31 | 15.67 | 0.005 | 6.894 | 8.178 | 192.752 | 193.229 | 191.286 | 192.23 |
| 152.639 | 202.837 | 264.765 | 15.59 | 0.005 | 6.897 | 8.106 | 202.276 | 202.605 | 200.352 | 201.403 |
| 154.36 | 214.229 | 314.067 | 15.4 | 0.005 | 6.911 | 7.97 | 213.901 | 214.381 | 211.578 | 212.478 |
| 155.439 | 227.721 | 327.105 | 15.09 | 0.005 | 6.915 | 7.96 | 227.371 | 228.046 | 225.213 | 226.381 |
| 155.587 | 239.587 | 339.754 | 11.42 | 0.004 | 6.914 | 7.799 | 239.032 | 239.505 | 237.622 | 237.601 |
| 156.042 | 249.655 | 349.787 | 11.16 | 0.005 | 6.938 | 7.738 | 248.938 | 249.581 | 247.595 | 247.626 |
| 155.543 | 259.089 | 360.251 | 11.06 | 0.005 | 6.95 | 7.71 | 257.86 | 258.588 | 256.614 | 256.522 |
| 155.767 | 266.121 | 367.479 | 10.92 | 0.005 | 6.958 | 7.773 | 264.764 | 265.592 | 263.719 | 263.697 |
| 156.446 | 272.009 | 372.995 | 10.74 | 0.005 | 6.974 | 7.948 | 270.511 | 271.194 | 269.276 | 269.367 |

Figure 3-107: This table shows an example of raw data output, with data gathered every 15 minutes interval.

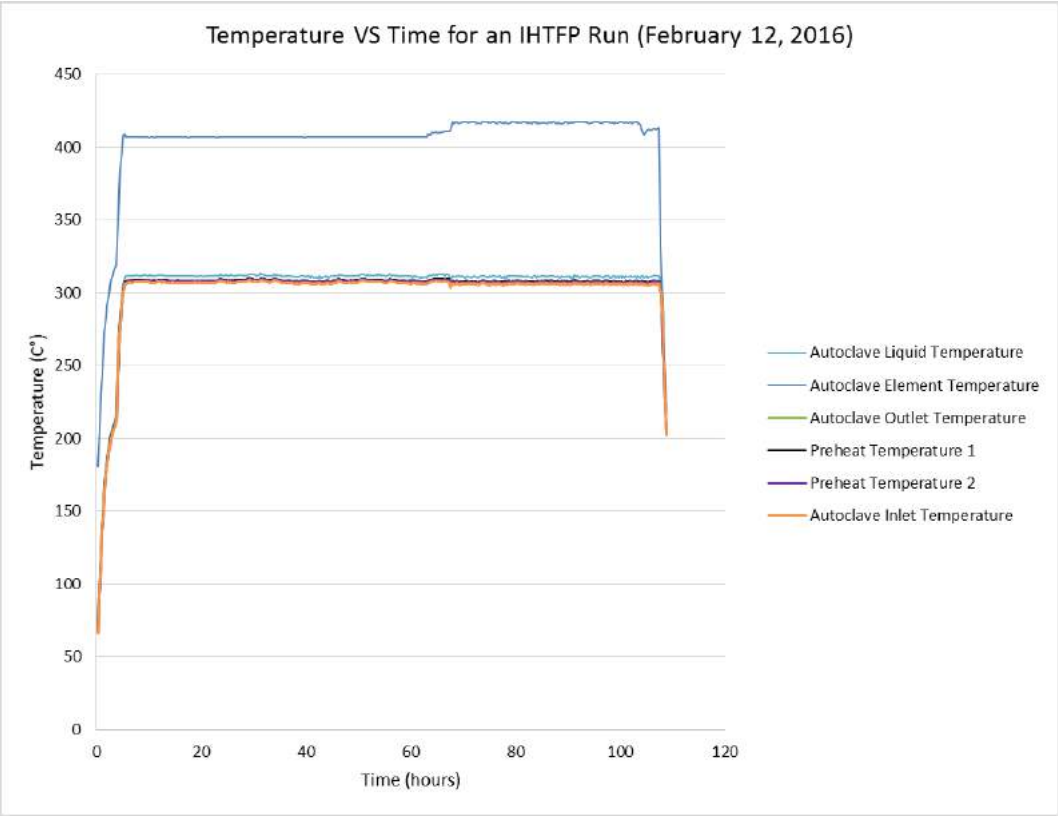


Figure 3-108: Graph of temperature (°C) VS time (hours) for the six thermocouples on the IHTFP. This particular graph is for February 12, 2016.

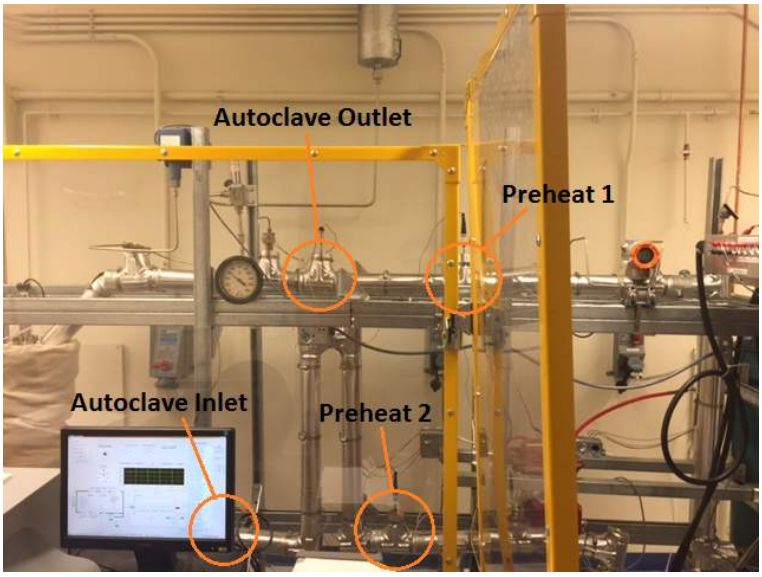


Figure 3-109: This figure shows four spots on the loop where thermocouples are placed.

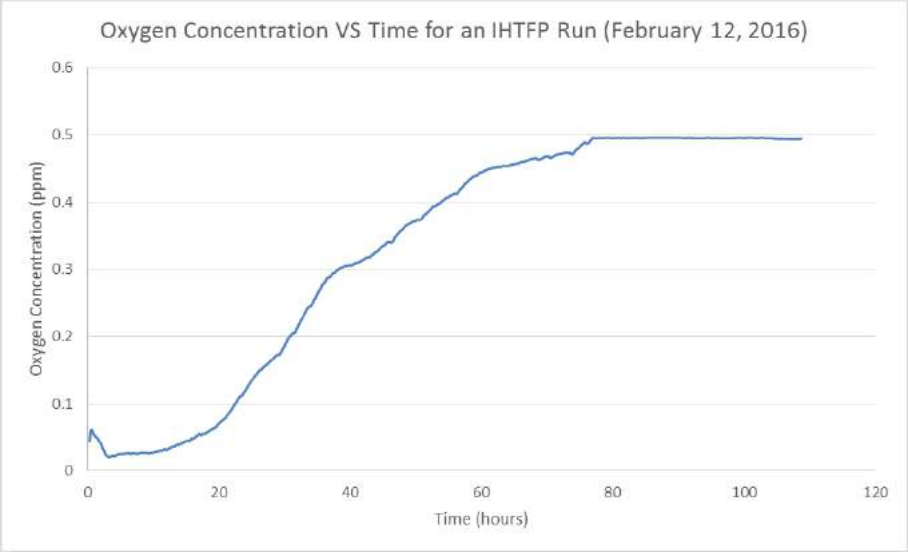


Figure 3-110: Graph of dissolved oxygen concentration (ppm) VS time (hours) for an the IHTFP experiment conducted on February 12, 2016. Note that the oxygen concentration rose in this case due to a very small leak.

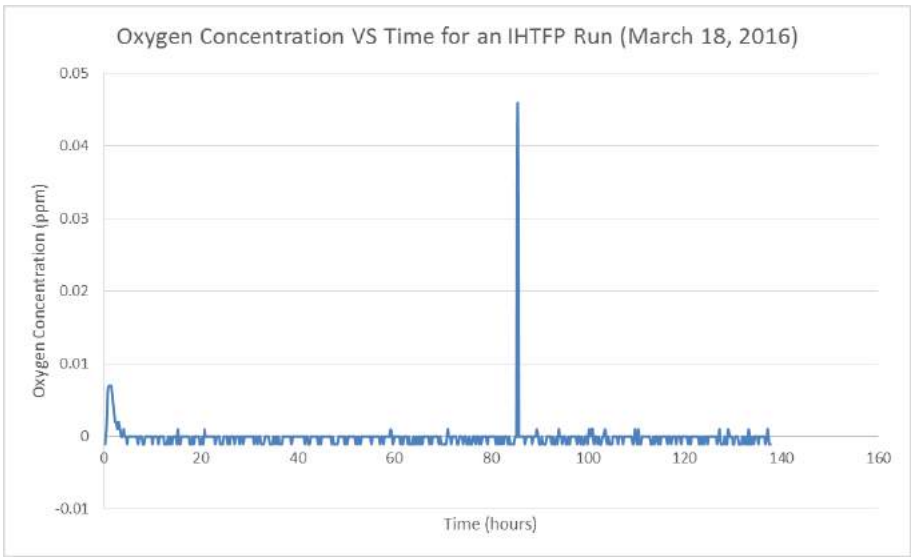


Figure 3-111: Graph of dissolved oxygen concentration (ppm) VS time (hours) for an the IHTFP experiment conducted on March 18, 2016. In this typical case without any leak, the dissolved oxygen remains close to zero at all time.

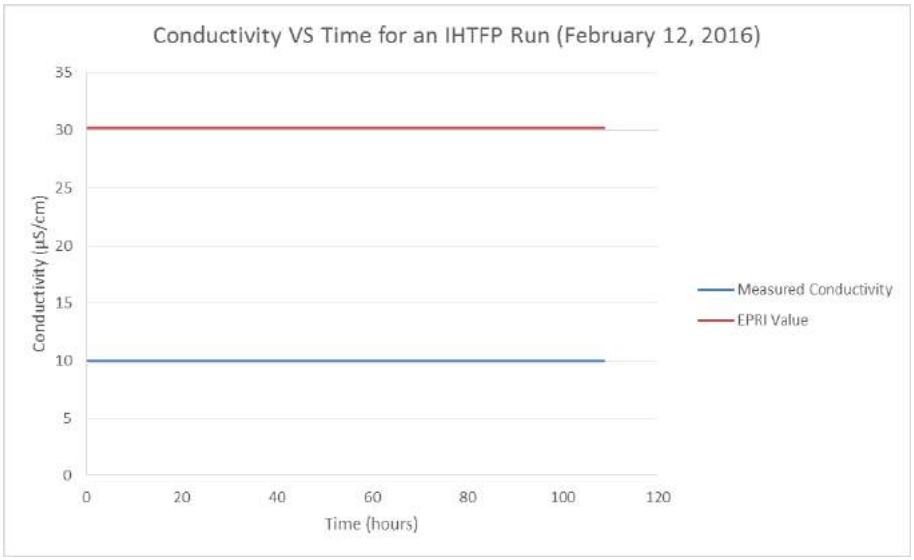


Figure 3-112: Graph of conductivity ($\mu S/cm$) VS time (hours) for an the IHTFP experiment conducted on February 12, 2016. The blue line is the measured conductivity from the experiment. The red line is the conductivity value from figure 3-22 by EPRI, given that water contains 1400 ppm of boron and 3 ppm of lithium hydroxide. The huge gap in theoretical and measured conductivity is likely due either an uneven mixing of solution or undissolved chemical species .

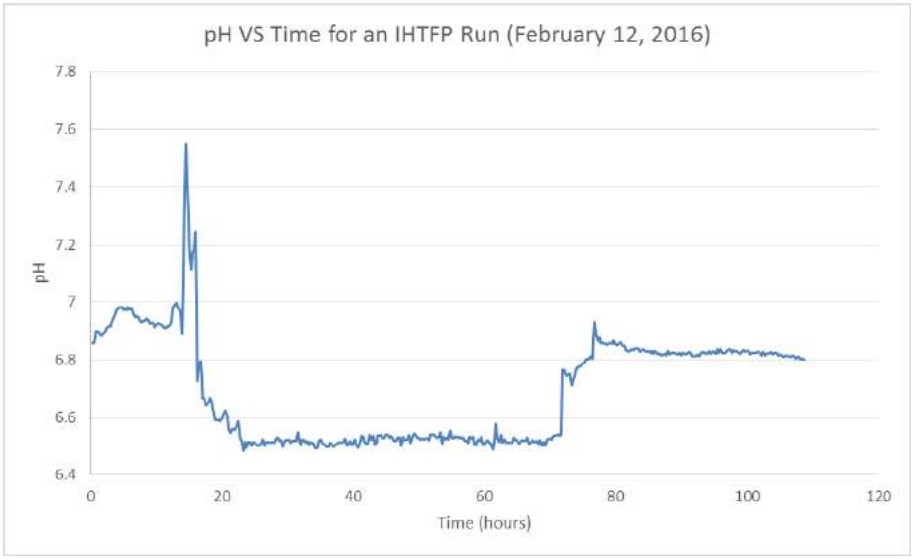


Figure 3-113: Graph of pH VS time (hours) for an the IHTFP experiment conducted on February 12, 2016.

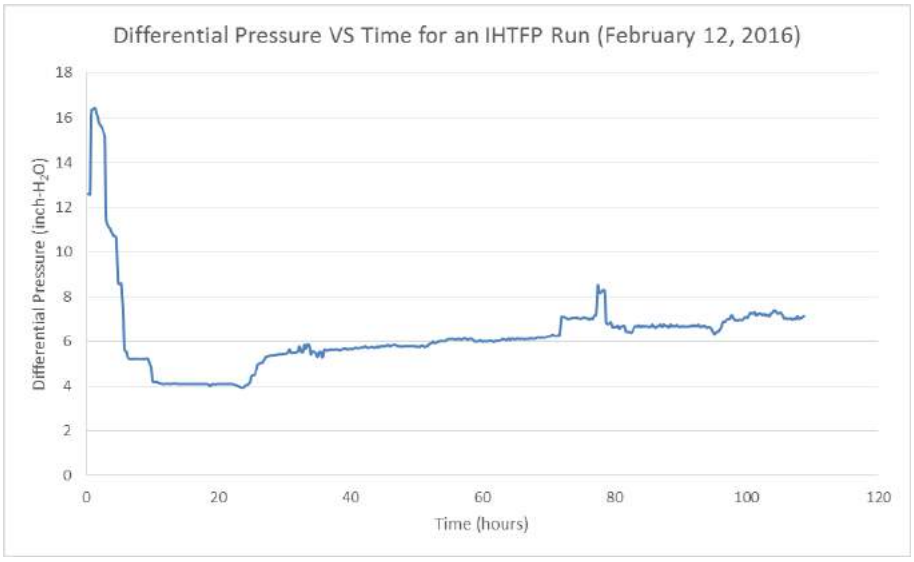


Figure 3-114: Graph of differential pressure ($Inch - H_2O$) VS time (hours) for an the IHTFP experiment conducted on February 12, 2016. Note that 6 $inches - H_2O$ corresponds to autoclave velocity of 2.98 m/s and the Reynolds number of 98,955.

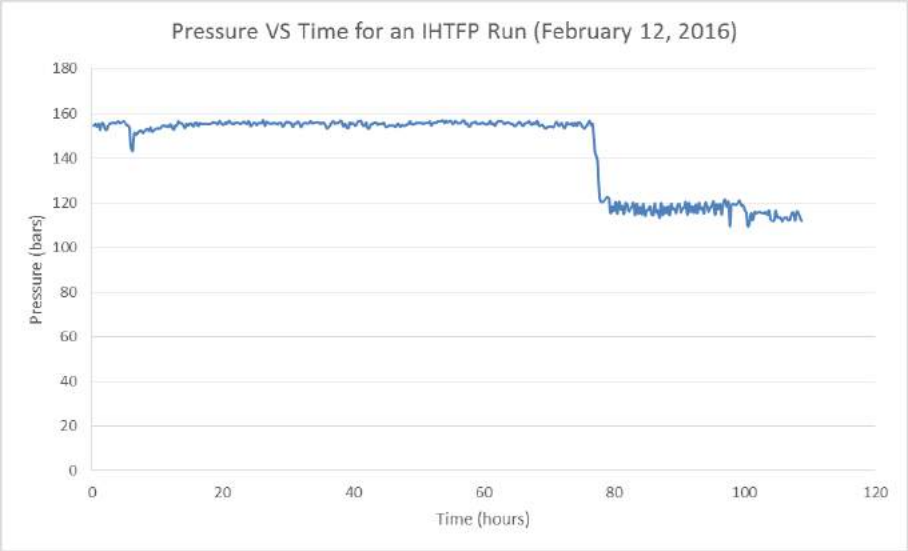


Figure 3-115: Graph of pressure (bars) VS time (hours) for an the IHTFP experiment conducted on February 12, 2016. The drop in pressure towards the end is because we decided that lowering pressure, and therefore allowing more boiling, might benefit crud growth.

- Liquid temperature: This value represents the liquid temperature in the autoclave as measured from the top of the test section within the autoclave.
- Element temperature: This value represents the temperature within the heating element measured by the thermocouple embedded in the center of the heating element.
- Differential pressure: This value represents the differential pressure from the differential pressure transmitter on top of the loop. This use useful for figuring out the flow rate.
- Dissolved Oxygen: This is the dissolved oxygen value measured by the measurement equipment cluster. It will measure either the dissolved oxygen content of the main loop or the water tank depending on the valve direction.
- pH: The pH measurement also measures from the measurement equipment cluster.
- Conductivity: The conductivity is another value from the measurement equipment cluster. It is useful for determining how much ions are flowing within the loop or the water tank.
- Temperature before cooler: Temperature from thermocouple on the top left side of the main loop
- Temperature after cooler: Temperature from thermocouple on the top right side of the main loop
- Temperature before preheater: Temperature from thermocouple on the lower right side of the main loop

- Temperature after preheater: Temperature from thermocouple on the lower left side of the main loop

# Chapter 4

# EXPERIMENTAL AND ANALYTICAL METHODOLOGY

## 4.1 Introduction

This chapter will present information regarding the experiments that we ran on the IHTFP. Its first section presents the summary of experiments that were planned and run successfully. In each of these experimental trials, crud is grown on coated test sample rings that cover the heater rod, as explained in section 4.3.3.3. The second section explains how the coatings for test sample rings were chosen, as well as how these test samples are fabricated. Once we get crud on the test samples, different analysis methods are applied to it. These analysis methods are explained in the third section of this chapter.

## 4.2 Experimental Matrix & IHTFP Parameters

In summary, there are four successful experimental trials. The first experiment tested the loop's ability to grow crud. The second trial aims to grow crud for the fractal analysis. and the effectiveness analysis of crud-resistant, surface-chemistry modification. The third and the fourth trials are similar trials that is designed to test all types of coatings we have. In each of these two trials, of the surface-chemistry, crud-resistant coatings are tested. Two of the same successful trials were conducted to ensure that the experiment is repeatable. Nine sample rings with surface-chemistry modifications were placed on the heating rod for each trial. This following table 4.1 summarizes what was done for each trial. The following subsections explain in detail what happened in each trial.

| | | Trial A | Trial B | Trial C | Trial D |
|---|---|---|---|---|---|
| Date | | August 28, 2015 | September 22, 2015 | February 12, 2016 | March 18, 2016 |
| Purpose | | First crud growth test trial | Fractal analysis | Test crud-resistant coating | Test crud-resistant coating |
| Condition | Pressure | 155 bars | 103-115 bars | 115 bars | 115 bars |
| | Temperature | 320 ºC | 305-310 ºC | 310-320 ºC | 310-320 ºC |
| | Boric acid | 1400 ppm | 1400 ppm | 1400 ppm | 1400 ppm |
| | Lithium hydroxide | 3 ppm | 3 ppm | 3 ppm | 3 ppm |
| | Crud particles | 20 $\mu g/ml$ of 50 nm diameter NiO | 20 $\mu g/ml$ of 50 nm diameter NiO | 20 $\mu g/ml$ of 50 nm diameter NiO | 50 $\mu g/ml$ of 50 nm diameter NiO |
| | Heat flux | 206 $kW/m^2$ | 206 $kW/m^2$ | 206 $kW/m^2$ | 206 $kW/m^2$ |
| | Total time | 7 days | 9 days | 4 days | 13 days |
| Analysis method | | -SEM -FIB | -SEM -FIB | -SEM | -SEM |

Table 4.1: Summary of all trials that containing data we used for result and analysis.

#### 4.2.0.1 Trial A: First Test Growth Trial (August 28, 2015)

The objective of this trial was to test whether the loop can actually grow crud. Similar to other trials, crud particles (50nm sized nickel oxides), boron, and lithium hydroxide were added to the water. Crud was grown at approximately 155 bars and $320°C$ over a period of seven days before heaters were switched off and left to cool for 48 hours. The chemicals added were nickel oxide at 20 $\mu g/ml$, boric acid at 1400ppm and lithium hydroxide at 3ppm. This chemical condition matches normal operating condition of PWR. In this experiment, the only sample ring added was a 5 cm long blank stainless steel sample ring.

#### 4.2.0.2 Trial B: Fractal Analysis Trial (September 22, 2015)

This second test trial's major goal was to grow crud thick enough to perform the fractal analysis. The crud growing conditions were approximately 103-115 bar and $310 - 320°C$. Chemical additives were nickle oxide (20 ppm), boric acid (1400 ppm) and lithium hydroxide (3 ppm). This trial ran with start up and cool down procedures similar to the first growth trial. The trial was originally planned for 14 days, but was terminated at 9 days because of the worry that high dissolved oxygen

concentrations during the later part of the trial might damage the loop.

In this particular trial, sample rings with coatings of titanium nitride ($TiN$), zirconium oxide ($ZrO_2$), molybdenum disulfide ($MoS_2$), and tungsten/titanium ($W/Ti$) were also tested as surface-chemistry modification crud-resistant material. However, their results are not used for crud-resistant coating analysis because the crud grown was too thick for proper area coverage analysis. The sample placements are four coated materials mentioned and blank stainless steel rings. The first and tenth stainless steel rings are used to stabilize the flow before it reaches important samples with coating materials. The middle four samples are placed at the viewing window because at the point of this trial, it was not yet known whether windows would significantly affect crud growth. Later on, it was found that the windows have a negligible effect on how crud grows. Table 4.2 summarizes the sample placement in this trial.

| Sample Number | Height Position from Rod Tip (mm) | Sample Type |
|---|---|---|
| 1 | 278.5 | 316 stainless steel |
| 2 | 266 | titanium nitride ($TiN$) |
| 3 | 253.5 | zirconium oxide ($ZrO_2$) |
| 4 | 241 | 316 stainless steel |
| 5 | 228.5 | 316 stainless steel |
| 6 | 216 | 316 stainless steel |
| 7 | 203.5 | 316 stainless steel |
| 8 | 191 | molybdenum disulfide ($MoS_2$) |
| 9 | 178.5 | tungsten/titanium ($W/Ti$) |
| 10 | 166 | 316 stainless steel |

Table 4.2: Sample placement for Trial B.

#### 4.2.0.3 Trial C: Crud-Resistant Trial (Febrary 12, 2016)

This trial is designed to test the crud-resistant, surface-chemistry modification coatings. The crud-growing conditions were approximately 115 bar and $310 - 320°C$. Chemical additives were nickel oxide (20 ppm), boric acid (1400 ppm), and lithium hydroxide (3 ppm). This trial was originally planned for 14 days but only lasted for 4 days because the heater rod failed. Nevertheless, scattered crud particles were found and the SEM images taken are still useful for determining the effectiveness of the coatings.

Sample placements are as follows. The zircaloy and stainless steel rings on the top and the bottom of the rod will act as both flow stabilizing ring and control sample ring. The reason that

we do not want to put coated rings on the ends is because we want to obtain accurate data from them. The heating cartridge in the heater rod has a length of 150 mm. The 12 sample rings also have a combined length of 150 mm (12.5 mm each). This means that the rings at the ends may not receive very uniform heat, and therefore may yield inaccurate results. As mentioned earlier in section 4.3.3.3, each coated sample ring is coated on only one side. The control group analysis is obtained from the uncoated side of coated samples. Table 4.3 summarizes the sample placements in this trial. Note that $Ti_2AlC$ (sample 11), is a coating that we helped test for another research group, and is not related to this thesis.

| Sample Number | Height Position from Rod Tip (mm) | Sample Type |
|---|---|---|
| 1 | 302.5 | zircaloy-4 |
| 2 | 290 | zirconium carbide ($ZrC$) |
| 3 | 277.5 | zirconium nitride ($ZrN$) |
| 4 | 265 | titanium carbide ($TiC$) |
| 5 | 252.5 | titanium nitride ($TiN$) |
| 6 | 240 | aluminum oxide ($Al_2O_3$) |
| 7 | 227.5 | titanium oxide ($TiO_2$) |
| 8 | 215 | titanium boride ($TiB_2$) |
| 9 | 202.5 | zirconium oxide ($ZrO_2$) |
| 10 | 190 | magnesium oxice ($MgO$) |
| 11 | 177.5 | $Ti_2AlC$ |
| 12 | 165 | 316 stainless steel |

Table 4.3: Sample placement for Trial C. Note that all coated samples are only coated on one side. The uncoated side is used as a control.

#### 4.2.0.4 Trial D: Crud-Resistant Trial (March 18, 2016)

Similar to trial D, trial C is designed to test the crud-resistant, surface-chemistry modification coatings. This test is done to ensure that the results of trial C are repeatable. The crud-growing conditions were approximately 115 bar and $310 - 320°C$. Chemical additives are nickel oxide (20 ppm), boric acid (1400 ppm), and lithium hydroxide (3 ppm). This trial lasted for 13 days. Scattered crud particles denser than trial C can be found in this trial.

Sample placements are almost the same as trial C, with the exception that trial D does not contain a $Ti_2AlC$ sample ring. Similar to trial C, each coated sample ring is coated on only one side. The control group analysis is obtained from the uncoated side of coated samples. Table 4.4

summarizes the sample placements in trial D.

| Sample Number | Height Position from Rod Tip (mm) | Sample Type |
|---|---|---|
| 1 | 290 | zircaloy-4 |
| 2 | 277.5 | zirconium carbide ($ZrC$) |
| 3 | 265 | zirconium nitride ($ZrN$) |
| 4 | 252.5 | titanium carbide ($TiC$) |
| 5 | 240 | titanium nitride ($TiN$) |
| 6 | 227.5 | aluminum oxide ($Al_2O_3$) |
| 7 | 215 | titanium oxide ($TiO_2$) |
| 8 | 202.5 | titanium boride ($TiB_2$) |
| 9 | 190 | zirconium oxide ($ZrO_2$) |
| 10 | 177.5 | magnesium oxice ($MgO$) |
| 11 | 165 | 316 stainless steel |

Table 4.4: Sample placement for trial D. Note that all coated samples are only coated on one side. The uncoated side is used as a control.

#### 4.2.0.5 Failed Trials

The IHTFP was built only recently. Building any new equipment, especially one that can imitate PWR conditions, entails a huge learning curve and many experimental failures. Nevertheless, its experimental failure rate improved immensely since its commissioning. We acquired a significant amount of experience on how to maintain and operate the IHTFP, through many experimental failures we had. The following paragraphs delve into detail of each experimental failure we faced, and what we learned from it.

**September ~4, 2015** This trial failed very early on. The heating rod never stabilized at temperatures higher than 100 $^{o}$C, where the measurements typically start. The failure was due to the use of manual power adjustment to accelerate the IHTFP heating process. In the typical heating procedure, an automatic PID power adjustment is used to heat up the IHTFP. In this trial, we attempted to accelerate the initial heating process by setting the power manually to 100 % when the liquid temperature was still low. The premise was that, at low temperatures, it is possible to use a sustained 100 % power as there are still large temperature buffers before boiling occur. The heating process went on for a few minutes without any problem. Then, suddenly, the heating rod failed. We suspect that this was due to the departure from nucleate boiling condition. When the

boiling regime transitions from the efficient nucleate boiling to the film boiling, heat transfer decrease immensely, leading to the overtemperature in the heating rod. In this failed trial, we learned to never use manual power adjustment, even at low temperature.

**October 9, 2015** After the more successful trial B on September 22, 2015, shown in section 5.2.1.1, we attempted to push the pressure limit to get more nucleate boiling, and therefore, crud growth. As demonstrated in section 5.2.1.1, the estimated difference between the wall temperature and the water saturation temperature is only 2 ºC. A difference of 5 to 10 ºC would be ideal according to figure 3-8. This led us to lower the saturation temperature by 5 ºC compared to the trial B; we did this by lowering the pressure from 103 bars to roughly 95 bars. During this trial, we started off with temperatures of roughly 105 bars similar to trial B. When we attempted to decrease the pressure to 95 bars, the heating rod failed at roughly 96 bars. This failed trial prompted us to become more conservative when pushing the pressure boundary. It also reinforced our hypothesis that the element temperature may not be a very accurate representation of the heating rod centerline temperature, because of manufacturing limitations. For instance, the element temperature thermocouple embedded in the heating cartridge may not be at its exact center. In addition, the heating cartridge may not have a completely uniform heat generation.

**October 14, 2015** Because of the failure of the experimental trial that started on October 9, we reverted back to using the pressure of 155 bars. Unfortunately, this trial failed to grow any visible crud. After this trial, the pressure of 155 bars was never used again, since it appears to hamper crud growth.

**November 10, 2015** As shown earlier, thick crud, suitable for fractal analysis, was successfully grown during the experimental trial B. However, trial B's samples contain machining grooves which can be seen on SEM images. The plan for November 10 was to create samples with thick crud on electropolished sample rings without any machining grooves. A more conservative pressure of roughly 120 bars was used ensure that the heating rod would not fail. Although this experimental trial successfully ran for the full planned three weeks, it did not grow any visible crud. In this failed trial, we learned that low pressure, combined with electropolished surfaces, can severely hamper crud growth. Moreover, this experimental trial also highlights how conditions might be more important than the time in impacting the growth of crud.

**March 14, 2015** Heater rod suddenly failed at the beginning of the trial with the pressure of roughly 125 bars and temperature of roughly 407 ºC. The failure of this heating rod without any easily identifiable cause demonstrates how unreliable the heating rod can be. This heating rod's failure emphasizes the importance of ordering spare heating rods for experiments, as well as the

importance of making backup plans to take into consideration the possibility of heating rod failure.

**Failed Trials Conclusion.** Overall, the major causes of failure are the heating rod failure and the lack of crud growth. Both problems are caused by the unreliability of heating rods. Heating rod failures happen because we cannot get a very accurate element temperature, and therefore, tend to push the heating rod beyond its limit. On the other hand, using more conservative pressures to combat heating rod failure leads to the lack of crud growth. Heating rod improvements, inspired by CRIEPI [118], as shown in section 6.4.1, may solve these problems.

## 4.3 Preparing Test Samples

As mentioned earlier in section 4.3.3.3, the samples are small, thin rings press-fitted onto the heating rod that is inserted into the autoclave. These sample rings have the inner diameter of 17.5 mm, which fits perfectly on the heater rod. They have the length of 12.5 mm and the thickness of 0.25 mm. This section will focus on the preparation of these test sample rings. The first subsection presents in detail the reasons that we decided to use sample rings. The second subsection delves into the material selection process and how the materials selected should work. Finally, the third subsection gives detail on how these coated/uncoated sample rings are fabricated.

### 4.3.1 Reasons for Using Sample Rings

There are several reasons that sample rings are used. First, instead of having to replace the whole heater rod each experiment, potentially making the experiment very costly and time-consuming, we press-fit the heater rod with sample rings that can be replaced every experiment run. Each heating rod is quite expensive and hard to fabricate. In this experiment, we are testing more than ten types of materials, with each material tested at least twice. This translates to at least twenty experiments, each of which takes two weeks and one heating rod. In addition, because the heating cartridge used in each experiment is custom-made and has exceptionally high heat density, there is a significant chance of these heating rods failing. If experimental success/failure rates are taken into account, it could very well take more than twenty experiments to reach a dependable conclusion. The cost and time consumption to carry out more than twenty experiments cannot be justified in our scenario. On the other hand, using sample rings grants us the ability to test all nine coated samples at once. Each experiment with nine coated samples can be repeated twice for experimental verification. In this case, only two experiments are needed. The heating rod can even be reused if it does not fail.

Second, it is significantly easier to sputter coatings onto sample rings, rather than the heating rod itself. The known methods for coating very thin layer are the sputtering and the electron beam vaporization method. For both of these methods, samples must be placed in their respective

chambers. A whole heating rod has a length of 715 mm, while a sample ring has a length of only 12.5 mm. This means that coating the whole heating rod would require a very large sputtering chamber or electron beam vaporization chamber. This large sputtering or electron beam vaporization chamber size isn't available to us, a problem that could otherwise hamper our experimental progress.

Third, sample rings greatly simplifies the sample preparation for the SEM/FIB analysis. Ultimately, all test samples must be analyzed with SEM/FIB. If the samples are heating rods, we must cut the heating rod claddings into small pieces for SEM/FIB without damaging crud. This is also very difficult since heating rod claddings are made of 316 stainless steel with a thickness of 2.5 mm. It is significantly easier to cut sample rings with only 0.25 mm thickness.

Using sample rings for crud growth as opposed to the heating rod has a disadvantage in that sample rings could affect the heat transfer or fluid flow profile. Nevertheless, our experiments had shown that sample rings' effect on crud growth is not easily distinguishable. In addition, when we analyze crud data of coated samples, we always use the uncoated side of those samples as control surfaces. This limits errors, since surfaces of the same sample ring are less likely to experience different heat flux and flow profile. Ultimately, as shown above, sample rings' benefit far exceeds its disadvantages, which is why they were used in the crud experiments.

### 4.3.2 Surface-Chemistry Modification for Crud Resistance

As shown in section 4.2, two core experiments for this thesis are the fractal analysis of crud and the testing of crud-resistant coatings. The crud-resistant coating experiments are attempts to mitigate or prevent crud by preventing crud particles from getting adsorbed onto the cladding surface. Nine different selected materials that may prevent or mitigate adsorption of crud particles are chosen. Each of these materials is sputtered onto sample rings which are used to test crud-resistant characteristics of each material. The focus of this section is to explain the idea behind the surface-chemistry modifications, and the material selection process we used.

#### 4.3.2.1 What Is Adsorption?

Adsorption is the adhesion of atom or molecules to a surface. Adsorption happens as a consequence of surface energy, similar to surface tension. Adsorption can be classified into two major types the physisorption or the adsorption via weak van der Waals forces, and the chemisorption or the adsorption via covalent bonding. The chemisorption involves a chemical reaction between the surface and the adsorbate. Since there is no evidence of chemical reaction between crud particles and fuel cladding, it is likely that the important adsorption process in crud formation is the physisorption. More information on this is available in section 2.4.2 of the background chapter.

#### 4.3.2.2 How Should It Work?

The main idea in a surface-chemistry coating experiment is to find a coating that does not adsorb crud particles. As mentioned in section 2.2.2.3, crud could form when a boiling bubble's liquid layer dry out. When looking at sub-cooled boiling bubble, the bubble bulges out, so there is a layer liquid between the bubble vapor and cladding surface. When this layer dries because of intense heat flux, crud particles stick to the surface. These crud particles stick to the surface via adsorption. Therefore, the premise is that if a cladding surface does not allow for adsorption of crud particle, the crud layer cannot start forming, making the cladding crud-resistant. In the case where there is no boiling, these surface-chemistry coatings will discourage crud particles from getting adsorbed to the coating surface. Under these conditions, we can hope that crud particles will never accumulate into a crud layer.

#### 4.3.2.3 Material Selection

Material selection was done through several processes. First, materials were narrowed down to the those that have a potential to survive in pressurized water reactor (PWR) conditions. These exclude most organic materials that cannot survive under the harsh pressure, temperature and flow condition of PWR. Materials also pass through analysis using Atomic-Force Microscopy (AFM) which measures the adhesiveness of the atom or molecule of each material to zircaloy surface. Several materials show good promise with AFM analysis. Figure 4-1 shows the adhesion of each material that was used in the crud experiment. Note that the adhesion forces of nickel oxide and iron oxide particles to zircaloy-4, the common PWR cladding, are the highest amongst materials tested. Therefore, we hypothesize that using other materials on figure 4-1 may lower iron oxide and nickel oxide crud particle stickiness, and therefore mitigate crud growth. Before being chosen to go into the IHTFP, some materials also underwent crud-resistant, pool-boiling experiments under atmospheric pressure. For some materials, such as zirconium carbide, pool-boiling experiment's results seem promising. Figure 4-2 shows how material such as zirconium carbide might prevent crud particles from sticking to the cladding surface.

### 4.3.3 Fabrication

This section highlights processes associated with fabricating the sample rings, from its inception to when it sits nicely on the autoclave heating rod. In summary, it starts with machining, electropolishing out the machine grooves, coating with crud-resistant materials, and press-fitting onto the autoclave heating rod.

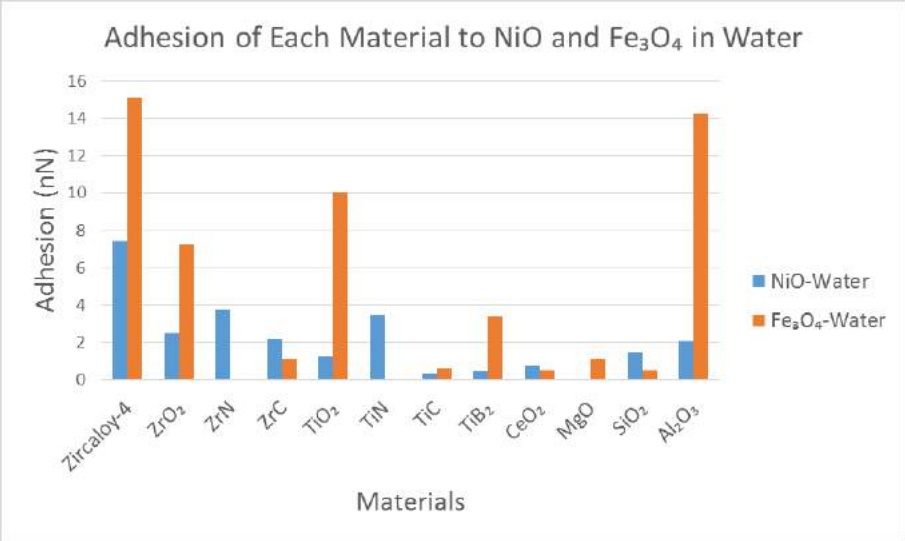


Figure 4-1: Bar graph showing adhesion of each material in x-axis to $NiO$ and $Fe_3O_4$ in water. This AFM data set was obtained by people in our group including Abdulla Alhajri, Rasheed Auguste, and Pavlina Karafilis.

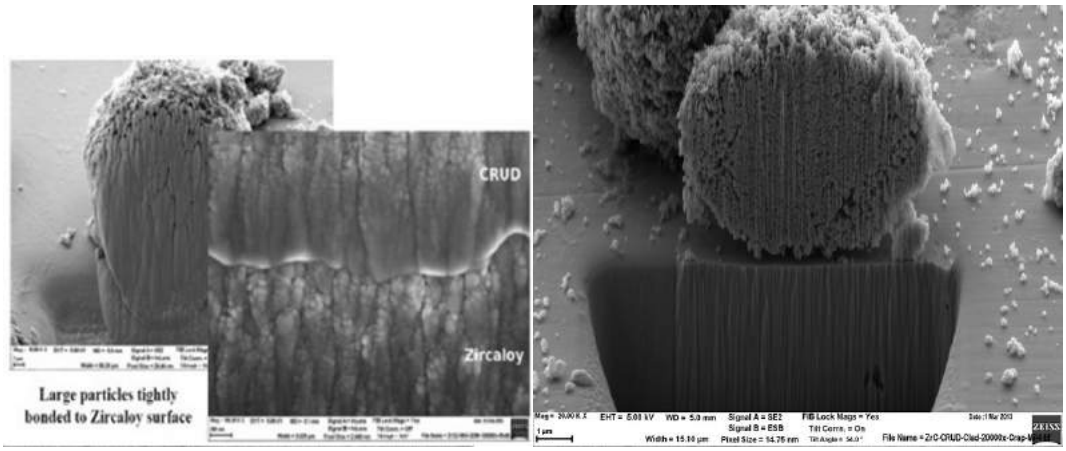


Figure 4-2: SEM image of crud particle getting adsorbed onto the cladding surface, obtained from pool-boiling sample [52]. The left image shows how crud particles actually bonded quite well to zircoloy, while the right image shows that on zirconium carbide, crud particles do not bond to it as well.

#### 4.3.3.1 Machining

The sample rings required to fit well inside the autoclave are not readily available in the market. Sample rings must be machined from stainless steel or zircaloy tubing of similar size. In this case, machining was done by the MIT machine shop using a driller to drill the raw tube inside and a lathe to carve the tube outside, to its exact dimension. Machining creates micron sized grooves, which is important to us because we use a scanning electron microscope (SEM) to analyze our samples. Therefore, the upcoming section presents a way to solve the problem of micro grooves with electropolishing.

#### 4.3.3.2 Electropolishing

The motivation of electropolishing is to remove machining grooves or other roughness that could affect our experimental results. Other forms of polishing usually do not produce resulting surfaces polished enough to appear smooth on SEM. Electropolishing is an electrochemical process in which the atoms of metal being polish get converted to ions and are removed from the surface. In doing so, metals are first removed from the rougher, pointier spots, which leaves a smoother surface profile. This is shown in the following figure. In electropolishing, the sample is the anode which is connected to positive terminal of the power supply. The cathode is connected to negative terminal of the power supply. In an electropolishing setup, the cathode is usually made of stainless steel, copper or lead. Both anode and cathode are submerged into an electrolyte solution, which is usually some mixture of acid or alcohol. When an electric potential is applied on the anode and cathode, rough and pointy parts of the metal surface get dissolved into the electrolyte. This is the opposite of electroplating where the metallic ions will travel through the electrolyte solution to deposit on a sample that needs to be coated.

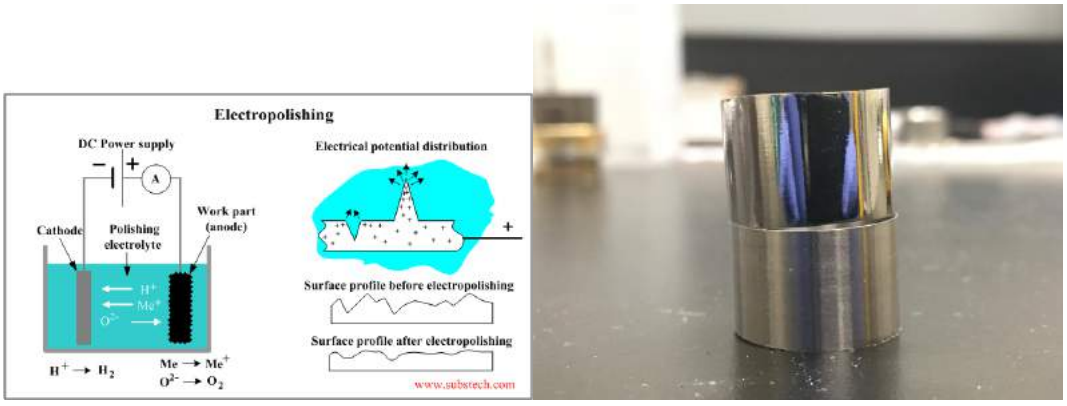


Figure 4-3: Left schematic shows how electropolishing works [215]. Right photo shows the electropolished sample ring (top) versus the unpolished ring (bottom). Notice that the electropolished sample ring looks shinier and smoother even by naked eye.

#### 4.3.3.3 Coating Sample Rings with Crud-resistant Materials

After sample rings have been fabricated, most of them must be coated with crud-resistant materials. The crud-resistant coating requires at least 10 nm so as not to feel the pull of the underlying substrate. The method of sputtering and electron-beam evaporation techniques are some typical methods of creating these very thin material coatings. The following subsections explain each of the processes and the logic that goes into choosing which process to use.

**Choosing Between Sputtering and Electron-Beam Evaporation Technique** Both sputtering and electron-beam evaporation technique can be used to deposit a thin coat of preferred material onto the fuel cladding surface. There are several other techniques such as cathodic arc deposition, etc., but these two methods of deposition are the ones available and suggested by the Microsystems Technology Laboratories (MTL) of MIT. Each technique has its own advantages and disadvantages.

Electron-beam evaporation starts with placing a target anode source, which contains the material we want to use for coating, into a vacuum chamber. The target is bombarded with an electron beam with a high amount of kinetic energy given off by a charged tungsten filament. The high kinetic energy beams of electron deposit its energy onto the material causing atoms from the material to heat up and transform into the gaseous phase. These vapor of material will deposit everywhere in the chamber, including the sample that we want to coat, forming a thin layer of the target anode material. The advantages of electron-beam evaporation include having a more even deposition compared to sputtering, having deposition rate that can be as low as 1nm per minute to as high as few microns per minute, and having better material utilization efficiency. Even deposition is something that could be useful for biphilic coating experiment because it will make sure that holes in the material mask are properly filled to form patches. The advantage in the allowance for high deposition rate and in material utilization efficiency is probably more useful to industry applications than in lab applications where production rate and efficiency is not as much of a concern. More information on biphilic coatings can be found in section 6.5.4.

Sputtering is a process of ejecting material from the target (source material) onto the substrate we want to coat. It is done by bombarding ionized inert gas, such as argon, on a target to eject material from the target, some of which will land on the substrate. In this process, an electric field is applied between the cathode target (source material) and the anode substrate. Both the target and substrate are placed within a chamber with inert gas. Free electrons driven by an electric field will bombard inert gas atoms causing them to ionize. Ionized inert gas will be attracted to the target cathode bombarding it and ejecting the target material atoms. This is the most basic form of sputtering called "DC (direct current) diode sputtering". A magnetic field can be used to trap electrons near the target to sustain plasma. By applying a magnetic field parallel to the target cathode surface, the electrons attempting to leave the cathode because of the applied electric field

may travel in circular motion back to hit the target cathode. As a result, deposition rate my increase significantly. This type of sputtering is called "DC magnetron sputtering." DC sputtering cannot be used on dielectric material targets because the insulating cathodes will cause charge build up when bombarded by charged inert gas. The solution to this problem is to use AC power instead. This type of sputtering is called "RF (radio frequency) sputtering." [216]

Sputtering's advantage, which is important to our experiment, is that even materials with a very high melting points are easily sputtered while evaporation of these materials is problematic. This is because sputtering depends on inert gas ions blasting atoms out of target, and is therefore less affected by the material's melting point. This advantage is very important to us since many of our materials are ceramics (including materials such as TiN, ZrN, ZrC), which have very high melting of around 3000 Celsius or more. Trying to evaporate these ceramics will be a difficult task.

Ultimately, the important advantage of the sputtering method is that it makes sputtering high melting point crud-resistant ceramics coating less troublesome. This advantage, along with its availability, made us choose the sputtering method over the electron-beam evaporation method. This is why, in the end, sputtering was chosen as a method of choice for coating our samples with crud-resistant coatings. All of the crud-resistant coatings made on sample ring were done using sputtering

#### 4.3.3.4 Press-Fitting

After electropolishing, samples are press-fitted onto the autoclave heating rod. The sample ring is designed to fit on autoclave heating rod very exactly. The current preferred way to press-fit is by using a press-fit shaft, a one-inch tubing section, and hammer. A press-fit shaft is basically a metal cylinder with a hole in it that was fabricated to have a diameter slightly larger than the diameter of the autoclave heating rod. The press-fit shaft can be used to slowly push or press-fit sample rings along the autoclave heater rod. The preferred way to push the press-fit shaft is with a hammer. A one-inch tube section is used as a shaft extension once the length from sample ring position to autoclave heater rod tip exceeds the press-fit shaft's length. Although the process is tedious and takes a long time, press-fitting this way has the clear advantage of complete control over the force used, since it is manual. Since the sample rings are only 0.25 mm in thickness, there is a huge risk of the ring getting crushed with using machine press-fit method, as opposed to the press-fit shaft method.

During the press-fitting process, there are two issues to keep in mind. First, since autoclave heating rod is reused many times, and the surface usually becomes quite rough in the process. This prevents proper press-fitting. The best way to get rid of this problem is to sand the outside surface of the heating rod to make it smooth. After each round of sanding, we make sure the rod is properly cleaned with alcohol using a lint free wipe before proceeding with the press-fitting process. Second,

the sample rings that we want crud to be on, must also be in a position that will get heat flux from the heating cartridge inside the heating rod. Only the 15 cm section in the middle of the rod has heating cartridge inside. We must vigilantly check to ensure that the first ring is fitted where the rest of the consecutive rings can fit nicely into this 15 cm section. After the press-fitting process is done for all the sample rings, the autoclave heating rod assembly is ready for crud growth experiment inside the autoclave, as shown in figure 4-4.

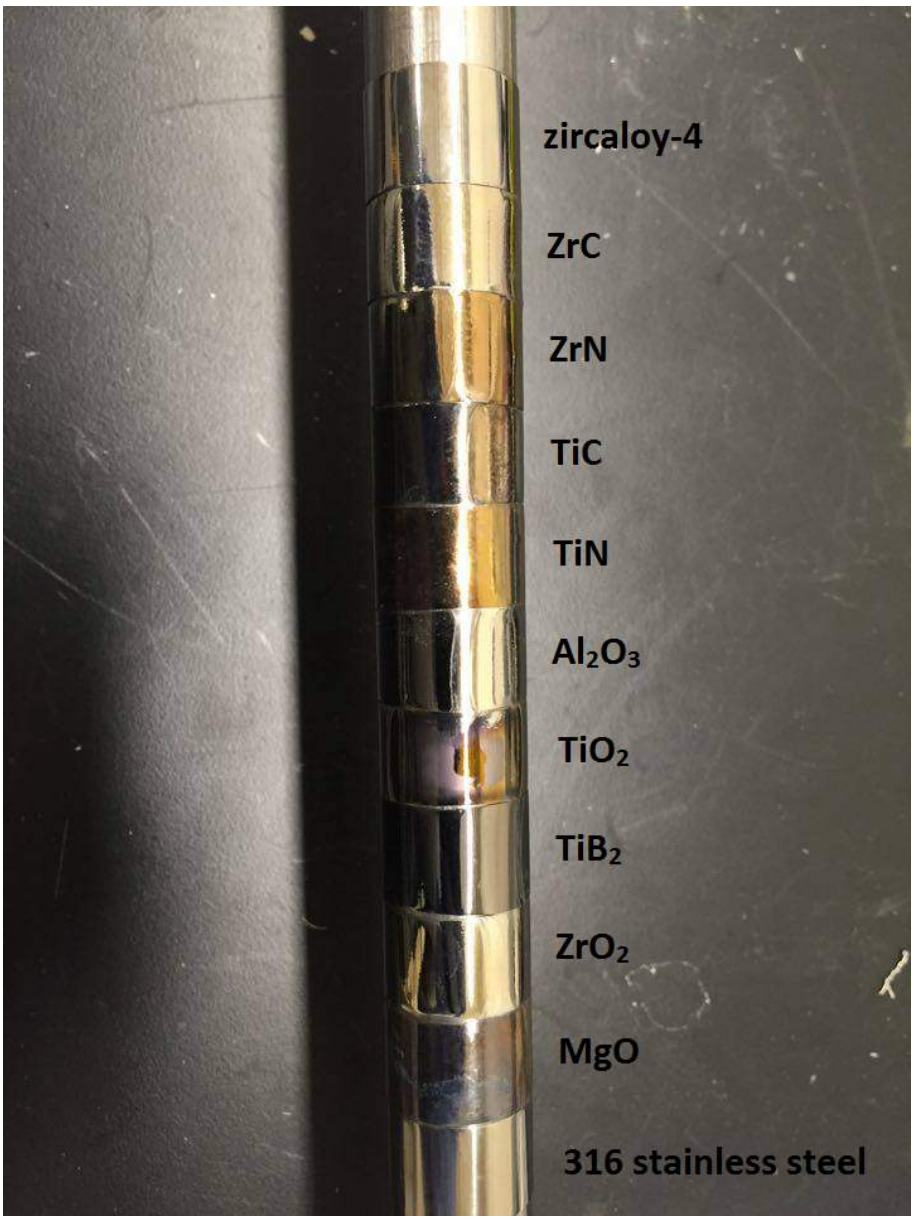


Figure 4-4: This figure shows the autoclave heating rod assembly with all its sample rings press-fitted on, ready to be heated in the autoclave.

## 4.4 Analysis Methodology

After crud is grown on fabricated samples in the IHTFP, the next step is the analysis of these samples. All of the analysis of samples in this thesis revolves around the application of image processing methods on SEM images. There are two major goals of crud analysis in this thesis. The first goal is to characterize crud and verify/provide more experimental information for the MAMBA crud model developed by our group to simulate crud. This goal focuses heavily on the fractal analysis of crud. Through finding patterns or characteristics of crud that have never been examined before, we hope to gain interesting insights into the science of crud formation and fouling deposit formation as a whole. This first goal uses SEM images of samples from trial B. The second goal is to determine the effectiveness of each chosen coating material at mitigating crud, as well as find any relationships between material properties and crud growth. This second goal uses SEM images of samples from trial C and D. This section explains the analysis methodologies applied to samples in order to obtain the data we need to reach our goals. The first subsection lays out the analysis methodology for the first goal, the fractal analysis of crud. Similarly, the second subsection lays out the analysis methodology for the second goal, the analysis of crud-resistant coating.

### 4.4.1 Fractal Analysis of Crud

The fractal analysis can be applied on SEM images of crud samples, both from the IHTFP and from the Westinghouse's WALT loop [8]. This section presents the analysis methodology used to obtain crud fractal dimensions, porosity, and thickness. The first subsection lays out the SEM images that have to be obtained from samples. The second section explains how binary images are obtained from these SEM images. The final two sections explain how values and plots can be obtained from these processed binary images. For all analysis done in this section, SEM images are taken with x10,000 magnification.

#### 4.4.1.1 SEM/FIB Images to Obtain

Samples that will be examined are from trial B of IHTFP run and from Westinghouse's WALT loop. Sample 1 and 5 of trial B grew the thickest crud in this thesis; therefore, they were chosen for this analysis. SEM images are taken for three cases, the trial B sample 5, trial B sample 1, and Westinghouse's sample. Westinghouse's sample is obtained from their test loop similar to the IHTFP. Each of these three cases requires 20 images — ten for top view and ten for cross-section view. Each image is randomly taken from different parts of sample areas to ensure that there is no location bias. In total, 60 images were taken for 3 samples, x2 views, and x10 images for each condition.

#### 4.4.1.2 Binary Image Processing

Fractal dimensions in this thesis are determined using the box-counting method, explained in section 2.3.9.2. The box-counting method requires binary images as inputs. A typical way to make a binary image is through the use of a global brightness threshold. Any pixel with brightness below the threshold would be black, and any pixel with brightness above or equal the threshold would be white. Figure 4-5 demonstrates how a binary image conversion works from a histogram point of view. If the number of pixels for each brightness are plotted, we will get the histogram represented by the blue line in figure 4-5. A global threshold, represented by the green line, can be calculated using a chosen image thresholding algorithm. In figure 4-5, the pixels in the part of histogram below the green threshold would become black pixels in the binary image. The pixels above the green threshold would become white pixels. A complete list of popular image thresholding algorithms is available in the ImageJ software is listed in section 2.3.9.1. In this thesis, the moment-preserving and the Otsu thresholding algorithm are chosen for reasons explained in section 2.3.9.1. Further explanations of the moment-preserving and the Otsu thresholding algorithm can be found in paragraph 2.3.9.1 and 2.3.9.1, respectively.

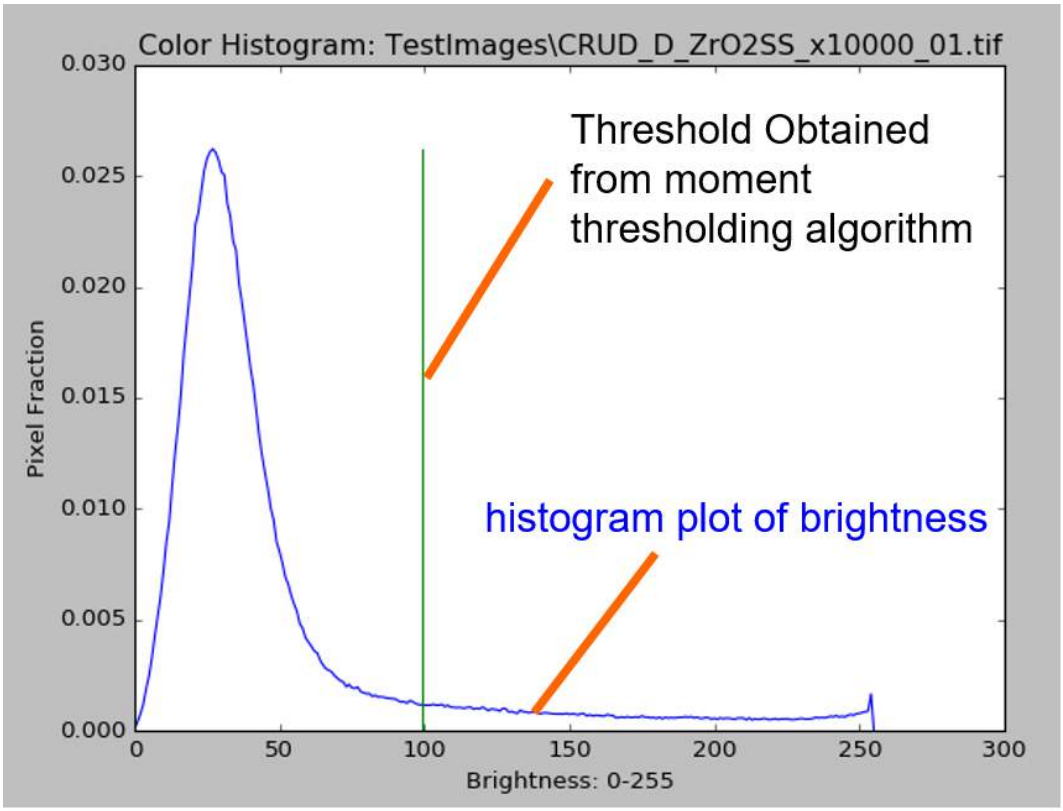


Figure 4-5: Histogram of pixel brightness in one example image, shown to illustrate how image thresholding works. The blue line represents the image's brightness histogram, while the green line represents the threshold found using moment-preserving thresholding algorithm.

Binary image conversions start with an input image such as the one shown in figure 4-6. If we create a binary image from a global threshold, determined using the moment-preserving thresholding and Otsu thresholding algorithm, we yield binary images shown in figures 4-7 and 4-8, respectively. With the use of global thresholds, the parts of both figures in orange squares are not properly converted to binary. Some crud particles are converted to black because of their darker local shading. This problem with image shading can be corrected with an adaptive thresholding algorithm.

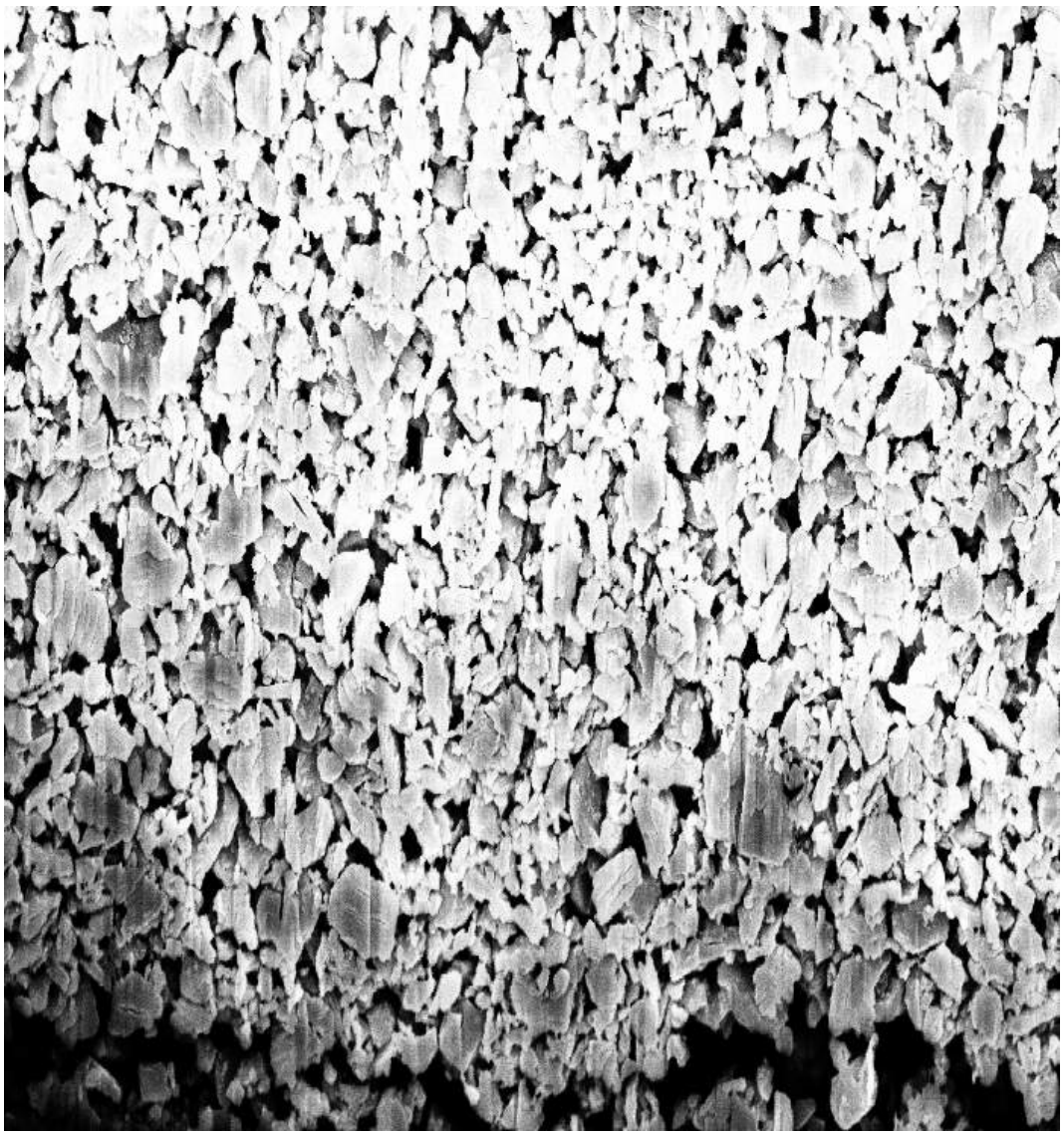

Figure 4-6: An example raw crud cross-section image.

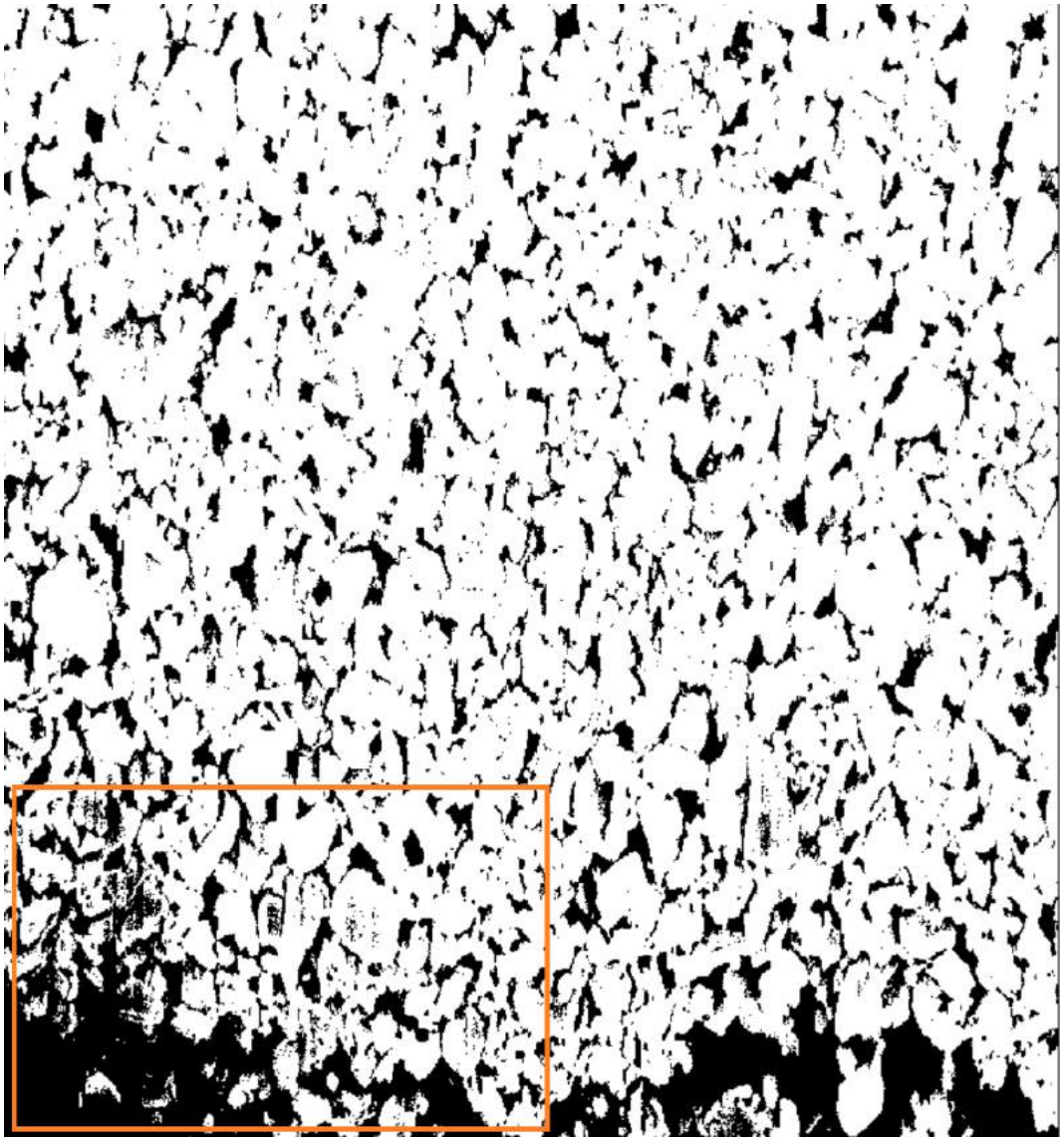

Figure 4-7: A binary image obtained by applying moment-preserving thresholding algorithm on figure 4-6. The part in the orange square is not very accurate. Some crud particles with darker shading were mistaken as holes.

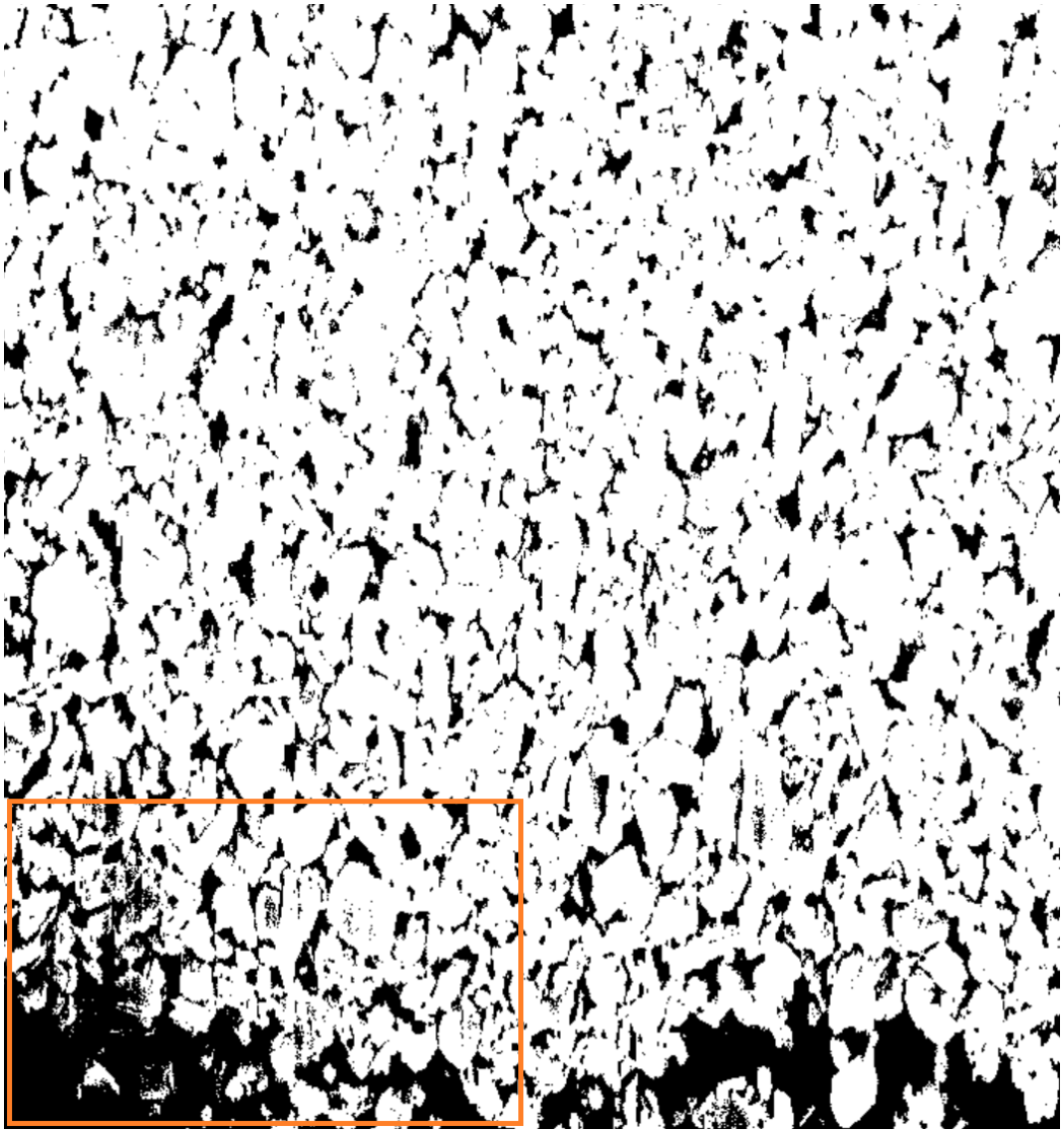

Figure 4-8: A binary image obtained by applying Otsu thresholding algorithm on figure 4-6. The part in the orange square is not very accurate. Some crud particles with darker shading were mistaken as holes. For this particular image, the fractal dimension is 1.574.

**Chow and Kaneko Adaptive Thresholding** An adaptive thresholding algorithm does not use a single global threshold as shown previously. Instead, it calculates local thresholds and interpolates among them to determine the final binary image. The standard technique for adaptive thresholding is the Chow and Kaneko approach [217]. This technique works by dividing the image into a regular array of overlapping sub-images. A local threshold is calculated for each sub-image that is not unimodal (an image is unimodal when its brightness histogram exhibits only one peak). Local thresholds can be calculated using any image thresholding algorithm including the moment-preserving and the otsu algorithm. Unimodal sub-images are ignored because they are unlikely to provide useful information. Local thresholds of unimodal sub-images are found by interpolating between sub-images with calculated local thresholds. After all the local thresholds for sub-images are found, the local threshold used in each pixel can be found through interpolation of sub-images' local thresholds. Figure 4-9 shows an illustration of the processes involved in Chow and Kaneko adaptive thresholding. Figures 4-10 and 4-11 demonstrates that Chow and Kaneko adaptive thresholding technique is superior to global thresholding techniques shown in figures 4-7 and 4-8. The inaccurate part in the orange squares of figures 4-7 and 4-8 are now properly corrected in figures 4-10 and 4-11. The fractal dimension changes from 1.574 to 1.559 when we added Chow and Kaneko thresholding to the process, for this example image. Despite its usefulness, Chow and Kaneko adaptive thresholding technique involves significant computing power. Nevertheless, in this thesis, this technique is chosen over the use of global threshold because we value data accuracy over computing time.

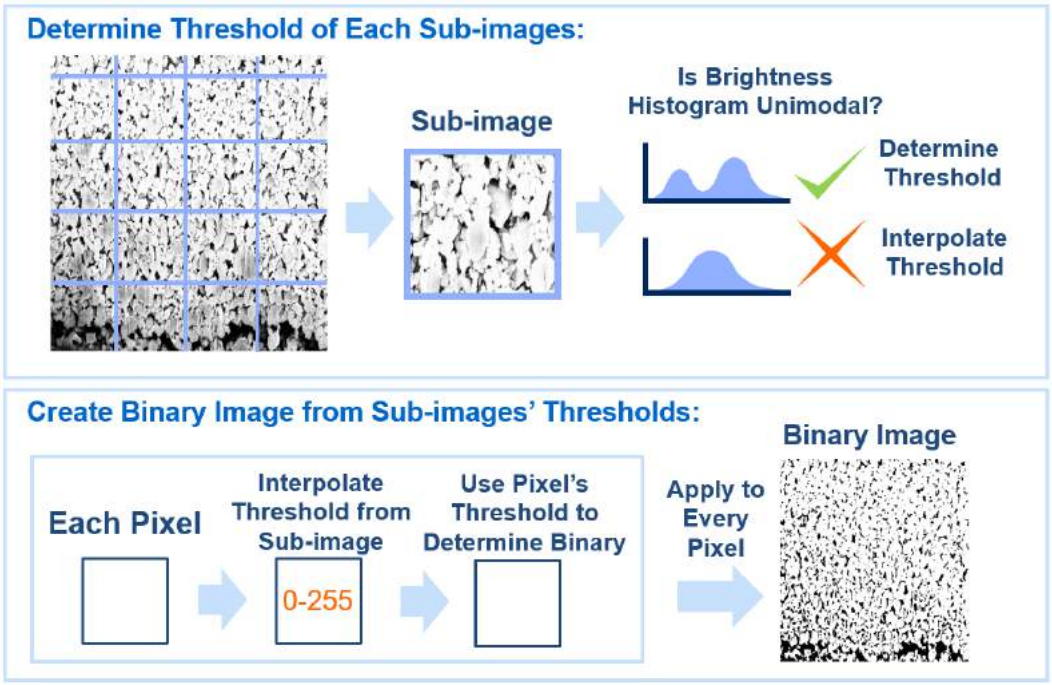


Figure 4-9: Illustration of the processes involved in Chow and Kaneko adaptive thresholding.

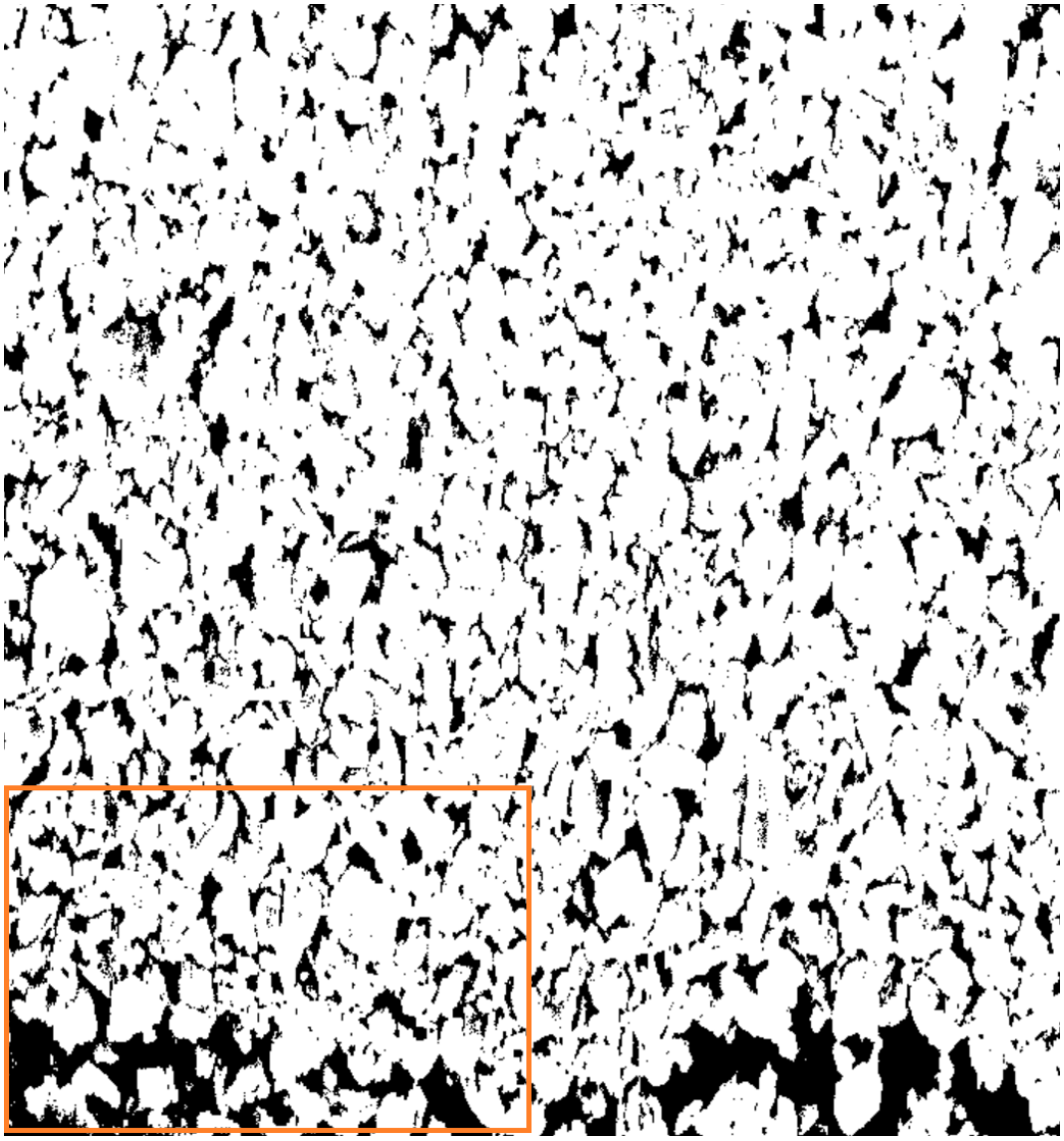

Figure 4-10: A binary image obtained by applying adaptive thresholding based on the moment-preserving thresholding algorithm on figure 4-6. The part in the orange square is now accurate with the help of adaptive thresholding algorithm.

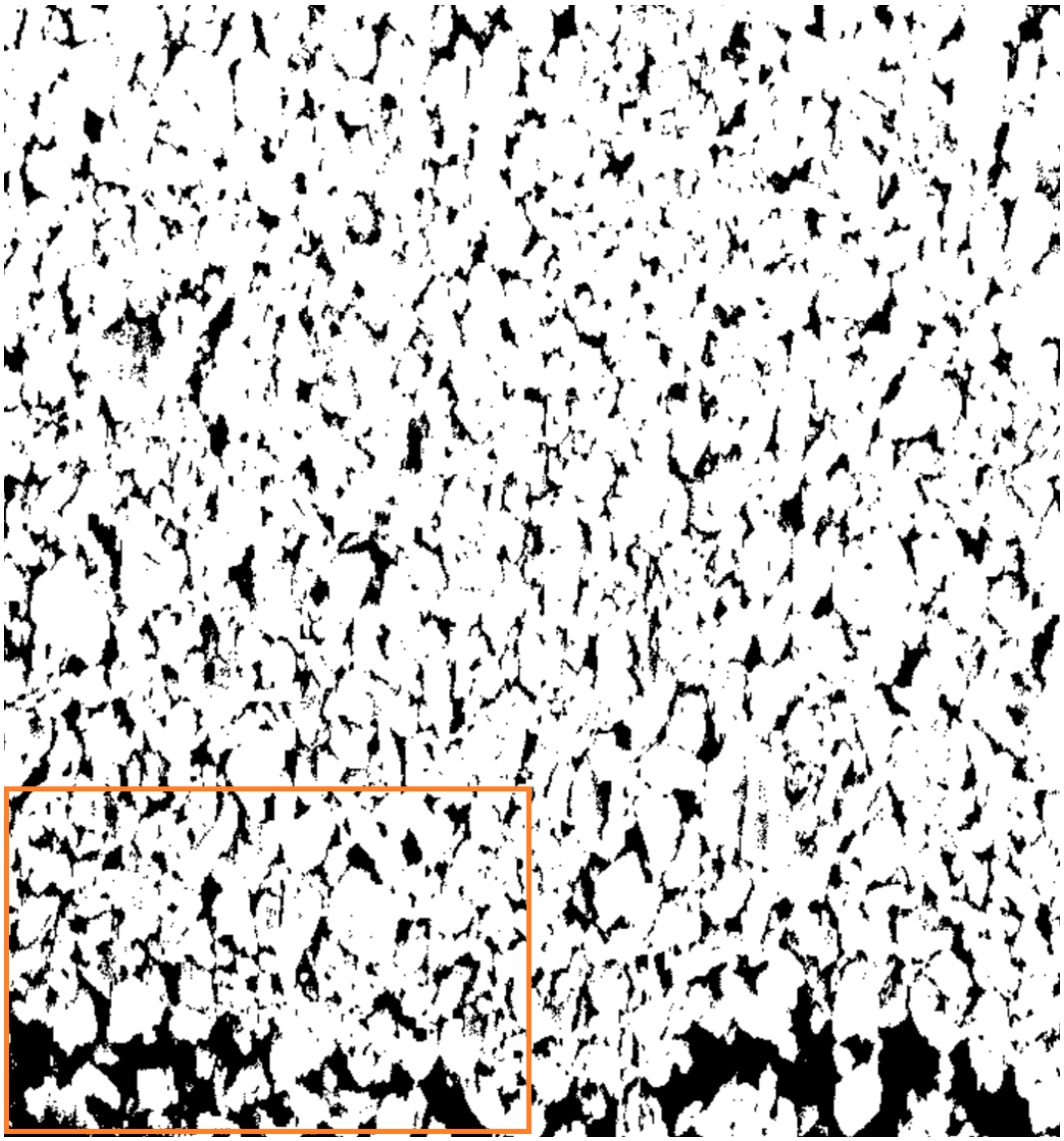

Figure 4-11: A binary image obtained by applying adaptive thresholding based on the Otsu thresholding algorithm on figure 4-6. The part in the orange square is now accurate with the help of adaptive thresholding algorithm. The fractal dimension of this image is 1.559 which is slightly lower than the fractal dimension of 1.574 from the binary image without adaptive thresholding.

**Morphological Image Processing** At this point, we have applied moment-preserving and Otsu thresholding with Chow and Kaneko adaptive thresholding. The results are decent but may still show some observable image artifacts. This artifacts problem can be alleviated with the use of morphological image processing as shown in figure 4-12. In morphological image processing, structuring elements are applied to each pixel. The structuring element is used to select some set of pixels around the pixel it applies to. An operator is applied to the structuring element to determine the outcome of the pixel that the structuring element is applied to. The 3x3 pixel box is chosen as the structuring element for its superior performance and simplicity. The closing operator is used to weed out black pixels without any surrounding pixels which are more likely to be artifacts. The closing operator works by counting the number of black pixels in the structuring element and determining if that number is more than some threshold. Figure 4-13 illustrate the process involved in morphological image processing used for this thesis. Using the same figure 4-6, applying the Otsu thresholding, the adaptive thresholding, and the morphological image processing yield the binary image with a fractal dimension of 1.525. This is lower compare to the fractal dimension of 1.559 when the morphological image processing was taken out of the process. Figure 4-14 shows how the morphological image processing affect the box-counting plots. We can see a slightly less box count among the smaller box sizes.

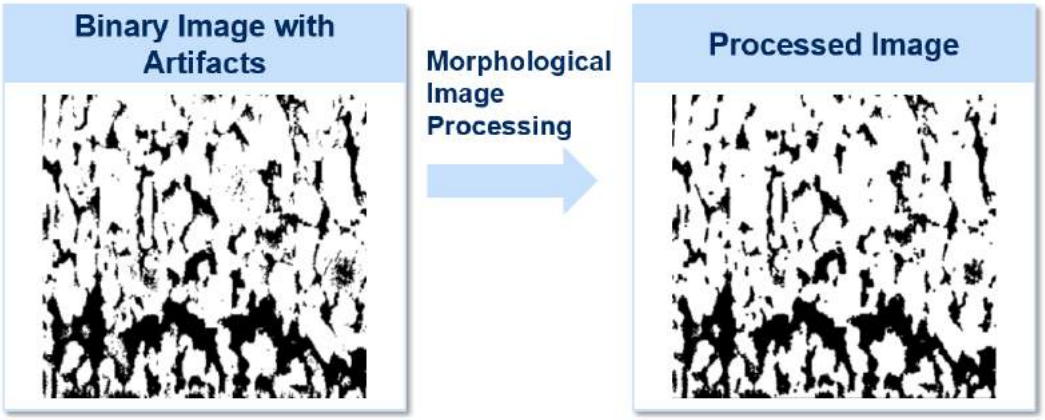


Figure 4-12: Illustration of how morphological image processing can alleviate an artifacts problem. The left binary image has black dots which are image-processing artifacts. There are noticably fewer black dots after morphological image processing was applied.

#### 4.4.1.3 Values to Obtain

After binary images are obtained from SEM images, we can use the binary images to obtain many useful crud parameters. These parameters are crud layer thickness, porosity, fractal area dimension, and fractal tortuosity dimension. The methodology used to obtain these values from binary images are explained in the following paragraphs. Note that more detailed background information related

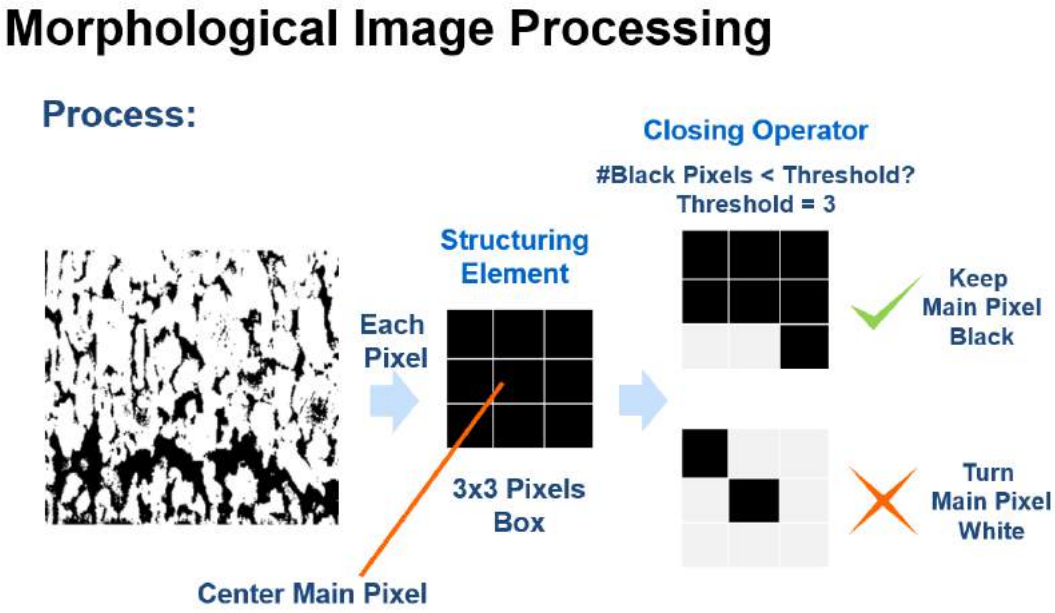


Figure 4-13: Illustration of morphological image processing applied in this thesis.

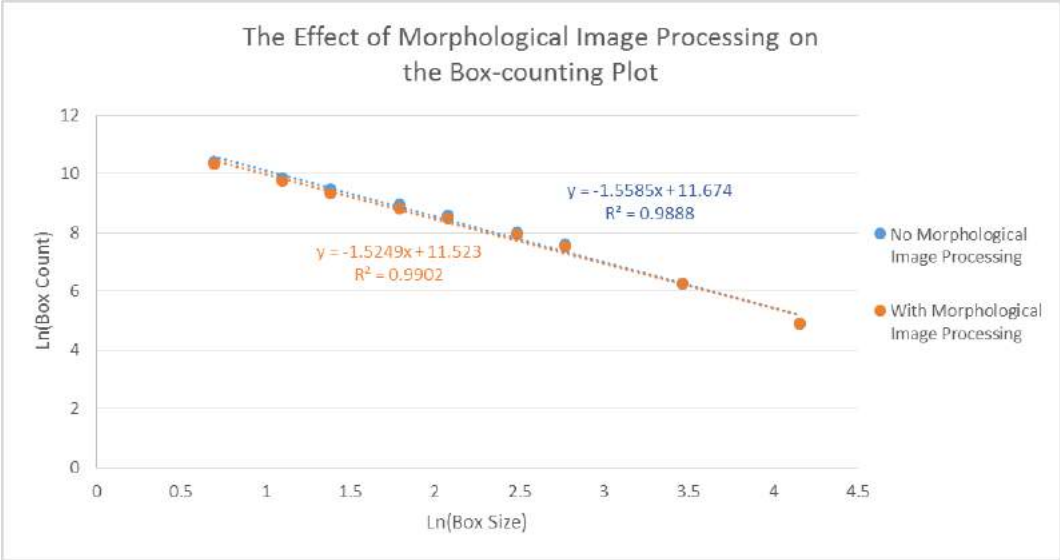


Figure 4-14: Box-counting plots for a case with and without morphological image processing. The Otsu thresholding and the adaptive thresholding algorithms are applied to the figure 4-6 in the base case.

to these parameters can be found in section 2.1.2.1 and 2.1.2.2 of the background chapter.

**Crud Layer Thickness** Crud thickness can be obtained through measuring thickness in the crud cross section SEM image obtained from FIB processing. SEM/FIB machines have built-in measurement tools with options to adjust the settings of the measurement tools for cross section measurements. In images without a measurement ruler, crud layer thickness can still be estimated using height in a number of pixels. In most SEMs, the ruler will remain at fixed length across the SEM screen as long as the magnification is fixed. This means that if the screen pixel size is also fixed, the ruler will remain at a fixed pixel length across images with the same magnification; therefore, we can calculate the ratio of the number of pixels length per actual micron length. After that, we can use this ratio to calculate the actual micron length given any length measured as the number of pixels. Crud thicknesses measured in the pixel unit can then be transformed to the micron unit by utilizing this ratio.

**Porosity** As mentioned earlier in section 2.1.2.2, porosity is the fraction of empty spaces in a material compared to its total volume. The value varies from 0 to 1 with 0 meaning the material is solid. Porosity is important in the study of crud because it affects the flow of water within crud as well as the heat transfer in the crud layer. In binary images obtained in the previous section, white color represents crud, while black color represents empty space. Determining the porosity from these binary images is simple: we can count the number of black pixels and divide them by the total number of pixels.

**Fractal Area Dimension** ($d_N$) Fractal dimension in this thesis is found via box-counting method, as explained in section 2.3.9.2. Fractal area dimensions are obtained from analyzing the images perpendicular to the flow. More background information on fractal area dimension can be found in section 2.3.7. The uncertainty for this value would be calculated using the standard error of the estimate $\sigma_{est}$, as explained in section 2.3.10.

**Fractal Tortuosity Dimension** ($d_T$) Tortuosity represents how twisted the flow pathways are. Fractal tortuosity dimension, $d_T$, represents the extent of convolutedness of capillary pathways in crud. In 2D, the fractal tortuosity dimension can range from 1 (straight path) to 2 (curve the filled the whole plane). More background information on fractal tortuosity dimension can be found in section 2.3.7. Similar to the fractal area dimension, the box-counting method is used to determine the fractal tortuosity dimension. Section 2.3.9.2 describes the box-counting method in detail. To determine the tortuosity of flow in the capillaries, the important images to analyze are parallel to the flow path. Hence, SEM images used in the box-counting analysis to compute fractal tortuosity dimensions must be the cross-section images. The uncertainty for this value can be calculated using

the standard error of the estimate $\sigma_{est}$, as explained in section 2.3.10.

#### 4.4.1.4 Plots to Obtain

The following plots are very useful in finding patterns in the experimental values obtained. In this thesis, we are particularly interested in understanding how fractal dimensions vary with position and porosity in crud. More information on parameters used in these plots can be found in section 2.1.2.1 and 2.1.2.2.

**Fractal Tortuosity Dimension vs Crud Height Position** One of the final goals of this section is to get a graph of fractal dimension versus crud height position ($\mu m$). Fractal dimensions will be on the y-axis and height positions will be on the x-axis. In this case, the crud height position is defined as the distance from the cladding surface. A cross-section SEM image of crud will be divided into overlapping sub-images with different crud height positions. Fractal analysis is applied to each of these sub-images to characterize its fractal tortuosity dimension. Note that the WALT loop's crud samples are in form of crud flake; therefore, they will not be used for this analysis, since we have no knowledge of their actual positions within the crud layers.

**Porosity vs Crud Height Position** The method of obtaining this plot is similar to that of the fractal tortuosity dimension vs crud height position plot, but porosities are calculated as opposed to the fractal tortuosity dimensions.

**Fractal Dimension vs Porosity** One interesting relationship we can obtain from our data is that between fractal dimension and porosity. Each point in this plot will represent a fractal dimension and a porosity of a particular image. All SEM images, taken according to section 4.4.1.1, will be plotted. Each point color on the plot will represent a set of data.

#### 4.4.1.5 Testing Fractal Dimensions on the MAMBA-BDM Crud Model

After the fractal dimension data were obtained, we are also interested in testing it on the MAMBA-BDM crud model to examine how these new experimental data affect our results. There are two modeling cases that we are interested in. In the first case, the porosity is fixed while the fractal dimension is varied with the height from the cladding. In other words, this modeling case will utilize the experimental relationship between the fractal dimension and the crud height position. In the second case, both the fractal dimension and the porosity will vary. This modeling case will utilize the experimental relationship between the fractal dimension and the porosity.

### 4.4.2 Crud-Resistant Surface Modification

The major goal of studying crud-resistant coatings is to determine their effectiveness in mitigating crud. This goal can be achieved by finding the area coverage of crud samples. The premise is that if a crud-resistant coating is effective in mitigating crud, there should be less crud sticking to the coating surface, and therefore, crud area coverage should also be reduced. This section presents the analytical methodology used to obtain these crud area coverages, as well as their related values and plots. The first section shows SEM images that are needed. The second section describes how binary images are obtained from these SEM images. The third section describes how crud area coverage and crud area reduction values are computed from these binary images. The last section describes interesting plots that can be obtained from our data. For all analysis done in this section, SEM images are taken with x10,000 magnification.

#### 4.4.2.1 SEM Images to Obtain

Each sample ring is coated with crud-resistant material on one side. The other uncoated side acts as the control area. Each type of material is tested two times in the trial C and the trial D to ensure that the data is repeatable. This means that for each material, SEM images are taken for the coated side of trial C and D, as well as the uncoated side of trial C and D. Each of these four cases requires ten images randomly taken from different parts of sample areas to ensure that there is no location bias. In total, 360 images were taken for 9 materials, x2 trials, x2 sides, and x10 images for each condition.

#### 4.4.2.2 Binary Image Processing

Crud obtained from trial C and trial D is composed of crud particles scattered on the cladding surface. As seen in the example SEM image in figure 4-15, the crud particles almost always appear whiter than the material background. This property is very useful for doing area coverage analysis, since it makes the job of processing the image into a binary image easier and more accurate. A binary image, as shown in figure 4-16 and 4-17, can be computed using the image thresholding algorithm mentioned earlier in section 4.4.1.2.

#### 4.4.2.3 Values to Obtain

In order to determine the effectiveness of crud-resistant coating for crud composed of scattered particles, crud area coverages (%) of different samples are needed. For each SEM image obtained according to section 4.4.1.1, crud area coverage must be determined. The mean and standard deviation of crud area coverage for each sample type can be found using the crud area coverage values obtained from the 10 SEM images taken for that particular sample type.

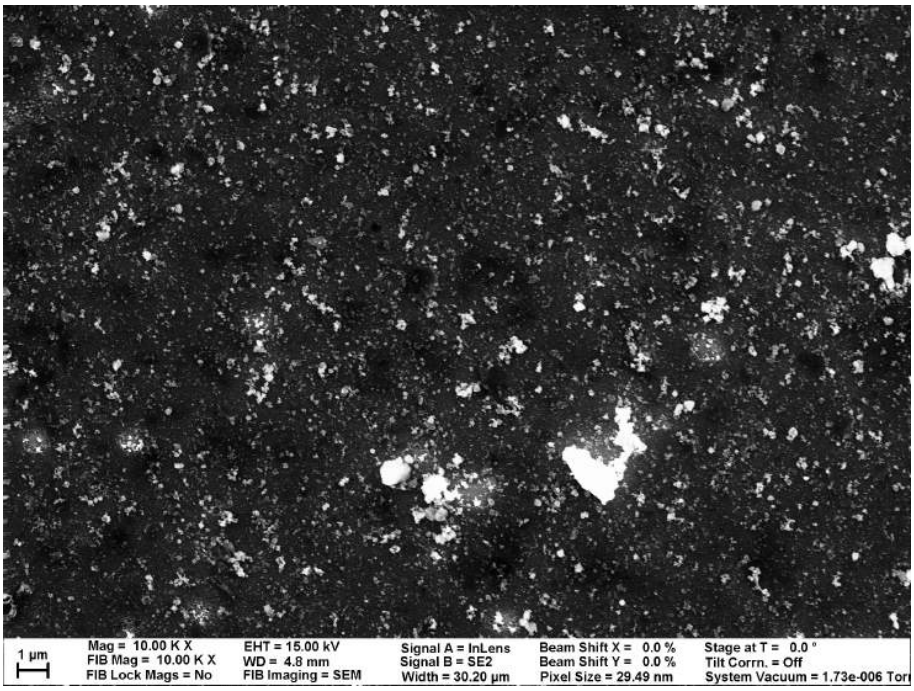


Figure 4-15: An example SEM image of the coated side of $ZrC$ sample ring.

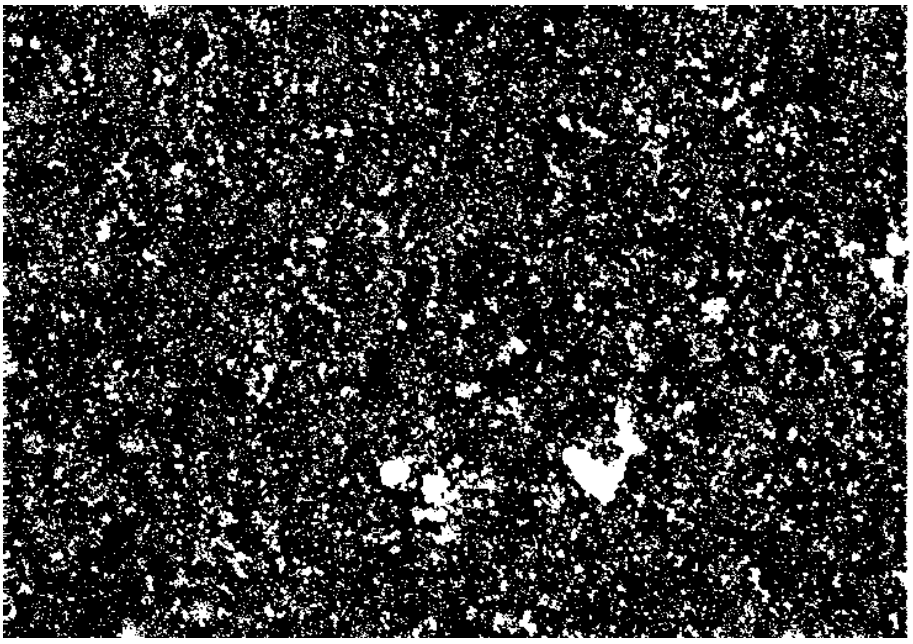

Figure 4-16: Figure 5-51 converted to a binary image using moment-preserving thresholding algorithm.

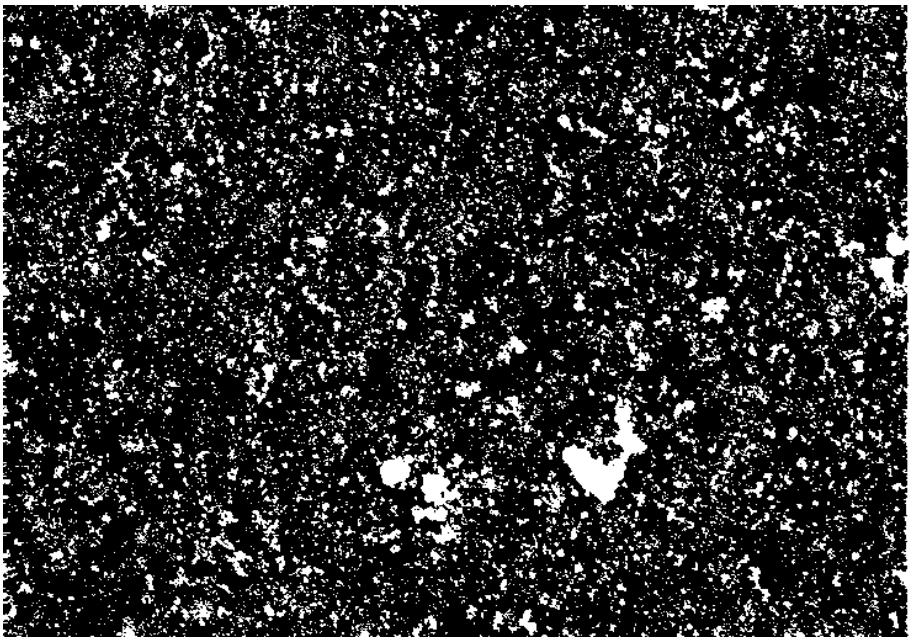

Figure 4-17: Figure 5-51 converted to a binary image using otsu thresholding algorithm.

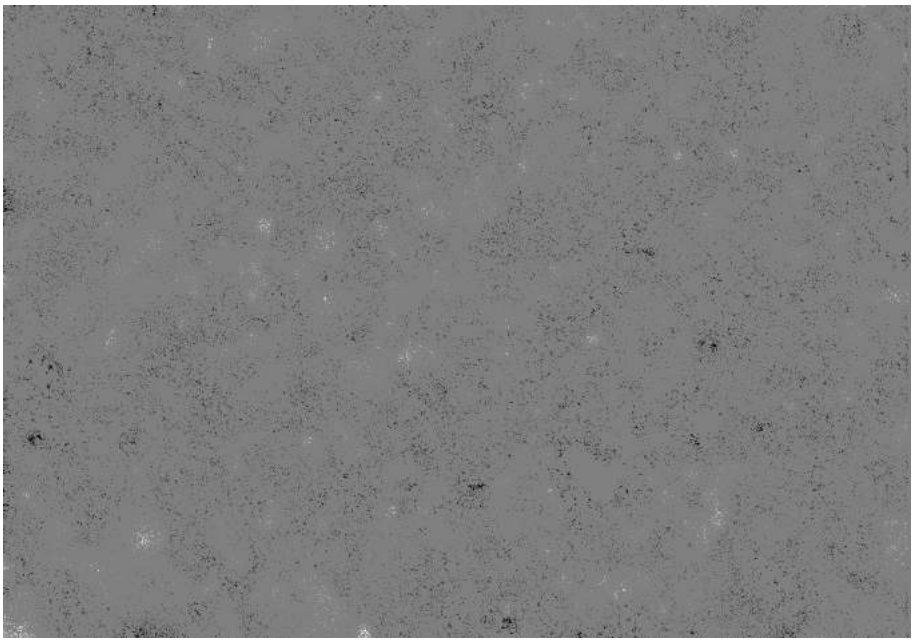

Figure 4-18: Image created by subtracting the Otsu thresholding's binary image in figure 4-16 from the moment-preserving thresholding's binary image in figure 4-16. The white pixels are where moment-preserving thresholding yield white pixels, while Otsu thresholding yield black pixels. Vice versa is true for black pixels. Gray pixels occur where both algorithms yield the same color.

**Crud Area Coverage (%)** Just as the name implied, the % crud area coverage is the percentage of area in the sample that is covered in crud. With binary images obtained in the previous section, finding the crud area coverage is a simple matter of counting the number of white pixels in a binary image, and dividing it by the total number of pixels.

**Crud Area Coverage Reduction (%)** This value is the mitigation of crud area coverage when the crud area coverages of coated areas are compared with their corresponding control area. As mentioned earlier, each sample ring contains a coated and an uncoated side, where the uncoated side acts as the control area. Crud area coverage reduction is computed using the following equation:

$$CoverageReduction = \frac{CrudAreaCoverage_{control} - CrudAreaCoverage_{coated}}{CrudAreaCoverage_{control}} \tag{4.1}$$

#### 4.4.2.4 Plots to Obtain

After the values of crud area coverage reduction are obtained, they should be compared to material properties to gain insights into how different material properties affect crud growth. One of the best ways to gain these insights is through plotting crud area coverage reduction versus properties such as AFM adhesion force, Hamaker constant, and refractive index. The following paragraphs explain how these comparison plots can be obtained.

**Crud Area Coverage Reduction vs AFM Adhesion force** A material's crud mitigation effectiveness will depend on how well crud particles adhere to the cladding surface. AFM experiments conducted in our group tested the adhesion force between crud particles and different material surfaces. Crud particles in the AFM experiments are taken as either iron oxide or nickel oxide particles. More details on this can be found in section 4.3.2.3.

**Crud Area Coverage Reduction vs Hamaker Constant** As mentioned earlier in section 2.4.2, Hamaker constants may be useful in estimating the adhesiveness of crud particles to different coating materials. By comparing the experimental crud area coverage reduction to Hamaker constant, we may get useful scientific insights into how Hamaker constant relate to crud growth. Hamaker constants can be obtained from the literature, as well as calculations that involve refractive index of the materials. Refractive indexes can be obtained from the literature and ellipsometery experiments conducted by our group.

### 4.4.3 Loop Conditions

For experimental trials used to obtain results for the fractal analysis of crud and effectiveness of crud-resistant materials, we also want to display the conditions at which the loop operates. Example plots

of sensor values from the IHTFP for a representative trial were shown in section 3.12. Other than presenting these IHTFP conditions' plots, the results chapter will also describe why the plots of the specific conditions take a particular shape and how those IHTFP conditions affect crud.

# Chapter 5

# RESULTS

## 5.1 Introduction

This chapter will present the results obtained from our experiments. Crud samples were obtained according to experimental procedures shown in chapter 4. SEM images of these crud samples, as well as Westinghouse WALT's crud flakes, are taken. All quantitative results are obtained from by applying image processing algorithms on SEM images of these crud samples. Section 5.2 presents the fractal analysis results obtained using the methods presented in section 4.4.1. Section 5.3 exhibits the crud-resistant coatings results obtained using the methods presented in section 4.4.2. Both sections 5.2 and 5.3 are divided into three sub-sections. The first subsection presents the loop conditions at which crud samples grew. The second subsection presents example crud SEM images. The third subsection shows the quantitive results that were obtained from the application of image processing algorithms on the crud SEM images.

## 5.2 Fractal Analysis of Crud

One of the two major goals of this thesis is the fractal analysis of crud samples. For background information on fractal analysis, visit section 2.3 from the background chapter. This section lays out the results acquired that are related to the fractal analysis including the conditions at which crud was grown, example SEM images of crud samples, and fractal analysis results.

### 5.2.1 Loop Conditions

Before diving into the SEM images results which are the core of this thesis, it is useful to first examine the conditions at which crud was grown. This section presents these conditions in detail, including the plot of how they vary over time and explanations of why they were chosen. In addition, any

anomaly during the experimental trial is also explained. Conditions used to conduct WALT loop's test can be found in section 2.2.6.2.

#### 5.2.1.1 Trial B (September 22, 2015)

The experimental trial B was chosen for use in crud fractal analysis because it is the trial that grew most crud in this thesis. Despite the fact that this trial ran for only 9 days as oppose to the planned 14 days, the crud found in this trial is 2 to 15 $\mu m$ thick, the thickest amongst all other trials. This heavier crud growth was likely due to two reasons. First, the sample contains machining marks visible under an electron microscope, as shown in section 5.2.2. These machining marks could act as nucleation sites for crud growth. All trials conducted after trial B uses electropolished sample rings that look smooth under SEM. More information on electropolishing can be found in section 4.3.3.2. Second, the pressure in trial B was also the lowest out of all the trials. Towards the end of trial B, the pressure hovers at around 103. The calculation in section 3.3.4 shows that temperature between the element centerline and the cladding surface should be roughly 95 ºC. The element temperature stays at roughly 410 ºC throughout the trial. This means that the cladding surface temperature would be roughly 315 ºC. The saturation temperature at 103 bars is 313 ºC according to ChemicaLogic SteamTab software [197]. The difference between cladding surface and saturation temperature is deduced to be only 2 ºC in this case. Figure 3-8 suggests that 5 to 10 ºC difference between cladding surface and saturation temperature would be ideal for nucleate boiling. In reality, the 2 ºC estimated is likely to be misleading, as explained in section 4.2.0.5. This temperature inaccuracy hypothesis is further reinforced when another trial with the same heating rod on October 9, 2015, failed when we try to decrease the saturation temperature by only 5 ºC, by lowering the pressure to roughly 95 bars.

A three-weeks trial was conducted later on November 10th, with electropolished sample rings and slightly higher pressure. Unfortunately, that trial yield no visible crud layer. Figure 5-3 shows how dissolved oxygen concentration vary with time in the IHTFP during trial B. The first peak was a mistake caused by wrong valve 1 direction. Valve 1 is the valve placed right after the backpressure regulator, as shown in figure 3-5, which can be used to redirect water coming from the main loop to either the water tank or the measurement equipment assembly. During the first 24 hours of trial B, this valve was accidently setup to redirect water to the water tank instead of the measurement equipment. This causes a continuous rise in apparent dissolved oxygen concentration since the stagnant water continuously receives more oxygen from the environment via diffusion or tiny leaks. In addition, this stagnant water volume in the measurement equipment tubing is separated from the water tank; therefore, its dissolved oxygen was not removed by argon gas bubbling. This mistake was corrected on the second day by redirecting valve 1 to push water from the main loop's outlet through measurement equipment. This is what caused the instantaneous drop in dissolved

oxygen level roughly 24 hours after the start of trial B. After around 100 hours, dissolved oxygen concentration rose for the second time, as shown in figure 5-3. This second dissolved oxygen rise never decrease back down again, which prompted loop shutdown at 9 days as oppose to the planned 14 days. The cause for oxygen rise was later determined to be tiny window leaks caused by sapphire window corrosion. Figure 3-106 is an example of sapphire window corrosion. Figure 5-2 is the graph of pressure versus time for trial B. As oppose to the 155 bars pressure in trial A, the pressure in trial B was set lower to generate more crud growth. The trial starts off with pressure around 115 bars. Later on, we lowered the pressure to around 103 bars which are the lowest we ever operate the IHTFP at. Figure 5-4 shows how water conductivity varies with time in the IHTFP during trial B. The plateau peak in the first 24 hours correspond to the dissolved oxygen peak which was caused by the mistake mentioned previously. Apart from the brief peak caused by the mistake, conductivity remains at around 8 $\mu S/cm$ which is typical for an IHTFP trial. Similarly, the pH graph, shown in figure 5-5, also exhibits a peak in the first 24 hours. 5-6

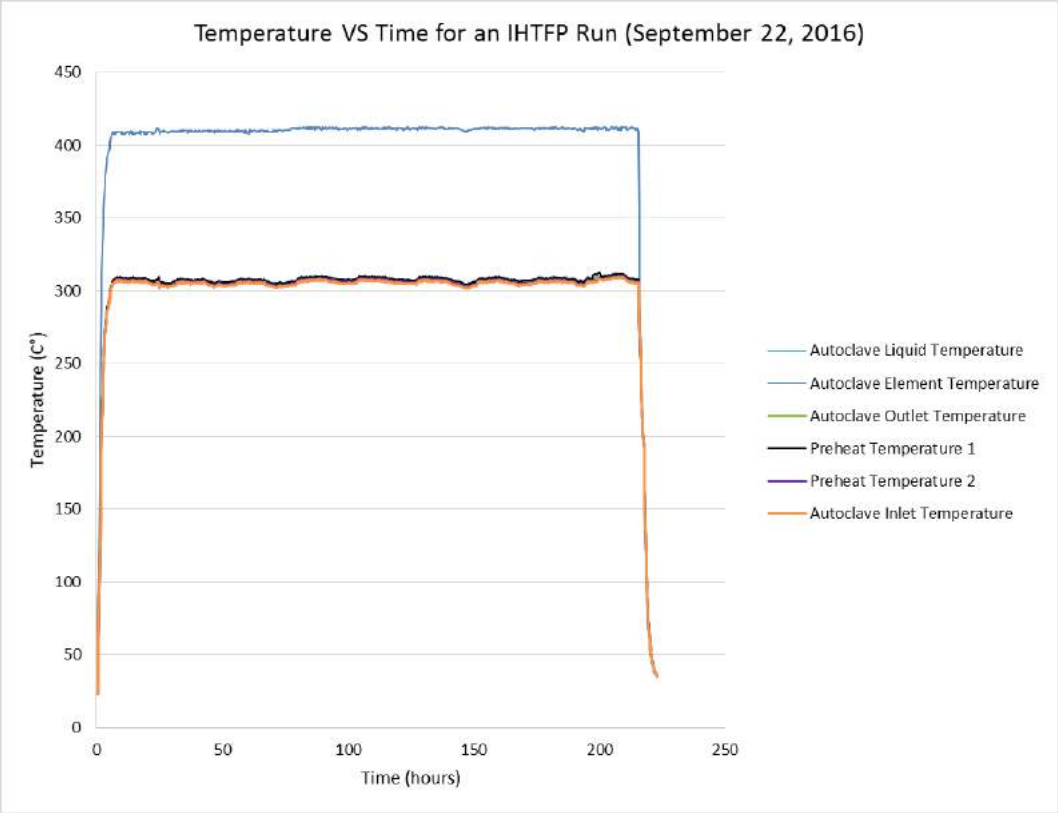


Figure 5-1: Temperatures at different spots in the loop versus time for the experimental trial B.

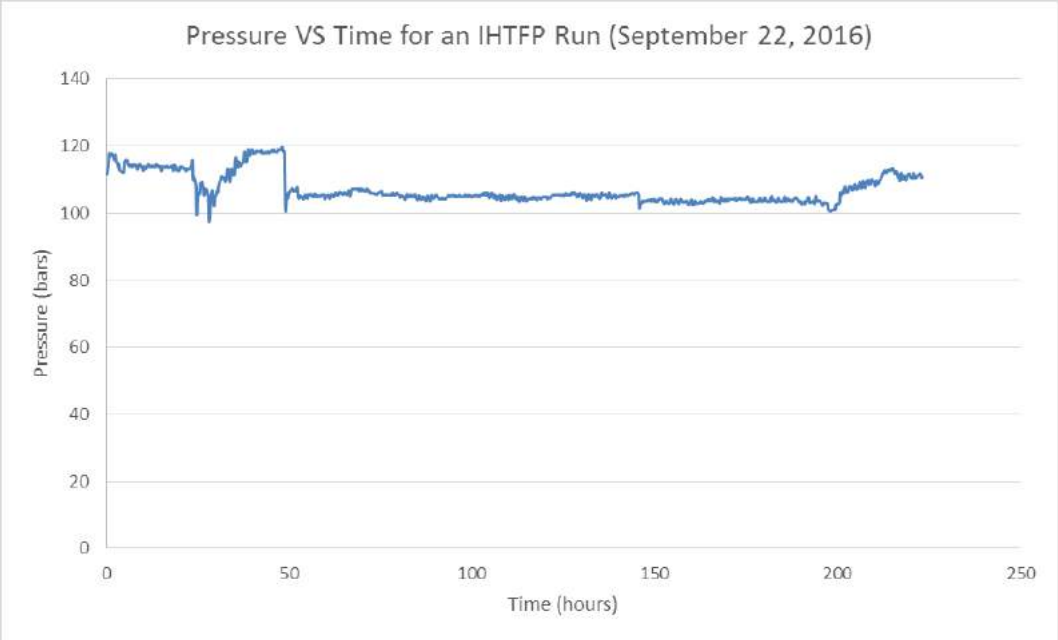


Figure 5-2: Pressure versus time for the experimental trial B.

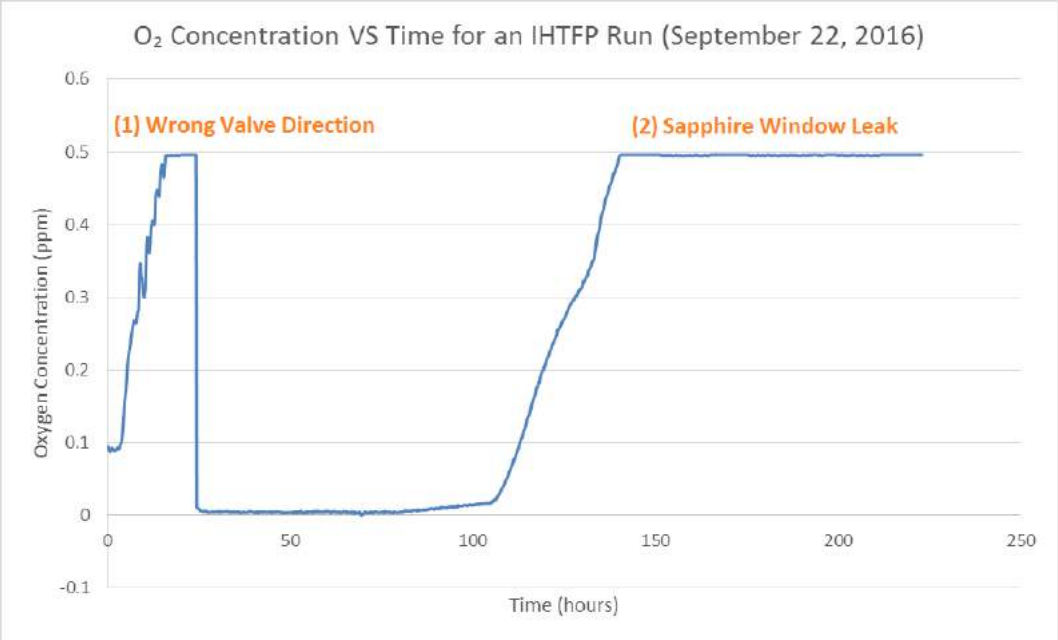


Figure 5-3: Dissolved oxygen concentration versus time for the experimental trial B.

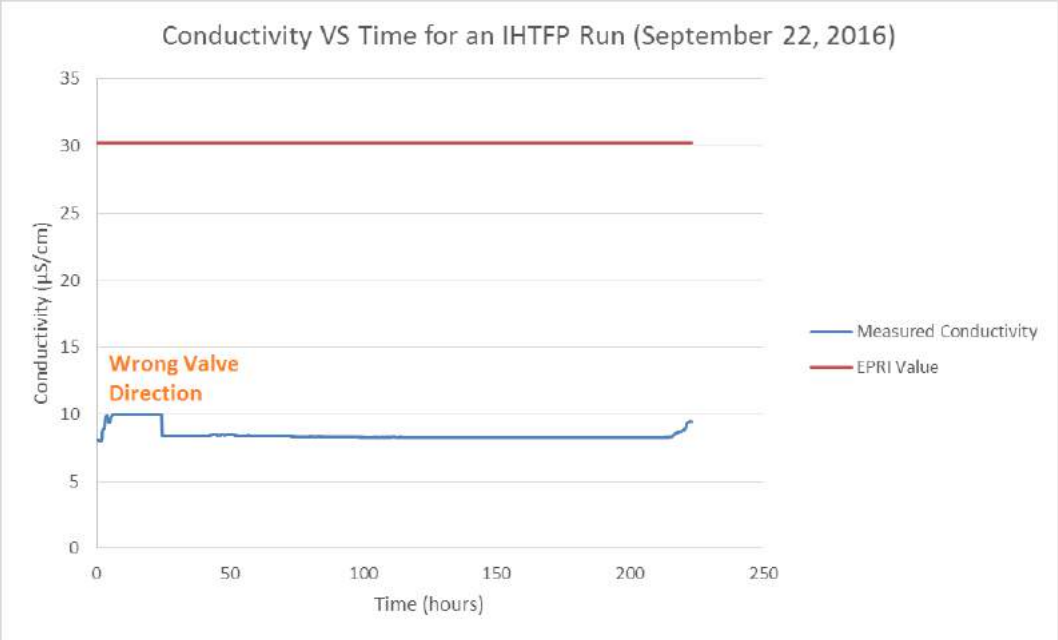


Figure 5-4: Water conductivity versus time for the experimental trial B.

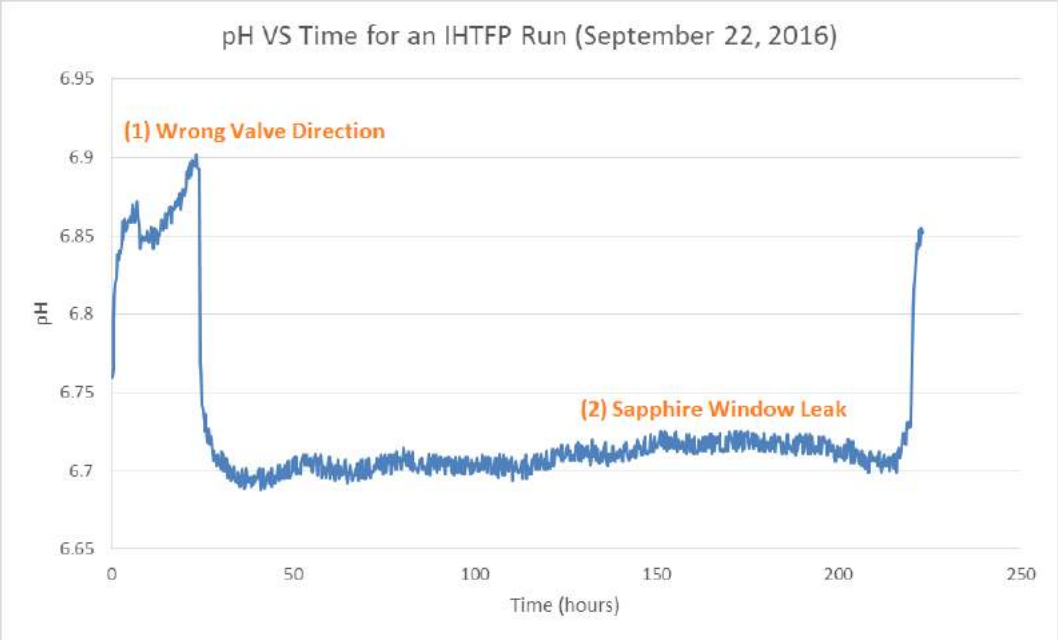


Figure 5-5: pH versus time for the experimental trial B.

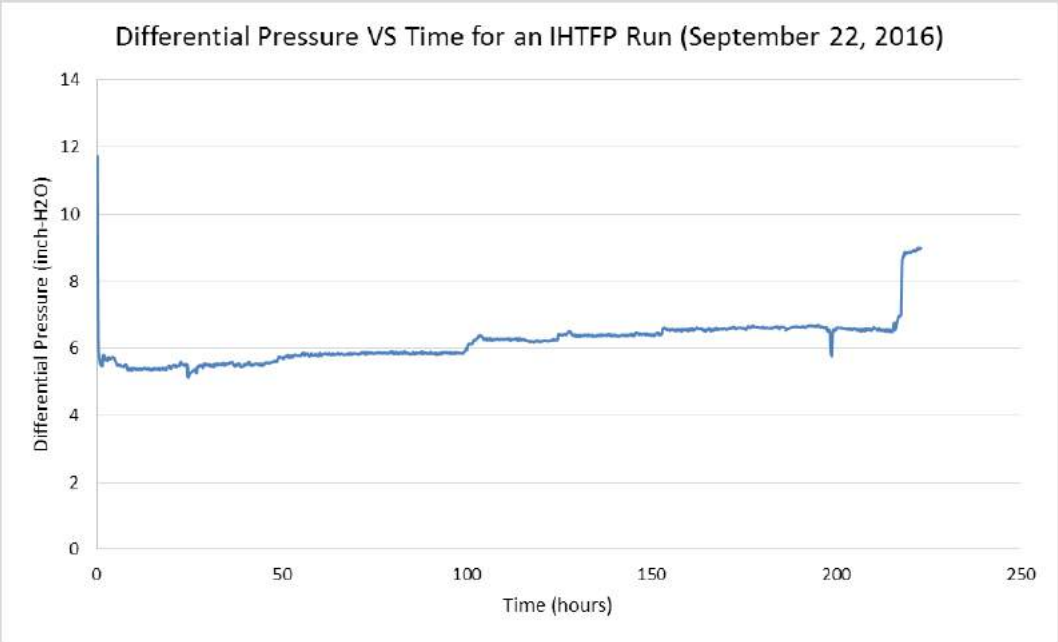


Figure 5-6: Differential pressure versus time for the experimental trial B. Note that 6 $inches - H_2O$ corresponds to the autoclave velocity of 2.98 m/s and the Reynolds number of 98,955.

### 5.2.2 Images

An important note is that images taken for binarization purposes are mostly taken with higher contrast than what is considered aesthetically pleasing to human. This is done to aid image thresholding algorithms. SEM images that are friendly to human eyes tends to be more gray overall. In these images, image thresholding algorithms are more likely to pick up the gray shadow shadings on crud particles as pores.

#### 5.2.2.1 Trial B (September 22, 2015)

In this trial, we grew a lot thicker crud than before as shown in the figures below. However, crud in this trials was grown in a very uneven fashion, as shown in figure 5-7. This was suspected to be because of the machining grooves could become boiling nucleation site. With boiling coming out of specific nucleation site, crud will be grown only around those nucleation sites creating an uneven crud formation. Figure 5-7 below also shows dark spots that could be interpreted as boiling chimneys. However, upon closer inspections, these chimney holes are very shallow which makes the assumptions that they are chimneys questionable.

**Sample 5** Sample 5 grows the most crud out of all samples from trial B. Figure 5-7 shows sample 5's top view. The blobs protruding out of the surface are crud formation. Note that the grooves are from machining defect which was fixed in later runs by electropolishing. These machine grooves,

however, is likely the major contributor to crud growth since trial B has the thickest crud out of all experimental trials conducted for this thesis. Following subsections will exhibit example images acquired for top and cross-section view of crud.

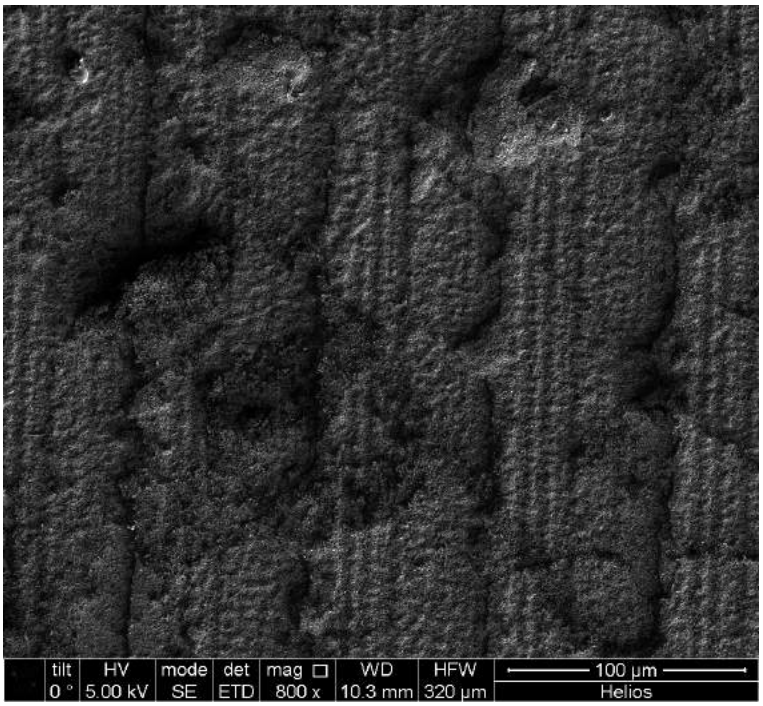


Figure 5-7: Zoomed out top view SEM image of trial B sample 5's crud. This image was taken using FEI Helios FIB/SEM.

**Top View** Figure 5-8 and figure 5-12 are examples of top view SEM images of crud from the sample 5. These images are taken with high contrast because it gives more accurate resulting binary images. When images are taken at normal contrast, shadings on the particles tend to get counted as pores. An important observation to make for figures 5-8 and 5-12 is that they have relatively little pores compare cross-section view images found in section 5.2.2.1. One possible cause for this observation is the gold coating applied on the samples. Gold coatings are applied to crud sample to alleviate the sample charging problems when taking SEM images. Gold coatings form layers around crud particles enlarging its size while filling up the pores. This leads to lower porosities obtained from top-view analysis of IHTFP samples analysis. Images were taken for this section using the FEI Helios FIB/SEM.

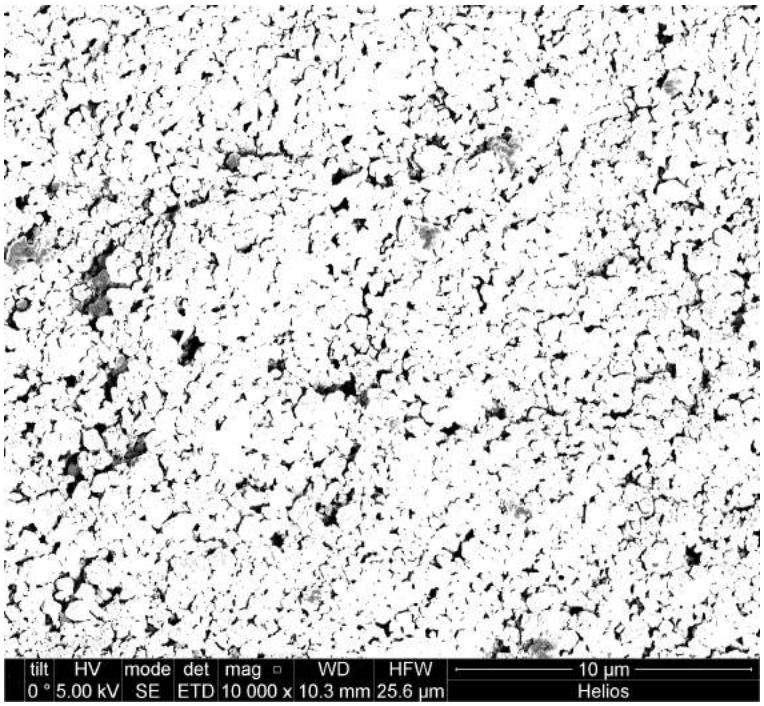


Figure 5-8: First example of the top view SEM image of thick crud from sample 5 of trial B.

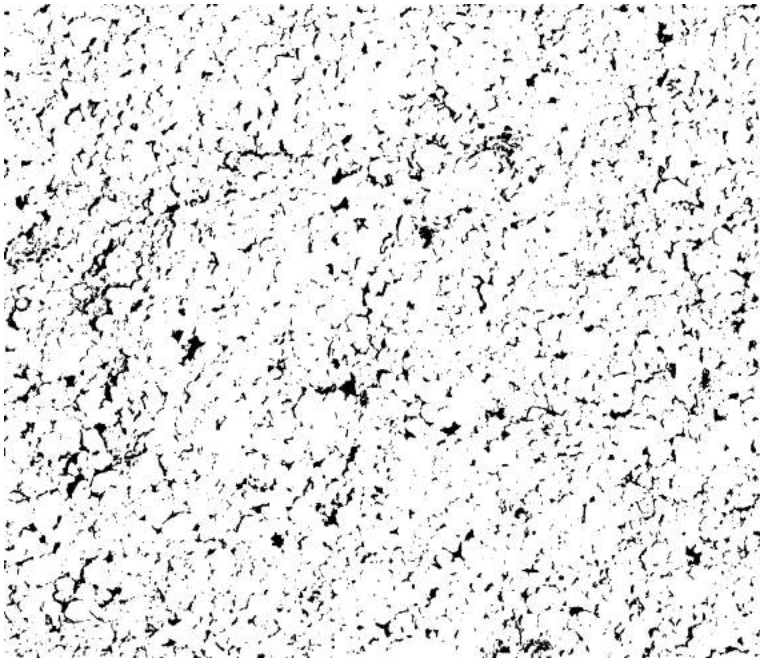

Figure 5-9: Binary image generated from figure 5-8 using the moment-preserving thresholding algorithm.

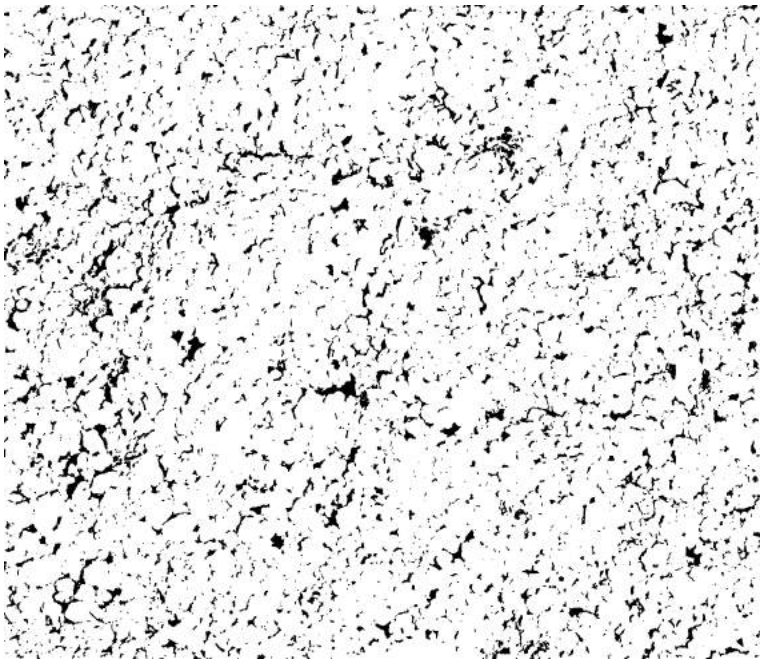

Figure 5-10: Binary image generated from figure 5-8 using the Otsu thresholding algorithm.

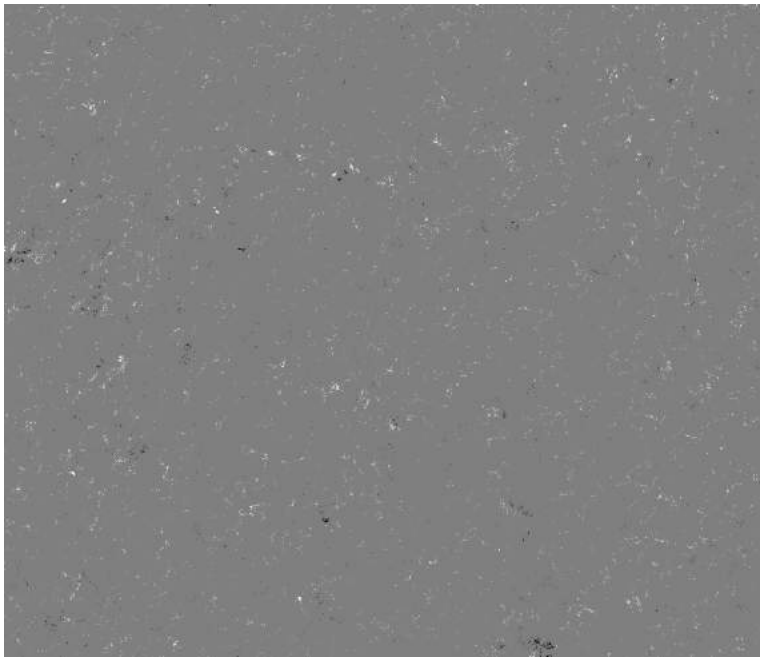

Figure 5-11: Figure demonstrating the difference between figures 5-9 and 5-10. Gray pixels are the pixels that both the moment and Otsu algorithms identified to have the same color. White pixels are the pixels that Otsu algorithm determined as black, while the moment algorithm determined as white. Black pixels are the pixels that moment algorithm determined as white, while the Otsu algorithm determined as black.

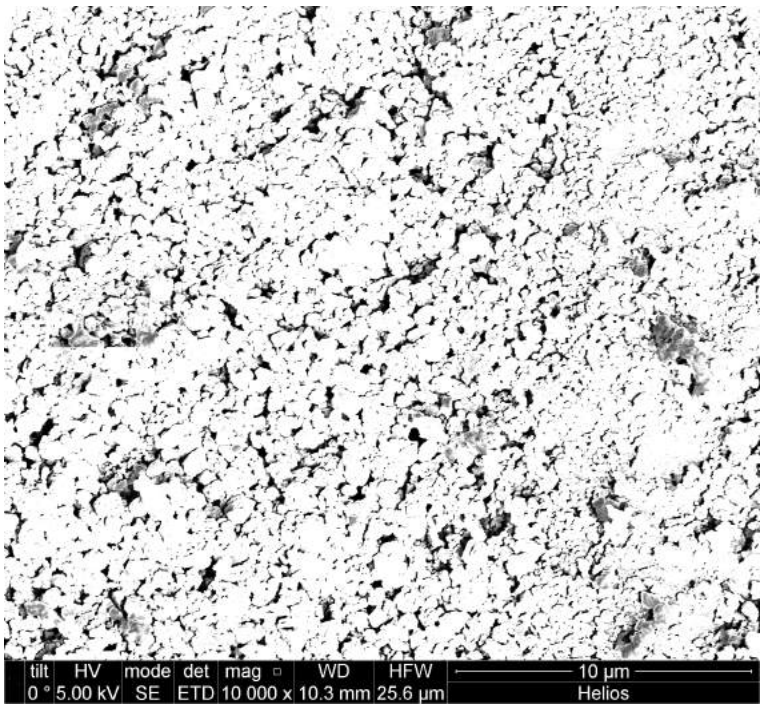


Figure 5-12: Second example of the top view SEM image of thick crud from sample 5 of trial B.

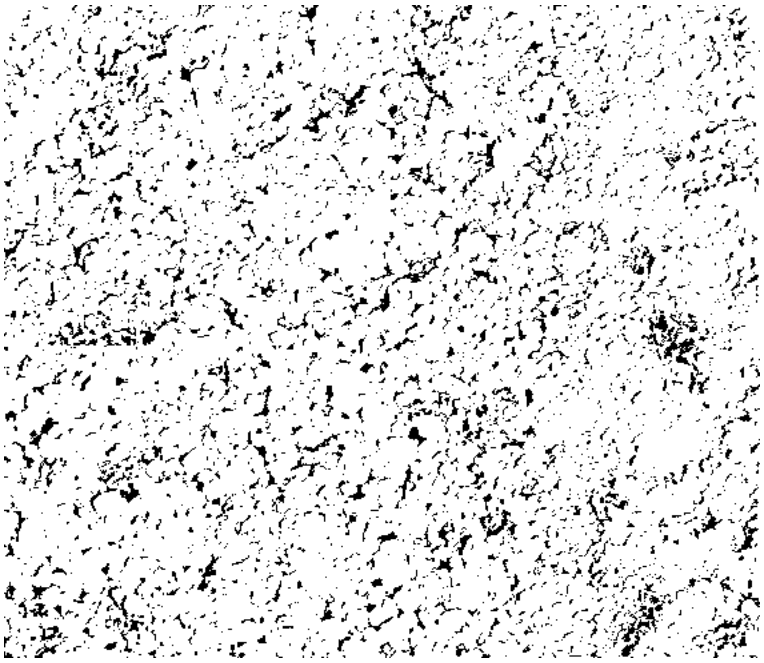

Figure 5-13: Binary image generated from figure 5-12 using the moment-preserving thresholding algorithm.

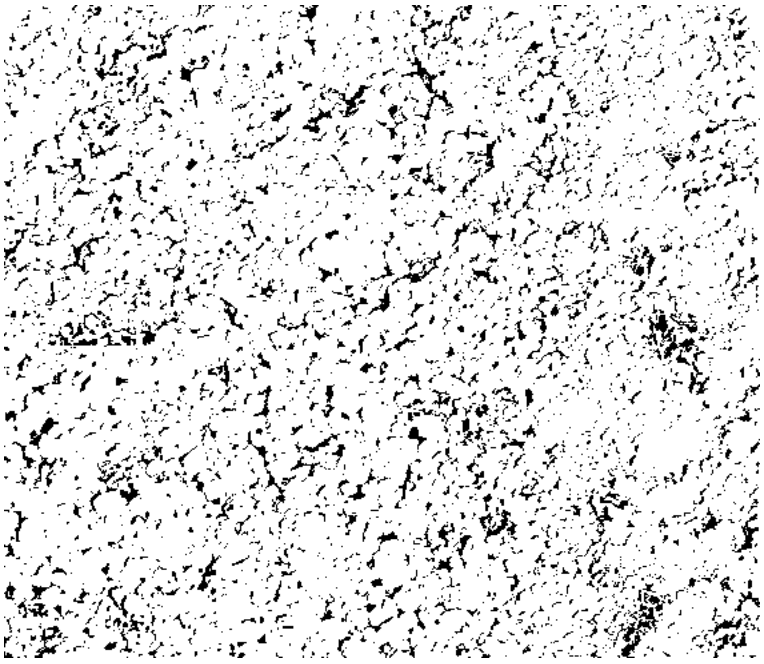

Figure 5-14: Binary image generated from figure 5-12 using the Otsu thresholding algorithm.

**Cross-section View** This subsection exhibits examples of sample 5's crud cross-sectional view. Figure 5-15 and 5-19 are the raw cross section images with high contrast of sample 5 and sample 1, respectively. The cross-section area that is suitable for fractal analysis is cropped off by hand, resulting in figure 5-16 and 5-20. The cropped images are turned into binary images using the moment thresholding algorithm resulting in figure 5-17 and 5-21. Similarly, binary images were also obtained using Otsu thresholding algorithm, as shown in figure 5-18 and 5-22. Images were taken for this section using the Zeiss Merlin Nvision FIB/SEM.

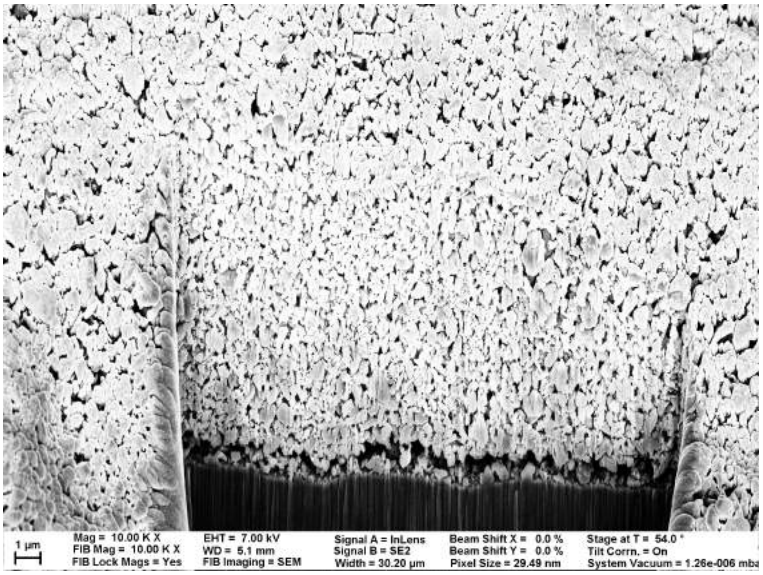


Figure 5-15: First example of the cross-section view SEM image of thin crud from sample 5 of trial B.

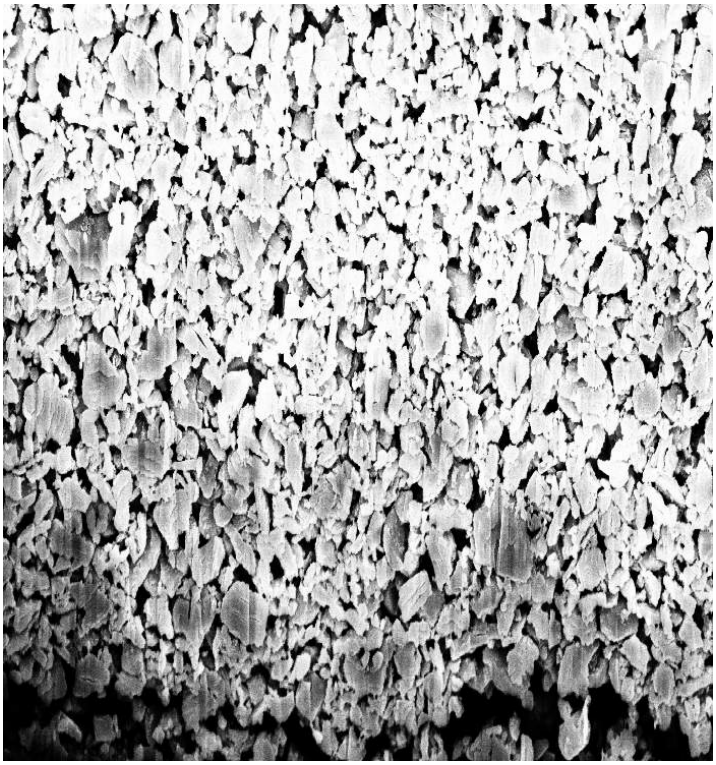

Figure 5-16: Cropped cross-section view SEM image of crud obtained from cropping figure 5-15.

Figure 5-17: Binary image converted from the cropped image in figure 5-16 using moment-preserving thresholding algorithm. This image is used to obtain the porosity and the fractal dimension.

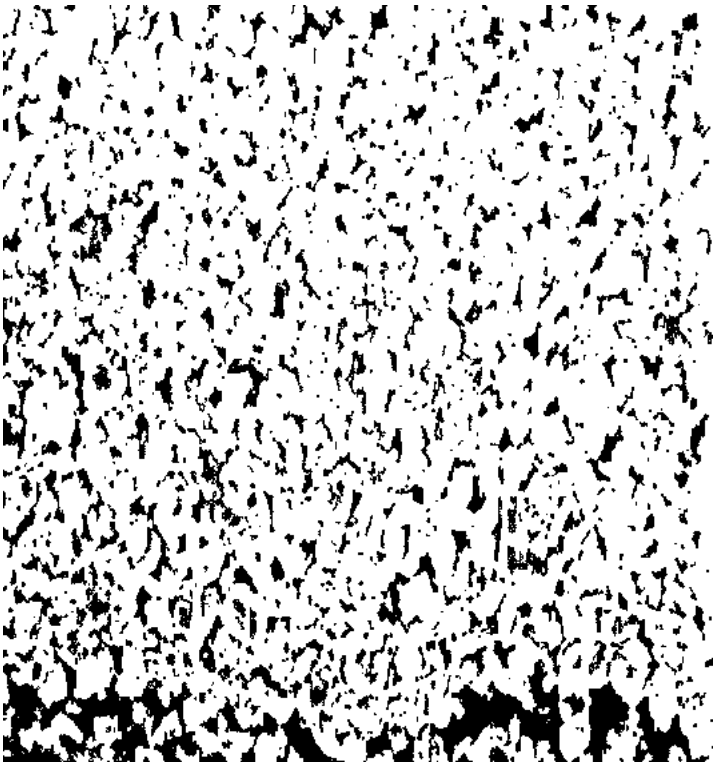

Figure 5-18: Binary image converted from the cropped image in figure 5-16 using Otsu thresholding algorithm. This image is used to obtain the porosity and the fractal dimension.

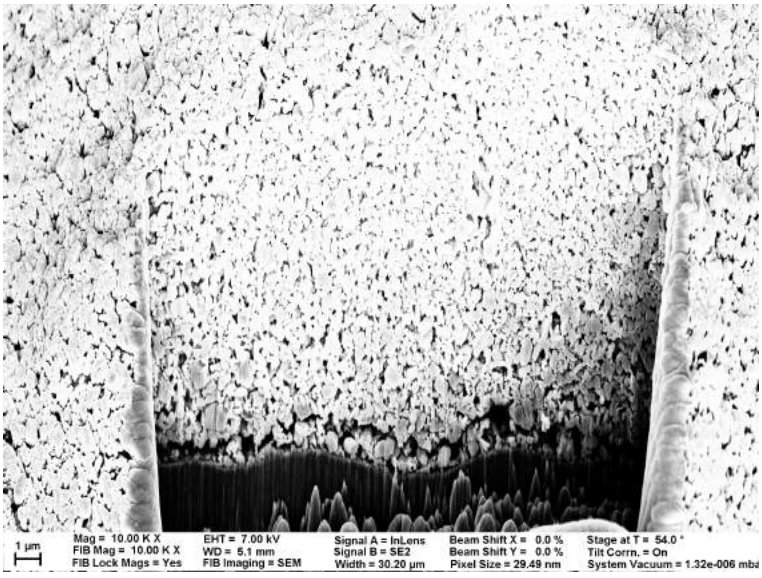


Figure 5-19: Second example of the cross-section view SEM image of thin crud from sample 5 of trial B.

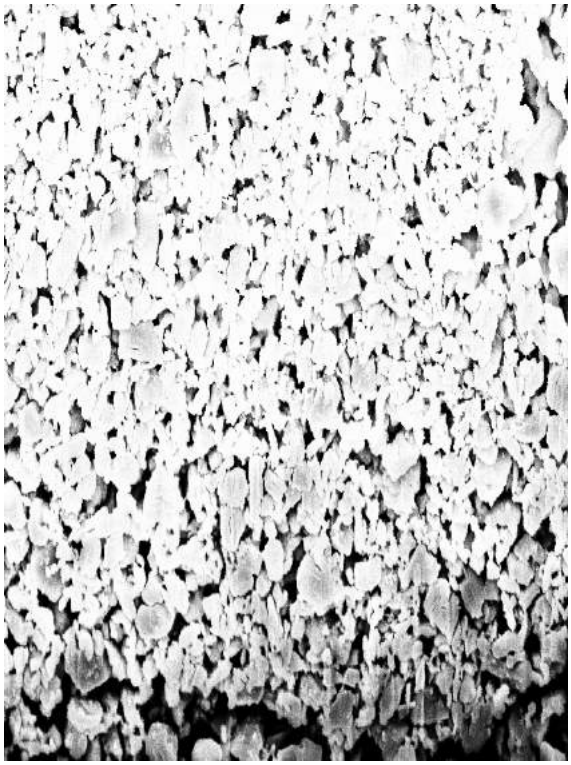

Figure 5-20: Cropped cross-section view SEM image of crud obtained from cropping figure 5-19.

Figure 5-21: Binary image converted from the cropped image in figure 5-20 using moment-preserving thresholding. This image is used to obtain the porosity and the fractal dimension.

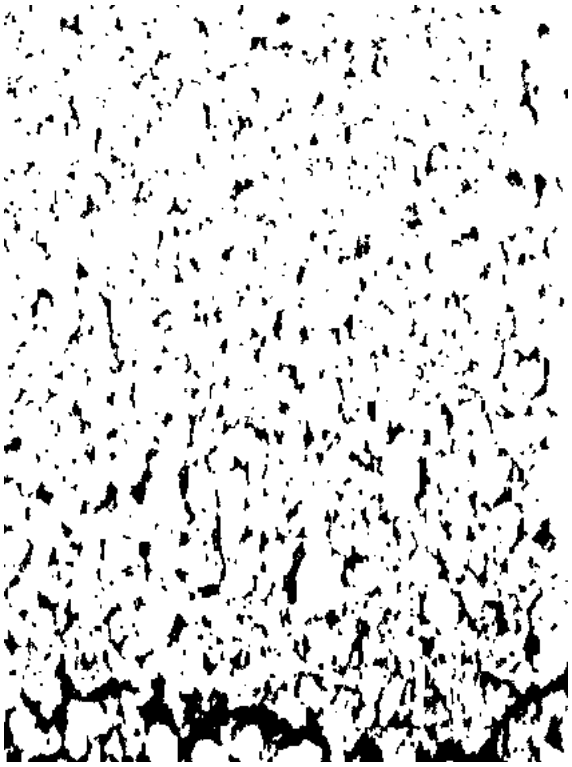

Figure 5-22: Binary image converted from the cropped image in figure 5-20 using Otsu thresholding. This image is used to obtain the porosity and the fractal dimension.

**Sample 1** In terms of overall crud thickness, sample 1 is similar to sample 5. Figure 5-23 shows how the surface of sample 1 generally looks. Similar to the sample 5, there are crud blobs, especially on machining grooves. By comparing figure 5-23 to figure 5-7, we can see that figure 5-7, which is from sample 5, has more crud blobs. Images taken for this section uses the FEI Helios FIB/SEM.

For all SEM images, we want to have 10,000x magnification as mentioned in section 4.4. However, all images we obtained from the FEI microscope have image captions that show 5,000x magnification. This is caused by a strange software behavior on the FEI microscope. The FEI microscope's default screen contains four subscreens which are for SEM, FIB, and the two light cameras. When switching from this default screen mode to full SEM screen display mode, the 10,000x magnification decreased to 5,000x magnification without any change in the actual image. We can confirm that these images with 5,000x caption are actually 10,000x by comparing the length ($\mu m$) to pixel ratio from SEM images of both Zeiss and FEI microscopes. Calculated the length to pixel ratio ($\mu m/pixels$) are 0.0098 for the FEI microscope at 5,000x and 0.0104 for the Zeiss microscope at 10,000x. These numbers being roughly equal imply similar actual magnifications.

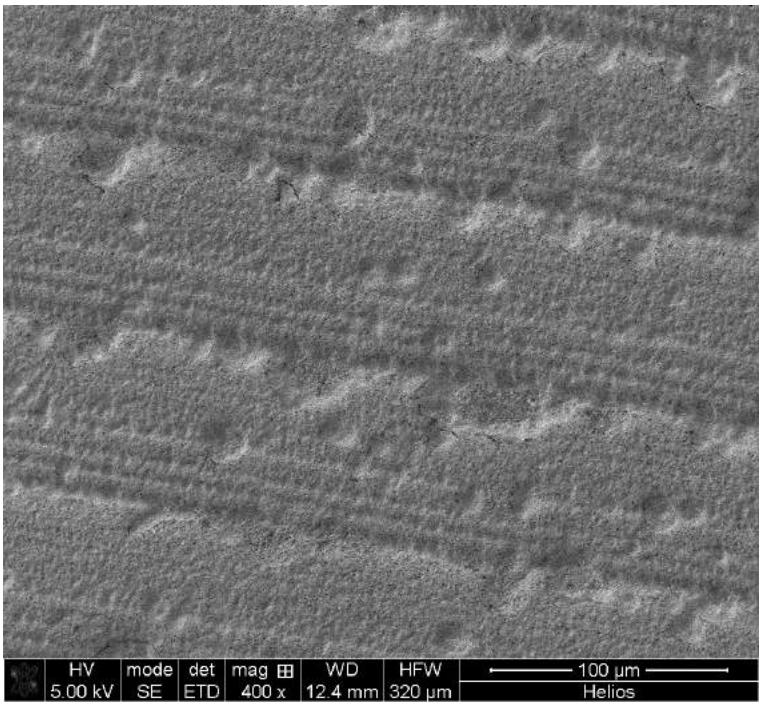


Figure 5-23: Zoomed out top view SEM image of trial B sample 1's crud.

**Top View** Figure 5-24 and 5-27 are example top view images of crud from sample 1. Similar to SEM images taken for sample 5, SEM images in figure 5-24 and 5-27 are taken so that the crevices between crud are more pronounced in black. This is done to aid image thresholding algorithms. Note that the particles look very densely packed as well. One explanation for this could be that the gold coating applied on the trial B's samples build up on the crud particles making them look bigger, and at the same time fill in some gaps. Figures 5-25 and 5-28 are binary images obtained using the moment-preserving thresholding algorithm. Figures 5-26 and 5-29 are binary images obtained using the Otsu thresholding algorithm. Images were taken for this section using the FEI Helios FIB/SEM.

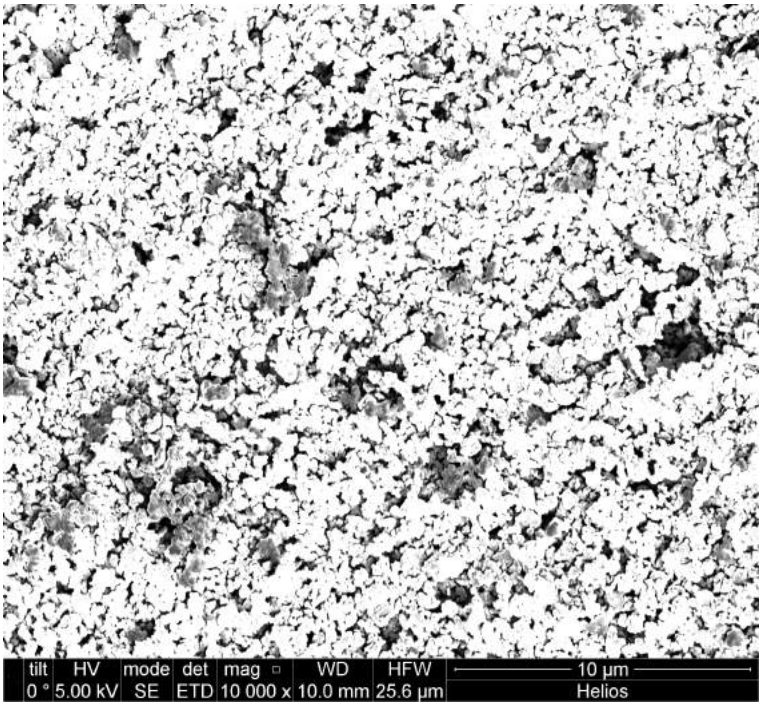


Figure 5-24: First example of the top view SEM image of thick crud from sample 1 of trial B.

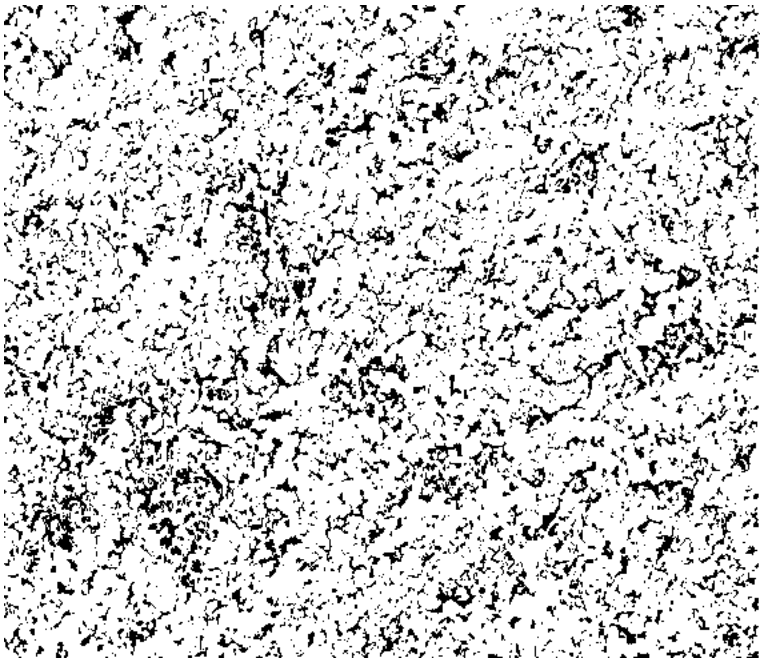

Figure 5-25: Binary image generated from figure 5-24 using the moment-preserving thresholding algorithm.

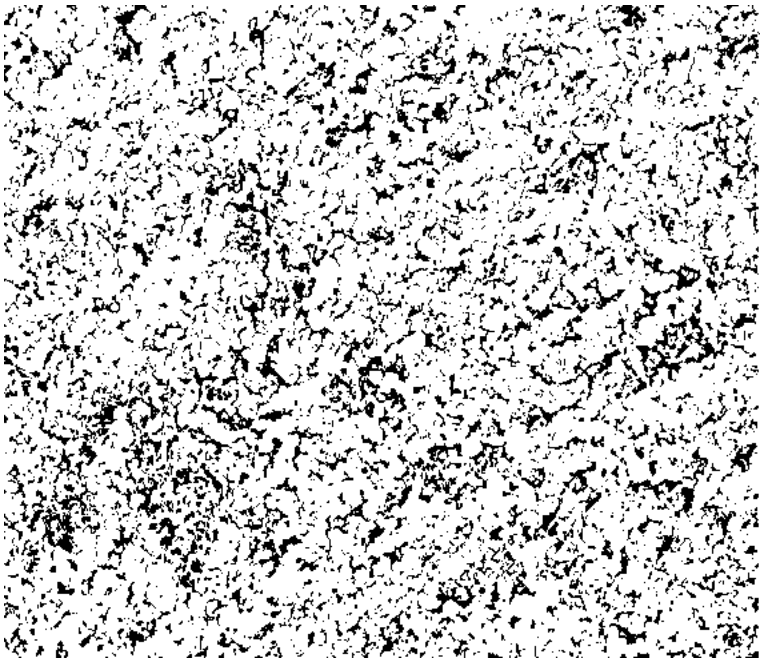

Figure 5-26: Binary image generated from figure 5-24 using the Otsu thresholding algorithm.

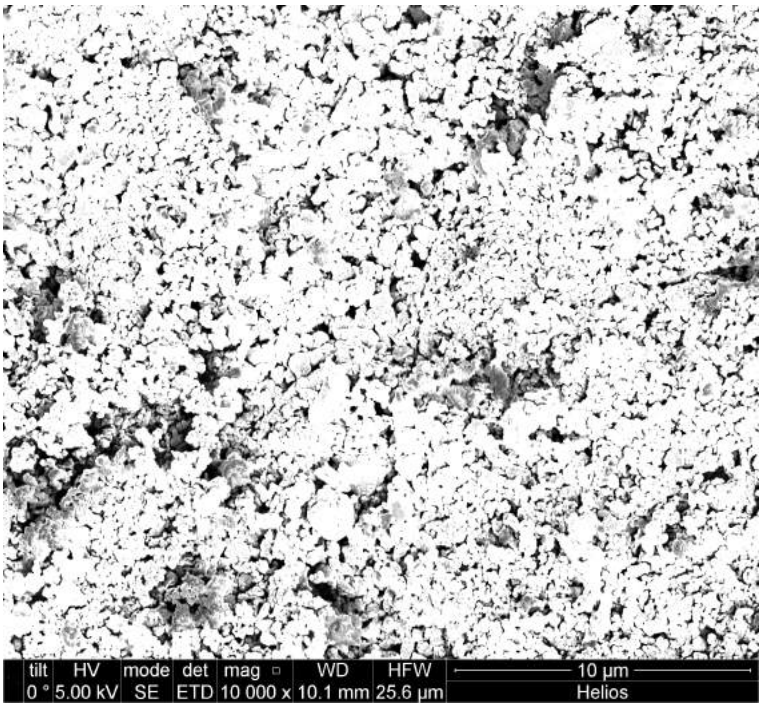


Figure 5-27: Second example of the top view SEM image of thick crud from sample 1 of trial B.

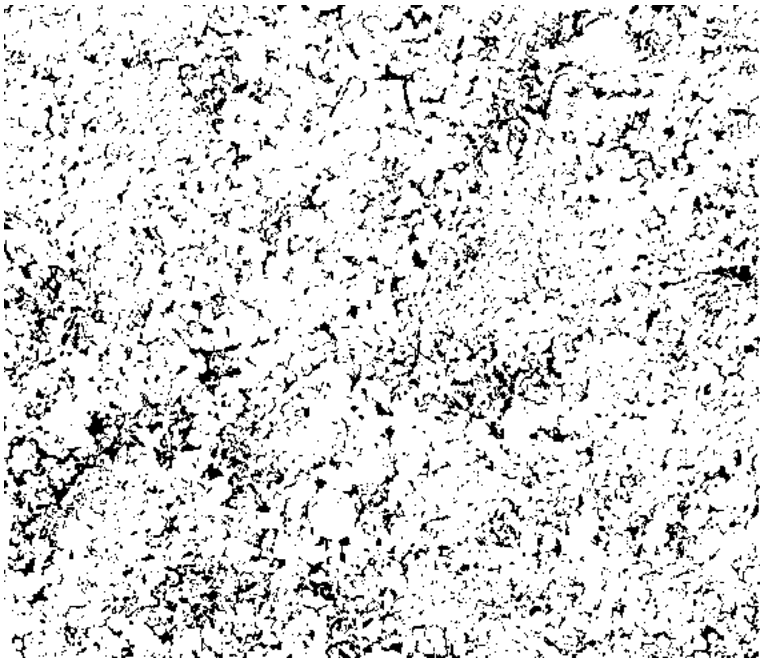

Figure 5-28: Binary image generated from figure 5-27 using the moment-preserving thresholding algorithm.

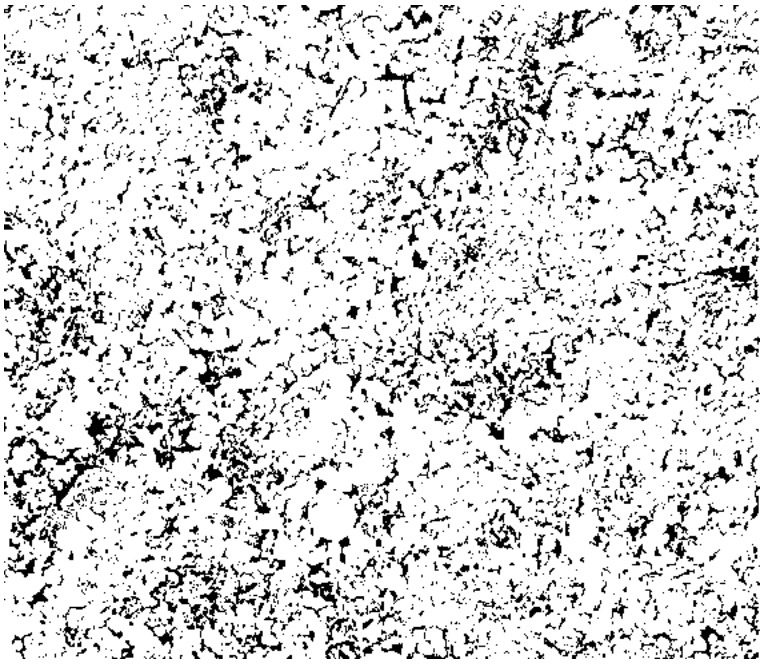

Figure 5-29: Binary image generated from figure 5-27 using the Otsu thresholding algorithm.

**Cross-section View** Figure 5-30 and 5-31 exhibits two examples of sample 1's crud cross-sectional view SEM images. Characteristics of SEM images taken in this section is largely similar to Sample 5's cross-section images. Images were taken for this section using the FEI Helios FIB/SEM. Since we had already shown many binary images demonstrating how binary image processing works, the rest of binary images will be skipped for the fractal analysis section.

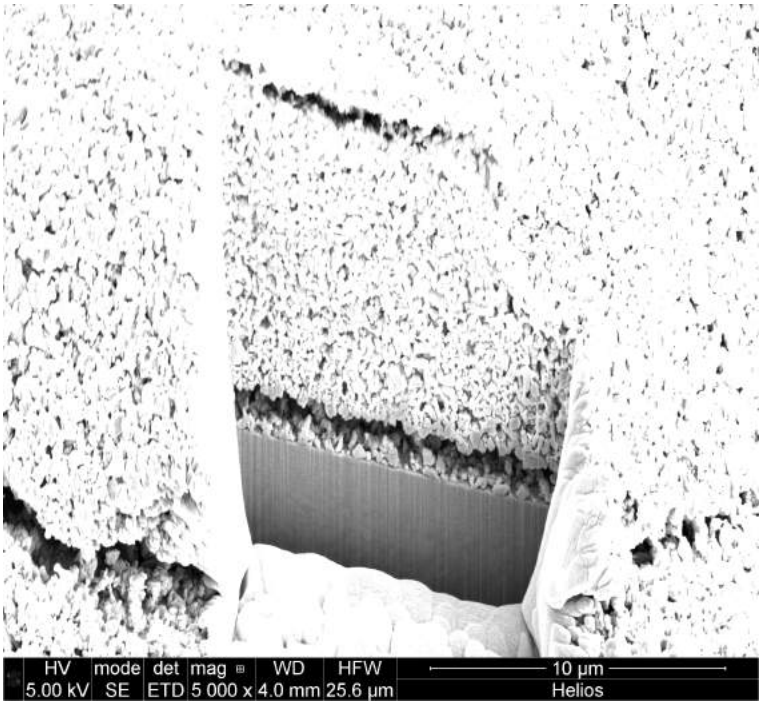


Figure 5-30: First example of the cross-section view SEM image of thin crud from sample 5 of trial B.

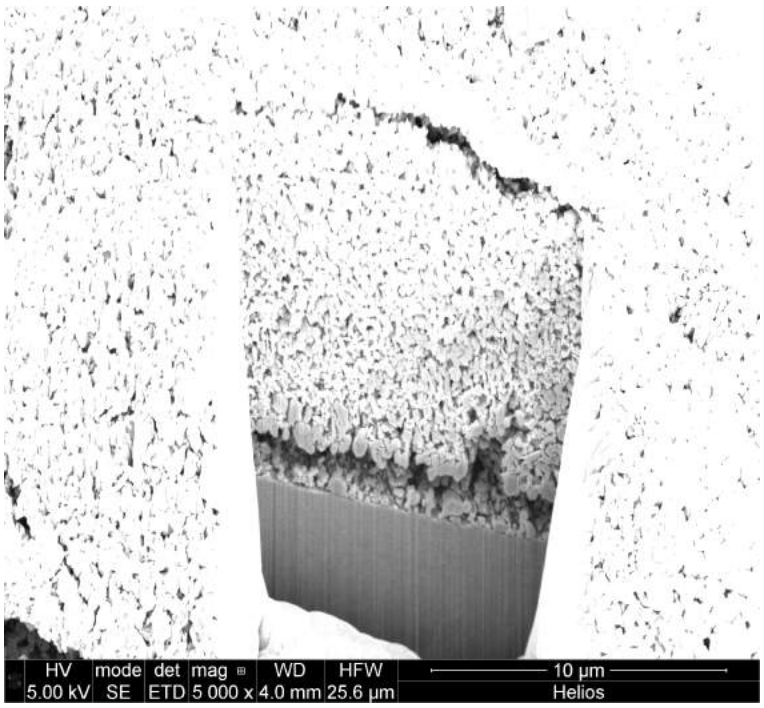


Figure 5-31: Second example of the cross-section view SEM image of thin crud from sample 5 of trial B.

#### 5.2.2.2 WALT loop sample

In addition to thick crud samples obtained from the experimental trial B performed using the IHFTP, WALT loop's team also provided us with some of their crud flake. Figure 5-32 shows the zoomed out view of the largest crud flake that was provided to us. In general, crud from WALT loop is more porous than crud grown in IHTFP. Other than, some of its parts also exhibit very clear chimney structures. In figure 5-32's top right, there are holes that are most likely boiling chimneys. Similar to trial B, SEM images of the top and cross-sectional view of crud were taken, all with x10,000 magnification. The rest of this section will exhibit these images.

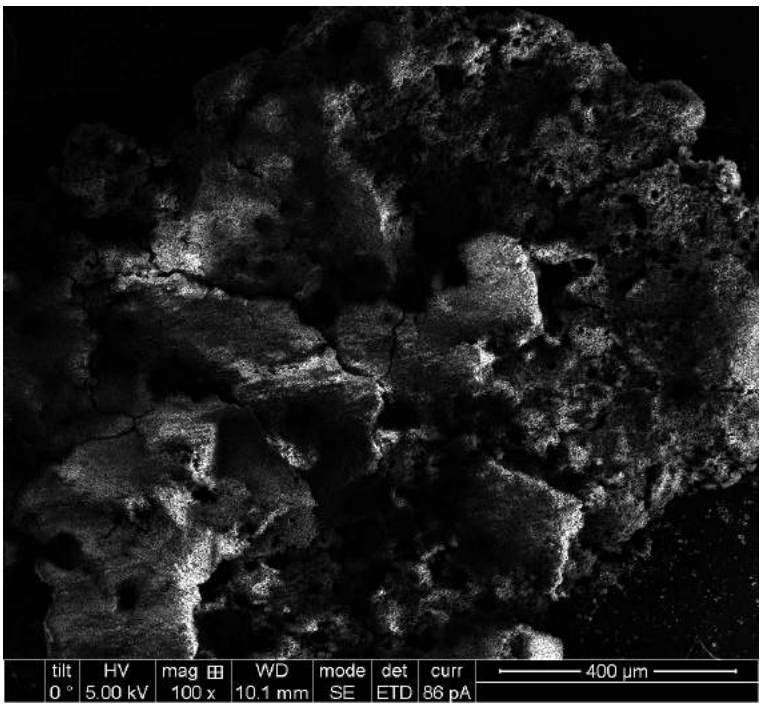


Figure 5-32: Zoomed out top view SEM Image of WALT loop's crud flake. The darker background part is the carbon tape holding the flake.

**Top View** Figures 5-33 and 5-34 are the top view SEM images of WALT loop's sample crud. These SEM images went through similar analysis to those from sample 1 and sample 5 of trial B. When compared to crud grown in the IHTFP, WALT loop's crud are generally more porous. Their significantly higher heat flux raises the porosity of their crud samples. The heat fluxes in the WALT loop range from 226.2 $kW/m^2$ to 1,000.0 $kW/m^2$, which are higher than the IHTFP's typical heat flux of 206 $kw/m^2$ [96]. WALT loop's crud images also show how WALT loop's crud particles vary more in size when compared to those grown in the IHTFP. This is likely due to the use of different types of crud precursors. The crud precursors used the IHTFP trial B are mainly nickel oxide particles with more uniform sizes of roughly 50 nm in diameter.

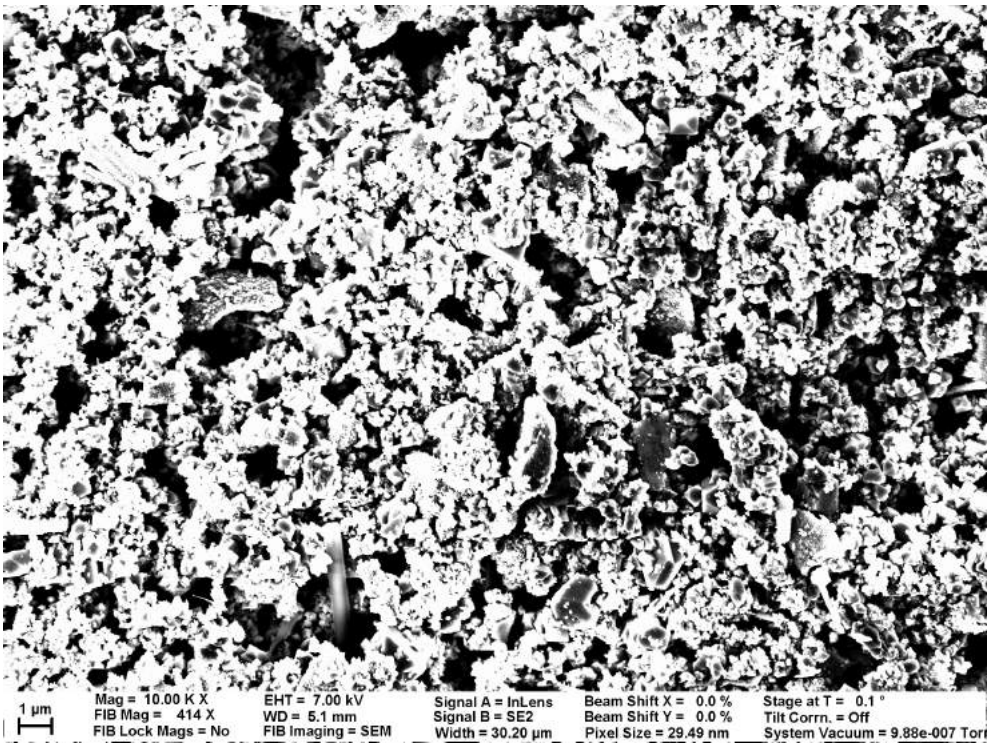


Figure 5-33: Top view SEM image of crud from the WALT loop.

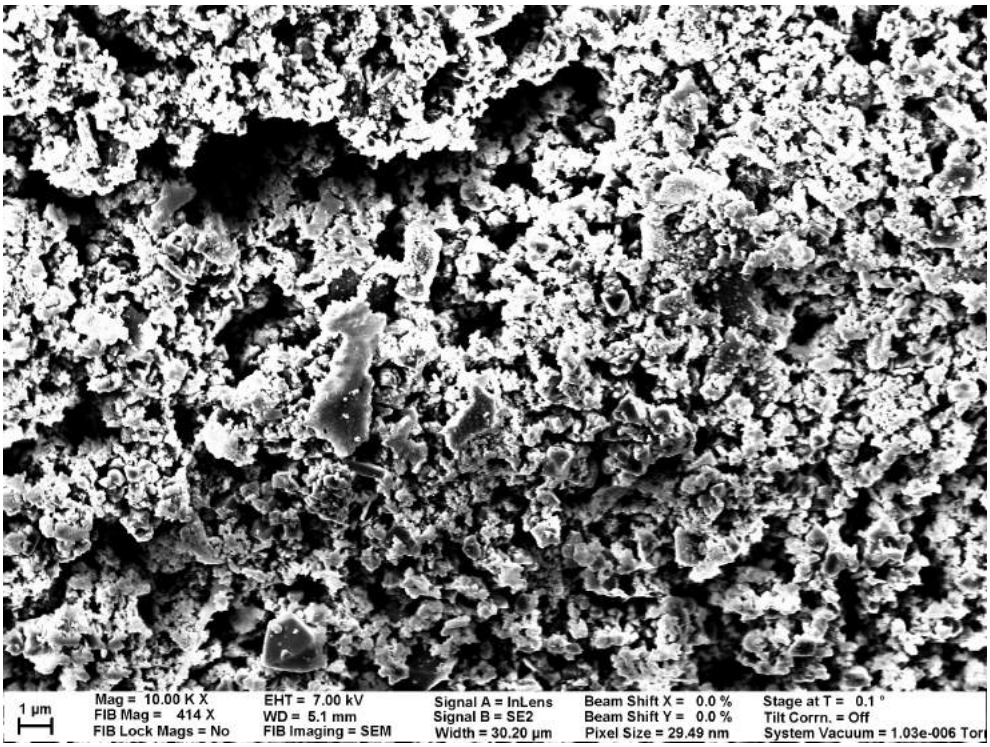


Figure 5-34: Top view SEM image of crud from the WALT loop.

**Cross-section View** Figures 5-35 and 5-36 are examples of high contrast raw SEM images used for fractal analysis. These images undergo similar binarization processes similar to those of sample 2. Those process images are omitted here to save space. Note that that contrast of these images are made more pronounced than crud images of trial B to combat the shading problems, where shades on crud particles counted as pores. Notice that crud cross-section towards the bottom is very dark. This shading is so pronounced that even Chow and Kaneko adaptive thresholding still fails to alleviate this shading problem. Therefore SEM images with higher than usual contrast are used to further alleviate the shading problem.

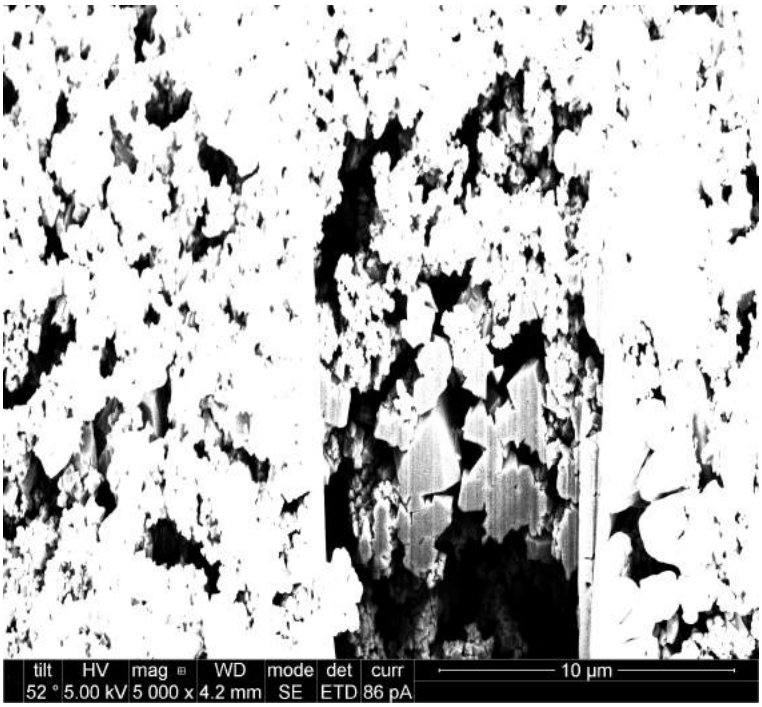


Figure 5-35: Cross-section view SEM image of crud from the WALT loop. The high contrast of this image is adjusted for image processing algorithms.

### 5.2.3 Quantitative Results

There are several parameters and plots that we wanted to obtain as laid out in sections 4.4.1.3 and 4.4.1.4. This section gives these parameters and plots obtained from analyzing SEM images from section 5.2.2. Values obtained are crud thickness, porosity, and fractal dimensions. Plots obtained are porosity vs height position, fractal dimension vs height position, and fractal dimension vs porosity.

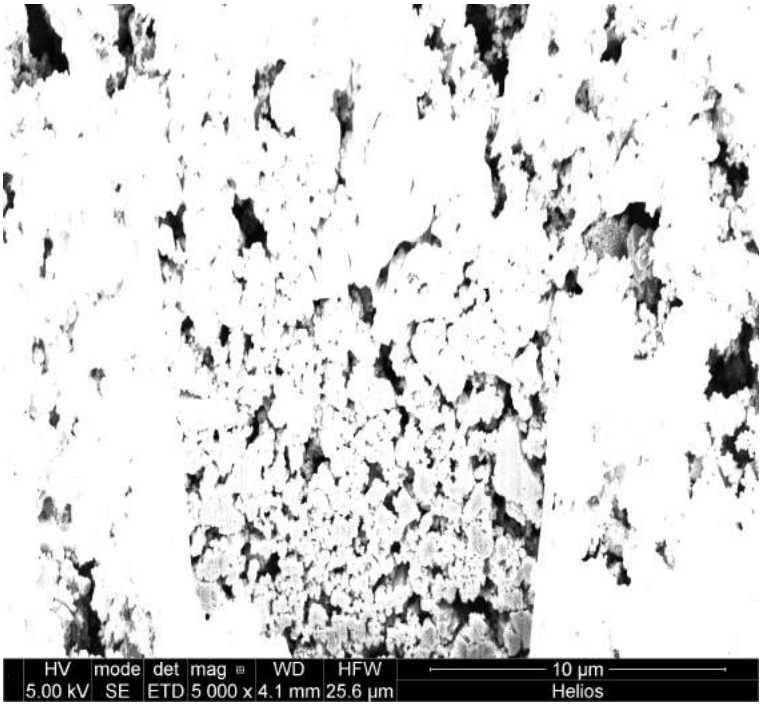


Figure 5-36: Cross-section view SEM image of crud from the WALT loop. The high contrast of this image is adjusted for image processing algorithms.

#### 5.2.3.1 Crud Thickness

The crud thicknesses of cross sections that we took SEM images of are shown in table 5.1. Thicknesses on this table are not representative of the overall thickness of a particular crud sample. This is because cross section images are usually taken from locations with crud blobs to ensure that crud at the location is thick enough to allow the application of the box-counting algorithm. The average measured thicknesses, in this case, will be significantly higher than the average thickness in the case where thickness measurements are taken at random locations on crud.

| Trial | Thickness ($\mu m$) |
|---|---|
| Trial B Thin Crud Sample 5 | $9.06 \pm 2.46$ |
| Trial B Thin Crud Sample 1 | $9.97 \pm 2.30$ |
| WALT Loop Crud | N/A |

Table 5.1: Table showing average and standard deviation crud thickness of the samples we analyzed. WALT loop crud's thickness is not available because the samples we got are crud flakes that are not attached to any surface.

#### 5.2.3.2 Porosity

After the SEM images are turned into binary images, porosity can be calculated by counting the number of black pixels which represent pores. Table 5.2 exhibits porosities calculated using different samples, views, and algorithms. WALT loop's crud is generally less dense than the trial B's IHTFP crud as clearly shown in the table. WALT loop's crud top views have very high porosity, partially due to a significant amount of shadow on crud particles that gets incorrectly classified as pores. Figure 5-33 and 5-34 illustrate how there are a significant amount of shadow in WALT loop top-view SEM images.

| Algorithm | Moment Preserving Thresholding | | | | Otsu Thresholding | | | |
|---|---|---|---|---|---|---|---|---|
| Sample | Top View | | Cross-section View | | Top View | | Cross-section View | |
| Trial B, Sample 5 | 11.3 | ± 1.7 | 14.9 | ± 4.5 | 12.1 | ± 1.8 | 15.4 | ± 4.7 |
| Trial B, Sample 1 | 18.5 | ± 2.8 | 18.5 | ± 5.3 | 19.9 | ± 2.9 | 19.3 | ± 4.8 |
| WALT Loop | 43.4 | ± 4.7 | 24.5 | ± 5.0 | 43.4 | ± 4.4 | 25.1 | ± 4.8 |

Table 5.2: Average percent porosity obtained from SEM images of each sample. The values shown are the average values from the sample sets. Each sample set contains 10 images. The uncertainties following "±" in this case are the standard deviations of porosities for each sample set.

#### 5.2.3.3 Fractal Dimensions

Table 5.3 exhibits the resulting fractal dimensions obtained from SEM images. Again, the fractal dimensions analyzed from top view SEM images are fractal area dimensions, while the fractal dimensions analyzed from the cross-section view SEM images are fractal tortuosity dimensions. Other than the fractal dimensions themselves, we also want to know the uncertainties associated with using the box-counting method. These uncertainties will also imply how well the box-counting method works on our SEM images. As explained in section 2.3.10, the important value for calculating the uncertainty in the box-counting method is the R-square value. The Table 5.4 shows the regression error in the form of R-square value. 0.996 R-square value means that 99.6% of the deviation in the values of sample set is explained by the regression line. This value being very close to 1 could be a supporting evidence that crud exhibit fractal property.

#### 5.2.3.4 Porosity vs Height Position

Figure 5-37 shows the relationship between porosity and height from the cladding surface. Each porosity is obtained from a sub-image that was made by cropping the source image with 64 pixels height at the height position. Note that these data points are taken from only sample 1 and sample 5 of trial B. WALT loop's data points are omitted because WALT loop's samples are crud flakes without any visible cladding. There is a general logarithmic downward trend in crud porosity as we

| Algorithm | Moment Preserving Thresholding | | Otsu Thresholding | |
|---|---|---|---|---|
| Sample | Top View | Cross-section View | Top View | Cross-section View |
| Trial B, Sample 5 | 1.38 ± 0.04 | 1.46 ± 0.08 | 1.40 ± 0.04 | 1.47 ± 0.08 |
| Trial B, Sample 1 | 1.53 ± 0.04 | 1.51 ± 0.09 | 1.55 ± 0.04 | 1.53 ± 0.08 |
| WALT Loop | 1.77 ± 0.03 | 1.61 ± 0.06 | 1.77 ± 0.03 | 1.61 ± 0.06 |

Table 5.3: Average fractal dimension obtained from SEM images of each sample. The values shown are the average values from the sample sets. Each sample set contains 10 images. The uncertainties following "±" in this case are the standard deviations of fractal dimensions for each sample set.

| Algorithm | Moment Preserving Thresholding | | Otsu Thresholding | |
|---|---|---|---|---|
| Sample | Top View | Cross-section View | Top View | Cross-section View |
| Trial B, Sample 5 | 0.996 | 0.989 | 0.996 | 0.989 |
| Trial B, Sample 1 | 0.995 | 0.995 | 0.995 | 0.995 |
| WALT Loop | 0.998 | 0.999 | 0.998 | 0.999 |

Table 5.4: R-square values for the box-counting method's regression lines.

go further from cladding surfaces. The last point has no error bar because there was only one crud cross section thick enough to get the data for that point.

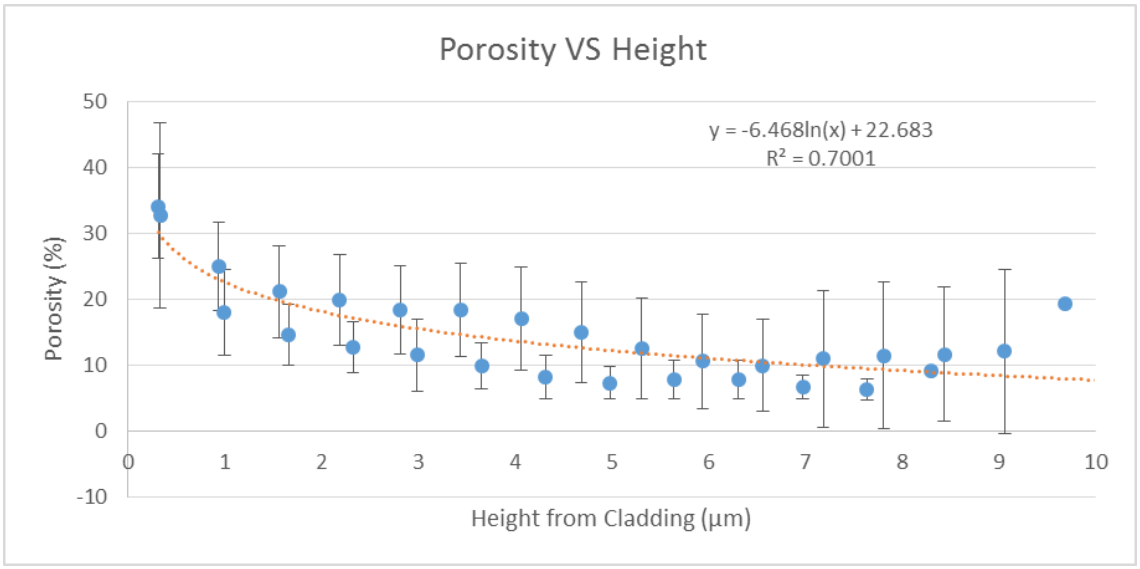


Figure 5-37: Plot of porosity versus height position within crud for sample 1 and sample 5 of trial B. Height positions used in this graph are the measured from where crud interface with cladding surfaces. Each point represents a set of values that are

#### 5.2.3.5 Fractal Dimension vs Height Position

Figure 5-38 is similar to figure 5-37, except that instead of porosity, fractal dimension is plotted against height from the cladding surface. In this case, fractal dimensions are fractal tortuosity

dimensions since they are all taken from analyzing cross-section images. Similar to porosity, there is a general logarithmic downward trend in fractal tortuosity dimension as the height from cladding increases. The last point has no error bar because there was only one crud cross section thick enough to get the data for that point.

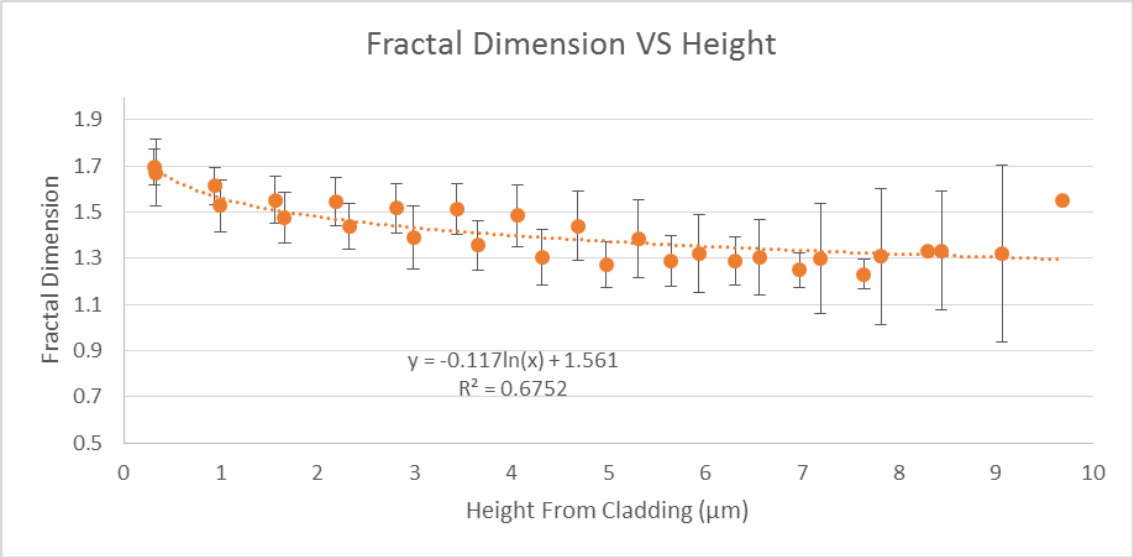


Figure 5-38: Plot of fractal dimension versus height position within crud for sample 1 and sample 5 of trial B. Since height can only be measured from cross-section views, the fractal dimensions are all fractal tortuosity dimensions in this case.

#### 5.2.3.6 Fractal Dimension vs Porosity

Figure 5-39 shows how fractal dimension related to porosity. The logarithmic trend fits nicely through all sample sets including the Westinghouse's WALT samples. The R-square value, 0.9925, is very close to 1 indicating that the data points fits particulary well onto the logarithmic trend. The fact that the WALT loop's and the IHTFP's crud give data points that lie on the same line suggests that there may be some underlying physical phenomena that generate the observed behavior.

## 5.3 Crud-Resistant Chemical Surface Modification

The resulting crud on the surface-modification trials is sparely covered by crud particles and did not form a thick layer. Therefore the analysis is geared toward the percent crud area coverage. The crud samples in this section are obtained from trial C and D. This section will first present the conditions at which crud was grown. Then it will show some example SEM images that were used in the crud area coverage analysis. Finally, the quantitative results will be presented.

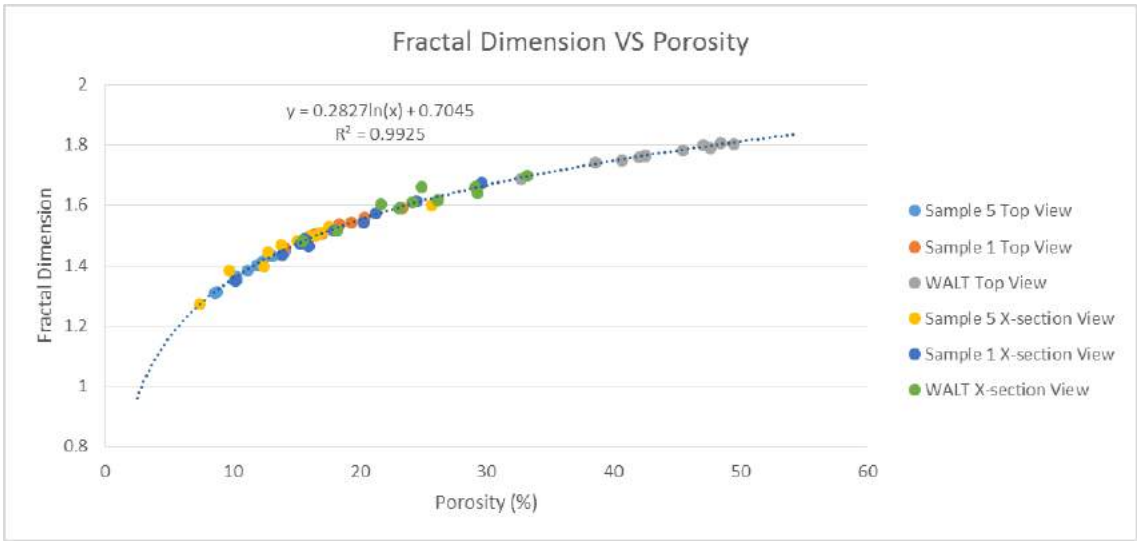


Figure 5-39: Plot of fractal dimension versus porosity of all samples.

### 5.3.1 Loop Conditions

This section presents these conditions of trial C and trial D in detail, including the plot of how they vary over time and explanations of why they were chosen. In addition, any anomaly during the experimental trial is also explained. In comparison to the trial B conditions shown in section 5.2.1, trial C and D has more conservative conditions with mostly higher pressure to prevent heater failure.

#### 5.3.1.1 Trial C (February 12, 2016)

There is a problem with differential pressure values recorded in trial C and D. Therefore, the differential pressure graph is not shown in this thesis since it would be misleading. Although the differential pressure was shown correctly on the differential pressure transmitter's screen, the output values recorded are inaccurate, sometimes by a factor of ten. This problem likely stem from electrical circuit problem that likely occurred when we tampered with the circuit prior to trial C and D. Throughout the trial, the differential pressure remains roughly 6 $inches - H_2O$, which corresponds to the autoclave velocity of 2.98 m/s and the Reynolds number of 98,955. The data acquisition system was broken for differential pressure; therefore, its graph is omitted.

Figure 5-40 shows temperatures at different spots and time during trial C. There was no significant temperature anomaly in this trial. Figure 5-41 shows the pressure which was set to 155 bars for most of the trial to prevent fuel failure. After a long period of the stable run, pressure was decreased to roughly 115 - 120 bars towards the end of the trial to speed up crud growth. The long initial phase with the pressure of 155 bars probably led to less crud growth observed in this trial. Figure 5-42 shows that dissolved oxygen was at almost zero when the trial starts. As the argon gas

bottle depletes slowly, the pressure of gas pushing through the gas regulator decreases. This pressure decrease causes the gas regulator to allow even less argon gas into the system to remove oxygen. As a result, the oxygen level slowly rose to 0.5 ppm. Water conductivity stayed at a constant value of around 10 $\mu S/cm$ for the whole trial as shown in figure 5-43. Figure 5-44 shows that although pH varies during the trial, it always lies in the desirable range.

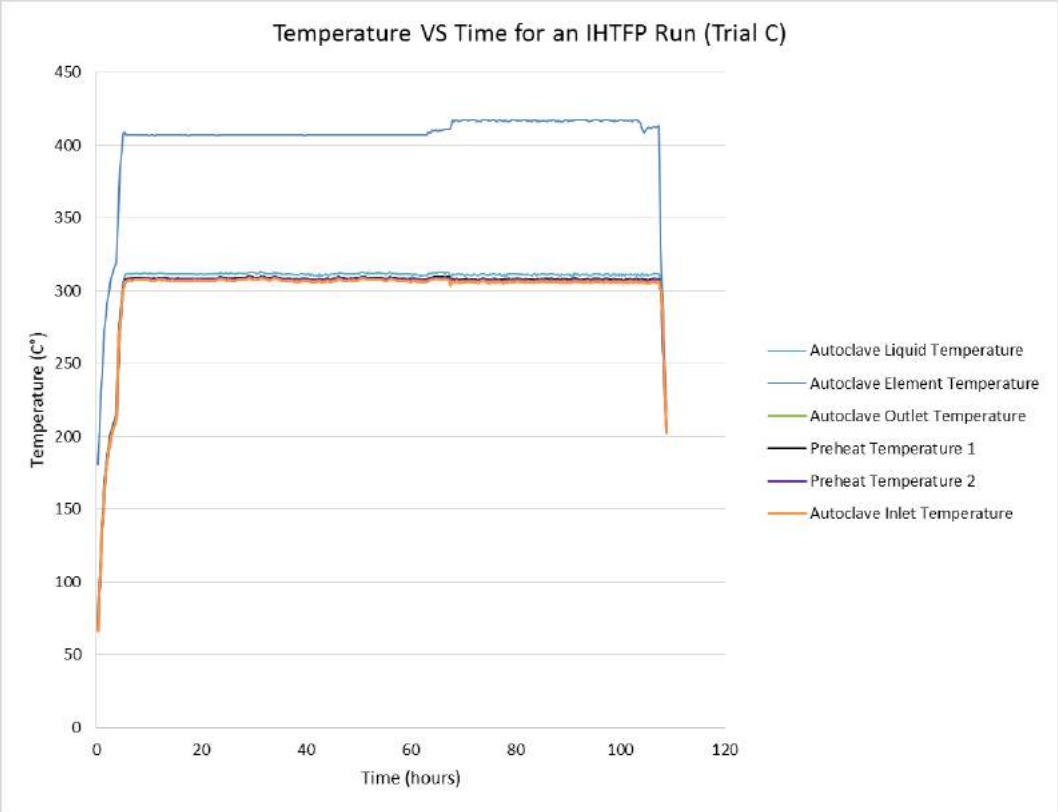


Figure 5-40: Temperature at different spots in the loop versus time for the experimental trial C.

#### 5.3.1.2 Trial D (March 18, 2016)

Figure 5-45 is the temperature versus time graph for trial D. In this run, the new heating rod used surprisingly exhibits the element temperature of only roughly 350 ºC. This is, by far, the lowest element temperature we have had in the middle of experimental trials. Nevertheless, there was no problem in pushing the IHTFP's liquid temperature to 310 ºC. The fact that the heating rod still provided enough power to reach 310 ºC suggests that its power output must be similar to its predecessors. That kind of power output makes it improbable for the element's centerline temperature to be 350 ºC. Therefore, the most reasonable explanation would be that the embedded thermocouple was not placed at the exact center of the heating rod. For the most part, the temperature at all measured spots stayed relatively stable during the whole run, with the exception of few anomalies. The true cause of sudden widening of temperature differences within the main loop around 235 hours

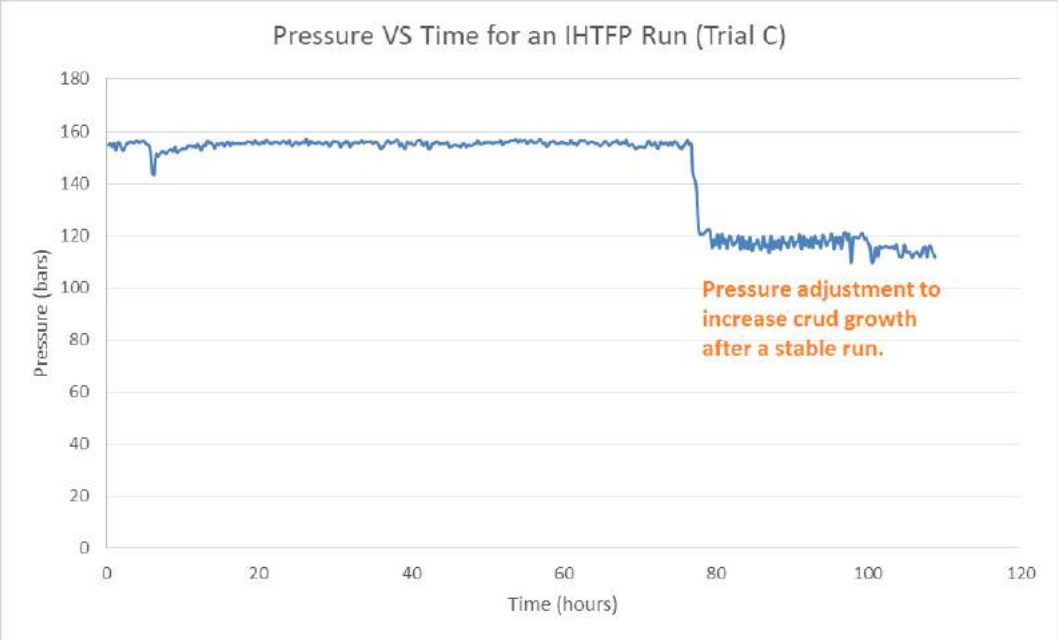


Figure 5-41: Pressure versus time for the experimental trial C.

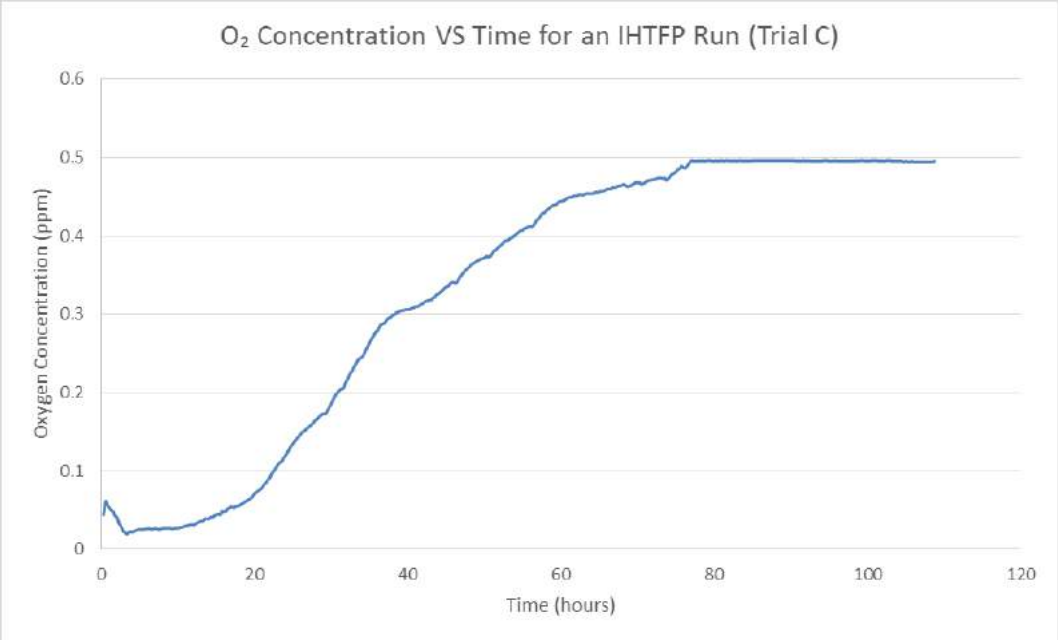


Figure 5-42: Dissolved oxygen concentration versus time for the experimental trial C.

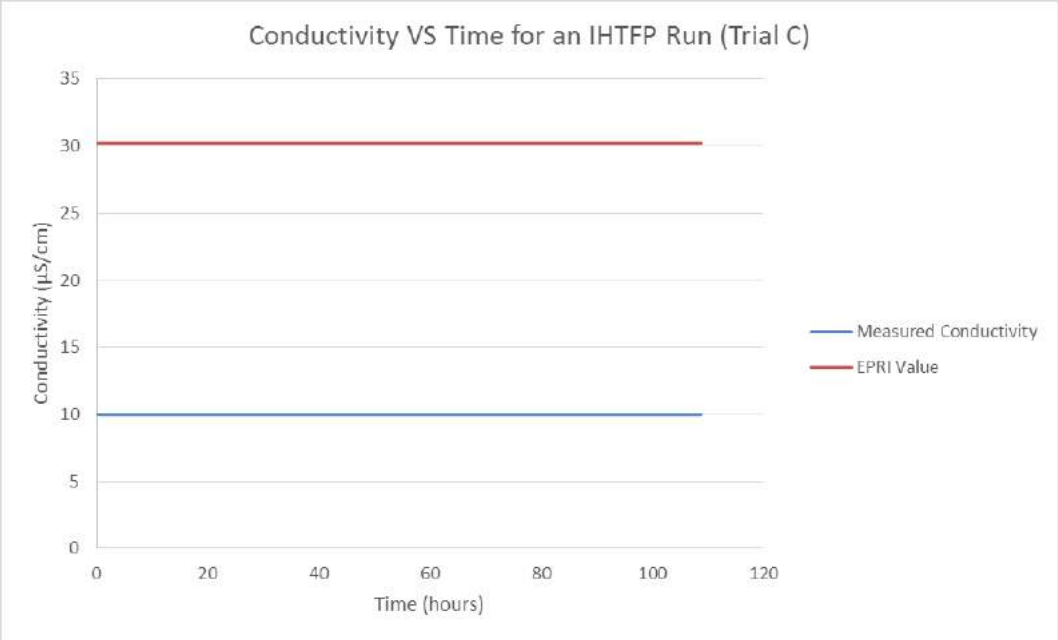


Figure 5-43: Water conductivity versus time for the experimental trial C.

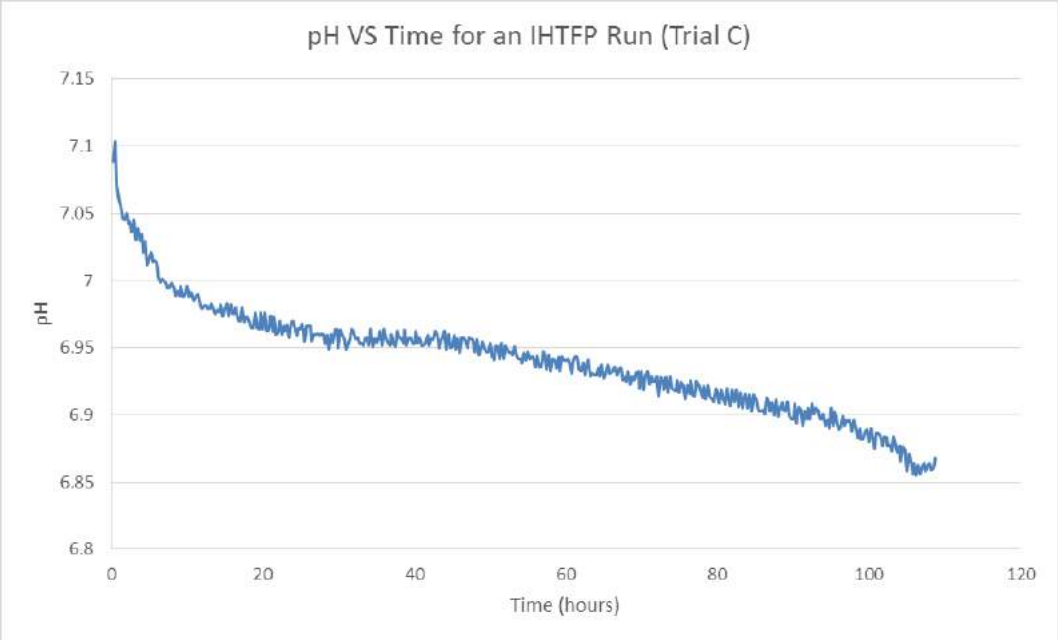


Figure 5-44: pH versus time for the experimental trial C.

is still unknown. One possible cause of the widening could have been the adjustment in room's air conditioning unit during the run. The actual cause of the slight drop around 270 hours in the temperature of preheat temperature 1 spot is also unknown. It is unlikely that the huge temperature drop is a physical phenomenon since that it is improbable for the temperature of circulating water to be that low. Additionally, the IHTFP was definitely not tinkered with during the run.

Figure 5-46 shows that pressure was quite stable throughout the run at around 120 - 135 bars. During trial C, the problem with oxygen regulation was caused by setting the gas regulator to allow too little argon gas through. Therefore, the gas regulator was set to allow more gas through in trial D. As shown in figure 5-47, the gas regulator adjustment worked well for more than half of the trial with oxygen concentration close to zero. However, towards the end of the trial, argon bottle starts to run out. The several downward slopes were because we decided to adjust the gas regulator. Water conductivity stayed at a constant value of around 10 $\mu S/cm$ for the whole trial as shown in figure 5-48. Figure 5-49 shows that although pH varies during the trial, it always lies in the desirable range. Similar to trial C, the data acquisition system was broken for differential pressure; therefore, its graph is omitted.

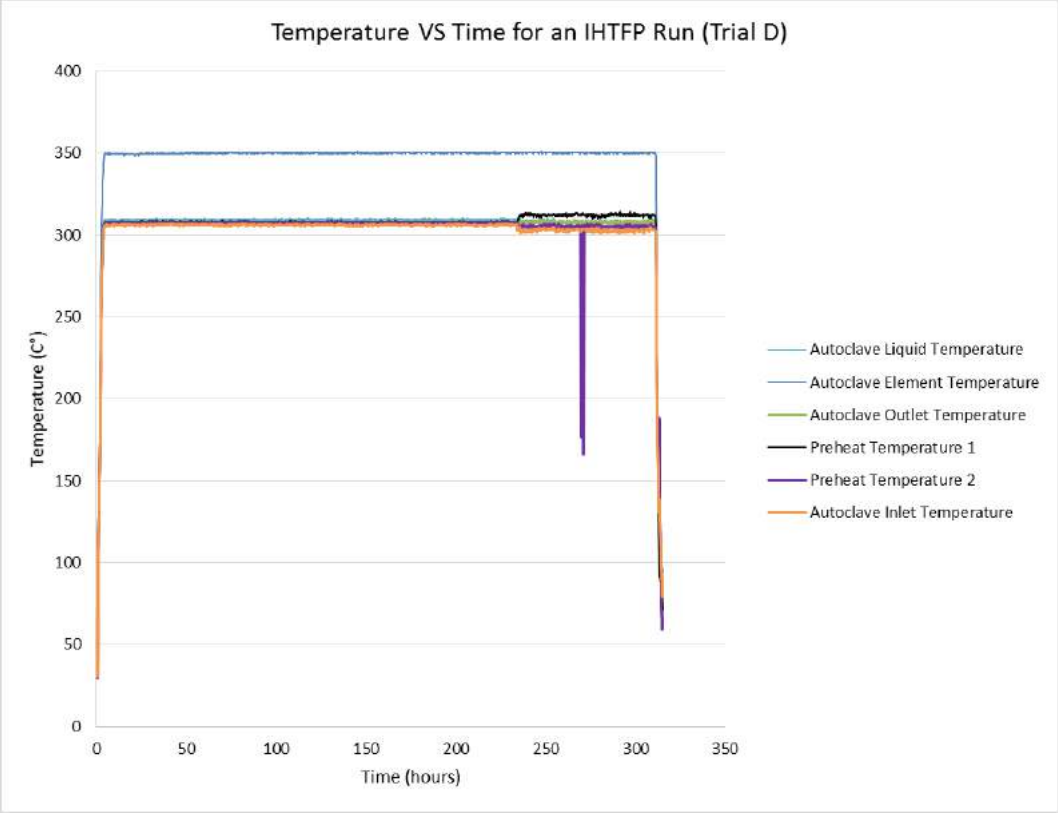


Figure 5-45: Temperature at different spots in the loop versus time for the experimental trial D.

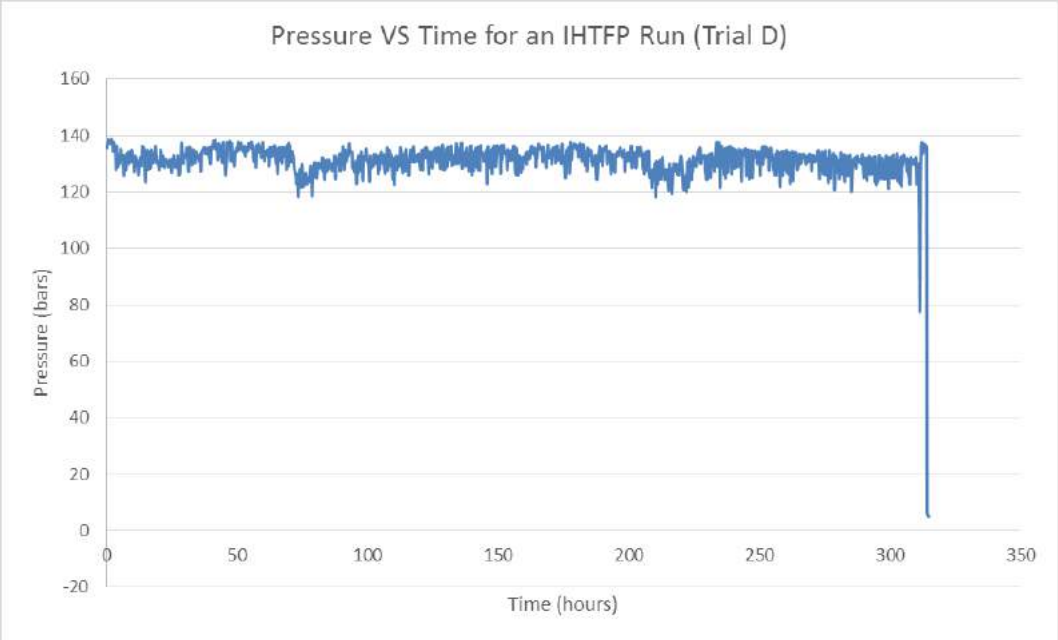


Figure 5-46: Pressure versus time for the experimental trial D.

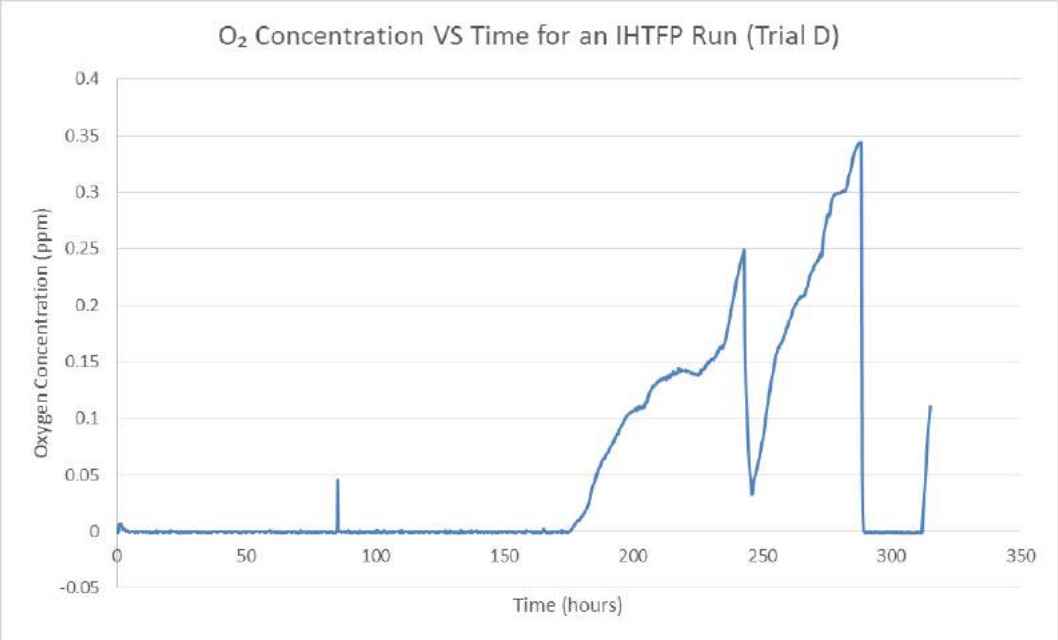


Figure 5-47: Dissolved oxygen concentration versus time for the experimental trial D.

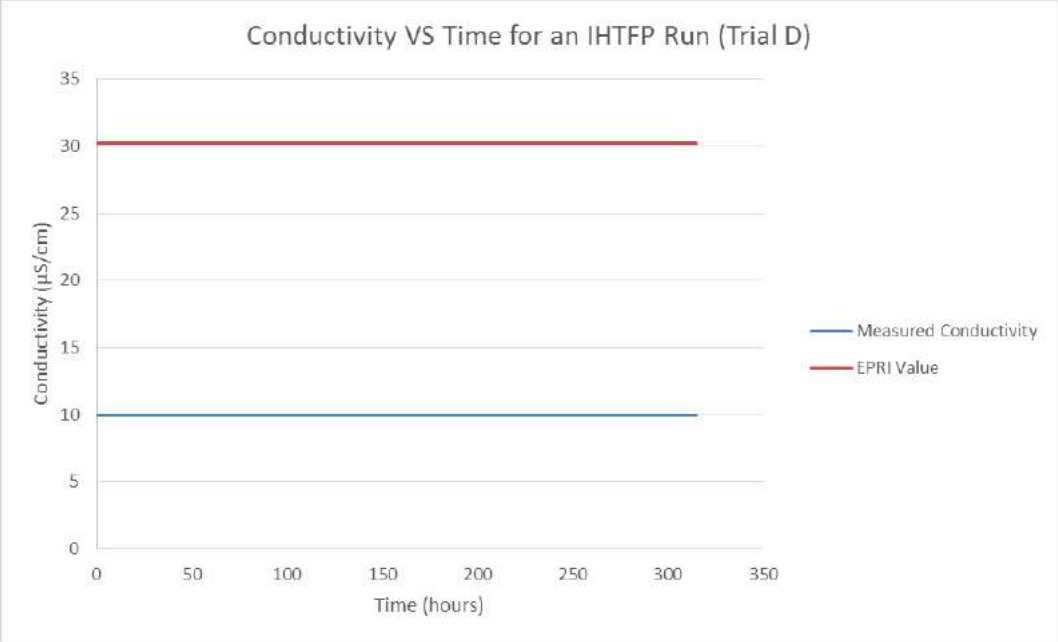


Figure 5-48: Water conductivity versus time for the experimental trial D.

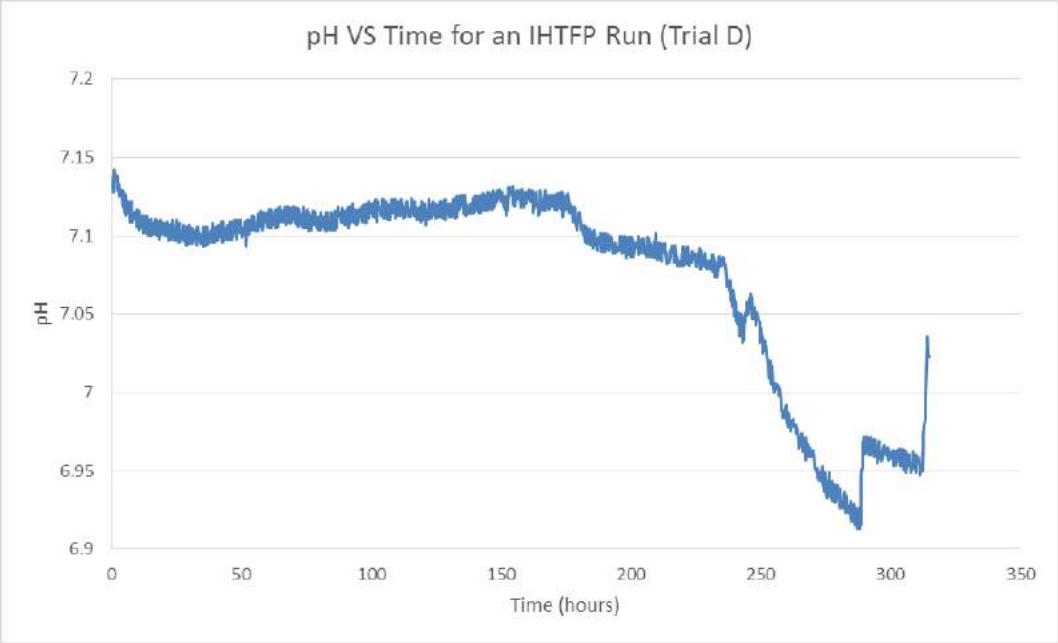


Figure 5-49: pH versus time for the experimental trial D.

### 5.3.2 Images

As mentioned in section 4.4.2, crud-resistant material analysis focus on the crud area coverage obtained from SEM images. Section 4.4.2.1 summarizes the types of images that were taken for crud-resistant material analysis. This section gives two example SEM images from each sample ring. SEM Images were taken for this section using the Zeiss Nvision FIB/SEM. As seen in the example SEM images throughout this section, the crud particles almost always appear whiter than the material background. This property is very useful for doing area coverage analysis since it makes the job of processing the image into binary image easier and more accurate. The process of image thresholding is explained in next section.

#### 5.3.2.1 Trial C (February 12, 2016)

This section shows example SEM images associated with each crud-resistant material for trial C. For first two materials, example binary images obtained from SEM images are also shown. Overall, trial C grew slightly less crud compare to trial D. This is likely due to the trial having high-pressure condition of 155 bars throughout most of the run.

[1]

**Zirconium Carbide ($ZrC$)** Figure 5-50 and 5-51 are example SEM images of crud on zirconium carbide coating surface. Figure 5-52 and 5-53 are binary image processed from figure 5-50 using moment thresholding and Otsu thresholding algorithm, respectively. All thresholding results use Chow and Kaneko's adaptive thresholding add-on, as explained in section 4.4.1.2. Moreover, all binary images underwent the morphological image processing, explained in section 4-13, to clean up image artifacts. These binary images can be used to determine crud area coverage, whereby the white area represents crud. In general, these two image processing algorithms perform well in separating crud particles from the background. Both cases yield very similar binary images. The only part in figure 5-50 where white areas of binary images do not represent crud particles very well is the bottom-left lighter area. If we look closely, we can see that the surface in this area is peeled off exposing the lighter material below the surface. Some parts of the lighter material has brightness that is easily above the threshold determined by the image thresholding algorithms. These parts are incorrectly identified as crud. It is important to note that this error stems from the use of threshold to determine binary image, rather than the problem with image processing algorithm determining bad threshold. If the thresholding were done manually on this image, one would see that increasing the threshold to prevent the misidentification in that particular area will lead to crud particles failing to be identified properly elsewhere in the image. Figure 5-54 and 5-55 are binary image processed

[1] Note that the ~200 images taken for this trial was taken with tilt correction on. Nevertheless, it should not affect the area coverage value since the area coverage would be the same even if the image is skewed.

from figure 5-51 using moment thresholding and Otsu thresholding algorithm, respectively.

Figures 5-56 and 5-56 are example SEM images of the uncoated side of zirconium carbide sample that are used for the control group. These two SEM images also have dark spots, which are not particles. If we zoomed close to these dark spots, we will see that they are darker surface without any peeling. We suspect that they may be related to the corroding stainless steel surface. Figures 5-57 and 5-61 are binary image processed from figure 5-57 using moment thresholding and Otsu thresholding algorithm, respectively. Likewise, figures 5-58 and 5-59 are binary image processed from figure 5-56 using moment thresholding and Otsu thresholding algorithm, respectively. It is hard to clearly determine whether zirconium carbide coating has more or less crud than its control sample with bare eyes. This is exactly why we use image processing algorithms to determine the actual numbers.

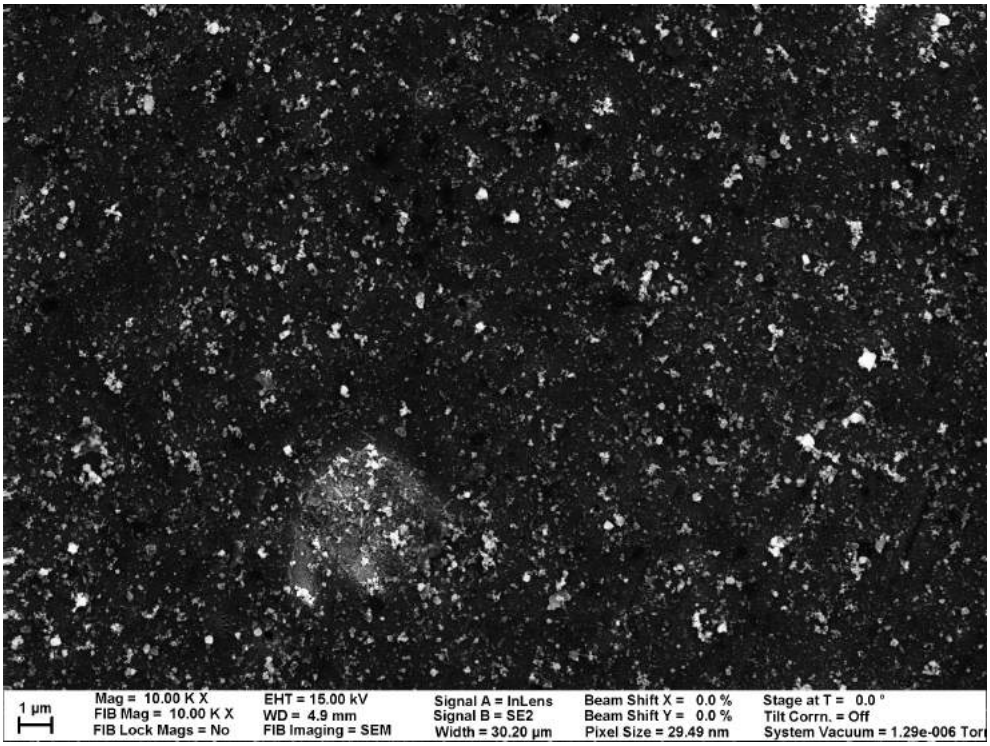


Figure 5-50: Example SEM image of the coated side of $ZrC$ sample ring.

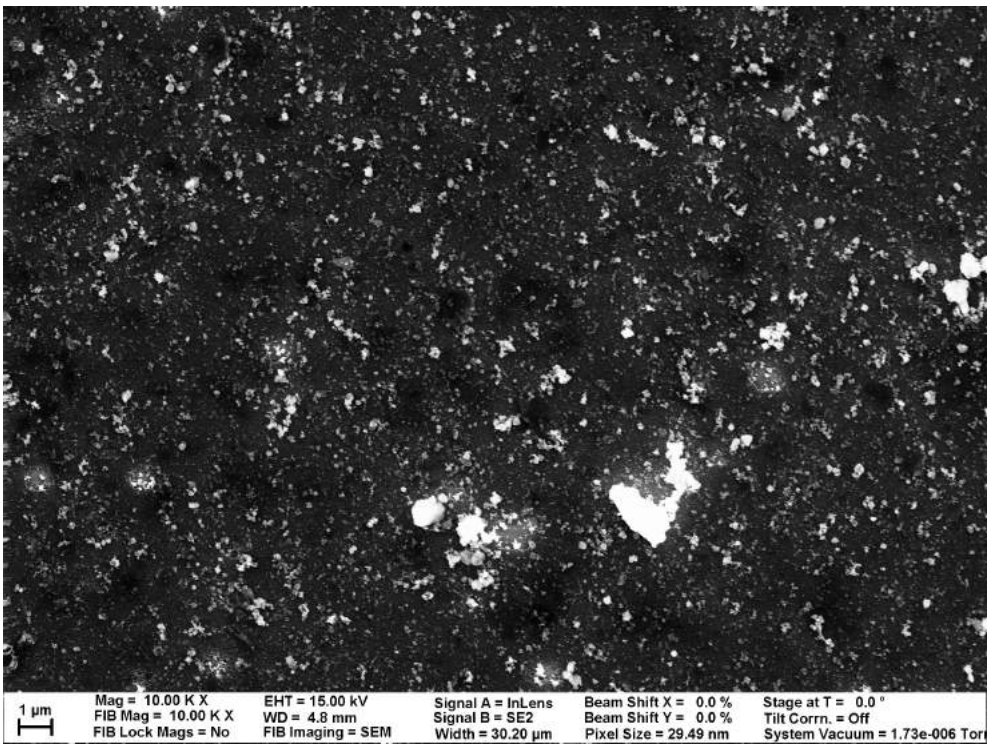


Figure 5-51: Another example SEM image of the coated side of $ZrC$ sample ring.

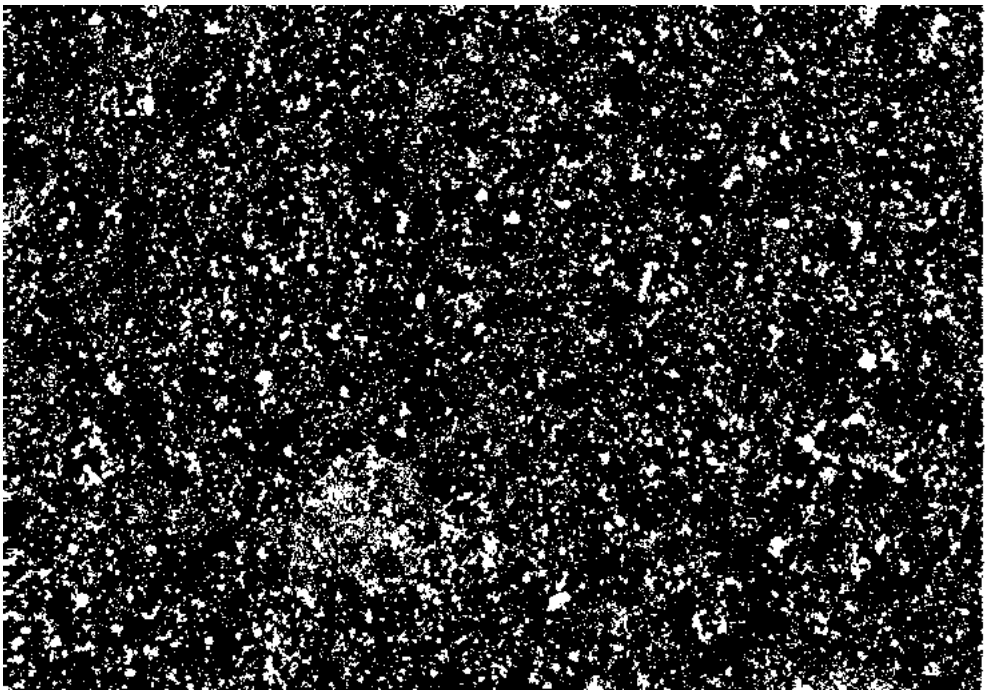

Figure 5-52: Figure 5-50 converted to a binary image using moment thresholding algorithm.

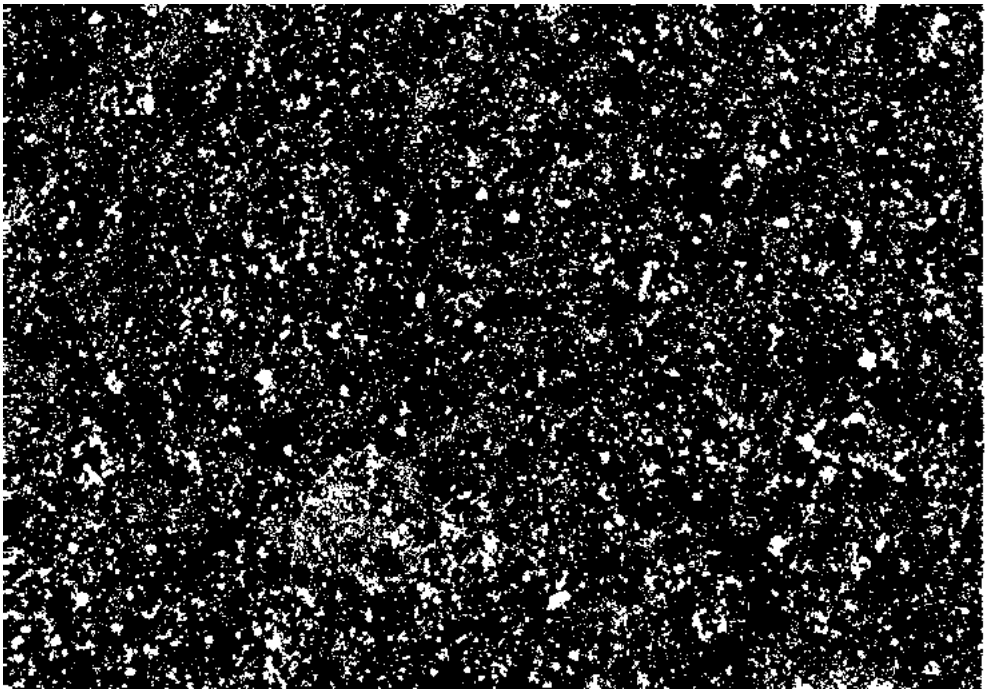

Figure 5-53: Figure 5-50 converted to a binary image using otsu thresholding algorithm.

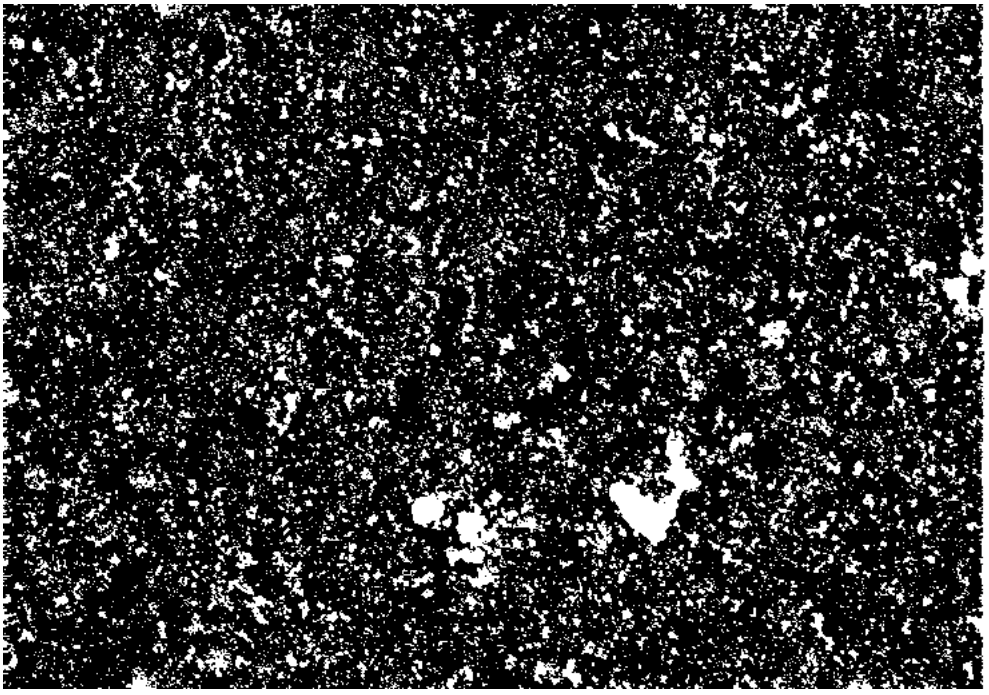

Figure 5-54: Figure 5-51 converted to a binary image using moment thresholding algorithm.

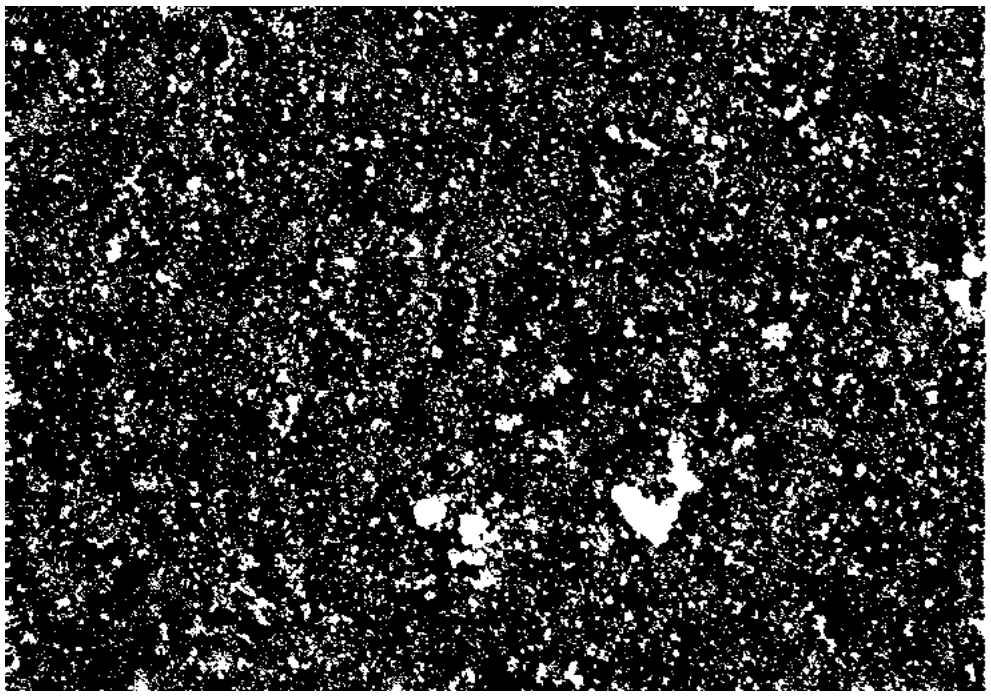

Figure 5-55: Figure 5-51 converted to a binary image using otsu thresholding algorithm.

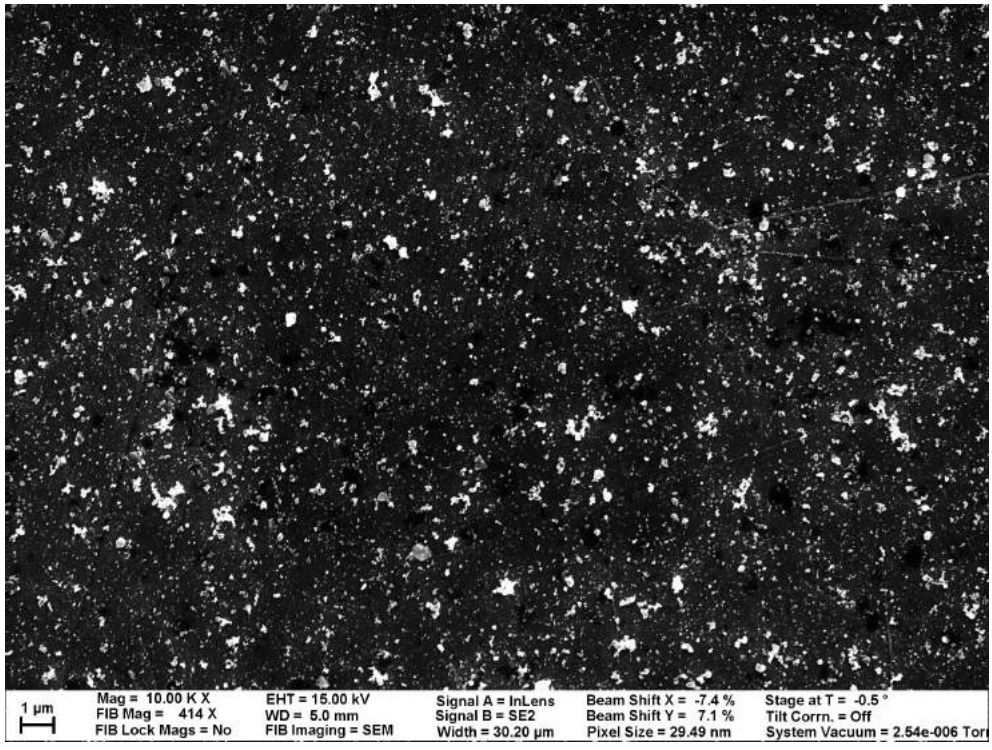


Figure 5-56: Example SEM image of the uncoated side of $ZrC$ sample ring.

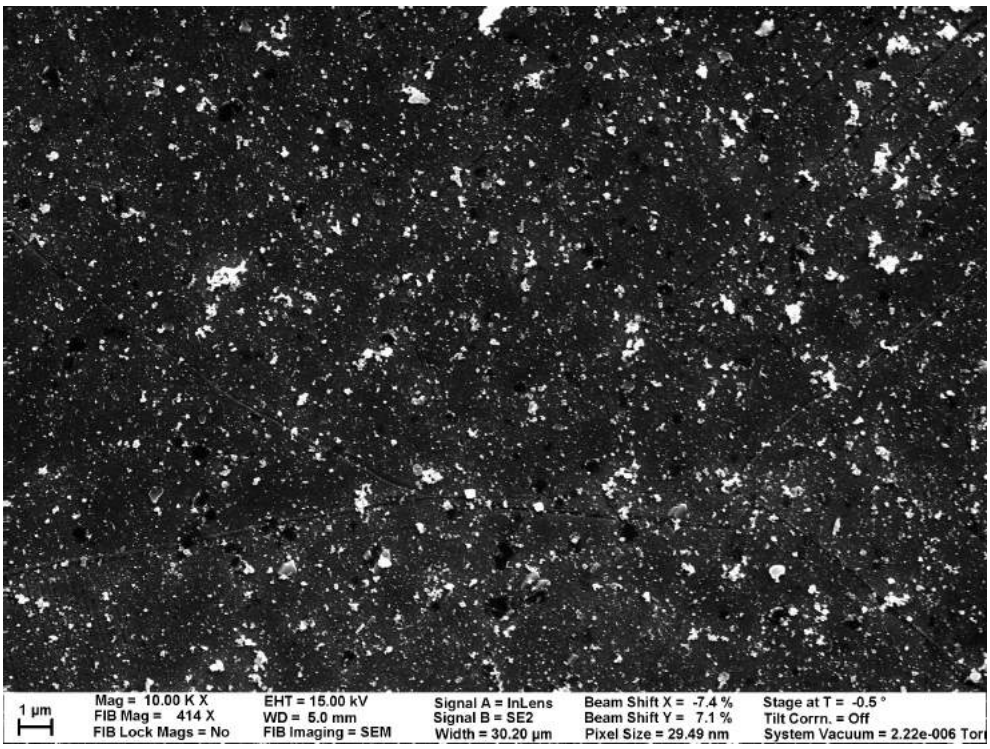


Figure 5-57: Another example SEM image of the uncoated side of $ZrC$ sample ring.

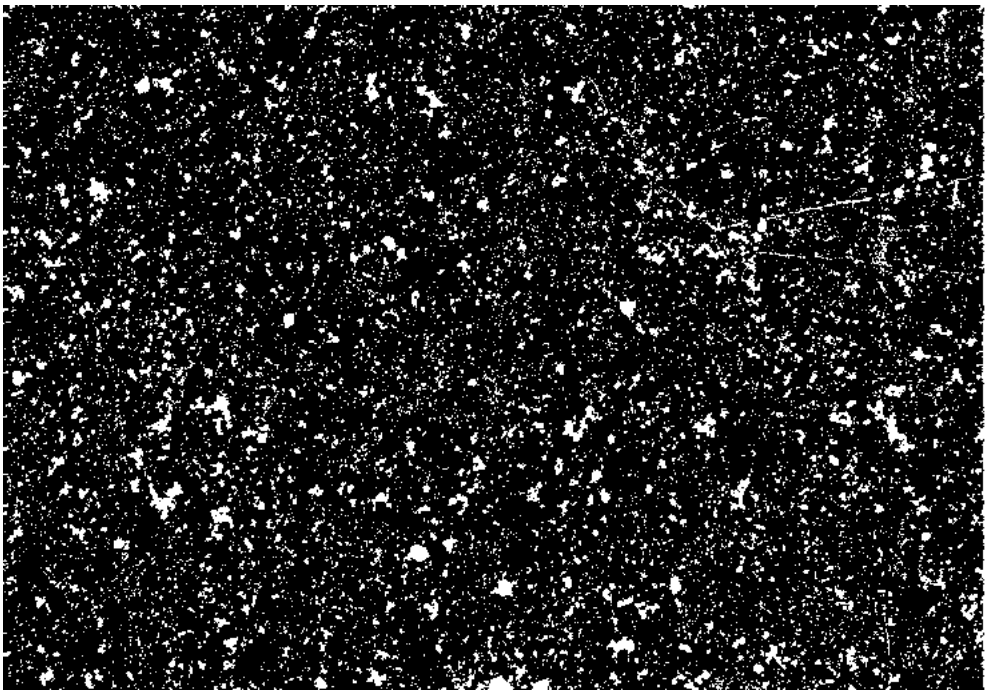

Figure 5-58: Figure 5-56 converted to a binary image using moment thresholding algorithm.

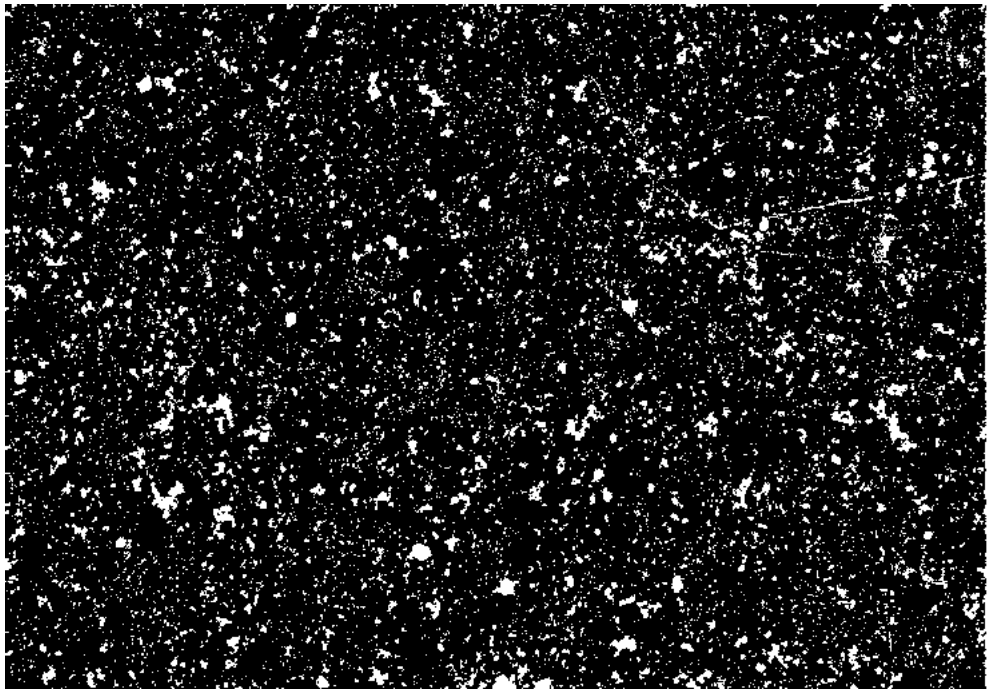

Figure 5-59: Figure 5-57 converted to a binary image using otsu thresholding algorithm.

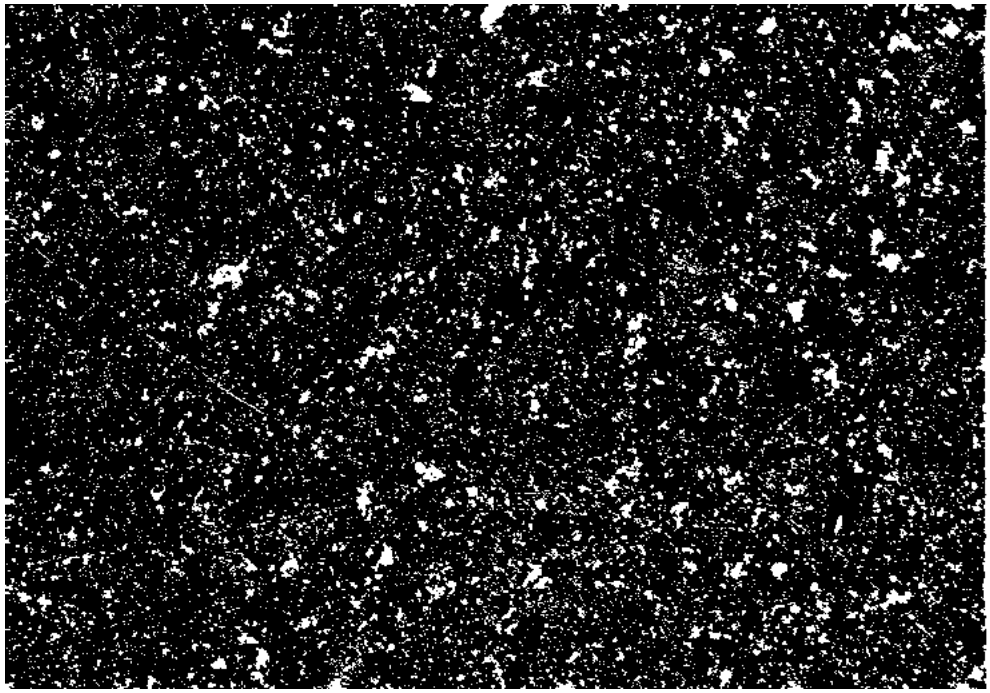

Figure 5-60: Figure 5-56 converted to a binary image using moment thresholding algorithm.

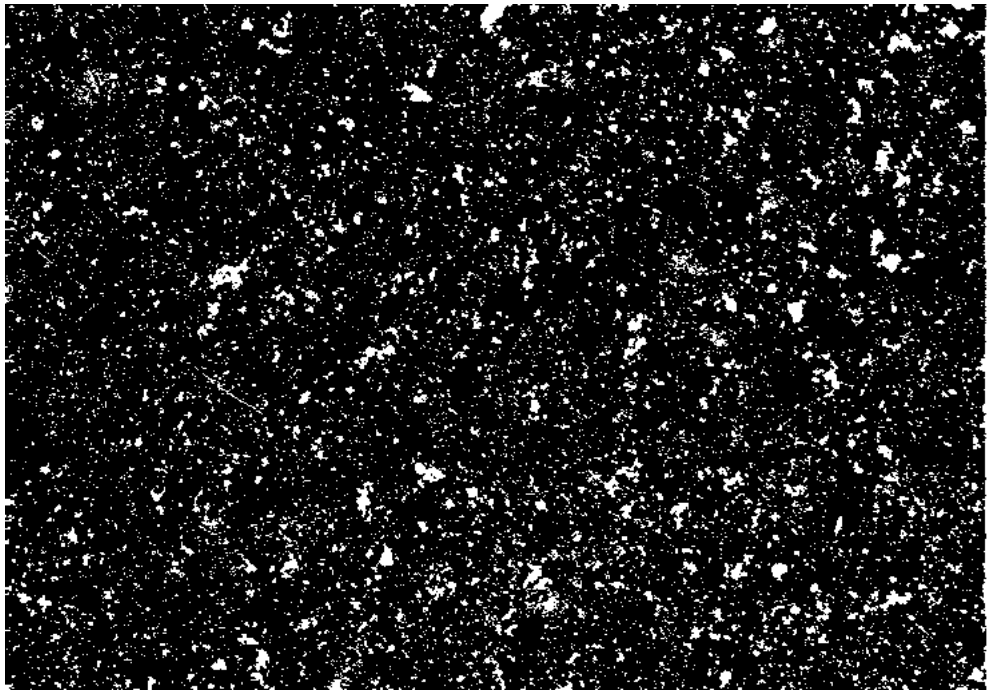

Figure 5-61: Figure 5-57 converted to a binary image using otsu thresholding algorithm.

**Zirconium Nitride ($ZrN$)** Figures 5-62 and 5-63 are SEM images of the coated side of the zirconium nitride sample. Figures 5-64 and 5-65 are binary image processed from figure 5-62 using moment thresholding and Otsu thresholding algorithm, respectively. Figures 5-66 and 5-67 are binary image processed from figure 5-63 using moment thresholding and Otsu thresholding algorithm, respectively.

Figures 5-108 and 5-109 are SEM images of the uncoated side of the zirconium nitride sample. Figures 5-70 and 5-71 are binary image processed from figure 5-108 using moment thresholding and Otsu thresholding algorithm, respectively. Figures 5-72 and 5-73 are binary image processed from figure 5-109 using moment thresholding and Otsu thresholding algorithm, respectively.

From observing these images, we can see that figure 5-69 of the uncoated side contains a very large particle which is likely an anomaly which does not appear in other SEM images from similar areas. Discounting that large particle, it is very hard to determine whether the coated or uncoated has more crud particles, just with bare eyes. It turns out that the crud coverage value found using image processing algorithms, shown in table 5.5, show that coated side has less crud coverage than the control side.

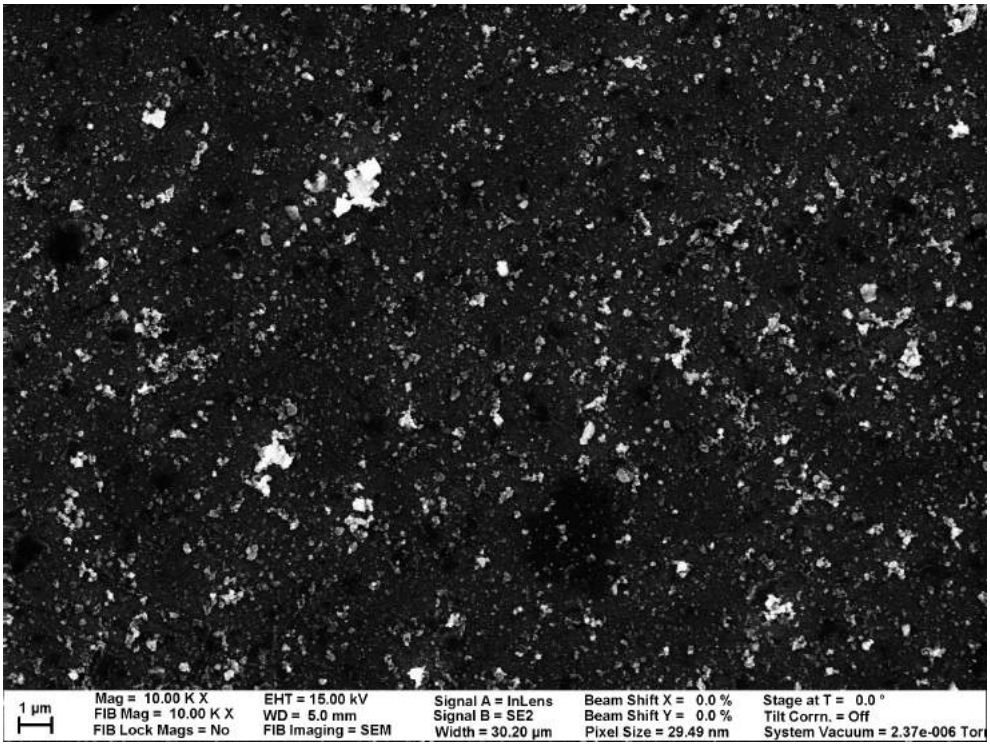


Figure 5-62: Example SEM image of the coated side of $ZrN$ sample ring.

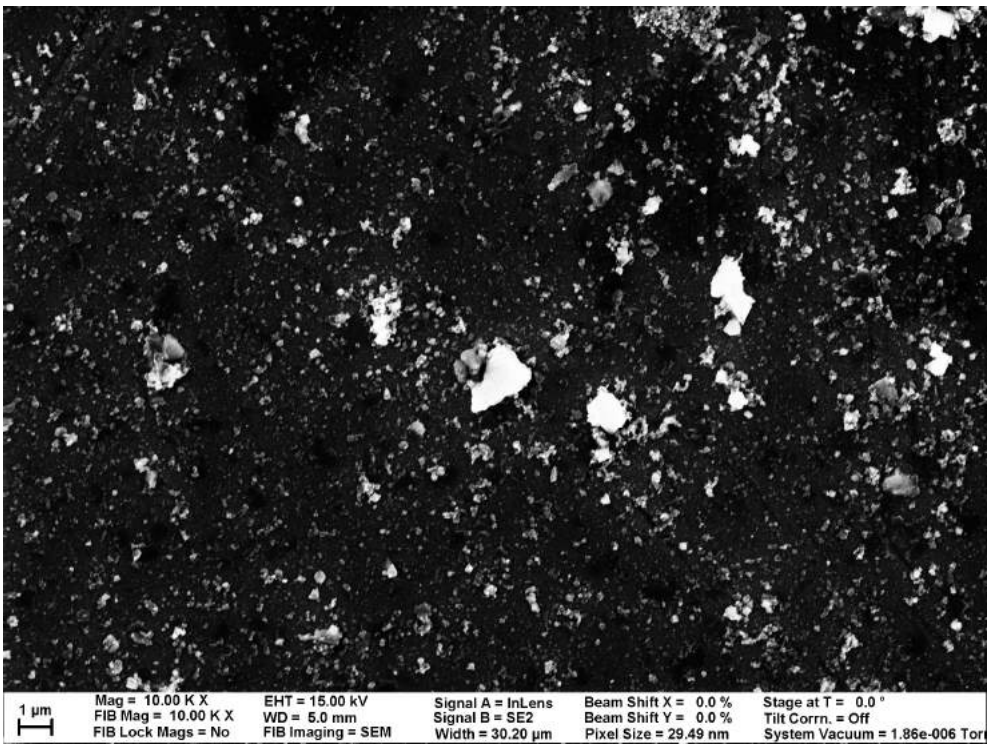


Figure 5-63: Another example SEM image of the coated side of $ZrN$ sample ring.

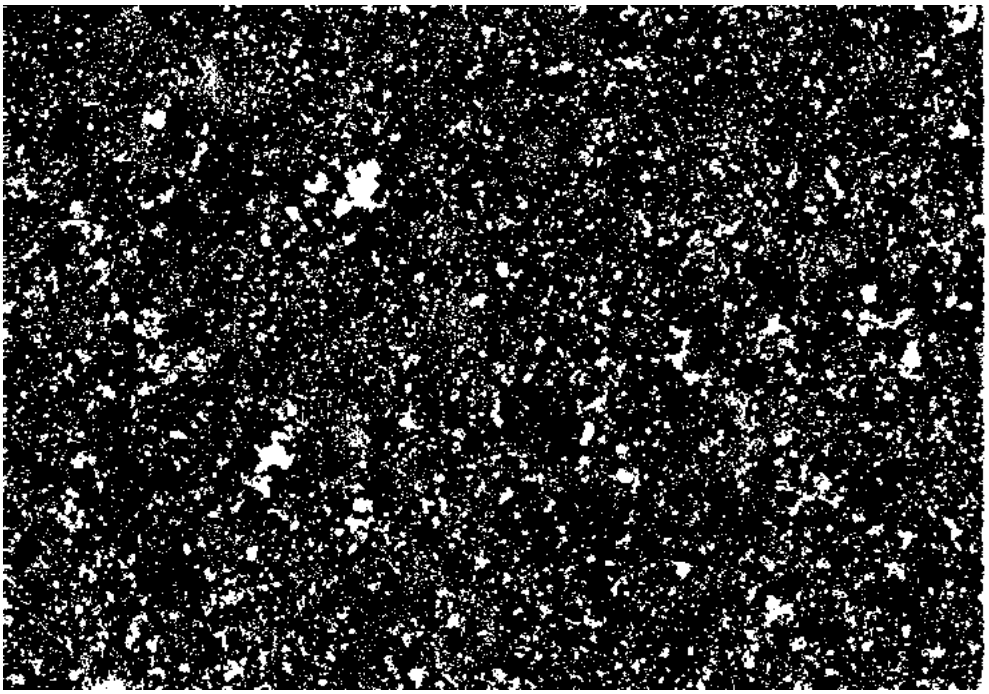

Figure 5-64: Figure 5-62 converted to a binary image using moment thresholding algorithm.

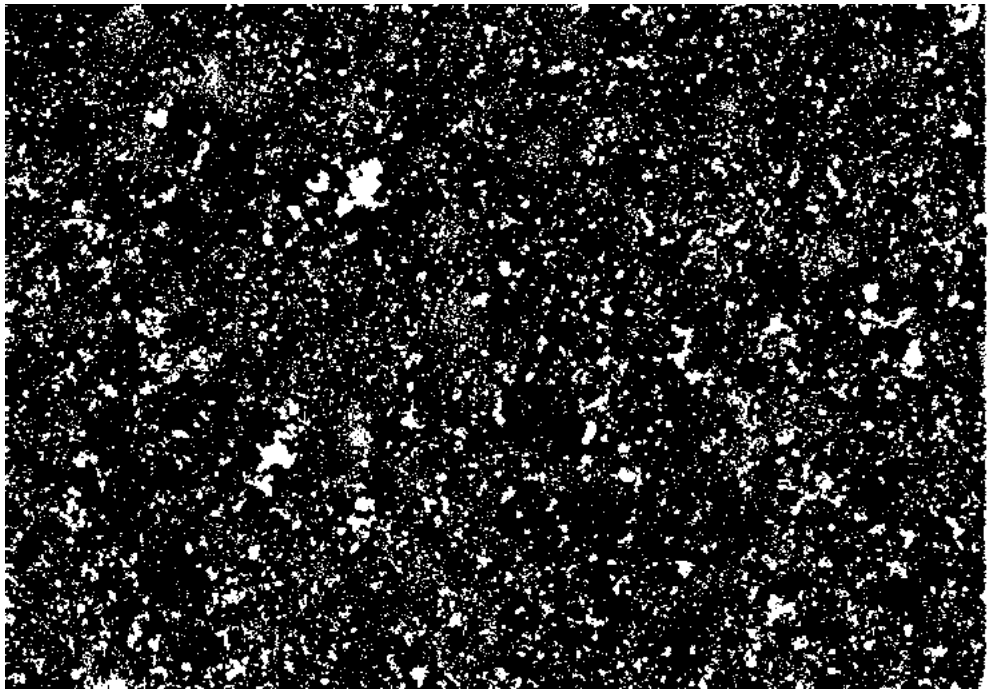

Figure 5-65: Figure 5-62 converted to a binary image using otsu thresholding algorithm.

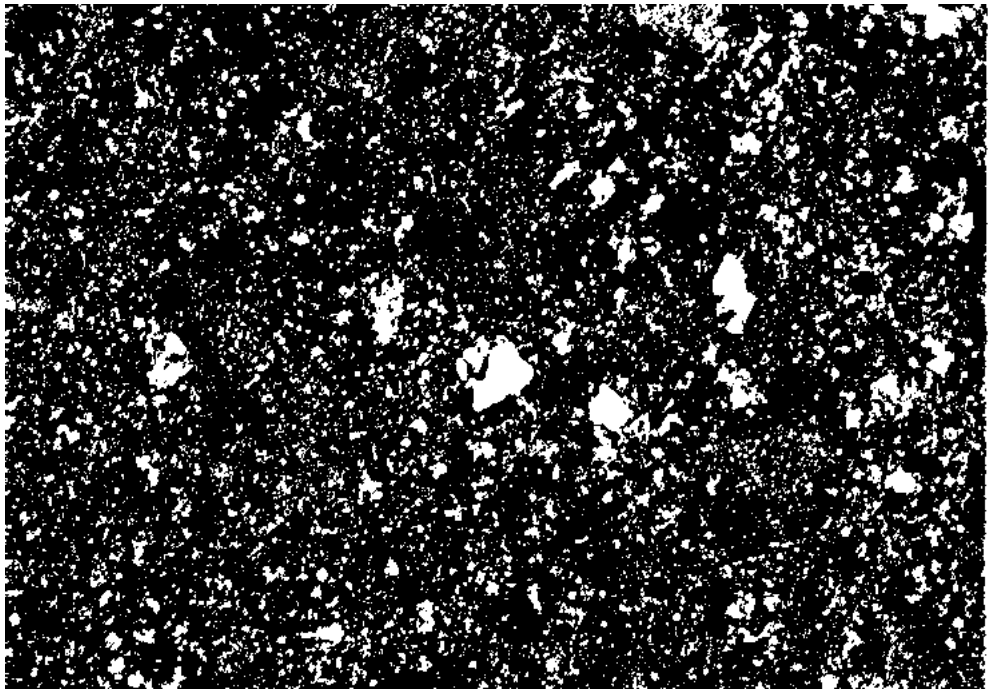

Figure 5-66: Figure 5-63 converted to a binary image using moment thresholding algorithm.

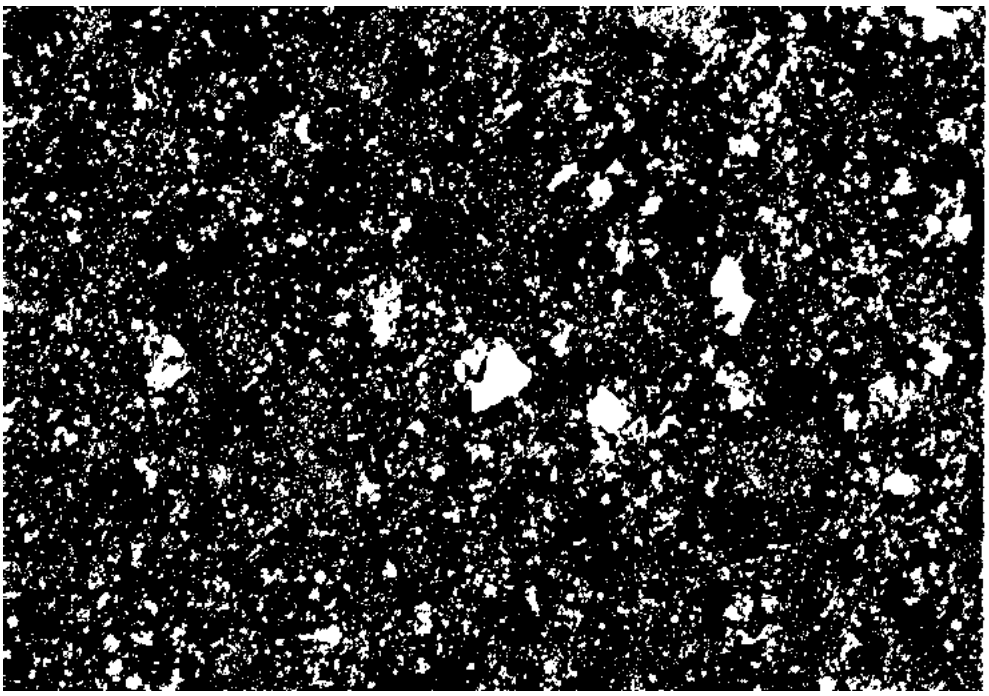

Figure 5-67: Figure 5-63 converted to a binary image using otsu thresholding algorithm.

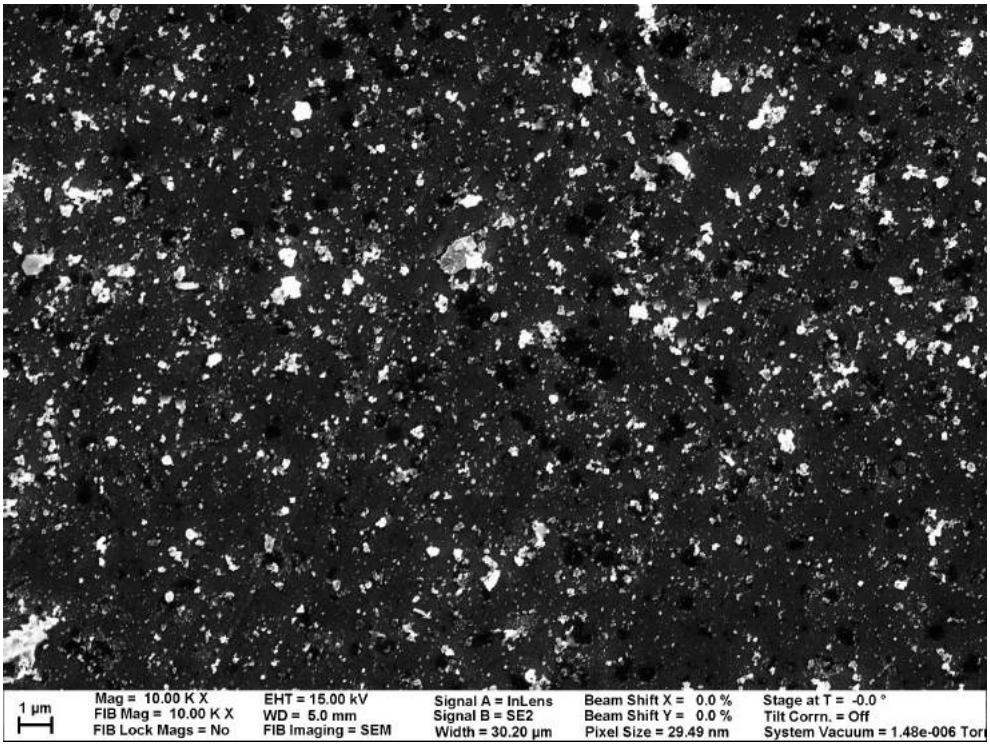


Figure 5-68: Example SEM image of the uncoated side of $ZrN$ sample ring.

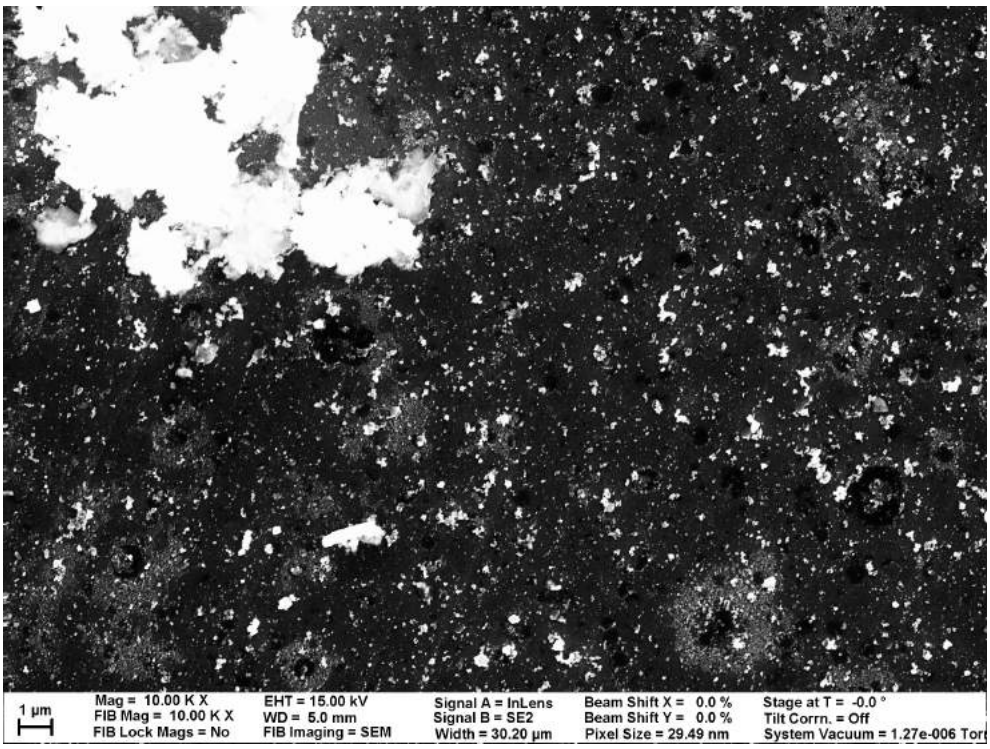


Figure 5-69: Another example SEM image of the uncoated side of $ZrN$ sample ring.

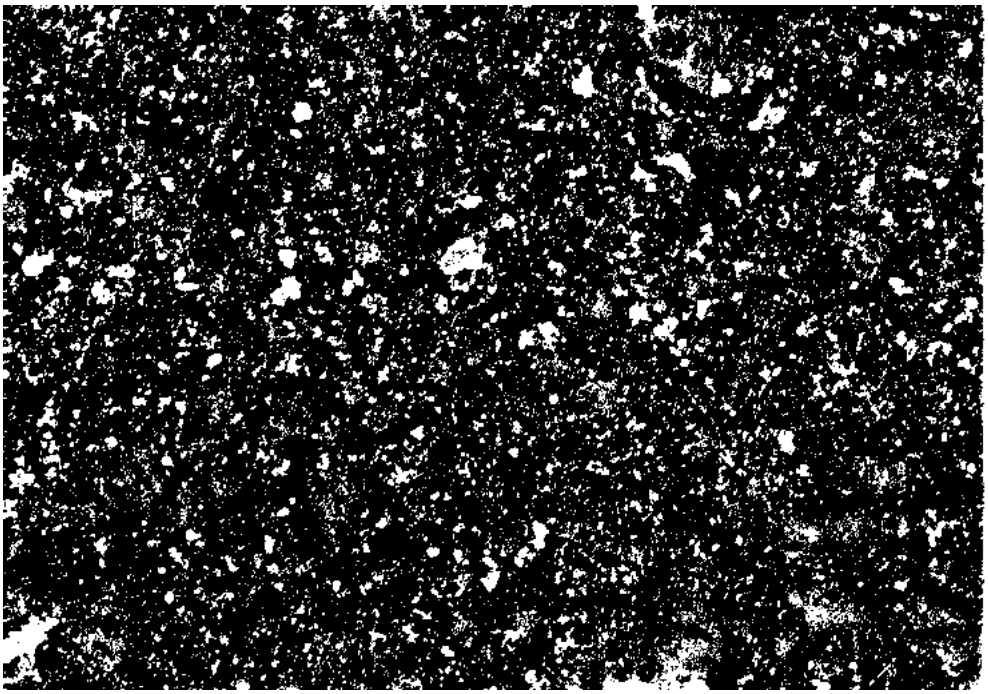

Figure 5-70: Figure 5-68 converted to a binary image using moment thresholding algorithm.

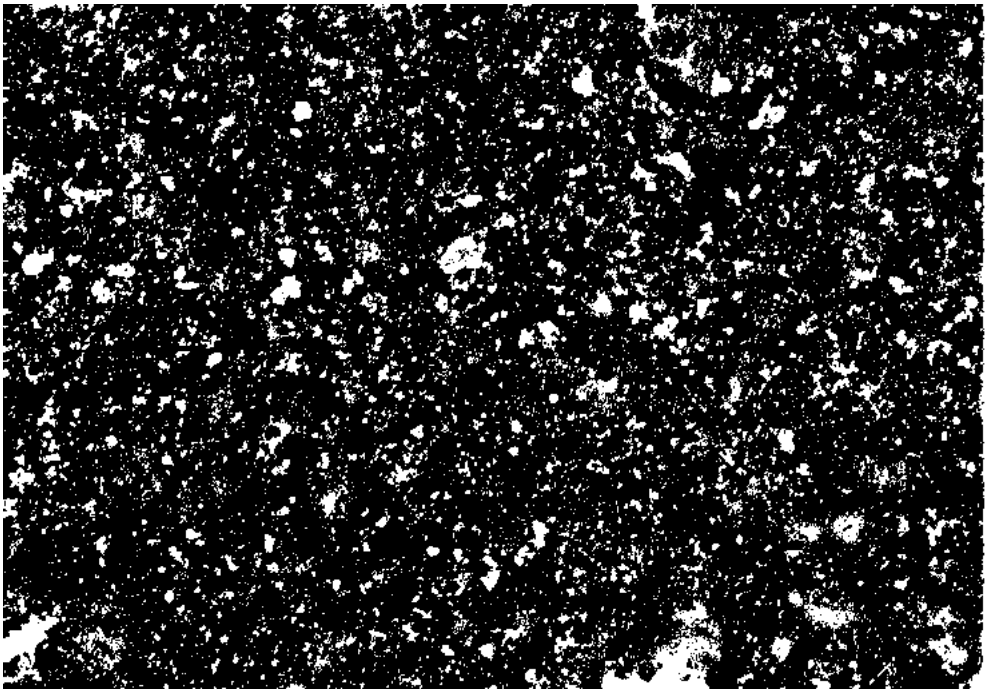

Figure 5-71: Figure 5-69 converted to a binary image using otsu thresholding algorithm.

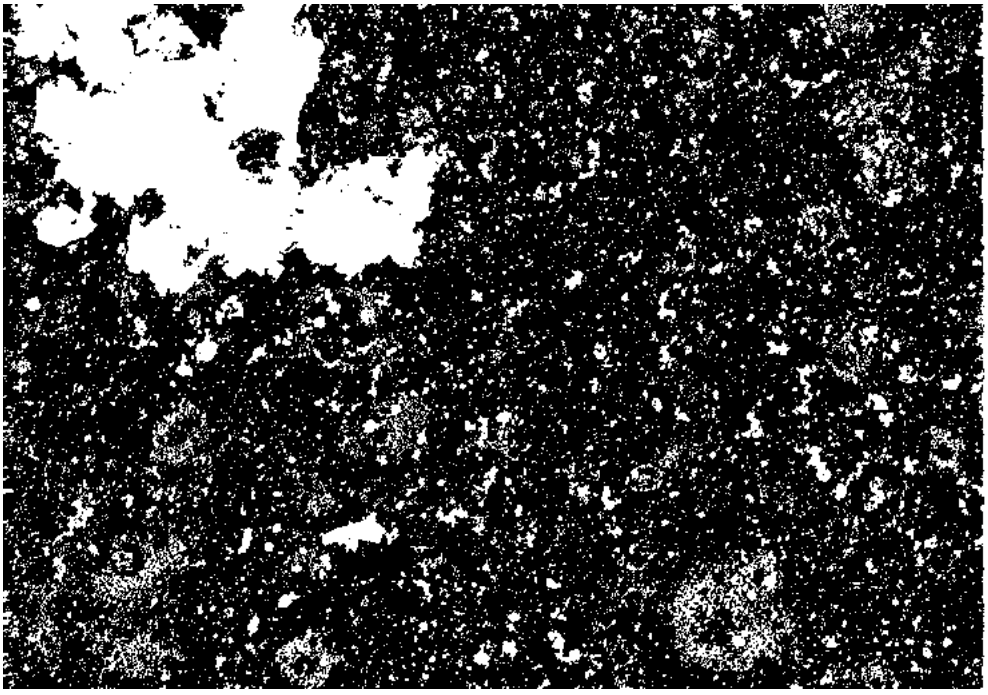

Figure 5-72: Figure 5-68 converted to a binary image using moment thresholding algorithm.

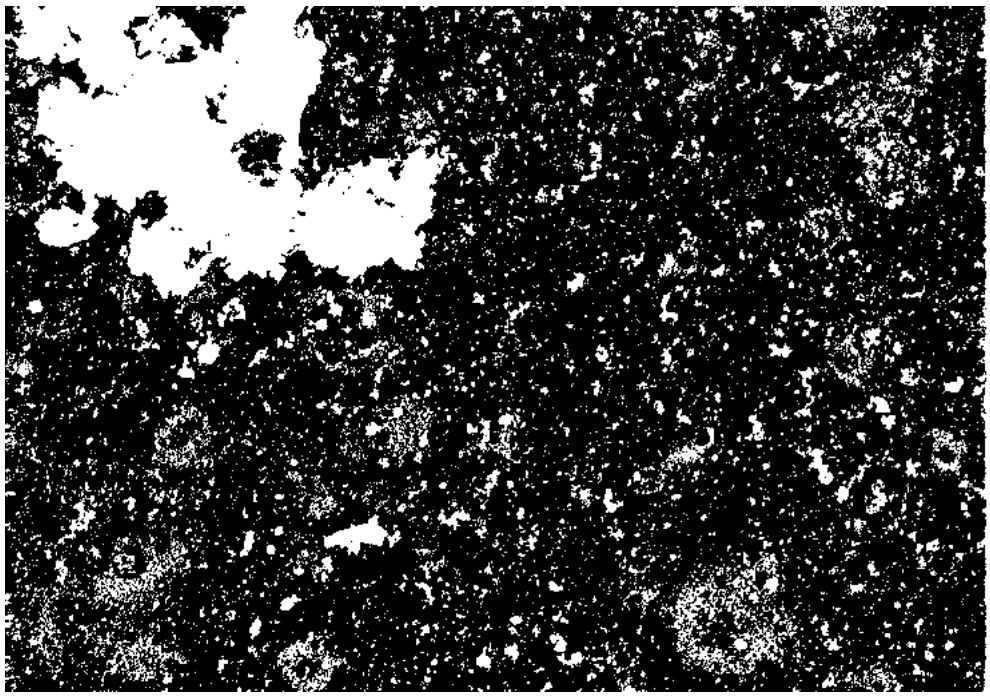

Figure 5-73: Figure 5-69 converted to a binary image using otsu thresholding algorithm.

**Titanium Carbide ($TiC$)** Figures 5-74 and 5-75 are SEM images of crud grown on the titanium carbide surface. Figures 5-76 and 5-77 are SEM images of the control side of the titanium carbide sample. From these images, the SEM images of control side seem to have slightly more crud coverage with larger sized particles.

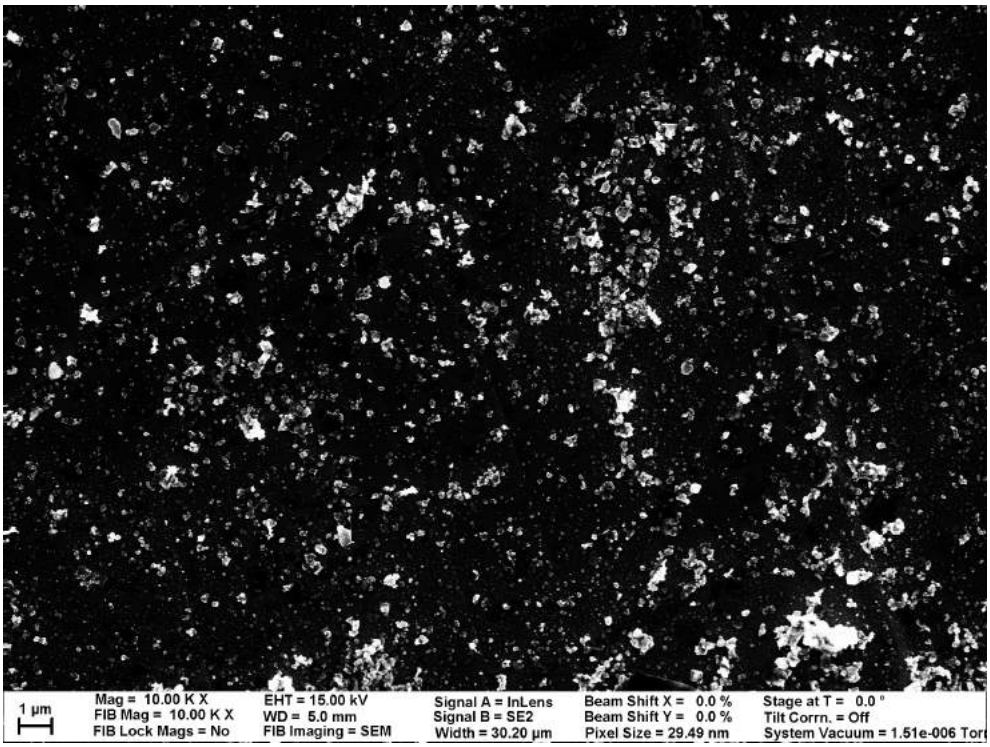


Figure 5-74: Example SEM image of the coated side of $TiC$ sample ring.

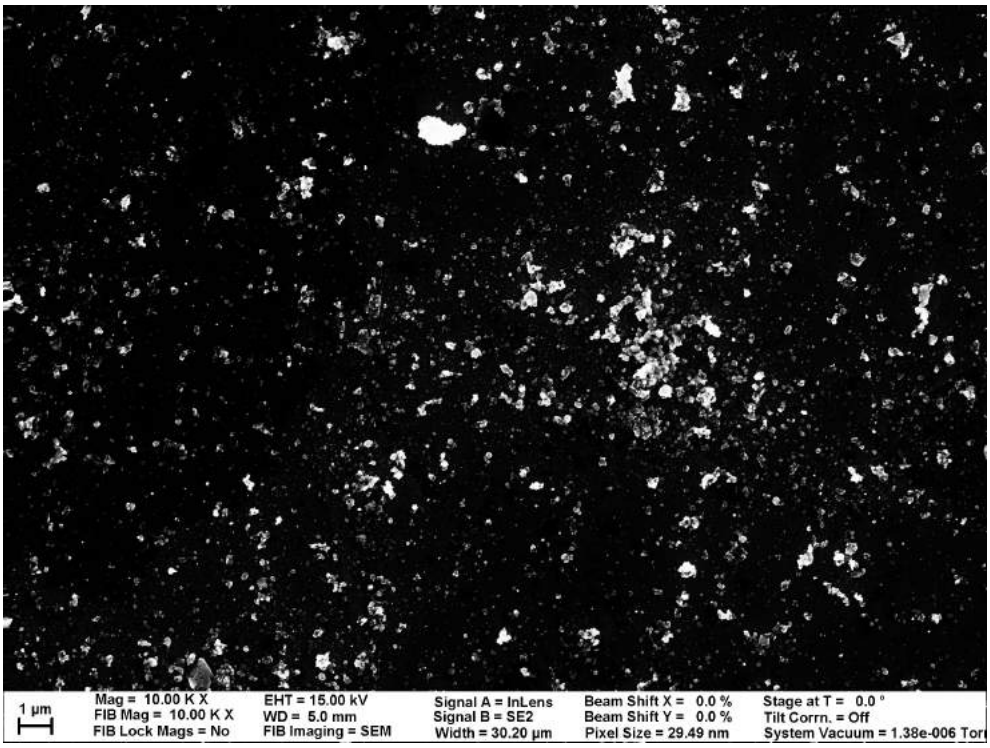


Figure 5-75: Another example SEM image of the coated side of $TiC$ sample ring.

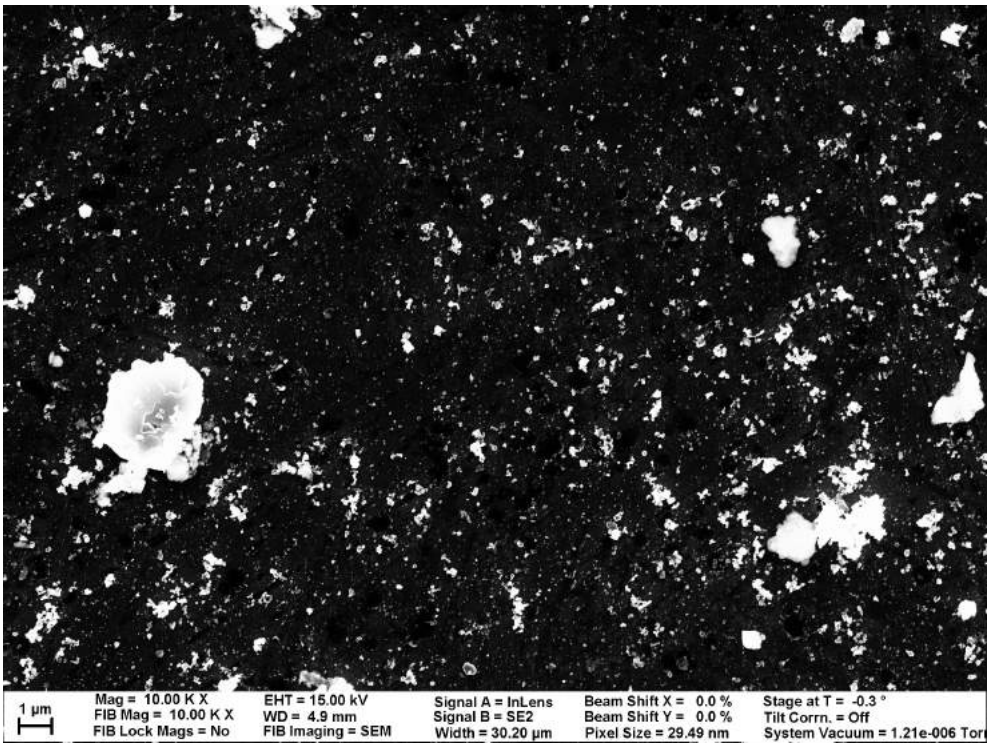


Figure 5-76: Example SEM image of the uncoated side of $TiC$ sample ring.

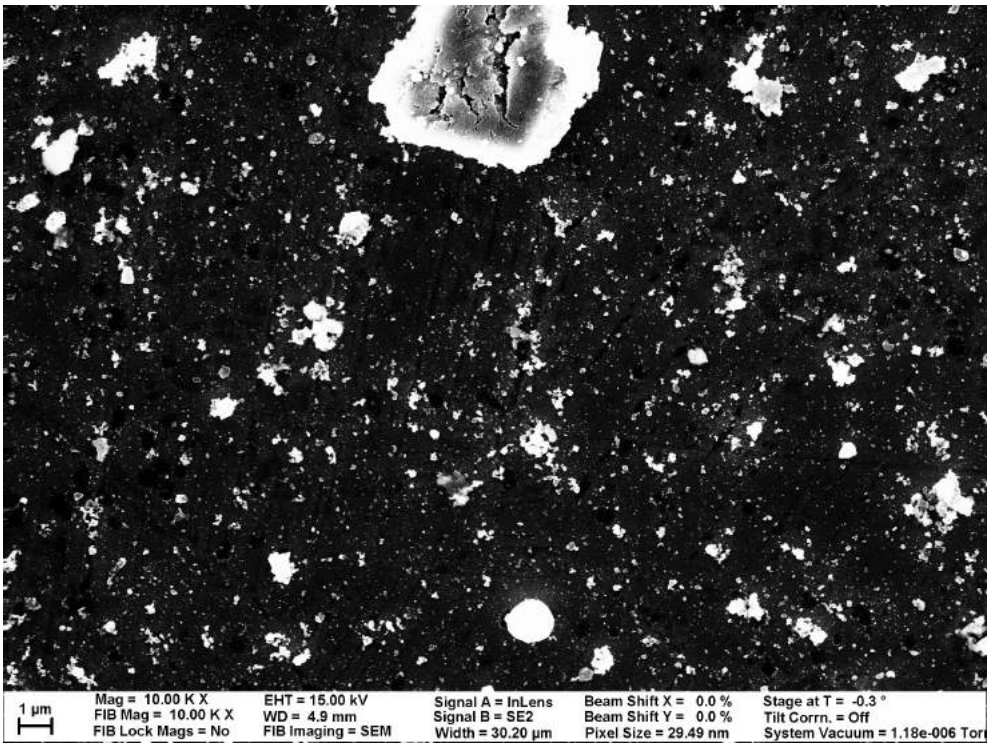


Figure 5-77: Another example SEM image of the uncoated side of $TiC$ sample ring. Since the added nickel oxide particles are only 50 $\mu m$ in diameter, the large particle on the top part of the image is likely an iron oxide particle that came from the corrosion within the loop.

**Titanium Nitride ($TiN$)** Figures 5-78 and 5-79 are SEM images of crud grown on the titanium nitride surface. Figures 5-80 and 5-81 are SEM images of the control side of the titanium nitride sample. Again, from observing these images, it is very hard to determine if the coating works.

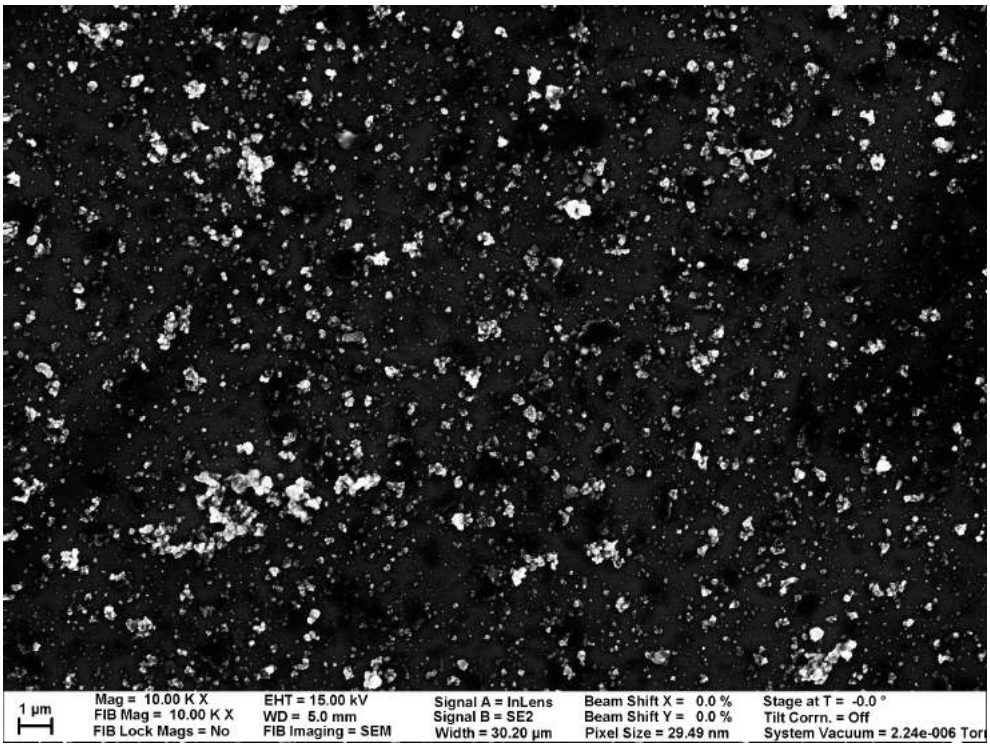


Figure 5-78: Example SEM image of the coated side of $TiN$ sample ring.

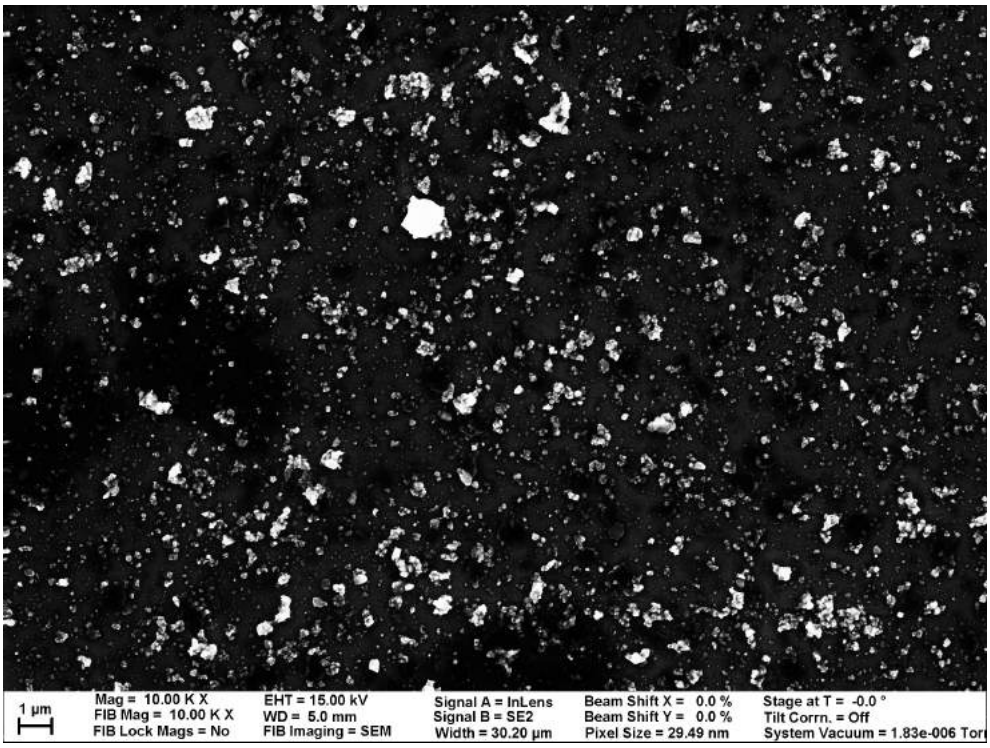


Figure 5-79: Another example SEM image of the coated side of $TiN$ sample ring.

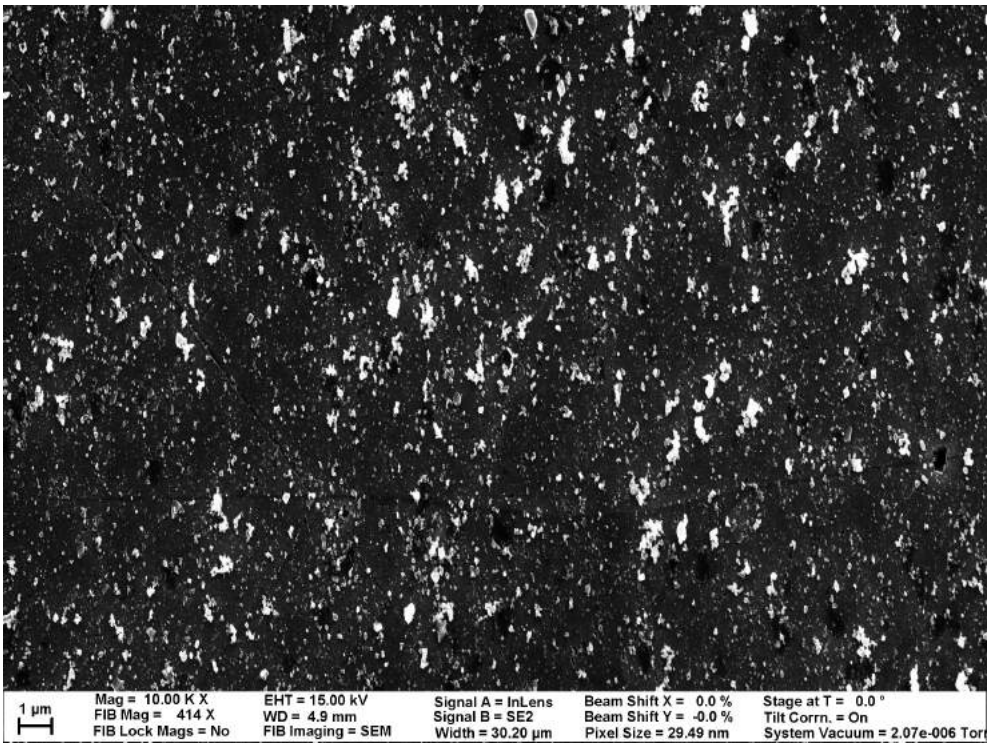


Figure 5-80: Example SEM image of the uncoated side of $TiN$ sample ring.

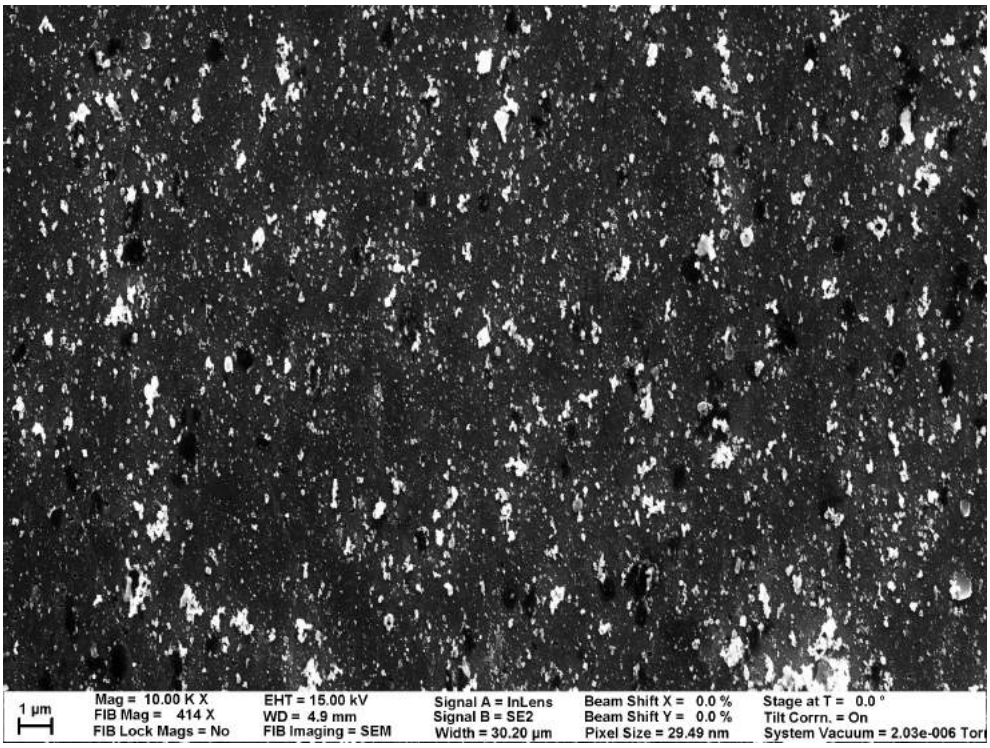


Figure 5-81: Another example SEM image of the uncoated side of $TiN$ sample ring.

**Aluminum Oxide ($Al_2O_3$)** Figures 5-82 and 5-83 are SEM images of crud grown on the aluminum oxide surface. Figures 5-84 and 5-85 are SEM images of the control side of the aluminum oxide sample. Again, from observing these images with bare eyes, it is very hard to determine if the coating works.

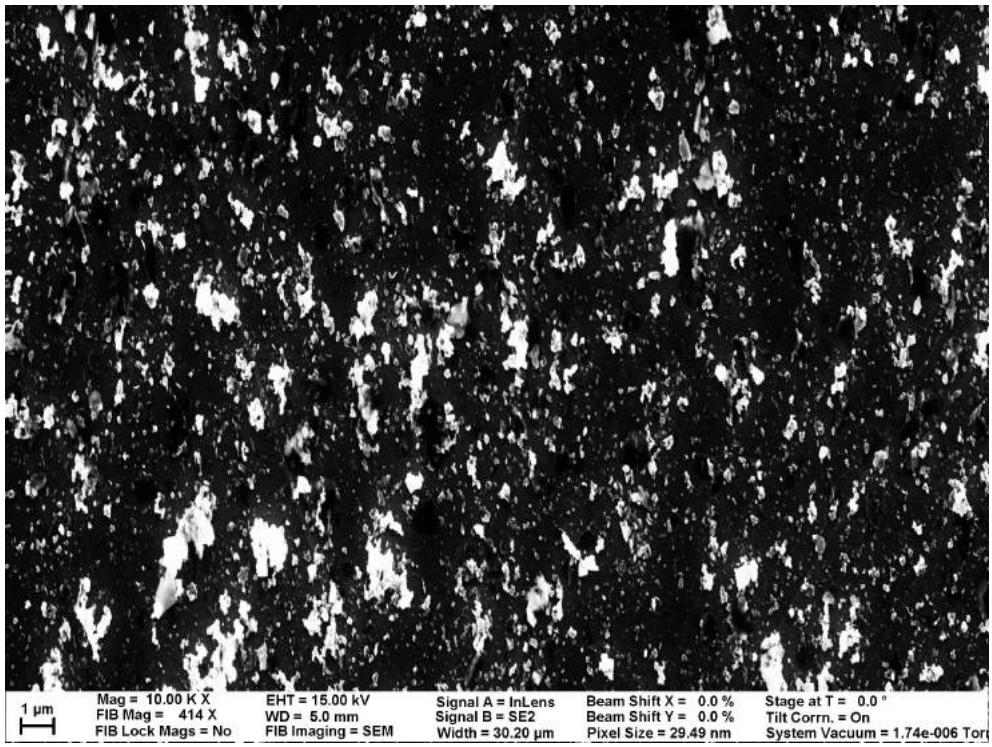


Figure 5-82: Example SEM image of the coated side of $Al_2O_3$ sample ring.

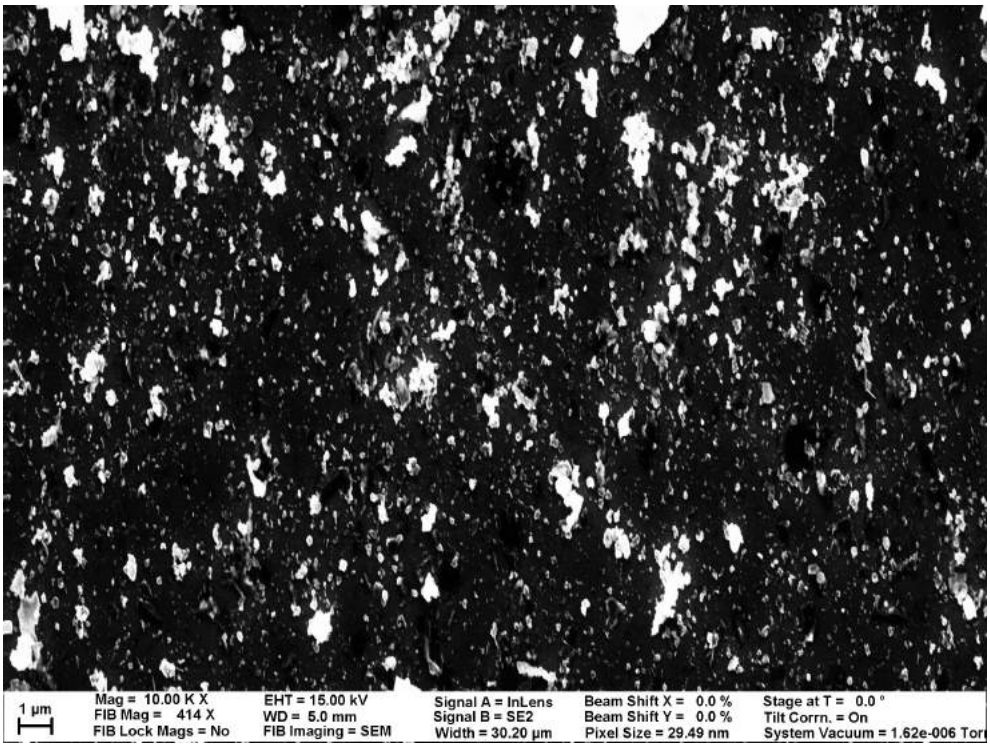


Figure 5-83: Another example SEM image of the coated side of $Al_2O_3$ sample ring.

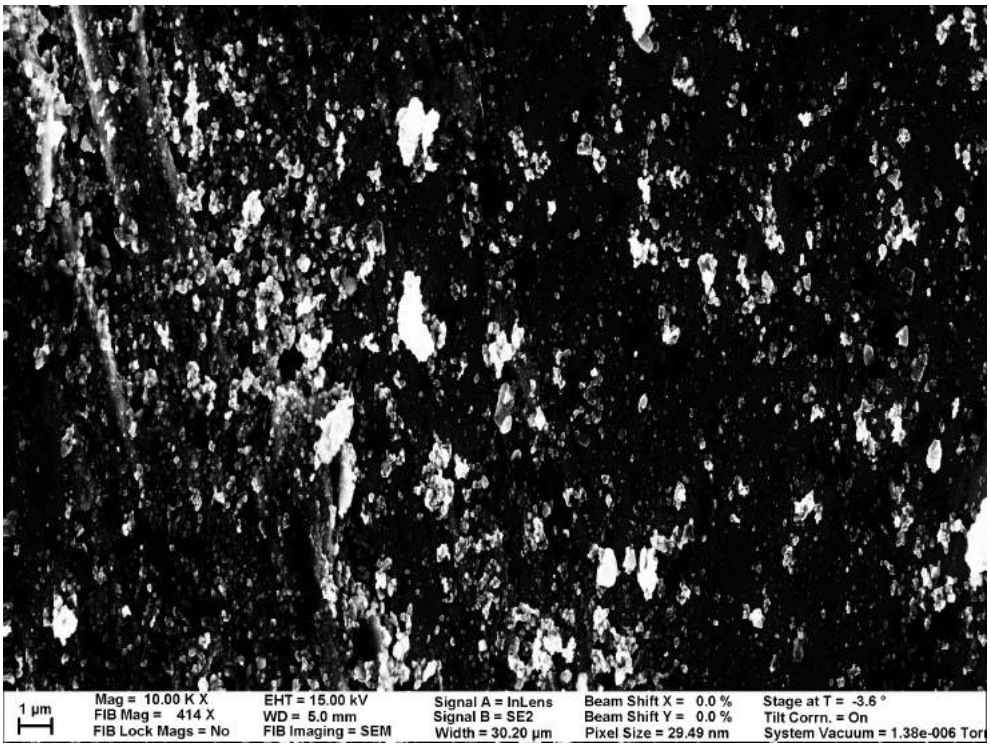


Figure 5-84: Example SEM image of the uncoated side of $Al_2O_3$ sample ring.

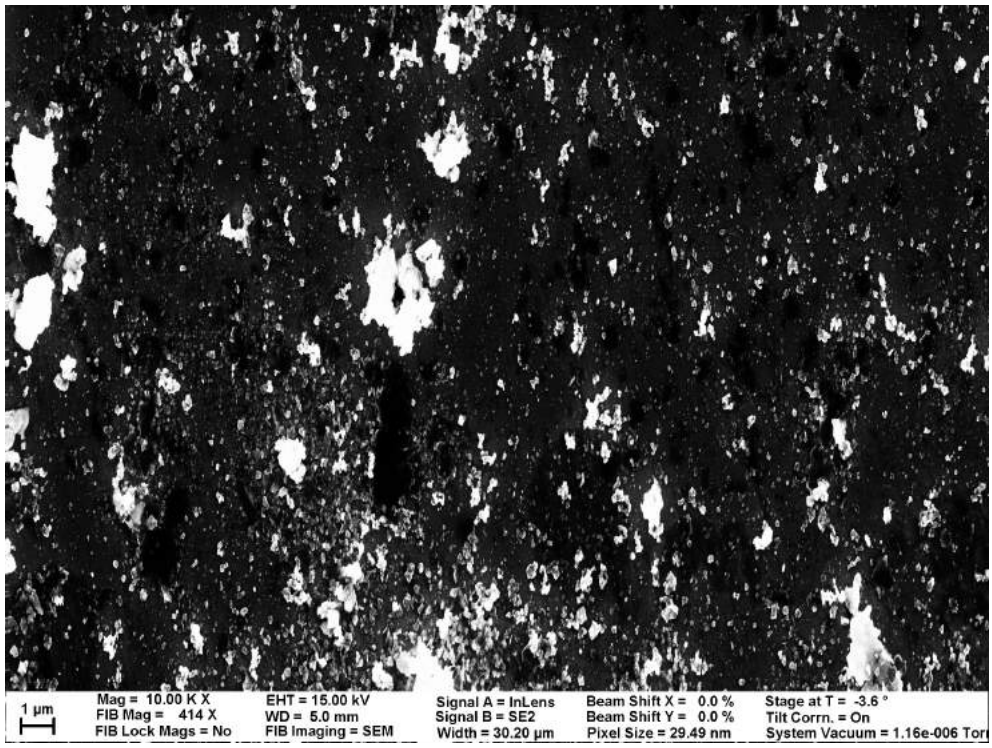


Figure 5-85: Another example SEM image of the uncoated side of $Al_2O_3$ sample ring.

**Titanium Dioxide ($TiO_2$)** Figures 5-86 and 5-88 are SEM images of crud grown on the titanium dioxide surface. Figures 5-89 and 5-89 are SEM images of the control side of the titanium dioxide sample. From observing these images with bare eyes, it seems that the SEM images of coated side show more crud particles than the images of the uncoated side. The crud coverage found from image processing algorithms, as shown in table 5.5 do agree with this observation.

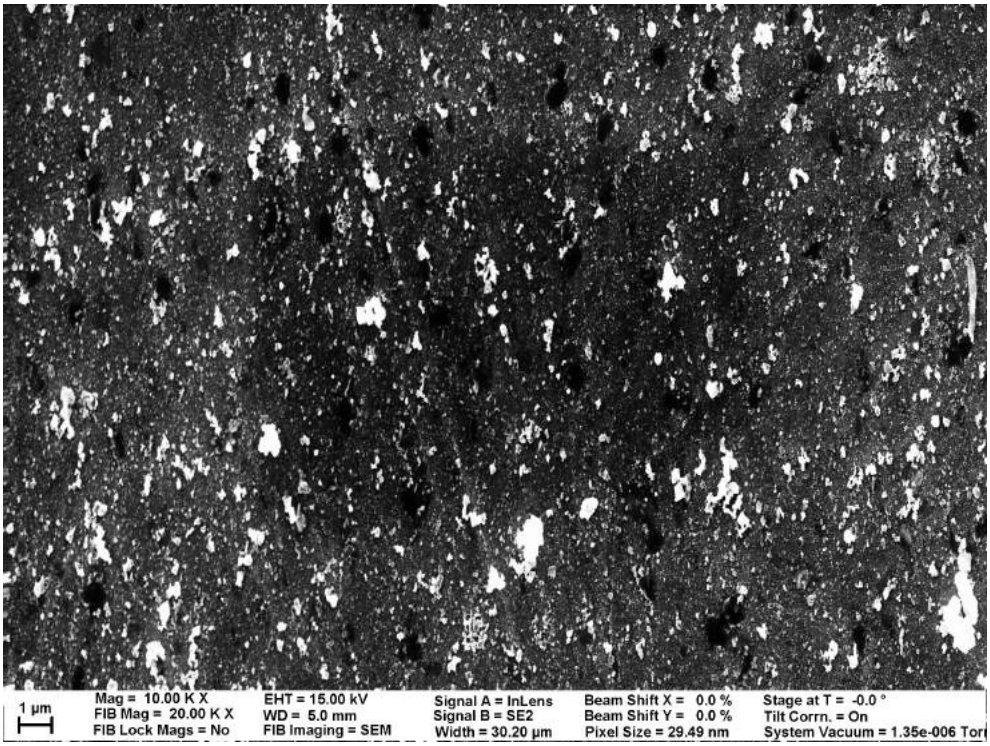


Figure 5-86: Example SEM image of the coated side of $TiO_2$ sample ring.

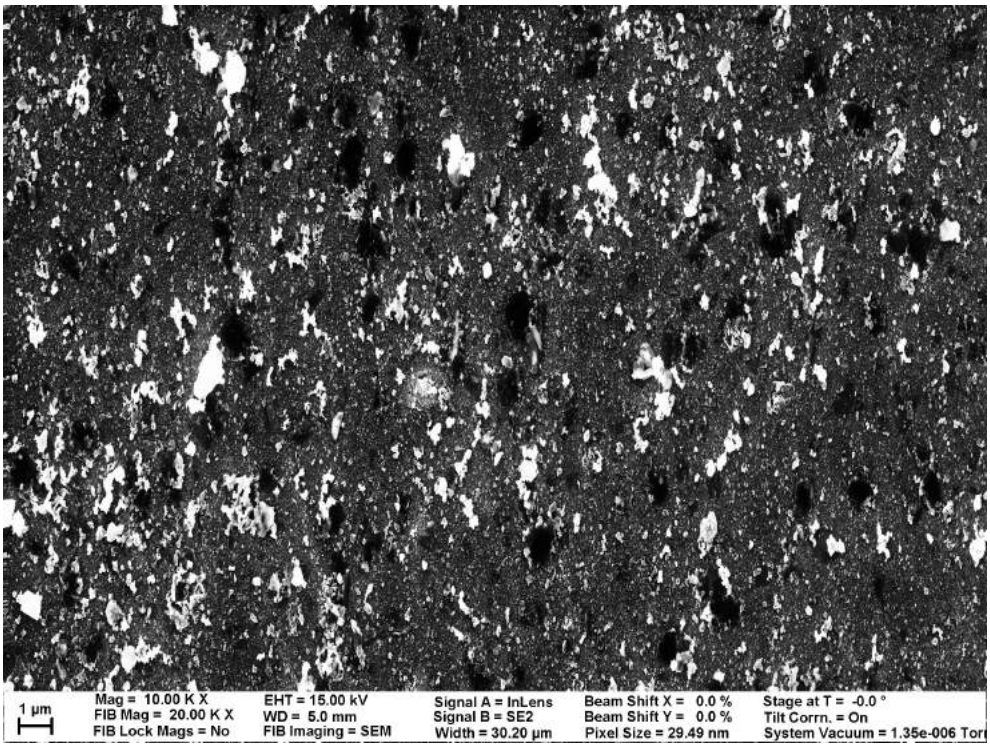


Figure 5-87: Another example SEM image of the coated side of $TiO_2$ sample ring.

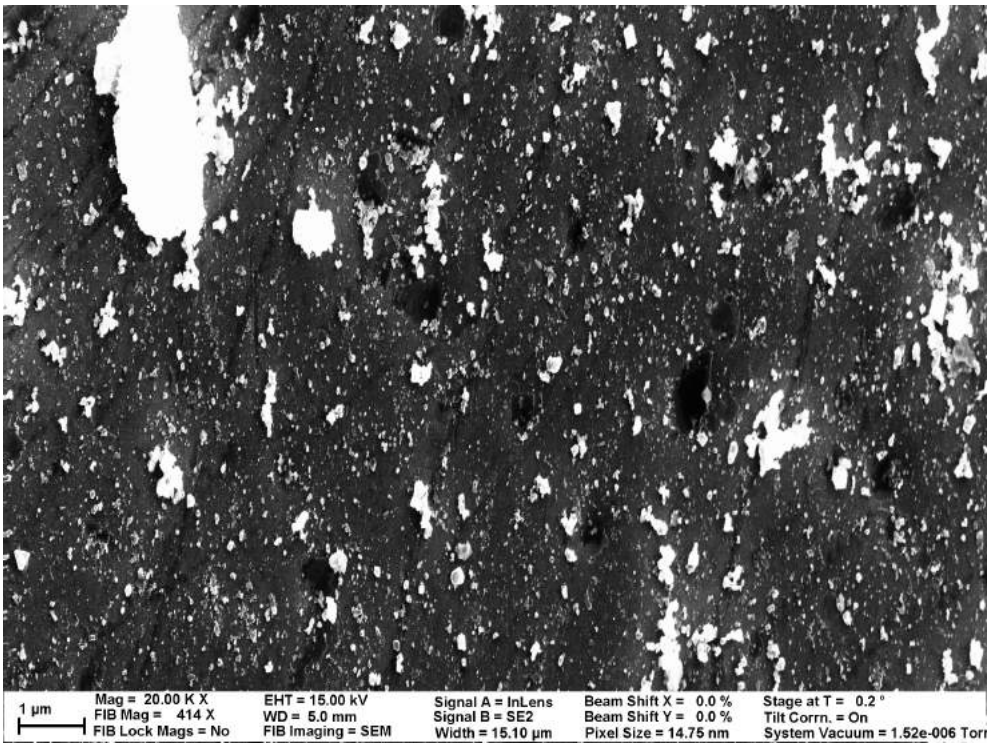


Figure 5-88: Example SEM image of the uncoated side of $TiO_2$ sample ring.

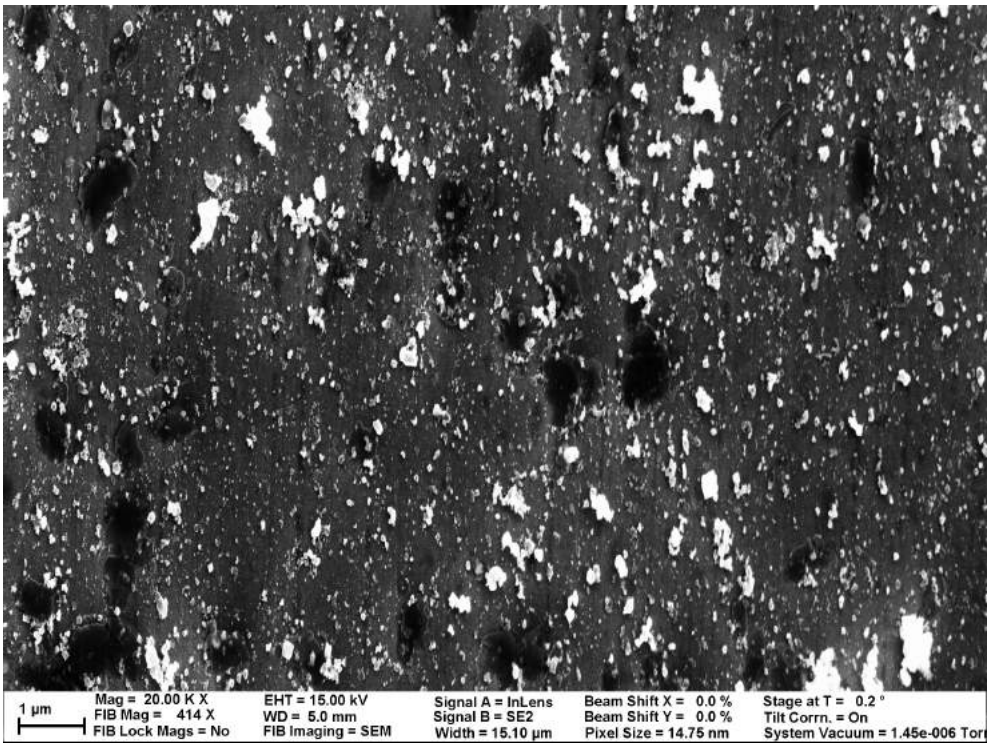


Figure 5-89: Another example SEM image of the uncoated side of $TiO_2$ sample ring.

**Titanium Diboride ($TiB_2$)** Figures 5-91 and 5-126 are SEM images of crud grown on the titanium diboride surface. Figures 5-92 and 5-93 are SEM images of the control side of the titanium diboride sample. From observing these images with bare eyes, it seems that the SEM images of the coated side show more crud particles than the images of the uncoated side. However, the actual values of crud area coverage from image processing, shown in table 5.5, shows very little difference between the coated and uncoated side. We could partially attribute this inconsistency to dark looking particles on the images of the coated surface that may be been mistaken by image processing algorithms as coating surface, as oppose to crud particle.

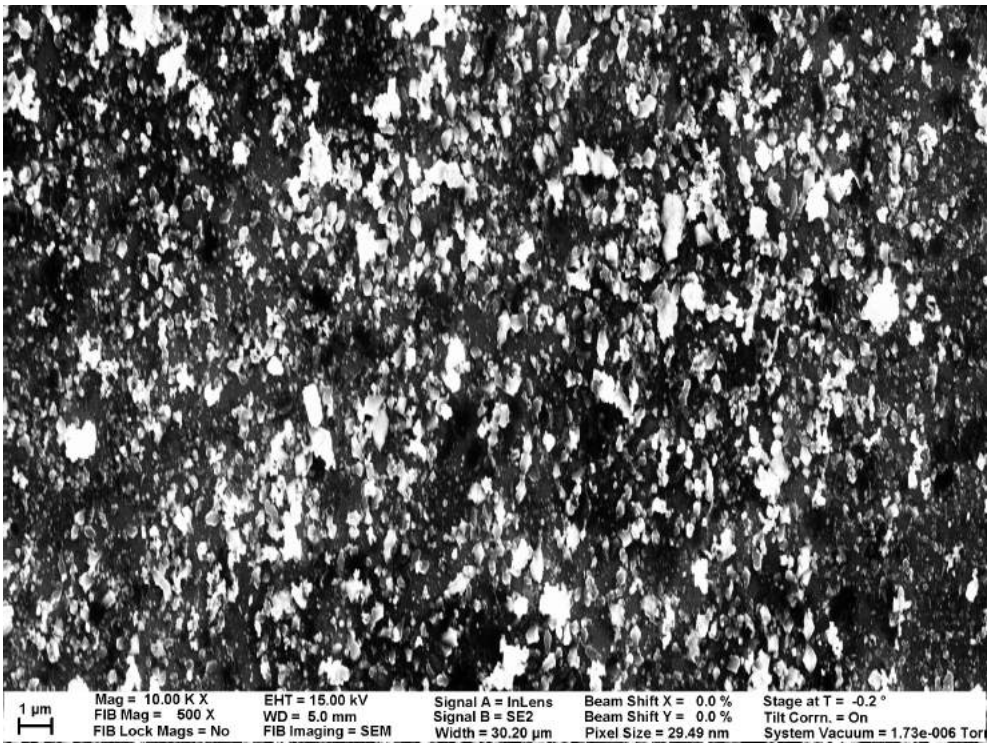


Figure 5-90: Example SEM image of the coated side of $TiB_2$ sample ring.

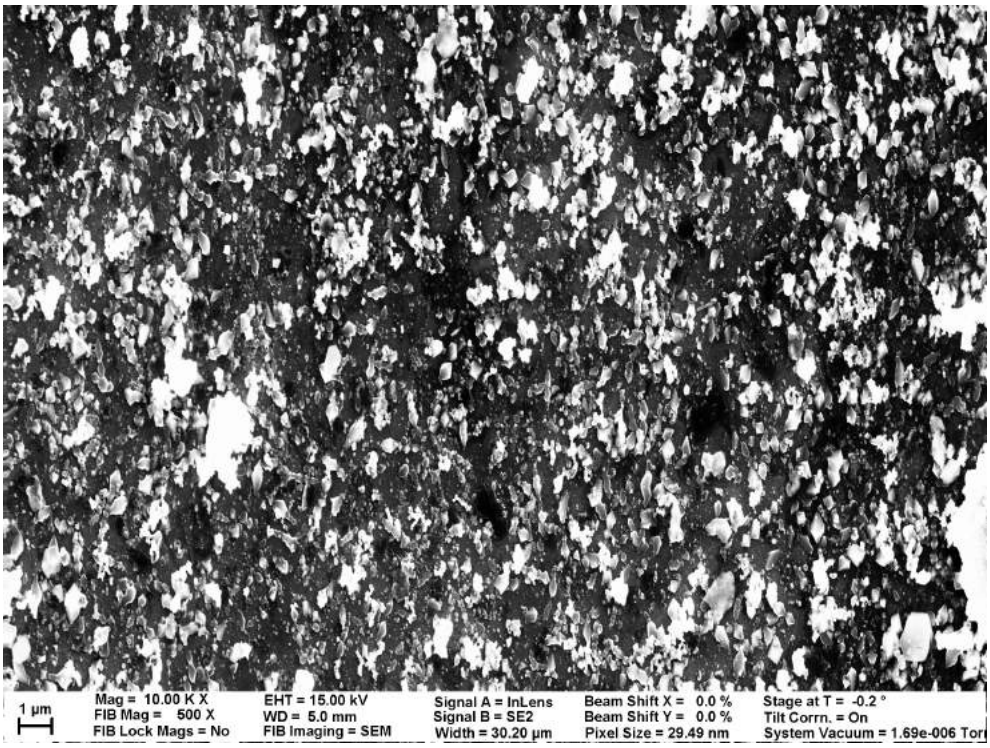


Figure 5-91: Another example SEM image of the coated side of $TiB_2$ sample ring.

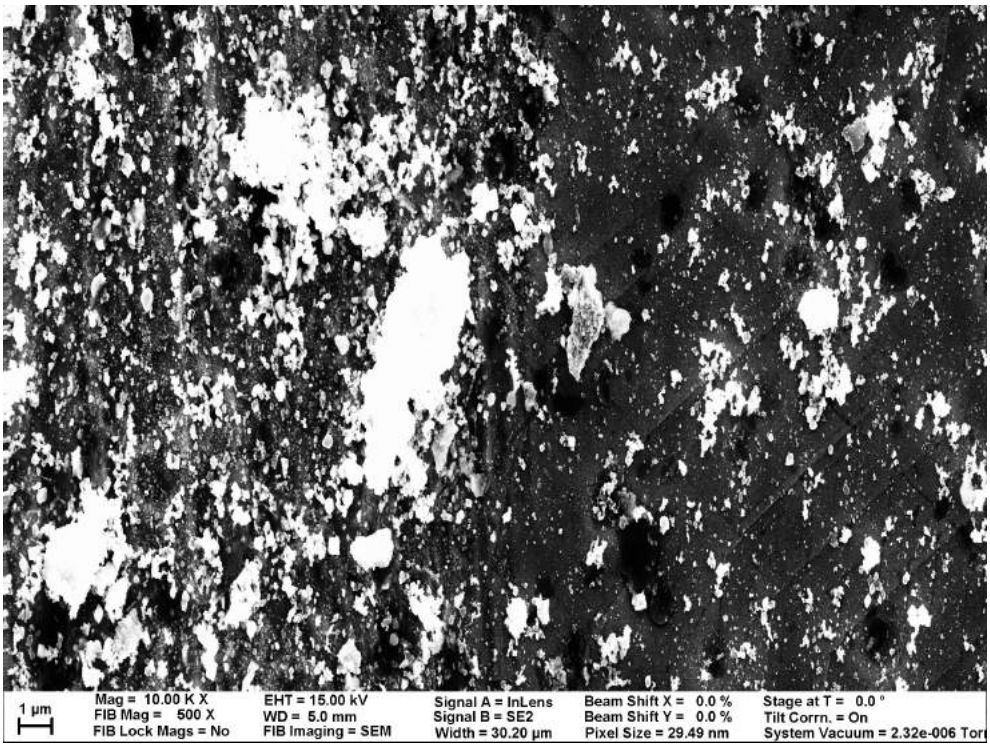


Figure 5-92: Example SEM image of the uncoated side of $TiB_2$ sample ring.

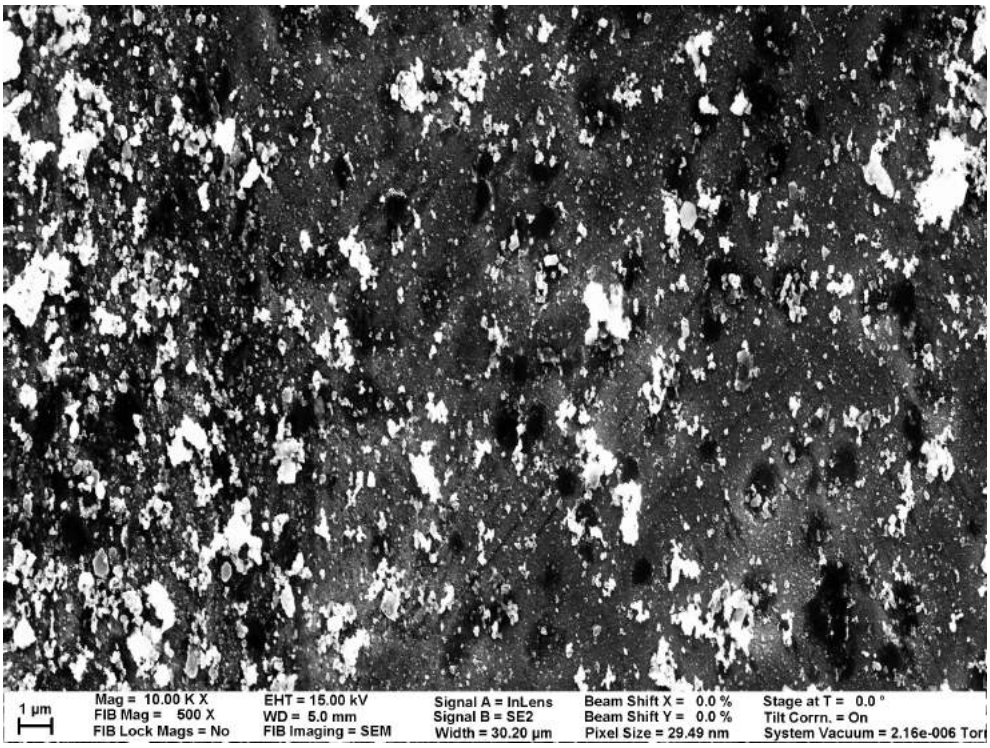


Figure 5-93: Another example SEM image of the uncoated side of $TiB_2$ sample ring.

**Zirconium Dioxide ($ZrO_2$)** Figures 5-94 and 5-95 are SEM images of crud grown on the zirconium dioxide surface. Figures 5-96 and 5-97 are SEM images of the control side of the zirconium dioxide sample. From observing these images with bare eyes, it is very hard to determine whether there is more or less crud on the coated side.

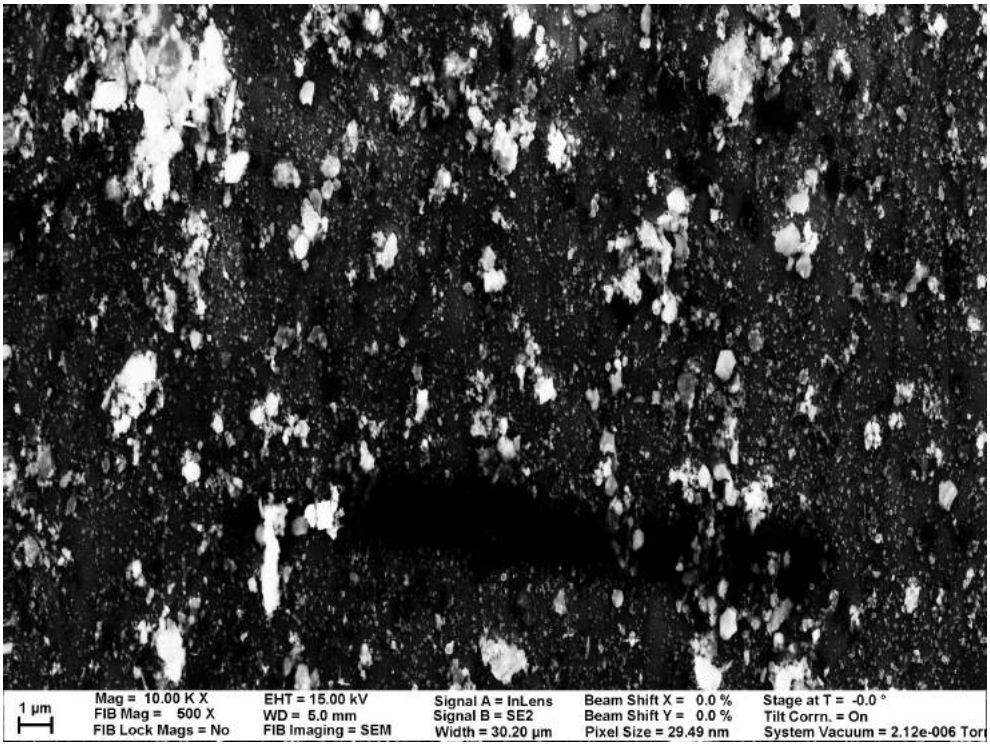


Figure 5-94: Example SEM image of the coated side of $ZrO_2$ sample ring.

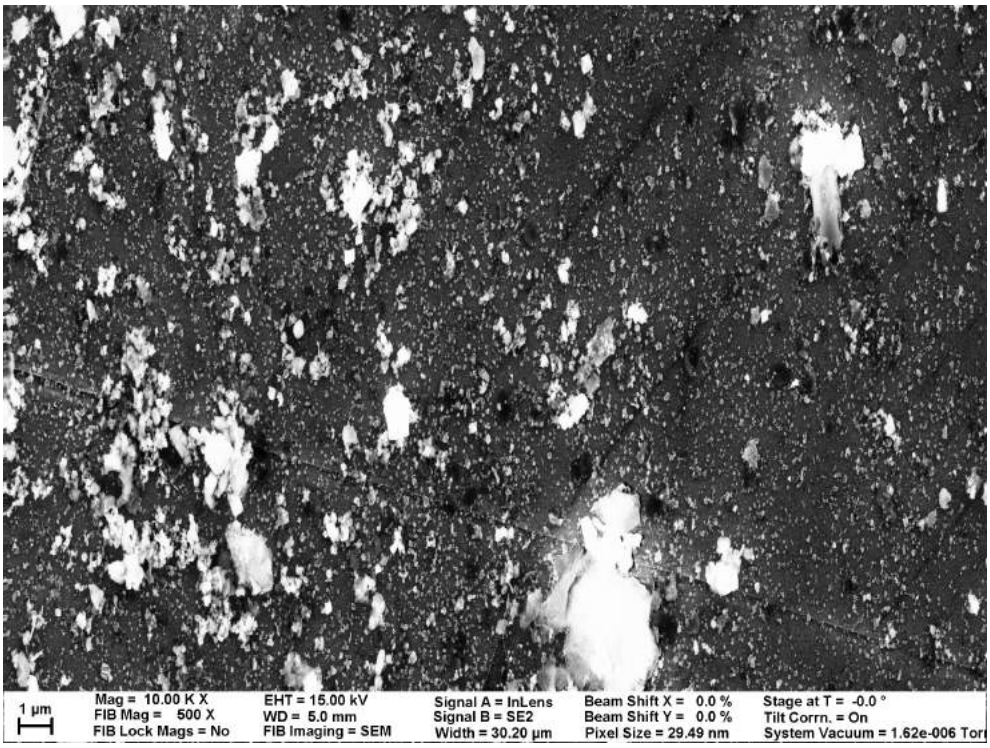


Figure 5-95: Another example SEM image of the coated side of $ZrO_2$ sample ring.

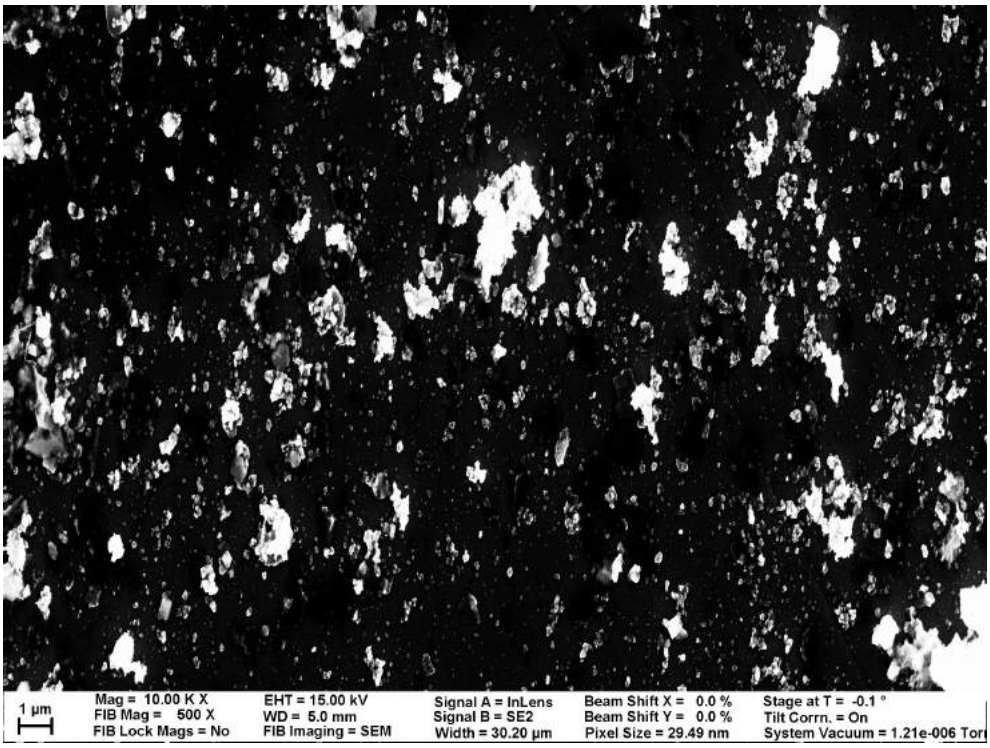


Figure 5-96: Example SEM image of the uncoated side of $ZrO_2$ sample ring.

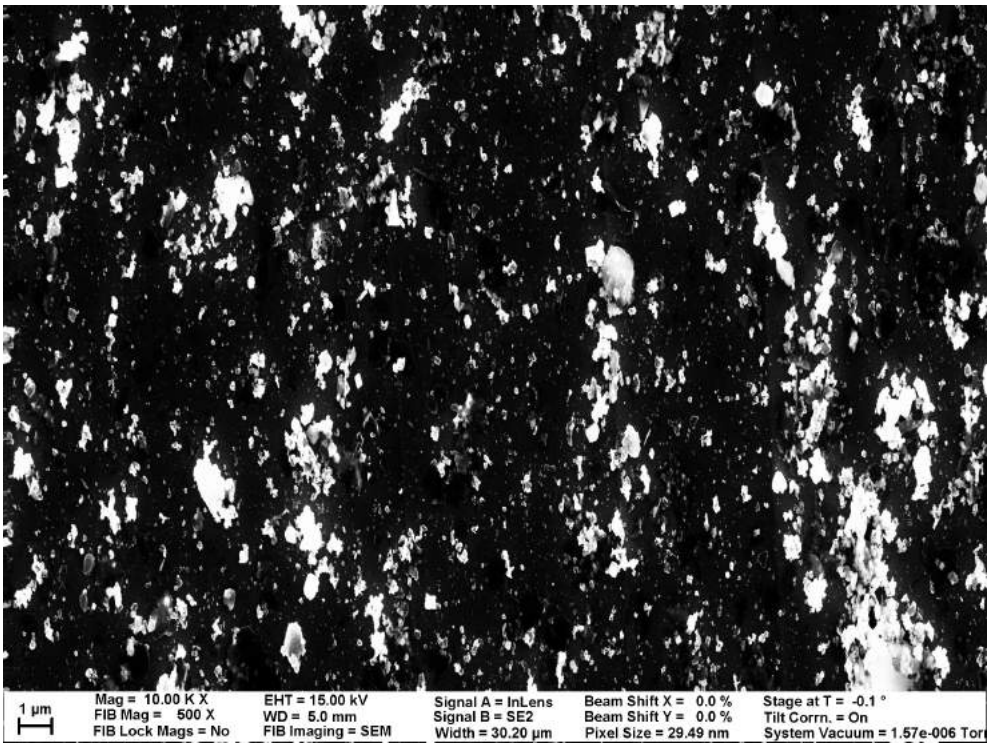


Figure 5-97: Another example SEM image of the uncoated side of $ZrO_2$ sample ring.

**Magnesium Oxide ($MgO$)** Figures 5-98 and 5-134 are SEM images of crud grown on the magnesium oxide surface. Figures 5-100 and 5-101 are SEM images of the control side of the magnesium oxide sample. From observing these images with bare eyes, the coated side seems to have slightly more crud coverage, especially with the larger particles in figure 5-98. The calculated crud coverages, shown in table 5.5, do agree with this observation.

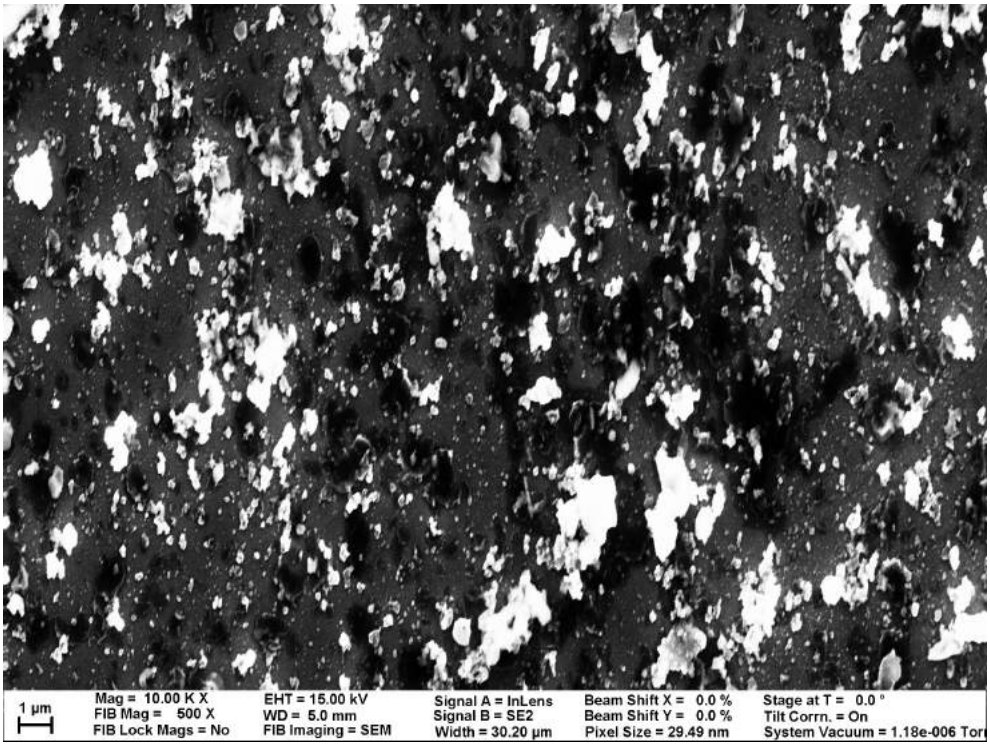


Figure 5-98: Example SEM image of the coated side of $MgO$ sample ring.

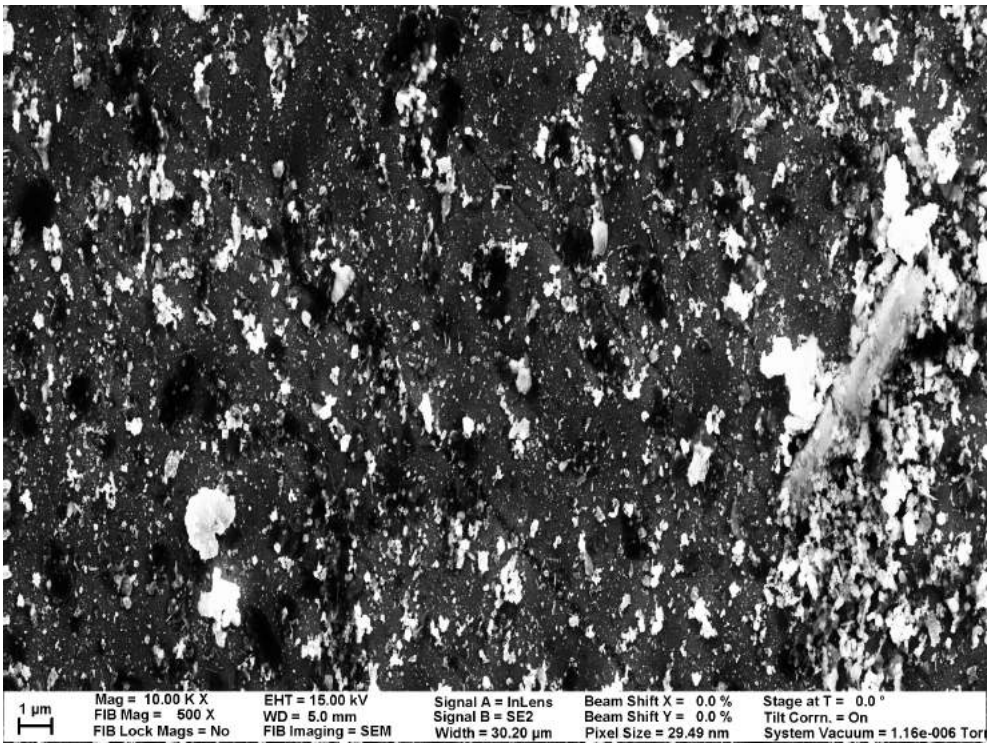


Figure 5-99: Another example SEM image of the coated side of $MgO$ sample ring.

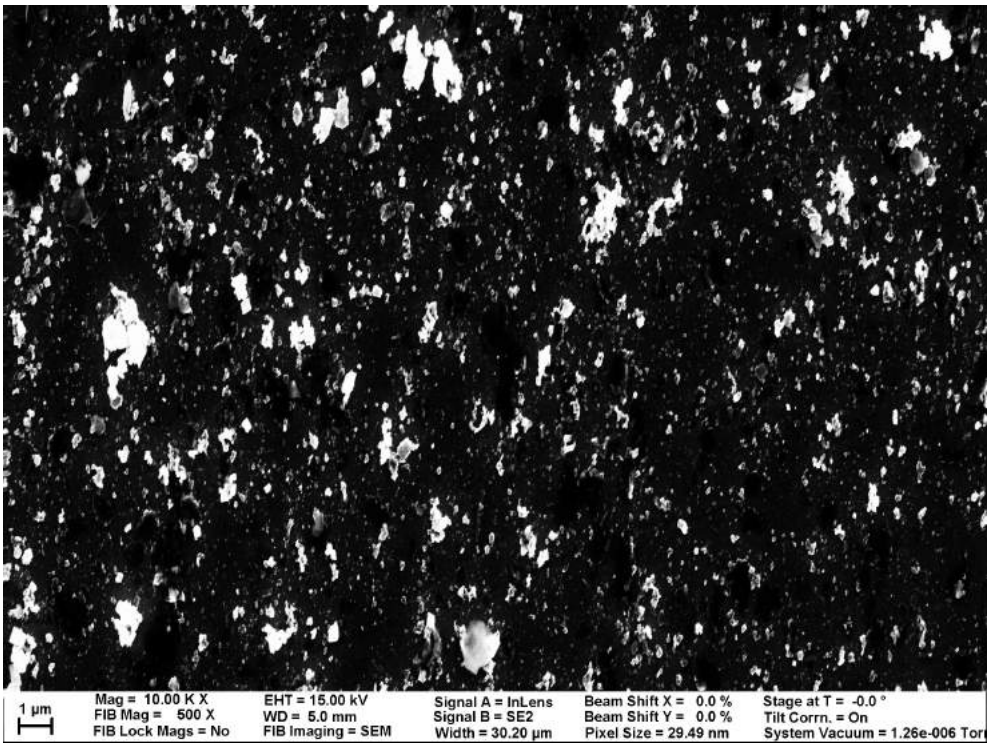


Figure 5-100: Example SEM image of the uncoated side of $MgO$ sample ring.

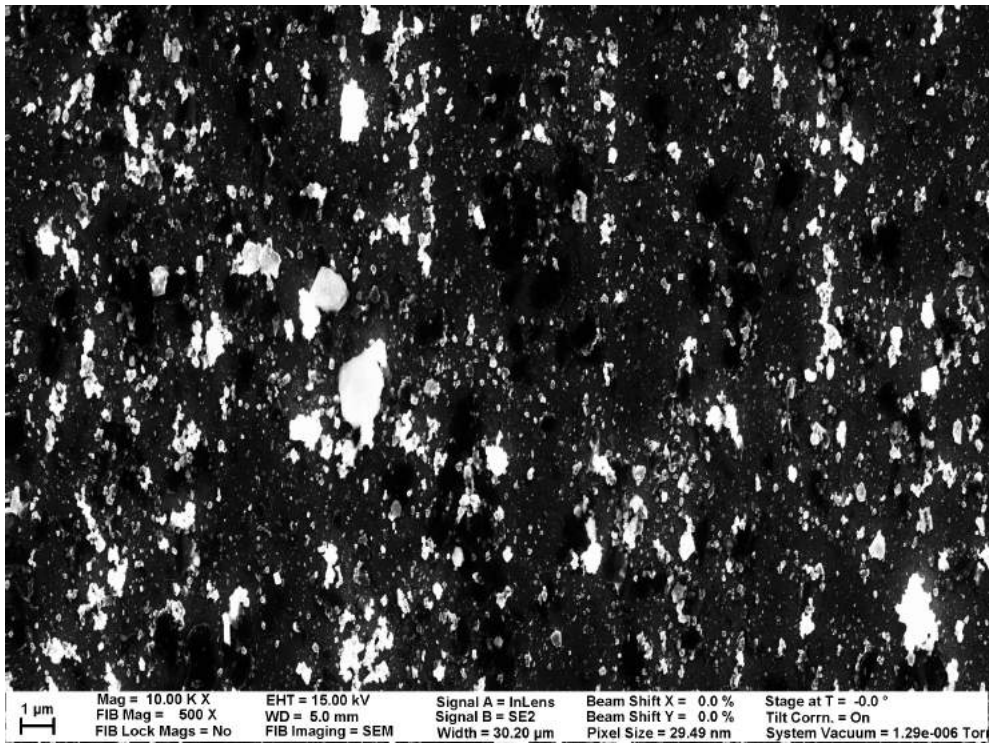


Figure 5-101: Another example SEM image of the uncoated side of $MgO$ sample ring.

#### 5.3.2.2 Trial D (March 18, 2016)

This section shows example SEM images associated with each crud-resistant material for trial D. Overall, trial D grew slightly more crud compare to trial C. One general observation is that trial D's crud has larger crud particles. This could suggest that crud forms from smaller particles initially. This could be because it is harder for larger particles to latch on to cladding or coating surfaces by itself. But, once there are already some small particles, it is easier for larger particles to fit in between smaller crud particles.

**Zirconium Carbide ($ZrC$)** Figures 5-102 and 5-103 are SEM images of crud grown on the zirconium carbide surface. Figures 5-104 and 5-105 are SEM images of the control side of the zirconium carbide sample. From observing these images with bare eyes, the coated side has slightly less crud coverage. Unlike the uncoated side where there are small crud particles covering virtually every spot, there are blank spots on coated side where there are almost no small crud particles. This could be seen as an evidence of resistance to crud particle bonding by zirconium carbides. In the locations where small crud particles successfully attach themselves to the coating surface, crud starts to form with larger particles also joining in. However, figure 5-112 also exhibits similar blank spots, which counter this hypothesis since figure 5-112 represents an uncoated surface.

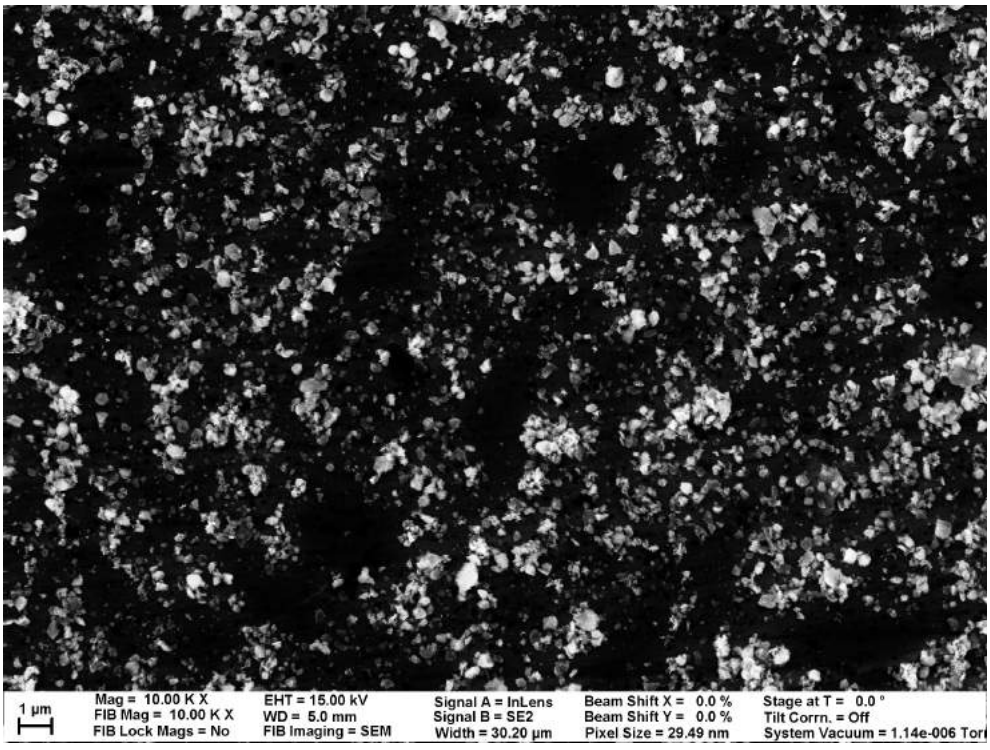


Figure 5-102: Example SEM image of the coated side of $ZrC$ sample ring.

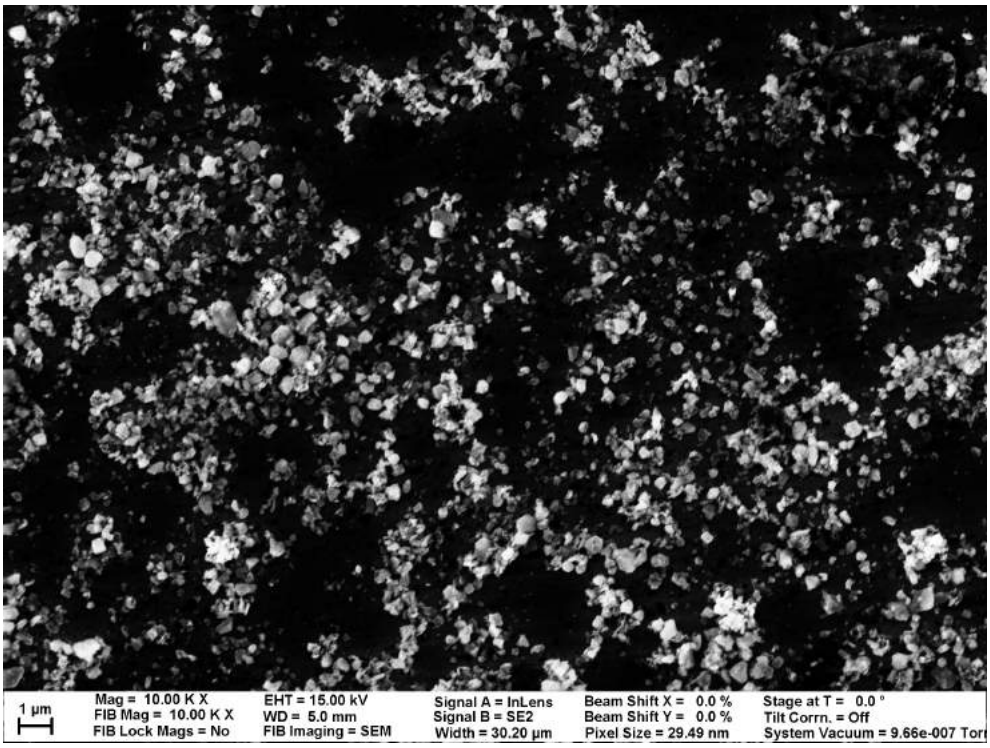


Figure 5-103: Another example SEM image of the coated side of $ZrC$ sample ring.

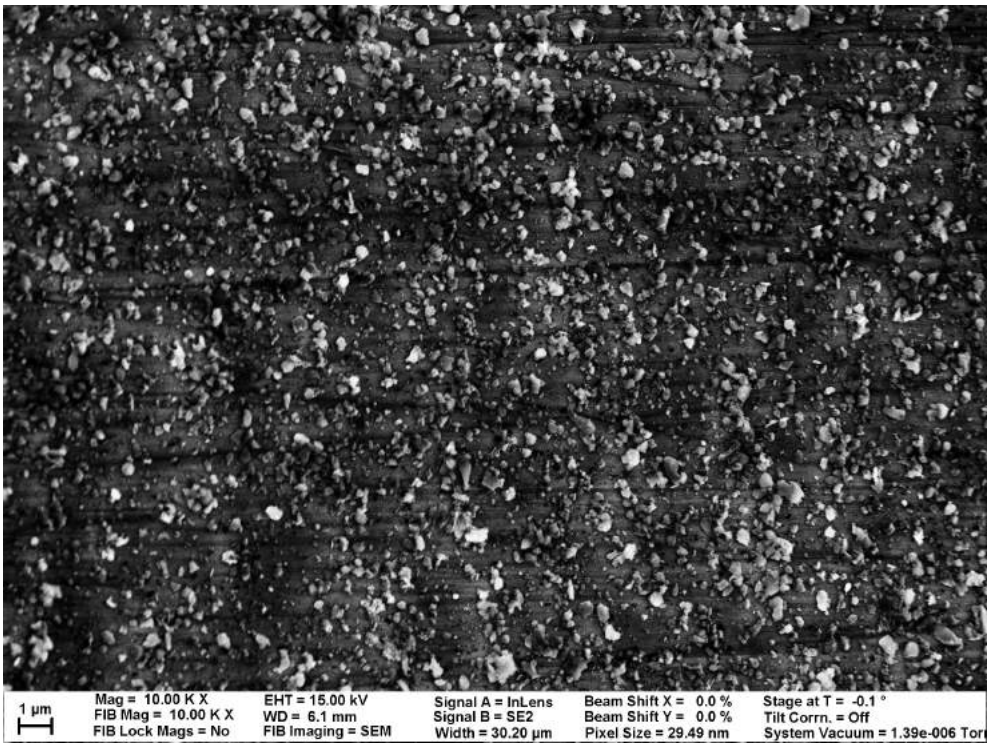


Figure 5-104: Example SEM image of the uncoated side of $ZrC$ sample ring.

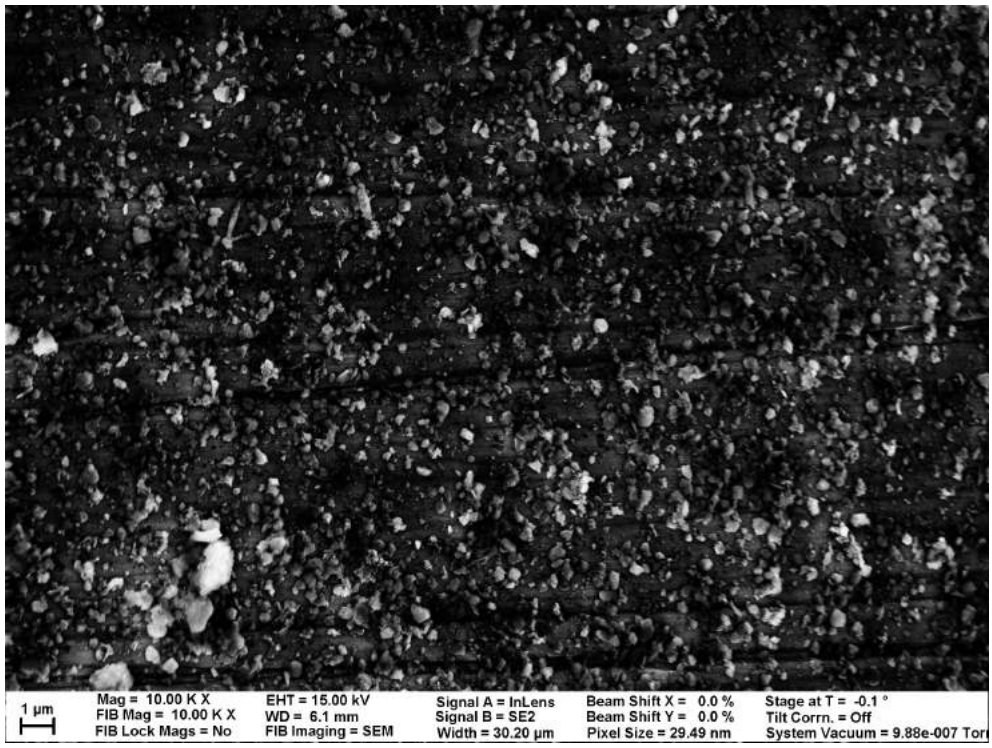


Figure 5-105: Another example SEM image of the uncoated side of $ZrC$ sample ring.

**Zirconium Nitride ($ZrN$)** Figures 5-106 and 5-107 are SEM images of crud grown on the zirconium nitride surface. Figures 5-108 and 5-109 are SEM images of the control side of the zirconium nitride sample. From observing these images with bare eyes, the coated side has slightly less crud coverage. The calculated crud area coverages in table 5.6 agrees with this observation.

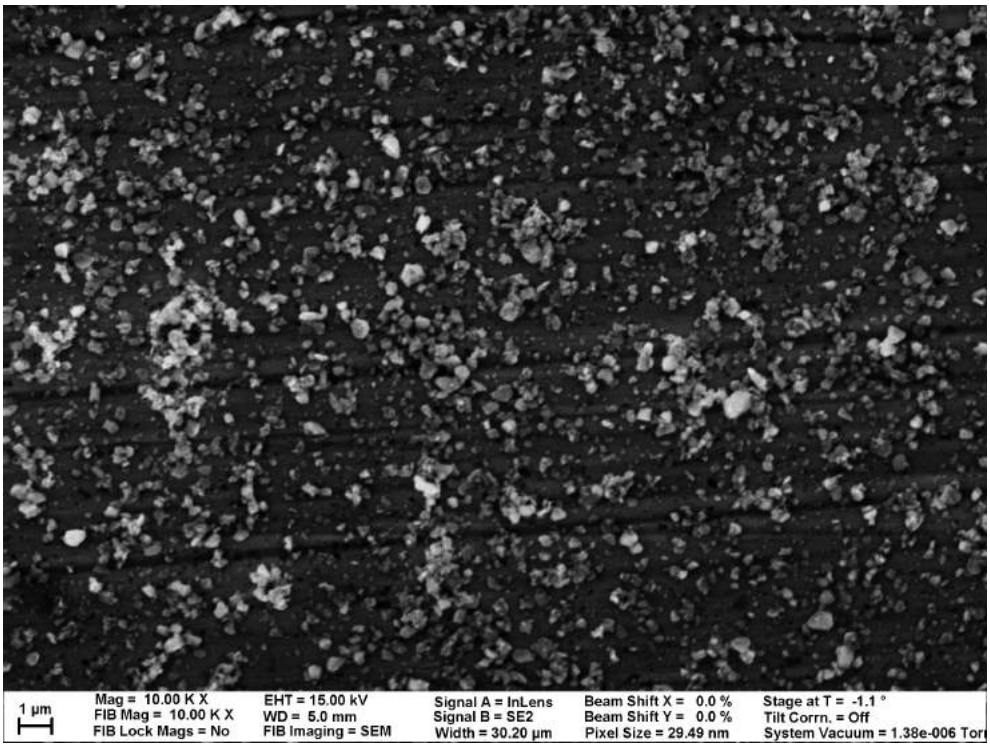


Figure 5-106: Example SEM image of the coated side of $ZrN$ sample ring.

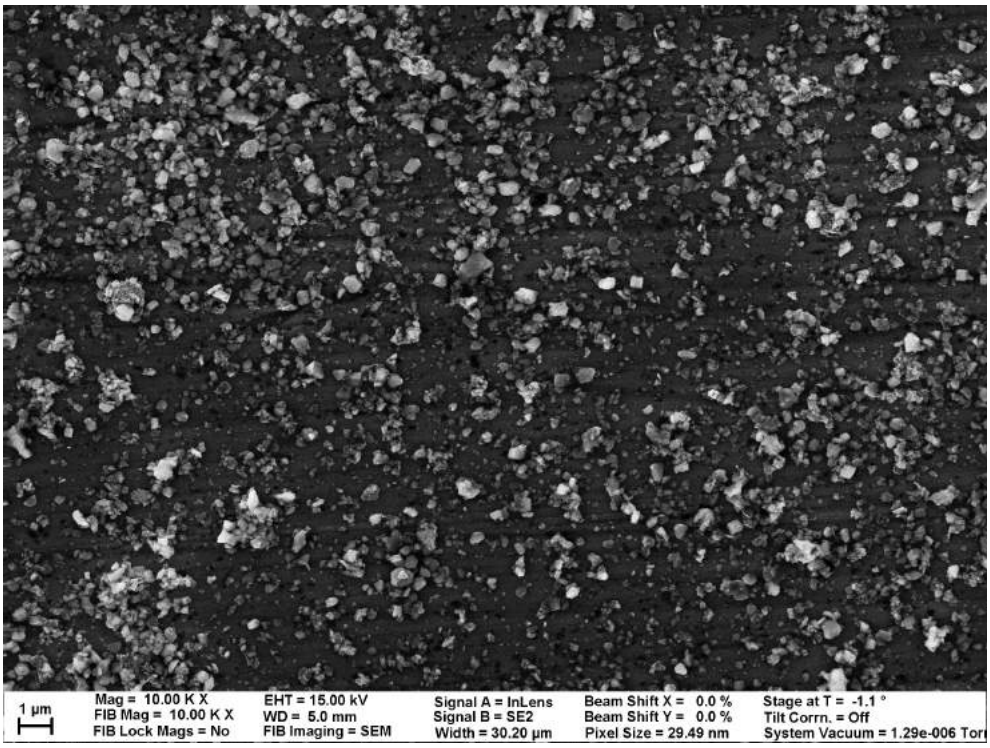


Figure 5-107: Another example SEM image of the coated side of $ZrN$ sample ring.

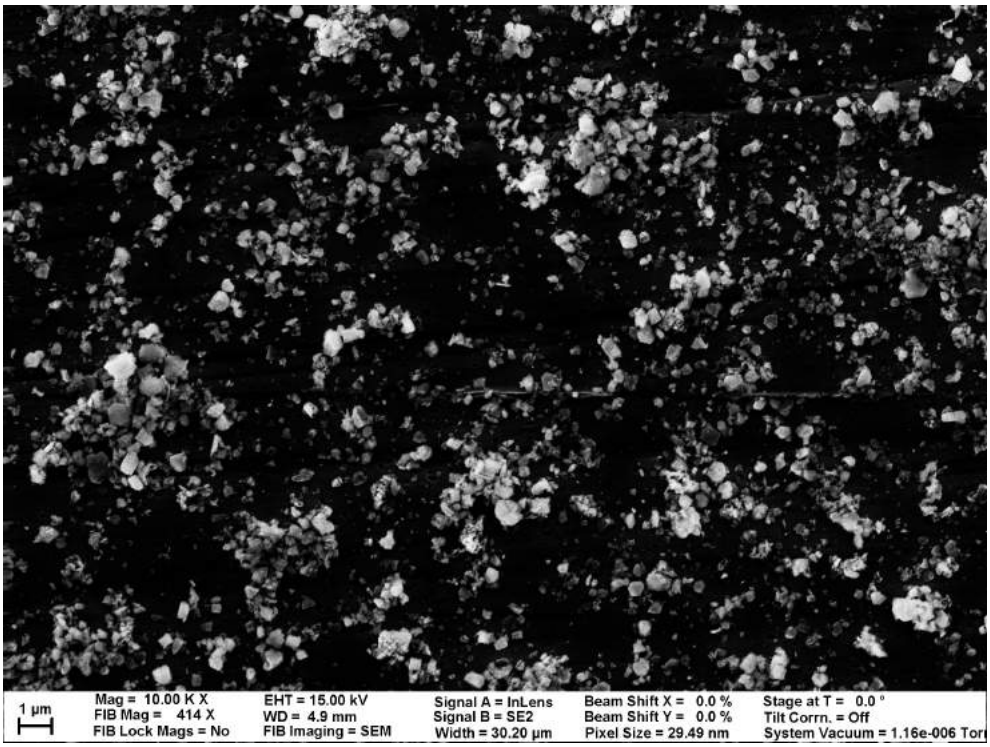


Figure 5-108: Example SEM image of the uncoated side of $ZrN$ sample ring.

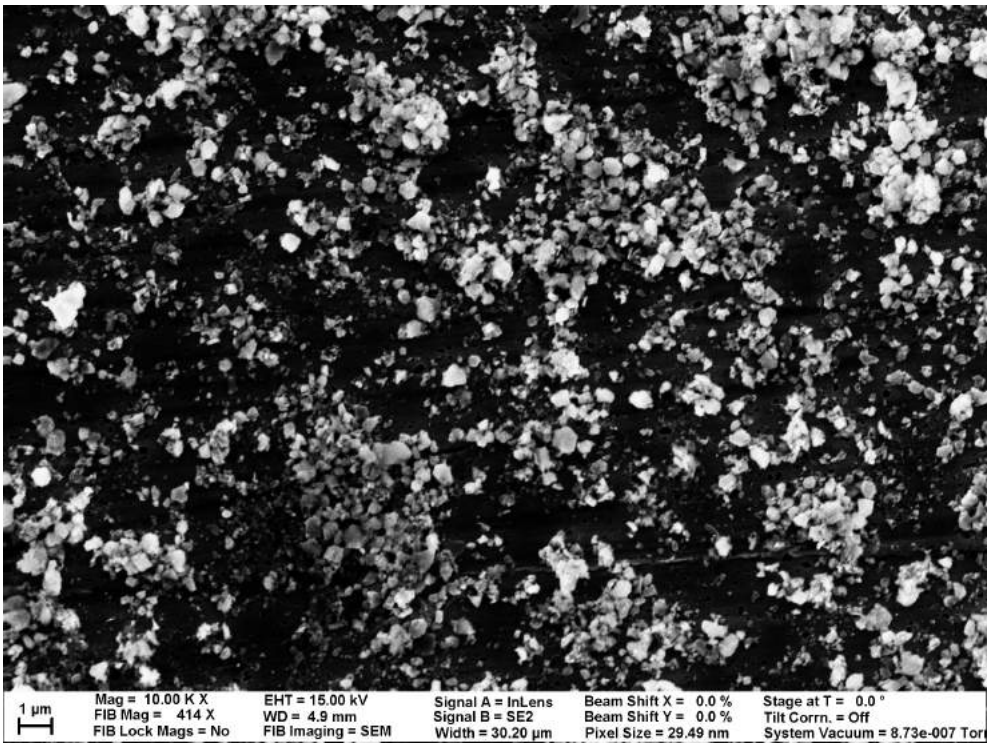


Figure 5-109: Another example SEM image of the uncoated side of $ZrN$ sample ring.

**Titanium Carbide ($TiC$)** Figures 5-110 and 5-111 are SEM images of crud grown on the titanium carbide surface. Figures 5-112 and 5-113 are SEM images of the control side of the titanium carbide sample. From observing these images with bare eyes, the coated side has slightly less crud coverage. The calculated crud area coverages in table 5.6 agrees with this observation.

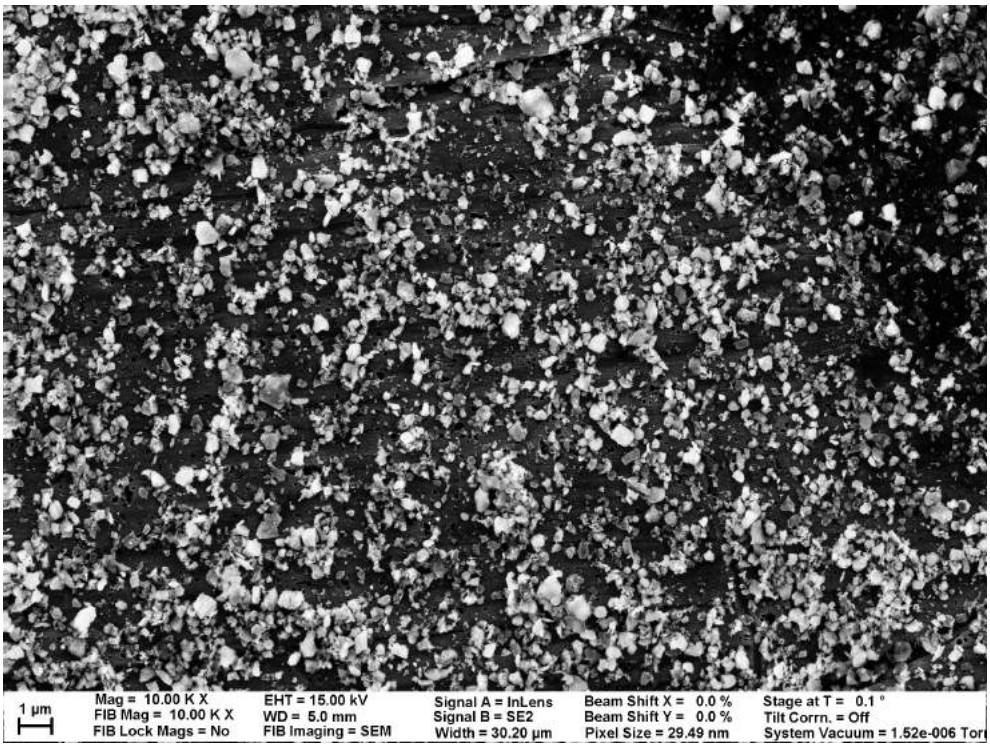


Figure 5-110: Example SEM image of the coated side of $TiC$ sample ring.

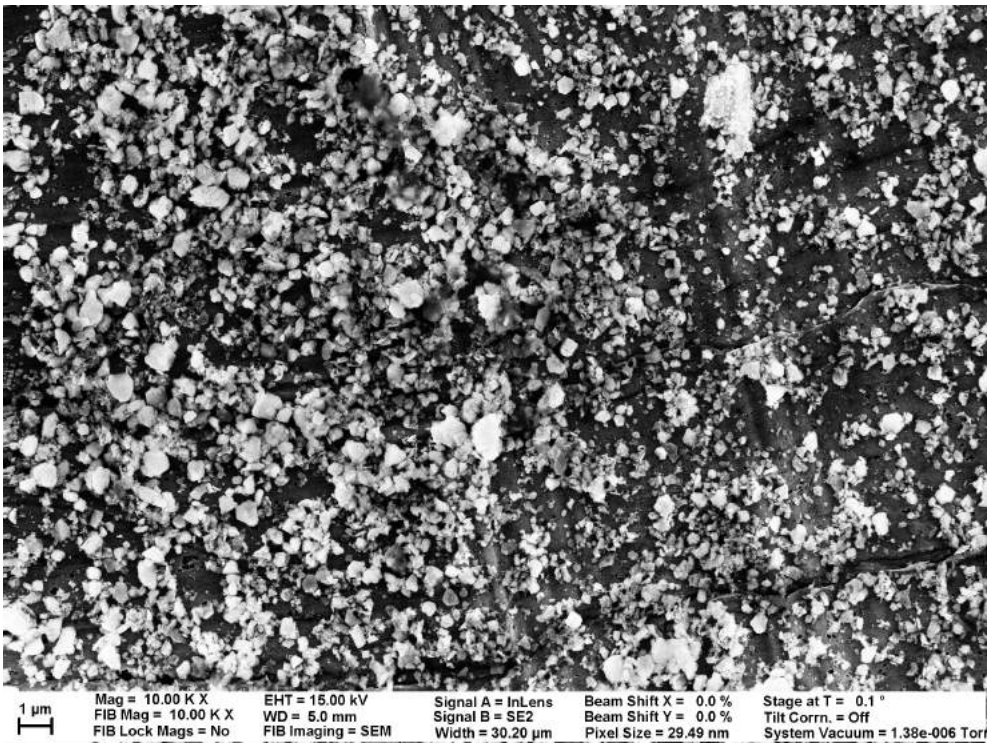


Figure 5-111: Another example SEM image of the coated side of $TiC$ sample ring.

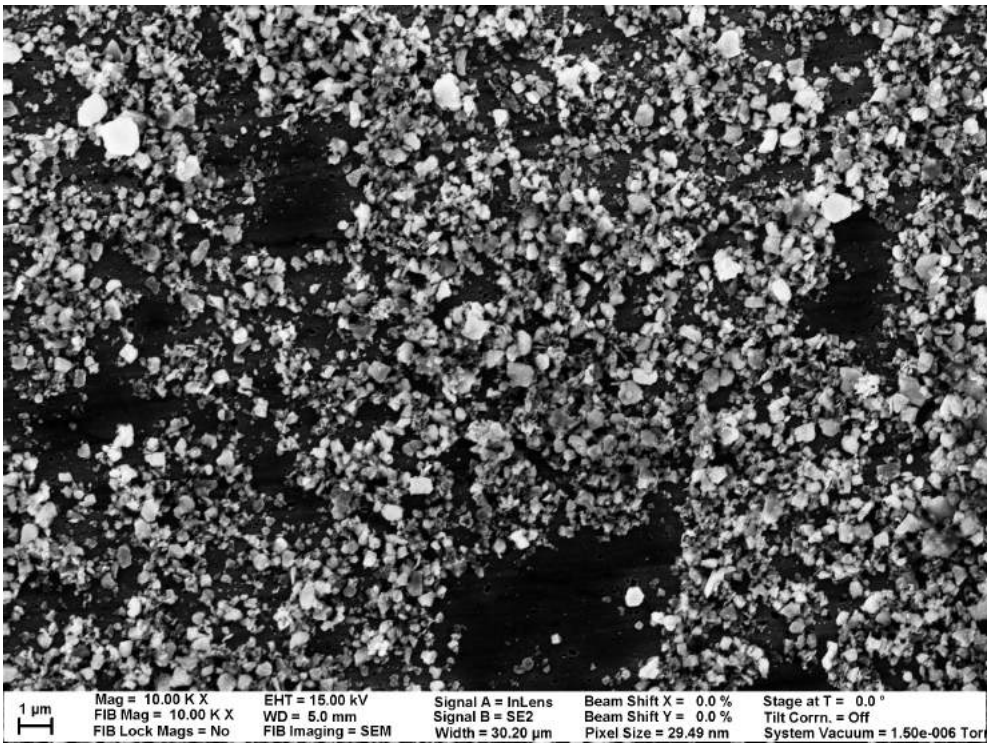


Figure 5-112: Example SEM image of the uncoated side of $TiC$ sample ring.

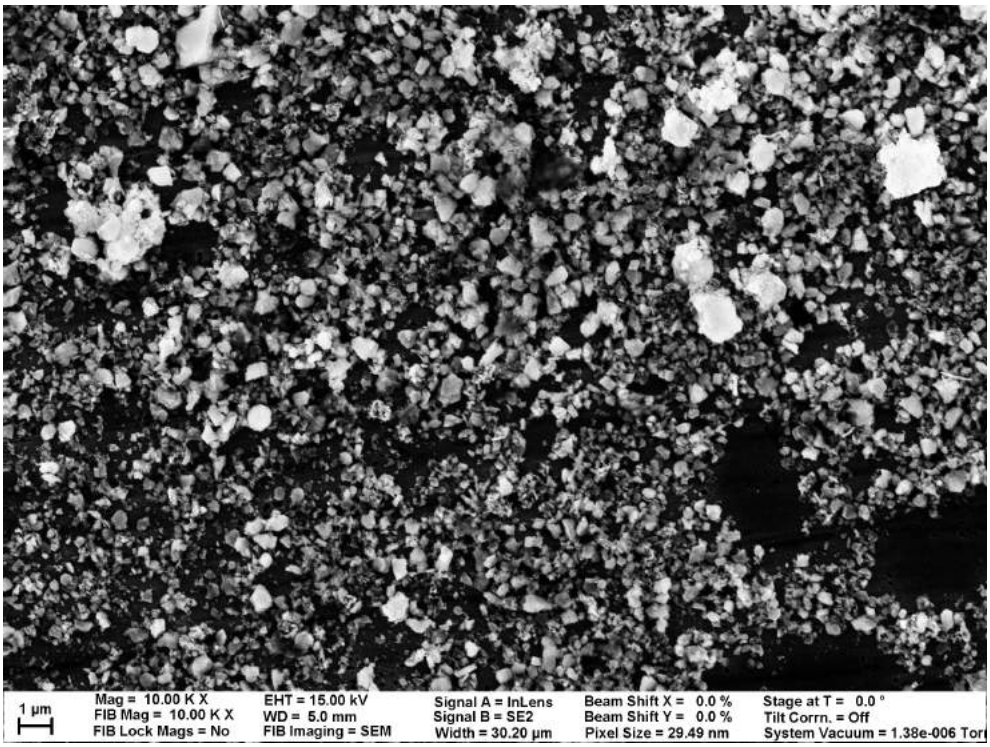


Figure 5-113: Another example SEM image of the uncoated side of $TiC$ sample ring.

**Titanium Nitride ($TiN$)** Figures 5-114 and 5-115 are SEM images of crud grown on the titanium nitride surface. Figures 5-116 and 5-117 are SEM images of the control side of the titanium nitride sample. From observing these images with bare eyes, we cannot really distinguish whether the coated side of the uncoated side has more crud. The calculated crud area coverages in table 5.6 shows that coated side have slightly less crud.

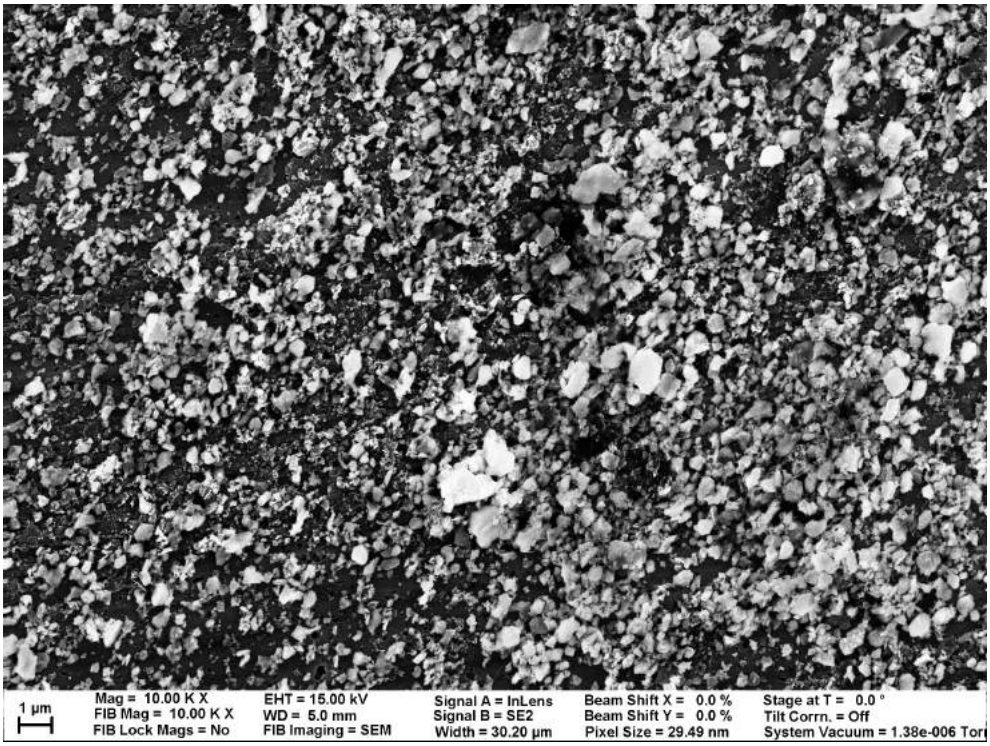


Figure 5-114: Example SEM image of the coated side of $TiN$ sample ring.

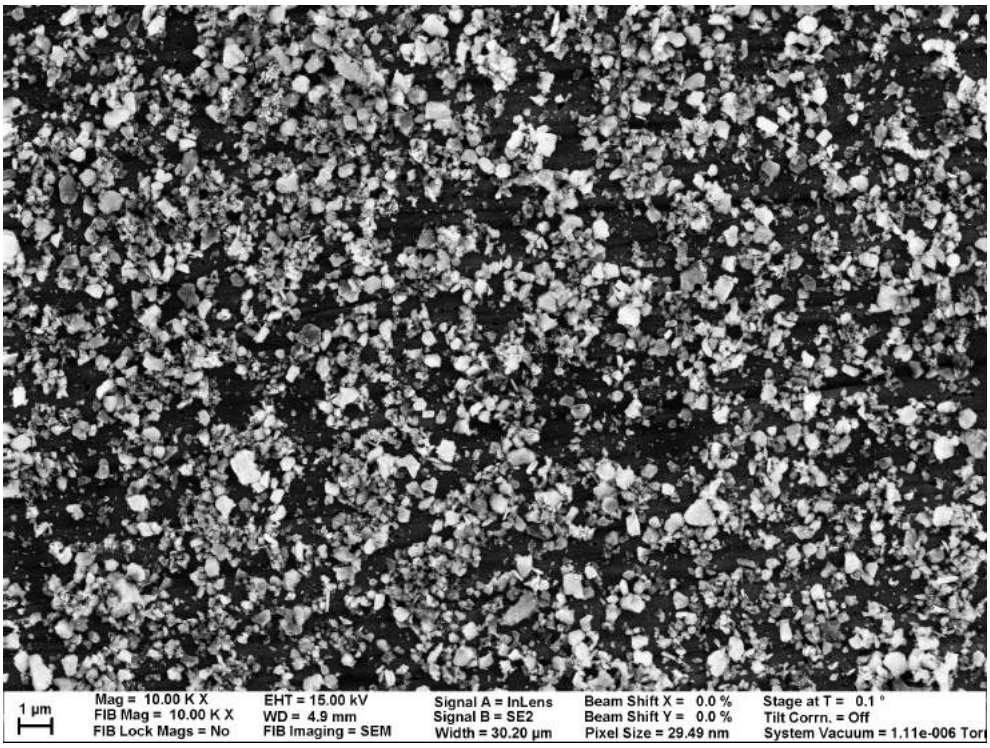


Figure 5-115: Another example SEM image of the coated side of $TiN$ sample ring.

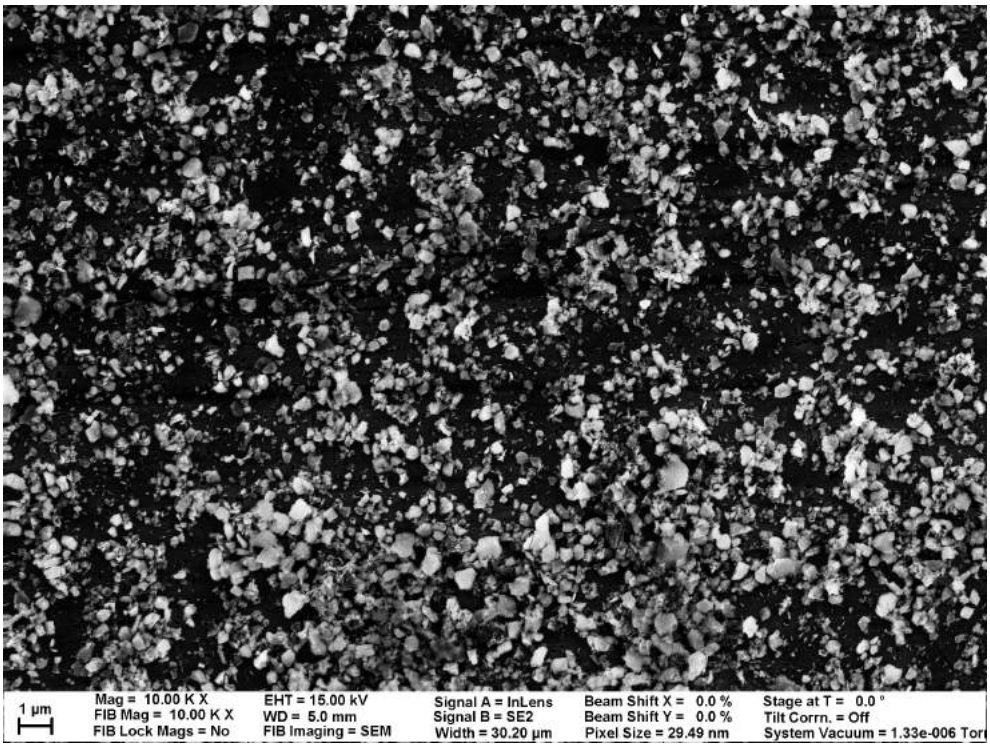


Figure 5-116: Example SEM image of the uncoated side of $TiN$ sample ring.

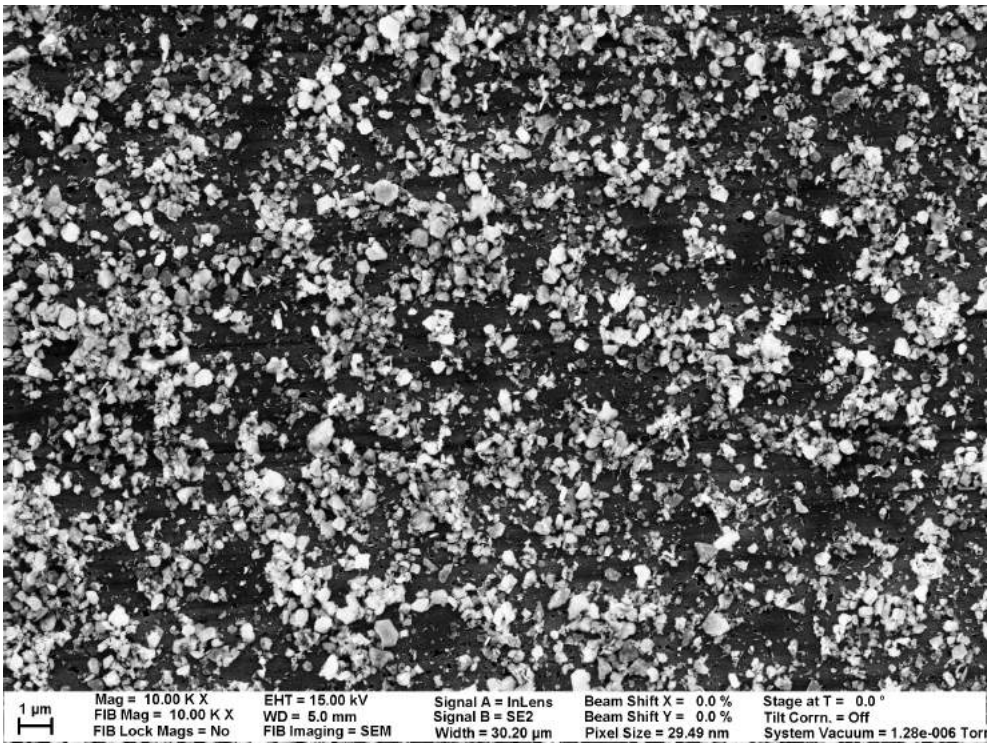


Figure 5-117: Another example SEM image of the uncoated side of $TiN$ sample ring.

**Aluminum Oxide ($Al_2O_3$)** Figures 5-118 and 5-119 are SEM images of crud grown on the aluminum oxide surface. Figures 5-120 and 5-121 are SEM images of the control side of the aluminum oxide sample. From observing these images with bare eyes, the coated side seems to have more crud. The calculated crud area coverages in table 5.6 agrees with this observation.

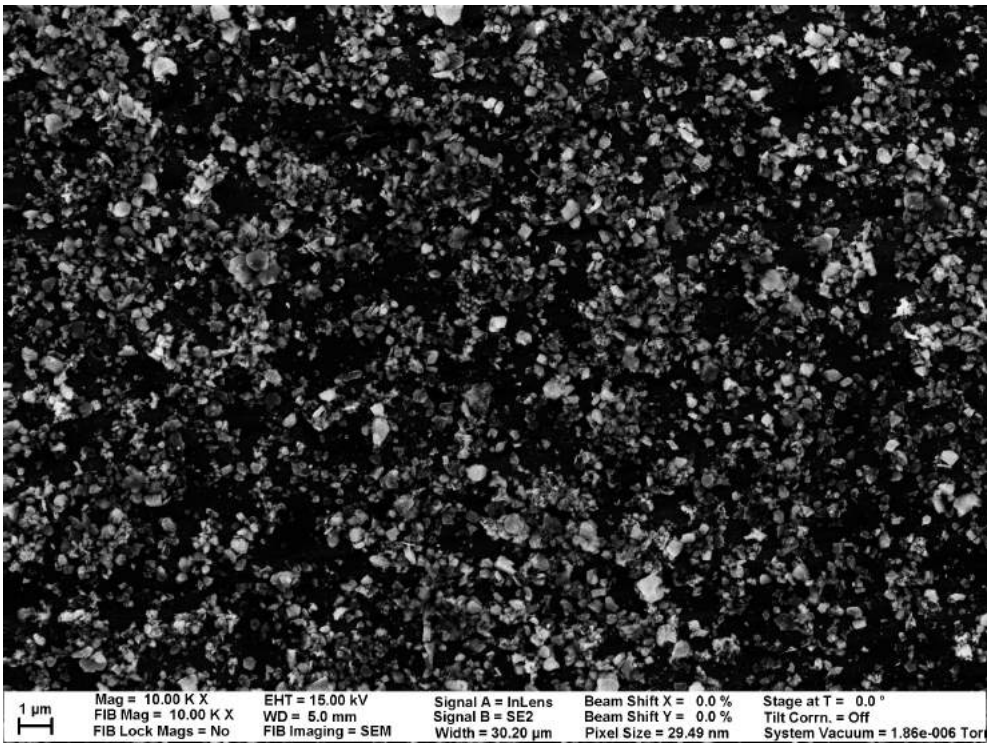


Figure 5-118: Example SEM image of the coated side of $Al_2O_3$ sample ring.

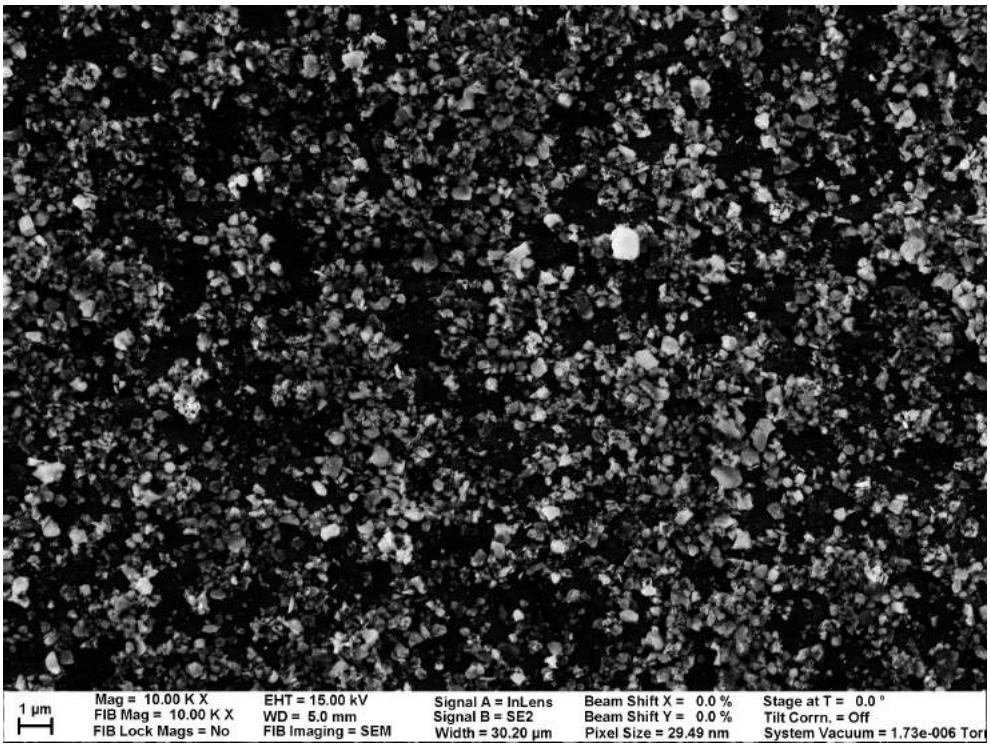


Figure 5-119: Another example SEM image of the coated side of $Al_2O_3$ sample ring.

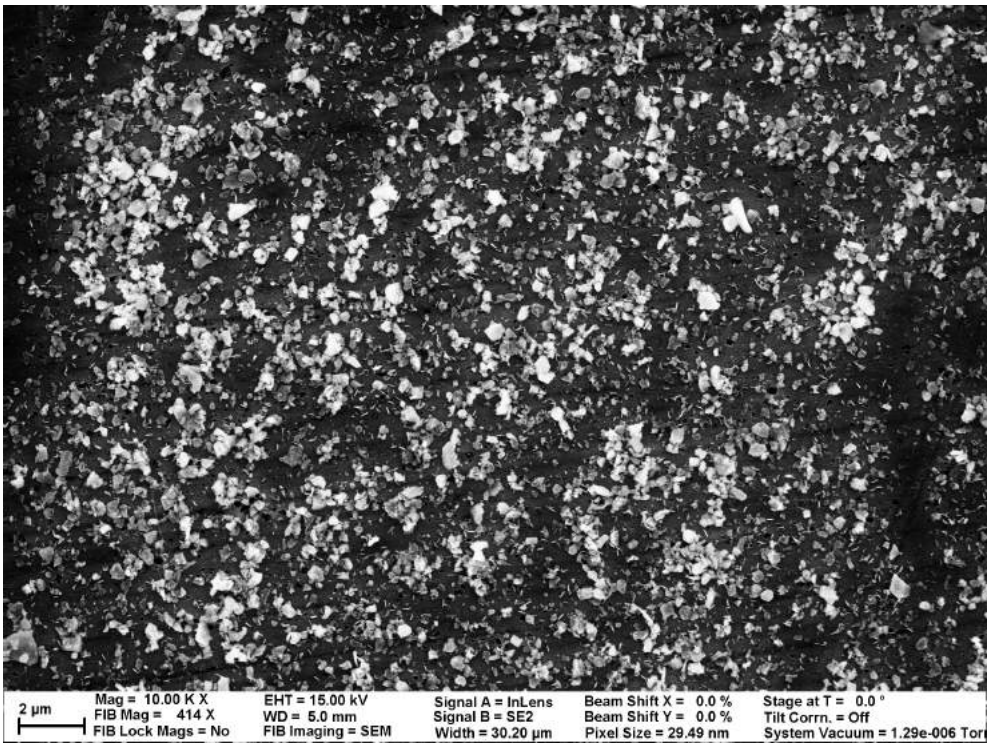


Figure 5-120: Example SEM image of the uncoated side of $Al_2O_3$ sample ring.

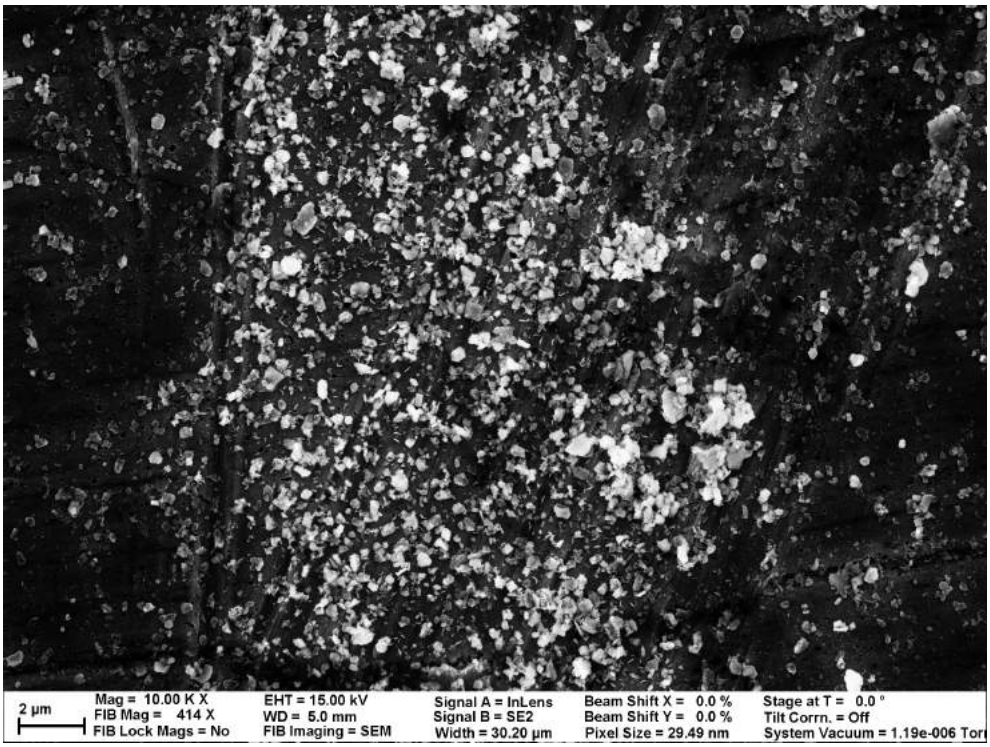


Figure 5-121: Another example SEM image of the uncoated side of $Al_2O_3$ sample ring.

**Titanium Dioxide ($TiO_2$)** Figures 5-122 and 5-123 are SEM images of crud grown on the titanium dioxide surface. Figures 5-124 and 5-125 are SEM images of the control side of the titanium dioxide sample. From observing these images with bare eyes, the coated side seems to have more crud. The calculated crud area coverages in table 5.6 agrees with this observation.

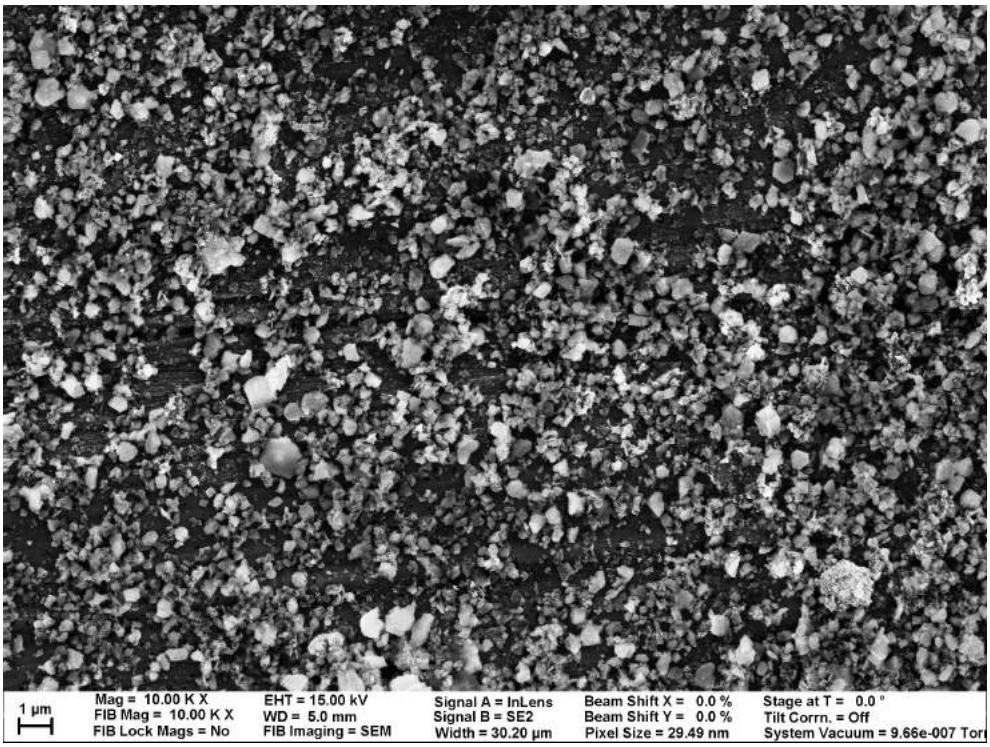


Figure 5-122: Example SEM image of the coated side of $TiO_2$ sample ring.

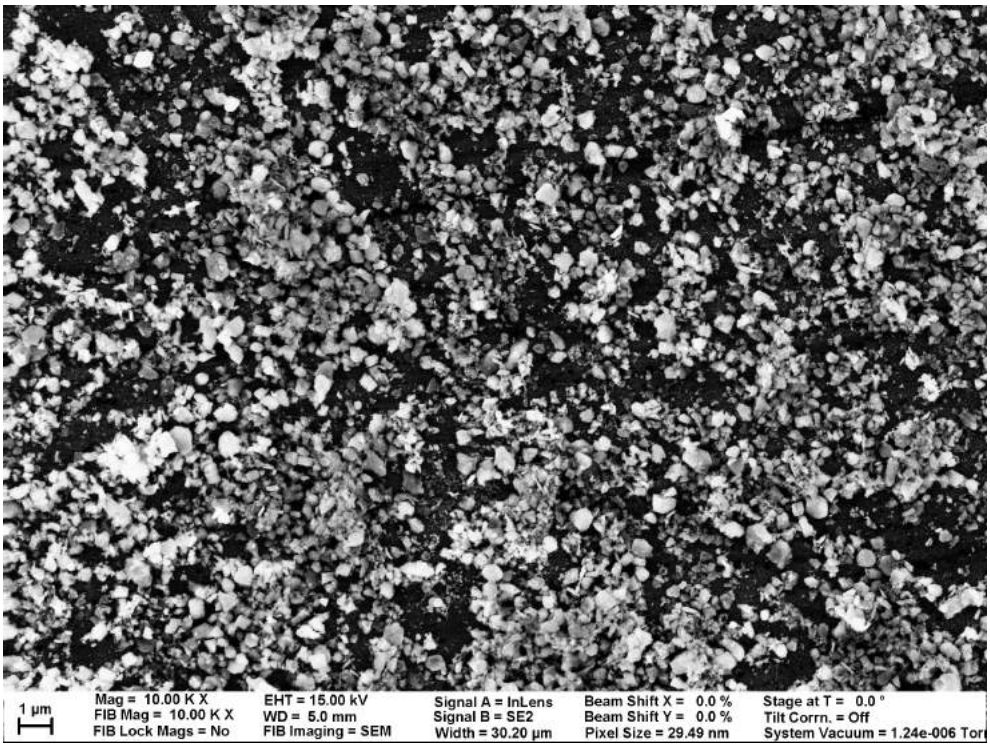


Figure 5-123: Another example SEM image of the coated side of $TiO_2$ sample ring.

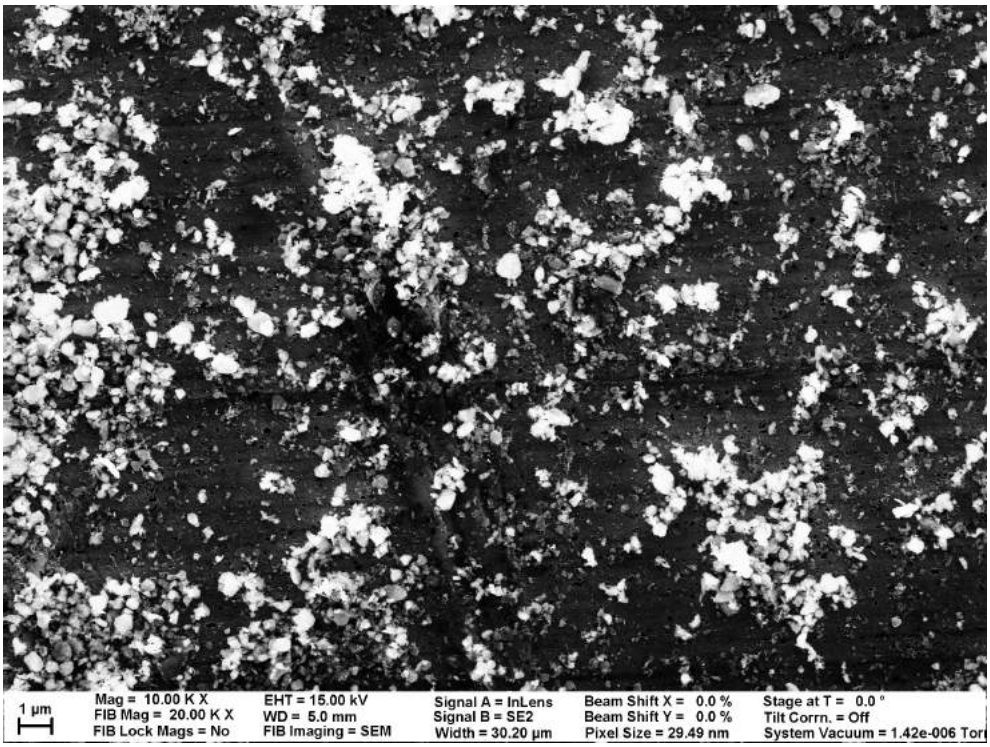


Figure 5-124: Example SEM image of the uncoated side of $TiO_2$ sample ring.

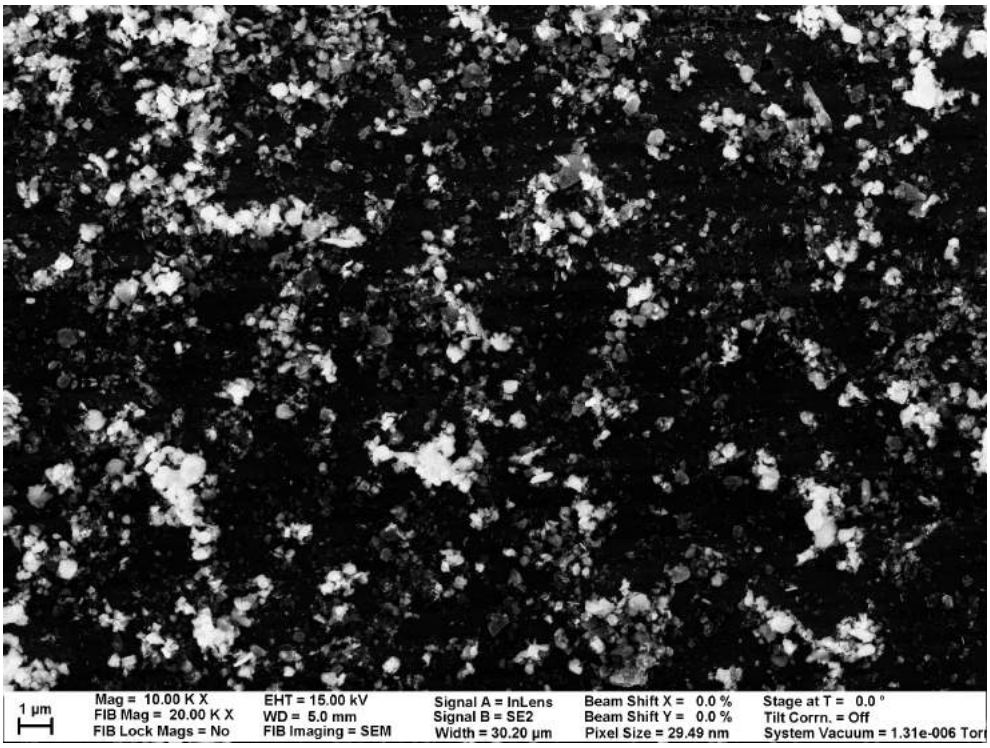


Figure 5-125: Another example SEM image of the uncoated side of $TiO_2$ sample ring.

**Titanium Diboride ($TiB_2$)** Figures 5-126 and 5-127 are SEM images of crud grown on the titanium diboride surface. Figures 5-128 and 5-129 are SEM images of the control side of the titanium diboride sample. From observing these images with bare eyes, the uncoated side seems to have more crud. The calculated crud area coverages in table 5.6 agrees with this observation.

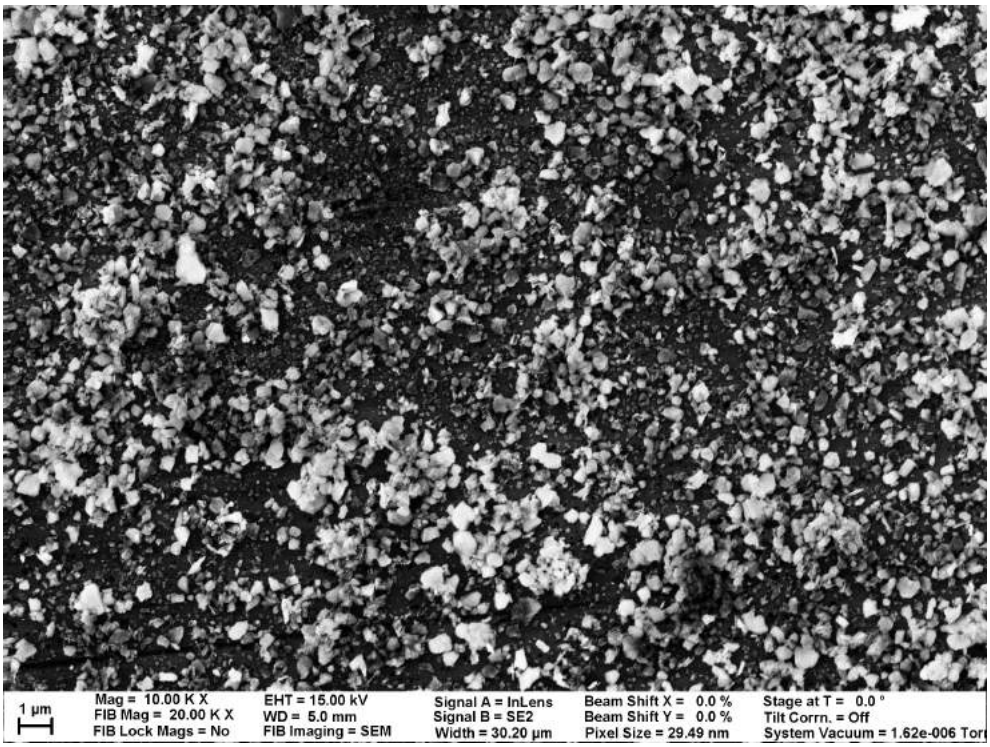


Figure 5-126: Example SEM image of the coated side of $TiB_2$ sample ring.

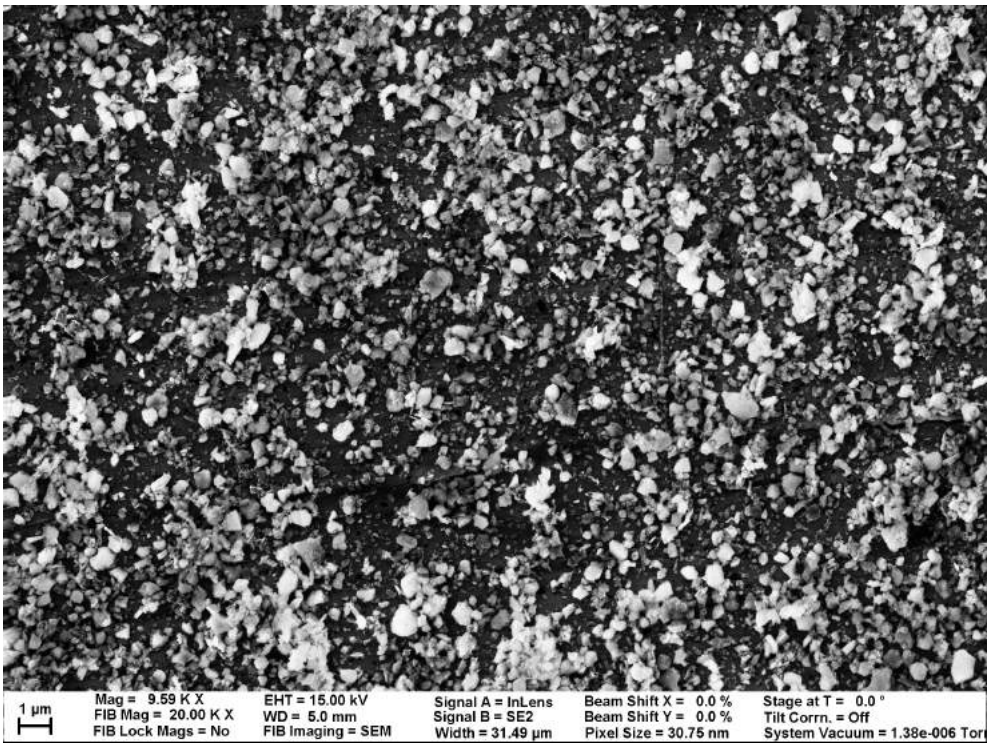


Figure 5-127: Another example SEM image of the coated side of $TiB_2$ sample ring.

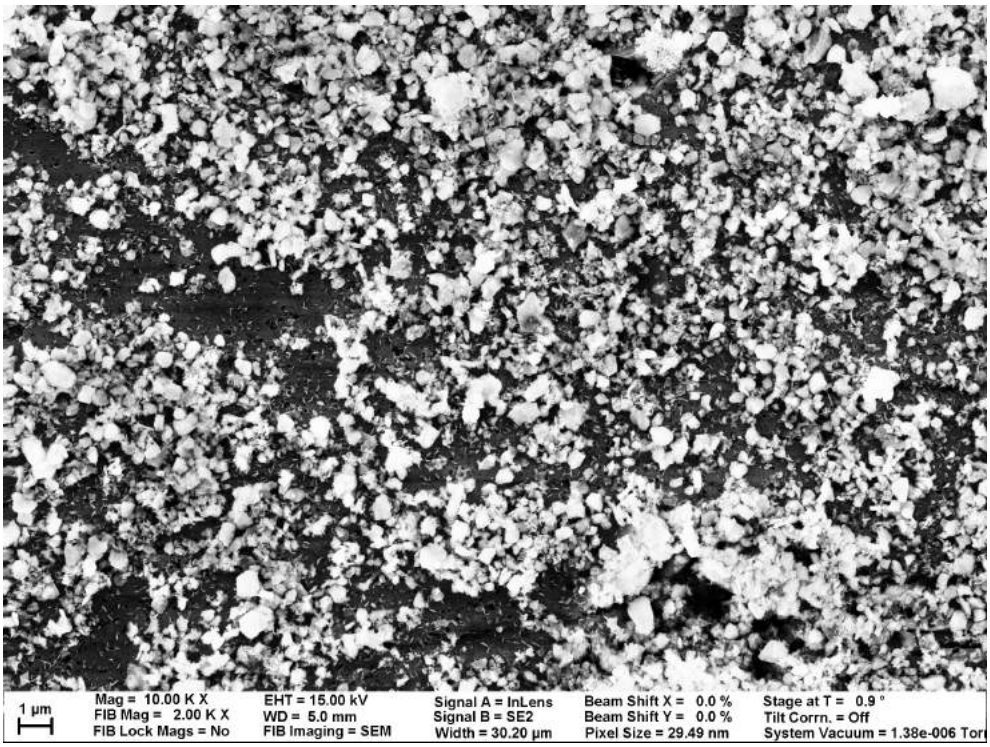


Figure 5-128: Example SEM image of the uncoated side of $TiB_2$ sample ring.

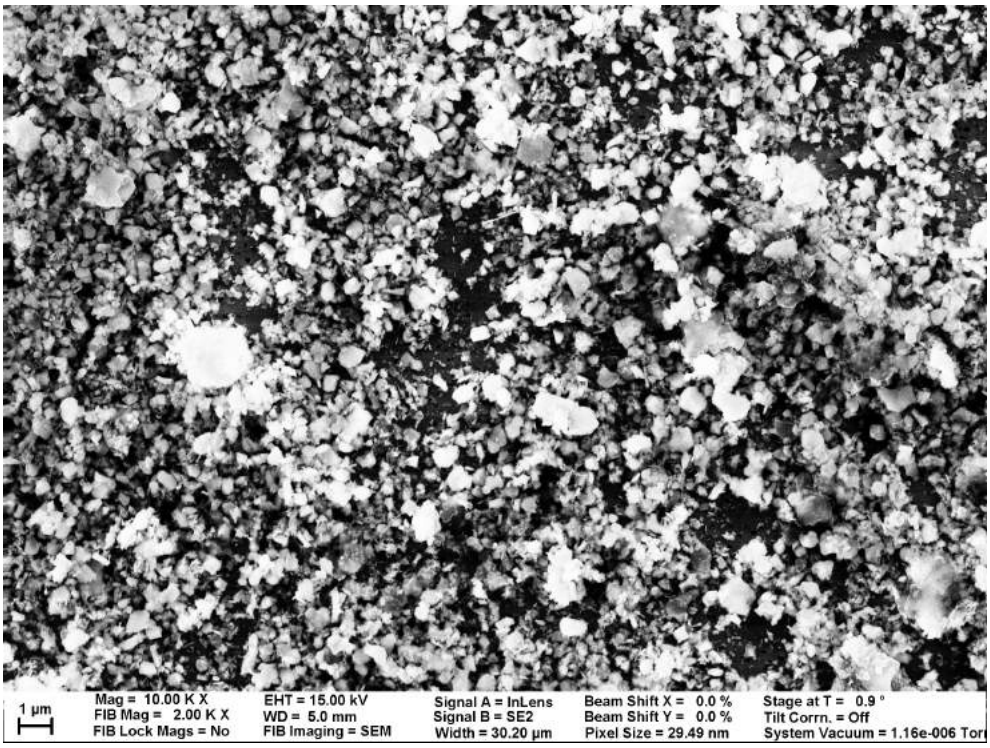


Figure 5-129: Another example SEM image of the uncoated side of $TiB_2$ sample ring.

**Zirconium Dioxide ($ZrO_2$)** Figures 5-130 and 5-131 are SEM images of crud grown on the zirconium oxide surface. Figures 5-132 and 5-133 are SEM images of the control side of the zirconium oxide sample. From observing these images with bare eyes, the uncoated side seems to have more crud. The calculated crud area coverages in table 5.6 agrees with this observation.

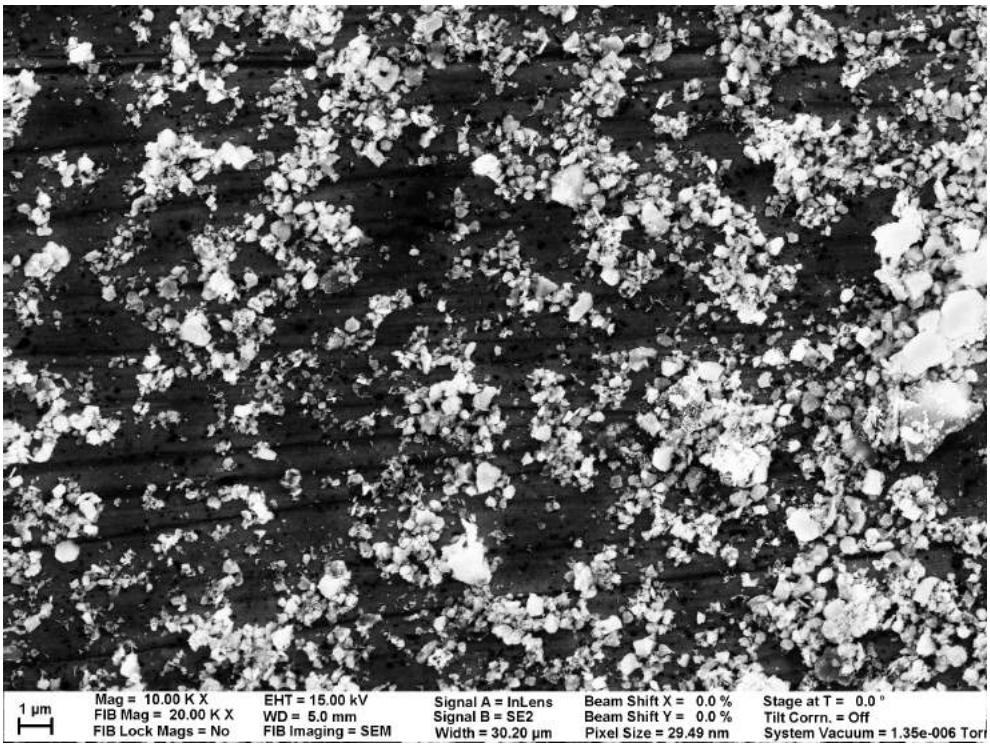


Figure 5-130: Example SEM image of the coated side of $ZrO_2$ sample ring.

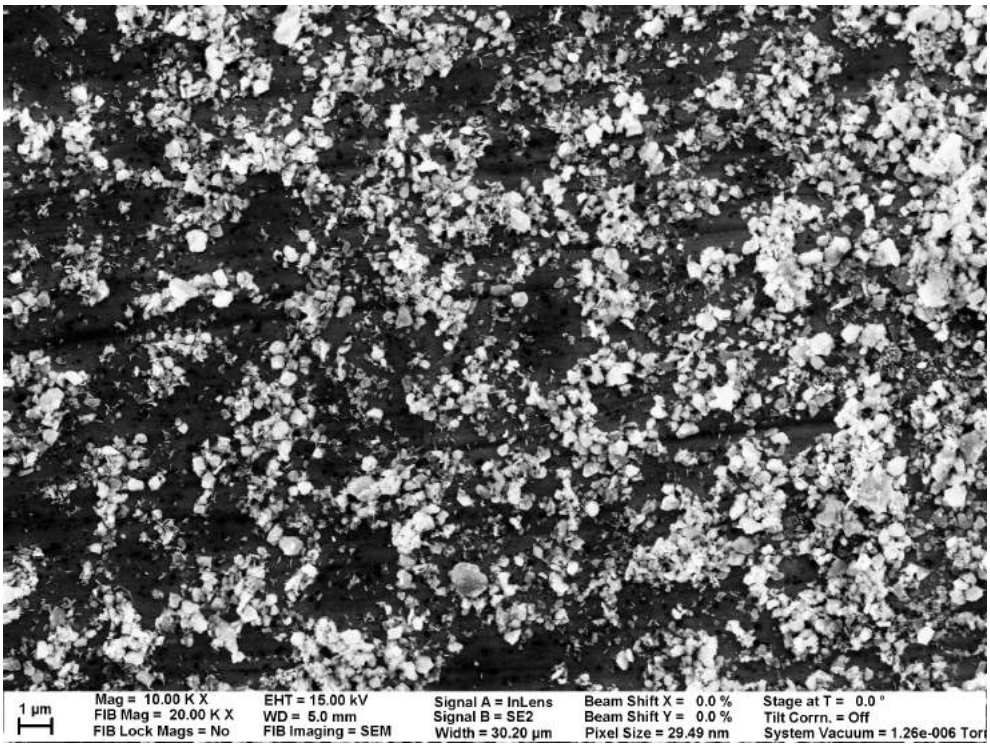


Figure 5-131: Another example SEM image of the coated side of $ZrO_2$ sample ring.

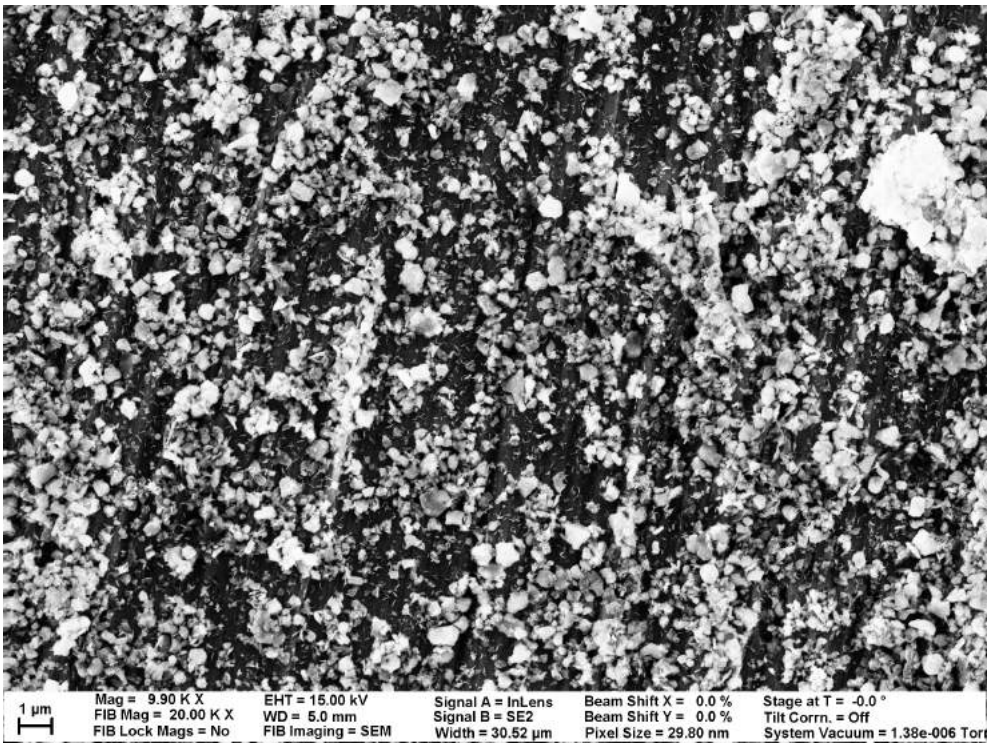


Figure 5-132: Example SEM image of the uncoated side of $ZrO_2$ sample ring.

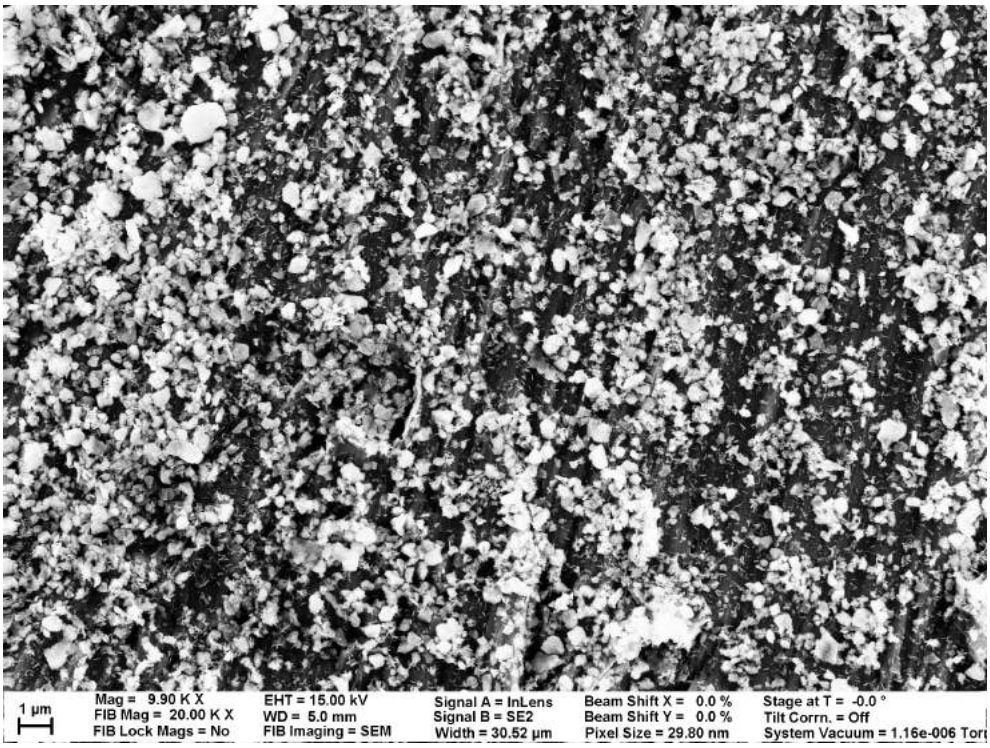


Figure 5-133: Another example SEM image of the uncoated side of $ZrO_2$ sample ring.

**Magnesium Oxide ($MgO$)** Figures 5-134 and 5-135 are SEM images of crud grown on the magnesium oxide surface. Figures 5-136 and 5-137 are SEM images of the control side of the magnesium oxide sample. From observing these images with bare eyes, we cannot determine whether uncoated or coated side has more crud. The calculated crud area coverages in table 5.6 shows that the crud area coverage is roughly the same on both sides with the coated side having slightly more crud.

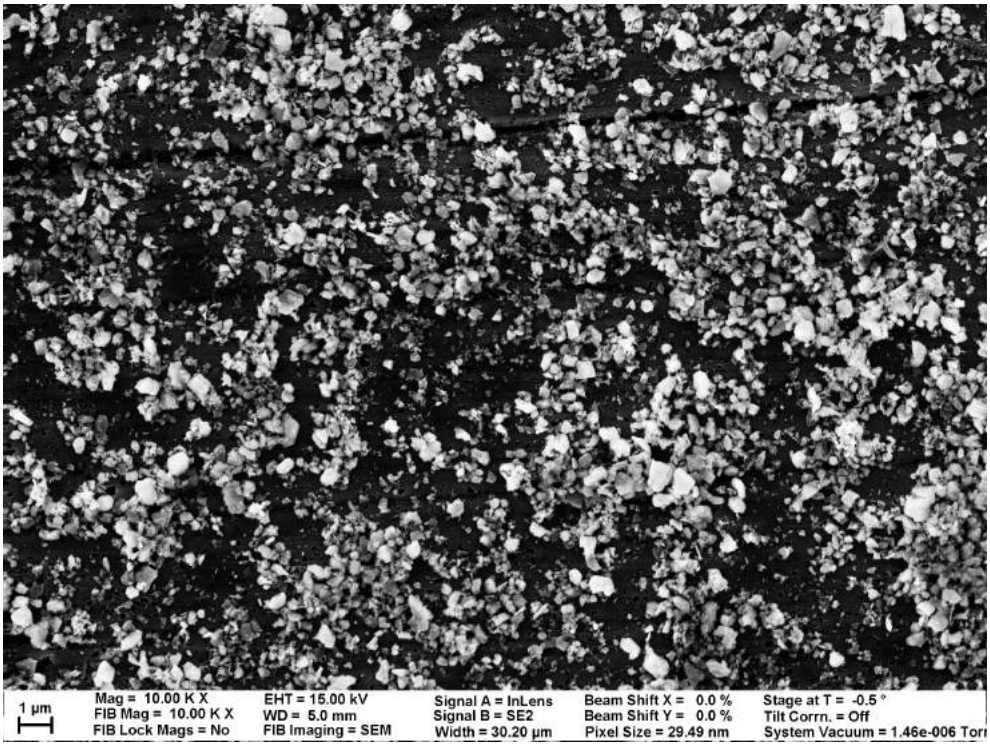


Figure 5-134: Example SEM image of the coated side of $MgO$ sample ring.

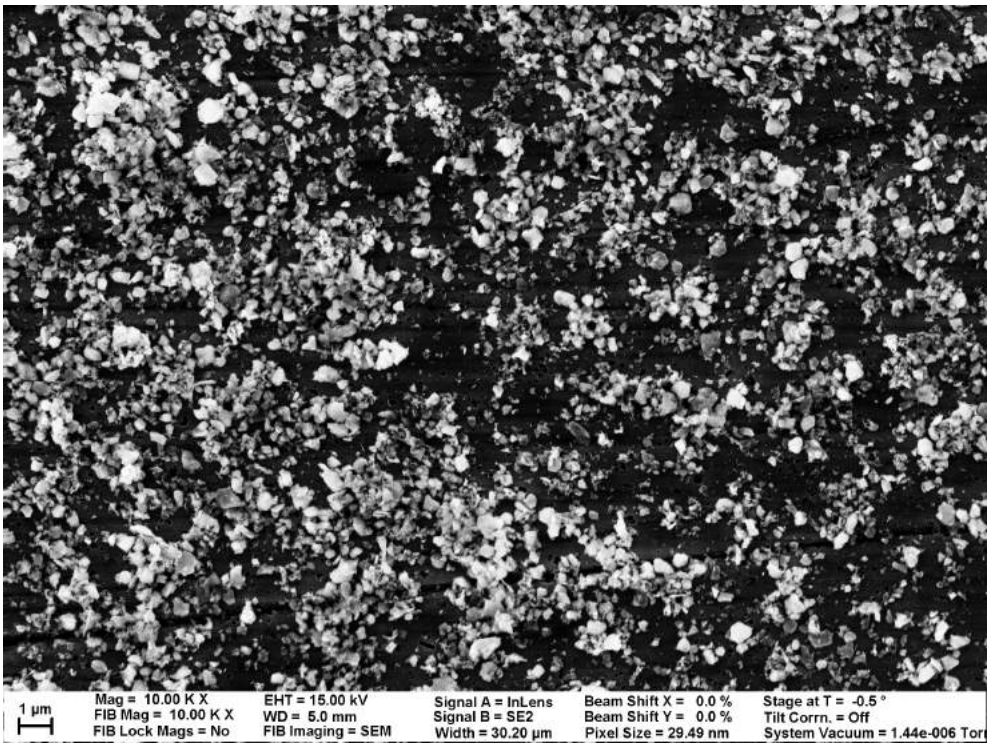


Figure 5-135: Another example SEM image of the coated side of $MgO$ sample ring.

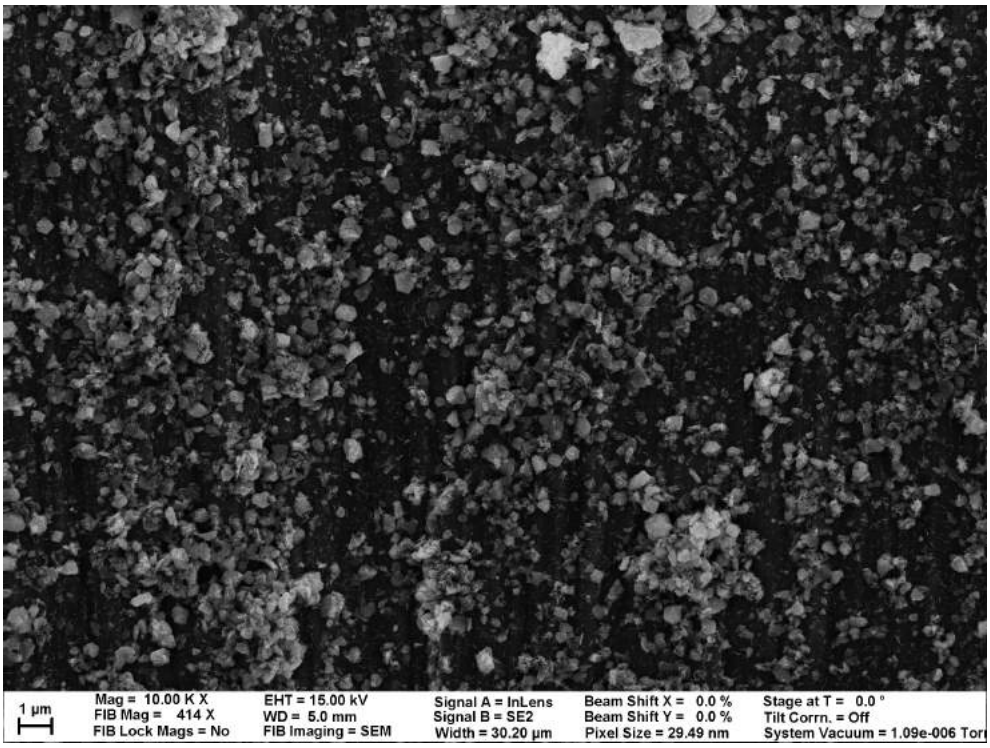


Figure 5-136: Example SEM image of the uncoated side of $MgO$ sample ring.

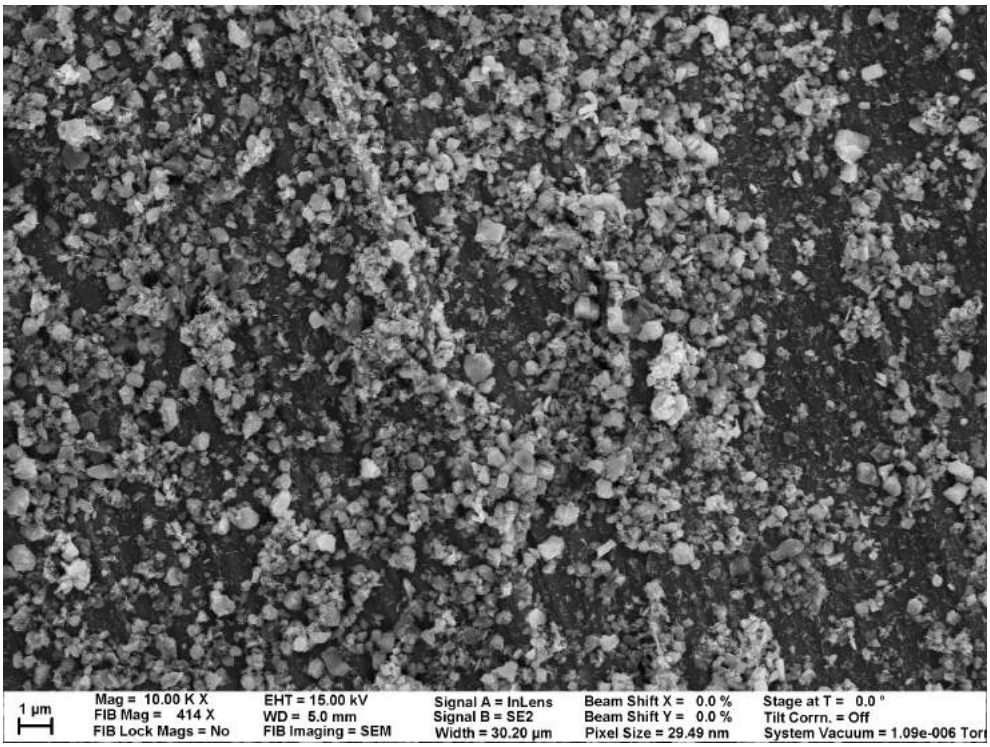


Figure 5-137: Another example SEM image of the uncoated side of $MgO$ sample ring.

### 5.3.3 Quantitative Results

Section 4.4.2 introduced, explained, and gave methods the quantitative results we are looking for to determine the effectiveness of each crud-resistant material. This section exhibits those quantitative results. After applying the percent crud area coverage analysis to SEM images obtained for each material from the successful trial C and D, we get the following results, summarized in the following tables 5.5 and 5.6, for trial C and trial D, respectively. Tables 5.5 and 5.6 showed that the same relationship (less/more crud) holds for most of the materials across both trial C and trial D, with the exception of $Al_2O_3$ and $ZrO_2$. In addition, tables 5.5 and 5.6 also demonstrate that the crud area coverage calculated by using the moment-preserving thresholding and Otsu thresholding yield very similar results.

If we calculate crud reduction from tables 5.5 and 5.6, we yield the results in table 5.7. Graphing these results, we get figure 5-138. In general, it is pretty clear that the nitrides/carbides are better than oxides for crud resistance. The data also generally agreed with AFM graph in figure 4-1 which suggests that $TiO_2$ may be adhesive to crud particles, while ZrC, ZrN, and TiC may be resistant to crud.

| Algorithm | Moment Preserving Thresholding | | Otsu Thresholding | |
|---|---|---|---|---|
| Material | Control Area Coverage (%) | Coated Area Coverage (%) | Control Area Coverage (%) | Coated Area Coverage (%) |
| zirconium carbide ($ZrC$) | 19.5 ± 2.6 | 21.9 ± 1.8 | 16.4 ± 2.2 | 19.8 ± 1.5 |
| zirconium nitride ($ZrN$) | 26.6 ± 4.2 | 20.3 ± 2.1 | 25.1 ± 4.2 | 19.0 ± 1.8 |
| titanium carbide ($TiC$) | 32.2 ± 8.7 | 14.8 ± 3.7 | 30.4 ± 8.4 | 14.1 ± 2.9 |
| titanium nitride ($TiN$) | 15.2 ± 1.5 | 13.5 ± 1.2 | 14.0 ± 1.0 | 13.2 ± 1.1 |
| aluminum oxide ($Al_2O_3$) | 34.3 ± 7.9 | 21.8 ± 2.4 | 33.4 ± 7.6 | 20.9 ± 2.1 |
| titanium oxide ($TiO_2$) | 19.9 ± 1.9 | 28.8 ± 1.8 | 17.7 ± 1.6 | 25.7 ± 1.9 |
| titanium boride ($TiB_2$) | 37.4 ± 8.5 | 38.8 ± 2.5 | 34.9 ± 8.3 | 37.5 ± 2.3 |
| zirconium oxide ($ZrO_2$) | 22.0 ± 5.3 | 32.7 ± 2.4 | 21.5 ± 4.7 | 30.8 ± 2.3 |
| magnesium oxide ($MgO$) | 20.6 ± 2.4 | 29.7 ± 3.8 | 19.6 ± 2.1 | 28.6 ± 4.0 |

Table 5.5: This table shows the crud area-coverage of the trial C samples. Each material represents each sample rings, where the control area coverage represents the uncoated side. Each number represent the mean of crud area coverage of 10 photos taken from the same sample and side. The uncertainty is obtained from the standard deviation of the crud area coverage for the 10 photos.

| Algorithm | Moment Preserving Thresholding | | Otsu Thresholding | |
|---|---|---|---|---|
| Material | Control Area Coverage (%) | Coated Area Coverage (%) | Control Area Coverage (%) | Coated Area Coverage (%) |
| zirconium carbide ($ZrC$) | 43.0 ± 6.6 | 34.1 ± 7.3 | 41.3 ± 6.3 | 34.0 ± 7.3 |
| zirconium nitride ($ZrN$) | 47.9 ± 9.6 | 35.0 ± 3.1 | 47.6 ± 9.4 | 32.4 ± 3.1 |
| titanium carbide ($TiC$) | 61.1 ± 8.8 | 44.6 ± 3.9 | 60.2 ± 8.5 | 44.2 ± 3.3 |
| titanium nitride ($TiN$) | 55.6 ± 8.0 | 50.3 ± 3.1 | 54.7 ± 8.0 | 50.4 ± 2.6 |
| aluminum oxide ($Al_2O_3$) | 37.3 ± 5.4 | 45.5 ± 7.5 | 35.4 ± 5.4 | 44.6 ± 7.1 |
| titanium oxide ($TiO_2$) | 36.0 ± 5.1 | 53.7 ± 4.7 | 34.9 ± 4.8 | 53.2 ± 4.9 |
| titanium boride ($TiB_2$) | 59.6 ± 3.8 | 52.9 ± 3.8 | 58.3 ± 3.7 | 51.6 ± 4.1 |
| zirconium oxide ($ZrO_2$) | 58.9 ± 7.1 | 49.8 ± 5.5 | 58.2 ± 7.0 | 48.2 ± 5.5 |
| magnesium oxide ($MgO$) | 45.6 ± 3.3 | 48.6 ± 3.5 | 45.6 ± 3.3 | 47.6 ± 3.3 |

Table 5.6: This table shows the crud area-coverage of the trial D samples. Each material represents each sample rings, where the control area coverage represents the uncoated side. Each number represent the mean of crud area coverage of 10 photos taken from the same sample and side. The uncertainty is obtained from the standard deviation of the crud area coverage for the 10 photos.

| Algorithm | Moment Preserving Thresholding | Otsu Thresholding |
|---|---|---|
| Material | Crud Area Coverage Reduction (%) | Crud Area Coverage Reduction (%) |
| zirconium carbide ($ZrC$) | 4.2 ± 13.0 | -20.7 ± 12.3 |
| zirconium nitride ($ZrN$) | 25.3 ± 14.8 | 24.3 ± 14.5 |
| titanium carbide ($TiC$) | 40.5 ± 19.1 | 53.6 ± 18.0 |
| titanium nitride ($TiN$) | 10.4 ± 10.5 | 5.7 ± 9.9 |
| aluminum oxide ($Al_2O_3$) | 7.2 ± 17.5 | 37.4 ± 16.8 |
| titanium oxide ($TiO_2$) | -46.9 ± 9.6 | -45.2 ± 9.3 |
| titanium boride ($TiB_2$) | 3.7 ± 14.2 | -7.4 ± 14.1 |
| zirconium oxide ($ZrO_2$) | -16.6 ± 14.8 | -43.3 ± 14.1 |
| magnesium oxide ($MgO$) | -25.4 ± 9.3 | -45.9 ± 9.2 |

Table 5.7: Crud area coverage reduction (%) of each material and its uncertainty. Tables 5.5 and 5.6 were used as the source data.

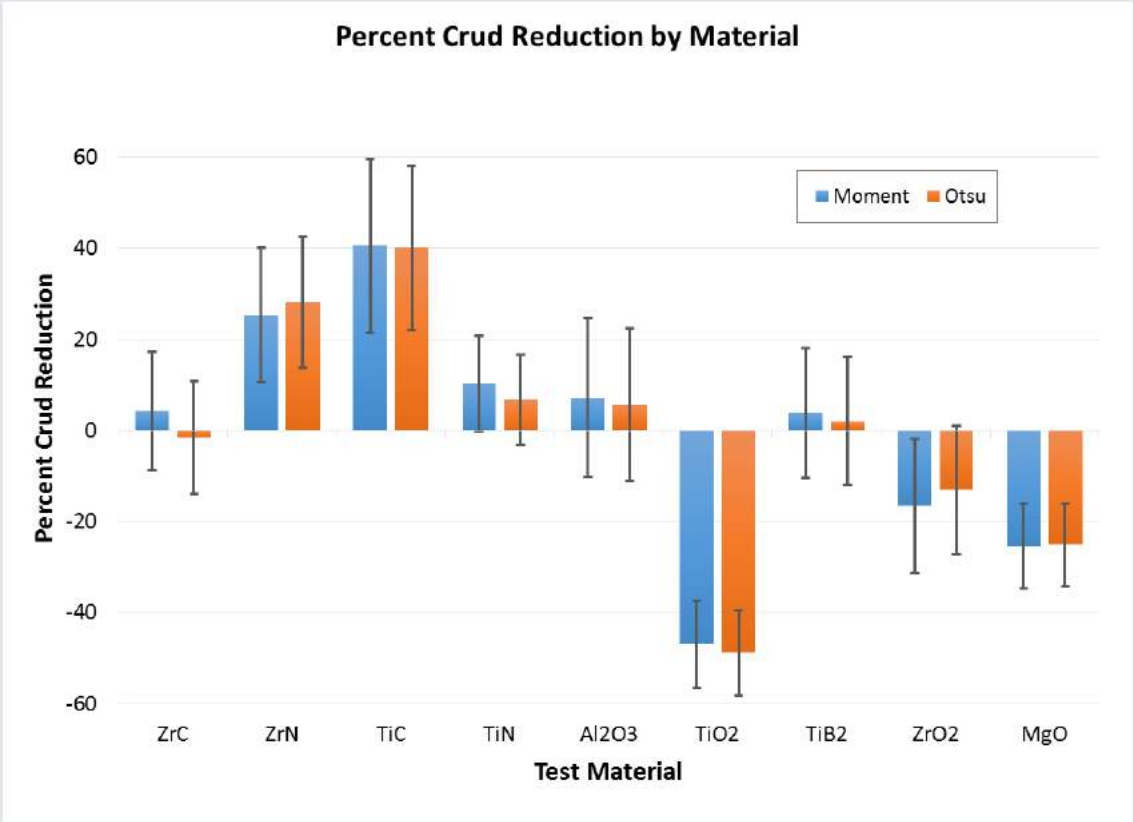


Figure 5-138: Percent crud reduction by the material. Both moment and Otsu thresholding algorithm give very similar results. The error bars represent 95% confidence interval.

# Chapter 6

# DISCUSSION

This chapter discusses the results that were laid out in chapter 5, as well as the possible tasks for the future. The first section discusses the fractal analysis results shown in section 5.2. The second section discusses the crud-resistant coatings experimental results shown in section 5.3. The third section describes the possible sources of experimental errors for all experimental trials conducted using the IHTFP. The fourth section highlights the possible improvements to the experimental methods and the IHTFP. The last section suggests interesting future experiments.

## 6.1 Fractal Analysis Discussions

This section examines the meaning behind the results from section 5.2 of the results chapter. The first subsection examines the question of whether crud is fractalline. The second subsection discusses the importance and the possible mechanisms behind the logarithmic relationships between porosity vs. height from cladding, as well as between the fractal dimension vs. height from the cladding. The third subsection discusses the strong logarithmic relationship found on the plot of fractal dimension vs. porosity.

### 6.1.1 Is Crud Fractalline?

The fractal analysis, if applicable to crud, could provide us with a simple and effective way to characterize the macro-scale behaviors of crud using its micro-scale properties. However, before the completion of the experiments conducted for this thesis, it was uncertain whether the use of fractal analysis on crud would be valid. At that point, we knew that the fractal analysis was already used in many soil studies including that of Annette Dathe (2005)[218] and Steven De Gryze et. al. (2006) [142]. However, this fact does guarantee that the fractal analysis is applicable to crud as well. In our fractal analysis of crud, the box-counting method was used. As explained in section 2.3.9.2, this

method consists of plotting the value of ln(box count) to ln(box size in pixels), similar to one shown in figure 6-1. An $R^2$ value obtained from a box-counting plot tells us the fraction of variation in the box-counting plot's points that can be explained by its trendline. An $R^2$ value closer to unity would suggest that the material image that the box-counting method was applied on is fractalline.

Figure 6-1 shows a box-counting plot of a random SEM image from an IHTFPs crud sample. Its maximum pixel box size is 128. Notice that in this case, the points towards the higher end starts to deviate down from the straight trendline. If we make another plot that only takes into account the lower box sizes before this deviation starts, we obtain a very close fit, shown in figure 6-2, with $R^2$ of 0.9994. On the other hand, the fit created in figure 6-1 has an $R^2$ value of only 0.9935. This suggests that crud is very fractalline at lower length scale, but starts to deviate to become less fractalline at higher length scale. The labels on data points in both figures 6-1 and 6-2 show box sizes in pixel converted to micron values. Notice that the lowest point box size of 0.0208 $\mu m$ or 20.8 $nm$. This is very close to the 50 $nm$ diameter size of NiO used in our experiment. The almost perfect box-counting fit near this length scale suggests that crud fractalline properties may be due to the shape and/or the arrangement of crud particles. As we increase beyond the box size of 332.8 $nm$, points starts to deviate from the general trend. This breakdown of fractalline properties is not surprising given that true fractal cannot exist in nature. All naturally observed fractals always only exist at a certain range of length scales. All data presented in this thesis uses 64-pixel max box size which is a good trade-off between including too little points and getting too much deviation from a straightline. Including too little points will lead to fractal dimension results that may deviate from reality. Getting too much deviation from including too many points will also lead to inaccuracy since the non-fractal regime will also be counted leading to fractal dimension values that are too high.

To examine all the $R^2$ values for the data sets we used, we compiled the $R^2$ values into table 5.4. Table 5.4 shows that $R^2$ values obtained from box-counting plots are very close to one regardless of the sample or the view. Even the highest average $R^2$ value of 0.989 suggests that 98.9% of the variation in the box-counting plot is explained by its linear regression, whose slope represents fractal dimension. For some comparison, box-counting method's $R^2$ value of pepper, eggplant, and tomato leaves are 0.9962, 0.9913, and 0.9972, respectively [134]. Although $R^2$ values by themselves are not proof that crud exhibits fractalline properties, they certainly act as supporting evidence. This may not be surprising given that the fractal theory itself was, from the beginning, designed to characterize the complex geometries that cannot be easily characterized by the standard geometry. Crud isn't alone as a naturally forming porous media that exhibits fractal properties; fractal analysis is also frequently applied in the studies of soil/sand/gravel. Section 6.1.3 will expand more on these studies.

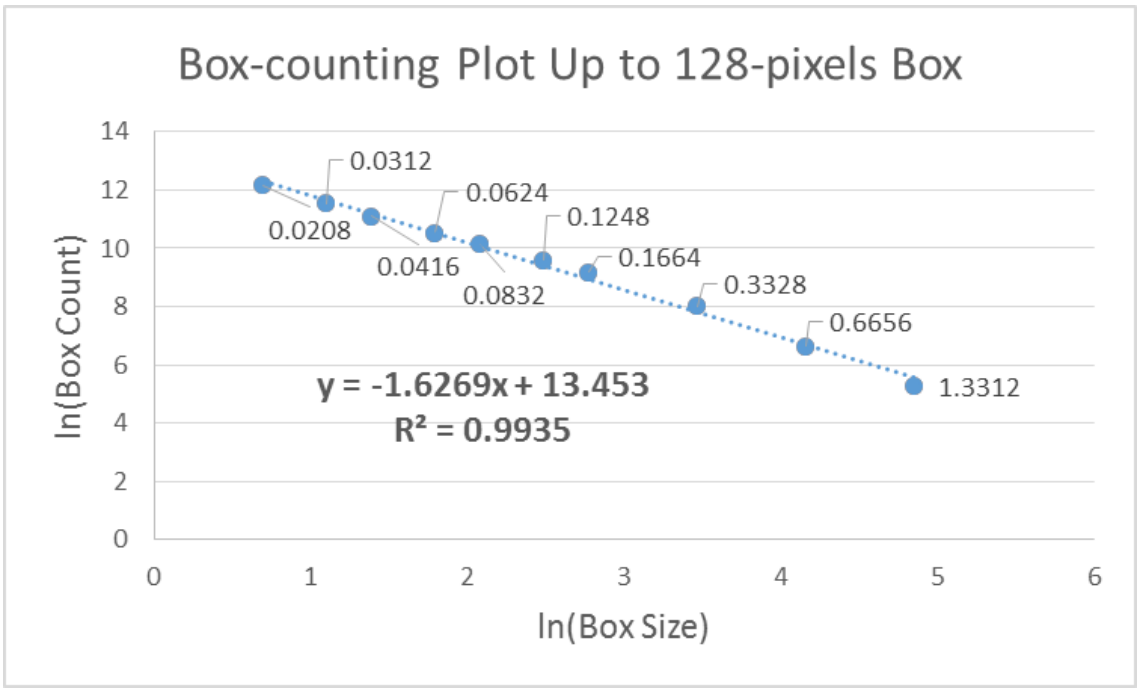


Figure 6-1: Plot of ln(box count) to ln(box size in pixels). The absolute value of the slope of its linear regression line is fractal dimension. This plot is generated from a random crud SEM image from an IHTFP's crud sample. The data-point label numbers are box sizes in microns.

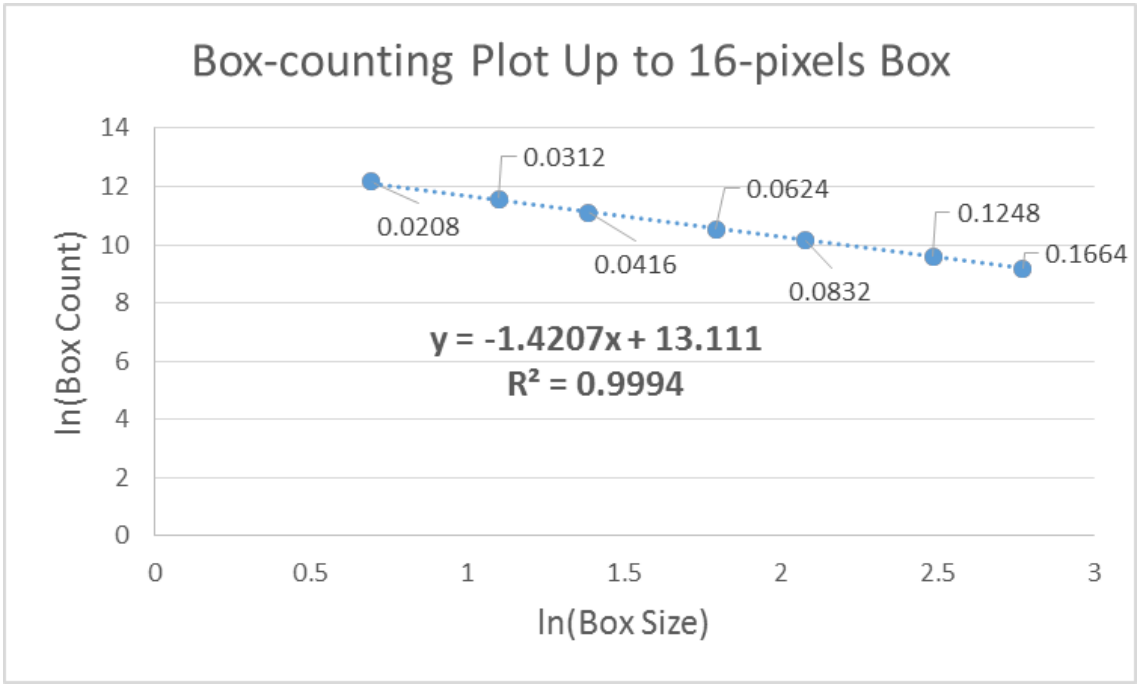


Figure 6-2: Same plot as 6-1 that only goes up to box size of 16 pixels.

### 6.1.2 Porosity/Fractal Dimension vs Height Relationship

Figure 5-37 demonstrates that crud porosity decreases with height. There are several theories that may explain why the porosity vs. height plot exhibits this relationship. The first theory is based on the assumption that crud does not grow indefinitely and tends to slow or stop growing at some thickness [98]. The reason for crud growth slowdown could be because the top layer of thicker crud is more likely to be washed away by the coolant. If this is the case, there could be a selection process, where crud particles depositing on thicker crud that does not fit tightly onto the crud deposit are more likely to get washed away. This creates a selection process where only crud particles that fit tightly onto crud surfaces will remain. Overall, this process will cause the crud to become more tightly packed with lower porosity. If crud particles are more likely to get washed away when they try to deposit on thicker crud, then the process will cause crud to become more tightly packed with lower porosity at greater height positions from the cladding. The second theory is based on the assumption that soft crud probably forms when there is more boiling. This is evident in the observations of soft crud from accidents. If crud is thin, water could turn to vapor very close to crud surface, leading to more boiling on the crud surface. As a result, crud at lower height might be "softer" from the boiling process. On the other hand, if crud is thick, the same phase change could happen within crud. This could lead to less boiling near crud surface, and therefore crud that accumulates on top of thicker crud might be "harder" with lower porosity. The third theory is that this relationship is caused by the cracking anomalies. The left SEM image of figure 6-3 shows crud cross-section image. There are cracks between crud and cladding which count as higher porosity for the image processing. This explains the steep rise in porosity near cladding. The reason crud cracked near the cladding boundary maybe due to the different rates of thermal contraction between crud and cladding. However, this theory is unlikely since several SEM images such as the second image of figure 6-3 demonstrate that even without a crack, crud still looks less tightly packed and weaker near cladding. Figure 5-38 shows that fractal dimension versus height relationship is similar to that of porosity versus height. This could be because fractal dimension follows porosity with their strong relationship shown in figure 5-39.

### 6.1.3 Fractal Dimension vs Porosity Relationship

The relationship of fractal dimension to porosity is shown to be very consistent for both top view and cross-section view of crud images. In addition, the relationship holds across not only the two samples from the IHTFP but also for the Westinghouse's sample. The logarithmic trend fits very nicely with $R^2$ value of only 0.9925 which suggests that there must be some underlying physics governing the trend.

Similar fractal dimension vs. porosity relationships are also observed in soil studies such as that

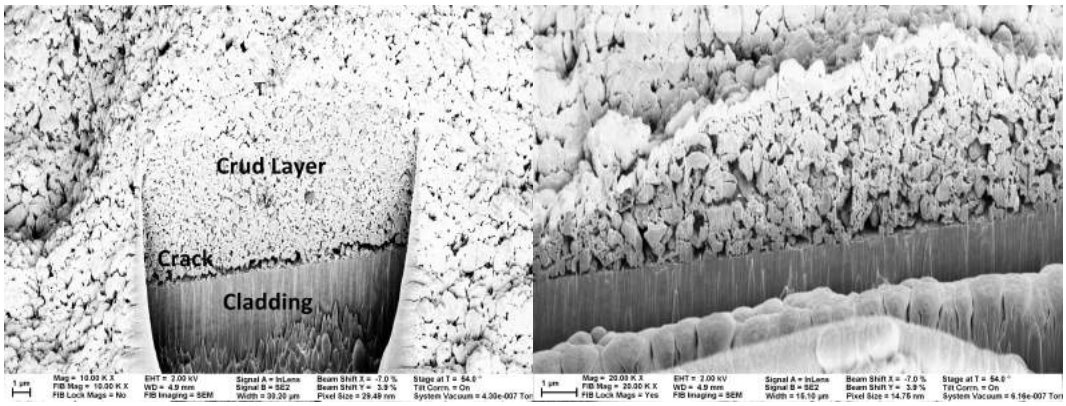


Figure 6-3: 1st (Left): crud cross-section image with a crack near crud to cladding interface. 2nd: crud cross-section image without a crack.

of Annette Dathe (2005)[218] and Steven De Gryze et. al. (2006) [142]. Steven De Gryze found a similar relationship in sandy and silt loam. Annette Dathe graphed the fractal dimension vs. porosity graph in order to quantify the effect of formation of micro-cracks made by microorganisms, and also found a similar relationship between fractal dimension and porosity. Anne Dathe's graphs in figure 6-3 also demonstrate that even the same kind of porous materials with different conditions do not necessary follow the same fractal dimension vs. porosity relationship. The observation that IHTFP sample's fractal dimension vs. porosity relationship follows closely with that of the Westinghouse sample is striking. It could mean that crud forming under the conditions close to those of PWR may follow the same fractal dimension versus porosity logarithmic trendline despite the difference in crud precursors and heat flux from the cladding. If this is the case, our group's crud model would definitely benefit from this new correlation. If our group's crud model works with real reactors, we could make very informed and accurate predictions of crud layer's effective thermal conductivity and perhaps crud's chemical interactions. This could, perhaps, alleviate the fear of crud growth and allow reactor operators faced with crud to make more informed decisions about how to react to crud problems.

### 6.1.4 Other Literature that Explored Fractal Dimension vs Porosity

Although the measurement of fractal dimension is a common practice in analyzing soil, as implied by the prolific number of papers available, there has not been any attempt so far to analyze crud in terms of fractal properties. Nevertheless, papers for soil fractal dimension vs porosity can still be useful in comparing their properties with crud fractal properties. In 2005, Annette Dathe [218] plotted the fractal dimension vs porosity to determine its relationship in soil. This plot is shown in figure 6-4. A similar relationship between fractal dimension and porosity were found in their paper, even though the paper calculated mass fractal dimension using pore-solid fractal (PSF) model.

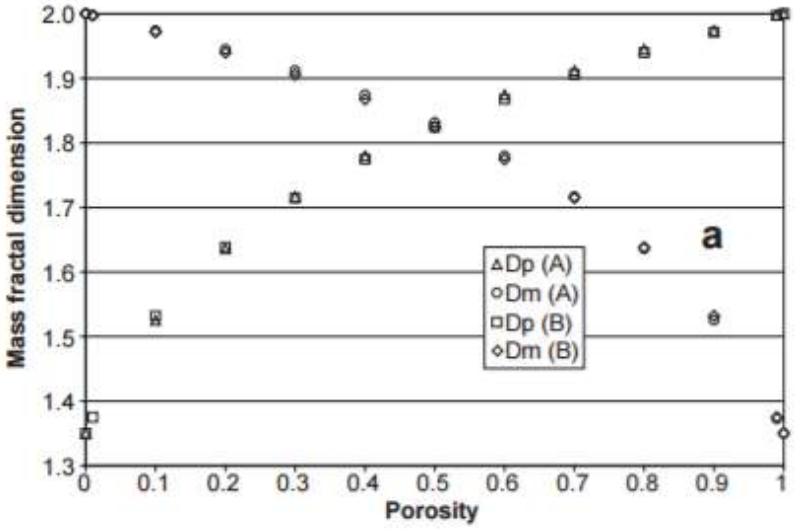


Figure 6-4: Plot of mass fractal dimension vs porosity from Anne Dathe [218]. Dp (A) and Dp (B) are the fractal dimensions of pores. The relationship between the fractal dimension of pore and porosity is very similar to the relationship observed in our experiment shown in figure 5-37.

Another noteworthy paper is the study by Steven De Gryze et. al. [142] in 2006 that also graphs the fractal dimension vs porosity graph in order to quantify the effects of formation of micro-cracks made by microorganisms. Their fractal dimension vs porosity graph is very similar to that of ours as shown in the following figure. The graph of fractal dimension vs porosity in sandy loam shows that sand of different condition can yield different fractal dimension vs porosity curve. This means that even the same kind of porous material with the different condition does not necessary follow the same fractal dimension vs porosity relationship. The fact that IHTFP's fractal dimension vs porosity relationship follows closely with that of Westinghouse's WALT Loop is striking.

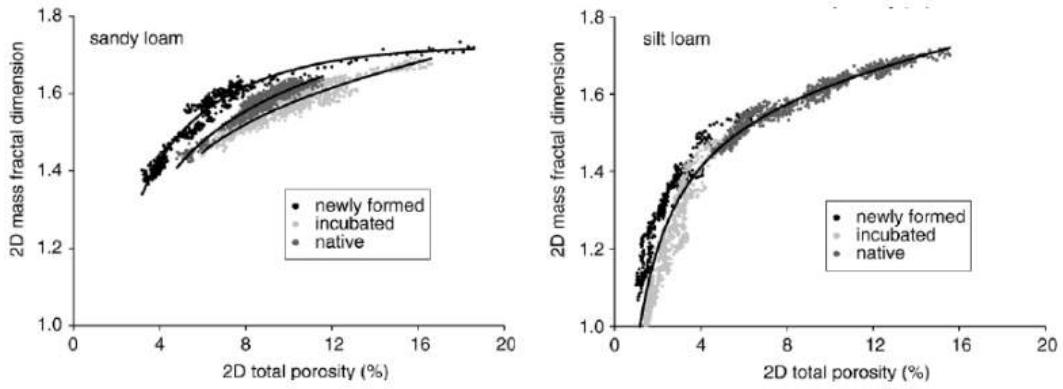


Figure 6-5: 2D mass fractal dimension vs porosity of aggregate from a sandly loam and a silt loam. The newly formed loams are aggregrates reformed from crushed material. The incubated loams are 21-day incubated newly formed loams [142].

### 6.1.5 Fractal Result's Effect on the MAMBA-BDM Crud Model

Fractal dimension data obtained from this study were applied on MAMBA-BDM crud model [44] with the help of Miaomiao Jin. We ran two general simulation cases. In case I, porosity and fractal dimension within crud vary spatially according to figure 5-37 and 5-38. This case I serves to examine how to porosity and fractal dimension spatial variation within crud affect crud's temperature and thermal conductivity. In case II, porosity and fractal dimension were made constant spatially. Ten simulation runs were made for ten separate points of porosity. The ten points of porosity vary uniformly between 7.5 % and 49.4 %. These two points represent the lowest and highest porosities from figure 5-39. Fractal dimensions are calculated from porosities according to the equation from figure 5-39.

Case I's resulting spatial temperature plot in figure 6-6. Because ten simulations were run for case II, we get ten separate resulting spatial temperature plots for the results. For brevity, the two spatial temperature plots for the two extreme 7.5 % and 49.4 % porosity values, are presented in figure 6-7 and 6-8. By observing these three selected spatial temperature plots, one can see that the case with the highest constant porosity of 49.4 %, shown in figure 6-8, has the highest temperature near the crud-cladding interface. The average temperature at the crud-cladding interface for 49.4 % porosity case is 621.78 K. This is higher than the average crud-cladding interface temperature of 619.52 K for the 7.5 % porosity case and 620.26 K for case I. This suggests that more porous, softer crud has more adverse effect on temperature than that of less porous, harder crud. Another interesting observation from these three temperature plots is that case I's plot has a slightly higher temperature at cladding compared to case II's 7.5 % porosity plot. The temperatures at crud-coolant interfaces for both plots, on the other hand, look similar to each other. If peak cladding temperature is plotted against porosity for case II, we yield the blue series in figure 6-9. If case I's porosity is taken as the average porosity from figure 5-37, we yield the red dot in figure 6-9. Figure 6-9 clearly shows that case I, with varying spatial porosity, exhibits a greater peak cladding temperature than the general trend from case II, with constant spatial porosity. This suggests that the heightened porosity near the crud-cladding interface leads to a higher temperature near cladding. This is significant because higher temperatures lead to more corrosion. In addition, figure 6-9 also exhibits a perfect fit, with R-square of one, when a polynomial fit is applied. Although one can say that this is the result of the logarithmic inputs for porosities and fractal dimensions, it is still, nevertheless, very interesting that two complex logarithmic input values will yield a simple polynomial trend on peak cladding temperatures that resulted from a complex crud simulation. Lastly, the effective thermal conductivity was found for all cases and plotted in figure 6-10. This plot shows a downward sloping exponential relationship between the effective thermal conductivity and porosity. Softer crud with higher porosity has lower effective thermal conductivity than harder crud with lower porosity. Moreover, varying spatial porosity and fractal dimension in case I lead to

a lower effective thermal conductivity shown by the red dot.

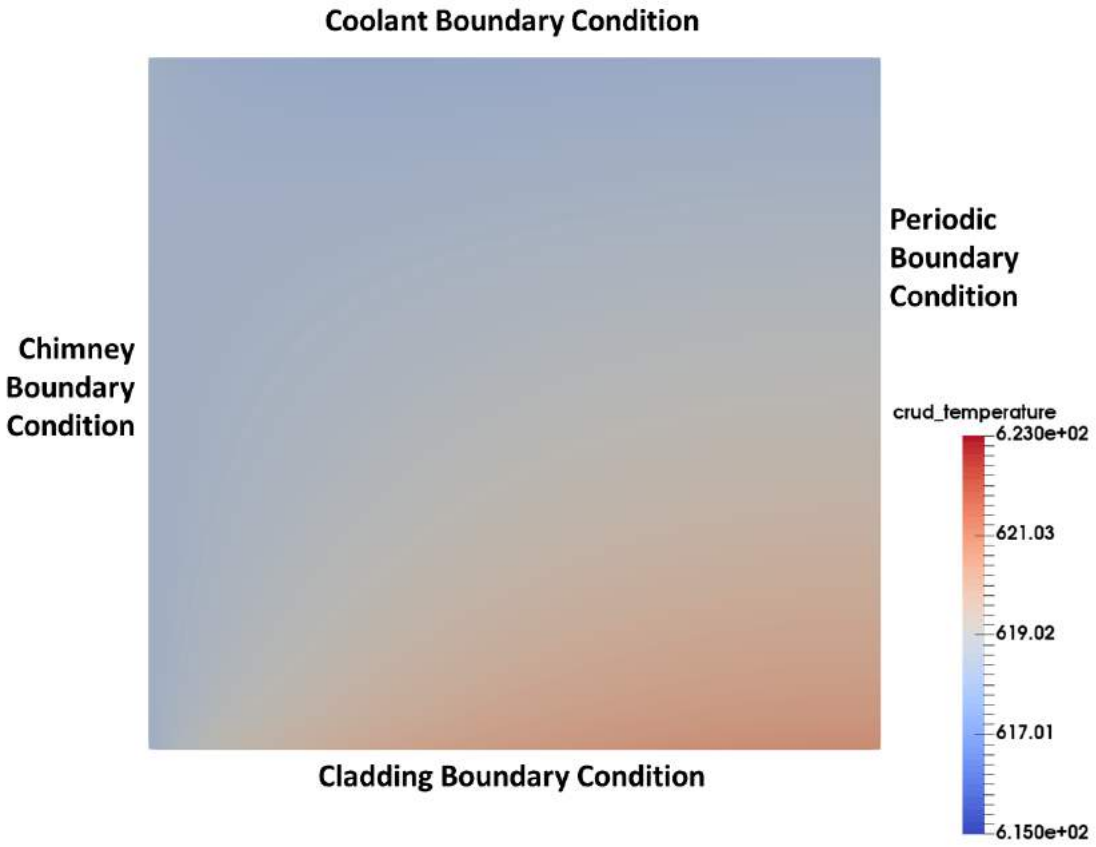


Figure 6-6: Spatial plot of temperature with in crud for case I. Crud temperature is in the unit of Kelvin. The plot represents the cross-section view of crud near a boiling chimney. The vertical axis represents the height from crud-clading interface. The bottom corner of the plot represents the crud-cladding interface, while the top corner represents that the crud-coolant surface. The thickness of crud in this case is taken as 10 microns. The horizontal axis represents the distance away from the boiling chimney. The left corner represents the surface within the boiling chimney.

[1]

## 6.2 Crud-resistant Surface Coating

This section examines the crud-resistant surface coating experimental results shown in section 5.3. The first subsection examines the effectiveness of crud-resistant coatings. The second section discusses the relationship between crud area reduction and refractive index as hypothesized in section 2.4.2.9.

[1]The MAMBA-BDM simulation was run by Miaomiao Jin [44]. The raw data from the simulation was processed for this thesis into the plots displayed.

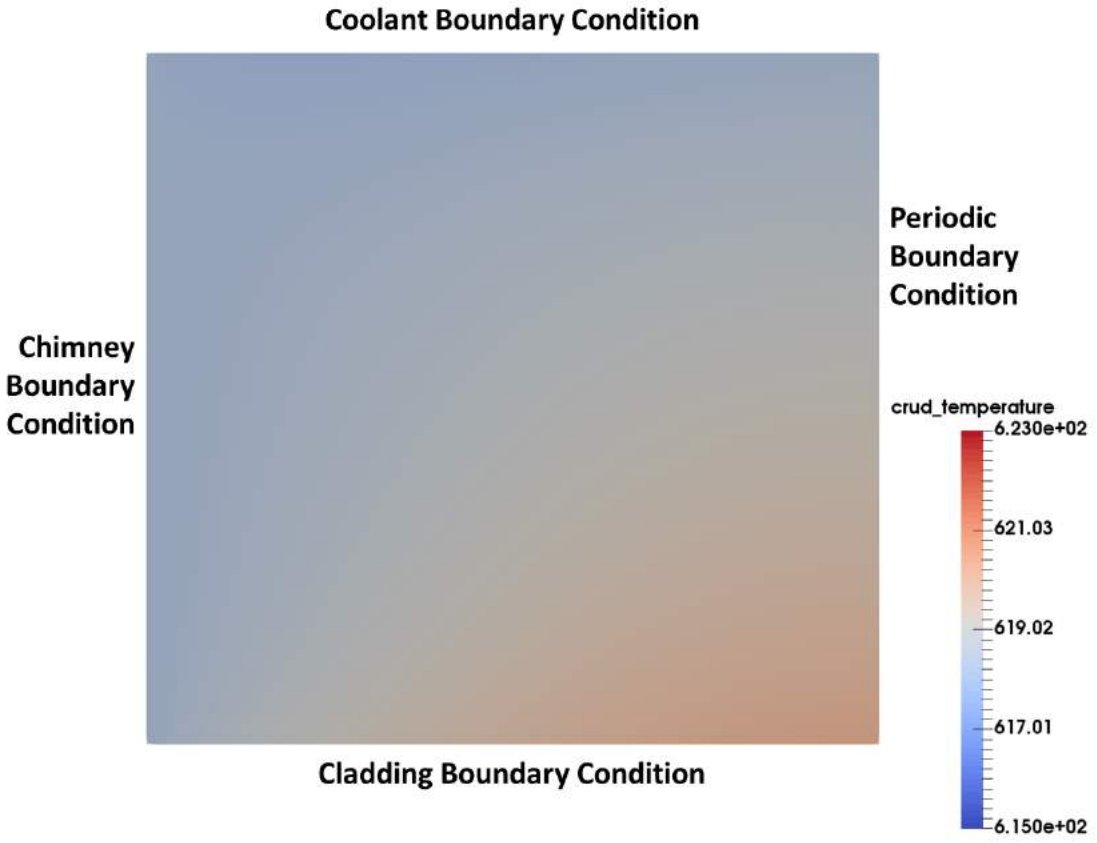


Figure 6-7: Spatial plot of temperature with in crud for case II, where porosity is constant at 7.5% throughout the crud layer and fractal dimension is calculated from porosity using equation from figure 5-39. Crud temperature is in the unit of Kelvin. The plot represents the cross-section view of crud near a boiling chimney. The vertical axis represents the height from crud-clading interface. The bottom corner of the plot represents the crud-cladding interface, while the top corner represents that the crud-coolant surface. The thickness of crud in this case is taken as 10 microns. The horizontal axis represents the distance away from the boiling chimney. The left corner represents the surface within the boiling chimney.

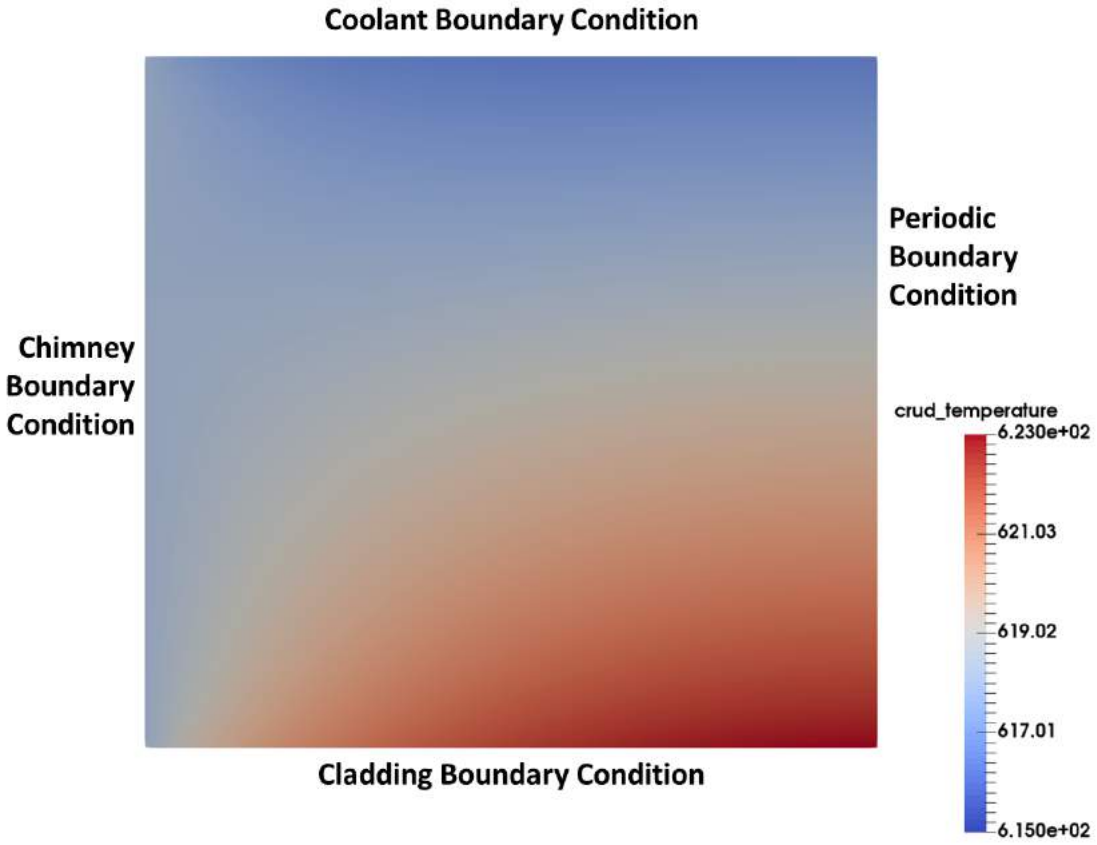


Figure 6-8: Spatial plot of temperature with in crud for case II, where porosity is constant at 49.4% throughout the crud layer and fractal dimension is calculated from porosity using equation from figure 5-39. Crud temperature is in the unit of Kelvin. The plot represents the cross-section view of crud near a boiling chimney. The vertical axis represents the height from crud-clading interface. The bottom corner of the plot represents the crud-cladding interface, while the top corner represents that the crud-coolant surface. The thickness of crud in this case is taken as 10 microns. The horizontal axis represents the distance away from the boiling chimney. The left corner represents the surface within the boiling chimney.

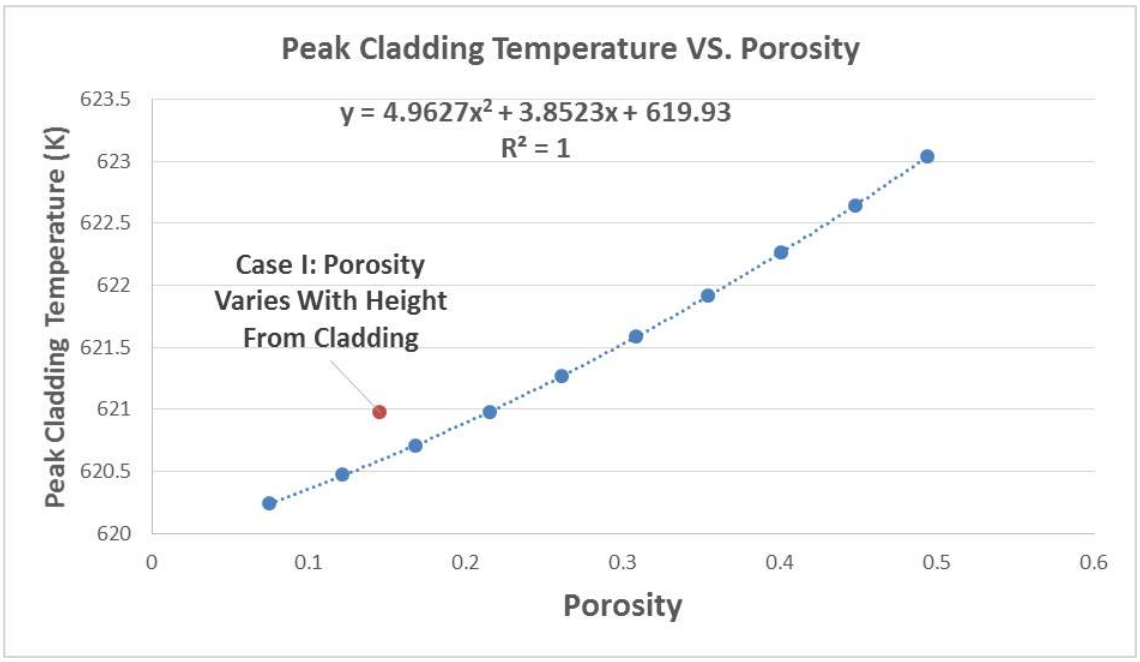


Figure 6-9: Plot demonstrating the relationship between peak cladding temperature (K) and porosity. The red point represents the result from case I.

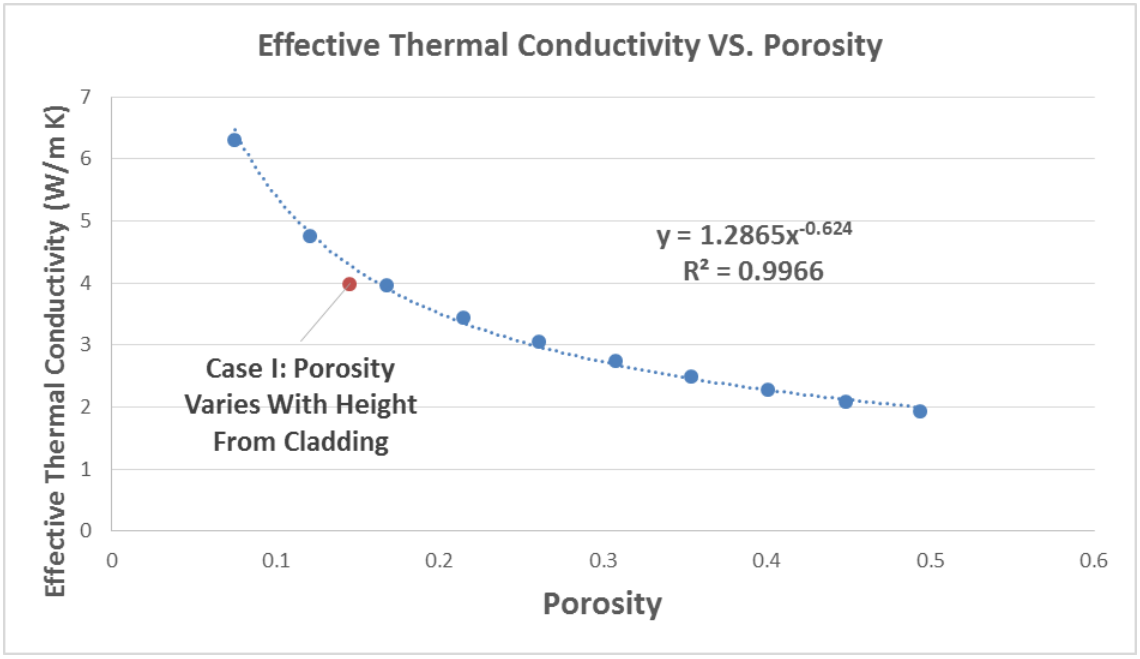


Figure 6-10: Plot demonstrating the relationship between effective thermal conductivity ($W/m \cdot K$) and porosity. The red point represents the result from case I.

### 6.2.1 Effectiveness of Crud-resistant Surface Coatings

The resulting crud on the surface-coating trials is sparsely covered by crud particles and did not form a thick layer. Therefore the analysis is geared toward the percent crud area coverage. The crud samples in this section are obtained from trials C and D. After applying the percent crud area coverage analysis to SEM images obtained for each material from the successful trials C and D, we get the results summarized in figure 5-138. $TiC$ and $ZrN$, the reductions in crud are as high as 40%. The error bars have a length of two standard deviations, which represents 95% confidence interval. Figure 5-138 shows repeatable crud reduction by $ZrN$, $ZrC$, $TiN$, $TiC$, along with crud coverage by $TiO_2$, $TiB_2$, and $MgO$ across both experiments and both image processing techniques. Only $ZrO_2$ and $Al_2O_3$ showed an increase in crud coverage between coated and control surfaces in one experiment and a decrease in another. This may be attribted to different heat fluxes across experiments that could be a result of sample ring dimensions. The higher crud concentration and the longer trial length in trial D led to an increase in crud growth compared to trial C. The choice of image processing algorithm does not change the sign of crud coverage except for the $Al_2O_3$'s case. The types of image processing algorithm and loop conditions used do not affect these conclusions. Six other materials tested failed to resist crud formation; MgO and $TiO_2$ appeared to encourage it. The important information left to be determined from this set of data is whether van der Waals (VDW) force is responsible for crud formation in PWRs. If the VDW force is responsible for crud formation, then we can use the knowledge to design crud-resistant materials.

### 6.2.2 Relationship Between Crud Area Reduction and Refractive Index

This section discusses the relationship between crud area reduction and refractive index as hypothesized in section 2.4.2.9. Figure 6-11 shows a comparison between the percentage crud area reduction and refractive that can be used for Tabor-Winterton approximation (TWA) Hamaker constants. Red dots are refractive indexes calculated using red visible light's wavelength of 633 nm, while blue dots represents refractive indexes calculated using UV's wavelength of 210 nm. The visible light's data set exhibits downward trend with the exception of TiC. TiC has the most resistance to crud despite having the highest refractive indexes at 633 nm. Tabor-Winterton approximation (TWA) works well with low refractive indices (n<1.7), but starts to break down at higher refractive index [219]. This has been verified by comparing both the TWA and the full spectral Hamaker constants for a number of materials with experimental measurements [220]. It also appears that the TWA is really only valid for material-fluid-material systems whose indices of refraction vary in similar ways across the relevant visible and ultraviolet ranges. Figure 6-12 shows a comparison of the refractive index spectra of seven of the tested materials. The important observation is that the seven materials with known refractive index in UV range almost line up in order of increasing crud resistance as the refractive

index decreases. Now, if we look back at figure 6-11 to see the trend for the blue 210 nm UV data, we can see that all materials including TiC now line up in a downward trend. This downward trend agrees with previous studies suggesting that the near-UV region is quite important in determining the Hamaker constant [221, 222]. In particular, ZrN has negative relative refractive index beyond around $0.34\,\mu m$ and suggests London-VDW repulsion at these higher wavelengths, which has been shown in previous systems [221]. These observable trends suggest that London-VDW forces are the controlling variables in designing crud-resistant materials.

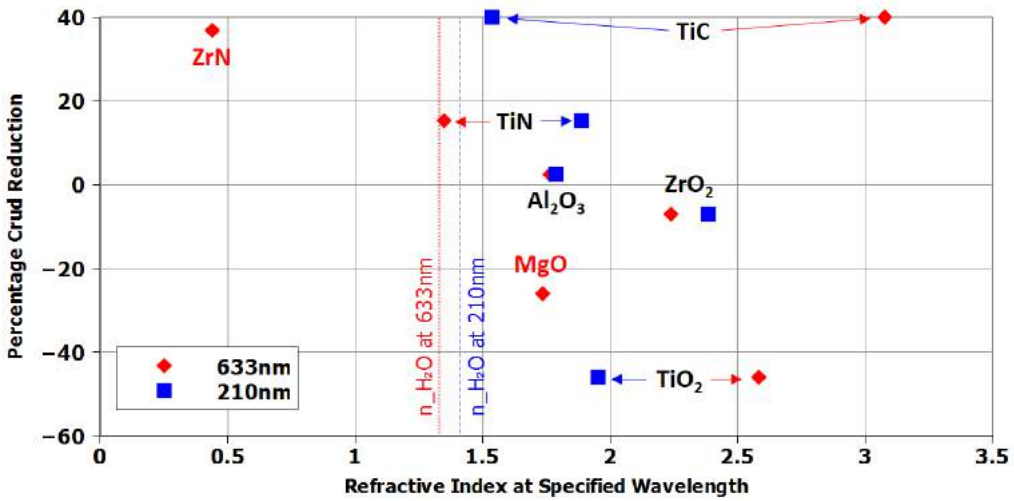


Figure 6-11: Percentage crud reduction vs. refractive index at two chosen wavelengths.

### 6.2.3 Relationship Between Crud Area Reduction and AFM Experimental Data

Chapter 4 explained the process of material selection in section 4.3.2.3. One of the determining factors for choosing coating materials to test in the IHTFP was through examining the atomic force microscopy (AFM) adhesion data by Abdulla Alhajri, Rasheed Auguste, and Pavlina Karafilis. Figure 6-13 plots the AFM adhesiveness versus crud area coverage reduction from figure 5-138 for each coating materials tested. The $NiO$ and $Fe_3O_4$ data sets represent the AFM done with $NiO$ and $Fe_3O_4$ particles, respectively. The plot shows that crud area coverage reduction increases as the $Fe_3O_4$ AFM adhesion decreases. On the other hand, we cannot see any significant correlation between the $NiO$ AFM adhesion and the crud reduction. However, the $TiC$ which is the material that we found to have the most crud reduction also have the lowest $NiO$ AFM adhesion for the and the second lowest $Fe_3O_4$ AFM adhesion. It is important to note that AFM adhesion experiment was conducted at room temperature, and therefore, may not accurately represent the actual adhesion at

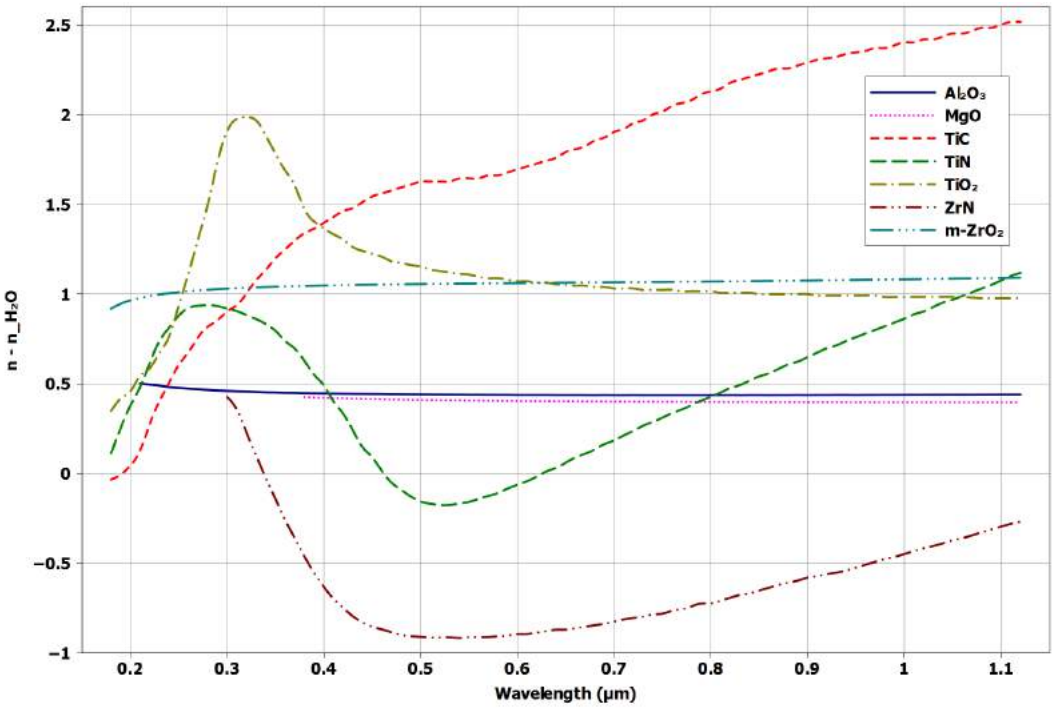


Figure 6-12: Refractive index spectra in the visible to near UV/IR ranges. The differences between refractive index of materials and the refractive index of water are used for better comparison. Source: [223] ($Al_2O_3$), [224] ($H_2O$), [225] (MgO), [226] (TiC & TiN), [227] ($TiO_2$), and [228] ($m - ZrO_2$), where 'm' stands for monoclinic.

PWR conditions.

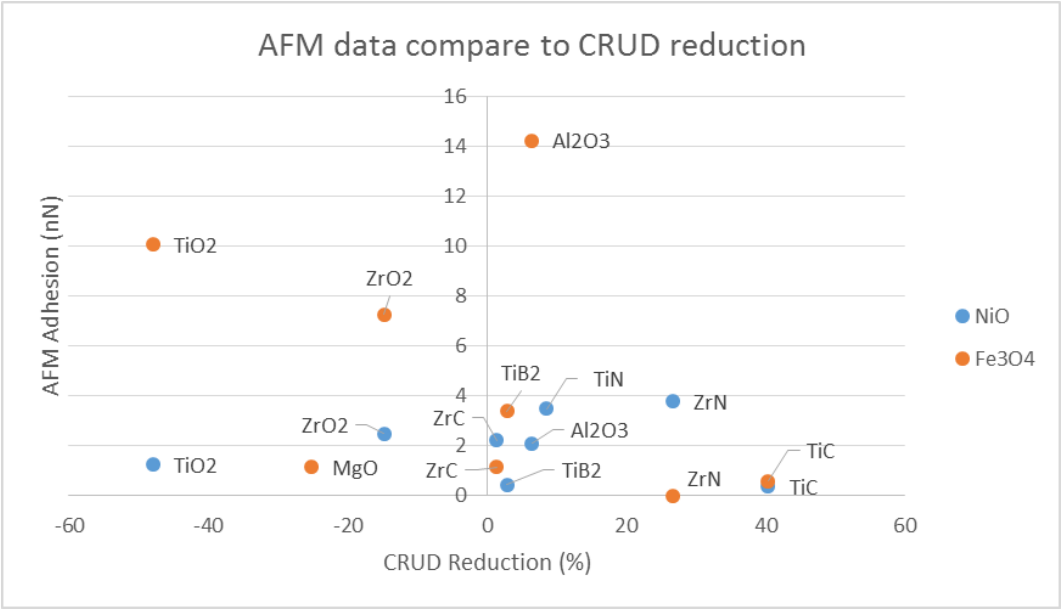


Figure 6-13: Plot comparing the AFM adhesion from figure 4-1 to the crud area coverage reduction from figure 5-138.

## 6.3 Sources of Experimental Error

There are several sources of experimental error which affect both the fractal dimension experiment as well as the surface-modification experiment. This section describes these sources of error, how they were handled, and their possible effects on the results.

### 6.3.1 Heating Element Manufacturing Imperfections

Different heating rods will yield very temperature behaviors during an experimental trial. The difference between their centerline element temperature and liquid bulk temperature will always differ by different amounts. The probable cause of this problem is that the centerline thermocouple may not be at the exact center of the heater. This problem could be solved through finding heaters with better quality. Since this error is systematic in nature, this error can be alleviated in fuel-rod coating experiments by having the control and the coated surface on the same sample ring. Each sample ring is coated with fuel-rod coating material on only one side. This way, the uncoated side can be used to gather control data. When comparing the data for crud area coverage for each material, we subtract the control data from the experimental data to understand how the fuel-rod coating can change the control data. Because both experimental data (coated) and the control data (uncoated) is on the same ring, we should get a more accurate result since the same ring should have similar conditions. This type of error does not affect the fractal analysis part of this thesis since this part deals with the characterization of crud. As long as thick crud samples can be obtained, the fractal analysis can be carried out.

### 6.3.2 Uneven Mixing of Nickel Oxide particles

The nickel oxide particles added may not mix equally within the water tank. This may lead to fluctuations of nickel oxide level between trials that can change crud amount between trials. This error would be systematic since it would happen throughout the trial. Since this is an error between trials, this error is mitigated through the use of coated/uncoated side in the fuel-rod coating experiments. This type of error does not affect the fractal analysis part of this thesis.

### 6.3.3 Uneven Roughness on Sample Ring Surfaces

The roughness of the surface on which crud grows can also have an effect on crud growth. The rougher surface will have more boiling nucleation point, which leads to more boiling and therefore more crud. This may lead to slight uneven crud growth throughout samples. This type of error leads to random errors that probably partially explains the uncertainty in crud area coverages.

### 6.3.4 Gap Between Sample Ring and Heater Tube

At the interface between the stainless steel tube covering the heater and the sample ring that crud was grown on, there should be no gap, to ensure even heat flux. However, in reality, accomplishing complete contact is very difficult. To do so, both surfaces would need to be completely smooth and the sample ring must be made so it could be press-fitted very tight to ensure better contact. But making both surfaces completely smooth is very difficult since the surfaces will still be slightly damaged during press fitting. Press-fitting sample rings too tight is also impractical since it increases the difficulty of press-fitting and increases the risk of ruining the sample ring. The differences in sample rings grip will lead to more/less contact with stainless steel heating tube which will affect the heat flux, and therefore crud growth. This is a random error. Since this is an error among sample rings, this error is mitigated through the use of coated/uncoated side in the fuel-rod coating experiments. This type of error does not affect the fractal analysis part of this thesis.

### 6.3.5 Unequal Heating Along the Heating Rod's Length

The heating rod in the middle of the test section could giving heat unevenly throughout its length. This problem originate both, from how well the heating rod is manufactured, and from how well it was press-fitted into the stainless steel tube housing it. Again, this problem is mitigated by coating only one side of sample ring. Simlar to other type of errors, this type of error does not affect the fractal analysis part of this thesis.

## 6.4 Experimental Improvements

There are several experimental improvements that can be useful for future experiments. First, we can attempt to procure new heating rods that have higher heat flux, more similar to that of PWRs. Second, the sapphire windows can be fixed so that other experimental opportunities may open up. Third, if the sapphire windows are fixed, we could revisit the idea of using laser triangulation to measure crud thickness in situ. Fourth, Raman spectroscopy can be applied to measure material composition in situ, given that the sapphire windows are fixed.

### 6.4.1 Heating Rod Procurement

Both the chapter 4 and chapter 5 demonstrated how much troubles we have had with heating rods. Heating rods made by Cormet are very expensive and have very long delivery time. The subsequent decisions were to use the MIT machine shop for manufacturing heating rods and procure heating cartridges from National Plastic Inc. This led to a significant decrease in price and delivery time. However, heater rods' reliability problems were never addressed. Section 4.2.0.5 demonstrated that

most experimental failures so far are either caused by heating rod failures or the lack of crud growth. In a way, these two problems have the same root, the unreliability of heating rods. Heating rod failures happen because we cannot get a very accurate element temperature, and therefore, tends to push the heating rod too far. The lack of crud growth happened because we use lower, more conservative pressures during the experimental trial.

Up until the time when this thesis is being written, we believed that these failure rates could be normal in custom-made, internally-heated heating rods. However, CRIEPI's crud experimental information [118], given to us with courtesy of Dr. Hirotaka Kawamura, demonstrated that it is possible to procure heating rods with a higher heat flux of 800 $kW/m^2$, as oppose to 206 $kW/m^2$ we currently use, as shown in table 2.5. Using a heating rod with higher heat flux will aid crud growth and make IHTFP's conditions closer to that of PWRs. Moreover, the same table shows that the heating rods that was procured for CRIEPI's loop had a smaller inner diameter of 9.48 mm and the outer diameter of 10.72 mm, as oppose to the inner diameter of 12.5 mm and the outer diameter of 17.5 mm we currently use. Smaller diameter for heating rods will widen flow areas and bring IHTFP's flow conditions closer to that of PWRs. The fact that CRIEPI's experiments can last for as long as 2,000 hours demonstrated their heating rod's reliability. If we can acquire the same type of heating rod as CRIEPI, the IHTFP's reliability and ability to imitate PWR conditions will improve immensely.

### 6.4.2 Sapphire Windows

At the point of writing this thesis, experiments conducted so far did not utilize the sapphire windows. This is because sapphire windows always turn opaque from corrosion after a week of running the loop. This problem can potentially be solved using the diamond disc to shield PWR conditions water from reaching the sapphire windows. Solving this sapphire windows problem should allow in situ laser triangulation, in situ Raman spectroscopy, and in situ observation of bubbles with a microscopic camera.

### 6.4.3 Laser Triangulation

The laser triangulation idea was shelved during this study because of the sapphire window problem. If sapphire windows are able to stay clear throughout the trial, laser triangulation can be used to measure crud thickness in situ. Measuring crud thickness in situ will allow us to obtain data on crud's actual growth rate over time, something that has never been done.

### 6.4.4 Raman Spectroscopy

If sapphire windows work properly, Raman spectroscopy can be used to identify the chemical composition of the cladding surface, in situ. This will allow us to observe how cladding coating composition changes with time, as crud grows on its surface. Gaining this data may yield insights into how crud grows.

## 6.5 Future Experiments

There are many interesting future experiments that can be conducted. They include both follow-up experiments, as well as alternate approaches to the current experiments. The future experiment ideas include AFM at PWR conditions, experimental measurement of refractive indexes, testing of materials with very low refractive index, testing of hydrophobic/biphilic coatings, and lastly testing of coatings with very low surface energy.

### 6.5.1 AFM at PWR conditions

As mentioned earlier, the experiments to obtain the AFM data were conducted at room temperature and atmospheric pressure. Since materials may not behave in a similar way at different temperature and pressure, this can lead to errors. Pressurized, heated chamber for AFM can be built for obtaining AFM data at PWR conditions. These PWR conditions AFM data may exhibit better correlations with crud area coverage reductions or theoretical Hamaker constants found in this study.

### 6.5.2 Experimental Measurement of Refractive Indexes

Refractive index data for many materials used in this study are still missing, especially in the near-UV range (10 - 400 nm). More resources should be dedicated to the experimental measurement of these and similar coatings. If we have full refractive index data, we can become more certain whether the full spectral refractive indexes comparison do indeed explain the crud area coverage reduction.

### 6.5.3 Testing of Materials with Very Low Refractive Index

Section 6.2.2 demonstrates that there may be a relationship between the refractive index and the crud reduction amount. This relationship indicates that London-van der Waals force is the major contributor to the intermolecular forces between crud particles and fuel-rod coatings. This means that a material with very low refractive index may be the answer to the crud-resistant fuel-rod coating. This idea is not entirely new. Teflon AF polymer, a material commonly used in non-stick pan employs similar ideas. Teflon is non-polar and, therefore, have no permanent dipoles. This means that Keesom-van der Waals and Debye-van der Waals forces are irrelevant to its intermolecular force.

The only relevant type of intermolecular force left is the London-van der Waals force, which correlates with the underlying material's refractive index. Teflon AF polymer has the lowest refractive index of any known polymer, as well as the lowest dielectric constant of any known solid polymer [229]. This explains why food does not stick to the Teflon AF polymer. Unfortunately, Teflon AF polymer has a melting point of 327 $^{o}$C which is not enough for it to work at PWR thermal conditions.

### 6.5.4 Hydrophobic/Biphilic Crud-Resistant Coatings

Crud particles in water attached itself to the cladding when liquid layer between bubbles and cladding surface dries out. By manipulating the bubble's contact angle with a hydrophobic and biphilic coating, we hope to prevent the liquid layer from forming, and therefore mitigate or prevent crud formation. As mentioned earlier, when sub-cooled boiling bubbles bulge out, there are liquid layers in between the bubble and the fuel rod cladding surface. This layer of liquid dries out from intense cladding heat flux and crud particles inside the liquid get deposited on the fuel rod cladding surface.

In an earlier section, surface chemistry modification for crud-resistant attempt to change how crud particles stick to the surface of fuel cladding. What if, instead, the sub-cooled boiling bubble is manipulated so that no layer exist to dry out happening in the first place. The hypothesis would be that if this layer of water does not exist, and does not dry out, no crud particles will get deposited. Following sections will explore the types of coatings that could possibly resist crud through manipulating boiling bubbles.

#### 6.5.4.1 Hydrophobic Crud Resistant Coating

The type of surface that might be able to manipulate bubble formation is hydrophobic surfaces. To understand how hydrophobic surface really works, there are several background concepts needed as present below.

**Background on Contact Angle and Hydrophobic/Hydrophilic surface** The contact angle is important in understanding the concept of hydrophobicity. In a system with droplet sitting on a flat horizontal surface, the contact angle is the angle made by the liquid-solid interface to liquid-vapor interface in the with a solid surface [230]. Figure 6-14 gives a good illustration of how contact angle is defined.

Contact angle help quantifies the wettability of a solid surface. When the contact angle is low, the liquid will spread better on the surface, implying better wettability. On the other than if the contact angle is very high, the liquid will avoid solid surface, generating less liquid spread and less wettability. A hydrophobic surface is defined as a surface that has a contact angle of more than 90 degrees, while the superhydrophobic surface is defined as a surface that has a contact angle of more than 150 degrees.

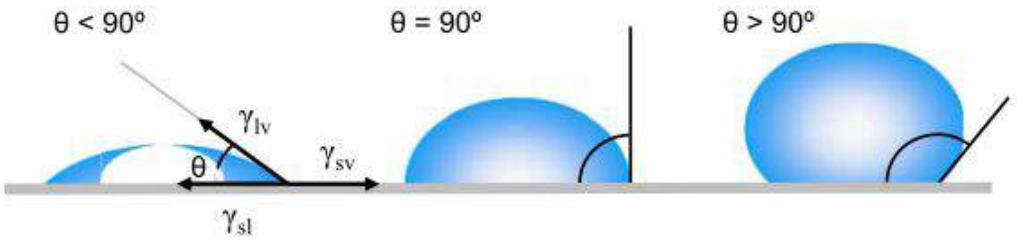


Figure 6-14: Illustration of what contact angle is, as appeared when there is liquid drop on a smooth surface [230].

**Explanation of Contact Angle, Surface Tension, and Surface Energy** In any liquid, molecules in the droplet will pull each other together. Where a liquid molecule is surrounded by other liquid molecules, the liquid molecule will get pulled by other liquid molecules in all direction, resulting in a net force of zero. On the exposed surface, however, where droplet does not have neighboring molecules in all direction to provide balance in force, neighboring molecules will pull the surface molecule inward, creating an internal pressure. Because sphere has the least surface area to volume ratio, liquid molecules will pull themselves together into a sphere, when the whole surface are in contact with are gaseous or empty. The intermolecular force between molecules that make this happens is called "surface tension" [230]. Figure 6-15 supports this explanation with an illustration.

In a solid surface, the similar situation happens, where surfaces are less energetically favorable than the bulk material, otherwise the material will try to form more surface, and ultimately lead to sublimation. "Surface energy" quantifies the amount of energy which has to be expended in order to increase the size of the surface. It is quantified in terms of energy per unit area created. In solid surface, the surface energy is usually applied. In liquid surface, surface energy and surface tension are identical, and surface tension is usually used instead.

Now, when a horizontal solid surface and gravity is added to the droplet system mentioned above, the droplet will sit on the solid surface with gravity pulling down. As a result, the droplet will no longer by spherical, as gravity will pull the droplet down and liquid molecules will be affected by the intermolecular force from the solid surface as well. If a solid surface is better at attracting liquid molecule, the liquid will spread better on the surface to take advantage of the solid surface's attraction force in balancing out its force. This leads to lower contact angle which defines the spread of liquid on the surface. On the other hand, in an opposite situation where the liquid does not get attracted well by the solid surface, the droplet liquid molecules will avoid the surface, and get attracted to each other instead. This will form a shape that is closer to a sphere, with the less liquid spread on the surface, and subsequently more contact angle. What affects this attraction between liquid and solid interface are the surface tension of the liquid, as well as the surface energy of solid. If a surface has more surface energy, it will better attract the liquid molecules, and therefore lead

to lower contact angle.

Figure 6-15: Illustration of the dynamics within the water droplet sitting on a surface. Circles are the liquid molecules which pull each other together by the force shown by the arrow [230].

**Young's Equation** The contact angle of a liquid drop on a surface is defined by the mechanical equilibrium of the drop under the action of three interfacial tensions [230]. This mechanical equilibrium is what defines Young's equation that can be used to characterize contact angle:

$$\gamma^{lv} cos\theta_c = \gamma^{sv} - \gamma^{sl} \tag{6.1}$$

where $\gamma^{lv}$ is the liquid-vapor interface surface tension $(J/m^2)$, $\gamma^{sv}$ is the solid-vapor interface surface tension $(J/m^2)$, $\gamma^{sl}$ is the solid-liquid interface surface tension $(J/m^2)$, and $\theta_c$ is the contact angle (degree or radian). Figure 6-16 is an illustration of this equation. Young's equation is only applicable for a static system for calculating static contact angle since one of the assumptions is that the system is in complete equilibrium.

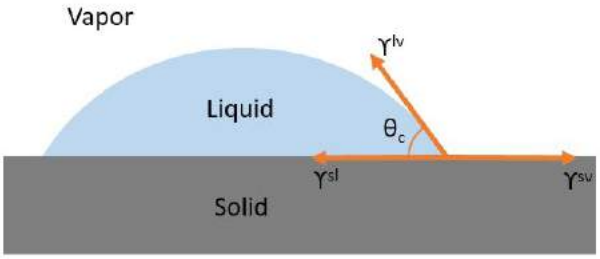


Figure 6-16: Illustration of surface energy balance on a liquid droplet on the solid horizontal surface. $\theta_c$ is Young's contact angle of the liquid droplet. $\gamma^{lv}$ is the liquid-vapor interface interfacial free energy. $\gamma^{sl}$ is the solid-liquid interface interfacial free energy. And, $\gamma^{sv}$ is the solid-vapor interface interfacial free energy. The balance of force between these three forces are what made up Young's equation.

**Contact Angle Hysteresis** In a dynamic system with movement, Young's equation is no longer applicable. Other than that, there also exist many states where contact angle may be different from theoretical Young's contact angle, that are theoretically unstable but so long-lived that it is stable for practical purposes. In a system that three-phase contact line is actually in motion, or was in recently in motion that the system did not adjust itself to equilibrium yet, the contact angle is

instead called “dynamic contact angle.”

Dynamic contact angle that is formed when liquid advances are called “advancing contact angle” while the dynamic contact angle formed when liquid recedes is called “receding contact angle.” Advancing contact angle’s value will be more than the static contact angle while receding contact angle will be less than the static contact angle. Dynamic contact angle will fall in a range between maximum advancing contact angle and minimum receding contact angle. This range is called “contact angle hysteresis.” Contact angle hysteresis arises from surface roughness and heterogeneity in the material. Surface roughness and heterogeneity present a barrier to three-phase contact line motion. Therefore the more roughness and heterogeneity will lead to more contact angle hysteresis.

**How Does Hydrophobic Coating Works?** Now that the background was explained on how hydrophobic coating works, we examine the relationship between contact angle and crud growth in bare zircoloy surface without any coatings. Zircaloy-4 has a static contact angle of 49.3 degrees [231]. When sub-cooled boiling bubbles are advancing on cladding surface, the contact angle used will be the receding contact angle. This because bubble advancement is the opposite of liquid droplet advancement. The receding contact angle will be somewhat lower than static contact angle depending on the roughness of zircaloy surface. So in bare zircoloy, as sub-cooled boiling bubbles advance, there will be liquid layer between this 49 degrees (or less) contact angle to dry off depositing crud particles. This is shown in figure 6-17, on the left.

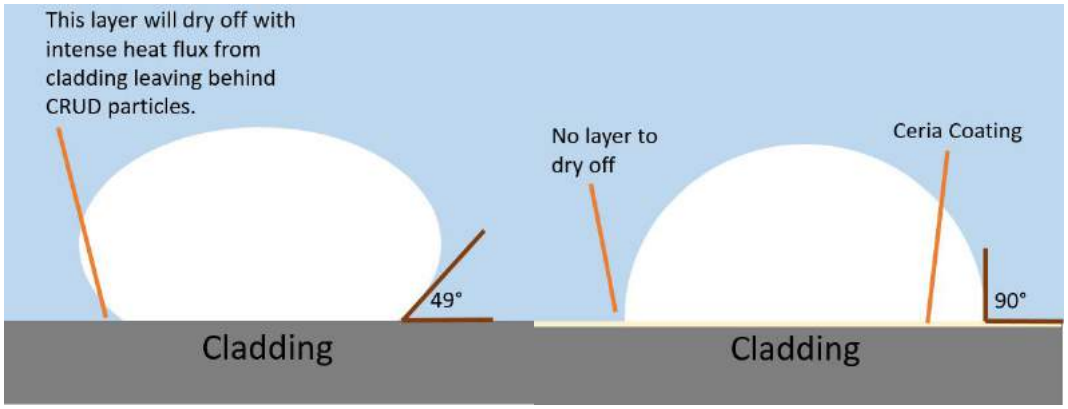


Figure 6-17: Illustration of the of how bubble should theoretically grow in bare zircaloy cladding (left) and on cladding with ceria (cerium oxide) hydrophobic coating [230].

On the other hand, if we have a layer that has very high contact angle, there should be no liquid layer to dry off and generate crud layer. These surfaces with high contact angle are called “hydrophobic” surface. In the illustration figure 6-17, the sub-cooled boiling bubble for ceria hydrophobic sputtered coating is shown. The receding contact angle, which represents the contact angle when sub-cooled boiling bubbles are advancing, is 90 degree [232]. Hence, if the cladding is coated with ceria, there should be no liquid layer to dry off and generate crud layer.

**Material Selection** Most existing hydrophobic materials are organic materials with low melting point. Most hydrophobic materials will not last at pressurized water reactor (PWR) pressure, temperature and flow. Fortunately, recent research conducted by Gisele Azimi at MIT discovered hydrophobic ceramics [232].

**Cerium Oxide Coated Sample** The central idea behind this experiment is to control boiling and crud deposition sites, by spatially altering the hydrophobicity of the cladding surface. It will be more likely for bubbles to grow outwards at hydrophobic patches than on the existing hydrophilic $ZrO_2$ surface since the higher contact angle allows less surface tension in the bubble. The higher contact angle on the hydrophobic areas should allow for the nucleation of bubbles that do not bulge out, so there should be a liquid layer between the bubble and the cladding surface that can dry out and induce deposition. The preferred materials to use as the hydrophobic patches are rare earth oxides, recently found to be hydrophobic [232]. This entire family of ceramics comprising the entire lanthanide oxide series is intrinsically hydrophobic. Figure 6-18 exhibits the contact angles of these hydrophobic ceramics.

| Surfaces | Measured contact angles ($\theta_{adv}$) | | | Contact angle hysteresis ($\theta_{adv,w} - \theta_{rec,w}$) |
|---|---|---|---|---|
| | Water | Ethylene glycol | Diiodomethane | Water |
| *Sintered* | | | | |
| $CeO_2$ | 103 ± 2 | 78 ± 2 | 55 ± 2 | 48 ± 1 |
| $Pr_6O_{11}$ | 102 ± 3 | 80 ± 3 | 64 ± 4 | 52 ± 2 |
| $Nd_2O_3$ | 101 ± 3 | 76 ± 4 | 58 ± 3 | 49 ± 2 |
| $Sm_2O_3$ | 107 ± 2 | 84 ± 3 | 58 ± 2 | 47 ± 3 |
| $Eu_2O_3$ | 104 ± 4 | 78 ± 4 | 55 ± 3 | 42 ± 1 |
| $Gd_2O_3$ | 109 ± 2 | 85 ± 5 | 67 ± 3 | 40 ± 1 |
| $Tb_7O_{12}$ | 107 ± 3 | 69 ± 4 | 45 ± 5 | 47 ± 2 |
| $Dy_2O_3$ | 105 ± 5 | 77 ± 3 | 55 ± 3 | 55 ± 1 |
| $Ho_2O_3$ | 115 ± 3 | 88 ± 2 | 60 ± 5 | 58 ± 2 |
| $Er_2O_3$ | 108 ± 5 | 82 ± 4 | 58 ± 5 | 58 ± 1 |
| $Tm_2O_3$ | 112 ± 4 | 87 ± 2 | 60 ± 2 | 52 ± 1 |
| $Yb_2O_3$ | 100 ± 5 | 73 ± 4 | 56 ± 5 | 45 ± 1 |
| $Lu_2O_3$ | 98 ± 3 | 79 ± 5 | 55 ± 4 | 47 ± 1 |
| *Sputtered* | | | | |
| $CeO_2$ on smooth silicon | 109 ± 3 | 80 ± 3 | 63 ± 2 | 19 ± 1 |
| $Er_2O_3$ on smooth silicon | 110 ± 2 | 81 ± 2 | 65 ± 2 | 30 ± 2 |

Figure 6-18: Table showing advancing contact angle and contact angle hysteresis measured in an experiment of rare earth oxides. These measurements are done at atmospheric pressure and room temperature [232].

**Why Cerium Oxide Coated Sample?** Figure 6-18 shows what Azimi found in her experiment which indicates what type of Rare-Earth oxides has good hydrophobic properties. Most

rare-earth oxides presented in this table are indeed rare and expensive except for Cerium Oxide. Because cerium oxide is very cheap, cerium oxide should be the most practical type of coating if we want to actually apply these coatings to industry. Hence, we chose cerium oxide as the material we will use for this experiment.

**Adapting Azimi's Data to Higher Pressure and Temperature** It is useful to note that the pressure associated with this table is atmospheric pressure and room temperature. In crud loop, pressure is 155 bars and temperature can be as high as 320 $^oC$, therefore the value of contact angle we expect in the reactor will be higher accordingly. The basis for the expectation that the contact angle will be higher comes from relevant molecular dynamics predictions and data from the literature [233]. Although studies on the influence of pressure and temperature on the contact angle of crud loop's exact system are not widespread, the $CO_2$-water contact angle system is widely studied since it ties directly $CO_2$ sequestration technology. They are similar systems with the gas-water-solid interfaces. As shown in figures 6-19 and 6-20, the influence of pressure on contact angle is that the contact angle increase with pressure increase, while there is no clear relationship between temperature and contact angle. Therefore, in crud loop where high pressure is expected, we expect the contact angle to be higher than shown on Azimi's data. Therefore, using Azimi's data as contact angle in crud loop system should be a low conservative estimate. Other than this, an experiment planned by Professor Buongiorno's group aim to get experimental data on contact angle at high pressure in the steam-water-solid system.

Table 1.
Molecular dynamics predictions for the influence of pressure and temperature on the water–$CO_2$–quartz contact angle $\theta$ and $CO_2$–water interfacial tension $\gamma$.

| Reference | Influence of pressure | Influence of temperature |
|---|---|---|
| Liu et al. [51][a] | $\theta$ increases | |
| Iglauer et al. [12] | $\theta$ increases; $\gamma$ decreases | $\theta$ decreases; $\gamma$ increases |
| McCaughan et al. [52] | $\theta$ increases | |
| Tsuji et al. [53] | Constant $\theta$; $\gamma$ decreases | $\gamma$ constant or decreases |
| Nielsen et al. [54] | $\gamma$ decreases | $\gamma \sim$constant |

a Liu et al. [51] simulated a β-cristobalite surface.

Figure 6-19: Table showing the influence of pressure and temperature on the contact angle of water-$CO_2$-quartz system predicted by molecular dynamics simulation. The general trend here is that pressure increase lead to increase in contact angle, while there are no clear influence of temperature on contact angle [233].

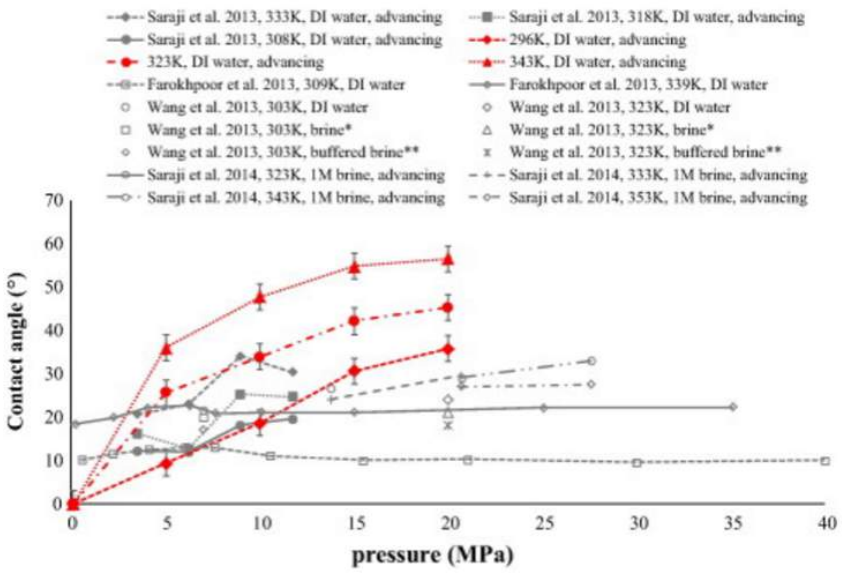


Figure 6-20: Table of data that shows the influence of pressure and temperature on the contact angle of water-$CO_2$-quartz system. The general trend shown here is that contact angle will either increase or stay constant as pressure increase. When temperature increase, contact angle may increase or stay constant [233].

**Conservative Contact Angle Prediction for Crud Loop System with Ce$O_2$ Sample** Another aspect to notice is that sintered Ce$O_2$ has a high contact angle hysteresis. This is not preferred because when bubbles are advancing on cladding surface, the contact angle used will be the receding contact angle. This means that if the contact angle hysteresis is 48 degree while advancing contact angle is 103 degree, the receding contact angle when the bubble is advancing will be 55 degrees. 55-degree contact angle is not very high which means that there might still be a liquid layer dries and leave crud particle. The reason that the contact angle hysteresis is quite high in sintered sample is because they are not smooth. As explained earlier about hysteresis, high hysteresis is most likely caused by the roughness pinning the liquid-vapor-solid interface in place. On the other hand, the sputtered Ce$O_2$ that will be used in our experiment has the contact angle of 109 degrees and the contact angle hysteresis of only 19 degrees. Because of this, the contact angle during bubble advancement is expected to be 90 degrees. This is how we arrived at the 90 degrees number shown in figure 6-17.

#### 6.5.4.2 Biphilic Crud Resistant Coating

The hydrophobic material has a potential for crud resistance. However, it also has its downside when it comes to increasing critical heat flux (CHF) of fuel. Critical heat flux is the maximum limiting heat flux tolerance for a reactor which should never be reached. Critical heat flux for PWR is usually

limited by departure from nucleate boiling (DNB), which is where the heat flux is high enough to turn nucleate boiling into film boiling. Film boiling is detrimental for heat transfer rate, so when it happens, fuel will heat up quickly and possibly fail. To prevent such problem biphilic coating is one way to tackle the problem. Biphilic surface also offers another benefit beyond prevention of DNB as well.

**Why Do We Want Biphilic Coating?** There are three major reasons behind why we might want to use biphilic coating as oppose to hydrophobic coating.

**Prevention of Departure from Nucleate Boiling Condition** First reason is because the hydrophobic coating is more likely to cause departure from the nucleate boiling condition. Departure from the nucleate boiling condition or film boiling condition is the condition that happens when the heat flux is so high that liquid water no longer touches the boiling surface. Vapor film is created throughout the boiling surface. This condition is characterized by decreased heat transfer rate which is detrimental to the fuel in transient scenarios where huge heat transfer rate is needed.

The related experiment of how contact angle affects DNB condition has been conducted by Ahn (2010) [231]. Although the experiment was designed to make the surface more hydrophilic, it still shows that the smaller contact angle will lead to higher DNB heat flux, while higher contact angle will lead to lower DNB heat flux. Table 6-21 shows that as contact angle decrease and the surface become more hydrophilic, the departure from the nucleate boiling increase to higher heat flux. Although not shown exactly on the table, this also implies that departure from nucleate boiling heat flux will decrease as contact angle becomes higher and the surface becomes more hydrophobic. Hence the statement above on hydrophobic surface causing departure from nucleate boiling.

**Table 2**
The surface characteristics of the typical test samples and CHF data.

| Anodization time (s) | Contact angle (°) | Average roughness (μm) | Spreading | ONB (°C) | CHF (kW/m²) |
|---|---|---|---|---|---|
| 600 | 0 | 0.32 | Large | 121 | 1924 |
| 600 | 0 | 0.31 | Large | 123 | 1770 |
| 300 | 2.1 | 0.07 | Small | 134 | 1406 |
| 180 | 3.2 | 0.05 | Small | 130 | 1669 |
| 60 | 9.1 | 0.15 | Small | 132 | 1352 |
| 45 | 14.6 | 0.11 | None | 121 | 1167 |
| 30 | 15.6 | 0.13 | None | 121 | 1148 |
| 15 | 25.7 | 0.16 | None | 123 | 1240 |
| 15 | 29.4 | 0.15 | None | 122 | 1272 |
| N/C | 49.3 (bare) | 0.15 | None | 121 | 1004 |

Figure 6-21: This table from Ho Seon Ahn's paper shows how contact angle relate to CHF (critical heat flux) condition. CHF, in this case, is essentially limited by departure from nucleate boiling condition. The table shows that as contact angle decrease and the surface become more hydrophilic, the departure from nucleate boiling increase to higher heat flux [231].

As explained earlier, for boiling on a hydrophilic surface, there will be a liquid layer between the boiling bubble and the hydrophilic surface. Although this liquid layer can dry off leaving crud particles behind, as explained earlier, it also gives a benefit when it comes to slowing the start of film

boiling. In hydrophilic surface, liquid water will be more likely to flood in between vapor in boiling bubbles and cladding surface, contacting the surface, cooling down the cladding surface. This makes the departure from the boiling condition, where liquid water is no longer in contact with cladding surface throughout the whole cladding surface, more unlikely. Now imagine the opposite for the hydrophobic surface. In hydrophobic surface, it is less likely for water to flood between the vapor bubble and the cladding surface. Hence, these bubbles are more likely to expand on the surface of hydrophobic cladding and eventually connect to form film boiling. This will make the heat flux that triggers the departure from nucleate boiling (DNB) condition lower, making reactor less safe.

In the case of a biphilic surface, we get the advantage of both worlds. The bubble expands within hydrophobic coating patches without generating liquid layer that can deposit crud. But if heat flux becomes too high, and sub-cooled boiling bubble expands enough to reach the bare hydrophilic surface, it will be restricted from further expansion by the hydrophilic surface. This will make it less likely for DNB to occur.

**Controlling Boiling Nucleation Sites and Bubble Expansions** Second reason why we might want a biphilic surface as oppose to the pure hydrophobic surface is related to controlling boiling nucleation site. It is hypothesized that the boiling will happens mostly at hydrophobic patches, for the reasons that will be explained in next sub-section. On full hydrophobic coating scenario, the sub-cooled boiling bubble can expand out of anywhere randomly. During the sub-cooled boiling bubble expansion, it is more likely for the bubble to form a liquid layer to dry-off. On hydrophobic patches, sub-cooled boiling expands in the patches until it is enough and eventually, part of it leave the surface, and another part will shrink somewhat before expanding again. When it shrinks down, the contact angle will be the same as droplet advancing contact angle, which is higher than receding contact angle. Another bubble will then grow out of this without moving around the liquid-vapor-solid interface very much. This minimizes the movement of sub-cooled boiling bubbles that could cause the liquid layer to form.

**Prospect of Improving Overall Heat Transfer** The Third reason for using biphilic coating is the prospect of improving heat transfer. Betz (2013) [234] reported better heat transfer for using biphilic surface on atmospheric pressure. It is entirely possible that this trend will continue into high-pressure and high-temperature system such as that of PWR. If the biphilic coating does offer both crud control capability and better heat transfer, it could be the new type of fuel upgrade that offers improve capabilities to all PWR.

**Why Will We Get Boiling at Hydrophobic Patches?** One big assumption of using biphilic coating is sub-cooled boiling bubbles will start on the surface of hydrophobic patches as oppose to randomly anywhere on the surface. This subsection will explore the hypothesis behind this

assumption. If the surface is hydrophilic, water can easily form layer underneath the bubble. This layer can expand to eventually flood the nucleation site and cut off the bubble from heating surface ending bubbling process in the nucleation site. On the other hand, if the surface is hydrophobic, this bubble layer underneath should not exist, therefore it is less likely for liquid water to flood and end boiling at the nucleation site. Therefore, our hypothesis is that over time, the nucleation site in hydrophobic part of the biphilic surface will stay, while it is less likely to get nucleation site in the hydrophilic surface. Therefore, with a biphilic surface which contains patches of hydrophobic material on the hydrophilic surface, it should be possible to control boiling nucleation to be within the patches.

**Determining Cerium Oxide Patch Size** To determine the cerium oxide patch size that makes sense, we use flow sub-cooled boiling correlation developed by Zeitoun in 1996 [235]. Cerium oxide patch should be somewhat larger than bubble size. This because the part that should work in preventing crud is the hydrophobic part. Therefore, we want the sub-cooled boiling bubbles to only grows on the hydrophobic surfaces. If cerium oxide patch is smaller than a bubble, then the bubble will grow out of the patch and the hydrophobic crud mitigation effect will be nulled.

There are two bubble size calculations that was done to determine how sub-cooled boiling bubbles might grow. The following equation is useful for deriving the smallest possible sub-cooled boiling bubble size. It is derived from surface tension mechanical equilibrium equation. If the bubble is larger than this smallest bubble size, it will grow. Otherwise, if the bubble is smaller than this smallest bubble size, it will shrink to nothing.

$$r_{bubble} = \frac{2\sigma T_{sat}}{\rho_g h_{fg} \Delta T} \tag{6.2}$$

Plugging in conditions of 115 bars and 310 Celsius, smallest bubble size of 6.616 microns are obtained. Zeitoun Shoukri Correlation [235] is useful for finding bubble mean Sauter diameter (or equivalent sphere diameter). Zeitoun Shoukri Correlation rearranged to get bubble radius is as follows:

$$r_{bubble} = \sqrt{\frac{\sigma}{g\Delta\rho}} \frac{0.0683(\frac{\rho_L}{\rho_g})^{1.326}}{Re^{0.324}(Ja + \frac{149.2(\frac{\rho_L}{\rho_g})^{1.326}}{(\frac{q^*}{Gh_{fg}})^{0.487} Re^{1.6}})} \tag{6.3}$$

The calculation by Zeitoun Shoukri Correlation, with conditions of 115 bars and 310 Celsius, shows that bubble mean Sauter diameter is around 54.5 microns. Since sputtered ceria has a receding contact angle of 90 degrees, we know that the base of the bubble of 54.5 microns size will be approximately 54.5 microns. This means that, at a bubble nucleation site, when a bubble left the site, it should also left behind small bubble attached to the surface. If the bubble left behind has the critical size to grow again (in 115 bar case, it is 6.6 microns) it will grow larger before departing

again. As mentioned before, since we want the bubble to grow in ceria patch to take advantage of its hydrophobic property, we decided to put the patch size at 60 microns slightly higher than 54.5 microns average bubble size.

#### 6.5.4.3 Text Matrix & Loop Parameter

The limitation of pitch in ceria patch was due to the coating procedure's equipment. Figure 6-22 and table 6.1 of ceria patch spacings that we planned for this experiment. All types of biphilic grids as well as hydrophobic coatings, in a total of five types of surfaces, are manufactured on a single sample ring.

| Grid number | Diameter ($\mu m$) | Pitch ($\mu m$) | Spacing ($\mu m$) | Number of Patches | Total Length ($\mu m$) |
|---|---|---|---|---|---|
| 1 | 60 | 70 | 10 | 6 | 410 |
| 2 | 60 | 80 | 20 | 5 | 380 |
| 3 | 60 | 100 | 40 | 5 | 460 |
| 4 | 60 | 120 | 60 | 4 | 420 |

Table 6.1: Table showing the four types of grids of ceria patches that will be tested in the experiment. The diameter is the diameter of each ceria patch. Pitch is the length between the center of each ceria patches. Spacing the length between the edge of each ceria patches. The number of patches represent the number of patches on the shorter side of the grid. Total length is the total length of the shorter side of the grid calculated from the number of patches, diameter, and spacing.

#### 6.5.4.4 Procedure in Fabricating the Biphilic Surfaces

To create biphilic surfaces with very small patches, the first method that seems obvious is the use of ion deposition capability of some SEM with FIB capability. However, because of the high melting point of the material that could be used for the biphilic purpose such as cerium oxide with 2400 Celsius melting point, it is impractical to deposit the patches using ion beam capability of some SEM. There are multiple ways to create biphilic surfaces in more roundabout ways.

One way to make biphilic surface is by using photoresist mask. In this procedure, photoresist coating such as PMMA coating may be applied on the relevant zircaloy surface. Then part of the surface that will be future patches can be exposed to UV light. Exposing photoresist coating to UV light will alter the coating chemically. This allows those altered photoresist portions to dissolve under specific solutions. This essentially creates a mask of photoresist. The patch material can then be sputtered on the surface that had the altered photoresist removed. This will allow partial exposure of patch material on the zircaloy surface. Lastly, solution can be used to dissolve away the rest of photoresist coating leaving only zircaloy surface with sputtered patch material. Figure 6-23 summarizes this method. This method has the main advantage that the photoresist mask or partially exposed photoresist can be bought with patterns already on them. This simplifies the process of making the pattern the photoresist coating. The downside is that manufacturer's equipment usually

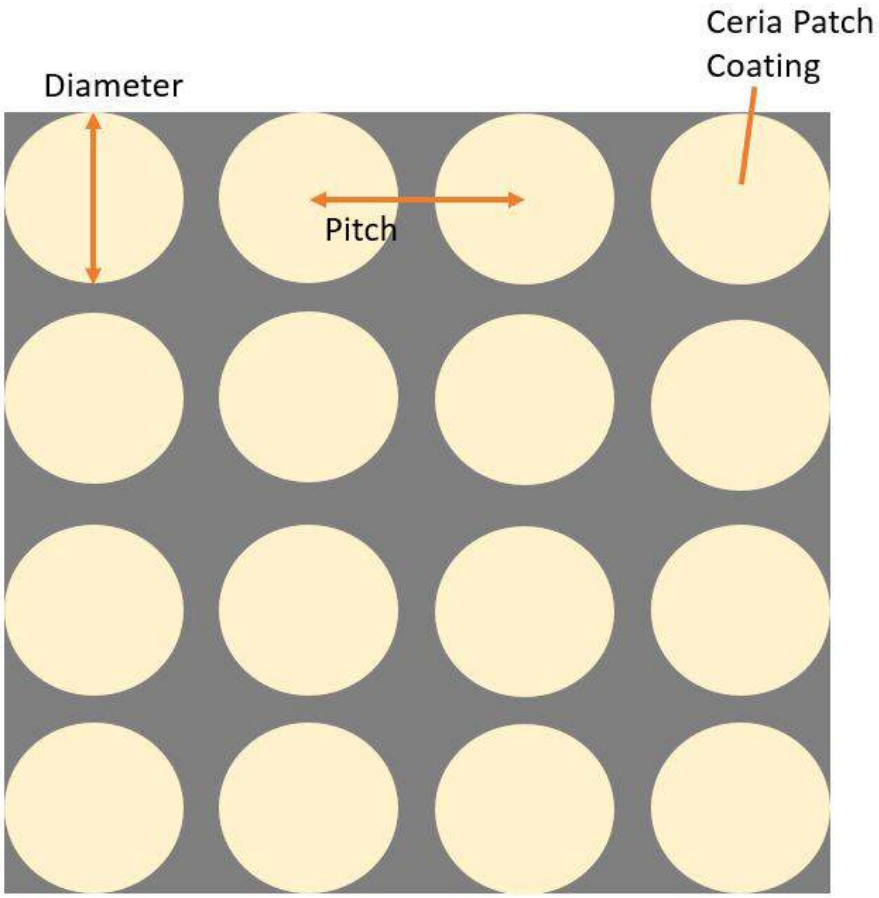


Figure 6-22: Illustration of a grid of ceria patch coating. Subcooled boiling bubbles are expected to appear on top of these ceria patches labeled with a beige color.

cannot make patch size smaller than around 25 microns. Using complete photoresist mask also means that only one type of pattern can be done per sample. This waste number of samples and lead to less effective comparison.

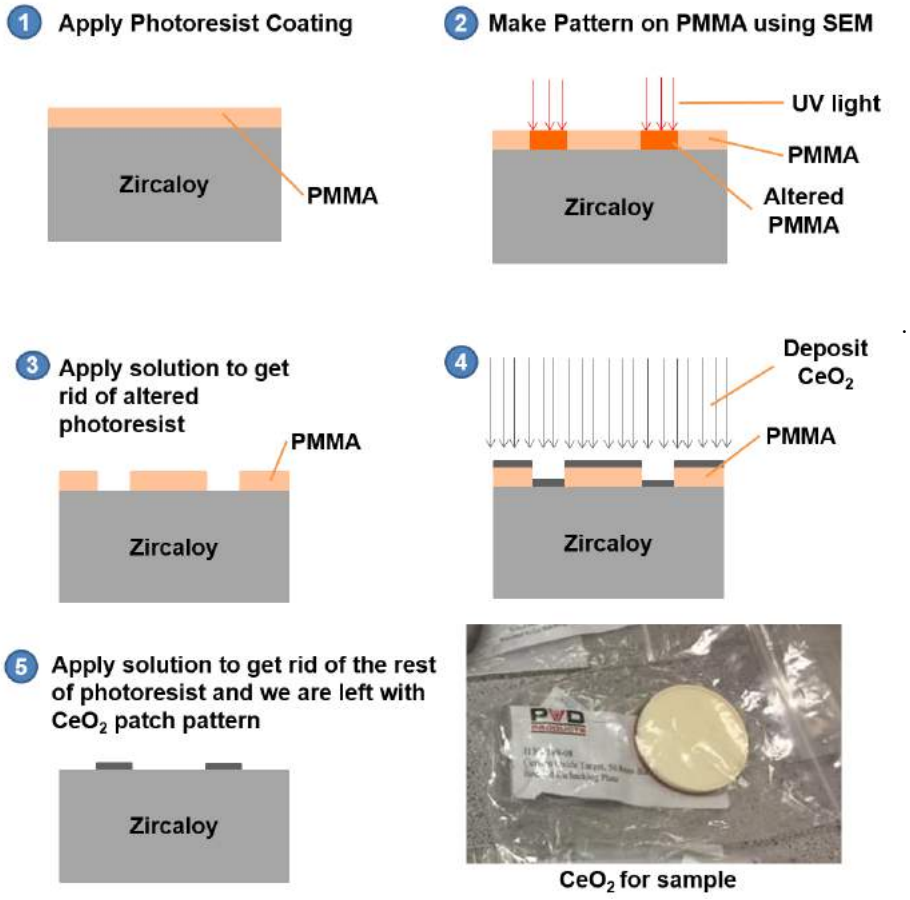


Figure 6-23: These two figures show the procedure for using photolithography to create a biphilic surface.

### 6.5.5 Low Surface Energy Material

Although the issue of van der Waals forces and hydrophobic/biphilic coatings were presented as two separate types of material, they are largely intertwined. Van der Waals force is one of the contributing force affecting the surface energy. A material with low surface energy will exhibit hydrophobic property. Our experimental results indicate that London-van der Waals force may be the major contributor in the crud-coating stickiness. This will also imply that it is the major contributor in the surface energy of coatings. So ultimately, it should be possible to have an ideal material with very low surface energy that will exhibit the prevention of adsorption, the superhydrophobicity property, and additionally, the self-cleaning property. Surface energy, by definition, is the energy associated with the intermolecular forces at the interface between two materials. It determines the attraction

and repulsion force that a material surface exert on another material. Measurement of contact angle is one way that is used to calculate surface energy using approaches such as Oss-Good-Chaudhury [236].

#### 6.5.5.1 Self-cleaning

If instead of using normal hydrophobic surface, we use superhydrophobic surface with a contact angle of 150 or more, we will also get the benefit of self-cleaning surface capability. The best natural example of the self-cleaning effect is on lotus leaves. Lotus leaves are superhydrophobic due to its low surface energy material as well as its roughness. Self-cleaning effect of lotus leaves or any other superhydrophobic surfaces works when water droplet rolls across them. Because of the extremely low surface energy, any contaminants are attracted to water drop instead of the solid surface. So as water drop rolls across the surface, it picks up all the contaminants. In sub-cooled boiling surface, the similar effect can happen. As vapor bubbles expand, crud particles get attracted to the water instead of the surface and get cleaned from superhydrophobic cladding coating.

Figure 6-24 shows how self-cleaning might work on sub-cooled boiling on cladding surface. When sub-cooled boiling bubble expands, its three-phase contact line moves along the surface. When the three-phase contact line reaches a crud particle sitting on the superhydrophobic surface, crud particle will either get stuck to the solid surface or gets attracted to water molecules. In the case of a superhydrophobic surface, the surface energy is so low that crud particle will be more attracted to water molecules. Therefore, as three-phase contact line moves along the surface with crud particles, it will lift up all the crud particles releasing them back into the water. Because of this, sub-cooled boiling bubbles will help clean the cladding surface of crud instead of causing crud build-up.

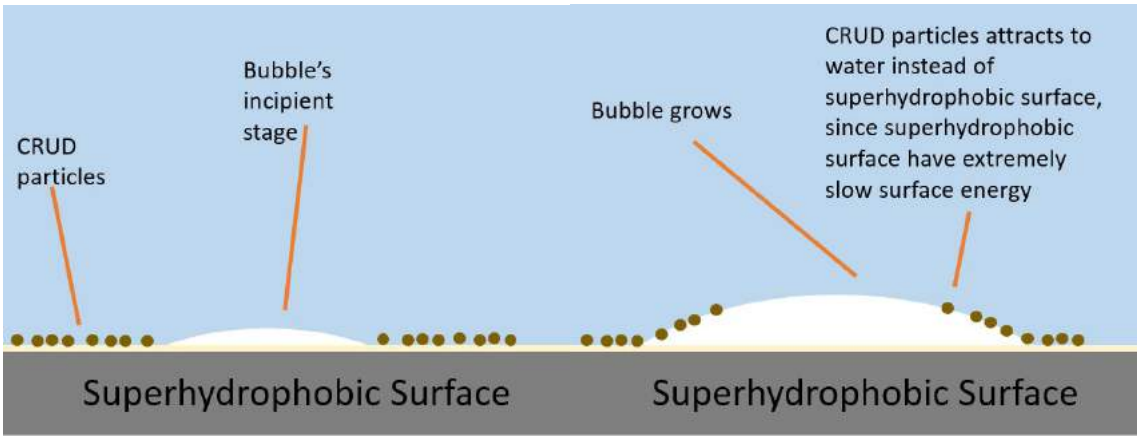


Figure 6-24: Illustration of how self-cleaning effect might work on sub-cooled boiling on superhydrophobic surface.

#### 6.5.5.2 Combination with Biphilic

If the ideal superhydrophobic material as explained above exist that can be used in a reactor, it will add a new problem with DNB which was discussed in hydrophobic material section. Again, this issue can be prevented by using the biphilic surface as explained in biphilic material section. So Ideally, if biphilic coating with superhydrophobic patches can be made, it might be possible to have an advanced fuel coating that can prevent crud and at the same time increase heat transfer.

#### 6.5.5.3 Limitations

There are many limitations to current experiment in terms of the materials we can choose as mentioned above. Unfortunately, most of the current superhydrophobic coatings rely on surface patterning or use of nanocoatings that disintegrate at high temperature or harsh abrasive condition, typical of a nuclear reactor. Most of the current superhydrophobic surface also have severe issues with decay in its property after an amount of time has passed. However, if these limitations change in the future, it may be worth revisiting these ideas.

# Chapter 7

# CONCLUSION

The crud formation on nuclear reactor fuel rods remains a significant problem to the worldwide fleet of light water reactors. The concerns for crud growth and effects had always prompted the nuclear reactor operators to increase operational margins to counter uncertainties associated with crud. If these margins can be reduced in some way, reactors around the world can potentially operate more efficiently. To study crud experimentally, the IHTFP was designed and built for this thesis' work. The IHTFP is capable of growing crud at PWR thermal-hydraulic and chemical conditions. All experimental crud samples analyzed for this thesis come from the IHTFP with the exception of crud flakes from the Westinghouse's WALT loop.

This study tackles the crud problem with two different approaches. The first approach is to prevent or mitigate crud formation through the use of fuel-rod coatings. In this approach, we tested different cladding coating materials to determine if any of them can prevent crud particles from sticking on to them. Moreover, we hope to examine the relationship between crud area coverages and different material properties. If crud-resistant fuel-rod coating material can be found in the future, these coatings can be applied to new fuel assemblies that can be deployed to existing reactors without any costly upgrades. Eliminating the crud formation will lead to reduced operating margins and more effective nuclear reactors. The current progress of fuel-rod coating material study advanced by this thesis is summarized in section 7.1.2.

In the case crud cannot be prevented, the second approach attempts to characterize crud in more detail. Having a better understanding of crud will allow better prediction of crud behaviors and therefore reduces overly conservative assumptions made to evaluate the impact of crud growth on reactor operation. Again, this will culminate in reduced operating margins and more effective nuclear reactors. The specific approach used in this thesis to characterize crud is the fractal analysis. The fractal analysis may potentially provide a simple and effective way of predicting crud behaviors at macro-scale with micro-scale fractal properties. The summary of crud fractal analysis study is

provided in section 7.1.1. In addition to the summary of findings, major contributions are listed in section 7.2, and recommendations for future works are listed in section 7.3.

## 7.1 Summary of Findings

The summary of key findings are separated into two areas: the fractal analysis and the crud-resistant fuel-rod coating.

### 7.1.1 Fractal Analysis

The four key findings for the fractal analysis study are described in the following subsections.

#### 7.1.1.1 $R^2$ Values Close to One in the Box-counting Method Indicates that Crud is Fractalline

The goal of fractal analysis work is to find a simple and effective way to characterize the macro-scale behavior of crud with its micro-scale properties. Our group sees fractal properties as great micro-scale property candidates. However, prior to this study, the usage of fractal properties in our group's crud model was based solely on theoretical assumptions. This experimental study found $R^2$ values to be very close to one when applying the box-counting method to crud, which is an important evidence to support the usage of fractal analysis on crud.

#### 7.1.1.2 Crud Porosity vs. Height from Cladding Relationship

The cross-section SEM images of crud were taken from holes carved by the focused ion beam (FIB). These cross-section images were used to plot crud porosity vs. height from cladding surface. The result was a downward sloping logarithmic relationship. This could be because, in thicker crud, boiling could potentially happen within crud as oppose to the surface of crud. If boiling occurs on top of crud, it could potentially speed up crud growth as well as generate porous crud since crud particles are more likely to attach to the crud layer surface despite having less contact. This means that as crud grows thicker and more boiling starts to happen inside the crud layer, newer crud top layer will become less porous.

#### 7.1.1.3 Crud Fractal Dimension vs. Height from Cladding Relationship

Similar to crud porosity vs. height from cladding relationship, fractal dimension vs. height from cladding relationship was also plotted. The result was also a downward sloping logarithmic relationship. Crud fractal dimension relates to crud porosity through the strong logarithmic relationship described in subsection 7.1.1.4 below. Crud fractal dimension vs. height from cladding relationship

is probably a combination of the porosity vs. height from cladding and the porosity vs. height from cladding relationships.

#### 7.1.1.4 Crud Porosity vs. Fractal Dimension Relationship

A strong logarithmic relationship trend between fractal dimension and porosity, with $R^2$ value of only 0.9925, was found. This relationship applies to both our crud samples and Westinghouse's crud sample, even though the two experimental setups used different crud precursors and heat flux. This finding indicates that crud fractal dimension is dependent only on crud porosity. If this is the case, it will simplify our group's crud model and lead to better ways to predict crud's behaviors. Application of better crud modeling will lead to less unnecessary fear of crud growth, and more efficient reactors in the future. Since this trend was only observed for three samples, further study to verify the trend with more samples could be beneficial.

#### 7.1.1.5 Fractal Result's Effect on the MAMBA-BDM Crud Model

It was found that varying porosity and fractal dimension spatially within crud according to experimental data lead to a higher peak cladding temperature and a lower effective thermal conductivity. Using the strong experimental relationship between porosity and fractal dimension, we also found that softer, more porous crud exhibits lower effective thermal conductivities and higher peak cladding temperatures.

[1]

### 7.1.2 Crud-resistant Fuel-rod Coating

The three key findings for the crud-resistant fuel-rod coating material study are described in the following subsections.

#### 7.1.2.1 Effectiveness of Crud-resistant Coating Materials

TiC and ZrN were both found to reduce crud deposition by roughly 40% with 95% confidence, compared to uncoated control surfaces. TiN reduces crud area coverage slightly at around 8% with almost 95% confidence. Six other materials tested failed to resist crud formation; MgO and $TiO_2$ appeared to encourage it.

#### 7.1.2.2 Crud Porosity vs. Fractal Dimension Relationship

It was hypothesized that if a material has a similar or lower refractive index profile when compared to water, that material would be resistant to crud formation. The closer a material's index of refraction

[1] Miaomiao Jin helped us run MAMBA-BDM Crud Model [44].

spectra is to that of water, the more likely that material will be resistant to crud formation. This hypothesis was supported by the IHTFP experimental data. A lower index of refraction of a material, especially in the UV region, correlates with higher crud resistance for the coating materials tested in this work.

#### 7.1.2.3 Crud Area Coverage Reduction vs. AFM Adhesion

It was found that crud area coverage reduction increases as the $Fe_3O_4$ AFM adhesion decreases. On the other hand, we cannot see any significant correlation between the $NiO$ AFM adhesion and the crud reduction. However, the $TiC$ which is the material that we found to have the most crud reduction also have the lowest $NiO$ AFM adhesion for the and the second lowest $Fe_3O_4$ AFM adhesion. It is important to note that AFM adhesion experiment was conducted at room temperature, and therefore, may not accurately represent the actual adhesion at PWR conditions. In the future, it is recommended to carry out a AFM measurement of adhesion values at PWR thermal-hydraulic conditions to solve this problem.

## 7.2 Major Contributions

The major contributions of this study include:

1. The design and construction of the IHTFP:
   (a) The first loop at the nuclear science and engineering department (NSE) of MIT that is capable of simulating the PWR thermal-hydraulic and chemical conditions.
   (b) One of the few experimental loops in the world capable of growing crud at PWR conditions.
   (c) The first loop at PWR condition to feature sapphire windows as large as 2 cm. In the future experiments where these windows are fully functioning, these windows will allow the use of insitu Raman spectroscopy, as well as the use of laser triangulation to measure the crud thickness.
2. The development of an image processing code capable of calculating the crud porosity and fractal dimensions, as well as their relevant statistics, from SEM images of crud. This custom-made code enables the analysis of the 420 SEM images that were used in the final results presented in this thesis.
3. Fractal analysis contributions:
   (a) Applied the fractal analysis on crud.

(b) The study obtained supporting evidence for the usage of fractal properties for understanding crud. This experimental study found $R^2$ values to be very close to one when applying the box-counting method to crud. This indicates that crud exhibits fractalline properties, which justifies the usage of fractal properties in modeling crud.

(c) The identification of how the crud porosity and the fractal dimension vary with the crud height position from cladding. These two relationships provide insights that enable more accurate predictions of crud behaviors.

(d) The discovery of a strong logarithmic relationship between the porosity and the fractal dimension. This strong logarithmic relationship with the $R^2$ value of only 0.9925 holds for both crud samples grown in the IHTFP and the Westinghouse's WALT loop. This suggests that the relationship may be universal.

4. Crud-resistant coatings contributions:

(a) Tested fuel-rod coatings as an approach to crud prevention and mitigation.

(b) Experimental data indicated that TiC and ZrN could potentially reduce crud area coverage by roughly 40% with 95% confidence.

(c) The discovery of a relationship between the refractive index and the crud area coverage reduction. This discovery implies that London-van der Waals dispersion force is the major contributor to the attraction between crud particles and fuel-rod claddings.

## 7.3 Recommendations for Future Work

**Recommended Future Work in Fractal Analysis**

- More thick crud samples should be obtained and analyzed to verify if the fractal relationships found will hold over many different conditions.
- If proper equipment is available, applying fractal analysis on crud from actual PWRs could provide verification and additional supporting data for the current study.

**Recommended Future Work in Crud-resistant coatings**

- Experimental measurements of the refractive indexes in the near-UV range (10 - 400 nm) for the materials tested in this thesis, as well as other similar materials. The existing data for these refractive indexes in the literature is still incomplete. The data for some materials are not available and many data sets fail to cover the near-UV range.

- AFM measurements of the adhesion values between crud particles and coating materials at PWR thermal-hydraulic conditions. In the past, AFM measurements was conducted at the room temperature and the atmospheric pressure, which may not be accurate.

- Experimental investigations into coatings with more extreme refractive index values. The materials tested in this thesis indicate that the lower refractive index values lead to less crud growth. Testing materials with very low refractive index values may provide the solution for crud prevention or mitigation.

**Recommended Future Improvements to the IHTFP**

- The experiments conducted for this thesis uses custom heating rods with heat fluxes of 206 $kW/m^2$. This is lower than the preferred design value of 600 $kW/m^2$. We settled for the lower heat flux because crud was grown regardless, and we did not to find any manufacturer that can manufacture heating rods with heat flux higher than 206 $kW/m^2$. However, CRIEPI's crud experimental information [118] given to us recently with the courtesy of Dr. Hirotaka Kawamura, demonstrated that it is possible to procure heating rods with a higher heat flux of 800 $kW/m^2$. The improvement goal for the IHTFP is to acquire and use the same type of heating rod as the one Dr. Hirotaka Kawamura used in his experiments.

- At the point of writing this thesis, experiments conducted so far did not utilize the sapphire windows. This is because sapphire windows always turn opaque from corrosion after a week of running the loop. This problem can potentially be solved using the diamond disc to shield PWR conditions water from reaching the sapphire windows. Solving this sapphire windows problem should allow in situ laser triangulation, in situ Raman spectroscopy, and in situ observation of bubbles with a microscopic camera.

# Bibliography


[1] S. Kazi, G. Duffy, and X. Chen, "Fouling and fouling mitigation on heated metal surfaces," *Desalination*, vol. 288, pp. 126 – 134, 2012.

[2] Y. Shi, J. Wang, and Z. Liu, "On-line monitoring of ash fouling and soot-blowing optimization for convective heat exchanger in coal-fired power plant boiler," *Applied Thermal Engineering*, vol. 78, pp. 39 – 50, 2015.

[3] S. Zhang, G. Shen, L. An, and G. Li, "Ash fouling monitoring based on acoustic pyrometry in boiler furnaces," *Applied Thermal Engineering*, vol. 84, pp. 74 – 81, 2015.

[4] T. C. Ho, "A study of crude oil fouling propensity," *International Journal of Heat and Mass Transfer*, vol. 95, pp. 62 – 68, 2016.

[5] H. A.-H. Ibrahim, *Fouling in Heat Exchangers*. INTECH Open Access Publisher, 2012.

[6] H. Muller-Steinhagen, M. R. Malayeri, and A. P. Watkinson, "Fouling of heat exchangers-new approaches to solve an old problem," *Heat Transfer Engineering*, vol. 26, no. 1, pp. 1–4, 2005.

[7] M. Short, D. Hussey, B. Kendrick, T. Besmann, C. Stanek, and S. Yip, "Multiphysics modeling of porous crud deposits in nuclear reactors," *Journal of Nuclear Materials*, vol. 443, no. 1-3, pp. 579 – 587, 2013.

[8] J. Deshon, "Simulated fuel crud thermal conductivity measurements under pressurized water reactor conditions," EPRI, Tech. Rep., 2011, report No. 1022896.

[9] J. G. Speight, "Chapter 1 - the concept of fouling," in *Fouling in Refineries*, J. G. Speight, Ed. Boston: Gulf Professional Publishing, 2015, pp. 1 – 30.

[10] N. Epstein, "Particulate fouling of heat transfer surfaces: Mechanisms and models," *NATO ASI Series*, vol. 145, pp. 143 – 164, 1988.

[11] J. N. Israelachvili, *Intermolecular and Surface Forces*, 3rd ed. Elsevier Science, 2011.

[12] F.-L. Wang, Y.-L. He, Z.-X. Tong, and S.-Z. Tang, "Real-time fouling characteristics of a typical heat exchanger used in the waste heat recovery systems," *International Journal of Heat and Mass Transfer*, vol. 104, pp. 774 – 786, 2017.

[13] M. G. Perez, E. Vakkilainen, and T. Hyppanen, "The contribution of differently-sized ash particles to the fouling trends of a pilot-scale coal-fired combustor with an ash deposition cfd model," *Fuel*, vol. 189, pp. 120 – 130, 2017.

[14] (2009, June) Slagging and fouling in coal-fired boilers. Website. IEA. Gemini House 10-18 Putney Hill, London SW156AA, UK. Last accessed 6 May 2017. [Online]. Available: http://www.iea-coal.org/documents/82175/7154/Slagging-and-fouling-in-coal-fired-boilers

[15] A. Watkinson and D. Wilson, "Chemical reaction fouling: A review," *Experimental Thermal and Fluid Science*, vol. 14, no. 4, pp. 361 – 374, 1997.

[16] (2014) Fouling. Website. H&C Heat Transfer Solution. 799 Esser Crescent Sarnia Ontario Canada N7S 5W8. Last accessed 6 May 2017. [Online]. Available: http://www.hcheattransfer.com/fouling1.html

[17] M. M. Awad, *Fouling of Heat Transfer Surfaces, Heat Transfer - Theoretical Analysis, Experimental Investigations and Industrial Systems*, A. Belmiloudi, Ed. InTech, 2011.

[18] E. F. Somerscales, "Fundamentals of corrosion fouling," *Experimental Thermal and Fluid Science*, vol. 14, no. 4, pp. 335 – 355, 1997.

[19] M. J. J. Moghadasi, H. Müller-Steinhagen and A. Sharif, "Scale deposits in porous media and their removal by edta injection," in *ECI Symposium Series, Volume RP5: Proceedings of 7th International Conference on Heat Exchanger Fouling and Cleaning - Challenges and Opportunities*, 2007.

[20] S. F. E. Boerlage, "Scaling and particulate fouling in membrane filtration systems," Ph.D. dissertation, Wageningen University, 2001.

[21] H. Weingärtner, *Water in Ullmann's Encyclopedia of Industrial Chemistry.* Wiley VCH, Weinheim, 2006.

[22] N. Misdan, A. Ismail, and N. Hilal, "Recent advances in the development of (bio)fouling resistant thin film composite membranes for desalination," *Desalination*, vol. 380, pp. 105 – 111, 2016.

[23] L. Chambers, K. Stokes, F. Walsh, and R. Wood, "Modern approaches to marine antifouling coatings," *Surface and Coatings Technology*, vol. 201, no. 6, pp. 3642 – 3652, 2006.

[24] (2016) Biofouling. Website. International Maritime Organization. Last accessed 6 May 2017. [Online]. Available: http://www.imo.org/en/OurWork/Environment/Biofouling/Pages/default.aspx

[25] J. Taborek, T. Aoki, R. Ritter, J. Palin, and J. Knudsen, "Predictive methods for fouling behavior," *Chem. Engng Prog., 68 (1972), pp. 69-78*, vol. 68, no. 7, pp. 69–78, 1972.

[26] T. Bott, *Fouling of Heat Exchangers (Chemical Engineering Monographs)*. Elsevier Science, 1995.

[27] Fouling in a condenser of a chiller and algae in the cooling tower. Website. Merus, the water conditioner company. Last accessed 6 May 2017. [Online]. Available: http://www.merusonline.com/fouling-condenser-and-cooling-tower

[28] R. F. (2015, June) Typical causes of slagging and fouling problems in boilers. Website. Power Magazine. Last accessed 6 May 2017. [Online]. Available: http://www.powermag.com/typical-causes-of-slagging-and-fouling-problems-in-boilers/?pagenum=2

[29] J. G. Speight, "Chapter 6 - asphaltene deposition and fouling," in *Fouling in Refineries*, J. Speight, Ed. Boston: Gulf Professional Publishing, 2015, pp. 129 – 154.

[30] M. Trafczynski, M. Markowski, S. Alabrudzinski, and K. Urbaniec, "The influence of fouling on the dynamic behavior of pid-controlled heat exchangers," *Applied Thermal Engineering*, vol. 109, Part A, pp. 727 – 738, 2016.

[31] W. H. O. Institute, *Marine Fouling and Its Prevention*. George Banta Publishing Co., 1952.

[32] T. Wellock, "Crud: Another acronym bites the dust," public-blog.nrc-gateway.gov, March 2015.

[33] N. Cinosi and S. Walker, "Cfd analysis of localized crud effects on the flow of coolant in nuclear rod bundles," *Nuclear Engineering and Design*, vol. 305, pp. 28 – 38, 2016.

[34] D. H. Lister, "Corrosion products in power generating systems," in *Fouling of Heat Transfer Equipment*, 1980.

[35] J.-W. Yeon, I.-K. Choi, K.-K. Park, H.-M. Kwon, and K. Song, "Chemical analysis of fuel crud obtained from korean nuclear power plants," *Journal of Nuclear Materials*, vol. 404, no. 2, pp. 160 – 164, 2010.

[36] N. Cinosi, I. Haq, M. Bluck, and S. Walker, "The effective thermal conductivity of crud and heat transfer from crud-coated {PWR} fuel," *Nuclear Engineering and Design*, vol. 241, no. 3, pp. 792 – 798, 2011, the International Conference on Structural Mechanics in Reactor Technology (SMiRT19) Special Section.

[37] P. Cohen, "Heat and mass transfer for boiling in porous deposits with chimneys," in *AlChE Symp. Ser., 70*, 1974.

[38] J. Deshon, "Pwr axial offset anamoly (aoa) guidelines," in *EPRI, 1008102*, 2004.

[39] J. Mahlon, "The simulation and study of conditions leading to axial offset anomaly in pressurized water reactors," Master's thesis, M.Sc., Georgia Institute of Technology, USA, 2004.

[40] C. O'Brien, Z. Rak, E. Bucholz, and D. Brenner, "First principles calculations predict stable 50 nm nickel ferrite particles in pwr coolant," *Journal of Nuclear Materials*, vol. 454, no. 1-3, pp. 77 – 80, 2014.

[41] J. R. Y. Solomon, "Measurement of fuel-element crud deposits in pressurized water reactors," *Nucl. Technol.*, vol. 29, pp. 166–173, 1976.

[42] IAEA, "Review of fuel failures in water cooled reactors, iaea nuclear energy series," International Atomic Energy Agency, Tech. Rep., 2010.

[43] P. Millett, "Pwr primary water chemistry guidelines," EPRI, Tech. Rep., 1999.

[44] M. Jin and M. Short, "Multiphysics modeling of two-phase film boiling within porous corrosion deposits," *Journal of Computational Physics*, vol. 316, pp. 504 – 518, 2016.

[45] C. Coyle, J. Buongiorno, and T. Mckrell, "Synthesis of crud and its effects on pool and subcooled flow boiling," Massachusetts Institute of Technology, Tech. Rep., 2015.

[46] Ventilation ducts - roughness & surface coefficients. Website. Engineering Tool Box. Last accessed 6 May 2017. [Online]. Available: http://www.engineeringtoolbox.com/surface-roughness-ventilation-ducts-d_209.html

[47] K. Kim, E. Park, H. Kim, S. Hwang, and K. Jeon, "Assessments of crud deposition effect on flow field in converging flow hole," in *Korean Nuclear Society Autumn Meeting*, 2003.

[48] M. Williams, "Uncertainty quantification in relation to crud behaviour in a pwr," *Annals of Nuclear Energy*, vol. 59, pp. 111 – 125, 2013.

[49] D. J. Walter, B. K. Kendrick, V. Petrov, A. Manera, B. Collins, and T. Downar, "Proof-of-principle of high-fidelity coupled crud deposition and cycle depletion simulation," *Annals of Nuclear Energy*, vol. 85, pp. 1152 – 1166, 2015.

[50] (1997, December) Information notice 97-85: Effects of crud buildup and boron deposition on power distribution and shutdown margin. Website. United States Nuclear Regulatory Commission (U.S., NRC). Last accessed 6 May 2017. [Online]. Available: http://www.nrc.gov/reading-rm/doc-collections/gen-comm/info-notices/1997/in97085.html

[51] D. H. Sean Bushart, "Highlights of epri radiation exposure management program," in *International ISOE Symposium March 23-26, 2004*, 2004.

[52] M. P. Short, "Finding the cure for crud: Combined simulation & experiments at casl & mit," Website, July 2013, presentation given by Michael P. Short to CASL. [Online]. Available: http://www.casl.gov/docs/CASL-U-2015-0109-000.pdf

[53] J. Buongiorno. (2010) Pwr description. Online course. MIT. Last accessed 6 May 2017. [Online]. Available: https://ocw.mit.edu/courses/nuclear-engineering/22-06-engineering-of-nuclear-systems-fall-2010/lectures-and-readings/MIT22_06F10_lec06a.pdf

[54] N. E. Todreas and M. S. Kazimi, *Nuclear Systems Volume I: Thermal Hydraulic Fundamentals, Second Edition*. Taylor and Francis, 2011.

[55] S. Grandgeorge, C. Jallut, and B. Thonon, "Particulate fouling of corrugated plate heat exchangers. global kinetic and equilibrium studies," *Chemical Engineering Science*, vol. 53, no. 17, pp. 3050 – 3071, 1998.

[56] K. Hooman and M. Malayeri, "Metal foams as gas coolers for exhaust gas recirculation systems subjected to particulate fouling," *Energy Conversion and Management*, vol. 117, pp. 475 – 481, 2016.

[57] M. Abd-Elhady, "Fouling problems in exhaust gas recirculation coolers in the automotive industry," in *International Conference on Heat Exchanger Fouling and Cleaning*, H. Muller-Steinhagen, Ed., 2009.

[58] T. Bott, "Chapter 11 - chemical reaction fouling," in *Fouling of Heat Exchangers*, ser. Chemical Engineering Monographs, T. Bott, Ed. Amsterdam: Elsevier Science B.V., 1995, pp. 185 – 221. [Online]. Available: http://www.sciencedirect.com/science/article/pii/B9780444821867500130

[59] P. Blanpain-Avet, C. Andre, M. Khaldi, L. Bouvier, J. Petit, T. Six, R. Jeantet, T. Croguennec, and G. Delaplace, "Predicting the distribution of whey protein fouling in a plate heat exchanger using the kinetic parameters of the thermal denaturation reaction of beta-lactoglobulin and the bulk temperature profiles," *Journal of Dairy Science*, vol. 99, no. 12, pp. 9611 – 9630, 2016.

[60] C. Boxler, W. Augustin, and S. Scholl, "Composition of milk fouling deposits in a plate heat exchanger under pulsed flow conditions," *Journal of Food Engineering*, vol. 121, pp. 1 – 8, 2014.

[61] N. Memisi, S. V. Moracanin, M. Milijasevic, J. Babic, and D. Djukic, "Cip cleaning processes in the dairy industry," *Procedia Food Science*, vol. 5, pp. 184 – 186, 2015.

[62] (2015) Cleanflow for milk heat exchangers. Website. SmartFlow. SmartFlow BVBA Zandpoortstraat 5 2800 Mechelen Belgium. Last accessed 6 May 2017. [Online]. Available: http://www.smartflow.eu/technology-cleanflow.php

[63] Scale and corrosion in 3 independent cooling systems stopped. Website. Merus. Last accessed 6 May 2017. [Online]. Available: http://www.merusonline.com/nuplas

[64] Effluent water pipe in a refinery - scale removed. Website. Merus. Last accessed 6 May 2017. [Online]. Available: http://www.merusonline.com/effluentq8

[65] J. R. Lines, "Understanding ejector systems necessary to troubleshoot vacuum distillation," *Oil and Gas Journal*, vol. 97, no. 7, pp. 40 – 45, 1999.

[66] T. S. Rao, "Biofouling and microbial corrosion prolem in the thermo-fuild heat exchanger and cooling water system of a nuclear test reactor," *Biofouling*, vol. 25, no. 7, pp. 581 – 591, 2009.

[67] FathomShipping. (2013) Hull fouling control: The era of innovation. Website. Last accessed 6 May 2017. [Online]. Available: http://gcaptain.com/hull-fouling-control-innovation/

[68] Algae cooling tower - fouling heat exchanger. Website. Merus. Last accessed 6 May 2017. [Online]. Available: http://www.merusonline.com/algae-cooling-tower

[69] T. W. Engler. Porosity measurement. Website. New Mexico Insitute of Mining and Technology. Last accessed 6 May 2017. [Online]. Available: http://infohost.nmt.edu/~petro/faculty/Engler524/PET524-porosity-2-ppt.pdf

[70] J. Sun, X. Dong, J. Wang, D. R. Schmitt, C. Xu, and T. Mohammed, "Measurement of total porosity for gas shales by gas injection porosimetry (gip) method," *Fuel*, vol. 186, pp. 694 – 707, September 2016.

[71] (2006, January) Volume and density definitions and determination methods. Website. Azom. Last accessed 6 May 2017. [Online]. Available: http://www.azom.com/article.aspx?ArticleID=3214

[72] H. Giesche, "Mercury porosimetry: a general (practical) overview," *Particle & Particle Systems Characterization*, vol. 23, pp. 9 – 19, 2006.

[73] S. Li and W. Huai, "United formula for the friction factor in the turbulent region of pipe flow," *PLoS ONE*, vol. 11, no. 5, p. e0154408, 2016.

[74] T. R. Bott, *The Fouling of Heat Exchangers.* DSIR, Wellington, New Zealand., 1981.

[75] M. W. Hubbell, *The Fundamentals of Nuclear Power Generation: Questions & Answers*. Author House, 2011.

[76] H. K. et al., "Applicability of chemical cleaning process to steam generator secondary side," *Journal of Nuclear Science and Technology*, vol. 41, pp. 44 – 54, 2012.

[77] H. Huang, Q. Yao, H. Chen, and B. Liu, "Scale inhibitors with a hyper-branched structure: preparation, characterization and scale inhibition mechanism," *The Royal Society of Chemistry*, vol. 95, p. 2016, 2016.

[78] A. M. Pritchard, L. F. Melo, T. R. Bott, and C. A. Bernardo, "Cleaning of fouled surfaces: A discussion, in fouling science and technology," *NATO ASI Series, Series E: Applied Science 1988. p. 721-726*, vol. 145, pp. 721 – 726, 1988.

[79] W. A. Byers and J. Deshon, "Structure and chemistry of pwr crud," in *International Conference on Water Chemistry in Nuclear Reactor Systems, San Francisco*, 2004.

[80] Alloy 600 data sheet. Website. Jacquet Metal Service. Last accessed 6 May 2017. [Online]. Available: http://www.jacquet.biz/JACQUET/USA/files/JCQusa-alloy-600.pdf

[81] R. A. Castelli, *Nuclear Corrosion Modeling*. Elsevier Science, 2010.

[82] D. B. Gomez and M. Serrano, "Alloy 690 in pwr type reactors," *Nuclear Espana*, vol. 250, pp. 17 – 22, 1996.

[83] F. Carrette, M. Lafont, G. Chatainier, L. Guinard, and B. Pieraggi, "Analysis and tem examination of corrosion scales grown on alloy 690 exposed to pressurized waterat 325 c," *Surface and Interface Analysis*, vol. 55, no. 19, pp. 5384 – 5392, 2002.

[84] M. Sennour, L. Marchetti, S. Perrin, R. Molins, M. Pijolat, and O. Raquet, "Characterization of the oxide films formed at the surface of ni-base alloys in pressurized water reactors primary coolant by transmission electron microscopy," *Mater. Sci. Forum*, vol. 34, no. 1, pp. 135 – 138, 2008.

[85] J. Sawicki, "Analyses of crud deposits on fuel rods in pwrs using mössbauer spectroscopy," *Journal of Nuclear Materials*, vol. 402, no. 2-3, pp. 124 – 129, 2010.

[86] L. Marchetti, S. Perrin, Y. Wouters, and M. Pijolat, "Photoelectrochemical study of nickel base alloys oxide films formed at high temperature and high pressure water," *Electrochimica Acta, Elsevier*, 2010.

[87] (1999, October) Assessment and management of ageing of major nuclear power plant components important to safety: Pwr vessel internals. Website. Engineering

Safety Section, International Atomic Energy Agency. Wagramer Strasse 5, P.O. Box 100, A-1400 Vienna, Austria. Last accessed 6 May 2017. [Online]. Available: http://www-pub.iaea.org/MTCD/publications/PDF/te_1119_prn.pdf

[88] D. Lister, R. Davidson, and E. McAlpine, "The mechanism and kinetics of corrosion product release from stainless steel in lithiated high temperature water," *Corrosion Science*, vol. 27, no. 2, pp. 113 – 140, 1987.

[89] T. Terachi, T. Yamada, T. Miyamoto, K. Arioka, and K. Fukuya, "Corrosion behavior of stainless steels in simulated pwr primary water—effect of chromium content in alloys and dissolved hydrogen—," *Journal of Nuclear Science and Technology*, vol. 45, no. 10, pp. 975 – 984, 2008.

[90] (2015, June) 304 vs 316l vs 2205 duplex stainless steel spigots and hardware. Website. Avant-Garde Glass. 1 McIntyre St, Gordon NSW 2072. Last accessed 6 May 2017. [Online]. Available: http://www.avantgardeglass.com.au/services/frameless-pool-fencing/spigots/

[91] Y. L. Sandler, "Structure of pwr primary corrosion products," *Corrosion 35(5):205-208*, vol. 35, no. 5, pp. 205 – 208, 1979.

[92] E. Partridge and A. White, "Mechanism of formation of calcium sulfate boiler scale," *Industrial & Engineering Chemistry, 21(9): 834-838*, vol. 21, no. 9, pp. 834 – 838, 1929.

[93] L. Zou, H. Zhang, J. Gehin, and B. Kochunas, "A coupled th/neutronics/crud framework in prediction of cips phenomenon," in *INL/CON-11-23766*, 2012.

[94] L. Kabanov, "Heat and mass transfer as related to corrosion product deposition," *Energia. Nucleare Vol. 18, pp. 285-294 (1971)*, vol. 18, no. 5, pp. 285 – 294, 1971.

[95] Me 314 heat and mass transfer laboratory: Boiling heat transfer. Website. Indiana University - Purdue University Indianapolis. Last accessed 6 May 2017. [Online]. Available: http://www.engr.iupui.edu/~mrnalim/me314lab/lab09.htm

[96] G. Wang, W. A. Byers, M. Y. Young, and Z. E. Karoutas, "Westinghouse advance loop tester (walt) update," in *16th International Conference on Nuclear Engineering*, 2008.

[97] Modeling porous corrosion deposits. Website. Center for Advanced Nuclear Energy Systems (CANES). Last accessed 6 May 2017. [Online]. Available: https://canes.mit.edu/research/modeling-porous-corrosion-deposits-crud-pwrs-casl

[98] J.-W. Yeon, Y. Jung, and S.-I. Pyun, "Deposition behaviour of corrosion products on the zircaloy heat transfer surface," *Journal of Nuclear Materials*, vol. 354, no. 1-3, pp. 163 – 170, 2006.

[99] Thermal resistance circuit. Website. MIT. Last accessed 6 May 2017. [Online]. Available: http://web.mit.edu/16.unified/www/FALL/thermodynamics/notes/node118.html

[100] W. H. Tsai, "Moment-preserving thresholding: a new approach," *Computer Vision, Graphics, & Image Processing*, vol. 29, pp. 377–393, 1985.

[101] M. Sezgin and B. Sankur, "Survey over image thresholding techniques and quantitative performance evaluation," *Journal of Electronic Imaging*, vol. 13, pp. 146–165, 2004.

[102] H. Anderson. Transmission electron microscope. Website. MicroscopeMaster. Last accessed 6 May 2017. [Online]. Available: http://www.microscopemaster.com/transmission-electron-microscope.html

[103] L. Corbari and M. A. C. B. et al., "Iron oxide deposits associated with the ectosymbiotic bacteria in the hydrothermal vent shrimp rimicaris exoculata," *Biogeosciences*, vol. 5, pp. 1295 – 1310, 2008.

[104] D. E. Janney and D. L. Porter, "Characterization of phases in 'crud' from boiling-water reactors by transmission electron microscopy," *Journal of Nuclear Materials*, vol. 362, no. 1, pp. 104 – 115, 2007.

[105] What is the mossbauer effect? Website. Mossbauer Effect Data Center. Last accessed 6 May 2017. [Online]. Available: http://www.mossbauer.info/mossbauer.html

[106] M. D. Dyar. Mossbauer spectroscopy. Website. Mount Holyoke College. Last accessed 6 May 2017. [Online]. Available: http://serc.carleton.edu/research_education/geochemsheets/techniques/mossbauer.html

[107] J. Woods. (2015, July) Photoelectron instrumentation. Website. University of California Davis. Last accessed 6 May 2017. [Online]. Available: https://chem.libretexts.org/Core/Physical_and_Theoretical_Chemistry/Spectroscopy/Photoelectron_Spectroscopy/Photoelectron_Spectroscopy%3A_Application

[108] S. Ray and A. G. Shard, "Quantitative analysis of adsorbed proteins by x-ray photoelectron spectroscopy," *Anal. Chem.*, vol. 83, no. 22, pp. 8659 – 8666, 2011.

[109] R. V. Macbeth, "Boiling on surfaces overlayed with a porous deposit: heat transfer rates obtained by capillary action." Tech. Rep., 1971, report No. AEEW-R–711.

[110] Neutron cross section boron. Picture Published on Wikipedia. Wikipedia. Last accessed 6 May 2017. [Online]. Available: https://en.wikipedia.org/wiki/Neutron_capture

[111] J. Kopecky. (1997, April) Atlas of neutron capture cross sections. Website. International Nuclear Data Committee. Last accessed 6 May 2017. [Online]. Available: http://www.iaea.org/inis/collection/NCLCollectionStore/_Public/28/060/28060364.pdf

[112] J. Henshaw, J. C. McGurk, H. E. Sims, A. Tuson, S. Dickinson, and J. Deshon, "A model of chemistry and thermal hydraulics in pwr fuel crud deposits," *Journal of Nuclear Materials*, vol. 353, no. 1-2, pp. 1 – 11, 2006.

[113] A. P. Grosvenor, B. A. Kobe, and N. S. McIntyre, "Activation energies for the oxidation of iron by oxygen gas and water vapour," *Surface Science*, vol. 574, no. 2-3, pp. 317 – 321, 2005.

[114] W. Davis. (2014, June) Nuclear power uprates: What, how, when, and will there be more? Website. American Nuclear Society. Last accessed 6 May 2017. [Online]. Available: http://ansnuclearcafe.org/2014/06/26/nuclear-power-uprates-what-how-when-and-will-there-be-more/#sthash.vPkMFxZw.dpbs

[115] C. Pan, B. G. Jones, and A. J. Machiels, "Concentration levels of solutes in porous deposits with chimneys under wick boiling conditions," *Nuclear Engineering and Design*, vol. 99, pp. 317 – 327, 1987.

[116] A. J. Elliot, D. R. McCracken, G. V. Buxton, and N. D. Wood, "Estimation of rate constants for near-diffusion-controlled reactions in water at high temperatures," *J. Chem. Soc., Faraday Trans.*, vol. 86, pp. 1539–1547, 1990.

[117] D. Gaston, C. Newman, G. Hansen, and D. Lebrun-Grandie, "Moose: A parallel computational framework for coupled systems of nonlinear equations." *Nuclear*, vol. 239, no. 10, pp. 1768 – 1778, 2009.

[118] H. Kawamura, "Empirical fuel crud deposition model in simulated pwr primary water," in *20th NPC International Conference*. Material Science Research Laboratory, CRIEPI, Japan, 2016.

[119] M. T. Armand J. Panson, "Reactor coolant crud control by particulate scavenging and filtration," US Patent US4 842 812 A, 1989.

[120] B. B. Emory, "Development of magnetic filters for the primary coolant circuit of a pwr," in *Water chemistry of nuclear reactor systems 3*, 1983.

[121] M. C. Song, S. I. Kim, and K. J. Lee, "Development of moving alternating magnetic filter using permanent magnet for removal of radioactive corrosion product from nuclear power plant," *Journal of the Korean Nuclear Society*, 2002.

[122] Y. D. Lukic and J. S. Schmidt, "Fuel assemblies in a reactor core and method of designing and arranging same," US Patent 6 891 912, 2005. [Online]. Available: http://www.google.ch/patents/US6891912

[123] B. B. Mandelbrot, *The Fractal Geometry of Nature*. International Business Machines, 1983.

[124] Fractal dimension. Website. Fractal Foundation. Last accessed 6 May 2017. [Online]. Available: http://fractalfoundation.org/OFC/OFC-10-4.html

[125] J. Jiang and R. E. Plotnick, "Fractal analysis of the complexity of united states coastlines," *Mathematical Geology*, vol. 30, p. 535, 1998.

[126] D. G. Tarboton and I. R. I. Rafael L. Bras, "The fractal nature of river networks," *Water Resources Research*, vol. 24, no. 8, pp. 1317 – 1322, 1988.

[127] N. Zhihui, W. Lichun, W. Ming-hui, Y. Jing, and Z. Qiang, "The fractal dimension of river length based on the observed data," *Journal of Applied Mathematics*, vol. 2013, p. 9, 2013.

[128] P. Prusinkiewicz and M. Hammel, "A fractal model of mountains with rivers," in *Proceeding of Graphics Interface*. Department of Computer Science, University of Calgary, May 1993.

[129] J. Walker. Fractal food: Self-similarity on the supermarket shelf. Last accessed 6 May 2017. [Online]. Available: https://www.fourmilab.ch/images/Romanesco/

[130] P. S. Addison, *Fractal and Chaos: An illustrated course*. Institute of Physics Publishing, 1997.

[131] M. Frame and A. Urry, *Fractal Worlds: Grown, Built, and Imagined*. Yale Univerity Press, 2016.

[132] D. Griffon and C. A. et al. Emergence, self-organization and network efficiency in gigantic terminte-nest-networks build using simple rules. Website. Universidad Simon Bolivar. Last accessed 6 May 2017. [Online]. Available: https://arxiv.org/ftp/arxiv/papers/1506/1506.01487.pdf

[133] S.-H. Kim. (2008, February) Fractal dimensions of a green broccoli and a white cauliflower. Website. Division of Liberal Arts, Mokpo National Maritime University. Last accessed 6 May 2017. [Online]. Available: https://arxiv.org/pdf/cond-mat/0411597.pdf

[134] S. Oancea. Fractal dimension of leaves from three species of solanaceae. Website. Universitatea de Stiinte Agricole si Medicina Veterinara lasi. Last accessed 6 May 2017. [Online]. Available: http://www.revagrois.ro/PDF/2008_1_62.pdf

[135] K. M. Kolwankar and N. N. Karle, "A simple method to estimate fractal dimension of mountain surfaces," vol. 16, no. 2, pp. 26 – 30, 2014.

[136] D. P. Agoris, V. P. Charalambakos, and A. L. Kupershtokh, "An approach to fractal dimension of lightning pattern," in *International Conference on Lightning Protection*, 2002.

[137] J. Mcnally. (2010, September) Earth's most stunning natural fractal patterns. Wired. Last accessed 6 May 2017. [Online]. Available: https://www.wired.com/2010/09/fractal-patterns-in-nature/

[138] E. W. Weisstein. (2017) Koch snowflake. Website. Wolfram Web Resource. Last accessed 6 May 2017. [Online]. Available: http://mathworld.wolfram.com/KochSnowflake.html

[139] J. Rial. Nonlinear geoscience fractals. Website. University of North Carolina. Last accessed 6 May 2017. [Online]. Available: http://ems.gphys.unc.edu/nonlinear/fractals/moreexamples.html

[140] B. N. Lopes R., "Fractal and multifractal analysis: a review." *Med Image Anal*, vol. 13(4), pp. 634–49, 2009.

[141] B. Ghanbarian and H. Daigle, "Fractal dimension of soil fragment mass-size distribution: A critical analysis," *Geoderma*, vol. 245–246, pp. 98 – 103, 2015.

[142] S. D. Gryze, L. Jassogne, J. Six, H. Bossuyt, M. Wevers, and R. Merckx, "Pore structure changes during decomposition of fresh residue: X-ray tomography analyses," *Geoderma*, vol. 134, no. 1-2, pp. 82 – 96, 2006.

[143] R. L. Devaney, "The fractal geometry of the mandelbrot set. ii: How to add and how to count," *Fractals 3*, vol. No. 4, pp. 629–640, 1995.

[144] M. I. Philipp and M. Khokha, *Fractal Geometry in Biological Systems: An Analytical Approaches*. CRC Press, 1996.

[145] R. Pitchumani and B. Ramakrishnan, "A fractal geometry model for evaluating permeabilities of porous preforms used in liquid composite molding," *International Journal of Heat and Mass Transfer*, vol. 42, no. 12, pp. 2219 – 2232, 1999.

[146] (2014, March) Fractional brownian motion. Website. Quant Education. Last accessed 6 May 2017. [Online]. Available: https://www.youtube.com/watch?v=w0uMT160wM0&index=10&list=PLRj8HuwfWZEsXW2pzAwAWYC8EZbD2ieOq

[147] A. Pentland, "Fractal-based description of natural scenes," *IEEE Transactions on Pattern Analysis and Machine Intelligence*, vol. PAMI-6, no. 6, pp. 661 – 674, 1984.

[148] A. V. Put, A. Vertes, D. Wegrzynek, B. Treiger, and R. V. Grieken, "Quantitative characterization of individual particle surfaces by fractal analysis of scanning electron microscope images," *Fresenius J Anal Chem*, vol. 350, no. 7, pp. 440 – 447, 1994.

[149] Fractal dimension of coastlines. Website. Fractal Foundation. Last accessed 6 May 2017. [Online]. Available: http://fractalfoundation.org/OFC/OFC-10-4.html

[150] S. Peleg, J. Naor, R. Hartley, and D. Avnir, "Multiple resolution texture analysis and classification," *IEEE Transactions on Pattern Analysis and Machine Intelligence*, vol. PAMI-6, no. 4, pp. 518 – 523, 1984.

[151] Y. Gong, C. Wu, J. Wang, and L. Kong, "Calculating the fractal dimension of the material fracture surface based on the triangular prism surface area method," in *International Conference on Automation, Mechanical Control and Computational Engineering (AMCCE 2015)*, 2015.

[152] N. S.-N. Lam. An evaluation of fractal surface measurement methods using icams (image characterization and modeling system). Website. Louisiana State University. Last accessed 6 May 2017. [Online]. Available: http://mapcontext.com/autocarto/proceedings/auto-carto-13/pdf/an-evaluation-of-fractal-surface-measurement-methods.pdf

[153] L. J. Quackenbush, "Calculating fractal dimension using the triangular prism method," in *ASPRS 2005 Annual Conference*, 2005.

[154] L. Huang and M. Wang, "Image thresholding by minimizing the measure of fuzziness," *Pattern Recognition*, vol. 28, no. 1, pp. 41 – 51, 1995.

[155] J. Prewitt and M. Mendelsohn, "The analysis of cell images," *Annals of the New York Academy of Sciences*, vol. 128, pp. 1035 – 1053, 1966.

[156] T. Ridler and S. Calvard, "Picture thresholding using an iterative selection method," *IEEE Transactions on Systems*, vol. 8, no. 8, pp. 630 – 632, 1978.

[157] C. Li and C. Lee, "Minimum cross entropy thresholding," *Pattern Recognition*, vol. 26, no. 4, pp. 617 – 625, 1993.

[158] J. Kapur, P. Sahoo, and A. Wong, "A new method for gray-level picture thresholding using the entropy of the histogram," *Graphical Models and Image Processing*, vol. 29, pp. 273 – 285, 1984.

[159] C. Glasbey, "An analysis of histogram-based thresholding algorithms," *CVGIP: Graphical Models and Image Processing*, vol. 55, no. 6, pp. 532 – 537, 1993.

[160] J. Kittler and J. Illingworth, "Minimum error thresholding," *Pattern Recognition*, vol. 19, no. 1, pp. 41 – 47, 1986.

[161] J. Prewitt and M. Mendelsohn, "The analysis of cell images," *Annals of the New York Academy of Sciences*, vol. 128, pp. 1035 – 1053, 1966.

[162] W. Tsai, "Moment-preserving thresholding: a new approach," *Computer Vision, Graphics, and Image Processing*, vol. 19, pp. 377 – 393, 1985.

[163] U. Gonzales-Barron and F. Butler, "A comparison of seven thresholding techniques with the k-means clustering algorithm for measurement of bread-crumb features by digital image analysis," *Journal of Food Engineering*, vol. 74, no. 2, pp. 268 – 278, 2006.

[164] N. Otsu, "A threshold selection method from gray-level histograms," *IEEE Trans. Sys., Man., Cyber.*, vol. 9, no. 1, pp. 62 – 66, 1979.

[165] W. Doyle, "Operation useful for similarity-invariant pattern recognition," *Journal of the Association for Computing Machinery*, vol. 9, no. 2, pp. 259 – 267, 1962.

[166] A. G. Shanbhag, "Utilization of information measure as a means of image thresholding," *Graph. Models Image Process*, vol. 56, no. 5, pp. 414 – 419, 1994.

[167] G. Zack and W. Rogers, "Automatic measurement of sister chromatid exchange frequency," *Histochem. Cytochem.*, vol. 25, no. 7, pp. 741 – 753, 1977.

[168] Y. J.C., C. F.J., and C. S., "A new criterion for automatic multilevel thresholding," *Journal of Electronic Imaging*, vol. 4, no. 3, pp. 370 – 378, 2002.

[169] B. Battat and D. Rose. Application of fractals to materials science. Website. Department of Defense. AMPTIAC, Rome, NY. Last accessed 6 May 2017. [Online]. Available: http://citeseerx.ist.psu.edu/viewdoc/download?doi=10.1.1.384.1715&rep=rep1&type=pdf

[170] A. L. Barabasi and H. E. Stanley, *Fractal Concept in Surface Growth.* Cambridge, 1995.

[171] W. contributors. (2016, Jul.) Box counting. Pictures Published on Wikipedia. Wikipedia, The Free Encyclopedia. Last accessed 6 May 2017. [Online]. Available: https://en.wikipedia.org/w/index.php?title=Box_counting&oldid=728066885

[172] A. L. Karperien, H. F. Jelinek, and N. Milosevic, "Lacunarity analysis and classification of microglia in neuroscience," in *European Conference on Mathematical and Theoretical Biology*, 2011.

[173] J. Ibanez, R. Perez-Gomez, and F. S. J. Martinez, "The spatial distribution of soils across europe: A fractal approach," *Ecological Complexity*, vol. 6, no. 3, pp. 294 – 301, 2009, special Section: Fractal Modeling and Scaling in Natural Systems.

[174] K. M. Bialowiec A, Randerson PF, "Using fractal geometry to determine phytotoxicity of landfill leachate on willow." *Chemosphere*, vol. 79, no. 5, pp. 534–540, 2010.

[175] H. Hamaker, "The london-van der waals attraction between spherical particles," *Physica*, vol. 4, no. 10, pp. 1058 – 1072, 1937.

[176] R. S. Tanaka, "Quantifying the adhesion of noble metal foulants on structural materials in a molten salt reactor," Master's thesis, MIT, 2017.

[177] L. Bergström, "Hamaker constants of inorganic materials," *Advances in Colloid and Interface Science*, vol. 70, pp. 125 – 169, 1997.

[178] R. H. French, H. Mullejans, and et. al, "Dispersion forces and hamaker constants for intergranular ffilm in silicon nitride from spspatial resolved-valence electron energy loss spectrum imaging," *Acta Metallurgica*, vol. 46, no. 7, pp. 2271 – 2287, 1998.

[179] H. D. Ackler, R. H. French, and Y.-M. Chiang, "Comparisons of hamaker constants for ceramic systems with intervening vacuum or water: From force laws and physical properties," *Journal of Colloid and Interface Science*, vol. 179, no. 2, pp. 460 – 469, 1996.

[180] A. A. Andreev, *An Introduction to Hot Laser Plasma Physics.* Nova Science Publishers, 2000.

[181] G. Lefevre and A. Jolivet, "Calculation of hamaker constants applied to the deposition of metal oxide particles at high temperature," in *International Conference on Heat Exchanger Fouling and Cleaning*, 2009.

[182] J. R. DeVore, "Refractive indices of rutile and sphalerite," *Journal of the Optical Society of America*, vol. 41, no. 6, pp. 416–419, 1951.

[183] H. R. Philipp, "Optical properties of silicon nitride," *J. Electrochim. Soc.*, vol. 120, pp. 295–300, 1973.

[184] L. Zhao and P. Choi, "2 - molecular modelling of polymer surfaces and interfaces," in *Molecular Interfacial Phenomena of Polymers and Biopolymers*, ser. Woodhead Publishing Series in Biomaterials, P. Chen, Ed. Woodhead Publishing, 2005, pp. 48 – 71.

[185] V. A. Parsegian, *Van der Waals Forces: A Handbook for Biologists, Chemists, Engineers, and Physicists.* Cambridge University Press, 2005.

[186] The dielectric constant and the refractive index. Website. University of Cambridge. Last accessed 6 May 2017. [Online]. Available: https://www.doitpoms.ac.uk/tlplib/dielectrics/dielectric_refractive_index.php

[187] H. Fox and W. Zisman, "The spreading of liquids on low energy surfaces. i. polytetrafluoroethylene," *Journal of Colloid Science*, vol. 5, no. 6, pp. 514 – 531, 1950.

[188] M. K. Bernett and W. Zisman, "Effect of adsorbed water on the critical surface tension of wetting on metal surfaces," *Journal of Colloid and Interface Science*, vol. 28, no. 2, pp. 243 – 249, 1968.

[189] J. L. Gardon, "Relationship between cohesive energy densities of ppolymer and zisman's critical surface," *J. Phys. Chem*, vol. 67, no. 9, pp. 1935 – 1936, 1963.

[190] A. Agrawal. (2005) Surface tension of polymers. Website. MIT. Last accessed 6 May 2017. [Online]. Available: http://web.mit.edu/nnf/education/wettability/summerreading-2005short.pdf

[191] A. Rothen, "The ellipsometer, an apparatus to measure thickness of thin surface films," *Review of Scientific In*, vol. 34, no. 5, pp. 494 – 501, 1945.

[192] Buntgarn. (2008, January) Ellipsometry. Picture Published on Wikipedia. Wikipedia. Last accessed 6 May 2017. [Online]. Available: https://en.wikipedia.org/wiki/Ellipsometry

[193] A. G. Al-Rubaye, A. Nabok, and A. Tsargorodska, "Spectroscopic ellipsometry study of gold nanostructures for {LSPR} bio-sensing applications," *Sensing and Bio-Sensing Research*, vol. 12, pp. 30 – 35, 2017.

[194] M. Stoger-Pollach. Optical properties. Website. University Service-Einrichtung. Last accessed 6 May 2017. [Online]. Available: http://www.ustem.tuwien.ac.at/service/optical_properties/EN/

[195] J. Green. (2016, January) More doom and gloom: Nuclear power industry us. Website. Wise International. Last accessed 6 May 2017. [Online]. Available: https://www.wiseinternational.org/nuclear-monitor/824/more-doom-and-gloom-nuclear-power-industry-us

[196] Pressure drop in pipes. Website. Abu Dhabi Pipe Factory. Dubai Investment Park, Jebel Ali, Dubai 120700, U.A.E. Last accessed 6 May 2017. [Online]. Available: http://www.adpf.ae/images/Page-A.pdf

[197] Steamtab. Software. ChemicaLogic Corporation. 222 Stoney Gate Carlisle, MA 01741. Last accessed 6 May 2017. [Online]. Available: www.chemicalogic.com/Pages/SteamTab.aspx

[198] Pool boiling regimes. Website. Thermal-Fluid Central. Last accessed 6 May 2017. [Online]. Available: https://www.thermalfluidscentral.org/encyclopedia/index.php/Pool_Boiling_Regimes

[199] Stainless steel high temperature properties. Website. Specialty Steel Industry of North America. 3050 K Street, N.W. Washington, DC 20007. Last accessed 6 May 2017. [Online]. Available: http://www.ssina.com/composition/temperature.html

[200] Variable area flow meters model e. Website. Kytola. Last accessed 6 May 2017. [Online]. Available: http://www.kytola.com/us/products/flow-meters/variable-area-flow-meters/model-e

[201] R3a series externally adjustable relief valves maintenance instructions. Website. Swagelok. Last accessed 25 May 2017. [Online]. Available: https://www.swagelok.com/downloads/webcatalogs/en/MS-CRD-0013.pdf

[202] M12 thermocouple sensors for spring loading in thermowells. Website. Omega. Last accessed 6 May 2017. [Online]. Available: http://www.omega.com/pptst/M12-TC-SL.html

[203] Lewa ecoflow diaphragm metering pump. Lewa. Last accessed 6 May 2017. [Online]. Available: http://www.lewa.com/en/pumps/metering-pumps/lewa-ecoflow-diaphragm-metering-pump/

[204] Pad - heavy-duty industrial differential pressure transmitter. Website. Kobold. 1801 Parkway View Drive Pittsburgh PA, 15205. Last accessed 6 May 2017. [Online]. Available: http://koboldusa.com/products/pressure-transmitters/pad-heavy-duty-industrial-differential-pressure-transmitter

[205] *Severe Service Control Valve Type 1711*, Badger Meter, 2013. [Online]. Available: https://www.badgermeter.com/business-lines/flow-instrumentation/severe-service-type-1711/

[206] *MagnePump Recirculation MagnePumps*, Autoclave Engineers Operation, 8325 Hessinger Drive Erie, PA 16509-4679, 2016, last accessed 25 May 2017. [Online]. Available: http://www.autoclaveengineers.com/ae_pdfs/MP_ParkerAE_MagnePumps_06_0058SE.pdf

[207] *Relief Valve*, Autoclave Engineers Operation, 8325 Hessinger Drive Erie, Pennsylvania 16509-4679 USA, 2013, last accessed 25 May 2017. [Online]. Available: http://www.autoclave.com/products/relief_valves/rvp_series/

[208] *General Purpose pressure Switches in NEMA 4X (IP66) enclosures*, Omega, 800 Connecticut Ave. Suite 5N01 Norwalk, CT 06854, last accessed 25 May 2017. [Online]. Available: http://www.omega.com/pptst/PSW-100.html

[209] Smart sensors. Website. Thornton. Last accessed 6 May 2017. [Online]. Available: http://50.244.15.10/techlib/Thornton/DS_Smart_Sensor_770MAX_EN_Jul2012.pdf

[210] Flr 1000/1000br/1000st series user's guide. Website. Omega. 800 Connecticut Ave. Suite 5N01 Norwalk, CT 06854. Last accessed 6 May 2017. [Online]. Available: https://www.omega.com/manuals/manualpdf/M4574.pdf

[211] (2011, February) Electric actuators. Website. Swagelok. Last accessed 6 May 2017. [Online]. Available: https://www.swagelok.com/downloads/WebCatalogs/EN/MS-01-35-E.pdf

[212] Model a-10 pressure transmitter operating instructions. Website. WIKA Instrument, LP. 1000 Wiegand Boulevard Lawrenceville, GA 30043 USA. Last accessed 6 May 2017. [Online]. Available: http://www.wika.us/upload/OI_A_10_en_de_fr_es_6240.pdf

[213] U. of Cambridge. Back pressure regulator. Website. University of Cambridge. Last accessed 6 May 2017. [Online]. Available: http://www.phy.cam.ac.uk/internal_resources/hands/hazards/gases2

[214] *TLF Sample Cooler*, Sentry Equipment, 856 E. Armour Rd. PO Box 127 Oconomowoc, WI 53066 USA, last accessed 25 May 2017. [Online]. Available: http://sentry-equip.com/Public/BrochuresandDataShee/Sample-Cooler-TLR.pdf

[215] D. D. Kopeliovich. Electropolishing. Picture Published on Website. SubsTech. Last accessed 6 May 2017. [Online]. Available: http://www.substech.com/dokuwiki/doku.php?id=electropolishing

[216] E. Chen. (2004) Thin film deposition. Website. Harvard. Last accessed 6 May 2017. [Online]. Available: http://www.mrsec.harvard.edu/education/ap298r2004/Erli%20chenFabrication%20II%20-%20Deposition-1.pdf

[217] E. R. Davies, *Machine Vision: Theory, Algorithms, Practicalities*. Elsevier, 2014.

[218] A. Dathe and M. Thullner, "The relationship between fractal properties of solid matrix and pore space in porous media," *Geoderma*, vol. 129, no. 3-4, pp. 279 – 290, 2005.

[219] R. H. French, R. M. Cannon, L. K. DeNoyer, and Y.-M. Chiang, "Full spectral calculation of non-retarded hamaker constants for ceramic systems from interband transition strengths," *Solid State Ionics*, vol. 75, pp. 13 – 33, 1995.

[220] J. N. Israelachvili, in *Intermolecular and Surface Forces*, 3rd ed., J. N. Israelachvili, Ed. San Diego: Academic Press, 2011, ch. 11, pp. 261, 263, 275.

[221] J. Visser, "On hamaker constants: A comparison between hamaker constants and lifshitz-van der waals constants," *Adv. Colloid Interface Sci.*, vol. 3, no. 4, pp. 331–363, 1972.

[222] L. Bergström, "Hamaker constants of inorganic materials," *Adv. Colloid Interface Sci.*, vol. 70, pp. 125 – 169, 1997.

[223] I. H. Malitson and M. J. Dodge, "Refractive index and birefringence of synthetic sapphire," *J. Opt. Soc. Am.*, vol. 62, p. 1405, 1972.

[224] M. Daimon and A. Masumura, "Measurement of the refractive index of distilled water from the near-infrared region to the ultraviolet region," *Appl. Opt.*, vol. 46, no. 18, pp. 3811–3820, 2007.

[225] R. E. Stephens and I. H. M., "Index of refraction of magnesium oxide," *J. Res. Nat. Bureau Standards*, vol. 49, no. 4, pp. 249–252, 1952.

[226] J. Pflüger, J. Fink, W. Weber, K. P. Bohnen, and G. Crecelius, "Dielectric properties of $tic_x$, $tin_x$, $vc_x$, and $vn_x$ from 1.5 to 40 ev determined by electron-energy-loss spectroscopy," *Phys. Rev. B*, vol. 30, pp. 1155–1163, 1984.

[227] T. Siefke, S. Kroker, K. Pfeiffer, O. Puffky, K. Dietrich, D. Franta, I. Ohlídal, A. Szeghalmi, E.-B. Kley, and A. Tünnermann, "Materials pushing the application limits of wire grid polarizers further into the deep ultraviolet spectral range," *Adv. Opt. Mater.*, vol. 4, pp. 1780–1786, 2016.

[228] N. M. Balzaretti and J. A. H. da Jornada, "Pressure dependence of the refractive index of monoclinic and yttria-stabilized cubic zirconia," *Phys. Rev. B*, vol. 52, pp. 9266–9269, 1995.

[229] M. K. Yang, R. H. French, and E. W. Tokarsky, "Optical properties of teflon af amorphous fluoropolymers," *J. Micro/Nanolith.*, vol. 7, no. 33, p. 033010, 2008.

[230] Y. Yuan and T. R. Lee, "Contact angle and wetting properties," *Springer Series in Surface Sciences*, vol. 51, pp. 3 – 34, 2013.

[231] S. Kim, H. Kim, H. Kim, H. Ahn, H. Jo, J. Kim, and M. Kim, "Effects of nano-fluid and surfaces with nano structure on the increase of chf," *Experimental thermal and fluid science*, vol. 34, no. 4, pp. 487 – 495, 2010.

[232] G. Azimi, R. Dhiman, H.-M. Kwon, A. T. Paxson, and K. K. Varanasi, "Hydrophobicity of rare-earth oxide ceramics," *Nature Materials*, vol. 12, p. 315–320, January 2013.

[233] M. Sarmadivaleh, A. Z. Al-Yaseri, and S. Iglauer, "Influence of temperature and pressure on quartz–water–co2 contact angle and co2–water interfacial tension," *Journal of Colloid and Interface Science*, vol. 441, pp. 59 – 64, 2015.

[234] A. R. Betz, J. Jenkins, and D. Attinger, "Boiling heat transfer on superhydrophilic, superhydrophobic, and superbiphilic surfaces," *International Journal of Heat and Mass Transfer*, vol. 57, no. 2, pp. 733 – 741, February 2013.

[235] O. Zeitoun and M. Shoukri, "Bubble behavior and mean diameter in subcooled flow boiling," *J. Heat Transfer*, vol. 118, no. 1, pp. 110–116, February 1996.

[236] P. C. Rieke, "Application of van oss-chaudhury-good theory of wettability to interpretation of interfacial free energies of heterogeneous nucleation," *Journal of Crystal Growth*, vol. 182, no. 3, pp. 472 – 484, 1997.